Enhanced Oil Recovery in Shale and Tight Reservoirs

James J. Sheng

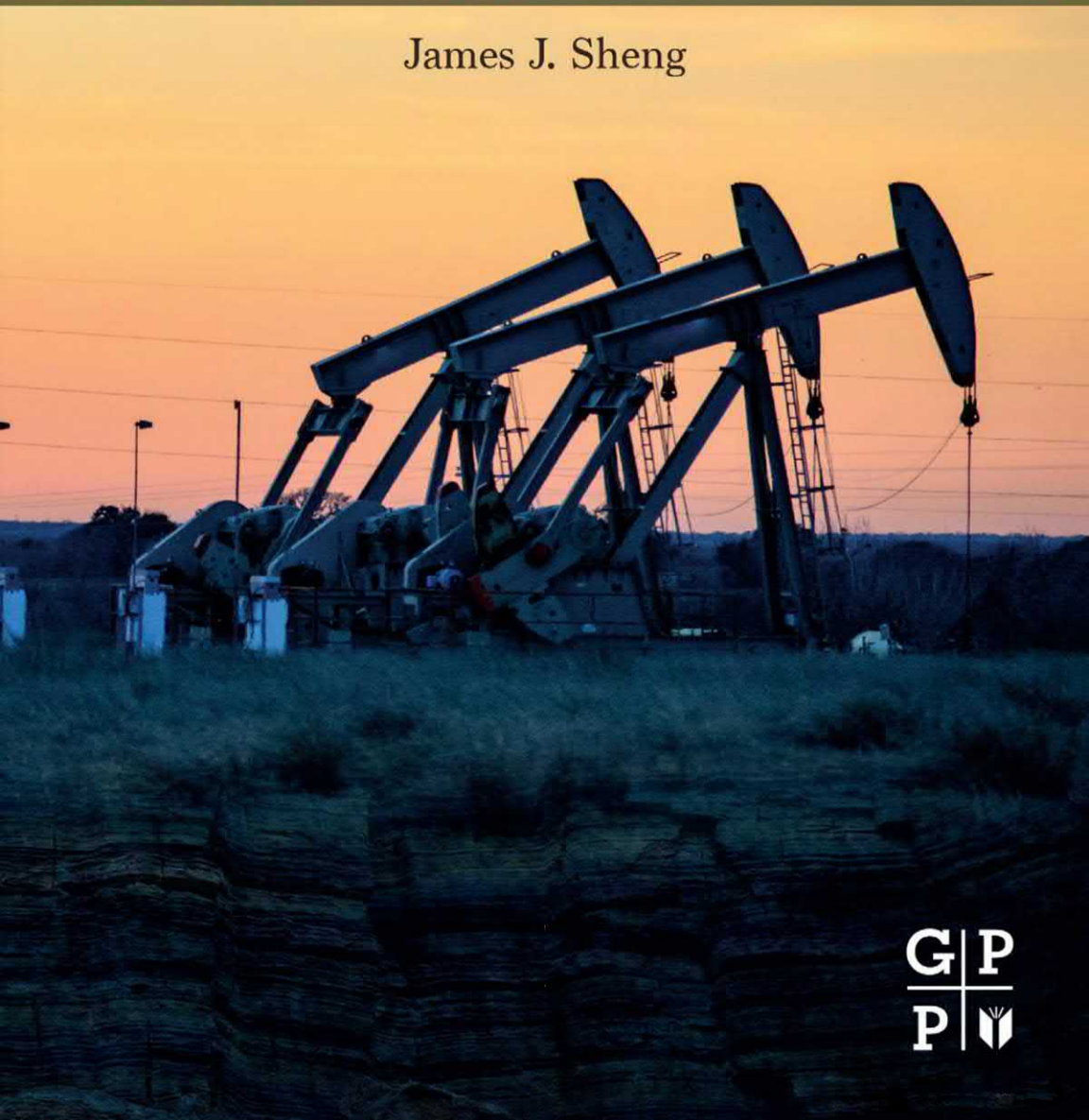

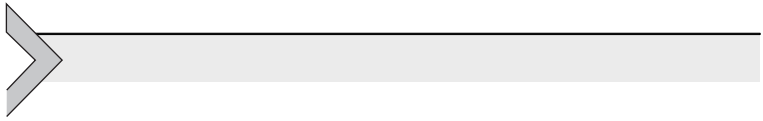

ENHANCED OIL RECOVERY IN SHALE AND TIGHT RESERVOIRS

JAMES J. SHENG

Gulf Professional Publishing
An imprint of Elsevier

Gulf Professional Publishing is an imprint of Elsevier
50 Hampshire Street, 5th Floor, Cambridge, MA 02139, United States
The Boulevard, Langford Lane, Kidlington, Oxford, OX5 1GB, United Kingdom

Notices
Knowledge and best practice in this field are constantly changing. As new research and experience broaden our understanding, changes in research methods, professional practices, or medical treatment may become necessary.

Practitioners and researchers must always rely on their own experience and knowledge in evaluating and using any information, methods, compounds, or experiments described herein. In using such information or methods they should be mindful of their own safety and the safety of others, including parties for whom they have a professional responsibility.

To the fullest extent of the law, neither the Publisher nor the authors, contributors, or editors, assume any liability for any injury and/or damage to persons or property as a matter of products liability, negligence or otherwise, or from any use or operation of any methods, products, instructions, or ideas contained in the material herein.

Library of Congress Cataloging-in-Publication Data
A catalog record for this book is available from the Library of Congress

British Library Cataloguing-in-Publication Data
A catalogue record for this book is available from the British Library

ISBN: 978-0-12-815905-7

For information on all Gulf Professional Publishing publications visit our website at https://www.elsevier.com/books-and-journals

Publisher: Joe Hayton
Senior Acquisition Editor: Katie Hammon
Editorial Project Manager: Aleksandra Packowska
Production Project Manager: Selvaraj Raviraj
Cover Designer: Mark Rogers

Typeset by TNQ Technologies

Acknowledgments

This book summarizes some of my research results about shale EOR technologies in the past decade. Some of the dissertation or research work from my ex-PhD students, ex-postdoctoral students, and current PhD students is used and cited to support my views in this book. They are Yang Yu, Lei Li, Ziqi Shen, Siyuan Huang, Yao Zhang, Sharanya Sharma, Xingbang Meng, Nur Wijaya, Srikanth Tangirala, Tao Wan, Samiha Morsy, Shifeng Zhang, Hu Jia, Junrong Liu, Talal Daou Gamadi, and Jiawei Tu. Some of the work published by other authors is cited. Their work is sincerely acknowledged.

I have devoted much of my time to my career development. I owe much to my wife Ying Zhang, my daughters Emily and Selena, and my parents Jifa Sheng and Shouying Liu. If my life could be rechosen, I would have reallocated my time to them.

Some of the research work was supported by the US department of Energy under Award Number DE-FE0024311, Apache Corporation, and ConocoPhillips.

CHAPTER ONE

Introduction to shale and tight reservoirs

Abstract

Preliminary definitions of shale and tight reservoirs are proposed after the definitions of shale and tight reservoirs in the literature are summarized and discussed. There are no widely agreed definitions of shale and tight formations. The definitions of shale oil and oil shale are differentiated; the former is the oil that exists in shale, whereas the latter is the rock that contains organic hydrocarbon materials. Shale and tight resources are presented. Current production technologies are briefly introduced.

Keywords: Oil shale; Shale; Shale oil; Shale resources; Tight formation.

1.1 Introduction

Oil production from shale and tight formations accounted for more than half of total U.S. oil production in 2015 (EIA, 2016). Such amount is expected to grow significantly as the active development of low permeability reservoirs continues. The current technique to produce shale oil is through primary depletion using horizontal wells with multiple transverse fractures. The oil recovery is less than 10% (Sheng, 2015d), or 3%–6% according to the EIA 2013 report (Kuuskraa, 2013). The oil recovery in tight formations is also low, e.g., 15%–25% (Kuuskraa, 2013). Clark (2009) showed that the results from several methods indicate that the most likely value for oil recovery factor in the Bakken shale is approximately 7%. The North Dakota Council website states "With today's best technology, it is predicted that 1%–2% of the reserves can be recovered." (North Dakota Council, 2012). The oil recovery factor for each of 28 US tight oil plays is below 10% (Advanced Resources International, 2013). It is certain that a large percentage of the oil remains unrecovered without enhanced oil recovery methods. There is a big prize to be claimed in terms of enhanced shale and tight oil recovery. Therefore, this book is dedicated to the enhanced oil recovery (EOR) in shale and tight reservoirs.

Enhanced Oil Recovery in Shale and Tight Reservoirs
ISBN: 978-0-12-815905-7
https://doi.org/10.1016/B978-0-12-815905-7.00001-3

In this chapter, shale and tight reservoirs are defined first. Then current production technologies are described. Detailed EOR methods are discussed in the subsequent chapters.

1.2 Definitions of shale and tight reservoirs

In this section, shale and tight reservoirs are defined. The terminologies of shale oil and oil shale are also differentiated. Different injection modes are defined.

1.2.1 Shale tight reservoir

Shale is a laminated or fissile claystone or siltstone. If claystones (or siltstones, not listed in Pettijohn, 1957) are neither fissile nor laminated but they are blocky or massive, they are termed *mudstone*. Claystone is indurated clay. A clay is a sediment with grains less than 0.002 mm (in radius or 1/256 mm in diameter (Pettijohn, 1957). A tight formation is a reservoir. One common and important characteristic about shale and tight formations is very low permeability. Tight formation oil permeability is less than 0.1 milliDarcy (mD) (air permeability is less than 1 mD) (Jia et al., 2012); and matrix shale formation permeability is in the order of nanoDarcies (nD). Zou et al. (2015) divided conventional and unconventional oil and gas reservoirs using 1 mD air permeability. Song et al. (2015) grouped shale formation, tight formations, coal-bed methane formations, and oil shale in unconventional reservoirs. Another related term is ultralow permeability formation whose permeability is 1 nD to 1 mD (Speight, 2017). In other words, ultralow permeability formations cover tight formations and shale formations. But ultralow permeability is defined 0.3−1 mD (air permeability) in China (Yang et al., 2013). Some shale formations, if not all, have small natural fractures, which can make the effective permeability higher than the order of nanoDarcies. Some key parameters about tight oil reservoirs are the porosity less than 10%, total organic carbon (TOC) higher than 1%, thermal maturity 0.6%−1.3%, and the API gravity higher than 40 (Jia et al., 2012). Based on the shale pore size distribution, the micropore is for the pore diameter $d \leq 2$ nm, mesopore 2 nm $\leq d \leq$ 50 nm, and macropore $d \geq 50$ nm (Fakcharoenphol et al., 2014). According to a DOE report, shale originated from mud deposition in low-energy environment and it primarily consists of consolidated clay-sized particles (Ground Water Protection Council and All Consulting, 2009).

The pore sizes are also used to define shale and tight formations. Zou et al. (2012) defined the pore throat diameters: shale gas 5—200 nm, tight oil limestone 40—500 nm, tight oil sandstone 50—900 nm, tight gas sandstone 40—700 nm. Some authors classified shale formations as the rocks where hydrocarbons were generated in situ (source rocks) (Aguilera, 2014), or migrated within a very short distance (Yang et al., 2015), and tight formations as the formations near source rocks (oil migrated in a short-distance) (Jia et al., 2014) or source rock-storage reservoir interbedded reservoirs (Zheng et al., 2017). Actually, a shale formation does not have to be a source rock. Strictly speaking, shale oil comes from shale formations like source rocks and mud shale rocks; tight oil comes from low-permeability sandstones, silty sands, and carbonates. However, in practice, there seems no clear or agreed difference between these two terms, and they are used synonymously. Apparently, the term *tight formation* is commonly used in China, while the term *shale formation* is commonly used in the rest of the world, especially in the United States. More discussion or review of the subject is provided by Zhou and Yang (2012).

Recently, Zhao et al. (2018) listed some differences between shale and tight formations which are summarized in Table 1.1.

Despite the above discussions about shale and tight oil reservoirs, the term *tight oil* does not have a specific technical, scientific, or geologic definition. Tight oil is an industry convention that generally refers to oil produced from very low-permeability shale, sandstone, and carbonate formations, with permeability being a measure of the ability of a fluid to flow through the rock. In limited areas of some very low-permeability formations, small volumes of oil have been produced for many decades (EIA, 2018a).

However, shale and tight formations should be defined. Table 1.2 may be used as preliminary definitions.

Table 1.1 Differences between shale and tight formations.

	Tight formation	Shale formation
Types of hydrocarbon	Converted (oil and gas) migrated from nearby source rocks	Converted (oil and gas) and unconverted organic materials
Rocks	Reservoirs (oil and gas)	Source rocks
Porosity	>6%	<3%
Permeability	<1 mD (air)	<1 nD (probably typo, should be < 1 μD)

Table 1.2 Preliminary definitions of shale and tight formations.

	Tight formation	Shale formation
Types of hydrocarbon	Converted (oil and gas) migrated from nearby source rocks	Unconverted organic materials and converted (oil and gas) and/or migrated from nearby sources, and
Rocks	Storage reservoirs	Interbedded source rocks and storage reservoirs
Matrix permeability	<0.1 mD	<1 μD

Because the same unconventional technology (horizontal well drilling and fracturing) has to be used to produce shale and tight reservoirs, it is convenient to combine the discussion of these two. Therefore, we do not differentiate the terms of shale oil and tight oil in this paper, except for some places where a differentiation is necessary. Note that sometimes shale oil includes oil from oil shale and shale formation (NPC, 2011; Jia et al., 2012). Such definition gradually loses its use because the technologies to produce oil from oil shale and shale formation are very different. Producing oil from oil shale generally uses high-temperature pyrolysis.

1.2.2 Shale oil versus oil shale

There is a huge difference between oil shale and shale oil. Oil shale is a rock that contains a solid organic compound known as kerogen—a precursor to oil. Oil shale is a misnomer because kerogen is not really a crude oil, and the rock holding the kerogen is not necessarily shale. Shale oil refers to hydrocarbons that are trapped in so tight formations that the oil and gas cannot easily flow into production wells.

To generate (before production) oil and gas synthetically from oil shale, the kerogen-rich rock is heated to a high temperature (about 950°F or 500°C) in a low oxygen environment, a process called *retorting*. There are two methods to heat the rock. One is to mine the rock and heat the rock at the ground surface. The other one is to heat the rock underground. To heat the rock underground, ExxonMobil has developed a process to create underground fractures in oil shale, to lay electrically conductive materials in the fracture, and pass electric currents through the shale to gradually convert the kerogen into liquid oil. The oil company Shell buries electric heaters underground to heat the oil shale. Compared to the technologies to produce hydrocarbon from oil shale, the current technology to produce shale oil is

much more publicly known, which is horizontal well drilling and fracturing. In the Chinese literature, there is a word "volume fracturing" if literally translated. It actually means massive fracturing which results in a large stimulated reservoir volume (SRV) (Qi, 2015).

1.2.3 Injection modes

A fluid, either water or gas, could be injected into reservoirs through a flooding mode or in a huff-n-puff (huff and puff) mode. For the flooding mode, a fluid is injected through a dedicated well and oil and gas are produced from a separate well or wells (see Fig. 1.1). For the huff-n-puff mode, after a fluid is injected through a well, in situ fluids (oil, gas and water) and a fraction of the injected fluid are produced from the same well (see Fig. 1.2). For the huff-n-puff mode, there is a period the well is shut-in in some situations. This period is called *soaking time*. The process of injecting-soaking-producing is repeated.

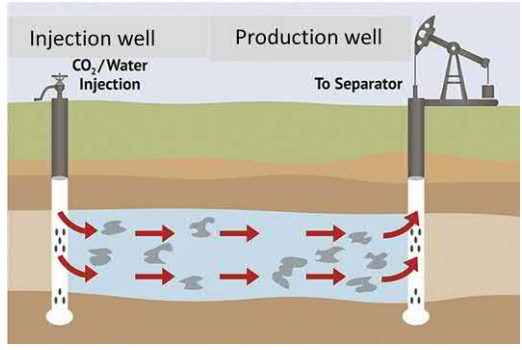

Figure 1.1 Schematic of flooding.

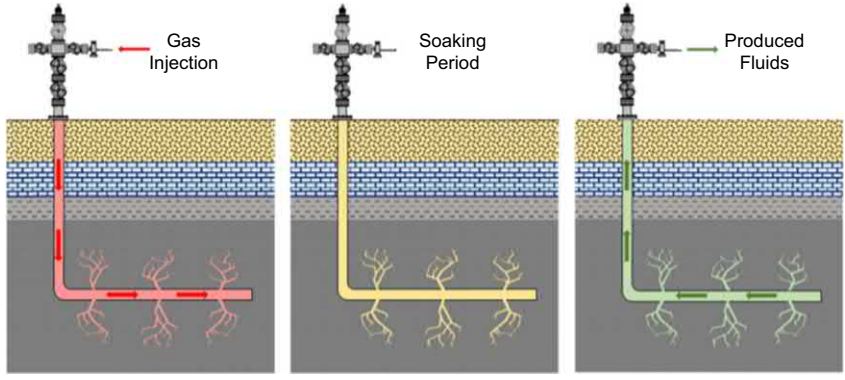

Figure 1.2 Schematic of huff-n-puff.

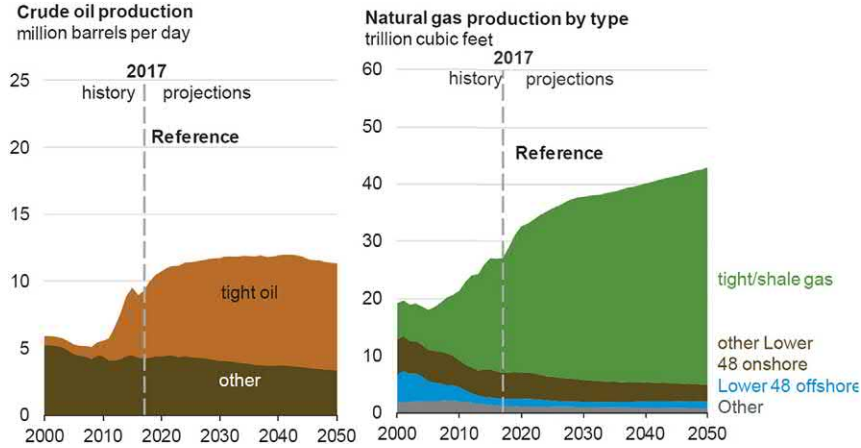

Figure 1.3 U.S. crude oil and dry natural gas production, Reference case (EIA, 2018b).

Produced fluids may be reinjected into reservoirs in some situations. Thus, the fluids are recycled. Such cyclic injection can be performed in both flooding mode and huff-n-puff mode. However, in the petroleum literature, cyclic injection, more often, refers to huff-n-puff injection.

1.3 Shale and tight resources

According to EIA, the future oil and gas production increases come from tight reservoirs, as shown in Fig. 1.3. The oil and gas production from tight resources is more than the total from other sources. It is similar in China.

1.4 Current production technologies

Current production technologies from shale and tight reservoirs are primary depletion using hydraulically fractures horizontal wells. In terms of enhanced oil recovery methods, Orozco et al. (2018) stated: "Up to now, most of the industry efforts for enhancing oil recovery from shales have been devoted to H&P gas injection." The Society of Petroleum Engineers had a forum on EOR in unconventional reservoirs in San Antonio, Texas, November 5–10, 2017. The huff-n-puff method of gas injection was discussed in the whole week of the forum. At the end of the form, it was asked: "Is there any other EOR methods feasible for shale and tight reservoirs?" Of course, potential EOR methods have been proposed. EOR methods and related topics are discussed in the rest of this book.

CHAPTER TWO

Huff-n-puff gas injection in oil reservoirs

Abstract

This chapter discusses huff-n-puff gas injection in shale and tight oil reservoirs. The effects of matrix size, pressure and pressure depletion rate, soaking time, gas composition, diffusion, water saturation, stress-dependent permeability on EOR potential are discussed. The EOR mechanisms are discussed. The minimum miscible pressure in huff-n-puff injection is found to be higher than estimated from the conventional slim-tube tests. The gas penetration depth is strongly related to natural fracture density. Some field projects are presented.

Keywords: Diffusion; Gas composition; Gas penetration; Huff-n-puff; MMP; Pressure depletion rate; Soaking time.

2.1 Introduction

In shale and tight reservoirs, because of the ultralow permeability and high injectivity of gas, it is intuitive that gas injection is preferred. Gas injection can be carried through flooding and huff-n-puff. Again, because of ultralow permeability, most of the pressure drop occurs near the injection well. It will take a long time for the injected gas to drive oil to the production well. Therefore, the flooding mode loses its advantages. By contrast, in the huff-n-puff mode, as gas injection and fluid production are performed at the same well, the pressure near the well can be quickly built up during the huff period, and fluid (gas, oil and water) can be produced immediately after the well is put in the puff mode (Sheng and Chen, 2014). The benefits of gas injection can be quickly returned. And the process of huff-soak-puff can be repeated (cycled). Thus, the benefits can be extended for a long time. Therefore, the huff-n-puff gas injection is a preferred mode. In this chapter, the huff-n-puff injection is discussed in detail, including mechanisms, field projects and experimental and numerical studies of the factors that affect the performance.

Enhanced Oil Recovery in Shale and Tight Reservoirs
ISBN: 978-0-12-815905-7
https://doi.org/10.1016/B978-0-12-815905-7.00002-5

2.2 Initial simulation studies of huff-n-puff gas injection

Chen et al. (2013) are among the first who simulated the effect of reservoir heterogeneity on huff-n-puff CO_2 injection enhanced oil recovery in shale oil reservoirs using the UT-COMP reservoir simulator (UT Austin's compositional simulator). Their conclusion was that if the reservoir was homogenous, injected CO_2 moved deep into the reservoir without much increase in the near-well reservoir pressure, and unable to carry oil back to the well in the production stage, resulting in a lower recovery factor compared to that in primary recovery. In their journal publication version (Chen et al., 2014), they concluded that the effect of reservoir heterogeneity was to expedite the decline of recovery rate in the production stage, leading to a reduced final recovery factor; the final recovery factor in the huff-n-puff was lower than that in the primary recovery because the incremental recovery in the production stage was unable to make up the production loss in the huff and shut-in stages.

Sheng (2015d) further analyzed Chen et al.'s (2014) data and results. In their models, the huff-and-puff process was from 300 to 1000 days; the injection pressure was 4000 psi, and the bottom hole producing pressure was 3000 psi. Sheng (2015d) believed that their result was due to the low production history and the low injection pressure. To support the argument, Sheng used a simulation model to mimic Chen et al.'s injection pressure, injection and production history. The model results showed that the oil recovery factor at 1000 days from the huff-and-puff process was 2.94% which was lower than 3% from the primary depletion. Thus, Chen et al.'s observation was repeated by Sheng's model. However, the model showed that the oil recovery factors at the end of 30, 50, and 70 years from the huff-n-puff process were all higher than those from the primary depletion, when the injection pressure of 7000 psi was used. Therefore, Chen et al.'s results were caused by the low injection pressure of 4000 psi which was lower than the initial reservoir pressure of 6840 psi. The injection pressure in the high-pressure reservoir should be raised to show the EOR potential of huff-n-puff.

Wan et al. (2013a) independently proposed huff-n-puff gas injection during almost the same time as Chen et al. did the above-mentioned work. Their simulation results showed that a significant increase in oil recovery could be obtained from huff-n-puff gas injection. After that, extensive experimental and numerical studies have been carried out in their research group. Some of those studies combined with other studies published in the literature are discussed next.

2.3 Experimental methods

In shale and tight cores, it is very difficult to do experiments, as the flow rate is very low, significant experimental errors can be resulted. In this section, several experimental setups are discussed.

2.3.1 Core saturation with oil

When an experiment is conducted, the core needs to be saturated with oil. A conventional process using a desiccator cannot be used, as the core permeability is too low, and the saturation pressure must be high. An experimental setup schematically shown in Fig. 2.1 may be used. The core is first vacuumed for 1 day, for example. The measured dry core weight is W_{dry}. Then oil is pumped through another pump until a desired high pressure in the container is reached. Stop pumping oil. Oil will gradually imbibe into the core because the oil pressure is high, and the core was vacuumed earlier and the pressure inside the core is low. Gradually, the pressure inside the core is increased until it reaches the oil pressure in the container. During the saturation period, the oil pump may be restarted, when the oil pressure inside the container is dropped owing to oil imbibition into the core. When the pressure inside the container no longer decreases, the core is almost fully saturated with oil. Then take the saturated core and measure its weight, W_{sat}. As is understood, oil cannot enter very narrow pores below some pressure. As the saturation pressure is higher, oil can enter narrower pores. What pressure should be used? Generally, the saturation should be several hundred psi

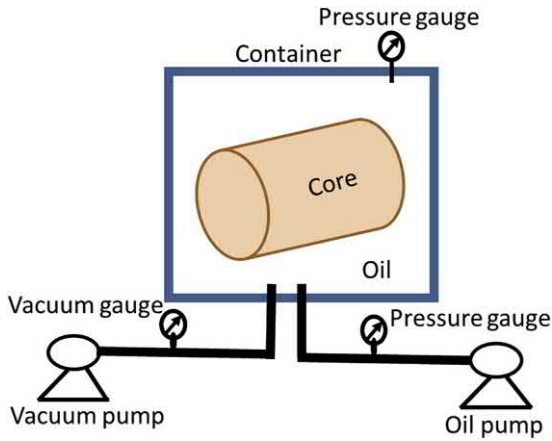

Figure 2.1 Schematic to saturate a core with oil.

higher than the initial reservoir pressure of the interest. Even at such a higher pressure, oil may not enter very small pores. A core cannot be fully saturated by oil in practice. This partial saturation is justified by the fact that oil in the very small pores (e.g., a few nanometers) cannot be produced anyway. Therefore, the oil recovery factor from laboratory may be at a higher side because of this partial oil saturation. The weight of the saturated oil is $W_{sat} - W_{dry}$. Our experience shows that this error is not significant, as we checked the oil weights at different saturation pressures; we also checked the oil weight in the core compared with the pore volume which was independently measured by nitrogen injection or a CT scanner.

When CT is used, the porosity calculation formula can be derived. If the porosity is known, the pore volume is known and the oil weight in the pore volume can be compared with the weight difference between the saturated core and the dry core. If the oil weight is equal to or very close to the weight difference, the core is fully saturated.

Assume the rock is fully saturated with oil, the total mass of the oil-saturated rock is equal to the total mass of oil and rock:

$$V_{or}\rho_{or} = V_o\rho_o + V_r\rho_r \tag{2.1}$$

In the above equation, V_{or}, V_o and V_r are the rock bulk volume whose pores are fully saturated by oil, oil volume, and solid rock volume, respectively, and ρ_{or}, ρ_o, and ρ_r are the densities for the rock bulk fully saturated by oil, oil and rock itself, respectively. Divided by V_{or} for each term, the above equation becomes

$$\rho_{or} = \phi\rho_o + (1-\phi)\rho_r \tag{2.2}$$

ϕ is the porosity. Assume that the density of a substance is proportional to the CT number measured in the substance; the above equation can be written as

$$CT_{or} = \phi CT_o + (1-\phi)CT_r \tag{2.3}$$

Similarly, for a dry rock which is saturated by air,

$$CT_{ar} = \phi CT_a + (1-\phi)CT_r \tag{2.4}$$

The subscripts o, r and a represent oil, rock, and air, respectively. From the above two equations, the porosity can be estimated by

$$\phi = \frac{CT_{or} - CT_{ar}}{CT_o - CT_a} \tag{2.5}$$

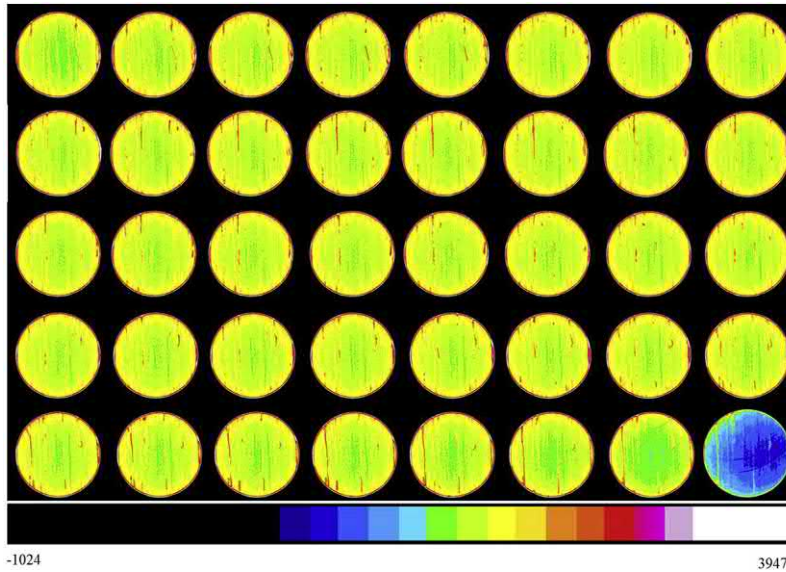

Figure 2.2 CT slice images of an oil saturated core plug (2″ in diameter and 2″ in length).

Whether the core is saturated with oil can be checked with the CT number or CT images. If the CT numbers in the central part of the core are close to those in the edge of core, the core is saturated. Fig. 2.2 shows 50 CT images from a core saturated with oil (Li and Sheng, 2016). It does show that some of the central parts had more greenish colors indicating lower CT numbers. But overall the color is relatively homogeneous. The degree of saturation may also be double-checked by comparing the CT numbers of each slice of the dry core and the saturated core, as shown in Fig. 2.3 as an example (Li and Sheng, 2016). It shows that at every slide, the CT number in the saturated core was higher than that in the dry core.

2.3.2 Huff-n-puff experiments

The experimental setup used for gas (N_2) huff-n-puff tests is shown in Fig. 2.4 (Yu et al., 2016a). It mainly includes a high-pressure nitrogen gas cylinder, a high-pressure vessel, a pressure gauge, a three-way valve, two pressure regulators, and a gas mass flow controller. The oil-saturated core weighing W_{sat} is placed in the vessel. The annular space between the inner diameter of the vessel and the core represents fracture spacing surrounding

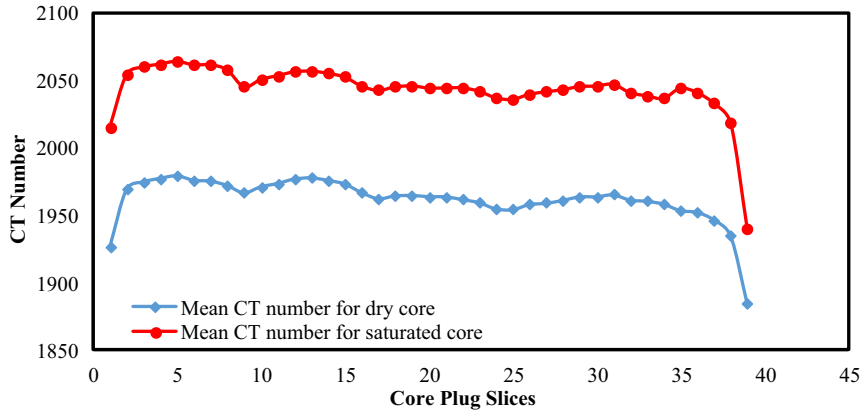

Figure 2.3 CT number comparison between a dry and the oil saturated core.

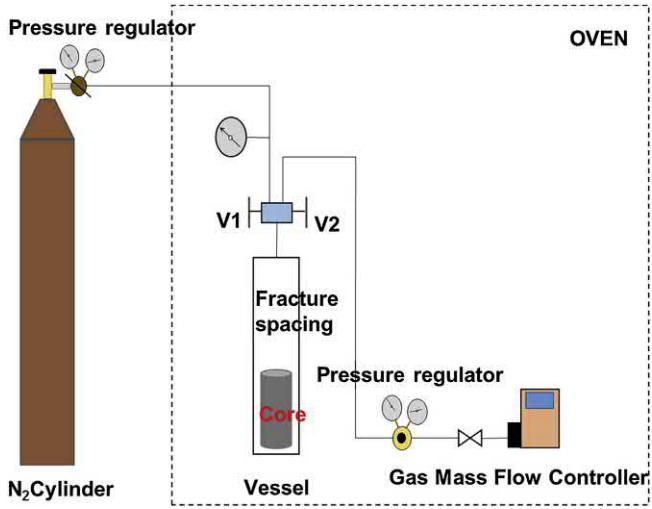

Figure 2.4 Schematic of the experimental setup for N_2 huff-n-puff tests.

the matrix. Before operating a huff-n-puff test, all valves are closed. The procedures for one cycle huff-n-puff process are as follows.

1. Open valve V1 and the N_2 cylinder valve to transfer the gas into the vessel until the system pressure reaches a designed injection pressure;
2. Close valve V1 to have a soaking period;
3. After the soaking period, open valve V2 and set a desired gas outlet flow rate to reduce the system pressure (linearly) to the atmospheric pressure;

4. Remove the core from the vessel, measure the weight (W_{exp}), and calculate the cumulative recovery factor as $(W_{sat} - W_{exp})/W_{sat}$.
5. Repeat the procedures 1 to 4 for a set of times (cycles).

In Akita et al.'s (2018) experimental setup, crushed shale samples instead of core plugs were used. In their experiments, the amount of fluid produced during each cycle was obtained by the difference between the NMR volumes before and after each cycle.

The oil recovery factor may also be derived from CT numbers. According to Akin and Kovscek (2003), the CT number of a core lies on the straight line connecting phase 1 to phase 2. They stated that the CT number of a core has a linear function with the attenuation coefficients of the constituting materials:

$$CT_{gor} = (1 - \phi)\mu_r + \phi S_o \mu_{or} + \phi S_g \mu_{gr} \tag{2.6}$$

where CT_{gor} represents the CT number for a system of gas, oil, and rock, μ_r, μ_{or}, and μ_{gr} are the attenuation coefficients for the rock only, for the *core* fully saturated with oil, and for the core fully saturated with gas, respectively S_o and S_g are the oil and gas saturations, respectively. Note that all the attenuation coefficients μ_{or}, and μ_{gr} are not the attenuation coefficients for oil only and gas only, although our intuition or logic think they are.

If only gas is in the pores, the above equation can be written as

$$CT_{gr} = (1 - \phi)\mu_r + \phi\mu_{gr} \tag{2.7}$$

If only oil is in the pores, the above equation can be written as

$$CT_{or} = (1 - \phi)\mu_r + \phi\mu_{or} \tag{2.8}$$

For a pure fluid, oil or gas, $\phi = 1$. From the above two equations, we can see that CT is equivalent to μ. Then from Eqs. (2.7) and (2.8), we have

$$\phi = \frac{CT_{or} - CT_{gr}}{\mu_{or} - \mu_{gr}} \tag{2.9}$$

The derived Eq. (2.9) is different from Eq. (2.5). Eq. 2.9 may be incorrect as it is derived based on Eq. 2.6. We think Eq. 2.6 should be written as Eq. 2.6': $CT_{gor} = (1 - \phi)CT_r + \phi S_o CT_o + \phi S_g CT_g$, as it will be further discussed later.

From Eqs. (2.6) and (2.7), we have

$$CT_{gor} - CT_{gr} = \phi S_o (CT_o - CT_g) \tag{2.10}$$

Combining Eqs. (2.9) and (2.10), we have

$$S_o = \frac{CT_{gor} - CT_{gr}}{CT_{or} - CT_{gr}} \tag{2.11}$$

Then the oil recovery factor (RF) is

$$RF = \frac{S_{oi} - S_o}{S_{oi}} \times 100\% \tag{2.12}$$

where S_{oi} is the initial oil saturation. Although several groups of authors (Shi and Horne, 2008; Li and Sheng, 2016; Meng et al., 2017) used the above equation, the derivation lacks rigidity. An alternative derivation is proposed below.

The mass balance equation for a core saturated with two fluids, gas and oil, is

$$\rho_{gor} = (1 - \phi)\rho_r + \phi S_o \rho_o + \phi S_g \rho_g \tag{2.13}$$

Assume the density of a system or material is proportional to its CT number,

$$CT_{gor} = (1 - \phi)CT_r + \phi S_o CT_o + \phi S_g CT_g \tag{2.14}$$

If the rock is saturated with oil or gas, we have

$$CT_{or} = (1 - \phi)CT_r + \phi CT_o \tag{2.15}$$

and

$$CT_{gr} = (1 - \phi)CT_r + \phi CT_g \tag{2.16}$$

By combining Eqs. (2.14 and 2.16), Eq. (2.11) is derived.

Fig. 2. 5 shows the cumulative distribution of CT numbers for the dry core, oil saturated core, and during eight cycles (Li and Sheng, 2016). The CT numbers in the cycles were between the one for the dry core and the one for the saturated core. The CT numbers decreased with cycle number. From the CT number in each cycle, oil saturation was calculated from Eq. (2.11), and the recovery factor was calculated from Eq. (2.12) as shown in Fig. 2.6.

In the Tovar et al. (2014) experimental apparatus (Fig. 2.7), the fracturing space between a core plug and the wall of a container is packed with glass beads to simulate hydraulic fractures. A CT scanner is used to monitor the oil saturation changes during the huff-n-puff CO_2 injection process. The oil recovery factor is calculated from CT numbers. The volume

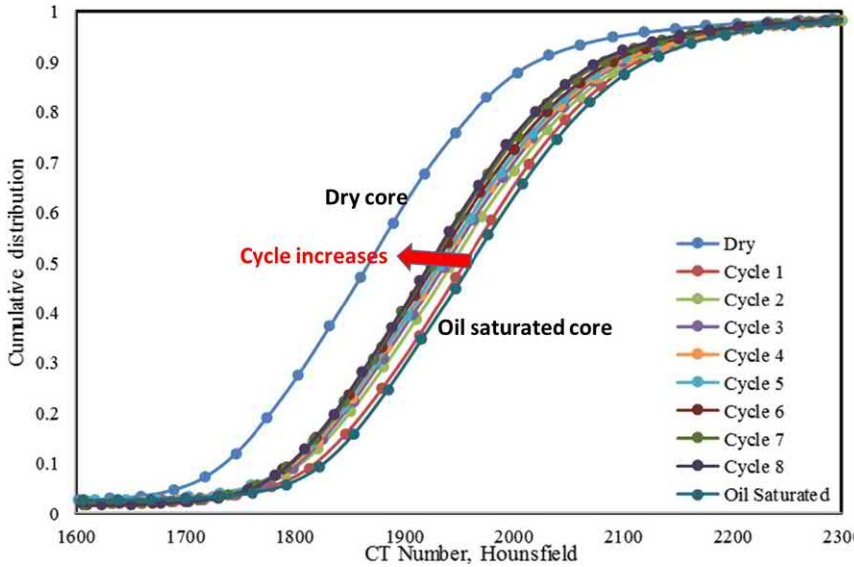

Figure 2.5 CT number cumulative distribution for the dry core, saturated core, and during 8 cycles.

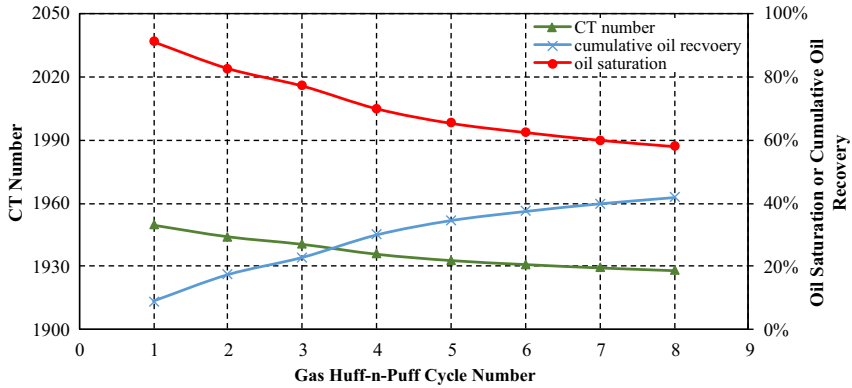

Figure 2.6 CT number, oil saturation, and cumulative oil recovery in every huff-n-puff cycle.

in the glass beads is much higher than that in the core so that the CO_2 saturation is almost one.

In the Alharthy et al. (2015) setup (Fig. 2.8), an ISCO pump injects CO_2 at 5000 psi at the inlet valve of the extraction vessel and the pressure is maintained during the entire experiment. The temperature inside the extraction

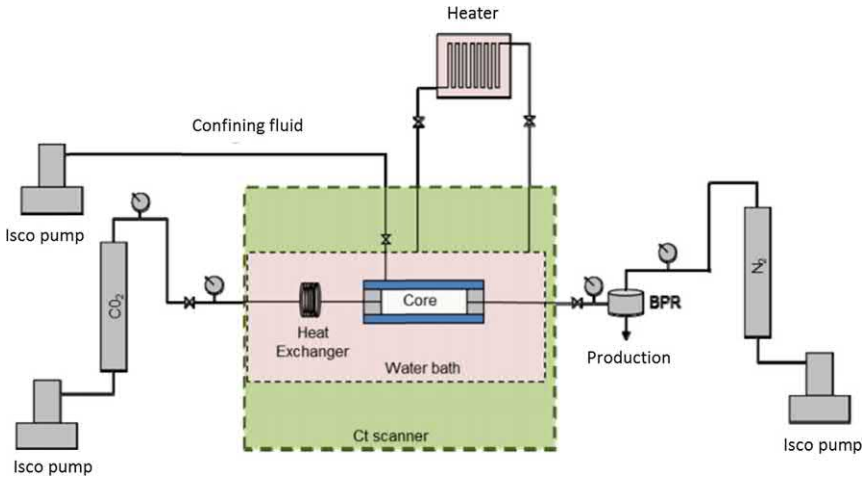

Figure 2.7 Schematic of the displacement equipment (Tovar et al., 2014).

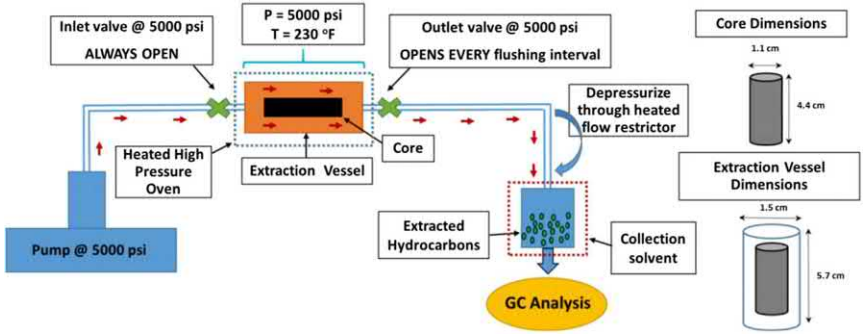

Figure 2.8 EOR experimental setup (Alharthy et al., 2015).

vessel is 230°F. The space between the core and vessel wall represents the fracture surrounding a matrix. During the injection (huff) phase, the outlet valve is closed, and the CO_2 pressure is maintained at 5000 psi for 50 min (soak time) or overnight if the experiment cannot be continued. Subsequently, the outlet valve is opened for 10 min only, while the inlet pressure is maintained at 5000 psi. This process flushes the CO_2 and extracted oil from the core to the collection vessel. This process does not fully represent a huff phase, as a displacement process occurs. It represents a CO_2 or a solvent flow through a fractured reservoir with the flow dominating in fractures. The process is indeed a solvent extraction (soaking) process.

The whole process lasts about 1 hour. And the experiment lasts 24 h or more hours for some experiments. The oil recovery factor is calculated from the collected fluid compositions by GC.

2.3.3 Experimental verification of huff-n-puff effectiveness

The simulation work from Wan et al. (2013a) and Chen et al. (2013) demonstrated the EOR potential of huff-n-puff gas injection in shale cores and shale reservoirs. The potential needs to be verified by experiments, as initial concerns were: (1) during the huff (injection) period, insignificant amount of oil could come out of the core by countercurrent flow of oil and gas, as the injected gas pressure was high and the gas was injected from all the core surfaces; (2) during the puff (production) period, because the oil compressibility was low, limited gas could enter the core, and thus the resultant pressure energy was limited that drove oil out of the core; (3) as a result of those two reasons, the huff-n-puff process might lead to a cycle of injecting and producing gas.

To verify the EOR potential, an experimental setup similar to that presented in Fig. 2.4 was first used by Gamadi et al. (2013). Outcrop core plugs (unfractured matrix cores) from Eagle Ford, Barnett, and Marcos shales were used. Soltrol 130 mineral oil and nitrogen were used. The effects of soak time, injection pressure, and other parameters were investigated. The results showed that huff-n-puff gas injection could increase a significant oil, as shown in Fig. 2.9 as an example.

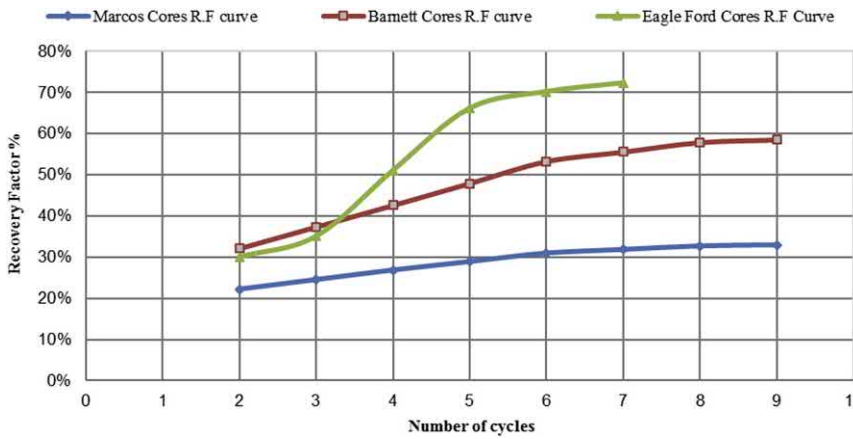

Figure 2.9 Huff-n-puff nitrogen injection performance from Mancos, Barnet, and Eagle Ford cores.

Tovar et al. (2014) used preserved sidewall cores (1in. diameter) under confinement. The cores were soaked in CO_2 at 1600 psi and 3000 psi and 150°F for several days. Production of oil was achieved by increasing the system pressure above a set pressure (similarly to puff period). After the 1 hour of production, the system pressure was maintained 100 psi below the set pressure again (similarly to a huff and soak period). The production was carried out twice a day. The oil recovery was between 18% and 55% of the original oil in the cores.

Alharthy et al. (2015) used their solvent soaking process (not huff-n-puff) and found that 95% oil was achieved by CO_2 for Middle Bakken cores and up to 40% for Lower Bakken cores. Note that the core diameters were 1.1 cm and the lengths were 4.4 cm. Other solvents like methane, methane-ethane mixture, and nitrogen were also used.

2.4 Effect of core size

Further to the preceding initial studies and experimental verification, many more experimental and simulation studies have been performed. The results are summarized and discussed next.

In the preceding verification experiments, very small cores were used so that high oil recovery was obtained. In real reservoirs, matrix is much larger. Therefore, the experimental results cannot directly be applied to reservoirs. The effect of core size needs to be studied.

Li and Sheng (2016, 2017a) did an experimental study about the effect of core size on gas huff-n-puff using two groups of cores from the Wolfcamp formation in West Texas. The first group contained core plugs with the same length of 2 inches but different diameters of 1″, 1.5″, 2″, 3″, 3.5″, and 4″. The second group core plugs had the same diameter of 1.5 inches but different in lengths of 1″, 2″, 2.75″, and 3.5″. The injection pressure was 2000 psi. Methane was used. All the experiments were performed at the temperature of 95°F in an oven. The huff-n-puff experiments were conducted following the procedures described in Section 2.3.2.

Fig. 2.10 shows the oil recovery factors for different diameters but the same length of 2 inches. It is understandable that as the diameter was increased, the surface-to-volume ratio was decreased, the diffusion area and flow area were relatively low, and the pressure gradient (dp/dr) became lower. Thus, the resultant oil recovery became lower.

Fig. 2.11 shows the oil recovery factors for different lengths but the same diameter of 1.5 inches. It shows that the oil recovery factors were not quite

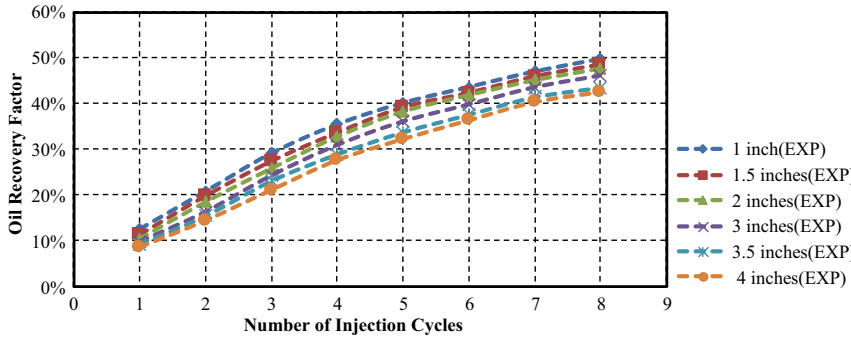

Figure 2.10 Oil recovery factors for cores of different diameters but the same length.

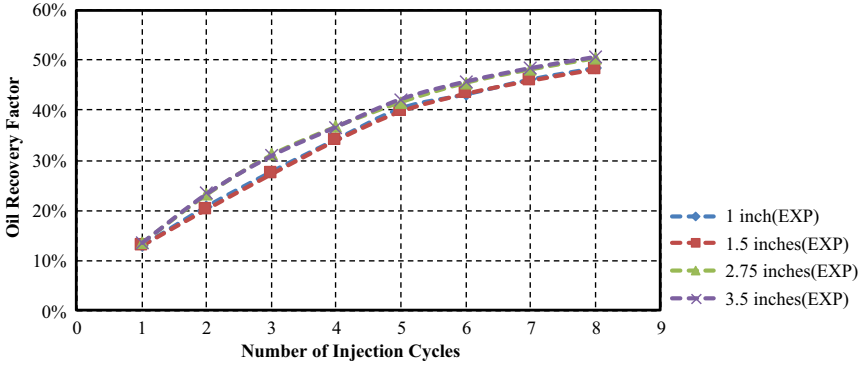

Figure 2.11 Oil recovery factors for cores of different lengths but the same diameter.

different, because the surface-to-volume ratio did not change, the diffusion area and flow area were not changed, and the pressure gradient (dp/dr) was the same when the length was changed.

The above experiments show that the oil recovery factor from a huff-n-puff gas injection varies with the core size. It can be predicted that it will vary with the matrix size in the field scale. To be able to use the experimental data, an upscale method is needed. Li and Sheng (2017b) proposed a curve of the oil recovery versus a dimensionless time for different sizes:

$$t_D = \frac{0.000264\,kt}{\phi\mu c_t (L^2)\left(p_D^2\right)} \tag{2.17}$$

where t_D is the dimensionless time; k is the permeability in mD; t is the operation time in hours; ϕ is the matrix porosity; μ is the oil viscosity in cP;

c_t is the total compressibility in psi^{-1}; L is the characteristic length in ft; p_D is the dimensionless pressure which is defined as

$$p_D = p_{huff} - p_{puff} = \frac{\int_0^{t_{huff}} p_{avg} dt}{S_{huff}} - \frac{\int_0^{t_{puff}} p_{avg} dt}{S_{puff}} \tag{2.18}$$

The subscripts huff and puff mean during the huff time and puff time, p_{avg} means the matrix average pressure. Refer to the areas marked in Fig. 2.12, p_{huff} and p_{puff} are defined as

$$p_{huff} = \frac{S1}{S2} = \frac{\int_0^{t_{huff}} p_{avg} dt}{S_{huff}} = \frac{\int_0^{t_{huff}} p_{avg} dt}{p_{max} \times t_{huff}} \tag{2.19}$$

$$p_{puff} = \frac{S3}{S4} = \frac{\int_0^{t_{puff}} p_{avg} dt}{S_{puff}} = \frac{\int_0^{t_{puff}} p_{avg} dt}{p_{max} \times t_{puff}} \tag{2.20}$$

where S_1, the blue area shown in the figure, represents the integral of average matrix pressure over the huff time in a cycle (t_{huff}), S_2, part of it being the yellow area shown in the figure, represents the area defined by the maximum average matrix pressure during the huff time, p_{max}, times t_{huff}; similarly, S_3, the green area shown in the figure, represents the integral of the average matrix pressure over the puff time in a cycle (t_{puff}), S4, part of it being the pink area shown in the figure, represents the area defined by the maximum average matrix pressure, p_{max}, times t_{puff}.

Using the above definitions, the curve of cumulative oil recovery factors versus the dimensionless time for the simulation models of different matrix sizes falls on almost the same curve, as shown in Fig. 2.13. In this figure, the oil mobilities (permeability divided by oil viscosity) of the different scales are the same. When the mobility is increased, the curve shifts to the right, although variation of well operation constraints (e.g., injection and production pressures) does not shift the curve. When the huff time and/or puff time are changed, p_D is changed. As p_D is increased, t_D is decreased, the curve shifts to the left. Simulation model results seem to indicate that the optimum p_D for oil recovery is 0.8 (Li and Sheng, 2017b).

2.5 Effects of pressure and pressure depletion rate

In the beginning of the type of research in laboratory, the injection pressure was in a few thousands of psi, and the pressure was suddenly released to the atmospheric. It was observed that as the injection pressure was

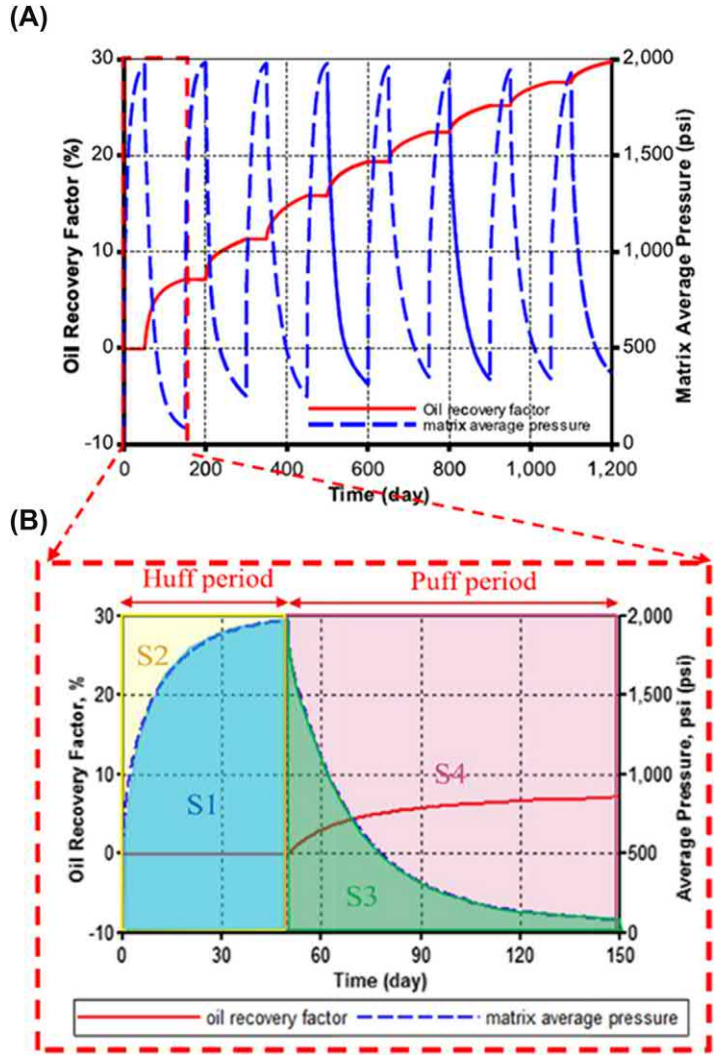

Figure 2.12 Oil recovery factor and matrix average pressure vs. operation time, (A) in a typical huff-n-puff injection time, (B) zoomed in a typical cycle.

increased, the oil recovery factor became higher (Gamadi et al., 2013). Such results were confirmed by other researchers in laboratory and simulation, e.g., Yu et al. (2016a) and Li et al. (2018). Liu et al. (2005) mentioned that if the gas injection pressure is lower, the gas penetration velocity become lower; then the injected gas (CO_2) may stay near the injector, reducing gas contact with oil. When the velocity is higher, gas may bypass

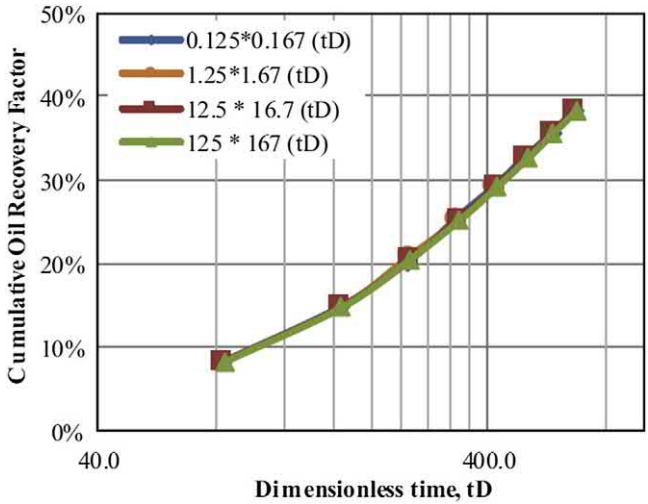

Figure 2.13 Oil recovery factor vs. dimensionless time from the simulation models of different scales.

oil and penetrate further into the reservoir, increasing gas contact with oil. But too high pressure may push oil far away from the well. Laboratory results show that intermediate velocity led to the best performance for conventional reservoirs. In shale and tight reservoirs, a higher injection pressure that corresponds to a higher velocity provides a better performance. However, as the pressure is further increased, the incremental oil is reduced so that the oil recovery factor is similar to that in a lower pressure, if huff-n-puff injection is long enough (Song and Yang, 2013).

The effect of huff pressure is opposite to that of puff pressure. When the puff pressure is lower, higher drawdown occurs. Then the recovery rate is higher. Sheng and Chen's (2014) and Sanchez-Rivera et al.'s (2015) simulation results show that a larger drawdown leads to a higher oil recovery factor; the benefit of larger drawdown is more important than maintaining miscibility near the wellbore by raising the puff pressure.

In laboratory, if the core size was the same, the effect of pressure was actually the effect of pressure depletion rate. In real reservoirs the pressure is depleted at a different or slower rate than in a typical experiment in laboratory. To make use of laboratory results for field performance prediction, it is necessary to study the effect of pressure depletion rate.

Yu et al. (2016a) used two Eagle Ford outcrops (LEF_3 and LEF_4) to study the effect of pressure depletion rate using the experimental apparatus

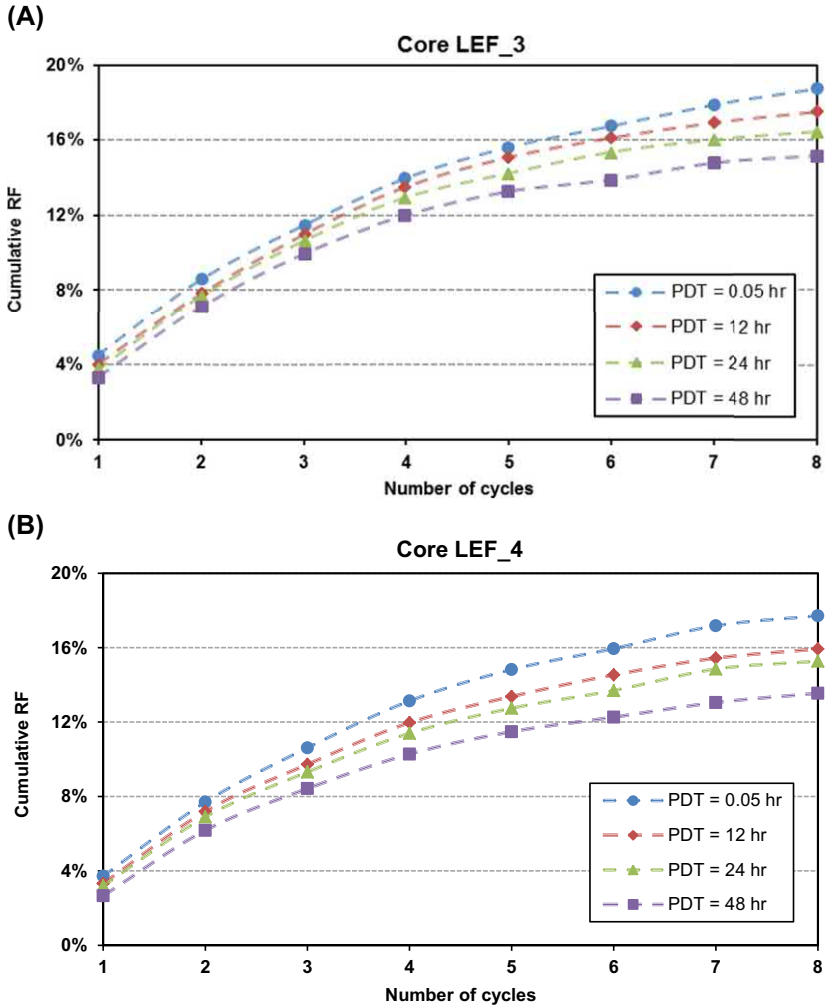

Figure 2.14 Effect of pressure depletion rate, (A) LEF_3 and (B) LEF_4.

shown in Fig. 2.4. The cores had the porosity of 9.7% and the permeability of 300–500 nD. Nitrogen and a Wolfcamp dead oil of 8 cP viscosity were used. The soak time was 12 h (hours). The soaking pressure of 1000 psi was depleted to the atmosphere within 0.05, 12, 24, and 48 h. The data in Fig. 2.14 shows that as the pressure depletion rate was decreased, the oil recovery decreased. They also used a simulation model to history matched the experimental data for the LEF-3 core, as shown in Fig. 2.15. More work was done earlier (Yu and Sheng, 2015).

When the pressure is depleted faster, more cycles can be performed within the same time, which helps further to produce more oil. When the pressure is depleted faster, more gas sites are nucleated. Small gas bubbles form at these gas sites. These gas bubbles grow or expand to provide energy to drive oil out of matrix. As more gas bubbles form, it will be more difficult for those gas bubbles to coalesce. In other words, if the pressure depletion rate is low, large gas bubbles form and they can more easily coalesce, forming a continuous flow path to flow out of matrix bypassing oil (Sheng et al., 1997; 1998).

Interestingly, Akita et al.'s (2018) experimental data of huff-n-puff gas injection showed that higher rate led to lower oil recovery. The attributed this lower recovery to a two-phase choke effect. Native core plugs were used. CO_2 was used as gas. The experimental temperature was at 150°F. The injected pressure was 3500 psi. The soak time was 1 h. Two pressure depletion rates were used. In the fast depletion experiment, the 3500-psi pressure was released to the atmospheric pressure in 3 min. In the other slow experiment, the 3500-psi pressure was released to the atmospheric pressure in 45 min. After the depressurization, the samples were removed from the pressure vessel to a desiccator to cool down to the room temperature for 1 h. The amount of fluid produced from the samples during each cycle was measured by the difference between the NMR volumes before and after each cycle. The NMR measurements were conducted at

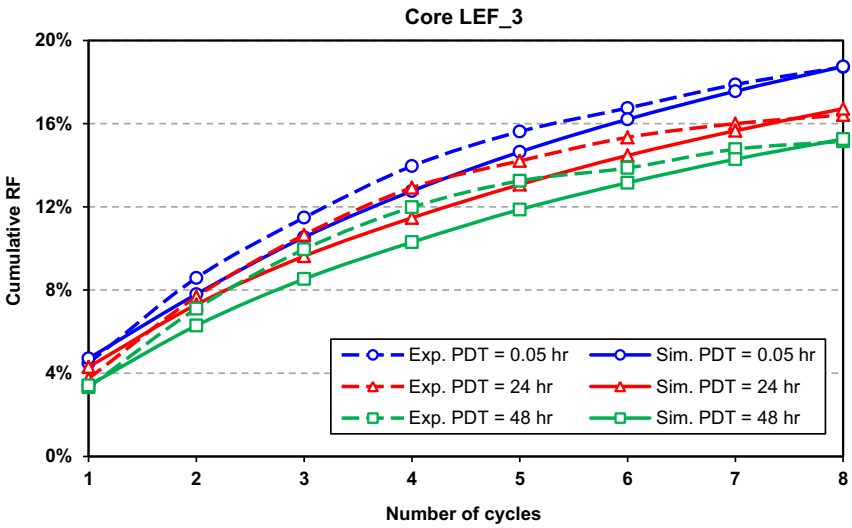

Figure 2.15 Comparison of experimental data and simulation data on the effect of pressure depletion rate.

12 MHz and a TE of 0.114 ms. Their experiments showed that the recovery of each cycle from the slow experiment was about twice that in each corresponding cycle from the fast experiment.

In their fast experiment, when the samples were immediately removed from the pressure vessel to a desiccator to cool down to the room temperature, the fluid in the sample could not come out any more, as both the pressure and the temperature were low at room conditions. Based on our experience, it takes time for the fluid in a tight core to come out. While in the slow experiment, the samples were kept in the high temperature (150°F), and the relatively higher pressure was maintained for 1 h. During this 1 h, a lot of fluid came out based on our experience.

2.6 Effect of soaking time

It is easy to predict that if soaking time is longer, injected gas has more time to diffuse into the matrix and dissolve into the oil, therefore, more oil can be produced in each cycle. Such results have been confirmed in the literature (Gamadi et al., 2013; Yu and Sheng, 2015; Li et al., 2016). Fig. 2.16 is an example (Yu et al., 2016a), in which an Eagle Ford outcrop sample was used. The soaking pressure was 1000 psi. This pressure was depleted in 0.05 h during the puff period. Nitrogen was used. This example showed that at the same sequential cycle number, the oil recovery was higher as the soaking time was increased. It also showed that when the soaking time was short from 0.025, 3–12 h, increasing soaking time significantly

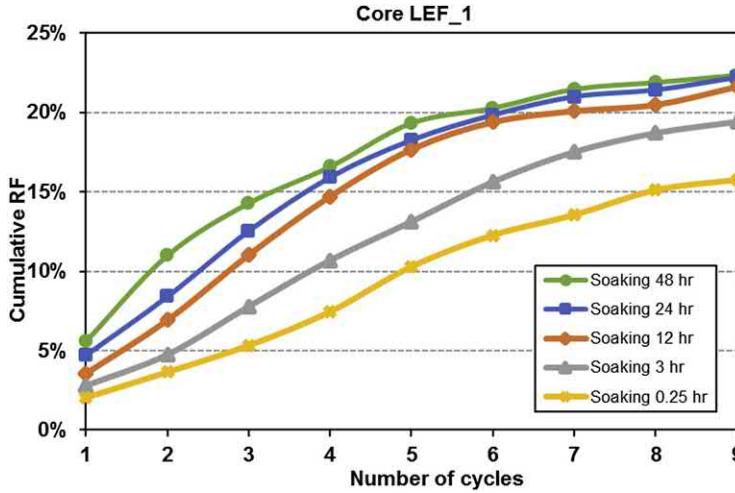

Figure 2.16 Soaking time effect on huff-n-puff oil recovery.

increased oil recovery, but not effectively as the soaking became long from 12, 24–48 h. Especially, after 4th cycle, the difference for different soaking times was marginal. Logically, there should be an optimal soaking time. In this example, 12 h seems to be an optimal.

Fig. 2.17 compares the experimental data with the simulation results. It can be seen that the simulation results match the experimental data, confirming the conclusions from the experiments. Using a simulation model, we can investigate more mechanisms by analyzing simulation data. Fig. 2.18 shows the matrix-fracture system pressure in the first six cycles for the test of 12 h of soaking and 3 h of production. Nitrogen is injected

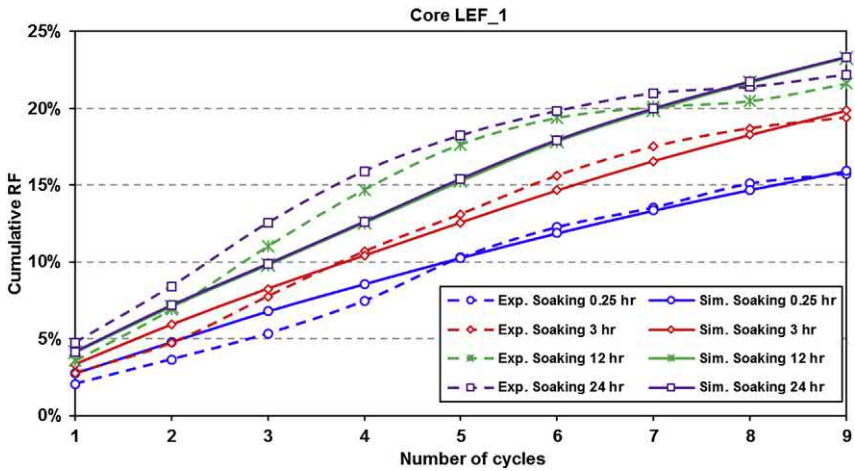

Figure 2.17 Comparison of experimental data and simulation results on soaking time effect.

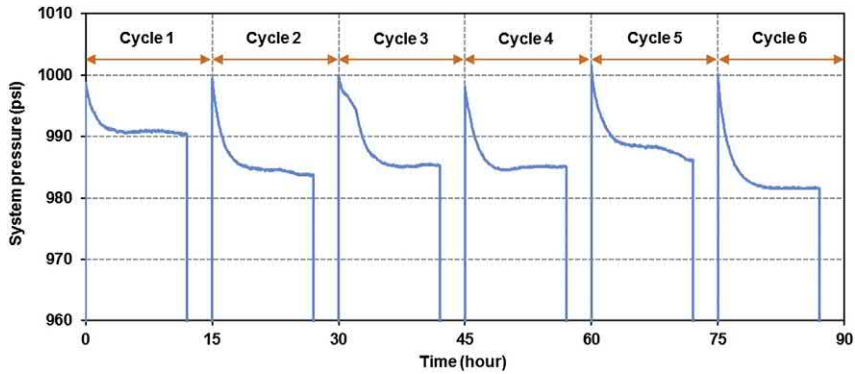

Figure 2.18 System pressure profile for 6 cycles of the test of 12 h of soaking time and 3 h of production time.

into the system quickly until the system pressure reaches 1000 psi, followed by 12 h of soaking. Then the system pressure is blown down to the atmosphere followed by 3 h of production. So, the total operation time for one cycle is 15 h. During the soaking phase, the system pressure declines rapidly in the first 3 h, and then the decline rate decreases gradually until the pressure levels off. The pressure drop (ΔP) in the first cycle is about 10 psi. This pressure decreases more in the subsequent cycles. This is because in the early cycles, oil saturation is high; it is difficult for gas to diffuse into the oil. At later cycles, some oil is produced leaving more gas channels for gas to enter the matrix and dissolve in the oil, the pressure decreases more (about 16 psi). It is 18 psi in the 6th cycle.

Fig. 2.19 further shows the pressure distribution in the system. After gas injection (huff phase), the pressure in fracture area builds up to 1000 psi quickly (in 30 s). With the gas diffusing into the shale matrix, the matrix pressure increases with soaking time from the outer to the inner sections. After about 8.5 h of soaking, the whole system reaches almost 1000 psi. Therefore, a soaking time longer than 8.5 h may not effectively help to improve oil recovery.

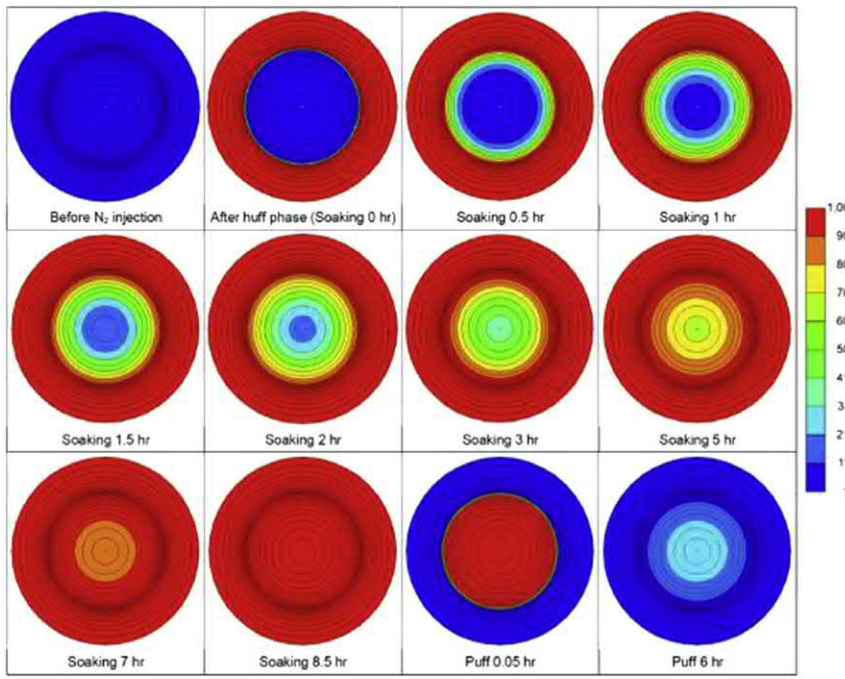

Figure 2.19 System pressure profile in 1 cycle of huff-n-puff process.

Although soaking improves oil recovery, the equal amount of production time is sacrificed. Fig. 2.20 presents the oil recovery histories for the four different soaking times. Note that the horizontal axis is the actual experimental (operation) time, instead of the cycle numbers as plotted earlier. Since there is no oil produced during the huff and soaking phases, the recovery factor (RF) curve remains flat from the beginning of the huff phase to the end of soaking phase, as the experimental RF data are collected at the end of each puff phase. The RF data at the end of the puff phase is connected to the RF data at the end of soaking phase. In the figure is shown a short line with a positive slope. So, in each cycle there are one flat line and one positive-slope line. It can be seen from the figure that within the same operation time, a higher cumulative RF was achieved for a shorter soaking time. Although within a single cycle, a shorter-soaking case had a lower RF, more cycles could be performed, and less production time was lost. This result was also confirmed by experiments in laboratory (Gamadi et al., 2014b; Li and Sheng, 2017a) and by numerical simulation (Sanchez-Rivera et al., 2015; Li et al., 2016; Kong et al., 2016; Li and Sheng, 2017a).

Based on the above discussion, it seems zero-soaking time is the best. Monger and Coma (1988) reported that a soak period was required to maximize ultimate oil recovery by huff-n-puff CO_2 injection in watered-out Berea cores. However, in the reservoir, 9 out of 14 successful CO_2

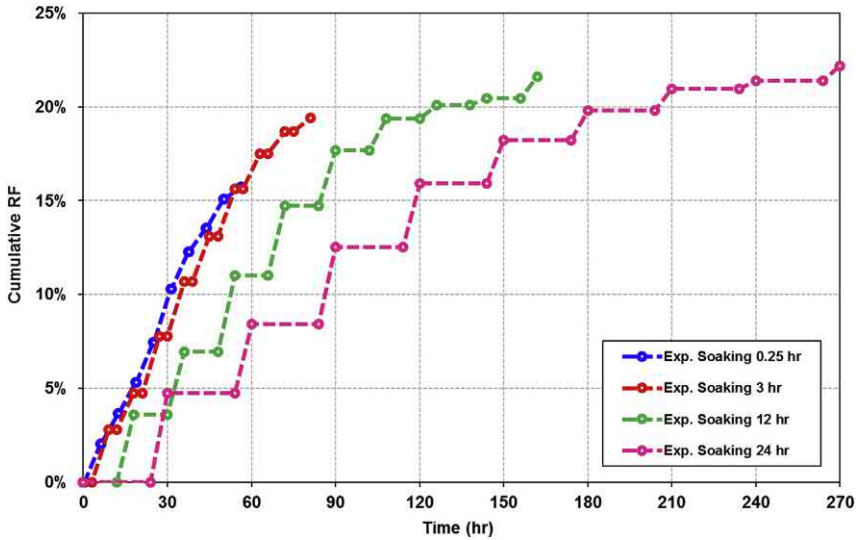

Figure 2.20 Oil recovery histories for different soaking times.

huff-and-puff field tests experienced soak periods ranging from 18 to 52 days, and the process performance appeared to be less sensitive to the soak duration. In few CO_2 huff-n-puff projects in shale reservoirs, soaking time was tens of days (Sheng, 2017a). From the experience of the author of this work, simulation models show zero-soaking time is preferred in terms of oil recovery.

2.7 EOR performance with number of cycles

Artun et al. (2011) did a parametric simulation study of a naturally fractured reservoir (a conventional reservoir). They found the optimum number of cycles was two to three based on net present value. However, Fig. 2.21 shows the pictures of a core of 2″ in diameter and 2″ in length from the first cycle to eighth cycle of huff-n-puff methane injection (Li and Sheng, 2016). The methane was injected at 2000 psi, the core was soaked for 1 day and then the pressure was released to the atmospheric pressure. The incremental recovery factors in each cycle for 10 cores are presented in Table 2.1. The figure and the table show that oil coming out from the core decreased with the cycle. This is because it was easier for

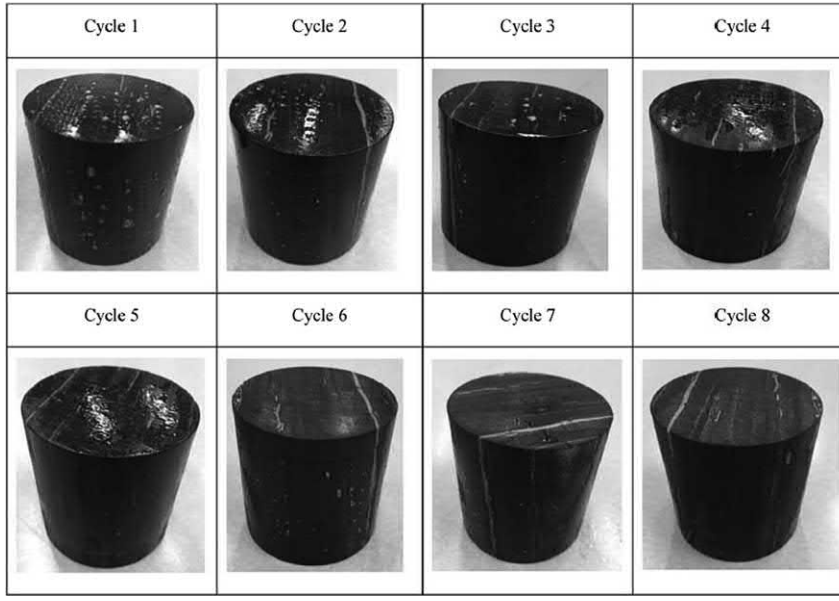

Figure 2.21 A core with released oil during 8 cycles of huff-n-puff injection.

Table 2.1 The incremental oil recovered in each cycle of all the 10 core plugs.

			Incremental oil recovered in each cycle							
Core No.	**Diameter inches**	**Length inches**	**Cycle 1**	**Cycle 2**	**Cycle 3**	**Cycle 4**	**Cycle 5**	**Cycle 6**	**Cycle 7**	**Cycle 8**
1	1	2	12.63%	8.21%	8.27%	6.30%	4.66%	3.47%	3.37%	2.74%
2	1.5		11.26%	8.47%	7.61%	6.24%	5.59%	3.18%	3.60%	2.62%
3	2		10.53%	8.05%	7.32%	6.96%	5.48%	3.61%	3.26%	2.55%
4	3		9.77%	6.54%	7.92%	6.69%	5.16%	3.73%	3.76%	2.58%
5	3.5		9.34%	6.18%	7.62%	5.83%	4.82%	3.86%	3.83%	2.07%
6	4		8.62%	5.84%	6.69%	6.54%	4.62%	4.12%	3.99%	2.22%
7	1.5	1	12.98%	7.85%	6.96%	6.48%	6.21%	2.78%	2.98%	2.30%
8		2	12.97%	7.30%	7.04%	6.75%	5.80%	3.53%	2.63%	2.26%
9		2.75	13.67%	9.63%	7.83%	5.64%	4.86%	3.82%	2.67%	2.19%
10		3.5	13.60%	9.77%	7.52%	5.75%	5.53%	3.48%	2.68%	2.21%

the oil to come to the core surface and the oil saturation gradient is higher in the earlier cycles.

Yu and Sheng (2015) did 10 cycles of huff-n-puff experiments under different pressure depletion rates, using Eagle Ford outcrop samples, the mineral oil Soltrol 130, and nitrogen. Their cumulative oil recovered continued to increase with the cycle. One of the example results is presented in Table 2.2.

Wan et al. (2015) history matched Yu and Sheng's experiments and their models also predicted the continuous increase with the cycle. Their simulation data showed that the cumulative oil recovered increased with the cycle almost linearly when the diffusion was not included in the model.

Sheng (2017b) simulated the huff-n-puff gas injection with 300 days of huff and 300 days of puff time but no soak time, for 32,850 days (about 90 years). The cumulative oil recovery factor keeps increasing, although the oil rate decreases with time as shown in Fig. 2.22. These results indicate that the huff-n-puff process in shale and tight reservoirs can be continued until an economic rate cut-off is reached. In a practical application, an economic cut-off may not allow too many cycles. Artun et al. (2011) did a parametric simulation study of a naturally fractured reservoir (a conventional reservoir). They found that the optimum number of cycles was 2 to 3. Sanchez-Rivera et al.'s (2015) simulation data shows that only the first cycle of huff-n-puff CO_2 injection was profitable. They assumed the oil price is \$90/STB and the CO_2 cost is \$2/Mscf. Reinjection of separator gas (about 50% CO_2 and 50% produced gas) make a project more profitable.

2.8 Effect of injected gas composition

N_2, CO_2, and C_1 are separately used by different researchers to study huff-n-puff gas injection in laboratory. To compare the performance of these gases, Li et al. (2017a) did experiments and simulation work at the same experimental setup and similar conditions. In their experiments, Wolfcamp dead oil was used. The injection pressure was 2000 psi. More experimental details are shown in Table 2.3. To check repeatability, two cores are used. Note that the experimental conditions for CO_2 are not the same as those for N_2 and C_1 which have the same experimental conditions. For Core 1, N_2 and C_1 oil recovery factors are similar in the first three cycles, but N2 is better than C_1 (Fig. 2.23a). For Core 2, N_2 was always better than C_1. It seemed that N_2 is better (Fig. 2.23b). Note the dead oil is

Table 2.2 Accumulative RF data for 10 huff-n-puff recovery cycles of the first round experiment (soaking for 1 day).

Core No.	p depletion time, hrs	Cycle 1	Cycle 2	Cycle 3	Cycle 4	Cycle 5	Cycle 6	Cycle 7	Cycle 8	Cycle 9	Cycle 10
EF #1	0.05	18.67%	23.75%	28.91%	32.82%	36.22%	39.51%	42.46%	45.40%	48.08%	50.51%
EF #2	4	15.39%	22.25%	26.40%	30.23%	33.88%	37.10%	40.28%	43.24%	46.27%	49.06%
EF #3	40	9.27%	15.34%	19.74%	24.01%	26.73%	30.34%	33.66%	37.06%	40.34%	43.39%

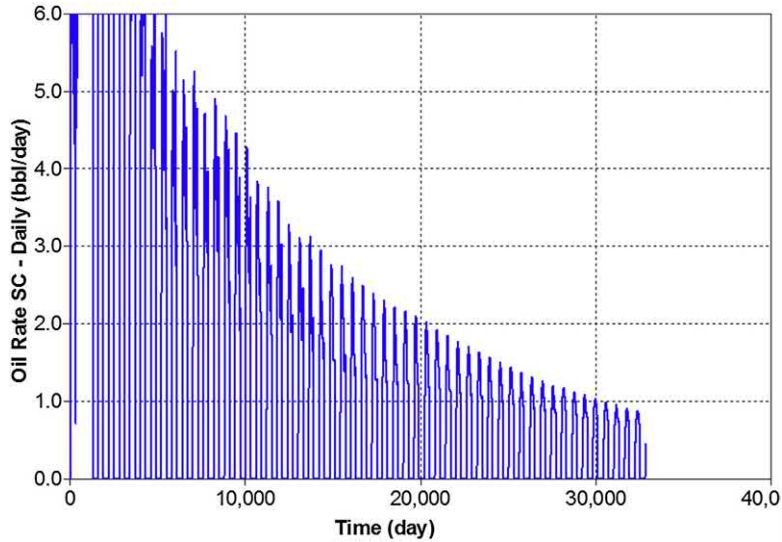

Figure 2.22 Oil rate versus time in an extended simulation case.

Table 2.3 Experimental conditions.

Test No.	Gas	Core no.	Injection time, hrs	Soaking time, hrs	Production time, hrs
1	CO_2	Core 1 Core 2	1	6	6
2	N_2	Core 1 Core 2	0.2	18	6
3	C1	Core 1 Core 2	0.2	18	6

used. C_1 was easier to dissolve in the oil, resulting in lower pressure to drive oil out of cores.

To avoid this performance difference that might be caused by an experimental error, simulation models in the experimental scale show that N_2 is better than C_1, and CO_2 is the best (Fig. 2.24). However, a field scale model simulation results seen in Fig. 2.25 show that C_1 is better than N_2; C_2 is better than CO_2. The huff time and puff time are the same 100 days. Other simulation studies (e.g., Wan et al., 2014a) also show that the oil recovery by CO_2 injection is higher than that by methane injection in shale oil reservoirs.

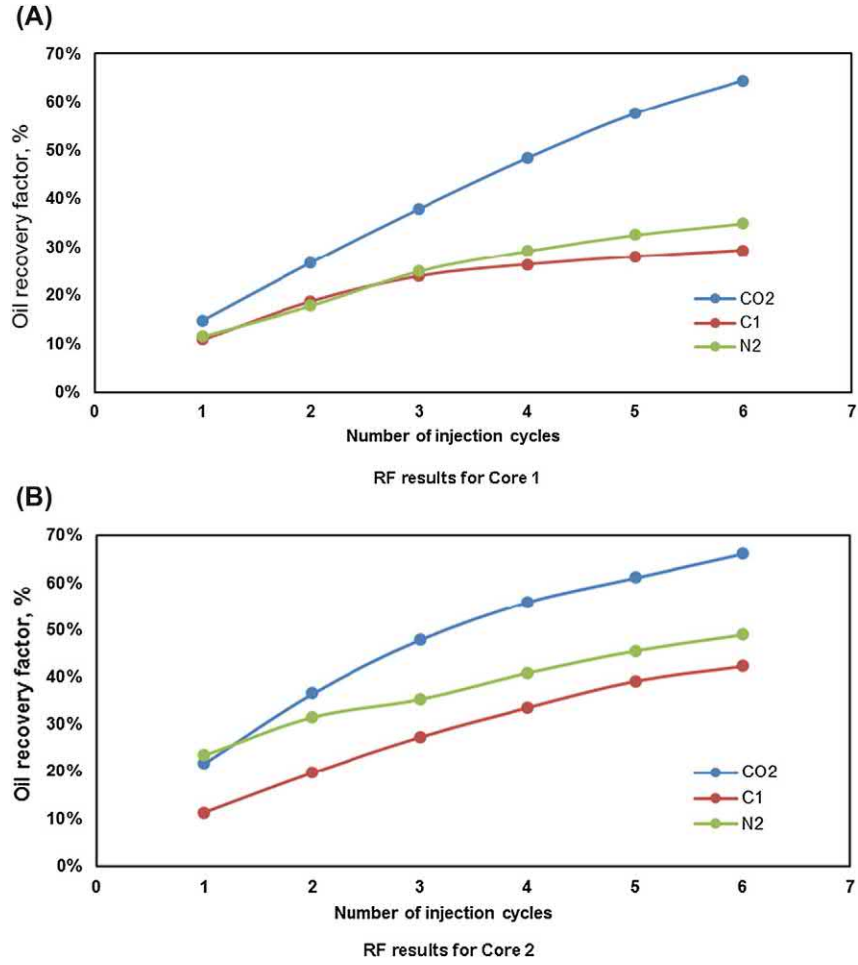

Figure 2.23 Effect of injection gases on huff-n-puff oil recovery. (A) RF results for Core 1 (B) RF results for Core 2.

In Shayegi et al.'s (1996) sandstone cores and Alharthy et al.'s (2015) shale core experiments, C_1 was better than N_2. Li et al. (2017a) attributed this inconsistency to the difference in oil components. Their field scale model shows in Fig. 2.26 that the performance of N_2 is better for a dead oil, but C_1 was better for a live oil. For a live oil, C_1 can easily dissolve in the oil, making oil viscosity lower, compared with N_2. But for a dead oil, their solubility and the oil viscosity reduction are not much different.

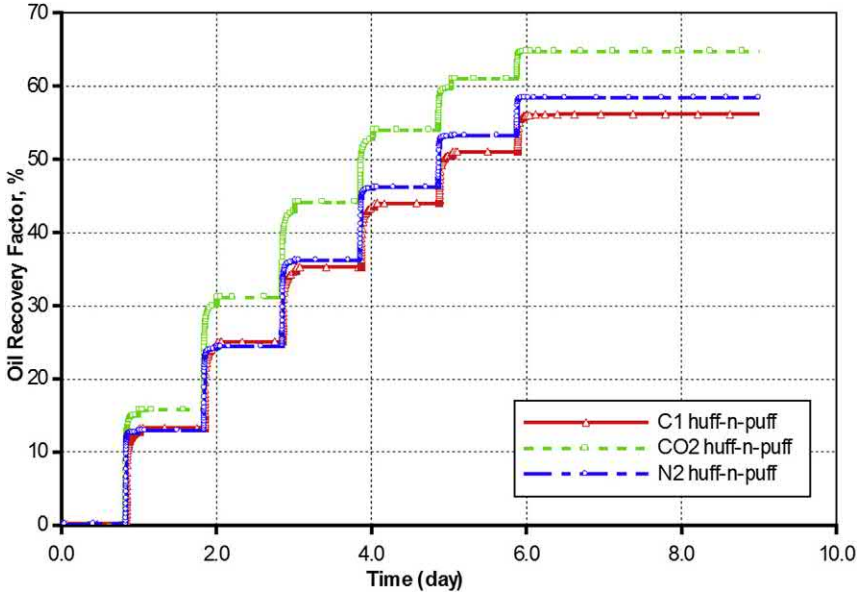

Figure 2.24 Effect of injection gases on oil recovery using an experimental simulation model.

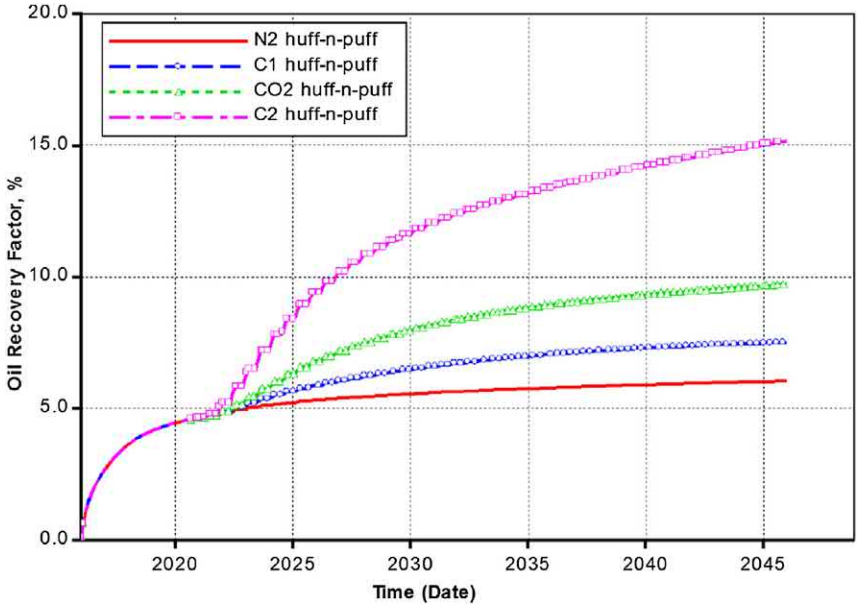

Figure 2.25 Effect of injection gases on oil recovery using a field-scale simulation model.

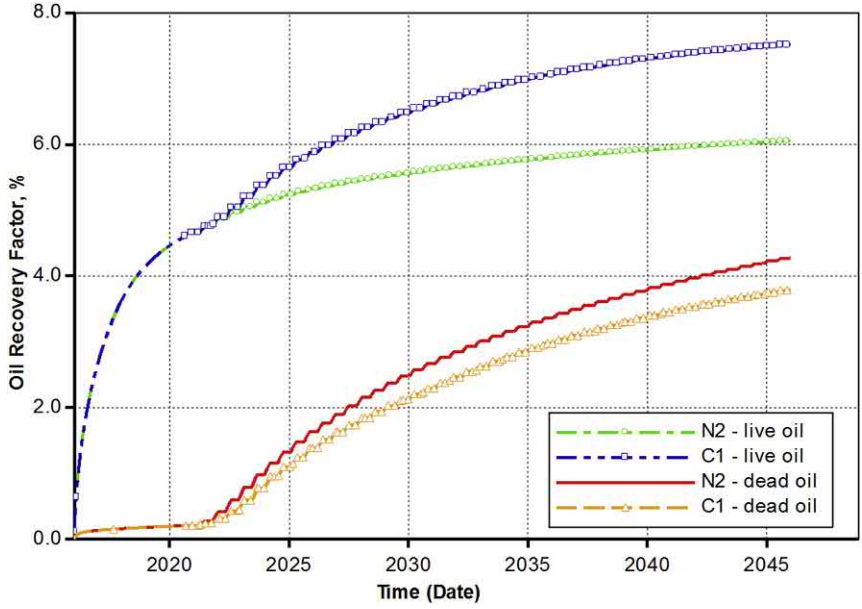

Figure 2.26 Comparison of oil recovery from N2 and C1 when live and dead Wolfcamp oils are used.

In condensate reservoirs, Sheng et al. (2016) observed from a simulation study that the liquid condensate recovery from CO_2 injection is little bit higher than that from the methane injection, but it is much higher than that from nitrogen injection because it is more difficult for nitrogen to be miscible with liquid oil. However, Sheng (2015b) observed that the liquid oil recovery from CO_2 injection is lower than that from C_1 injection because the total volume of injected CO_2 is 15% lower than that of injected C_1 for the same injection pressure. Sharma and Sheng (2017, 2018) found that ethane is the most effective agent to recover liquid condensate compared with methane and solvents like methanol and isopropyl alcohol (IPA).

In principle, if the injected agent is more similar in its properties to liquid oil, the liquid oil recovery will be higher under the same injection conditions and injection volume. Other operation issues need to be considered. For example, CO_2 injection may have issues like corrosion, hydrate and lack of availability near a large field operation; it may cause an asphaltene deposition issue (Shen and Sheng, 2017a; 2017b, 2018).

2.9 Minimum miscible pressure

For gas EOR, one of the important mechanisms is the miscibility of gas and oil. Then a miscibility pressure needs to be measured. One of the conventional methods is to use slimtube tests. One example of such an experimental setup is shown in Fig. 2.27. The part in the figure marked "Coil/Column" is a slimtube which is packed with sand and the sand is saturated with a dead oil initially. About 1.2 pore volumes (PV) of gas (CO_2 in this figure) are injected to the slimtube. Some of the gas is dissolved in the oil to swell the oil and to reduce oil viscosity; some of the gas bypasses the oil; and some of the gas displaces out the oil in the slimtube. The produced oil is collected at the downstream where a back-pressure regulator (BPR) is installed. It can be understood that as the injection pressure is higher, more oil can be displaced out. When the pressures are low, an increase in pressure will result in a significant increase in oil production. But when the pressures are high, the increase in pressure may not lead to as much increase as in the low pressures. One example of the oil recovery factors at different pressures is shown in Fig. 2.28. From this figure, it can be seen that the increase in oil recovery slows down when the pressure is higher

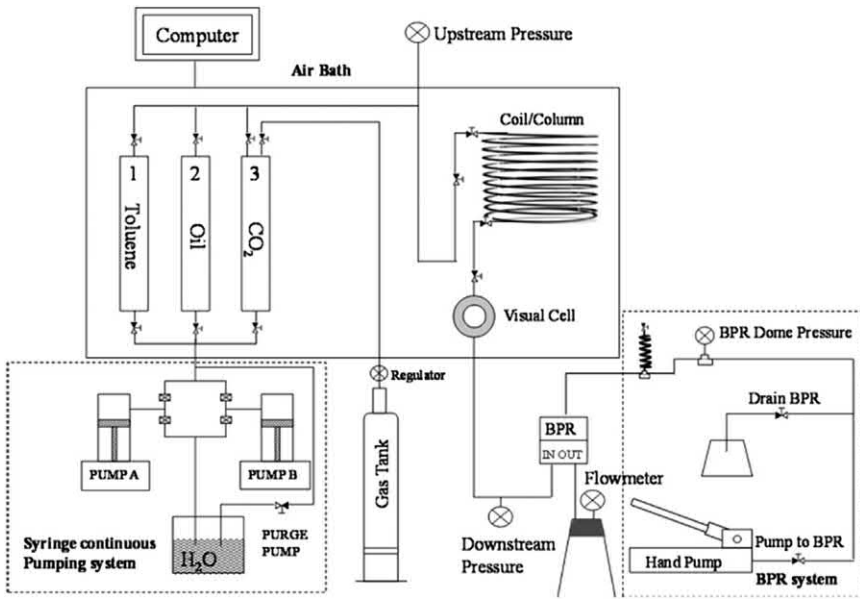

Figure 2.27 A schematic to measure the miscible pressure using slimtube tests.

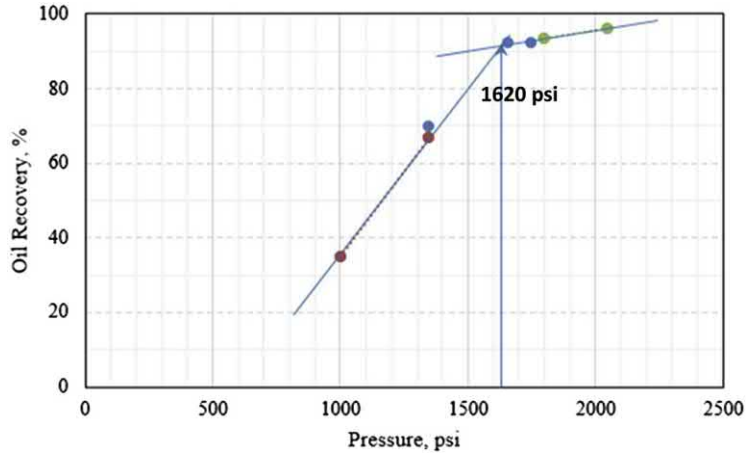

Figure 2.28 An example to determine MMP from slimtube tests.

than 1620 psi. It means that when the pressure reaches 1620 psi, gas and oil start to be fully miscible. Thus, it is called the minimum miscible pressure (MMP).

Li et al. (2017b) used the above experimental setup to determine the CO_2 MMP for Wolfcamp oil at 104°F. The MMP was 1620 psi.

After determining the MMP using slimtube tests, Li et al. (2017b) used the Wolfcamp oil and three Wolfcamp shale core samples to perform huff-n-puff CO_2 injection tests, with the pressures below and above the MMP (1200, 1600, 1800, 2000, and 2400 psi). At each pressure, seven cycles of huff-n-puff tests were performed. For each huff-n-puff test, the soaking time was 6 h. The soaking pressure was suddenly released to the atmospheric pressure, and the core stayed in that pressure for 6 h. The oil recovered was estimated from the weight difference of the core samples containing oil before and after the test. The experimental setup is shown in Figs. 2.29 and 2.30. The accumulator 1 was used to store high pressure CO_2. The core samples were put in the accumulator 2. The accumulator 3 contained the oil which was used to saturate the core samples. Three cores were used to repeat the tests. The results for Core 2 are presented in Fig. 2.31. Note that the oil recovery factors at different soaking pressures and different cycles were different. But the MMP determined from Core 2 at Cycle 6 was close to that from Cycle 7, and the MMP was close to those from other cores. The MMP was about 1800 psi. This MMP is about 200 psi higher than that obtained from slimtube tests.

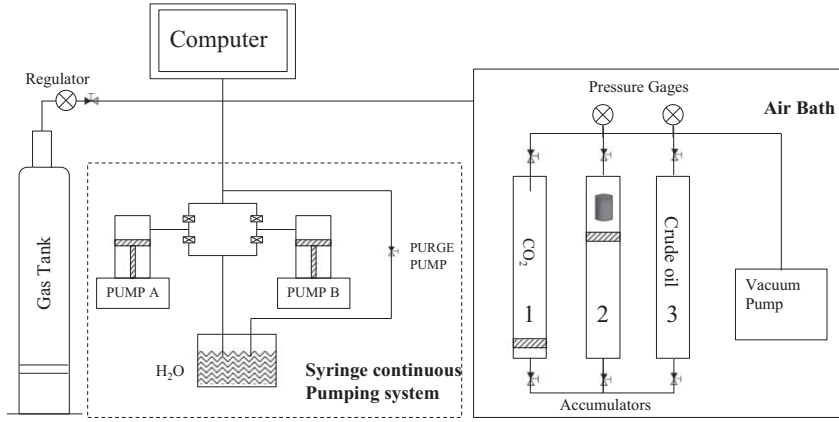

Figure 2.29 Experimental setup for the CO_2 huff-n-puff tests.

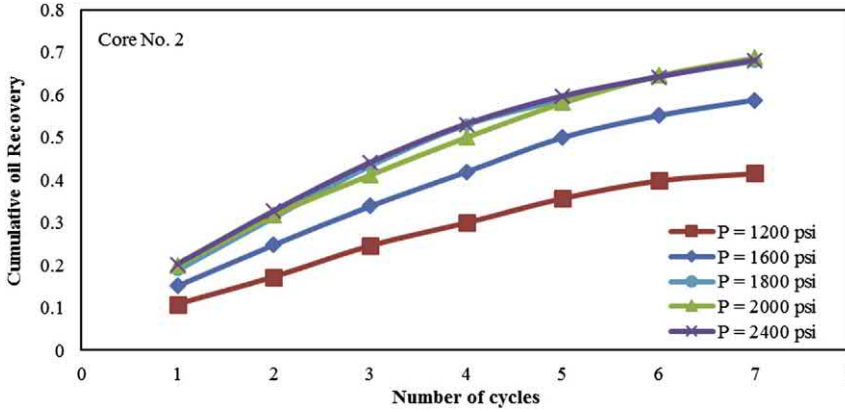

Figure 2.30 Oil recovery factors at different soaking pressures and different cycles for Core 2.

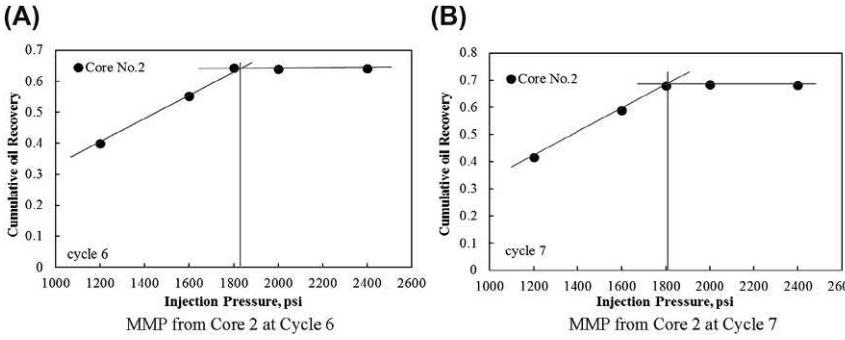

Figure 2.31 MMP determined from tests using Core 2 at Cycles 6 and 7. (A) MMP from Core 2 at Cycle 6 (B) MMP from Core 2 at Cycle 7.

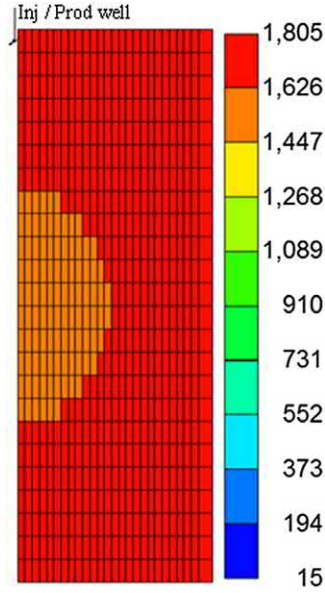

Figure 2.32 Pressure distribution in Core 2 at the end of soaking at Cycle 7.

Li et al. (2017b) used a simulation model to history match the tests for Core 2. Fig. 2.32 shows the pressure distribution in Core 2 at the end of soaking period at Cycle 7. It can be seen that the pressure in the central part of the core was lower than that near the core surface where the injection pressure was reported and plotted in Fig. 2.31. To make the central part miscible, the injection pressure near the core surface must be higher than the MMP (1620 psi) determined from the slimtube test. This phenomenon is less significant in a high-permeability case. Another fact that caused this MMP difference is the two methods used. One method is to measure MMP from the huff-n-puff tests in which the pressure depletion was fast and the pressure was actually lower than the MMP required in the puff period. The other is from the slimtube experiments in which the gas injection rate in the slimtube experiment was extremely slow to allow the gas to fully mix with oil. Therefore, the MMP required for huff-n-puff injection should be higher than the MMP estimated from the slimtube tests.

Similarly, the distributions of CO_2 mole fraction in oil inside the core at the end of soaking period in Cycle 7 (Fig. 2.33) shows that when the injection pressure was below 1800 psi, the CO_2 fraction in the core center was low, indicating the miscibility was not reached. When the pressure was at

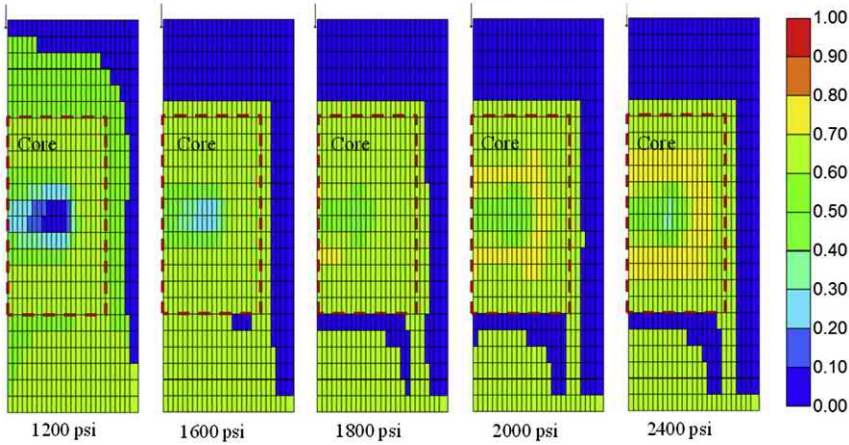

Figure 2.33 CO_2 mole fraction in oil at the end of soaking at different pressures in Cycle 7 for Core 2 (dotted line outlining the core area).

1800 psi, more CO_2 reached the core center. After that, the benefit of increasing pressure was not significant.

2.10 Effect of diffusion

It is our intuition that in shale and tight formations, diffusion is more important than in conventional formations as the convection is smaller; and it may be thought that diffusion plays a dominant role. However, in shale and tight formations, the diffusion is also smaller than in conventional formations. In the literature, a theoretical or experimental quantification has not been published regarding the huff-n-puff gas injection process. Researchers generally use simulation models to quantify their roles by comparing the oil recovery with and without inclusion of diffusion in their models. Wan and Sheng (2015a) simulated gas flooding in shale formations. Their simulation results show that the Péclet number in their model is in the order of 10^{-3}, indicating a diffusion-controlled flow regime. The Péclet number (N_{pe}) defines the ratio of the convective term (velocity multiplied by characteristic length L) to the dispersive coefficient (D). Figs. 2.34 and 2.35 shows the effect of diffusion on oil recovery in gas flooding at different natural fracture spacings. Diffusion does not show up as there is no gas injection in the primary production. In the gas injection process, as the fracture spacing is reduced, the effect of diffusion is enhanced. When the spacing is

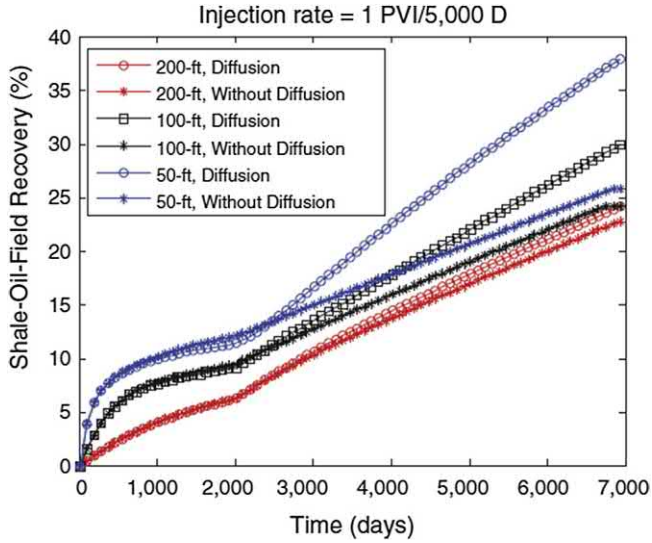

Figure 2.34 Effect of diffusion on gas flooding oil recovery at different fracture spacings.

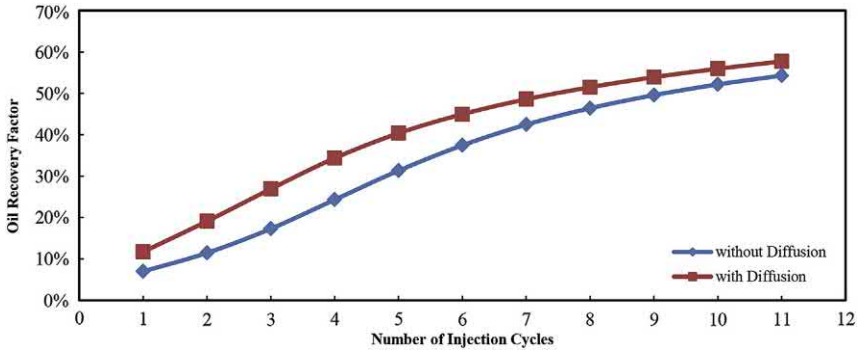

Figure 2.35 Effect of diffusion on huff-n-puff methane injection.

about 50 ft to 100 ft, the increase in oil recovery with diffusion compared with the case without diffusion is about 10%. Yu et al.'s (2014b) simulation shows that the incremental oil recovery factor is 3%–4% using a diffusion coefficient of 10^{-8} m^2/s. In their model, one huff-n-puff is 6 months of huff, 3 months of soaking, and 12 months of puff, and this cycle is repeated for 30 years.

Li and Sheng (2017a) simulated huff-n-puff CH_4 injection with and without diffusion. The molecular diffusion coefficients are calculated using

the Sigmund (1976) correlation. Fig. 2.35 shows that the oil recovery with diffusion is about 10% higher than that without diffusion in the first five cycles. The difference becomes lower with later cycles.

Li et al. (2018) used a simulation model which matched an experiment of huff-n-puff methane injection. The oil viscosity at different distances from the "fracture" are shown in Fig. 2.36A with diffusion and Fig. 2.36B without diffusion. The fracture was the open space between the core plug of 1.5 inches in diameter and the container wall in the experiment. The place with 0.75 inches to the fracture was at the edge of the core, 0.45 inches to the fracture was the middle of the core, and the 0.075 inches to the fracture was the center the core. In the figure, "H" represents the huff time (1 h) and soaking time (4 h), and "P" represents the puff time (4 h). The figure shows that with diffusion in (A), the oil viscosity in the center of the core increased during the huff and the soaking time, and the oil viscosity in the middle and the edge of the core decreased, as the methane diffused from the edge to the center. Without diffusion in (B), the oil viscosity did not change during the huff and the soaking time.

2.11 Effect of water saturation

In real reservoirs, some initial water and aqueous fracturing fluid exist. Li et al. (2018) studied the effect of this water on huff-n-puff CO_2 performance. Since the water and oil saturation in the core initially and at the end of a cycle were not known, oil recovery factor could not be calculated. Instead, a liquid recovery factor was calculated using the following equation:

$$\text{Liquid recovery factor at the end of cycle i} = \frac{W_{r+w+o} - W_i}{W_{r+w+o} - W_{dry}} \tag{2.21}$$

In the above equation, W_{r+w+o} is the weight of the rock saturated with water and oil initially, W_i is the weight of the rock with water and oil at the end of cycle i, and W_{dry} is the weight of dry rock. Three tests were conducted: one test with the core fully saturated with Wolfcamp dead oil, the other two tests with cores saturated with oil and water of 15% KCl for repeatability tests. During the tests, the soaking pressure of 2000 psi was released to the atmosphere. About 6 h of soaking time and 6 h of huff time were used. The experimental data are shown in Fig. 2.37. It showed that even the produced oil and water were added together, the liquid oil recovery is lower than the oil recovery, indicating the multiphase fluid system was not as

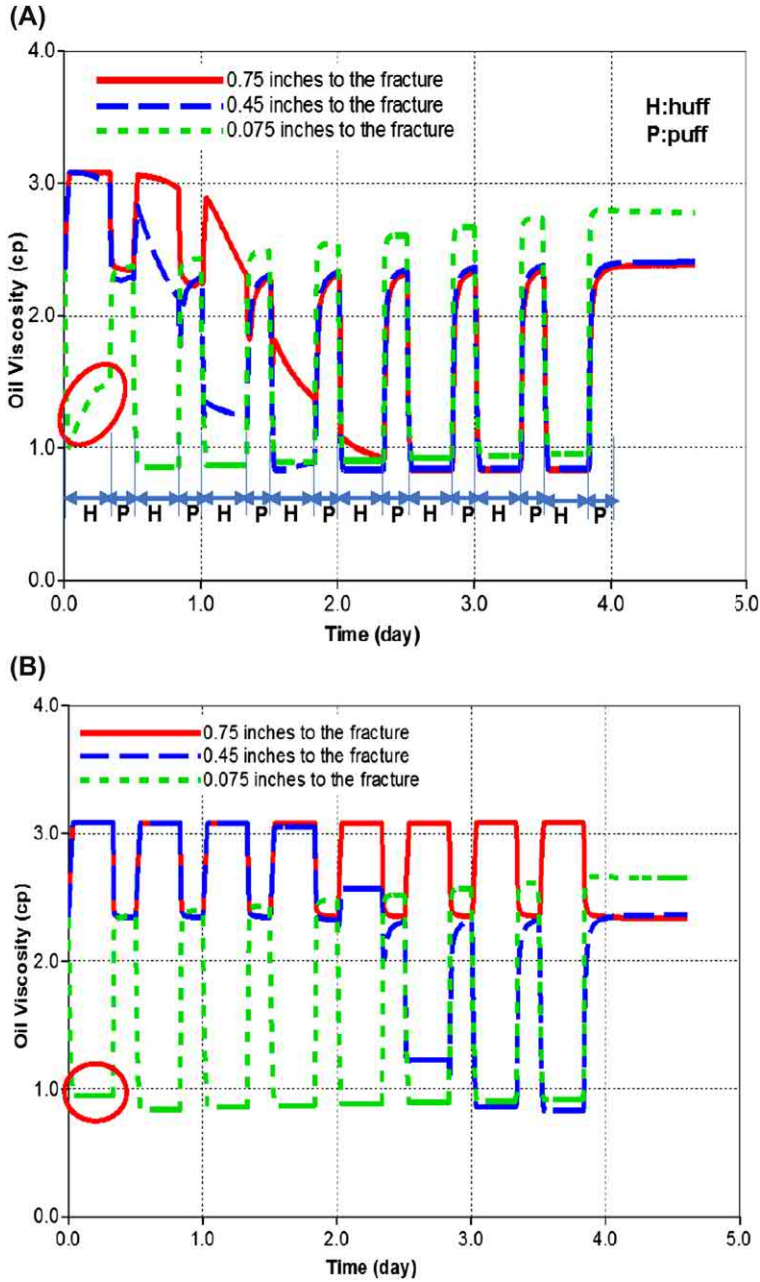

Figure 2.36 Oil viscosity at different places in the core during huff-n-puff methane injection. (A) With diffusion (B) Without diffusion.

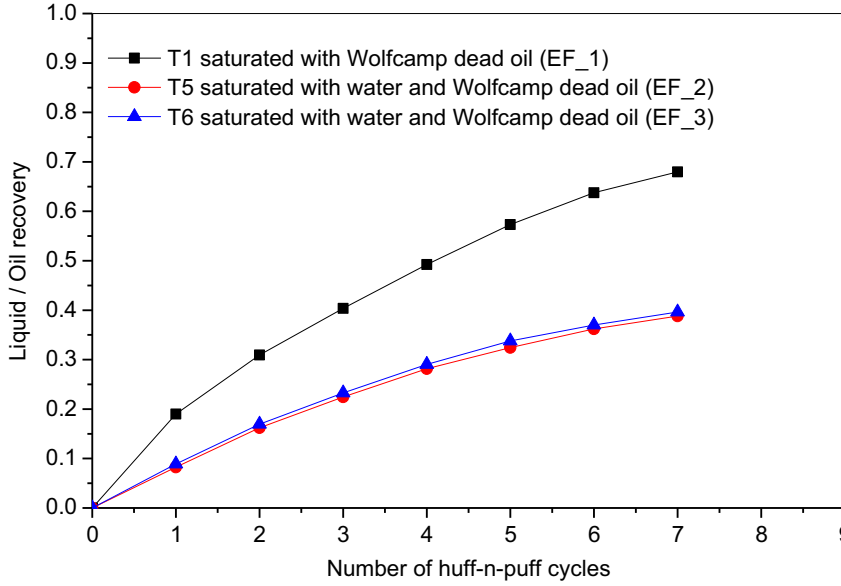

Figure 2.37 Liquid/oil recovery factors at the end of cycles with different oil saturations.

effective as the single oil fluid system to produce fluid in the huff-n-puff mode. This is another factor which needs to be considered when predicting a field performance.

2.12 Effect of stress-dependent permeability

After some years of primary production, the reservoir pressure (pore pressure) is reduced, and the formation effective stress is increased. As a result, the formation permeability is reduced. If huff-n-puff gas injection is carried out, the formation permeability will be increased during the huff period and the early puff period, because the formation of effective stress is reduced owing to the increased pore pressure. Therefore, the huff-n-puff process helps well injectivity and productivity. Gala and Sharma (2018) evaluated this benefit using reservoir simulation, as shown in Fig. 2.38. It shows the oil recovery factors for the cases of No Geomechanics (no stress-dependent permeability changes), Base Gamma = 5e-4 1/psi (middle curve), and Base Gamma = 10e-4 1/psi (bottom curve). The gamma is the permeability-stress exponent in an uploading/unloading cycle in the following equation:

$$k = k_0 e^{\beta(\sigma - \sigma_0)} \tag{2.22}$$

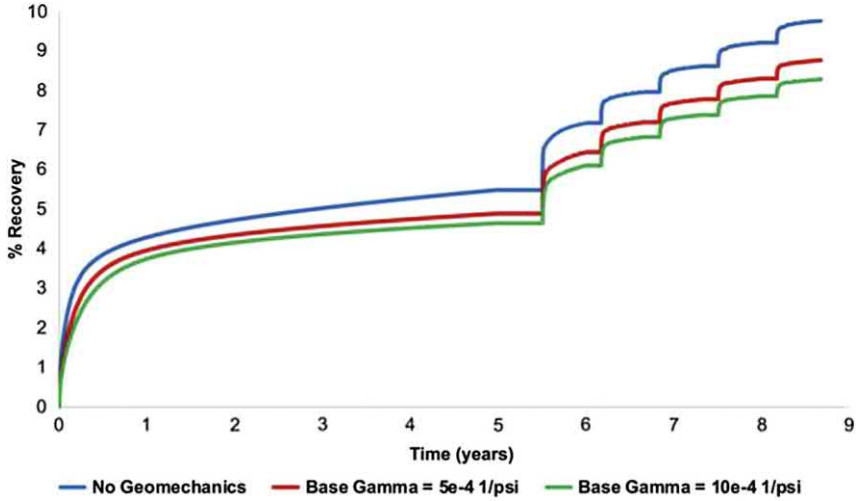

Figure 2.38 Oil recovery factors for the cases of No Geomechanics (no stress-dependent permeability changes, top curve), Base Gamma = 5e-4 1/psi (middle curve) and Base Gamma = 10e-4 1/psi (bottom curve) (Gala and Sharma, 2018).

where k is the permeability at the effective stress σ, k_0 is the permeability at the initial stress σ_0, β is the permeability-stress exponent. Apparently opposite to what we expect, this figure shows that the oil recovery is the highest when the permeability does not change with the effective stress (no geomechanics). This is because in their simulation model, the permeability is kept at the highest value k_0 at the initial effective stress σ_0 in the case of No Geomechanics. For a fair comparison, the permeability in the case of No Geomechanics should have been chosen at the value at the end of 5 years of primary depletion, so that the benefit of permeability increase from the huff-n-puff process can be shown.

The benefit of huff-n-puff injection can be seen from Fig. 2.39 in which the ratios of oil production from the huff-n-puff cases to that from the non-huff-n-puff case are plotted. It can be seen that the ratio from the case of No Geomechanics is lower than those from the other two cases. In other words, in real reservoirs where the permeability is stress-dependent, the huff-n-puff beneficial is enhanced.

2.13 Huff-n-puff mechanisms

Many EOR mechanisms have been proposed in the literature for huff-n-puff gas injection, including increase in reservoir pressure, volumetric

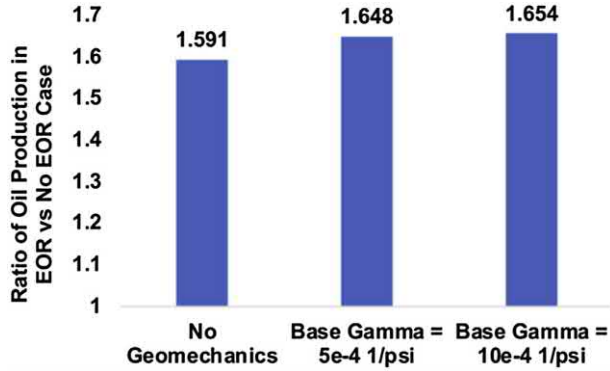

Figure 2.39 Ratios of oil production from the huff-n-puff cases to that from non-huff-n-puff case (Gala and Sharma, 2018).

swelling, viscosity reduction, relative permeability hysteresis, miscibility, gas extraction, gas solubility, and diffusion. But few are quantified.

Swelling effect stores the energy during the huff period, and it provides the driving force in the puff period. Swelling also increases the oil volume so that oil saturation and thus oil relative permeability is increased. Liu et al. (2005) reported that the swelling factor in the huff period is higher than that in the puff period at the same pressure. During the huff period, the injected gas is in a continuous phase, whereas the gas may lose some continuity during the puff period. Some gas is trapped. This may result in the relative permeability hysteresis by which gas relative permeability is reduced during the puff period (imbibition process). As gas diffuses into the oil phase, oil viscosity is reduced. This mechanism may be important for heavy oil but not for light oil. Experiments show that less soaking time leads to higher oil recovery within the same operation time (Yu et al., 2016a), although longer soaking time makes the oil recovery in a single cycle higher (Gamadi et al., 2013; Yu and Sheng, 2015). Many simulation results show that without soaking, the oil recovery is the highest with a fixed operation time (e.g., Li et al., 2016; Fragoso et al., 2018a). These imply that diffusion effect cannot be significant in improving oil recovery. Experiments showed that higher injection pressure resulted in miscibility and more oil could be produced (Li et al., 2017b). Next, solvent soaking mechanism is discussed in more detail.

Hawthorne et al. (2013) believed that the flow in shale and tight reservoirs is dominated by the flow in fractures, and the oil displacement mechanisms in conventional reservoirs do not apply. Based on that, they proposed

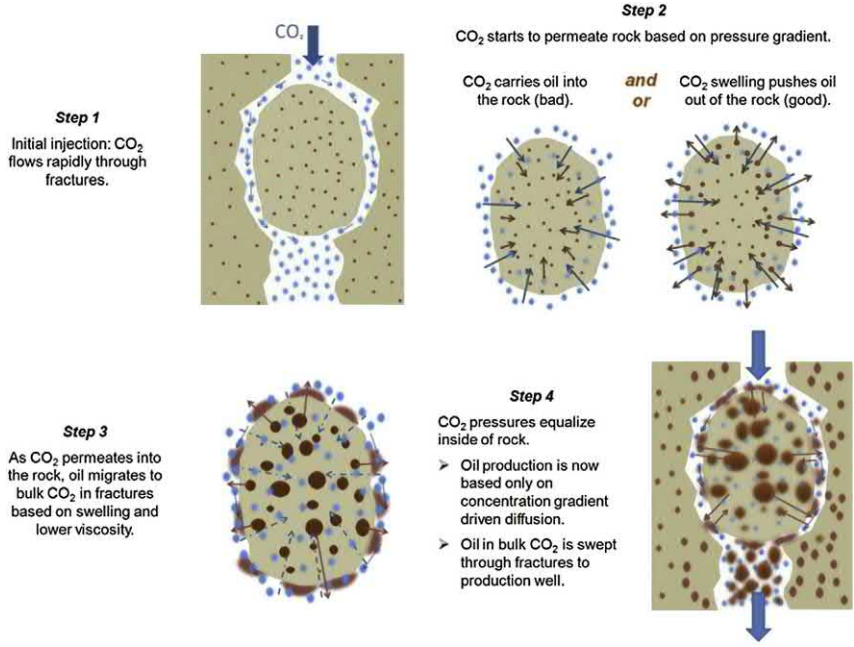

Figure 2.40 Conceptual steps for CO_2 EOR in fractured shale and tight reservoirs (Hawthorne et al., 2013).

CO_2-based EOR mechanistic processes, as explained in Fig. 2.40. These processes are related to what occurs in a huff-n-puff process and are reviewed here.

Hawthorne et al. (2013) used the experimental setup in Fig. 2.41 and used very small rock samples to have conducted CO_2 extraction experiments. In their experiments, a small core plug was inside the vessel and there is an empty space between the vessel wall and the plug, mimicking the flow through fractures in fractured shale and tight reservoirs. Fig. 2.42 shows the oil recovery of different molecular weight alkanes. It shows that there was no apparent lag in oil recovery even in the first 10 min of exposure. This observation indicates that the mechanism in Step 2 in Fig. 2.40 that CO_2 carries oil into the matrix so that oil production is reduced in the early time pressurization is not significant. Similarly, the absence of a very fast recovery in the first few minutes indicates that the initial oil swelling is not a significant recovery mechanism.

According to Step 3 in Fig. 2.40, oil swelling and lowered oil viscosity caused by CO_2 dissolution into the oil can likely enhance oil recovery. Fig. 2.40 shows that lower-molecular weight oil had a higher recovery,

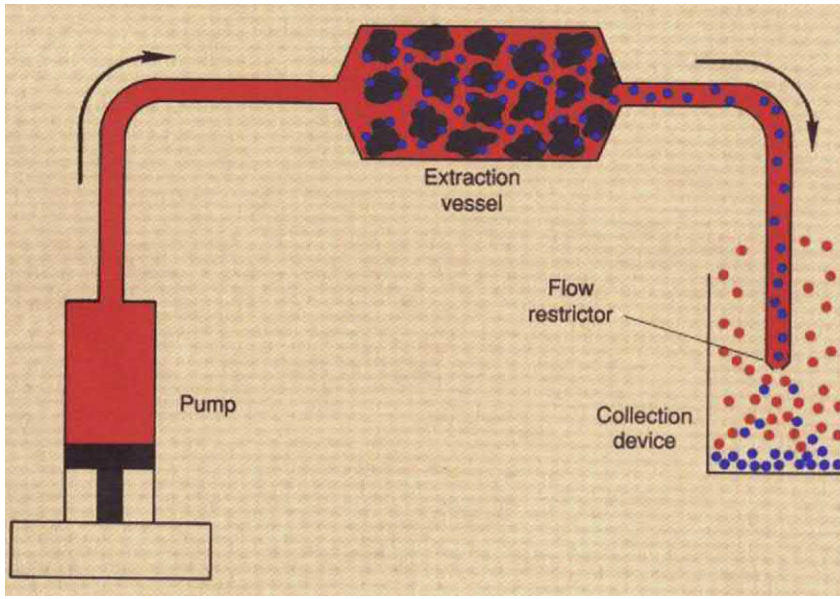

Figure 2.41 Schematic of a supercritical fluid extraction system. The supercritical fluid (e.g., CO_2) (red [light gray in print version]) is pumped to the extraction vessel where the analytes (purple [dark gray in print version]) are extracted from the sample matrix (brown [black in print version]). The analytes are then swept through the flow restrictor into the collection device, and the depressurized supercritical fluid (now a gas, for most fluids) is vented (Hawthorne, 1990).

indicating that mobilization of hydrocarbons into CO_2, rather than dissolution of CO_2 into the bulk oil, is a dominant recovery process. This could be due to solvation of oil into CO_2 phase and/or generation of a new "miscible" mixture of CO_2 and oil because both processes favor lighter oils.

The facts that the rock sample was so small, but the oil recovery process took hours indicate that the mechanism in Step 4 in Fig. 2.40 that oil concentration-gradient driven diffusion is very slow.

Alharthy et al. (2015) summarized the mechanisms in the extraction of oil from tight matrix during the solvent soaking process: repressurization (solution gas drive), viscosity and interfacial tension reduction through oil swelling, wettability alteration, and relative permeability hysteresis. By history matching soaking extraction experiments using numerical models, they investigate the EOR roles of different mechanisms, as shown in Fig. 2.43. It shows that the gravity only or gravity and diffusion only plays a negligible role in hydrocarbon recovery; the pressure gradient

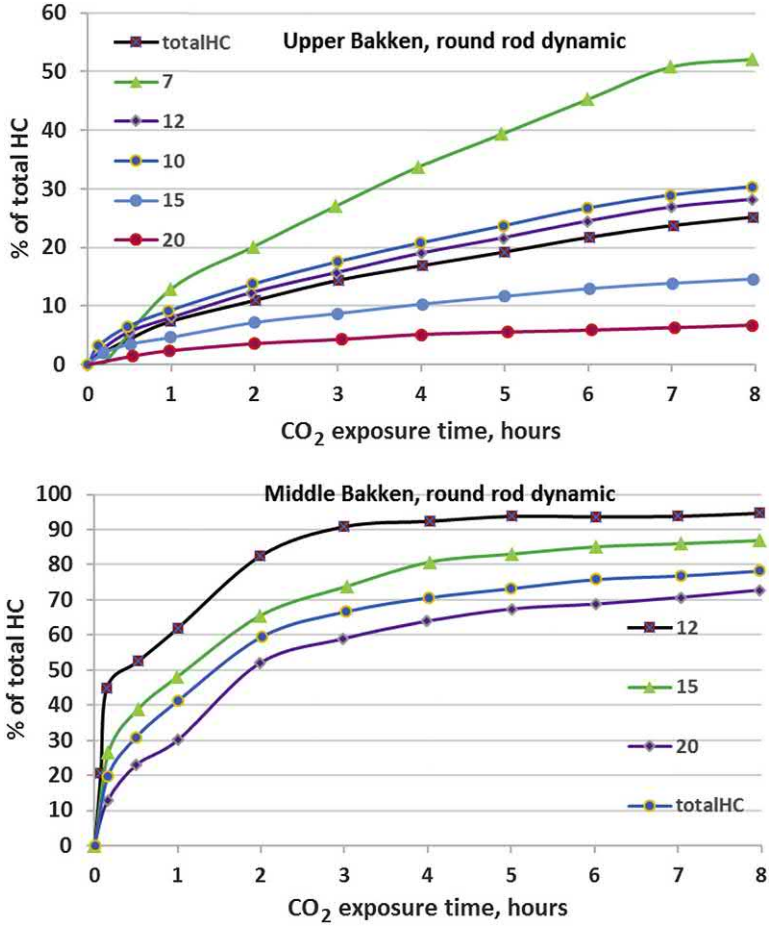

Figure 2.42 Oil recovery of different molecular weight alkanes under dynamic CO_2 exposure at 5000 psi and 110°C from rock samples of the round rod geometry of 1 cm diameter and 4 cm length. The numbers in the legend represent the hydrocarbon components, e.g., 7 represents C7; "total HC" represents the total hydrocarbon mass recovered regardless of molecular weight (Hawthorne et al., 2013).

(shown in DARCY in the figure) from matrix to fractures combined gravity plays an important role; inclusion of the gravity, pressure gradient, and diffusion in the simulation model makes the experimental data matched. They also showed the hydrocarbon recovery by solvent soaking with the mixture of 85% C_1 and 15% C_2, and nitrogen. Their study shows that the synergy between diffusion and pressure gradient plays the dominant role in solvent soaking; the dominant mechanism is diffusive-advective

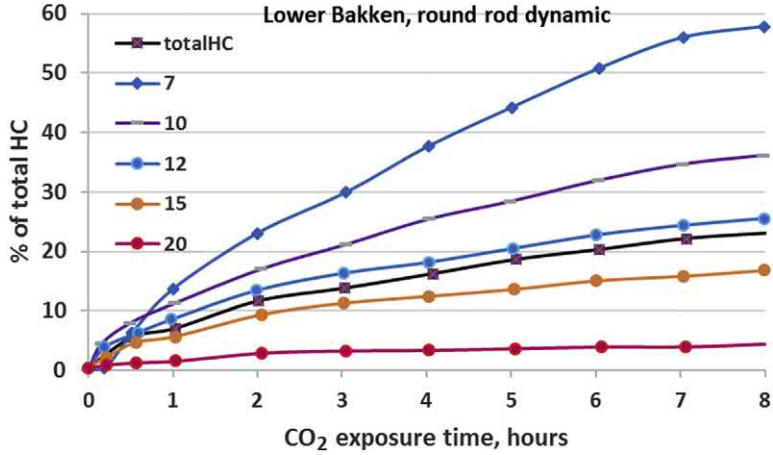

Figure 2.42 Continued

mass transfer. However, in their field-scale simulation of real huff-n-puff gas injection process, inclusion and without inclusion of molecular diffusion do not lead to a significant difference in oil recovery (less than 1%).

2.14 Gas penetration depth

It can be understood that gas penetration depth is critically important to effective huff-n-puff gas injection. A high injection rate and the formation heterogeneity will promote gas fingering, resulting in a higher penetration depth. In the case of CO_2 injection, it is easier to inject liquid CO_2. However, gaseous CO_2 will penetrate deeper into formation. From this point of view, preinjection of nitrogen or other dry gas to create a gas network will help make the subsequent liquid CO_2 penetrate deeper into the reservoir.

Li et al. (2018) studied gas penetration by simulation. They first did experiments using a core of 1.5 inches diameter which was saturated with oil. Methane was used as the gas. One huff-n-puff cycle has 1 h of huff, 7 h of soaking, and 4 h of puff. They used a simulation model to history match the experiment. Fig. 2.44 shows that methane mole fraction in oil, C_{1oil}. The model data indicated C_{1oil} reached 0.525 inches which was 70% of the core radius (0.75 inches) by the end of puff (1 h). At this distance, C_{1oil} is 0.1 which is an arbitrarily selected value. The experiment indicates the penetration velocity was 1 inch per hour

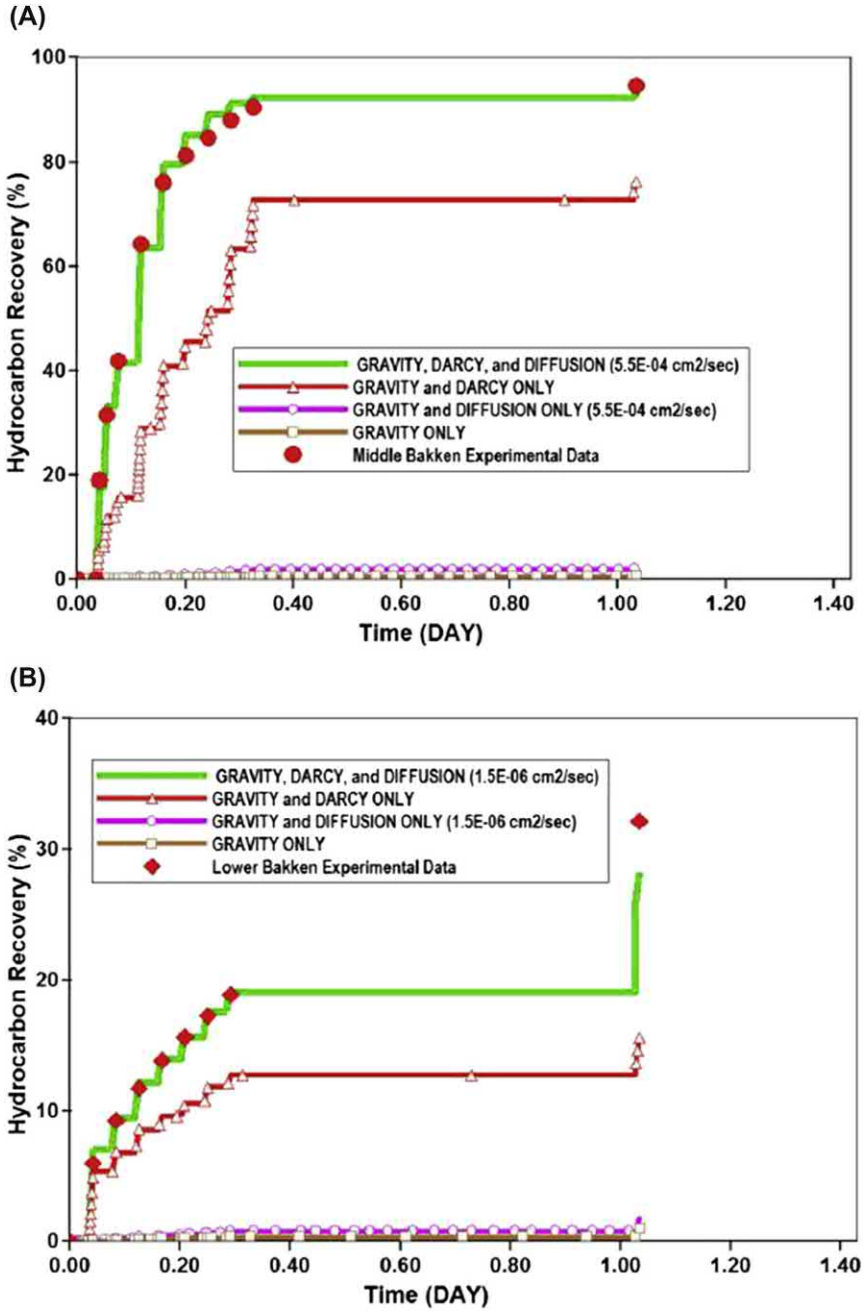

Figure 2.43 Hydrocarbon recovery by CO_2 solvent soaking (simulation vs. experiments), (A) from a Middle Bakken rock sample; (B) from a Lower Bakken rock sample (Alharthy et al., 2015).

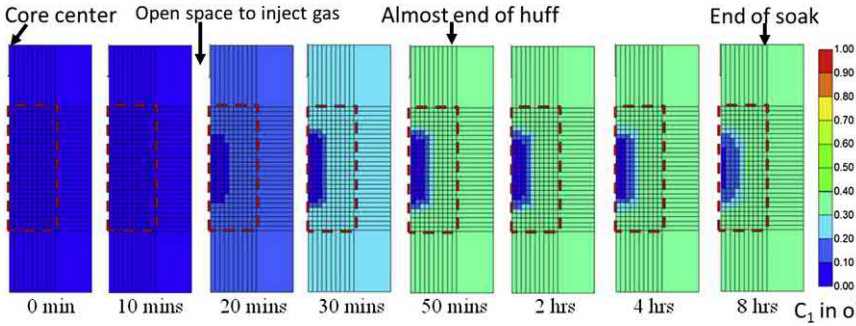

Figure 2.44 C_1 mole fraction in oil phase (C_{1oil}) during the injection time and soaking time in the third cycle.

(2 ft per day). This apparently fast penetration velocity may not be extended to a large field scale. This figure also shows that methane did penetrate fast in the first hour, but it did not penetrate further too much toward the core center during the 7 h of soak. This observation implies that long soaking is not effective in gas huff-n-puff in terms of gas diffusion into the oil phase, which is consistent with the results by Sheng (2015d; Yu et al., 2016a).

For a large-scale field model, injected gas may not penetrate uniformly into the matrix as there are some natural and induced fractures, in addition to hydraulic fractures, as an example of CO_2 mole fraction in oil (CO_{2oil}) is shown in Fig. 2.45. In such field model, the penetration depth is defined as

$$\sum V_i \phi_i S_{oi} y_i = A_f D \frac{\sum \phi_i V_i S_{oi}}{\sum \phi_i V_i} \times \frac{\sum \phi_i y_i}{\sum \phi_i V_i} \tag{2.23}$$

In the above equation, the summations are carried over the block i where gas mole fraction in oil (y) is above 0.4, V is the block volume, ϕ is the porosity, S_o is the oil saturation, A_f is the fracture surface area, and D is the penetration depth. Note $y = 0.4$ is arbitrarily used because in a base field model, the average y in the penetrated area is found as 0.4.

Based on the above definitions, for a field-scale model which was validated by Sheng (2017b), one cycle has 100-day huff time, 100-day puff time, and no soaking time. In the model, the matrix permeability is 300 nD, the natural fracture spacing is 2.27 ft, and the induced fracture spacing near the hydraulic fracture is 0.77 ft. The injected CO_2 diffusion coefficients in the oil phase and in the gas phase are 2.12e-6 cm^2/s and 2e-5 cm^2/s,

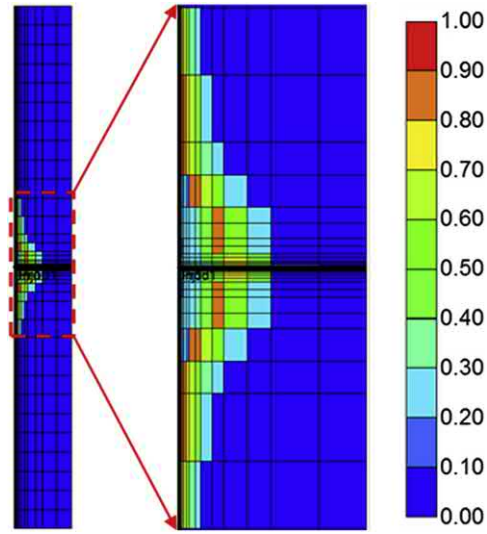

Figure 2.45 Distribution of CO_{2oil} in a field-scale model at the end of huff period.

respectively. The predicted gas penetration depth is shown in Fig. 2.46. At the end of 100-day injection, the CO_2 penetrates 105.6 ft (Li et al., 2018).

Li et al. (2018) did more sensitivities using the field-scale base model. Interestingly, when the matrix permeability is increased from 300 nD to 3000 nD, the CO_2 penetration depth is only increased from 105.6 ft to 106.5 ft. Fractures play a very important role. When the induced fracture spacing is increased from 0.77 ft in the base model to 7.7 ft to no fracture, the penetration depth is decreased from 105.6 ft to 68.7 ft to 0.31 ft. It is expected that gas diffusion coefficient in the oil phase is very sensitive. However, Sorensen et al. (2018) estimated that the CO_2 penetration radius may be 50-70 ft around the wellbore based on the amount of CO_2 injected, the matrix porosity of 0.06-0.08 and CO_2 saturation of 0.4-0.6, for their field injection test in an unfractured vertical well. Their simulation model estimated a maximum penetration depth of 140 ft in some layers. Their model was a dual-porosity model with the matrix permeability being in the order of microdarcies.

2.15 Field projects

Table 2.4 summarizes the field projects for huff-n-puff gas injection in shale and tight reservoirs published so far. Field project with some detailed

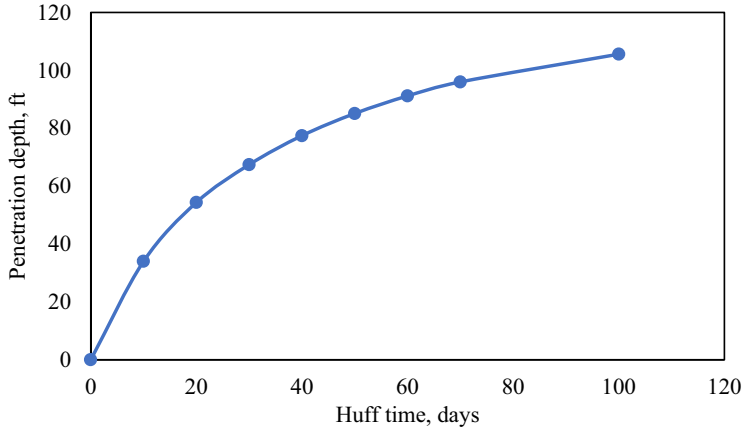

Figure 2.46 CO_2 penetration depth at different injection time in the first huff-n-puff cycle.

data are discussed. A performance summary is provided at the end of this section.

2.15.1 CO_2 huff-n-puff in Bakken formation, Elm Coulee field

Early in 2008 before the shale boom, a CO_2 huff-n-puff injection pilot was conducted in the Elm Coulee field in the Bakken formation in the North Dakota part (Hoffman and Evans, 2016). No injectivity problem was observed, with injection rate being 1 MMSCF/day at the injection pressure of 2000–3000 psi. Having 30 days of injection, the pilot showed little to no rate increase.

2.15.2 CO_2 huff-n-puff in Burning Tree-State No. 36-2H well in the Montana part of Bakken formation

Continental Resources, Enerplus, and XTO Energy jointly carried out CO_2 huff-n-puff injection in the Burning Tree-State No. 36-2H well in Richland County in the Montana part of the Bakken formation in early 2009. The horizontal well was completed in the Middle Bakken and was stimulated using single-stage hydraulic fracturing. During 45 days of injection from January to February 2009, approximately 45 million cubic feet (2570 tons) of CO_2 were injected. The injection rate was 1.5–2 MMSCF/d at 2000–3000 psi. After that the well was soaked for 64 days before production (Hoffman and Evans, 2016).

Table 2.4 Summary of field projects for huff-n-puff gas injection.

Start year	Field or shale	Inj. Gas	Huff, days	Soak, days	Puff, days	# Wells	Injection rate and pressure	Performance	References
2008	Elm Coulee, Bakken, ND	CO_2	30			1	1 MMSCF/d, 2000−3000 psi	Little or no oil increase	Hoffman and Evans, 2016
2009	36-1H well, Bakken, MT	CO_2	45	64		1	1.5−2 MMSCF/d, 2000−3000 psi	Gas breakthrough	Hoffman and Evans, 2016; Sorensen and Hamling, 2016
2014	Bakken, ND	CO_2	20−30	20				Gas breakthrough at 900 ft away	Hoffman and Evans, 2016
2008	Farshall field, Bakken, ND	CO_2	11			1		Gas breakthrough in 11 days of injection, oil rate increased	Sorensen and Hamling, 2016
	Eagle Ford, TX	Methane	100	0	100			20% increase in oil recovery for 114 months (predicted)	Orozco et al., 2018
2012	Eagle Ford, Gonzales, TX	lean gas	28−42			1	2−3 MMSCF/d, 6000 psi	Oil rate increased	Hoffman, 2018
2015	Eagle Ford, Gonzales, TX	lean gas?				4		Oil increased 17% after 1.5 years	Hoffman, 2018
2015	Eagle Ford, Gonzales, TX	lean gas?				6		Oil increased 20% after 2.5 years	Hoffman, 2018
2015	Eagle Ford, la Salle, TX	lean gas?	56−70, 28−42		60−90, 60	4	2−4 MMscf/d, below fracture pressure	Oil rate doubled	Hoffman, 2018
2015	Eagle Ford, Atascosa, TX	rich gas				1	2.5 MMscf/d, below fracture pressure		Hoffman, 2018
2015	Eagle Ford, Atascosa, TX	rich gas				1	2.5 MMscf/d, below fracture pressure		Hoffman, 2018
2016	Eagle Ford, Gonzales, TX	lean gas?				32			Hoffman, 2018
2017	Middle Bakken	CO_2	3.2		14.6	45 minutes (?)	16-12 gallos/min., 9400-9470 psi	CO_2 preferentially produced light oil	Sorensen et al., 2018

From January to March 2010, there was a gradual oil productivity increase. The peak oil rate reached 44 bbl/d in March 2010 (a higher rate than what was achieved during any of the 14 months immediately prior to the injection test). However, the operator confirmed that the higher production rate might be related to workover activities on the well as opposed to delayed CO_2 effects. Although the Burning Tree well did not see a dramatic production increase, CO_2 was able to be injected (no injectivity issue) (Sorensen and Hamling, 2016).

One reason for the poor performance in the above tests in Montana and North Dakota could be the too short injection duration (45 and 30 days, respectively). In the North Dakota test, CO_2 broke through an offset well about 5000 feet away in less than 2 weeks. This could be another reason for the poor performance. The third reason may be too low injection pressure (2000−3000 psi for both the tests).

2.15.3 Huff-n-puff CO_2 injection in Parshall field

EOG conducted a CO_2 injection test in NDIC 16713 in the Parshall field in the Mountrail County in late 2008. A horizontal well was drilled into the Middle Bakken and was completed using a six-stage hydraulic fracture treatment. An estimated 30 MMSCF of CO_2 were injected using a huff-and-puff approach. After 11 days of injection, CO_2 broke through the offset well NDIC 16768, located one mile west of the NDIC 16713. The oil rates for the test well and offset wells increased after injection.

The Parshall field has a high degree of natural fracturing, and the high mobility of CO_2 in this fractured system indicates that conformance control is likely a major factor in designing EOR operations. Of interest is the fact that three other offset wells located within one mile of the injector did not see CO_2 breakthrough, suggesting that understanding the local natural fracture system is key to EOR planning (Sorensen and Hamling, 2016).

2.15.4 Eagle Ford project in La Salle County, TX

Four wells are in huff-n-puff injection starting in 2015. Initially gas was injected for 6 months to fill up the reservoir void. Then wells produced for 2−3 months followed by 8−10 weeks. This pattern was repeated for four cycles. After that, a shorter cycle of 4−6 weeks of injection and soak time and 2 months of production was used. The average well oil rate and the cumulative production within the lease are shown in Fig. 2.47. The oil rate clearly shows the increase (about doubled) from huff-n-puff

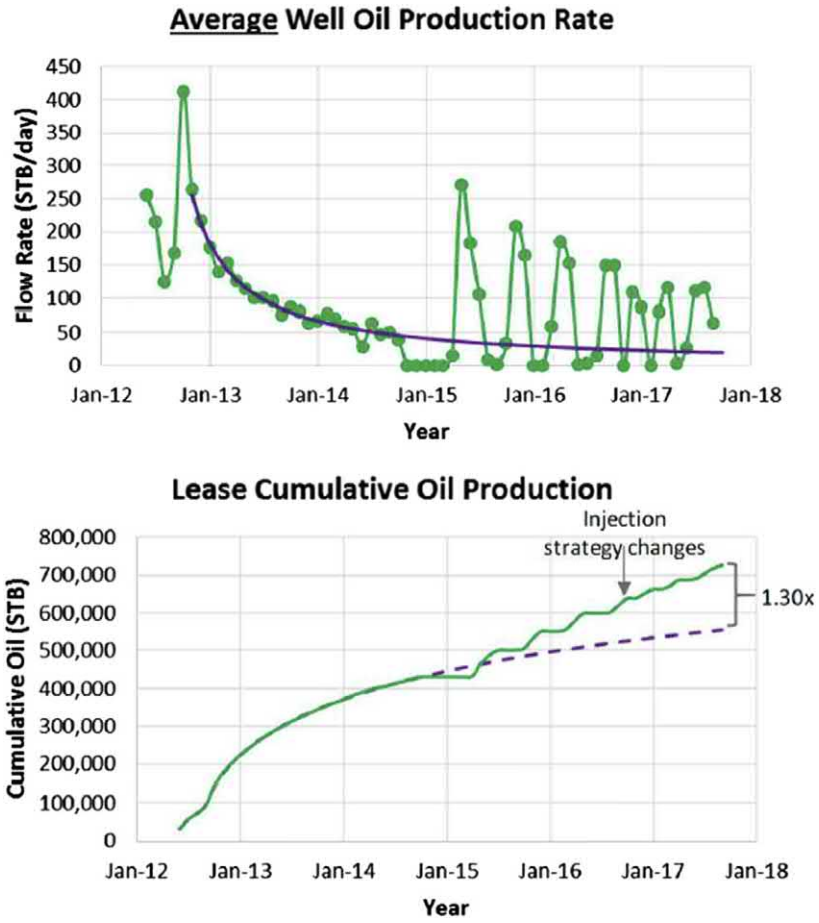

Figure 2.47 Average well oil rate and the cumulative production within the pilot lease (Hoffman, 2018).

injection. The cumulative oil production in 6 years had been increased by 30%. Hoffman (2018) did a simple economic estimate. It was assumed that the infrastructure/capital costs were $1 million per well that included the installation costs, well workover, and other costs; the gas price was $2.5/Mscf, and oil price was $50/bbl; the discount rate was 15%; the gas used for the initial fill up was considered "purchased," and 20% of the subsequent gas injected was considered the gas cost because most of the injected gas would be produced back; 10% of the amount of injected gas was needed to operate the fired compressors. Under those assumptions, the pilot internal rate of return was 17.7% and the payback was 2.3 years. This pilot project appeared to be a little over breakeven.

2.15.5 CO_2 injection in an unfractured vertical well in the Middle Bakken

In shale and tight reservoirs, fractured wells are commonly used. However, fractured wells may induce small fractures to form a stimulated reservoir volume, which may complicate the study of CO_2 diffusion in the matrix. The heterogeneity of formation may leave a long horizontal well unideal well type to study EOR mechanisms. To avoid these complexities, the Energy and Environmental Research Center (EERC) and XTO Energy conducted a pilot CO_2 injection in an unfractured vertical well in one virgin Middle Bakken area (Sorensen et al., 2018). The well name is Knutson-Were 34-3WIW, North Dakota state well ID number 11413. First, a small scale pretest was carried out on April 3, 2017. 16 tons of CO_2 was injected enough to infill the tubing and build pressure on the perforations. When the pressure was built to 9113 psi that was higher than the reservoir pressure of 8668 psi, the upper packed that isolated the injection zone failed. CO_2 did not enter the formation. After the packer was repaired, the well was swabbed and 62 barrels of fluid was produced. After swabbing, the bottom-hole pressure (BHP) was about 7500 psi. Then a main test was initialed at 7 pm MDT (Mountain Daylight Time) on June 24, 2017 and concluded at 5 am June 28, 2017. Total 98.9 tons of CO_2 were injected for about 3.2 days. On June 27, the well was shut in for a about 5 hours to run a pressure falloff test.

After the injection was ended on June 28, the well was shut in for soaking until it was opened on July 7 (about 9 days of shut in). At this time, the BHP was 8740 psi close to the early reservoir pressure. After opening the well, gas flowed 8.5 hours, essentially CO_2 from the tubing with some traces of hydrocarbons in the last 2 hours. The BHP dropped to 100 psi. Those data indicated that a significant amount of injected CO_2 was voided from the reservoir. Because the well could not sustain flow, the well was put back to shut in for another 6 days until July 13. The total soak time was about 13.6 days. The BHP was built up to 3116 psi, which might result from the reservoir oil migration to the near wellbore zone. After the well was open and produced a mix of CO_2 and hydrocarbon gas for 10.5 hours, some oil started to flow to the surface at a rate of about one eighth of a barrel per minute. By that time, the BHP was decreased to 1890 psi that was below the saturation pressure. Within 45 minutes of flow, 9 barrels of oil was produced. Analysis of produced oil compositions shows that the oil composition produced after CO_2 injection was lighter than that before.

2.15.6 Summary of gas huff-n-puff performance

Overall, some learnings from those gas huff-n-puff pilots presented above may be summarized in the following.

- Gas injectivity did not seem to be a problem.
- Gas breakthrough was observed in some projects. The success of a project required the confinement of the injection pattern.
- Later projects performed better than the earlier one.
- Tens of CO_2 huff-n-puff field tests including some large-scale field projects have been carried out in Chinese low-permeability sandstone reservoirs. Most of those tests were claimed to be successful. Some tests were in tight oil reservoirs.
- One of the important economic parameters is gas utilization factor. The above projects did not report this data. In conventional reservoirs, the CO_2 utilization factors reported are 1.3 MSCF/bbl (Thomas and Monger-McClure, 1991), and 0.3–10 MSCF/bbl for light oils and 5–22 MSCF/bbl for heavy oils (Mohammed-Singh et al., 2006). For shale reservoirs, Gamadi et al.'s (2014a) simulation data showed to be about 10 MSCF/bbl.

CHAPTER THREE

Asphaltene precipitation and deposition in a huff-n-puff process

Abstract

Asphaltene precipitation and deposition may cause formation damage in conventional reservoirs. In shale and tight reservoirs, pore and throat sizes are smaller than those in conventional reservoirs. This problem could be more serious in shale and tight reservoirs. This chapter is dedicated to the asphaltene precipitation and deposition in a huff-n-puff process. Experimental results and numerical analysis are presented. The mechanisms of asphaltene deposition are discussed. Effect of asphaltene deposition on huff-n-puff optimization is also discussed.

Keywords: Asphaltene precipitation; asphaltene deposition; formation damage; pore throat.

3.1 Introduction

It has been reported that asphaltene precipitation and deposition may cause formation damage in conventional reservoirs. In shale and tight reservoirs, pore and throat sizes are smaller than those in conventional reservoirs. This problem could be more serious in shale and tight reservoirs. From another angle, huff-n-puff has been found to an effective EOR method. This chapter is dedicated to the asphaltene precipitation and deposition in a huff-n-puff process. Experimental results and numerical analysis are presented.

3.2 Experiments of asphaltene precipitation and permeability reduction

Maroudas (1996) found that particles with a size greater than 1/3 of the size of a pore or a throat would block the pore or the throat. It was found that if the 1/7 rule was used, oil recovery was improved. Ershaghi et al. (1986) suggested to use the more stringent 1/7 rule. The known 1/3-1/7

Enhanced Oil Recovery in Shale and Tight Reservoirs
ISBN: 978-0-12-815905-7
https://doi.org/10.1016/B978-0-12-815905-7.00003-7

rule-of-thumb was used in the industry. Partz et al. (1989) evaluated this rule-of-thumb.

To study the asphaltene precipitation, Shen and Sheng (2016) first measured the asphaltene sizes under CH_4 and CO_2 injection. The dead oil sample from a Wolfcamp shale reservoir was used. The viscosity was 3.66 cP and the density was 0.794 g/cm^3. The experimental setup is shown in Fig. 3.1. It mainly consisted of a reservoir cylinder, a filter cylinder, and a

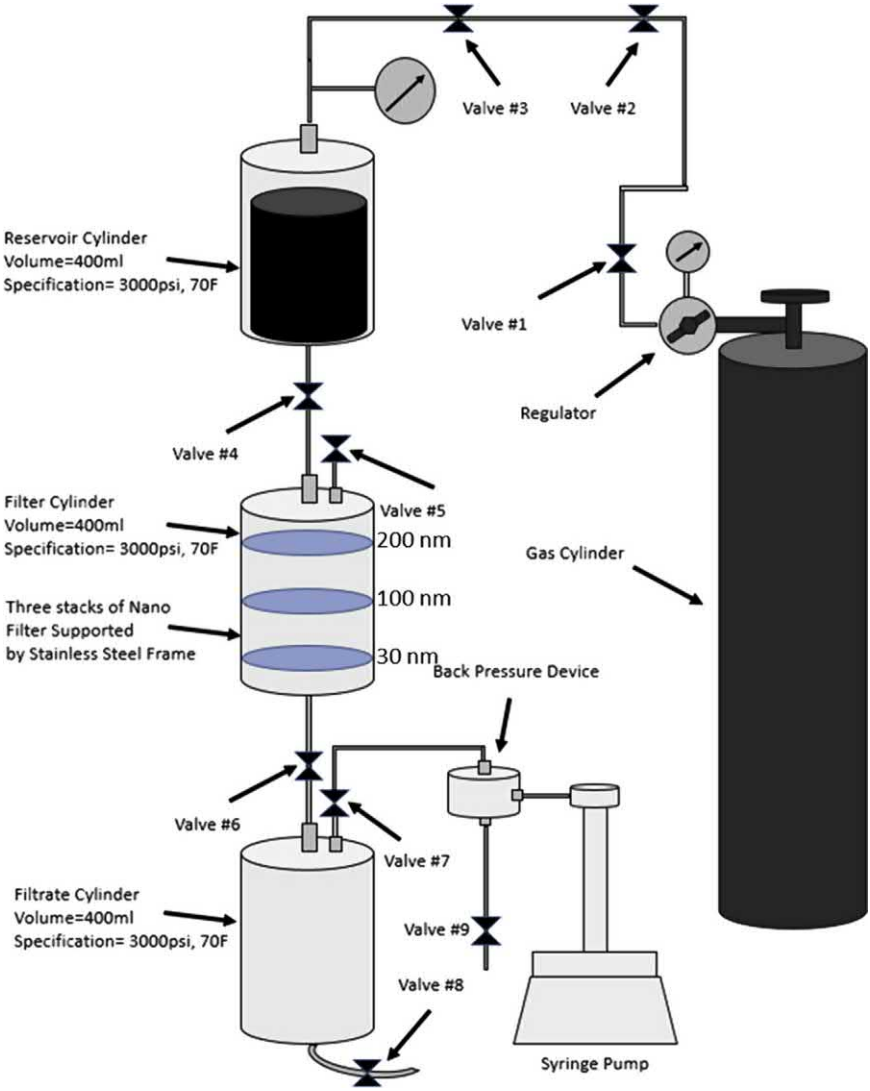

Figure 3.1 Schematic to measure asphaltene particle sizes.

filtrate cylinder. The reservoir cylinder is a 400 mL stainless steel core holder to store the dead crude oil and injected gas. Three stacks of nanomembranes of 200, 100, and 30 nm were placed from the top to the bottom in the filter cylinder, and they are supported by a stainless-steel frame. The filtrated crude oil was deposited in the filtrate cylinder.

The apparatus was designed to study the effect of gas concentration on asphaltene precipitation. For each test, 200 mL of oil was poured into the reservoir cylinder. Then the gas cylinder was connected to the reservoir cylinder, and the oil was saturated at a constant pressure. The pressure was maintained for 8 h for equilibrium. The dissolved gas mole fraction at each pressure was obtained from the gas solubility curve obtained prior to the experiment. The filter cylinder and filtrate cylinder were precharged with the gas at a pressure of 50 psi lower than that in the reservoir cylinder using a back-pressure regulator to let the crude oil go through the membranes. Then hot heptane was injected into the reservoir cylinder and forced through the membranes to wash away the oil left in the membrane and in the system, as asphaltene does not dissolve in heptane. This washing process was continued until heptane collected from the outlet of filtrate cylinder was clean. The amount of asphaltene precipitated on each membrane was measured using a modified IP143 standard test method (Muhammad et al., 2003).

Fig. 3.2 shows the total amount of precipitated asphaltene at different injected CO_2 and CH_4 concentrations. The total amount of precipitated

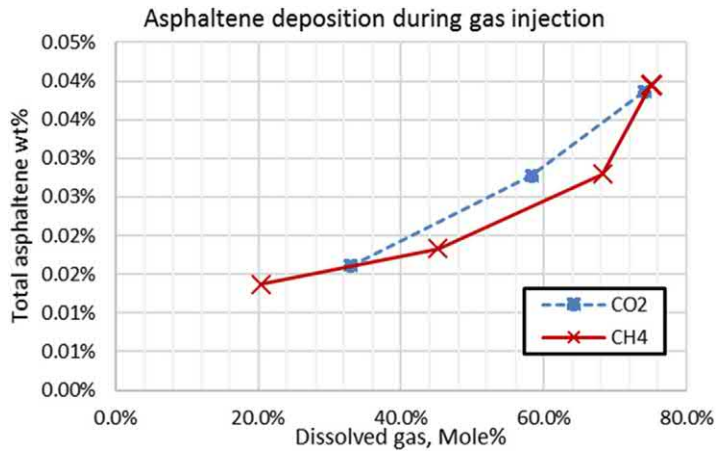

Figure 3.2 Total amount of precipitated asphaltene content at different injected CO_2 and CH_4 concentrations.

asphaltene content is the sum of the amount of asphaltene precipitated on each membrane. It shows that with the increase in injected gas concentration, more asphaltene precipitated. It seems that the precipitated asphaltene content for the Wolfcamp shale oil was very low.

Fig. 3.3 shows the fraction of amount of precipitated asphaltene on each of the membranes over total amount of precipitated asphaltene. In the filtration process, the crude oil flowed through the 200 nm membrane firstly, then through 100 nm of the membrane, and finally through 30 nm of the membrane. Asphaltene particles with a size larger than 200 nm could not go through the membrane of a 200 nm pore size. This part of asphaltene particles would precipitate on the 200 nm membrane. Asphaltene particles of a size smaller than 200 nm but larger than 100 nm could pass through the 200 nm membrane but would precipitate on the 100 nm membrane. Thus, the asphaltene that precipitated on 200 nm, 100 nm, and 30 nm membranes had the sizes >200 nm, 100 ~ 200 nm, and 30 ~ 100 nm, respectively. The amount of asphaltene precipitation on the 200 nm membrane increased along with the increment of injected gas concentration, which indicated that the injected gas helped asphaltene form larger aggregates. CO_2 had a stronger effect on increasing the asphaltene aggregation size than CH_4.

The above data show that more than half of asphaltene aggregates had the sizes larger than 30 nm. However, the pore throats of several shale cores shown in Fig. 3.4 suggest that majority of pore throat sizes were smaller than 30 nm. According to the 1/3-1/7 rule of thumb, asphaltene aggregates cannot flow through these shales. Fortunately, the asphaltene contents shown in Fig. 3.3 were very low. In other words, asphaltene content was

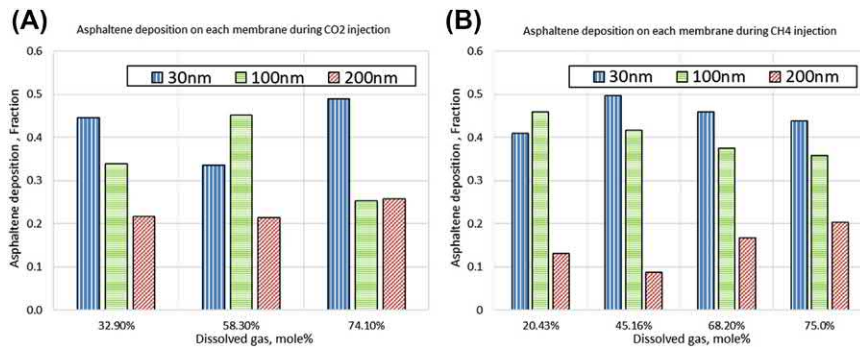

Figure 3.3 Fractions of asphaltene precipitation on each membrane during (A) CO_2 and (B) CH_4 injection.

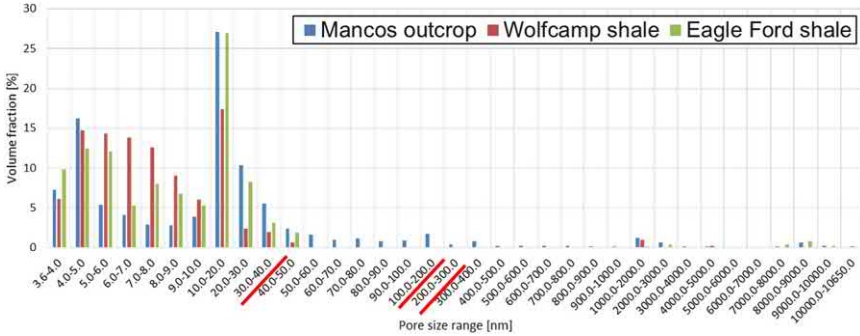

Figure 3.4 Pore throat size distribution for several shale cores.

very low, although the asphaltene aggregates were large, the resulting formation damage may not be serious. Next, we will study the degree of formation of damage during huff-n-puff gas injection.

Shen and Sheng (2017a) compared the pore size distributions (PSD) before and after huff-n-puff CO_2 injection. The PSD was measured by mercury injection. The Wolfcamp oil was used for EF#1 and EF#2 cores. For the comparative purpose, the mineral oil decane was also used for EF#5 core. Decane did not have asphaltene. Six cycles of huff-n-puff CO_2 injection were carried out. Fig. 3.5 shows the log differential pore volume (dv/dlogD) versus pore diameter (D). It gives the distribution of pore throats with different diameters in the tested core samples. The peak of such plot indicates the dominant pore size range. The peak of EF#1 lies in the range from 0.0036 to 0.020 μm (*red*), and the peak of EF#2 lied from 0.02 to 0.10 μm (*dot light blue*) before huff-n-puff. After huff-n-puff, the pore throats of EF#1 (*solid blue*) had higher peaks in small diameter ranges, but lower peaks in larger diameter ranges. The PSD curve for EF#2 (*dotted orange*) shifted left from 0.05 to 0.7 μm after huff-n-puff, indicating the pore throats becoming smaller. For EF#5 core, the peak of the PSD curve lies from 0.10 to 1 μm before (*light green*) and after (*light purple*) huff-n-puff, because the mineral oil decane did not have asphaltene. The above results become more obvious when the histogram and accumulative percentage of the PSD versus pore throat diameter are plotted, as shown in Figs. 3.6–3.8, respectively for EF#1, EF#2, and EF#5.

Two more cores EF#3 and EF#4 were used to compare the permeability before and after huff-n-puff CO_2 injection. For the huff and puff injection, the huff pressure was 8.27 MPa, the soaking time was 6 h, and

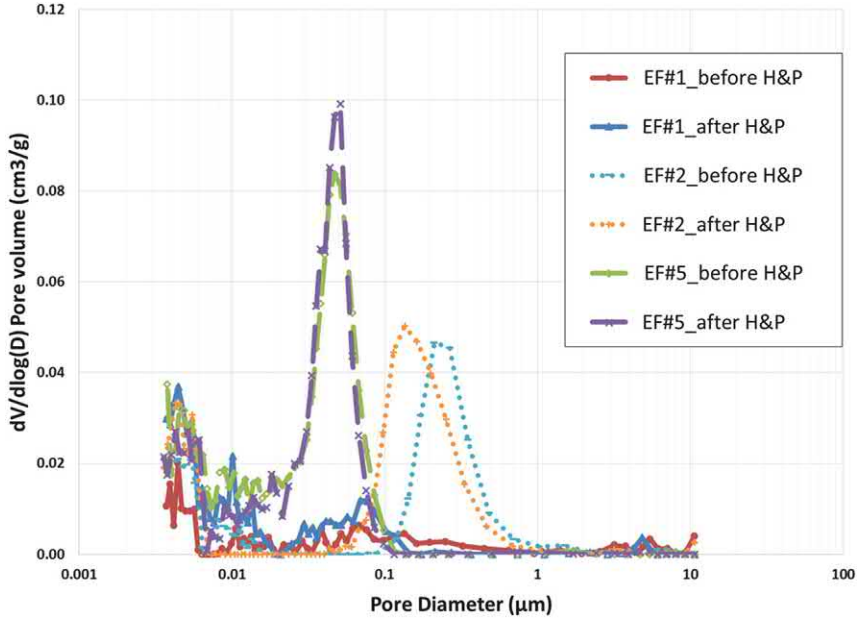

Figure 3.5 PSD of tested core samples before and after CO_2 huff and puff injection.

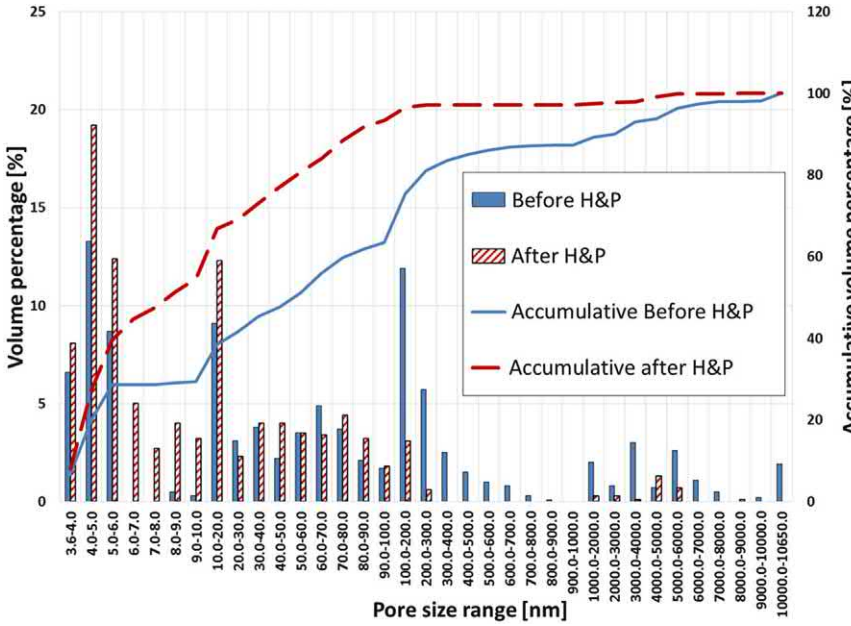

Figure 3.6 PSD for EF#1 core before and after huff and puff CO_2 injection.

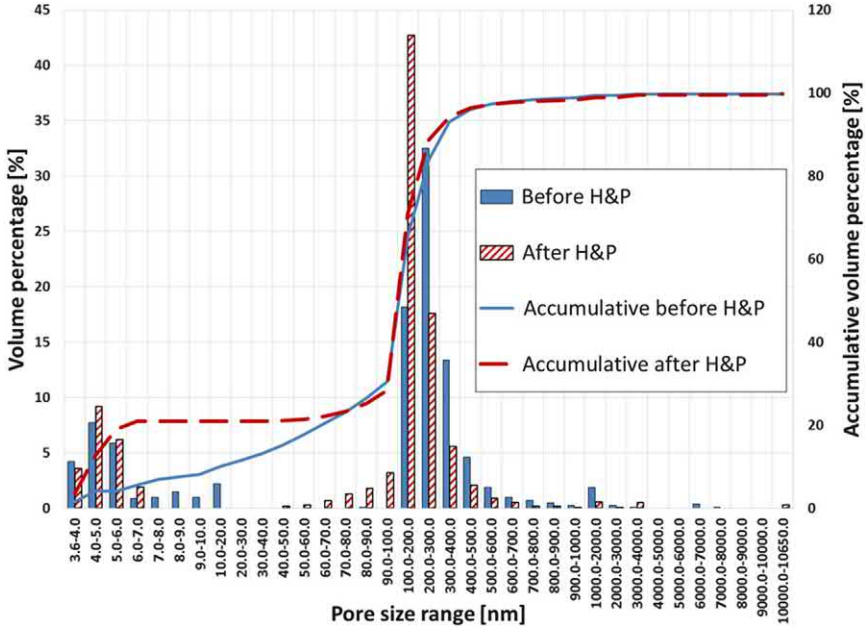

Figure 3.7 PSD for EF#2 core before and after huff and puff CO_2 injection.

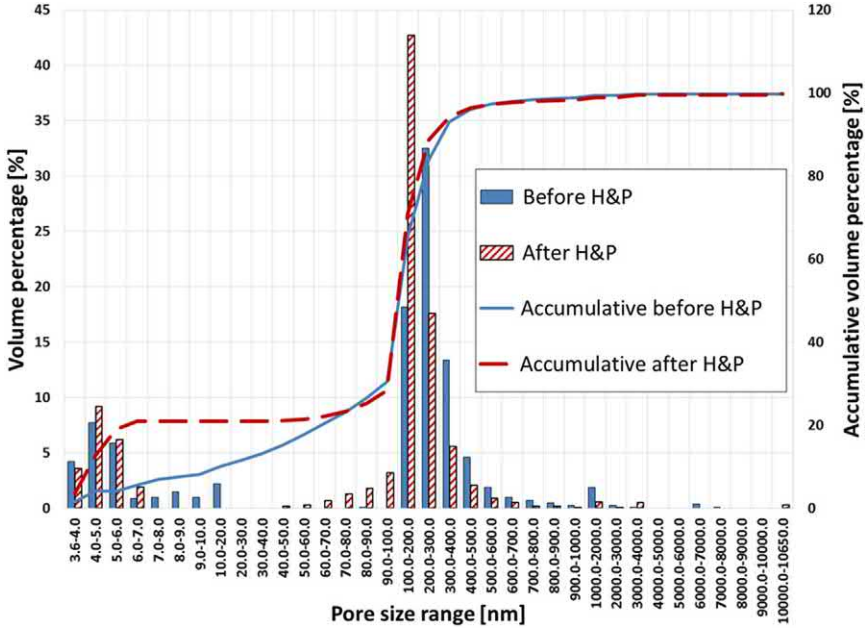

Figure 3.8 PSD for EF#5 core before and after huff and puff CO_2 injection.

the puff time was 18 h. The whole injection process is performed isothermally at 21°C. Before the huff and puff injection, EF#3 and EF#4 were saturated with Wolfcamp oil and decane, respectively. Their measured permeabilities were 126 nD and 86.7 nD for EF#3 and EF#4, respectively. After six cycles of huff and puff injection, their remeasured permeabilities were 78.5 nD and 81.7 nD for EF#3 and EF#4, respectively. The permeability for EF#3 using Wolfcamp oil was decreased by 47.5 nD after huff and puff injection, while the permeability for EF#4 using decane was almost unchanged, as shown in Fig. 3.9.

The permeability reduction is consistent with the changed PSD. After asphaltene deposits onto the rock surface, the pores become smaller or blocked. Behbahani et al. (2013) found that 60%–80% of the total damage by asphaltene deposition was caused by mechanical plugging that was recovered by cyclohexane reverse flooding; 20%–40% by adsorption that was recovered by toluene reverse flooding, but the recovery process took a long time. In another experimental study, Behbahani et al. (2015) observed that the carbonate cores experienced more particle plugging compared to the sandstone cores. In carbonate, the inner surfaces of a core contain more polar groups that can exert polar interactions with asphaltene surface group (Hamadou et al., 2008), which results in a high adsorption rate. In low permeability cores such as carbonate, the plugging mechanism acts

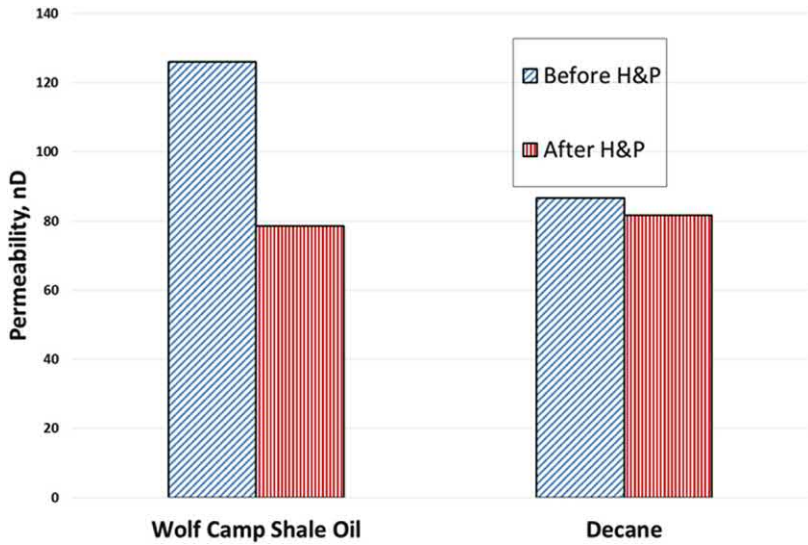

Figure 3.9 Comparison of permeability before and after huff and puff injection.

like a snowball growth. The complete plugging could happen after a continuous asphaltene adsorption. In shale, clay is a polar component. A higher adsorption rate would be expected. And nanometer pores may lead to the snowball growth of asphaltene to plug the pores. It needs to be mentioned that the Wolfcamp shale oil used in this study was dead oil. Permeability reduction by asphaltene deposition for live reservoir fluid flooding was found higher than that for dead oil flooding (Behbahani et al., 2015).

3.3 Deposition mechanisms

In another study, Shen and Sheng (2017b) conducted experiments to quantify the asphaltene deposition mechanisms during CO_2 huff-n-puff injection in an Eagle Ford shale core using Wolfcamp shale oil. After six cycles of CO_2 huff-n-puff were completed, a piece of core of 0.9 cm length was cut from the core plug using hacksaw for the n-heptane and toluene reverse flooding tests. These tests were used to measure permeability. The schematic of the flooding system is shown in Fig. 3.10. A shorter piece of core was used instead of the whole core to shorten the flooding test time.

Firstly, the n-heptane was injected at 0.01 cc/min by using the combination of two syringe pumps so that the n-heptane injection could be continued until a stable differential pressure between the two ends of the core sample was reached. Alternatively, a Quizix pump could replace two syringe pumps for continuous pumping. The first period of the n-heptane reverse flooding lasted for around 3000 min until the differential pressure between the two ends of the core sample became stable (see Fig. 3.11).

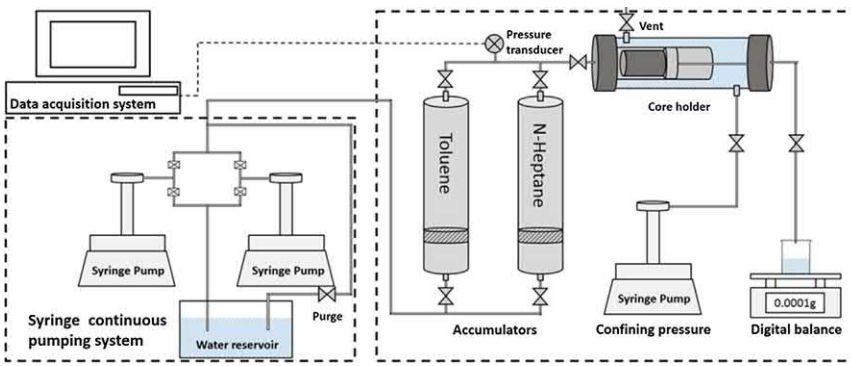

Figure 3.10 Schematic of the core flooding system.

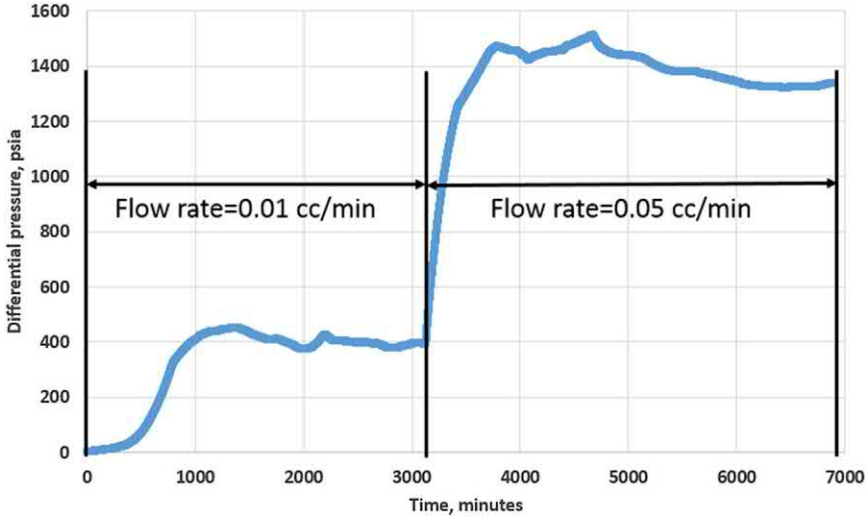

Figure 3.11 History of differential pressure between the two ends of core sample during the n-heptane reverse flooding.

The stabilized differential pressure was 2.69 MPa (390 psia). Given that the viscosity of n-heptane at 2.69 MPa (390 psia) at room temperature is 0.399 cP (Sagdeev et al., 2013; Zhang and Liu, 1991), the permeability was calculated to be 198.8 nD using Darcy's Law. This permeability is considered the permeability with adsorption but without entrainment because the entrainment of asphaltene particles only occurs when the interstitial velocity is higher than a critical velocity (Behbahani et al., 2012; Behbahani et al., 2015; Bolouri et al., 2013; Wang et al., 1999), and n-heptane cannot dissolve asphaltene. This rate of 0.01 cc/min was considered below the critical velocity, as the differential pressure was not significantly reduced as the flood continued. The higher pressure drop in the early time was caused by the existence of residual oil of higher viscosity.

To quantify the effect of entrainment (mechanical plugging) of asphaltene particles, the flow rate of n-heptane injection was increased from 0.01 to 0.05 cc/min. The differential pressure increased fast first owing to the increased rate, but it decreased later indicating the removal of asphaltene plugging. The flow rate of 0.05 cc/min was approximately equivalent to 0.0008 cm/s for this core plug. This velocity was considered above the critical velocity, as the plugging was removed at this velocity. Using the stable differential pressure at around 7000 min and the viscosity of n-heptane of 0.427 cP at 9.24 MPa (1340 psia) at room temperature (Sagdeev et al., 2013; Zhang

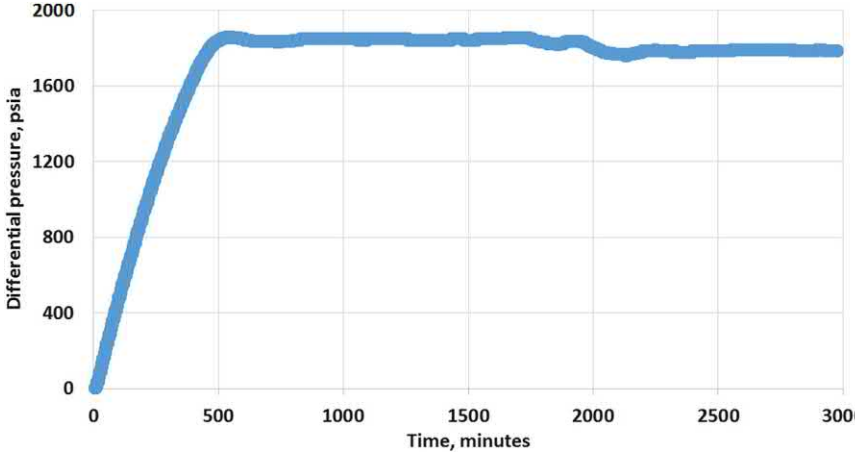

Figure 3.12 History of the differential pressure between the two ends of the core sample during the toluene reverse flooding.

and Liu, 1991), the permeability was calculated to be 309.7 nD by Darcy's equation. Thus, the permeability reduction caused by asphaltene mechanical plugging during huff-n-puff CO_2 injection was 110.9 nD (309.7−198.8).

Since toluene could dissolve asphaltene, the deposited asphaltene by the adsorption mechanism might be removed by toluene reverse flooding. After the n-heptane reverse flooding, toluene reverse flooding was carried at 0.05 cc/min continuously until a stable differential pressure was reached (see Fig. 3.12).

The stable differential pressure was 12.3 MPa (1785 psia). Using the viscosity of toluene of 0.617 cP at 12.3 MPa (1785 psia) at room temperature (Krall et al., 1992), the estimated permeability was 332.9 nD. After the n-heptane and toluene reverse flooding, asphaltene deposition by both mechanical plugging and adsorption mechanisms might be removed. The total permeability reduction by the asphaltene deposition was 134.1 nD (332.9−198.8). Among the total reduction, 110.9 nD (309.7−198.8) was caused by the mechanical plugging mechanism (83%) and 23.2 nD (332.9−309.7) was caused by the adsorption mechanism (17%). Based on the above discussions, formation damage caused by asphaltene mechanical plugging can be alleviated by a huff-n-puff process (back and forth flow).

3.4 Numerical analysis

Shen and Sheng (2018) did a further numerical simulation study. Asphaltene precipitation and deposition processes were simulated using

respective Winprop and GEM simulators developed by Computer Modeling Group.

The Winprop simulator uses the asphaltene precipitation model proposed by Nghiem et al. (1993). The model splits the heaviest component into two components: the nonprecipitating component and precipitating component. The two components have the same critical properties and acentric factors but different interaction coefficients with light components. The precipitating component has relatively larger interaction coefficients with light components, which leads to greater incompatibility between the precipitating component and the light components. As a result, the precipitating component will transfer to a solid phase, and thus precipitate. The nonprecipitating component includes heavy paraffin, resins, asphaltene/resin micelles that will not dissociate. The precipitating component is asphaltenes and asphaltene/resin micelles that could dissociate and precipitate. The precipitating asphaltene component in crude oil is considered as a pure dense phase which can either be a liquid or solid. This phase is referred to as the asphalt phase.

Shen and Sheng (2018) lumped together 24 components of an oil into five pseudocomponents: C_{3-4}, C_{5-8}, C_{9-19}, C_{20-40}, C_{41+}. The heavy precipitating component was $C_{41\pm asphaltene}$. The interaction coefficients of the split precipitating asphaltene component with the light components and the molar volume of asphaltene phase were tuned to match the asphaltene precipitation data from the model with the experimental data. The tuned parameters are listed in Table 3.1. The predicted asphaltene precipitation data and the experimental data are compared in Fig. 3.13. The molar volume of precipitating asphaltene component was tuned to be 0.92 L/mol.

The GEM simulator uses the asphaltene deposition model developed by Wang et al. (1999):

$$\frac{\partial E_A}{\partial t} = \alpha C_A \phi - \beta E_A (\nu_L - \nu_{Lc}) + \gamma u_L C_A \tag{3.1}$$

The first term on the right side of the above equation is the surface deposition. α is the surface deposition rate coefficient that should be a positive

Table 3.1 Binary interaction coefficients between asphaltene component and other components used in the precipitation model.

Components	CO_2	CH_4	C_{3-4}	C_{5-8}	C_{9-19}	C_{20-40}	C_{41+}	$C_{41\pm asphaltene}$
$C_{41\pm asphaltene}$	0.27	0.2	0.2	0.04	0	0	0	0

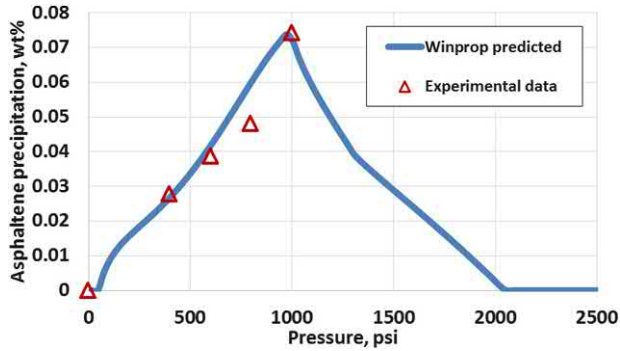

Figure 3.13 Comparison of Winprop predicted asphaltene precipitation with experimental data.

constant and is dependent on the rock type. C_A is the precipitated asphaltene concentration in the liquid phase and ϕ is the local porosity. The second term is the entrainment of asphaltene deposition. β is the entrainment rate coefficient, E_A is the fractional pore volume occupied by the asphaltene deposition, v_L is the interstitial velocity, and v_{Lc} is the critical interstitial velocity. The third term represents the pore throat plugging rate. γ is the plugging deposition rate coefficient, u_L is the superficial Darcy velocity. The entrainment of asphaltene will occur when v_L is higher than v_{Lc}; otherwise the entrainment rate will be set to zero. The term γ is defined as

$$\gamma = \gamma_i(1 + \sigma E_A), \text{ when } D_{pt} \leq D_{ptc} \tag{3.2}$$

$$\gamma = 0, \text{ when } D_{pt} \geq D_{ptc} \tag{3.3}$$

where γ_i is the rate coefficient for instantaneous plugging deposition, σ is the deposition constant for the snowball effect, D_{pt} is the average pore throat diameter, D_{ptc} is the critical pore throat diameter. If D_{pt} is smaller than D_{ptcr}, the pore throat plugging caused deposition will occur. The local porosity after asphaltene deposition is calculated by

$$\phi = \phi_0 - E_A \tag{3.4}$$

where ϕ_0 is the initial porosity. The flow resistance factor is calculated by the Kozeny-Carman type formula. The calculation of resistance factor is done recursively for time step. The current permeability is equal to the original permeability divided by the resistance factor calculated in the current time step.

In the GEM simulator, the asphaltene deposition is controlled by five parameters: α, β, v_{Lc}, γ_i, and σ. The five parameters were tuned to match

Table 3.2 Tuned parameters of the asphaltene deposition model.

Parameters	α, 1/day	β, 1/ft	v_{Lc}, ft/day	γ_i, 1/ft	σ, [-]
Value	1800	0	0	15	30

the experimental permeability reduction data in the first cycle and the last cycle. Their values are presented in Table 3.2.

Note that the entrainment of asphaltene deposition is not enabled in the model ($\beta = 0$). The high content of polar clay in shale strongly attracts polar functional groups in asphaltene molecules, resulting in strong asphaltene adsorption and making the entrainment more difficult. Wang et al. (1999) and Behbahani et al. (2015) showed that the critical interstitial velocity for entrainment was 0.01 to 0.04 cm/s in sandstone and carbonate. The critical velocity in shale is expected to be high. The maximum velocity is in the order of 10^{-5} cm/s in the model of this study. Then it is not possible that the critical velocity in shale can be exceeded. Therefore, the entrainment which causes mechanical plugging can be disabled. However, it was shown earlier that a higher percentage of permeability reduction data was caused by mechanical plugging. The mechanisms and the quantification of asphaltene deposition in huff-n-puff need more work.

Using the asphaltene model described above and a core-scale grid model, the oil recovery factor of a huff-n-puff CO_2 injection experiment can be matched with oil and gas relative permeabilities tuned, as shown in Fig. 3.14. It shows that without asphaltene deposition, the oil recovery can be increased by 3.5% over 15.5%.

Now we choose Block (11,1,12) that is 0.16 cm away from the interface between the core plug and the annual space. CO_2 is injected, and oil and CO_2 are produced through the annual space. Refer to Fig. 3.15 for the histories of CO_2 mole fraction, precipitated and deposited asphaltene in block (11,1,12). First, look at the CO_2 global (total) mole fraction (*dashed blue curve*). It increases during the huff and soaking period (6 h) and decreases during the puff period (18 h). For the asphaltene precipitation (*solid green curve*), during the injection and soaking time, as more CO_2 diffuses into this block, more asphaltene precipitates. However, as more CO_2 diffuses into the inner blocks, asphaltene precipitation decreases. There is a peak during this period. During the puff period, initially more oil flows into this block from the inner block and oil flows out of this block to the outer block. Because the inner block has a higher oil saturation or higher asphaltene content, the net asphaltene precipitation increases first, then decreases. There is a

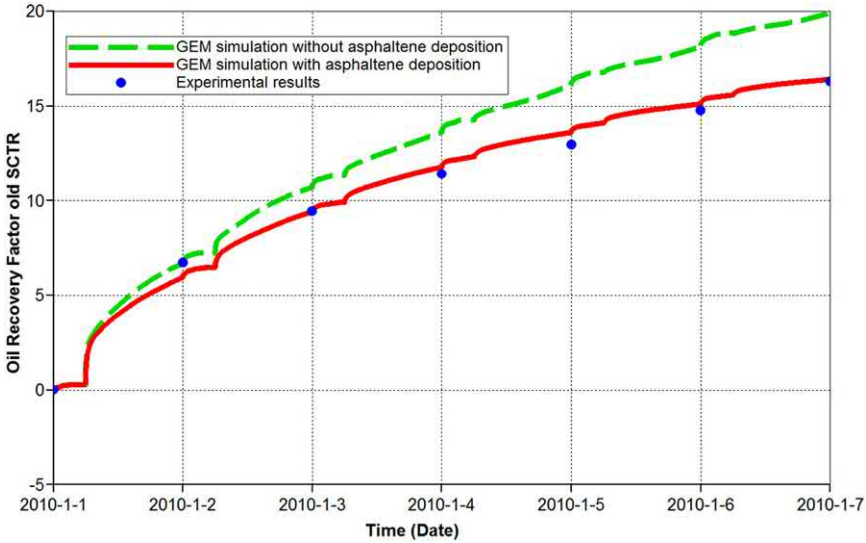

Figure 3.14 Comparison of the predicted oil recovery with experimental data.

small peak. At later cycles, because less oil flows into this block, and oil flows slower, the asphaltene precipitation show-up in this block delays the puff period. And the peaks become lower and lower with cycle.

For the asphaltene deposition (*dotted red curve*), more and more asphaltene deposits with cycle in this block. In other words, asphaltene deposition accumulates in this block. The asphaltene precipitation and deposition in different blocks may change differently. How they change depends on the net changes of CO_2, oil, and asphaltene content in the oil.

3.5 Effect of asphaltene deposition on huff-n-puff optimization

Asphaltene deposition is affected by pressure. The huff-n-puff performance strongly depends on the optimization of huff pressure, puff pressure, huff time, and puff time. Sheng (2017) proposed that a huff-n-puff should be optimized so that the huff time should be long enough for the pressure near the wellbore to reach the set maximum injection pressure, and the puff time should be long enough for the pressure near the wellbore to reach the set minimum production pressure. In other words, to improve or optimize

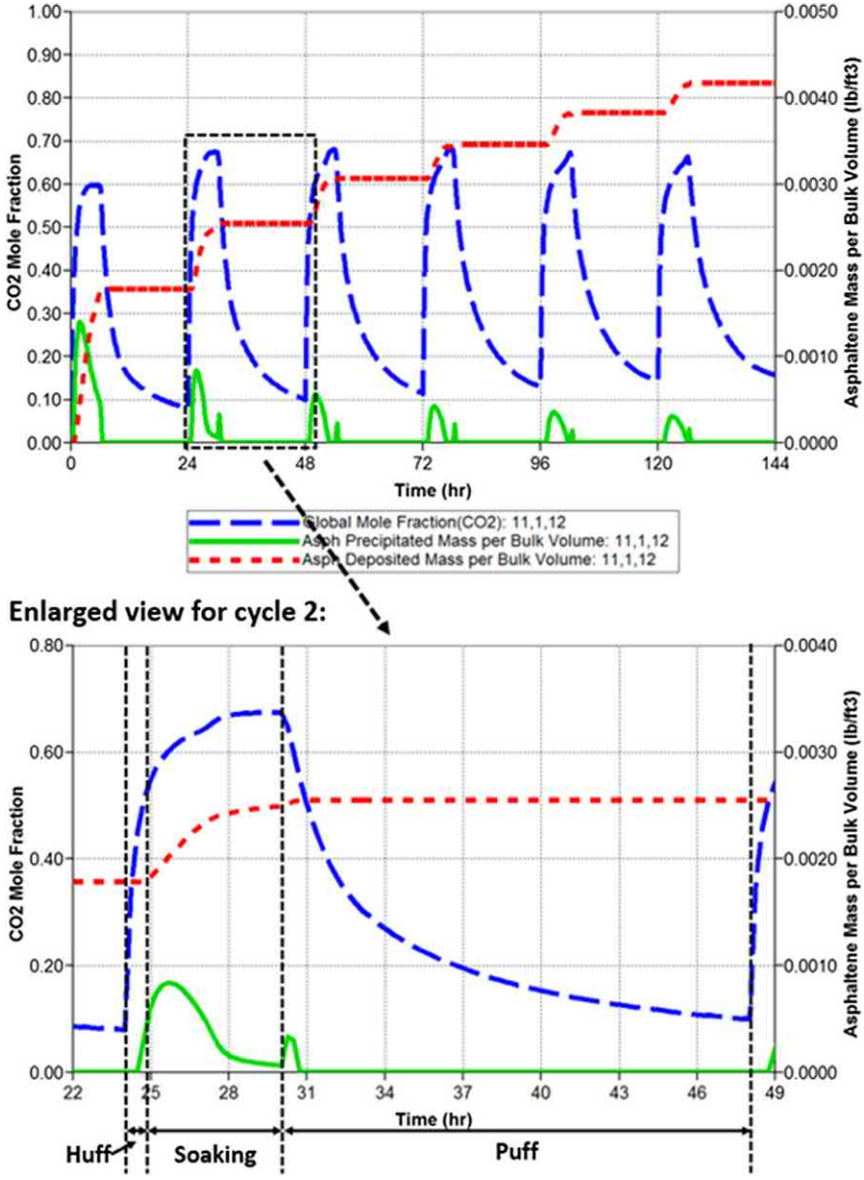

Figure 3.15 Histories of CO_2 mole fraction, precipitated and deposited asphaltene in Block (11,1,12).

oil recovery, a maximum allowable huff pressure should be used and a minimum allowable puff pressure should be used. Shen and Sheng (2019) studied how asphaltene deposition affects this optimization principle by simulation, as briefly presented below.

The basic reservoir grid model from Sheng (2017) is used. The PVT and compositional data of a live oil sample reported by Ashoori and Balavi (2014) are used. They measured the amount of asphaltene precipitation during primary depletion and CO_2 injection process. Shen and Sheng (2019) used a CMG PVT simulator, Winprop, to match the asphaltene precipitation data. The asphaltene deposition model described in the preceding section is used. For the base model, during the primary depletion of 1800 days, the bottom hole pressure is 1000 psi. During the huff-n-puff CO_2 injection, the puff pressure is 8000 psi, and the puff pressure is 1000 psi. The huff time and puff time are set to 100 days without a soaking time. The oil recovery factors from this base case with and without including asphaltene deposition are shown in Fig. 3.16. During the primary depletion, the oil recovery factors from the two cases are very close, no CO_2 is injected, and asphaltene deposition is insignificant. At the end of huff-n-puff CO_2 injection of 5600 days, the asphaltene deposition reduces 3.25% oil recovery. The simulation is repeated and the reductions in oil recovery factors caused by asphaltene deposition are shown in Fig. 3.17, when the huff pressures are 7000,

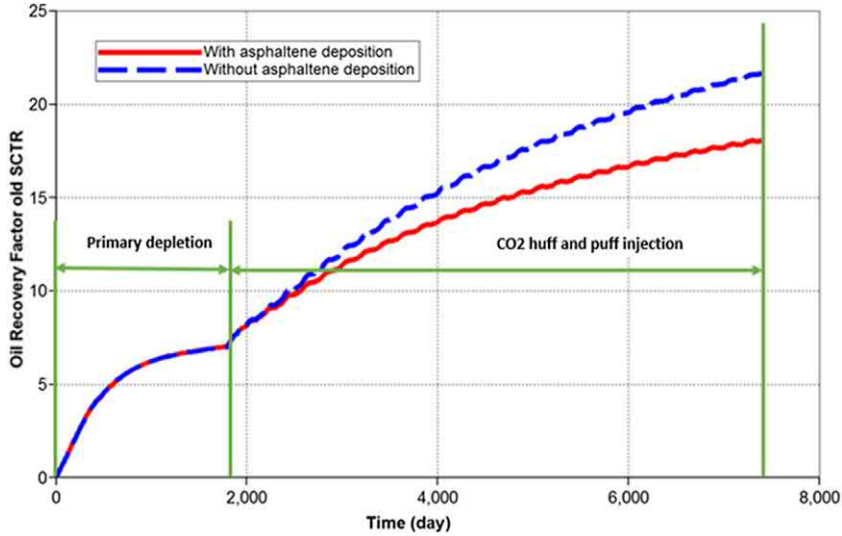

Figure 3.16 Oil recovery factors with and without including asphaltene deposition.

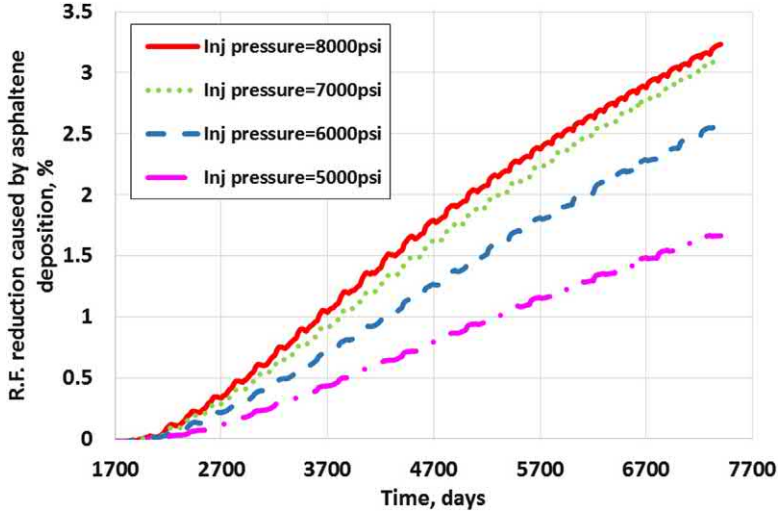

Figure 3.17 Reductions by asphaltene deposition in oil recovery factor at different huff pressures.

6000, and 5000 psi. It shows that as the huff pressure is increased, the reduction in oil recovery is higher. It implies that a lower huff pressure should be used to decrease the effect of asphaltene deposition. However, Fig. 3.18 shows that the oil recovery factor at a higher huff pressure is still higher than that at a lower huff pressure, even asphaltene deposition is included in the simulation. It means that the negative effect of asphaltene deposition on oil recovery is less than the positive effect of higher pressure. Then a higher huff pressure should be chosen to improve oil recovery. This conclusion is drawn when asphaltene is not taken into account (Gamadi et al., 2013; Yu et al., 2016a; Li et al., 2018).

Similarly, Fig. 3.19 shows that as the puff pressure is decreased, the reduction in oil recovery by asphaltene deposition is higher. However, Fig. 3.20 shows that the oil recovery factor at a lower puff pressure is still higher than that at a higher puff pressure, when asphaltene deposition is included in the simulation. The negative effect of asphaltene deposition on oil recovery is less than the positive effect of lower puff pressure. Therefore, a lower puff pressure should be chosen to improve oil recovery. This conclusion is drawn when asphaltene is not taken into account (Sheng and Chen, 2014; Sheng, 2015b; Sanchez-Rivera et al., 2015).

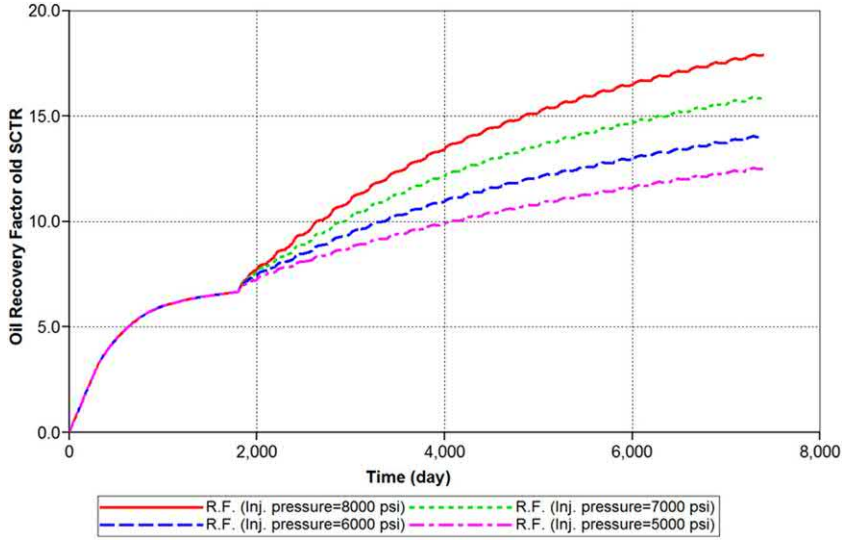

Figure 3.18 Oil recovery factors at different huff pressures with asphaltene deposition included.

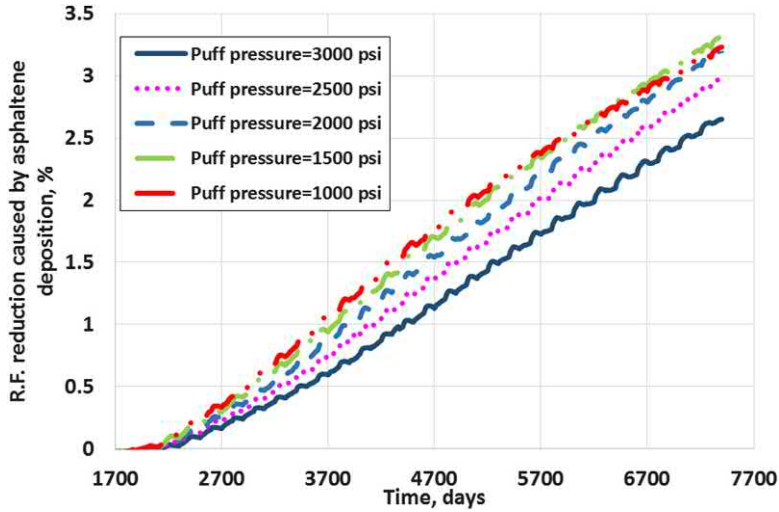

Figure 3.19 Reductions by asphaltene deposition in oil recovery factor at different puff pressures.

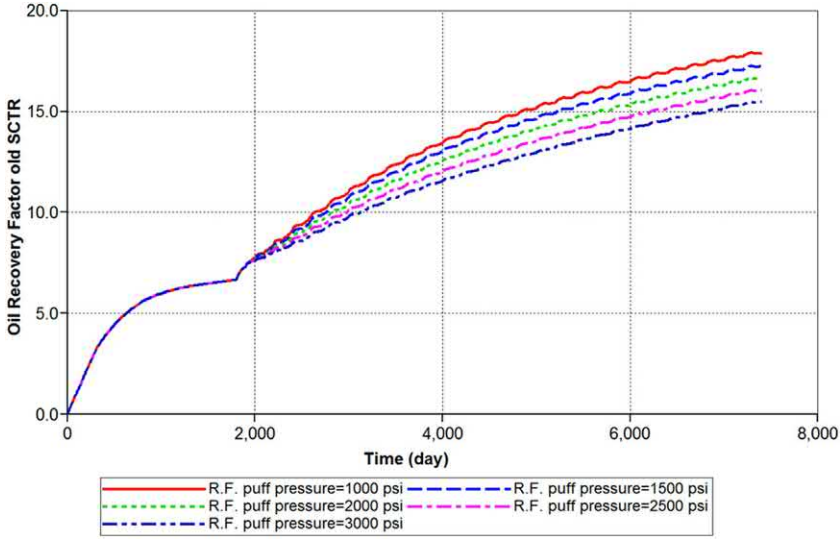

Figure 3.20 Oil recovery factors at different puff pressures with asphaltene deposition included.

The above results show that the conclusions about choosing a higher huff pressure and a lower puff pressure to improve oil recovery remain the same, regardless whether asphaltene deposition is considered or not.

CHAPTER FOUR

Huff-n-puff injection in shale gas condensate reservoirs

Abstract

This chapter discusses huff-n-puff gas injection in shale and tight gas condensate oil reservoirs. Huff-n-puff gas injection is compared with gas flooding in terms of their potential to enhance liquid recovery and remove liquid blockage. Huff-n-puff gas injection is also compared with huff-n-puff solvent injection in core scale and field scale. The solvents are methanol and isopropanol. The capacity of surfactants to remove liquid blockage is also studied. Factors that affect huff-n-puff gas injection performance are discussed. Mechanisms of huff-n-puff injection are discussed. Optimization of huff-n-puff injection is proposed.

Keywords: Gas condensate; Gas flooding; Huff-n-puff; Liquid blockage; Liquid recovery; Solvents; Surfactants.

4.1 Introduction

To understand the problem and solution of a gas condensate reservoir, first look at the phase diagram of a gas condensate (Fig. 4.1). When a gas condensate reservoir is produced, the pressure near the production well is depleted along the path 1 to 5 at the initial reservoir temperature. The pressure initially is at point 1 at the initial reservoir pressure. When the pressure is decreased at point 2 (dew point), some heavy components in the gas phase start to condense. From point 2 to point 3, more condensation occurs, and at point 3, the liquid condensate reaches the maximum between 15 and 20 shown in the figure. From point 3 to point 4, the liquid condensate starts to vaporize, and the vaporization is completed at point 5 (back to the dew point). At this point, the fluid becomes gas again. Because some pressure is needed to produce the well, the pressure near the bottom of the well cannot be as low as the pressure at point 5. Thus, some liquid condensate forms from the bottom of wellbore to some distance deep into the reservoir, as shown in Fig. 4.2. From this figure, it is obvious that the liquid condensate blocks the gas flow into the wellbore. As liquid is more difficult to flow than gas, the wellbore productivity is reduced.

Enhanced Oil Recovery in Shale and Tight Reservoirs
ISBN: 978-0-12-815905-7
https://doi.org/10.1016/B978-0-12-815905-7.00004-9

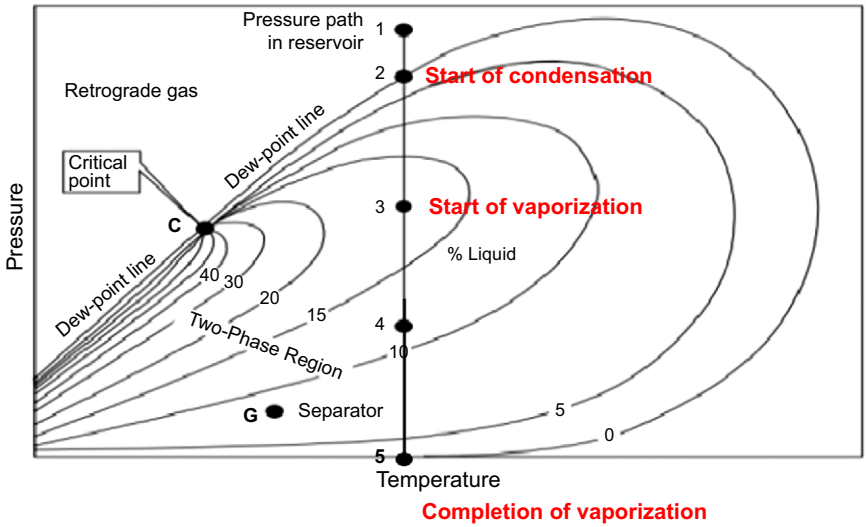

Figure 4.1 Phase diagram of a gas condensate. *Modified from McCain (1989).*

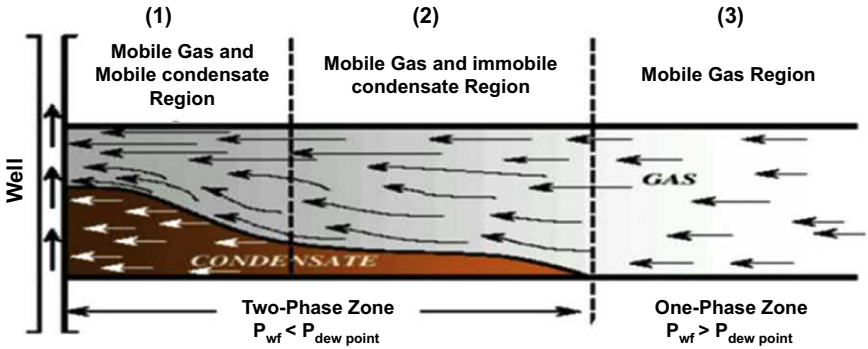

Figure 4.2 Gas and liquid condensate distribution when the near-wellbore pressure is below the dew point pressure (Al-Yami et al., 2013).

Even worse, some immobile liquid condensate accumulates near the wellbore, permanently blocking gas flow. This is the formation damage that forms near a typical gas condensate well. In shale and tight reservoirs, this formation damage zone is much larger owing to the ultralow permeability. Since the liquid condensate is composed of heavy hydrocarbon components, it has a great energy value. Therefore, the liquid condensate should be produced for the energy value; after it is produced, the formation damage is removed, and gas productivity can be restored.

From the above discussion of the problem, one easy way is to increase the pressure near the wellbore or in the reservoir above the dew point pressure by gas and/or water flooding (Hernandez et al., 1999). Surfactants may be injected to reduce interfacial tension or alter wettability so that residual liquid oil saturation is reduced (Kumar et al., 2006; Ahmadi et al., 2011; Ganjdanesh et al. (2015). Solvents may be injected to mitigate the impact of liquid blockage (Al-Anazi et al., 2005; Sayed and Al-Munstasheri, 2014). These methods have been proposed for conventional reservoirs. This chapter proposes huff-n-puff gas injection in shale and tight reservoirs to mitigate the liquid condensate blocking. The method is compared with solvent injection and surfactant treatment.

4.2 Experimental setup

Fig. 4.3 is a general experimental setup for flooding and huff-n-puff. During the huff (injection) period, a single-phase gas condensate is injected from Accumulator 2 into the two ends of core through Valves C, A, and B. During the puff period, the valve G for Accumulator 2 and Valve F for Accumulator 1 are closed, the valve E for the back-pressure regulator is open, and Valves A, B, C, and H are open. The flowback fluid is stored in Accumulator 3. The core is placed inside a CT scanner. The average

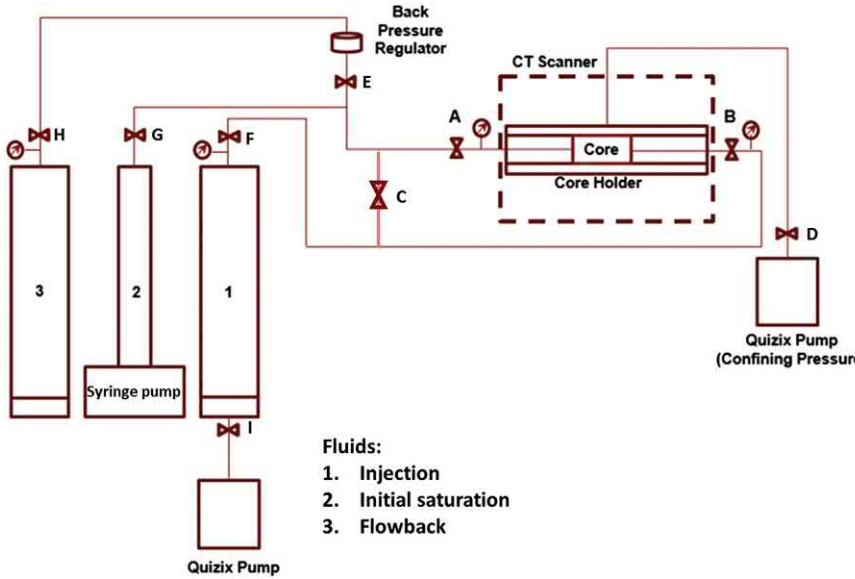

Figure 4.3 A general experimental setup for flooding and huff-n-puff.

liquid oil saturation in the core is calculated using CT numbers following Eq. 2.11, and the liquid condensate oil recovery factor can be calculated by Eq. 2.12.

For a flooding mode, first a condensate saturation is established. Valve C is closed. Valves A and B are open, but Valves E, F, and H are closed initially. The core is saturated by a gas condensate at a set pressure above a dew point pressure by opening Valve G. Then open Valves E and H at a pressure lower than the dew point pressure, some condensate forms in the core. Then increase the syringe pump rate at a set pressure higher than the earlier pressure, making the pressure in the core higher but the pressure at the exit end near Valve A lower than the dew point pressure. By doing so, the liquid condensate in the core is reduced. The average liquid oil saturation and the oil recovery in the core are calculated using CT numbers following the method for huff-n-puff.

4.3 Huff-n-puff gas injection

Meng et al. (2017) did huff-n-puff experiments. An Eagle Ford outcrop core of 1.5 inches in diameter and 4 inches in length was used. The porosity was 6.8% and the permeability was 100 nD. To make experiment easier to run and analyze, a synthetic gas condensate of 0.85 mol fraction of methane and 0.15 mol fraction of n-butane was used. Its phase diagram is shown in Fig. 4.4. The experiment was conducted at the room temperature of 68°F. The liquid drop of this mixture at this temperature is shown in Fig. 4.5. The dew point pressure of this gas condensate mixture at 68°F is 1860 psi. Thus, the initial pressure of the mixture was set 2200 psi at the Accumulator 2 but the injection pressure was set 1900 psi. The injection and soaking time was 30 min. After that, the back-pressure regulator was set 1460 psi (below the dew point pressure of 1860 psi). Valves B, A, E, and H were open while other valves were closed. The core was depleted at 1460 psi from both ends of the core for 30 min. This was one cycle. After that, gas mixture was injected from Accumulator 2 again followed by depletion to Accumulator 3 again. This process is repeated for 5 cycles. The liquid condensate saturation was measured by CT numbers which were obtained the end of every puff period. The condensate recovery was calculated by CT numbers.

As shown in Fig. 4.6, the condensate saturation after the primary depletion was 10%, and it was 9.1% at the end of the first puff process. The saturations at the end of remaining cycles are shown in the figure.

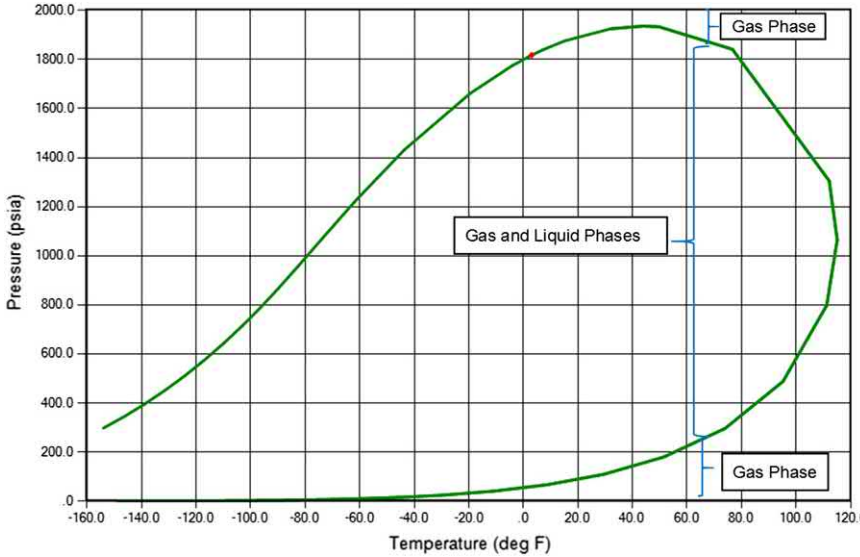

Figure 4.4 Phase diagram of the methane-n-butane mixture.

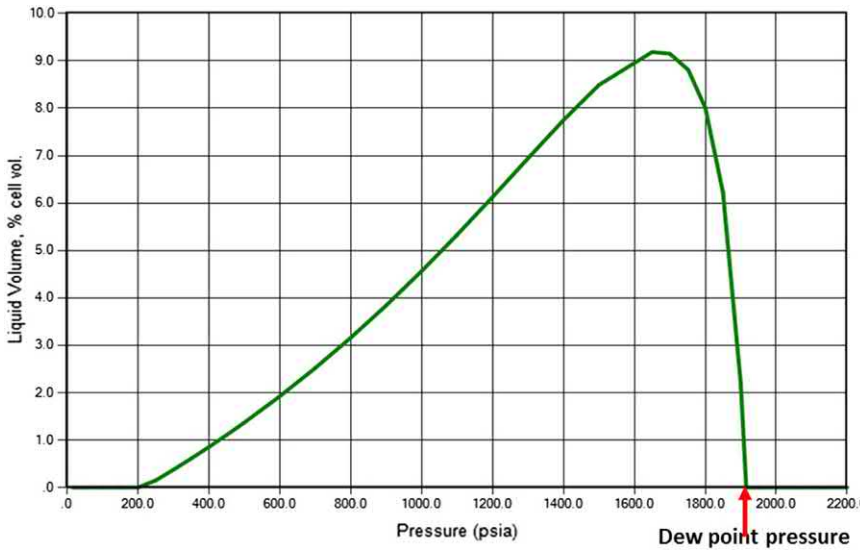

Figure 4.5 Liquid dropout curve of the methane-n-butane mixture.

The condensate recovery was calculated by Eq. 2.12, as shown in Fig. 4.7. It shows that the 25% of condensate was recovered after 5 cycles of huff-n-puff methane injection. A numerical simulation model was able to match the experimental data by tuning relative permeabilities.

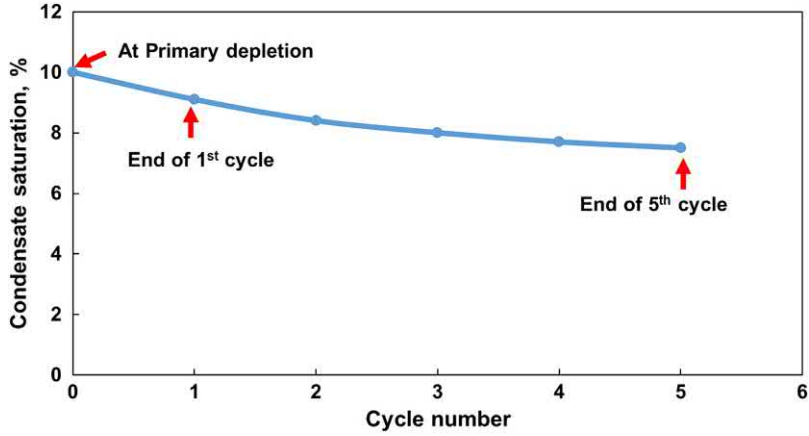

Figure 4.6 Condensate saturation at every cycle.

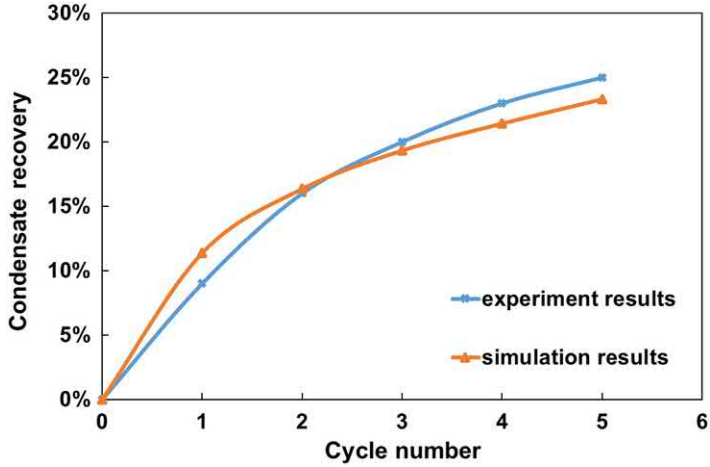

Figure 4.7 Condensate recovery at every cycle.

4.4 Huff-n-puff versus gas flooding

As described earlier in Section 4.2, gas flooding can be performed using the experimental setup in Fig. 4.3 to increase the core pressure so that the liquid drop can be reduced. Under the same injection pressure and outlet pressure as those in the huff-n-puff experiment described in the last section, the condensate recovery is shown in Fig. 4.8 with the predicted performance from a numerical simulation model.

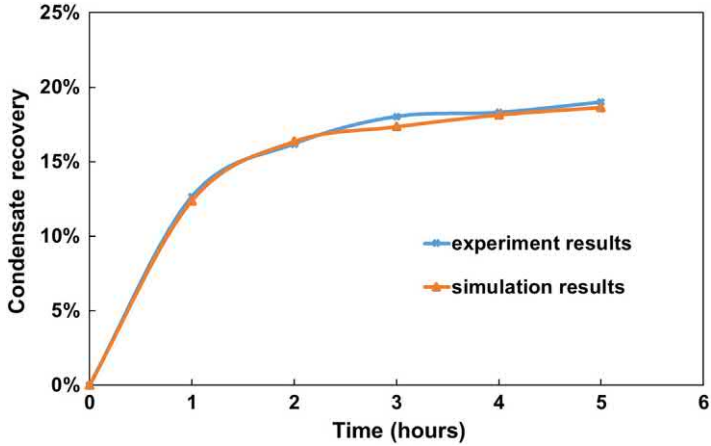

Figure 4.8 Condensate recovery during a gas flooding experiment.

For the huff-n-puff experiment, one cycle took 30 min of injection (puff) and soaking time and 30 min of production (puff) time, totaling 1 h. One cycle lasted 1 h, and total five cycles took 5 h. Thus, the condensate recovery can also be plotted in terms of experimental time (similar to the operation time in a field project). The condensate recovery from the huff-n-puff injection and the flooding is compared in Fig. 4.9. For the same period of 5 h, the condensate recovery was increased by 23.3% by huff-n-puff gas injection; but it was increased by 18.6% by gas flooding. This comparison showed outperformance of huff-n-puff gas injection over gas flooding. For huff-n-puff gas injection, the pressure near the well dropped and is depleted during the puff period; during the huff period, the pressure can

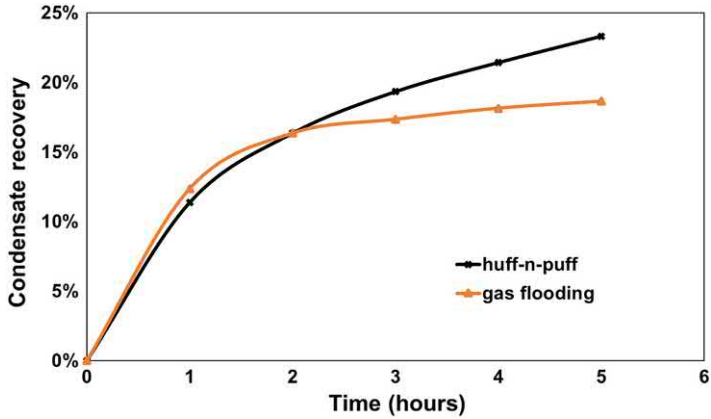

Figure 4.9 Performance comparison of huff-n-puff with gas flooding.

quickly be increased because gas is injected in the same low-pressure zone. In other words, the pressure can be effectively increased. As the pressure is increased, revaporization occurs. However, in the flooding mode, it takes a long time for the pressure to transmit from the injection side to the production side because of ultralow permeability.

Sheng (2015b) used a reservoir model to compare huff-n-puff gas injection with gas flooding. Orangi et al.'s (2011) gas condensate composition was used. The dew point pressure is 3988 psi. The matrix permeability is 100 nD. The huff time and puff time are 100 days, and no soaking time is used. The cumulative liquid oil produced from huff-n-puff and methane flooding is shown in Fig. 4.10. It shows that more oil is produced from huff-n-puff methane injection. The performance data are shown in Table 4.1. It shows that the huff-n-puff injection produces 8.7% higher liquid oil than the gas flooding. In the table, the net gas produced is the total gas produced minus total gas injected in the huff-n-puff. Both gas and oil produced are higher in the huff-n-puff injection. The revenue from oil and gas production in the huff-n-puff case is also higher than that from the gas flooding. The oil price of $100/STB and the gas selling price of $4/MSCF are used in the calculation. The difference in capital investment and facility and operation costs are not included. A discount rate is not taken into account. If a discount rate is considered, the performance of huff-n-puff will look even better than that of gas flooding, as the former liquid oil is produced in the earlier time, as shown in Fig. 4.10.

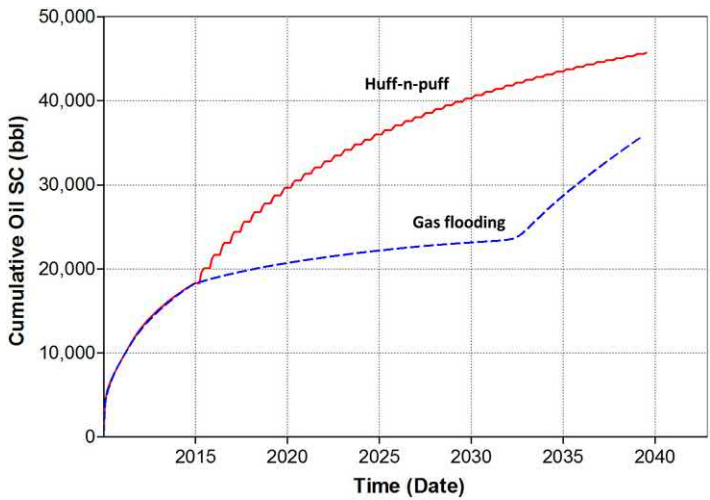

Figure 4.10 Cumulative oil production from methane flooding and huff-n-puff injection.

Table 4.1 Performance comparison of different scenarios (100 nD).

	Primary	Gas flooding (A)	Huff-n-puff (B)	Ratio (B/A)
Total gas produced (MMSCF)	357.01	275.43	3133.7	11.38
Gas injected (MMSCF)	0	216.36	3008.3	13.90
Net gas produced (MMSCF)	357.01	59.07	125.4	2.12
Oil produced (MSTB)	30.385	36.5	46.666	1.28
Oil recovery factor (%)	26	31.23	39.93	1.28
Value of produced oil and gas (MM$)	4.46654	3.88628	5.1682	1.33

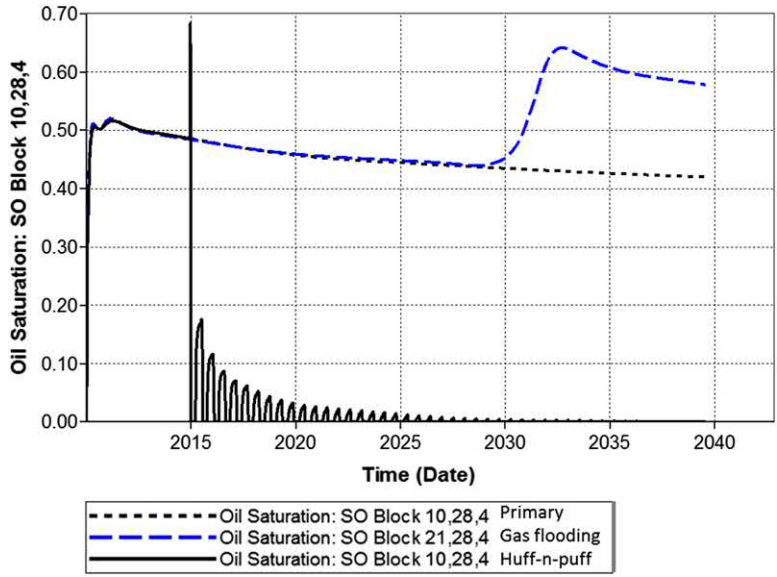

Figure 4.11 Block oil saturations near the well fracture blocks during the primary production, gas flooding and huff-n-puff gas injection.

In the simulation models, Block (10,28,4) is a neighbor block to the fracture block where the huff-n-puff well is in the huff-n-puff mode; Block (21,28,4) is a neighbor block to the fracture block where the production well is in the flooding mode. Fig. 4.11 shows that the oil saturation in Block (10,28,4) in the huff-n-puff mode quickly decreases to almost zero. In the primary and gas flooding modes, the oil saturations in Blocks (10,28,4) and (21,28,4) remain high. Note the oil saturation in the gas flooding mode starts to build up near year 2023 because the oil bank reaches the

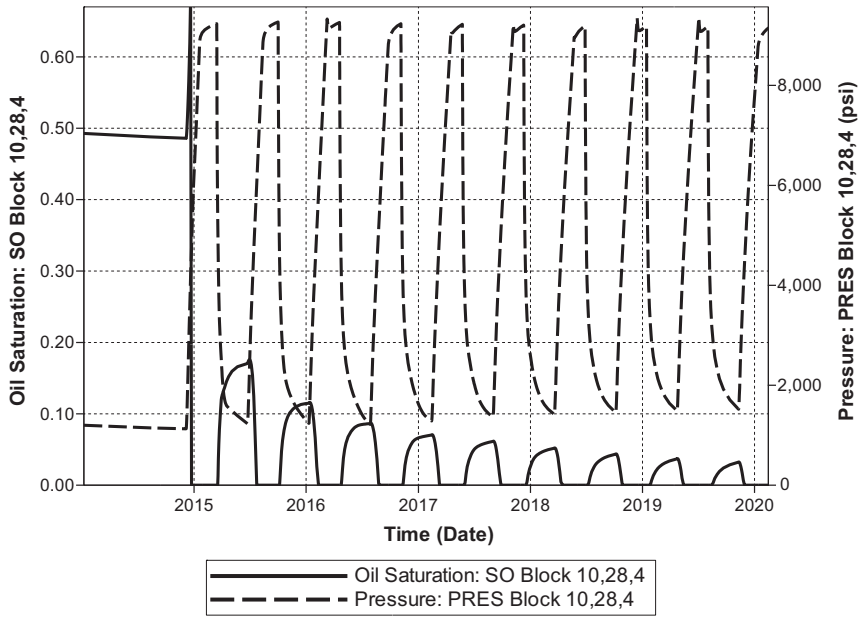

Figure 4.12 Pressure and oil saturation at Block (10,28,4) near the producing fracture in the gas huff-n-puff mode.

producing fracture. In the gas huff-n-puff mode, the oil saturation at Block (10,28,4) shoots up at the first huff because oil in the producing fracture block (11,28,4) is displaced to this block.

Fig. 4.12 shows the pressure and oil saturation at Block (10,28,4) near the producing fracture in the huff-n-puff mode. It shows that when the pressure increases during the huff period, the oil saturation decreases almost to zero, as oil is vaporized and flows with the gas stream, or some oil is displaced to the producing fracture; when the pressure is decreased during the puff period, the oil saturation is increased because of condensation or some oil from the deep matrix flows into the block.

In conventional reservoirs, generally gas is flooded to maintain a high reservoir pressure so that less condensate will occur (Thomas et al., 1995). In shale or tight gas condensate reservoirs, for example, when the matrix permeability of 100 nD in this studied model, higher liquid saturation occurs at the producing fracture, because the pressure there is low (about 500 psi), although the pressure in the injection fracture is 9500 psi, as shown in the left-hand side of Fig. 4.13. The pressure near the injection side cannot propagate to the production side in the low matrix permeability reservoir. For the

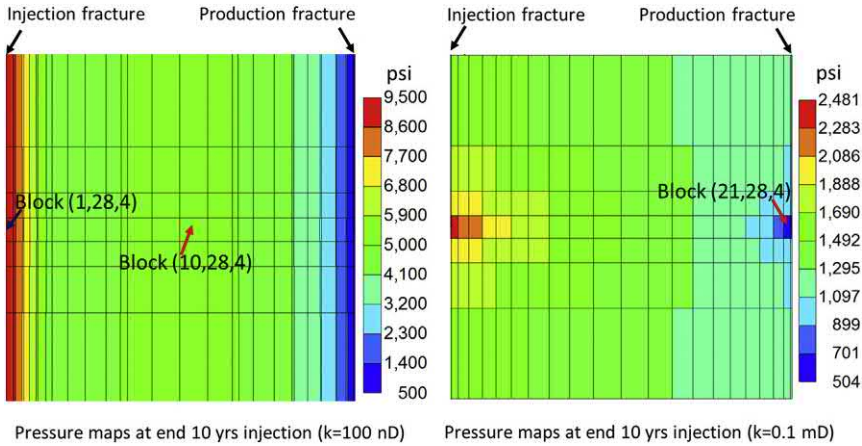

Figure 4.13 Pressure distributions at the end of 10 year of gas flooding for two reservoirs of 100 nD and 0.1 mD matrix permeability.

comparison, the right-hand side of Fig. 4.13 shows the pressure distribution when the matrix permeability is simply increased to 0.1 mD. The pressure in the injection fracture is about 1000 psi higher than that in the production fracture. In other words, the pressure does not decrease significantly from the injection side to the production side. Note that in the 0.1 mD case, the pressure near the injector cannot be built up to 9500 psi, because the pressure is able to dissipate to the production end. If the injection rate is increased, the pressure in the injection is increased to about 9500 psi, then the pressure in the production side will be about 8500 psi. Then no liquid will be condensed. That is why gas flooding will eliminate or mitigate the liquid dropout problem in a reasonably high permeability reservoir.

To further demonstrate that huff-n-puff injection is preferred in a shale reservoir of very low permeability than gas flooding, the performance in a higher matrix permeability reservoir of 0.1 mD is compared in Table 4.2. It shows that the oil recovery factor from gas flooding is 14.12% higher than that from huff-n-puff, opposite to the 100 nD case shown in Table 4.1. The revenues from produced oil and gas from gas flooding are also higher than those from huff-n-puff.

4.5 Core-scale modeling of gas and solvent performance

As mentioned earlier, solvents may also be injected to mitigate condensate blocking. Different gases may be used as well. Sharma and Sheng (2017,

Table 4.2 Performance comparison of different scenarios (0.1 mD).

	Primary	Gas flooding (A)	Gas huff-n-puff (B)	Ratio (B/A)
Total gas produced (MMSCF)	427.22	7491.5	3989.4	0.53
Gas injected (MMSCF)	0	7200	3600	0.50
Net gas produced (MMSCF)	427.22	291.5	389.4	1.34
Oil produced (MSTB)	55.046	111.36	83.167	0.75
Oil recovery factor (%)	47.1	95.28	71.16	0.75
Value of produced oil and gas (MM$)	7.21348	12.302	9.8743	0.80

2018) compared the performance of gases (methane and ethane) with that of solvents (methanol and isopropanol). Their approach was to analyze simulation results both in core-scale and in reservoir-scale. The core-scale model was validated by history-matching an experiment published by Al-Anazi (2003). The reservoir-scale model was built based on the core-scale parameters which were calibrated from history-matching the experiment. One key step is to calibrate the core-scale model which is presented next.

Al-Anazi (2003) used a Texas Cream Limestone core to conduct an experiment for gas condensate accumulation and methanol treatment (Experiment 17 in his dissertation). The core was 1 inch in diameter and 8 inches in length. Its permeability was 3.15 mD. The porosity was 0.2. The gas condensate mixture (Fluid A) had 0.8 C_1, 0.15 C_4, 0.038 C_7, and 0.012 C_{10} (mole fraction). The experimental temperature was 145°F. The dew point pressure was about 2795 psi. There was no initial water saturation in the experiment. During the experiment, the upstream injection pressure was at 3000 psi, and the downstream (outlet) pressure was at 1200 psi. The flow rate was 2 cc/h. His experimental data are shown in Fig. 4.14 as dot points. Two simulation models (in the solid blue line by Rai (2003) and in the solid thick red curve by Sharma and Sheng (2017) predicted the experimental trend.

Note that the model predictions and the experimental data were not well matched. The experimental data showed that as more gas was injected, initially the pressure drop increased owing to condensate accumulation; but when the injection volume was at about 2 pore volumes, the pressure

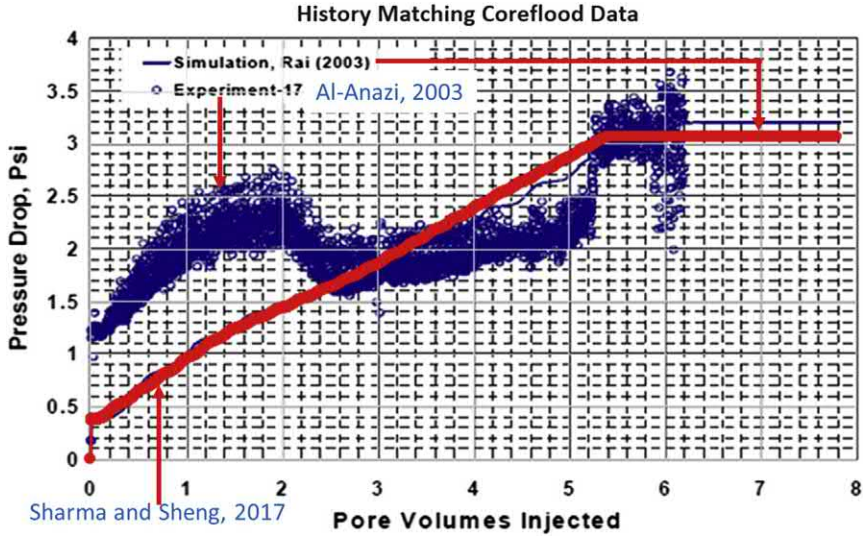

Figure 4.14 Coreflood experimental data of gas condensate fluid and two model predictions.

drop decreased. This observation was not seen in Al-Anazi's (2003) other experiments. Neither Rai's (2003) model nor Sharma and Sheng's (2017) model was able to capture this phenomenon. An alternative experiment should have been simulated. However, it is important for a simulation model to match the steady state pressure across the core with respect to the injected pore volume when the two-phase flow of gas and condensate was established. The experiment simulated was the only one of a low flow rate in which a steady-state flow was achieved. For other high rate experiments, it was observed that some of the accumulated condensate was stripped and carried because of the velocity effect. As a result, when the flow rate was increased, the measured pressure drop actually decreased, and a large pore volume of gas condensate had to be flooded to achieve a steady state flow (Al-Anazi, 2003). A simulation model cannot predict such trend.

Using the above described one-dimensional model, Sharma and Sheng (2017) compared the performance of methane, ethane, and solvent methanol. Huff-n-puff injection tests are run for 130 days. The injection pressure and the puff pressure are 2850 psi and 1200 psi, respectively. When the pressure at Block (4,1,1) (total 24 blocks in the core) reaches 2850 psi, the huff is changed to the puff period.

Because different gases or solvents produce different compositions, to evaluate their performance, the total produced hydrocarbon at different times should be compared. Such recovery factor (RF) is defined:

$$\frac{\text{(Total hydrocarbons produced after primary} - \text{total production of the injected fluid) in BOE}}{\text{(total hydrocrbons in place at the end of primary depletion in BOE)}}$$

Total hydrocarbons include methane, butane, heptane, and decane. Note that the unit of barrels of oil equivalent (BOE) is used. The volumes used for calculations are at the standard condition of 14.7 psi and 60°F. The BOE volume at the end of primary depletion is taken as the base volume to calculate the recovery factor. 1 BOE = 5800 SCF gas.

Since no ethane and solvent is in the original fluid (Fluid A), the produced compositions are from the injected fluid. For methane, the total production volume of the injected methane is equal to the total injected volume minus the additional methane volume in the core that is the remaining volume in the core minus the methane volume in the core at the end of primary depletion. The total hydrocarbon recovery factors from different gases and solvent are shown in Fig. 4.15. Note that the time in the horizontal axis is huff-n-puff time (excluding the primary depletion time). It shows that ethane produces the highest recovery of the total hydrocarbon volume in BOE based on the hydrocarbons in place at the end of primary depletion,

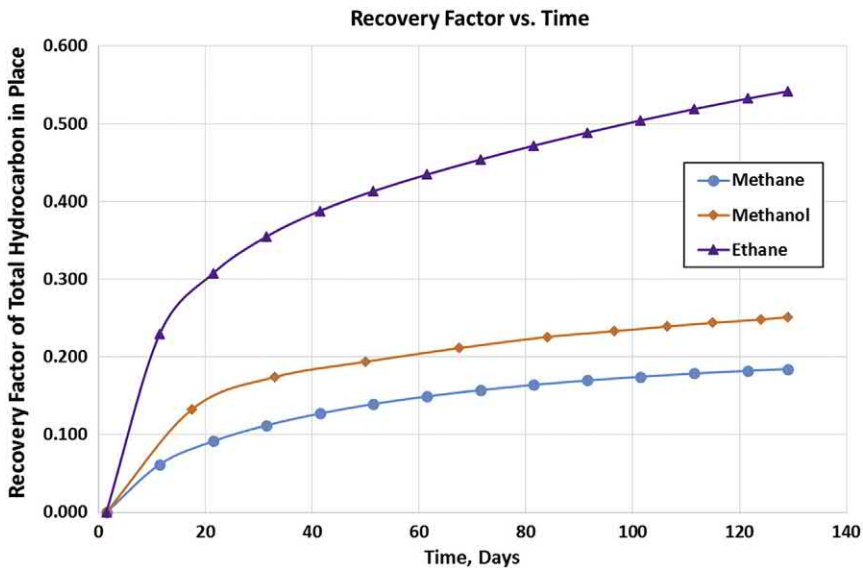

Figure 4.15 Total hydrocarbon recovery factors in different huff-n-puff time.

with the recovery factor of 54% followed by 25.1% from methanol injection and 18.4% from methane.

However, different volumes of gases and solvent are injected during the same huff-n-puff time. Fig. 4.16 shows the total hydrocarbon recovery factors versus their injection pore volumes. It shows that their performances rank the same as those in terms of huff-n-puff time. Further for a proper comparison, their difference costs should be taken into account. Fig. 4.17 compares their performances in terms of costs. When calculating the cost, these prices are used: \$3.17/Mscf for methane, \$0.88/gal. for methanol, \$1.35/gal. for isopropanol, and \$4.15/Mscf for ethane according to McGuire et al. (2016). Because it is a small core scale, the absolute costs are low. These costs should be interpreted at their relative values.

The above comparisons are based on the total hydrocarbons, and the performances are ranked as ethane, methanol, methane. To understand their EOR mechanisms, the recovery factors of individual components should be compared. Fig. 4.18 shows that methanol has good recoveries for methane and butane, but not as good for heptane and decane. The injected methane hardly produces the original methane (0.2%, not visible in the figure). In other words, the produced methane is almost the same amount as the injected methane. But methane recovers higher volumes of butane, heptane, and decane than methanol. Since the condensate dropouts in the core are

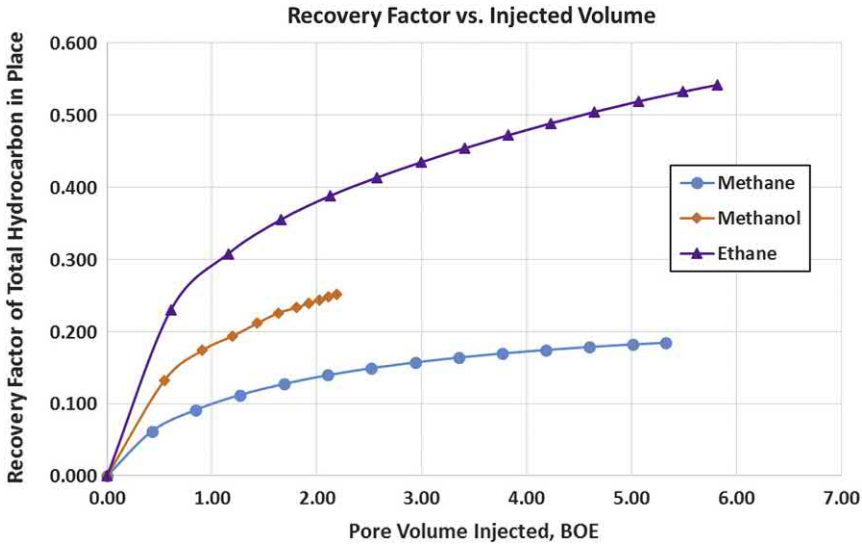

Figure 4.16 Total hydrocarbon recovery factors in different injected pore volume.

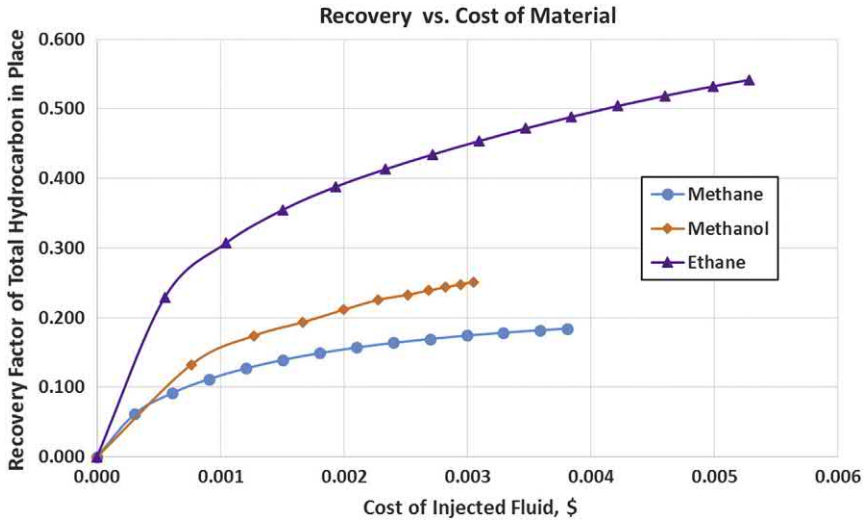

Figure 4.17 Total hydrocarbon recovery factors in terms of their costs.

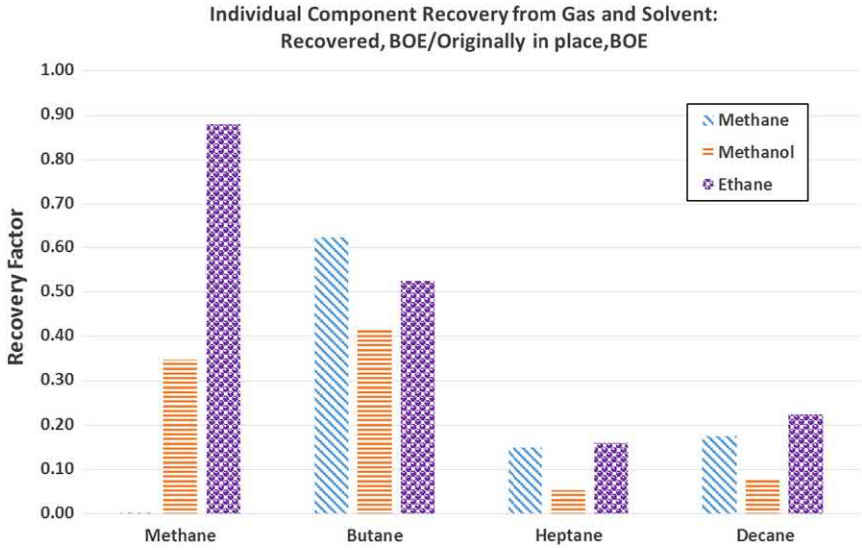

Figure 4.18 Individual hydrocarbon recovery factors from methane, ethane, and methanol.

C_4, C_7, and C_{10} components, methane is more effective than the methanol to recover the condensate. This is more obvious in Fig. 4.19 which shows the recovery factors of the intermediate and heavy components (excluding methane). Methane and ethane perform better than methanol.

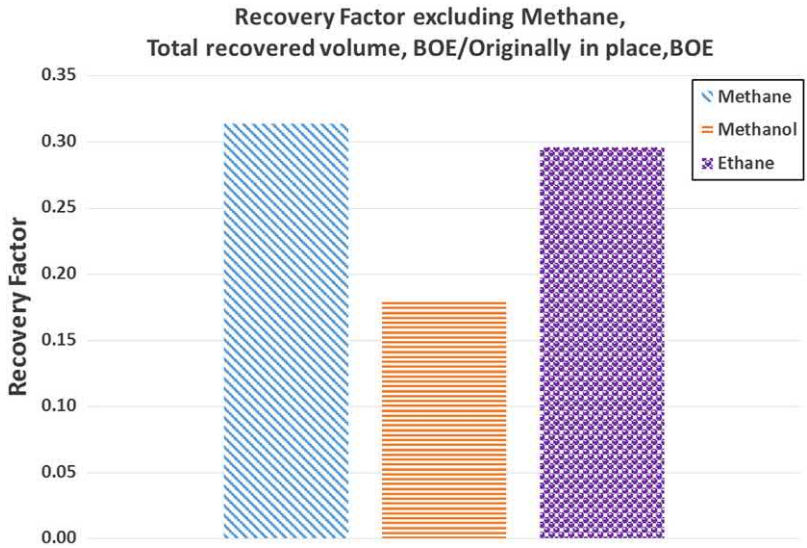

Figure 4.19 Recovery factors of total hydrocarbons except methane from methane, ethane, and methanol.

Sharma and Sheng (2017) also compared the performances of gases (methane and ethane) and solvents (methanol and isopropyl alcohol (commonly called isopropanol)) to recover Fluid B. Fluid B is composed of 0.81 mol fraction C_1, 0.05 C_4, 0.06 C_7, and 0.08 C_{10}, richer than Fluid A. There is 25% initial water saturation in the experiment. The experimental temperature is 300°F. Overall, the isopropanol (IPA) performance is similar to the methanol performance, with the former a little bit better than the latter with higher cost. As IPA is heavy than methanol, IPA outperforms methanol to recover heavy condensates. The ranking of these four gases and solvents from high to low recovery factors is ethane, methane, IPA, and methanol.

Generally, it is easier for gases to penetrate the liquid condensate, and liquid solvents are more likely to solubilize the condensate. Since ethane mixes with the condensate, it is difficult to split the produced condensate and ethane in laboratory experiments. Simulation work proves that ethane is the best injection fluid in recovering the total hydrocarbon in place. It revaporizes condensate and reduces the dew point pressure of initial reservoir fluid. Its supercritical fluid properties enable it to recover high volumes of the total hydrocarbon fluid in place for relatively small volumes of injection.

With richer compositions of a reservoir fluid, the performance difference in gas and solvent huff-n-puff is magnified, with significantly higher recovery factors from methane and ethane injection. Solvents recover intermediate fluids really well and can be competitive with gas huff-n-puff for lean gas condensate fluids. Isopropanol is a better solvent than methanol for recovering heavier components; however, higher costs may not favor its application.

4.6 Reservoir-scale modeling of gas and solvent performance

The preceding section is based on core-scale modeling. This section focuses on reservoir-scale modeling. The grid blocks of the reservoir-scale model are shown in Fig. 4.20. The matrix permeability is 304 nD, and the porosity is 5.6%. The fracture spacing is 2.27 ft in the non-SRV (stimulated reservoir volume) zone and 0.77 ft in the SRV zone. For more details, refer to Sheng et al. (2016).

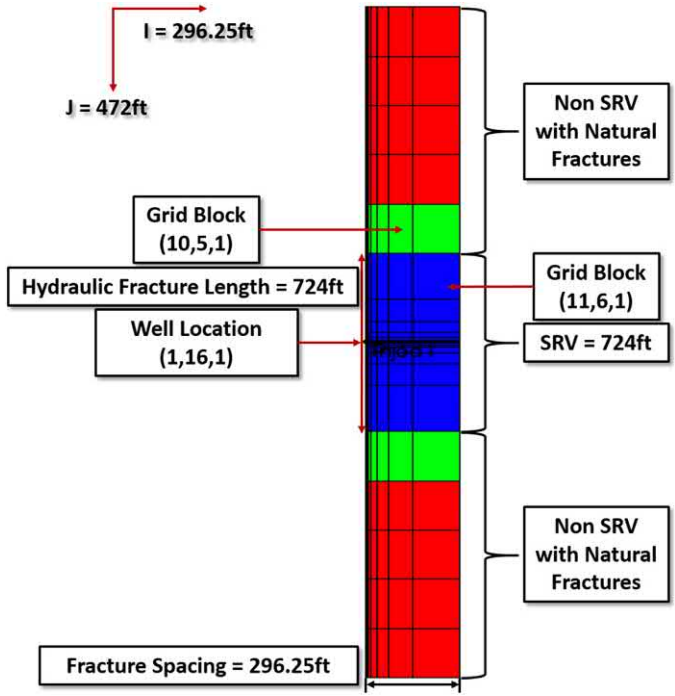

Figure 4.20 Reservoir-scale grid model based on Sheng et al. (2016).

Fluid B described in the preceding section is used in the model; the binary interaction parameters among components are from Bang et al. (2010). The initial reservoir pressure is 7800 psi. The reservoir is under 5 years of primary depletion before huff-n-puff. During the huff-n-puff injection, the injection pressure is 7800 psi which is above the dew point pressure. When the pressure in the well block (2,16,1) adjacent to the hydraulic fracture reaches the injection pressure of 7800 psi, the operation is switched to the puff period. The puff pressure is 1200 psi. When the pressure at the Block (2,16,1) approximately reaches 1200 psi, operation is switched back to the huff period again. Such process is repeated for 10,585 days or 29 years. For gases, the huff time is 175 days and the puff time is 920 days. For methanol, the huff time is 575 days and the puff time is 1500 days. For isopropanol, the huff time is 775 days and the puff time is 1750 days. No soaking time is used.

In this section, the recovery factor (RF) in % at any time is calculated using this equation:

$$\mathrm{RF} = \left[\frac{\text{Total original hydrocarbon moles in place} - \text{remaining total hydrocarbon moles in place}}{\text{Total original hydrocarbon moles in place}}\right] * 100$$

Using moles of components makes the RF independent of the reservoir or surface pressure and temperature conditions. The recovery factors for different gases and solvents are shown in Fig. 4.21. Similar to those results

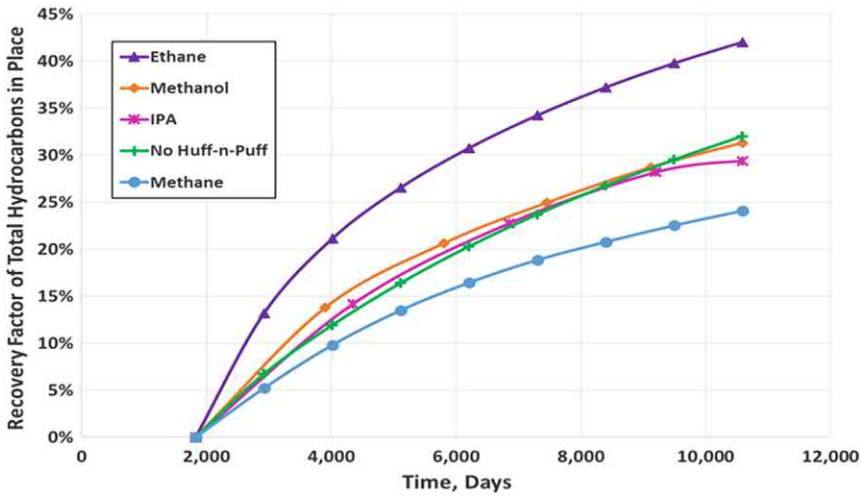

Figure 4.21 Total hydrocarbon recovery factors versus time from different operation schemes.

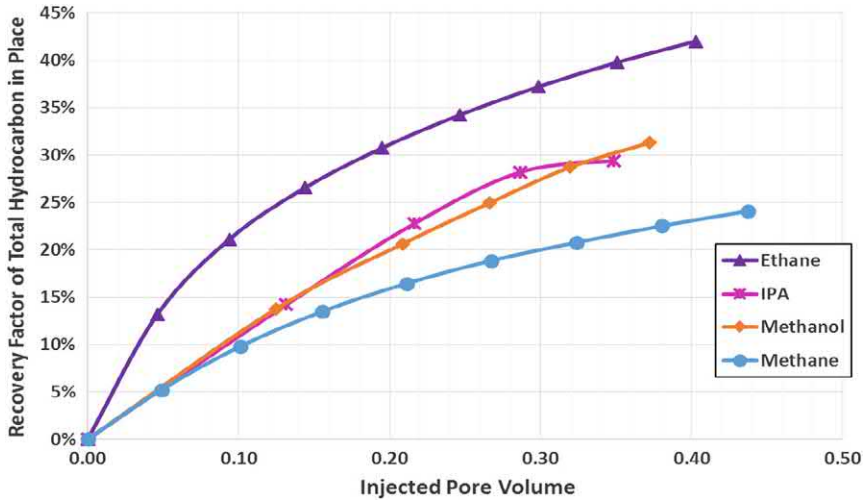

Figure 4.22 Total hydrocarbon recovery factors versus injected BOE volume from different operation schemes.

in the core-scale, ethane provides the highest recovery; the RFs from methanol and IPA are similar and close to that from no huff-n-puff; the RF from methane is the lowest. Part of the reasons for the lowest recovery can be better explained from the individual RFs later. Similar results are obtained when the total hydrocarbon recovery factors are plotted again the BOE volumes injected (Fig. 4.22).

The RF for an individual component follows the above equation except that "total hydrocarbon moles" is replaced by "total component i moles." Component i can be methane, butane, heptane, or decane. The component moles in the oil and gas phases are added together. The RFs of individual components are shown in Fig. 4.23. It can be seen that methane performs almost as well as ethane to recover condensate components (butane, heptane, and decane), but RF of methane is the lowest. The lowest recovery is because the RF definition excludes the remaining methane. Part of the remaining methane may be from the injected methane. But the RFs of other components do not have their own components injected and thus no exclusion is in their RF calculation. Apparently, this definition of RF is not perfect. But the earlier definition in the preceding section seems to have the effect. The objective to inject a gas or solvent is to recover condensate components. We need to pay attention to those recoveries when evaluating the recovery performance. Also note that methane

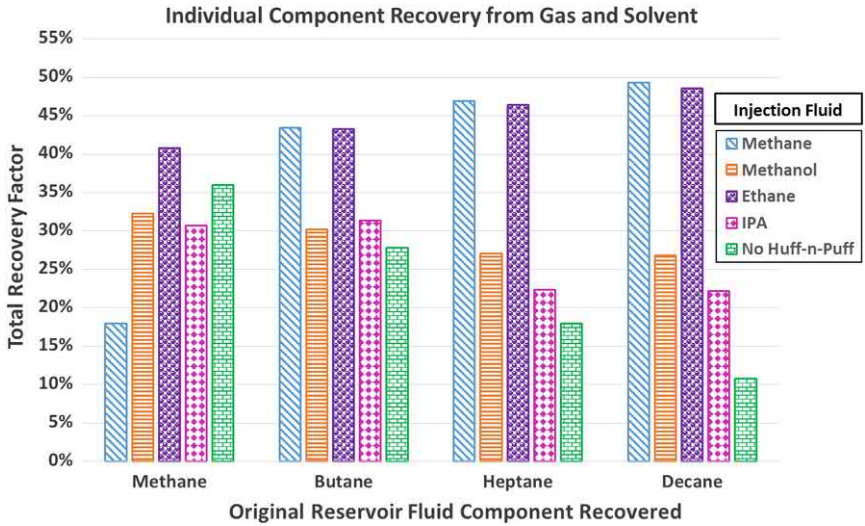

Figure 4.23 Total individual hydrocarbon recovery factors from different operation schemes.

injection recovers more methane than the solvents and butane similar to the solvents.

To include the effect of total injection volume and its cost, the recovery factors are corrected (called corrected recovery factor, RF_c). It is defined as:

$$RF_c = \frac{RF}{(\text{Unit volume cost of fluid}^*\text{Total volume of fluid injected})} \frac{\%}{\$MM}$$

The unit volume costs of the injection fluids are listed in the preceding section. This defined RF is only used to compare the relative economic performance. The corrected recovery factors for different gases and solvents are shown in Fig. 4.24. Gases outperform solvents. Although the corrected recovery factors for the two gases decrease with time, the corrected recovery factors for solvents stay relatively flat.

4.7 A field case of methanol injection

Hatter's Pond gas field had permeability of 2–6 mD, and porosity of 12%–15%. The dew point pressure was 3030 psi which was higher than the initial reservoir pressure of 2700 psi and the well flowing pressure of 2000 psi. The liquid dropout at 2000 psi was 33%. Such rich gas made a studied well production rate gradually decrease from 2.7 MMscf/d gas and

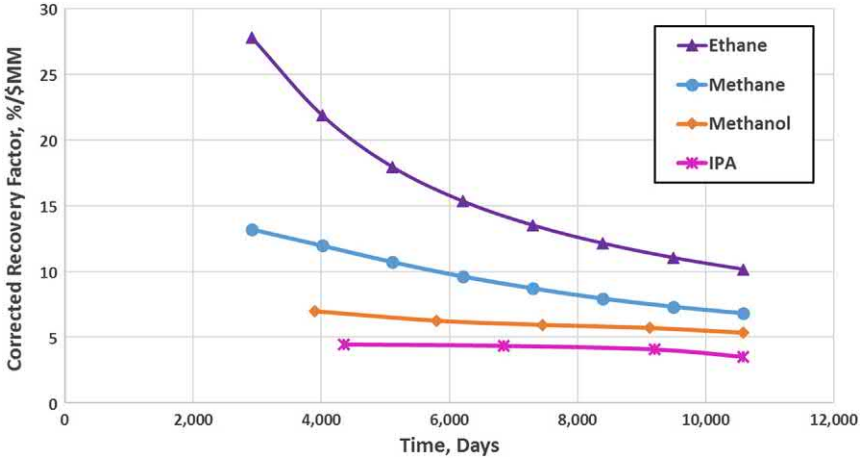

Figure 4.24 Corrected recovery factors from different operation schemes.

348 bbl/d condensate to 0.25 MMscf/d and 87 bbl/d, respectively. The production decline might be caused by water-base-mud filtrates, completion fluids, and condensate blanking. Well tests estimated permeability of 0.039 mD and a total skin of 0.68.

The well was treated by bull heading 1000 bbl methanol down the tubing at a rate of 5—8 bbl/min. After the treatment, the well production increased from 0.25 to 0.5 MMscf/d gas, and 87 to 157 bbl/d condensate. Although the permeability was almost unchanged, the total skin improved from 0.68 to 1.9, indicating wellbore damages were removed by the methanol. This production rates increased in 2 for 4 months and 50% thereafter (Al-Anazi et al., 2005).

4.8 Surfactant treatment

The principle of using surfactants to treat condensate blocked wells is wettability alteration of a strongly oil wet formation to a preferential gas wet formation (Li and Firoozabadi, 2000). Application of a nonionic fluorinated polymeric surfactant in sandstone cores has shown to increase both the gas and condensate relative permeabilities by a factor of 2 to 3 (Kumar et al., 2006). Their surfactant solution was prepared in a methanol-water mixture. A fluorinated surfactant was prepared in a mixture of isopropanol and propylene glycol (Bang et al., 2008) and in a 2-butoxyethanol-ethanol mixture (Bang, 2007). When the surfactant treated sand-filled propped fractures, relative permeability of gas was improved by the order of

1.5—2.5 (Bang et al., 2008). When a surfactant was used to treat reservoir and outcrop sandstone rocks, the relative permeability of the gas condensate at a connate water saturation was improved by a factor of 2 (Bang et al., 2009, 2010). The improvement remained after a large pore volume of the gas-condensate flood. However, Ahmadi et al. (2011) found that a polyamine primer preflush was necessary to make fluorinated chemicals durable. Karandish et al. (2015) used an anionic fluorosurfactant mixture to have altered the Sarkhun carbonate cores from water-wet to intermediate gas-wet. Their gas relative permeability was improved by 1.7 times.

Li et al. (2011) treated tight cores with the permeability less than 0.1 mD using a fluorocarbon surfactant. Water and decane imbibition tests were conducted to demonstrate wettability alteration from water wet to gas wet.

Sharma et al. (2018) treated Eagle Ford outcrop cores using a fluorocarbon surfactant. The porosity ranged from 8% to 9% and the permeability ranged between 700 nD to 900 nD. A gas-condensate mixture of 0.85 mol fraction methane and 0.15 mol fraction n-butane was used as a reservoir fluid. Its phase properties are presented earlier in this chapter. In this section, the experiments were carried at the room temperature of 74°F at which the dew point pressure of the fluid was 1870 psi. The maximum liquid dropout was 6.5% at 1500 psi. The nonionic fluorinated surfactant with 95% additives was used in experiments. Its fluoroalkyl group provided the oil- and water-repelling characteristics, resulting in gas wetting, while the alkylene oxide head group associated with the rock surface by hydrogen bonding caused by adsorption. The solution was prepared by diluting the 2 wt.% surfactant, 94 wt.% methanol, and 4 wt.% deionized water. The contact angle measurements for the treated cores showed significant wettability alteration to preferentially gas wetting. The water/air/rock contact angle increased from 60° to 80°, and the n-decane/air/rock contact angle increased from 0° to 60°.The experimental setup is shown in Fig. 4.3.

To perform a huff-n-puff experiment to remove condensate blockage, a condensate banking needed to be established. The core was first saturated with the single-phase gas-condensate mixture. Then the outlet A was set at 1500 psi at which the maximum liquid dropout occurred. The gas mixture was continuously flooded through the other end of the core B, until the average CT number did not change, indicating a steady flow through the core. Then the condensate saturation gradually decreased from the maximum at the outlet B to zero at some distance from the inlet B. Such condensate saturation represented a real liquid saturation profile from a well to some point in the reservoir.

For the purpose of comparison, methane huff-n-puff injection was performed. During a huff period, gas (methane) was injected into the core through the valve A (with B and C) closed for 30 min at 2000 psi which was higher than the dew point pressure. During a puff period, the core was depleted through A as well to the BPR for 30 min. No soaking time was applied. The CT number was recorded at the end of puff period. The liquid saturation in the core was calculated accordingly. The cycle was repeated 5 times. Within these 5 cycles, the condensate saturation was reduced from 0.2745 to 0.0957, resulting in 65.14% liquid recovery factor.

During a huff period of surfactant solution injection, the surfactant solution was injected into a core in 2.5 h at 2000 psi through the valve A with B and C closed. After that, the surfactant solution could not be further injected because of the low compressibility. And it was difficult to flow back because of the higher liquid viscosity and low shale permeability. As a result, only one cycle of surfactant huff-n-puff injection was performed in the experiment. The condensate saturation was reduced from 0.225 to 0.2218 with 1.42% liquid recovery factor. Note that any condensate whose saturation was lower than a critical condensate saturation could not be recovered by huff-n-puff surfactant injection. Injected surfactant could only change rock wettability to preferentially gas welling so that gas and liquid condensate relative permeabilities might be improved. One problem is that the radius or penetration of the surfactant treatment during huff-n-puff injection was small. Compared with methane huff-n-puff injection (65.14% RF), the RF from surfactant huff-n-puff ($1.42\% \times 5 = 7.1\%$) was about 10 times lower, even assuming 5 cycles had been able to be performed. Methane injection could have the revaporization mechanism which could recover liquid condensate both at higher and lower the critical condensate saturation. Note that the two cores in the two experiments were from the same Eagle Ford outcrop.

To further evaluate the feasibility of surfactant huff-n-puff injection, surfactant durability and economics were studied. The surfactant adsorption increased almost linearly with pore volumes injected. It reached 6.1 mg/g rock after 14 pore volume injection. The data indicates that the adsorption could be very high as a high pore volume of surfactant solution is injected because shale and tight rocks have a high surface area. Our laboratory experience revealed that it was difficult to change wettability using this surfactant after more than 15 pore volumes of flooding treatment (such treatment is not feasible in real reservoirs).

Earlier, huff-n-puff methane and methanol injection in shale gas-condensate cores are compared. Because of the ease of methane injection and flowback compared with methanol, methane injection is preferred to methanol injection. This surfactant is solubilized in the solution which consists of 94% methanol. Obviously, this surfactant cannot be more economic than methane injection.

4.9 Factors that affect huff-n-puff gas injection performance

To better understand the mechanisms and optimization of huff-n-puff gas injection, several relevant factors that affect the performance are discussed in this section. These factors include initial reservoir pressure, huff pressure, puff pressure, cycle time, soaking time, and CO_2 gas component.

4.9.1 Effect of huff pressure

From Fig. 4.7, it can be seen that the first cycle produced the highest condensate recovery. Meng et al. (2015a) found that higher injection (huff) pressure resulted in higher condensate recovery; with the pressure higher than the dew point, the effect of pressure became less significant, as shown in Fig. 4.25. A gas condensate mixture of 85% methane and 15% butane was used in the experiment.

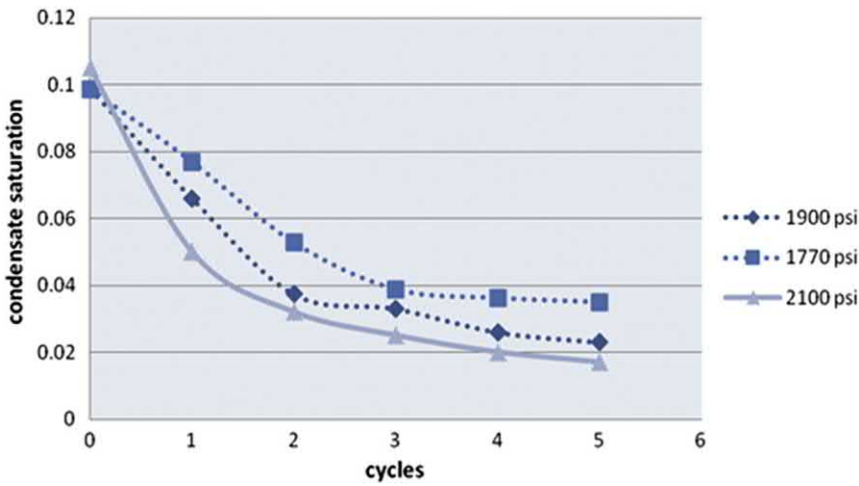

Figure 4.25 Effect of injection pressure on condensate recovery.

Table 4.3 Effect of huff pressure.

	P_i = 9088 psi			P_i = 5000 psi		
	Primary (PA)	H-n-P (A)	(A-PA)/ PA	Primary (PB)	H-n-P (B)	(B-PB)/ PB
Net gas produced (MMSCF)	357.01	125.40	−0.65	286.62	115.70	−0.60
Oil produced (MSTB)	30.39	46.67	0.54	17.83	23.42	0.31
Oil recovery factor (%)	26.00	39.93	0.54	19.00	24.91	0.31
Revenues of produced oil and gas (MM$)	4.47	5.19	0.16	2.93	2.80	−0.04

Based on the base model described in Section 4.4, the dew point of the gas condensate is 3988 psi, and the initial reservoir pressure is 9088 psi. In principle, the huff pressure should not be higher than the initial reservoir pressure to avoid fracture of the reservoir. Of course, it should be higher than the dew point pressure. To test the effect of huff pressure, two huff pressures of the initial reservoir pressure of 9088 psi and 5000 psi were used. The results are presented in Table 4.3. It shows that for the huff pressure of 9088 psi and 5000 psi, the incremental oil recovery of huff-n-puff injection over primary depletion are 54% and 31%, and the incremental revenues of produced oil and gas are 16% and −4%, respectively. These results show that higher huff pressure is better.

4.9.2 Effect of puff pressure

To simplify the discussion of the effect of puff pressure, the puff pressure should be below the dew point pressure (3988 psi ~ 4000 psi). Otherwise, there is not liquid blockage issue. Table 4.4 shows that the gas produced in the primary decreases with the puff pressure, because the production drawdown becomes lower. However, the oil recovery increases with the

Table 4.4 Effect of puff pressure.

Puff pressure, psi	Primary gas, MMSCF	Primary oil, MSTB	Huff-n-puff, MSTB	Inc. RF, %
500	357.01	26.00	39.93	53.6
1000	337.87	26.43	39.33	48.8
2000	285.84	27.97	38.81	38.7
4000	167.85	28.90	34.68	20.0
6000	85.13	15.27	25.32	65.8

puff pressure because higher puff (production) pressure results in less liquid oil dropout and then more oil produced.

For the huff-n-puff injection, the liquid oil produced decreases with the puff pressure, indicating that the lower production drawdown is less beneficial because less gas or energy is injected to boost the production of gas and liquid condensate. Therefore, the incremental oil recovery of huff-n-puff injection over the primary depletion decreases with the puff pressure.

To further discuss the effect of puff pressure, a case of 6000 psi puff pressure is added in the table. The primary gas production, primary oil production, and huff-n-puff oil production are all the lowest. This also implies that wells in a gas condensate reservoir should be produced below the dew point pressure.

4.9.3 Effect of cycle time

Table 4.5 shows the effect of cycle time. Here the cycle time is equal to the huff time and the puff time. As the cycle is shorter, more net gas is produced. However, the total liquid oil produced peaked at 100 days. The revenues from produced oil and gas also peaked at 100 days, implying that produced oil has higher economic value.

4.9.4 Effect of soak time

In Table 4.6, 100-0-100 means 100-day huff, 0-day soak, and 100-day puff. The first number is the huff time, the middle soak time, and the last puff time. The results show that when the first 100 days are split into 50-day huff and 50-day soaking, oil recovery and the revenues from oil and gas produced become lower, except the net gas produced. This means soaking is not effective. The benefit of soaking is to facilitate the injected gas to

Table 4.5 Effect of cycle time.

	200 d	100 d	50 d	25 d
Total gas produced (MMSCF)	2232.2	3133.7	3783.1	3814.4
Gas injected (MMSCF)	2161.6	3008.3	3621.5	3572.0
Net gas produced (MMSCF)	70.6	125.4	161.6	242.4
Oil produced (MSTB)	43.816	46.666	44.668	40.891
Oil recovery factor (%)	37.49	39.93	38.22	34.99
Revenues of produced oil and gas (MM$)	4.664	5.1682	5.1132	5.0587

Table 4.6 Effect of soak time.

	100-0-100	50-50-100	50-50-100 + diffusion	Diffusion effect, %
Total gas produced (MMSCF)	3133.7	2017.9	2028.2	0.5
Gas injected (MMSCF)	3008.3	1798.2	1790.3	−0.4
Net gas produced (MMSCF)	125.4	219.7	237.9	8.3
Oil produced (MSTB)	46.666	40.582	40.92	0.8
Oil recovery factor (%)	39.93	34.72	35.012	0.8
Revenues of produced oil and gas (MM$)	5.1682	4.937	5.0436	2.2

diffuse into oil. However, every performance parameter is lower than the case without soaking except net gas produced because of less gas injected. This means soaking cannot add benefits. Such conclusion is supported by Meng and Sheng's (2016a) simulation results. In some cases where the injection pressure is close to dew point pressure, soaking time propagates the pressure deep into the reservoir, leaving the pressure near the producing well or fracture below the dew point pressure, resulting in more condensate formation.

When soaking time is added, diffusion should be implemented in the model, which is done in the case of 50-50-100 + diffusion. By adding diffusion, every parameter is slightly improved except gas injected. The improvements shown in the column of "Diffusion effect, %" are marginal. That could be a reason that the effect of soaking time is not significant. The Sigmund (1976) method is used to calculate the molecular binary diffusion coefficients between components in the mixture.

4.9.5 CO_2 injection performance

CO_2 EOR is very interesting, and many studies have been conducted. And it is believed that CO_2 performs better than dry gas injection. However, Table 4.7 shows that oil recovery factor from C_1 injection is higher than CO_2. This is because the injected C_1 volume is higher than the CO_2 volume, as the well injection is controlled by the same injection pressure.

In another simulation study, Sheng et al. (2016) compared huff-n-puff performance from C_1, CO_2, and N_2. The oil recovery from the CO_2 injection is little higher than that from the C_1 injection, but it is much higher than that from the N_2 injection. The lower oil recovery in the N_2 injection

Table 4.7 Huff-n-puff CO_2 injection performance.

	C_1	CO_2
Total gas produced (MMSCF)	3133.2	2709.6
Gas injected (MMSCF)	3008.0	2626.0
Net gas produced (MMSCF)	125.2	83.6
Oil recovery factor (%)	39.93	37.09

is due to its high minimum miscible pressure. The effect of gas composition in gas condensate reservoirs is complex. It depends on gas injectivity and gas miscibility with the condensate. For shale oil reservoirs, the oil recovery by CO_2 injection is higher than that by C_1 injection (Wan et al., 2014a).

4.10 Optimization of huff-n-puff injection

From the above discussion of factors that affect huff-n-puff injection, we may have following designs to improve a huff-n-puff project in a condensate reservoir:

- Maximum allowable huff pressure,
- Minimum allowable puff pressure,
- Zero soaking time.

Cycle time needs to be optimized. Meng and Sheng (2016a) simulated the effect of injection time in a model of a single hydraulic fracture of 724 ft. They assume the simulated area is 724 ft by 592 ft. The matrix permeability is 100 nD. The puff time is 200 days. The dew point pressure is 2750 psi. The injection times of 10, 50, and 100 days are studied. Table 4.8 presents the results. From the point of view of oil production, longer injection is better. But the revenue from 50-day injection is the best.

Table 4.8 Effect of injection time.

	10 d	50 d	100 d
Total gas produced (MMSCF)	315	381	407
Gas injected (MMSCF)	30	117	164
Net gas produced (MMSCF)	285	264	243
Oil produced (MSTB)	12.933	14.113	14.678
Oil recovery factor (%)	13.3	14.5	15.1
Revenues of produced oil and gas (MM$)	2.433	2.467	2.439

The main condensate zone at the end of primary depletion is encompassed by the red dotted lines in Fig. 4.26. When the injection time is 10 days, the pressure in most of the zone is about 1500 psi. When it is 50 days, the pressure in half of the zone is below 2000 psi. When it is 100 days, the pressure in the entire zone is about 2400 psi, then the average pressure in the zone is close to the dew point of 2750 psi, and the oil recovery is the highest. From this discussion, it seems that the required injection time is so long that the pressure in the condensate zone should be above the dew point pressure. The final injection time should be optimized by economics, as long as injection requires more gas to be injected. In this example, it is 50 days. We may extend this statement more generally: the huff-n-puff injection should be optimized so that the pressure in the main condensate zone at the end of injection should be above the dew point pressure.

If a long puff time is used, less cycles will be needed for a fixed project time, less gas volume is injected, and more production time is obtained. Based on the above simulation model, Meng and Sheng (2016a) further studied the effect of puff time. They extended the puff time from 200 to 400 days with 50 days of puff time unchanged. They found the oil recovery factors for the two cases are almost the same, but the incremental revenues from the 400-day puff time case are more than two times those from the 200-day puff time case. The gas rate at the end of 200-day puff time is 38% of the rate in the beginning, while the gas rate at the end of 400-day puff time is 10%. Therefore, they proposed that the puff time should be determined so that the gas rate at the end of puff period should be 10% of the gas rate in the beginning. We have to say this 10% is not a general rule. A longer production is carried out at a relatively low pressure (energy) mode, which may not be optimal.

4.11 Mechanisms of huff-n-puff injection

Energy supply or pressure maintenance is probably the most important and obvious mechanism in huff-n-puff injection. Mechanisms re-vaporization, solubilization and improved phase behavior are discussed in this section.

4.10.1 Revaporization by gas

In Section 4.5, a one-dimensional simulation model is used to simulate gas and solvent performance. Fig. 4.27 shows the changes in oil viscosity,

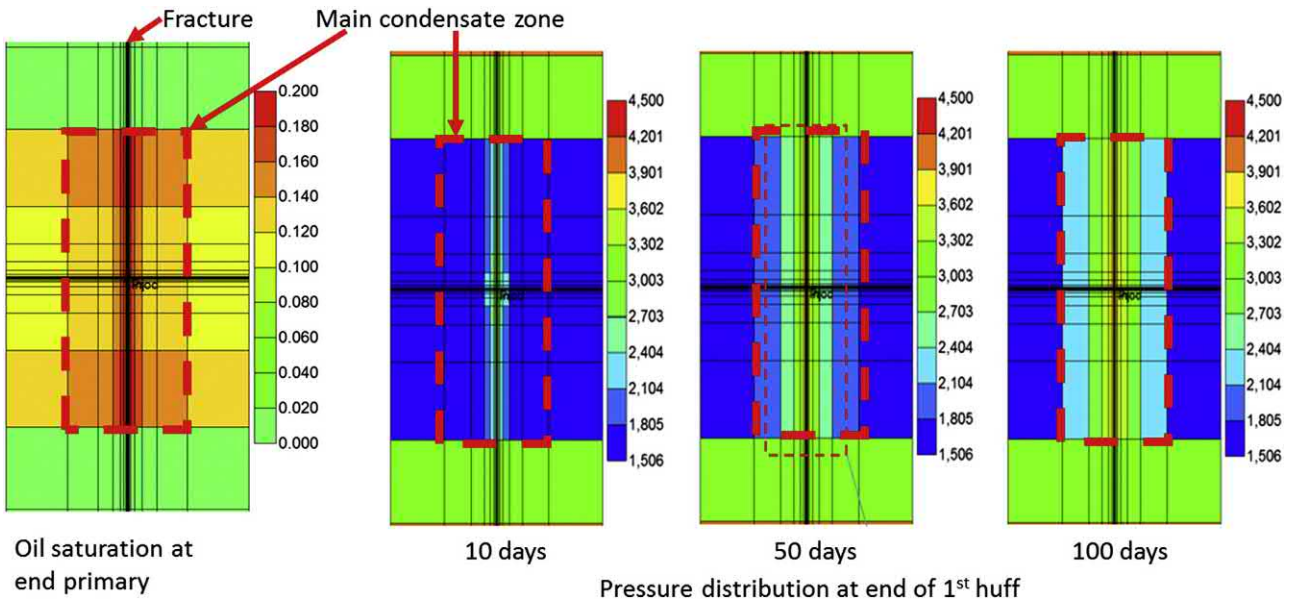

Figure 4.26 Oil saturation at the end of primary depletion and pressure distributions at the end of first huff.

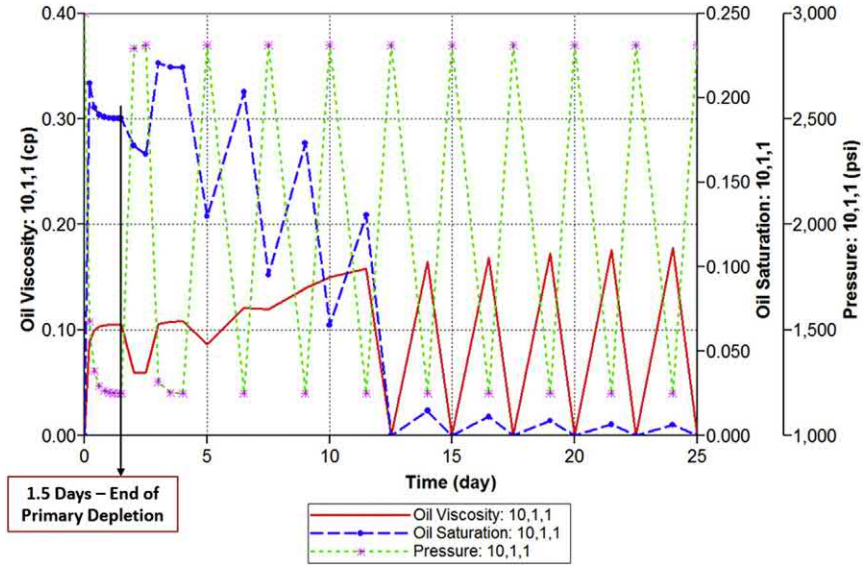

Figure 4.27 Changes in oil viscosity, pressure, and oil saturation at Block (10,1,1) for methane injection into a core of Fluid A.

pressure, and oil saturation at Block (10,1,1) for methane injection into a core of Fluid A. Keep in mind that total 24 blocks are used in the model with the huff-n-puff block in (1,1,1). On the pressure curve, every peak represents the end of huff or injection period, and every trough represents the end of puff or production period. Within a cycle of huff and puff, the trend of oil saturation change is opposite the trend of pressure change. In other words, when the pressure increases during the huff, the oil saturation decreases because higher pressure vaporizes the oil (the dew point pressure is 2795 psi). Note that the oil saturation is below 0.2 in almost the entire huff-n-puff process. The residual oil saturation in the model is 0.25. Therefore, the oil saturation decreases because of vaporization. Overall, the oil saturation decreases with cycle, and the peaks of oil viscosity slightly increase with cycle. The increase in oil viscosity with cycle is because light components are vaporized preferentially in early cycles, resulting in heavy components remaining in later cycles. Fig. 4.28 shows the mole fraction of butane at Block (10,1,1) decreases, while the mole fraction of decane increases with cycle. The discussion here also reveals viscosity reduction may not be a dominant mechanism for a low-viscosity condensate recovery.

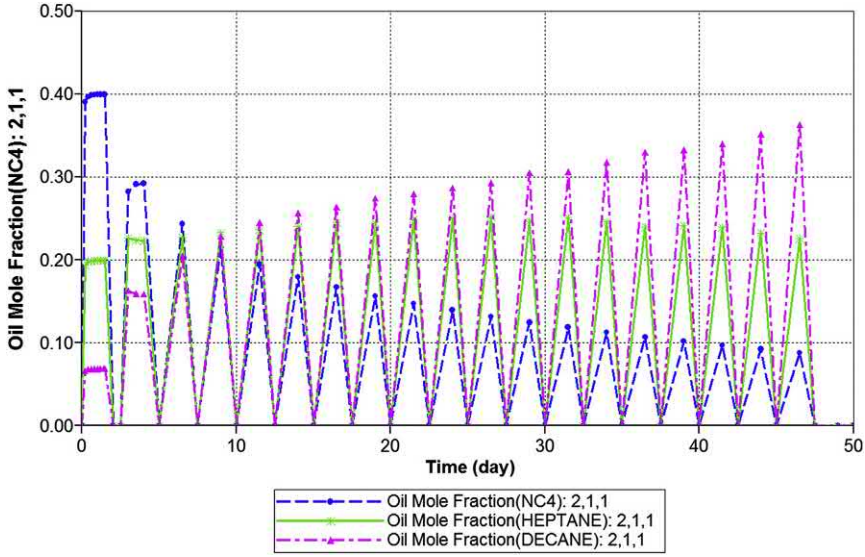

Figure 4.28 Component mole fractions at Block (10,1,1) for methane injection into a core of Fluid A.

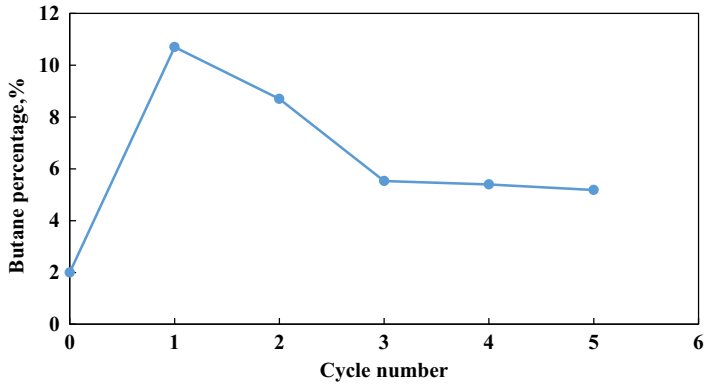

Figure 4.29 Butane content after primary depletion and huff-n-puff cycles.

Meng and Sheng (2016b) did huff-n-puff experiments using a mixture of 15% butane and 85% methane. At the end of primary depletion, the butane content in the produced stream was 2% (Fig. 4.29). It increased during the first cycle because of revaporization as the pressure was increased. At later cycles, it decreased as less butane was available and more methane flowed into the production stream.

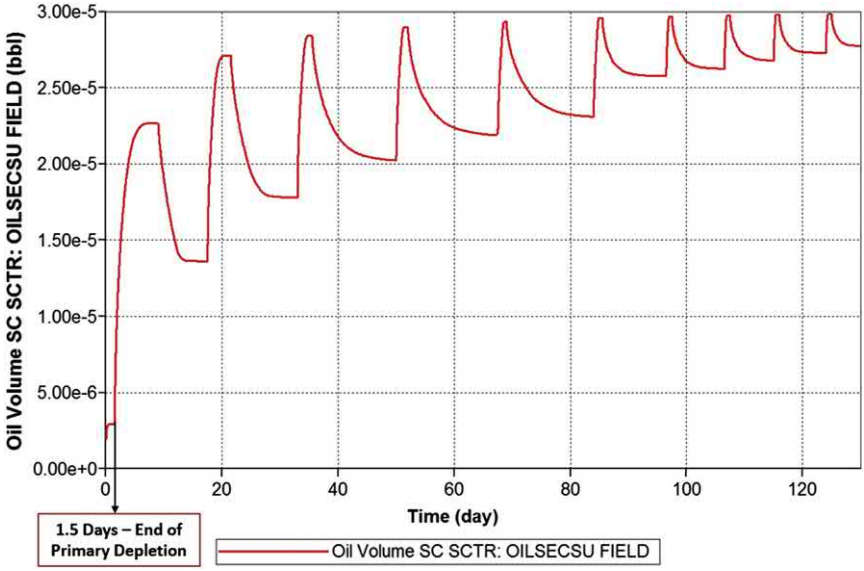

Figure 4.30 Oil volume changes with time in huff-n-puff methanol injection.

4.10.2 Swelling by a solvent

Methanol can solubilize the liquid condensate and dissolve gas. Fig. 4.30 shows the oil volume in the model consistently increases with cycles. Since oil is constantly produced, the original oil volume must decrease; the increase in oil volume is due to methanol solubilization. The oil volume in place is actually a mixture of solvent and hydrocarbons.

Although solvents displace some condensate near the wellbore, they also occupy the space that is occupied by the condensate. Thus, they cannot effectively increase gas permeability. However, they generally have lower interfacial tension (IFT) with the condensate. It is easier for them to flow back with the condensate with lower IFT. Solvents may also dissolve wax or asphaltene blockage.

4.10.3 Changed phase behavior

Gases and solvent may convert a contacted condensate to a more volatile fluid, reducing the dewpoint and liquid dropout. For example, when Fluid A is added with 15% mole fraction of methane, ethane, propane, and CO_2, the dew point and dropout are reduced (Fig. 4.31). When methane or ethane is injected, the dew point of the earlier mentioned Fluid B is reduced (see Fig. 4.32).

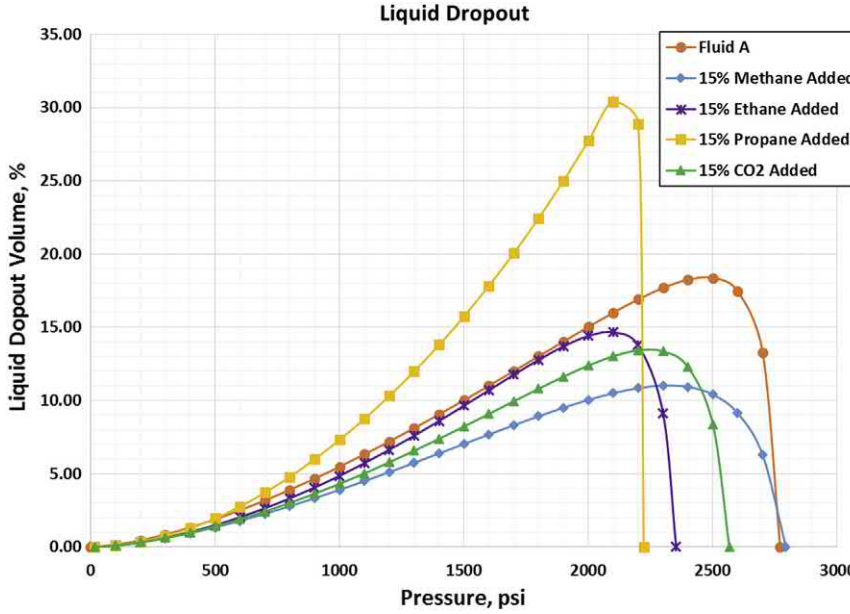

Figure 4.31 Reduced liquid dropout and dewpoint pressure of Fluid A when 15% gases are added.

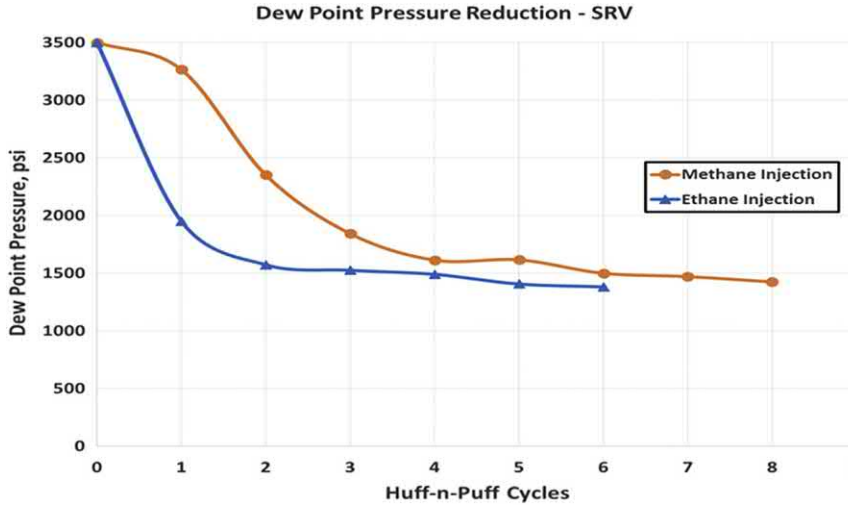

Figure 4.32 Reduction in dew point pressure in an SRV block after huff-n-puff ethane or methane injection.

CHAPTER FIVE

Optimization of huff-n-puff gas injection in shale and tight oil reservoirs

Abstract

This chapter is to discuss the optimum huff-n-puff times, number of cycles, and soaking time under practical operational and reservoir conditions. The operational and reservoir conditions dictate the maximum injection and production rates and the maximum injection pressure and minimum production pressure. Optimization principles and optimization criteria for huff-n-puff gas injection are proposed. It is also found that the benefits of soaking may not compensate the loss in injection and production due to the time lost in the soaking period. Therefore, soaking may not be necessary during the huff-n-puff gas injection in shale and tight oil reservoirs.

Keywords: Huff-n-puff gas injection; Maximum injection pressure; Minimum production pressure; Optimization criteria; Optimization principle; Soaking time.

5.1 Introduction

Since Wan et al. (2013a) proposed huff-n-puff gas injection to improve oil recovery in shale and tight oil reservoirs, many papers have been published on the subject, as reviewed by Sheng (2015d). However, Chen et al. (2014) showed that the final recovery factor from huff-n-puff CO_2 injection is lower than that in the primary depletion because the incremental oil recovery in the production stage is unable to compensate the loss during the injection and shut-in stages. In their models, the huff-n-puff time is from 300 to 1000 days; the bottom-hole injection pressure is 4000 psi and the producing pressure is 3000 psi. Using his model, Sheng (2015d) was able to repeat Chen et al.'s (2014) results (i.e., the huff-n-puff oil recovery is lower than the primary oil recovery). However, using the same model, by raising the injection pressure to 7000 psi, Sheng (2015d) demonstrated that all the oil recovery factors from the huff-n-puff process are higher than those from the primary depletion at the end of 30, 50, and 70 years. In other words, Chen et al.'s (2014) results

Enhanced Oil Recovery in Shale and Tight Reservoirs
ISBN: 978-0-12-815905-7
https://doi.org/10.1016/B978-0-12-815905-7.00005-0

are caused by the low injection pressure of 4000 psi. The initial reservoir pressure is 6840 psi. Generally, we try to use a high injection pressure to make the huff-n-puff more effective. This example shows that huff-n-puff optimization is so important that without optimization, a wrong conclusion about the effectiveness may be made. This chapter discusses the optimization of huff-n-puff gas injection in shale oil reservoirs. Huff time, puff time, and soaking time are investigated using simulation approach combined with some laboratory results.

5.2 Setup of a base simulation model

Middle Bakken data were used to build a validated base model. The compositional simulator GEM developed by Computer Modeling Group (2014) is used. A horizontal well is fractured with 15 fractures. The model has a half-fracture connected through a vertical well block (1,16,1). Then the production data from this model represents the 30th of a horizontal well production.

The schematic of the simulation model is shown in Fig. 5.1. Its dimensions are 296.25 ft × 4724 ft × 5 ft. The stimulated reservoir volume (SRV) has the fracture length of 724 ft in the J direction, the half-fracture spacing of 296.25 ft in the I direction, and 50 ft (formation thickness) in the K direction. The half-hydraulic fracture width is 0.5 ft. The detailed block sizes of this base model are below.

The block sizes in feet in the I direction from I = 1 to I = 11 are:

0.5	0.257312051	0.522150017	1.059571985	2.150134547	4.363156667	8.85392783
17.96681715	36.45913142	73.98462696	150.1331714			

The block sizes in feet in the J direction of total 31 blocks are:

5*200	187.1636568	90.39505341	43.65839939	21.08584226	10.18389932	4.918551703
2.375529264	1.147317264	0.554123632	0.267626932	0.5	0.267626932	
0.554123632	1.147317264	2.375529264	4.918551703	10.18389932	21.08584226	
43.65839939	90.39505341	187.1636568	5*200			

One block is used in the K direction with its size 50 feet.

Table 5.1 summarizes the matrix and fracture property data in the non-SRV and SRV regions in the Middle Bakken shale (Kurtoglu, 2013).

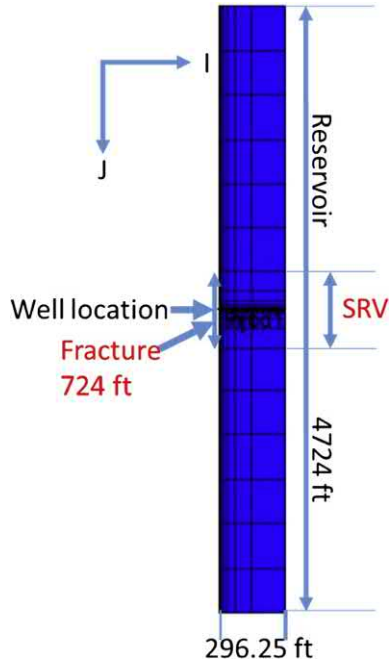

Figure 5.1 Schematic of the base model.

Table 5.1 Matrix and fracture properties.

	Non-SRV	SRV
Thickness, ft	50	50
Matrix permeability, mD	3.0E-04	3.0E-04
Matrix porosity, fraction	0.056	0.056
Fracture porosity, fraction	0.0022	0.0056
Fracture permeability, mD	2.16E-03	3.13E-02
Fracture spacing, ft	2.27	0.77
Hydraulic fracture porosity, fraction		0.9
Hydraulic fracture permeability, mD		100

The dual permeability model was used to simulate the matrix, natural fractures and hydraulically stimulated reservoir volume. The shale matrix permeability is 0.0003 mD. The natural fracture effective permeability is 0.0313 mD in the SRV and 0.00216 mD in the unstimulated reservoir region.

The reservoir fluid composition and the Peng-Robinson EOS parameters are from Yu et al. (2014b) as represented in Table 5.2. The binary

Table 5.2 Peng-Robinson EOS fluid description of the Bakken oil.

Comp.	Initial mole fraction	P_c (atm.)	T_c (° K)	V_c, L/mol)	Acentric factor	MW g/ mole	Parachor coeff.
CO_2	0.0001	72.80	304.2	0.0940	0.013	44.01	78.0
N_2–C_1	0.2203	45.24	189.7	0.0989	0.04	16.21	76.5
C_2–C_4	0.2063	43.49	412.5	0.2039	0.0986	44.79	150.5
C_5–C_7	0.1170	37.69	556.9	0.3324	0.1524	83.46	248.5
C_8–C_{12}	0.2815	31.04	667.5	0.4559	0.225	120.52	344.9
C_{13}–C_{19}	0.0940	19.29	673.8	0.7649	0.1848	220.34	570.1
C_{20+}	0.0808	15.38	792.4	1.2521	0.7527	321.52	905.7

Table 5.3 Binary interaction coefficients for Bakken oil.

	CO_2	N_2–C_1	C_2–C_4	C_5–C_7	C_8–C_{12}	C_{13}–C_{19}	C_{20+}
CO_2	0						
N_2–C_1	0.1013	0					
C_2–C_4	0.1317	0.013	0				
C_5–C_7	0.1421	0.0358	0.0059	0			
C_8–C_{12}	0.1501	0.0561	0.016	0.0025	0		
C_{13}–C_{19}	0.1502	0.0976	0.0424	0.0172	0.0067	0	
C_{20+}	0.1503	0.1449	0.0779	0.0427	0.0251	0.0061	0

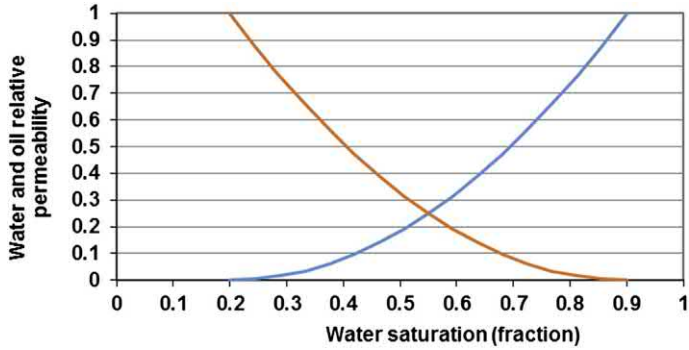

Figure 5.2 Water and oil relative permeabilities.

interaction coefficients are presented in Table 5.3. In Table 5.2, P_c, T_c, and V_c are the critical pressure, critical temperature, and critical volume, respectively, and MW means the molecular weight. The reservoir temperature is 245°F, and the initial reservoir pressure is 7800 psi. The initial water saturation is 0.4. The history-matched relative permeabilities are shown in Figs. 5.2 and 5.3.

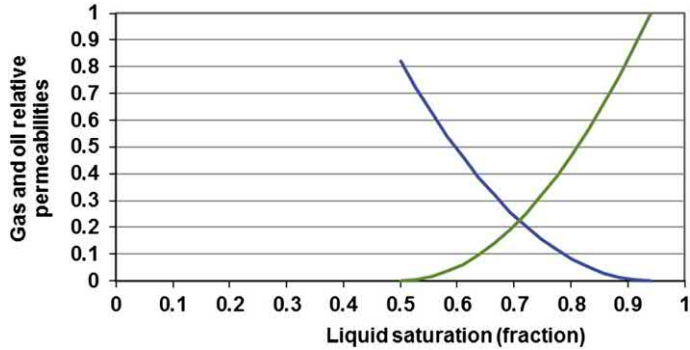

Figure 5.3 Gas and oil relative permeabilities.

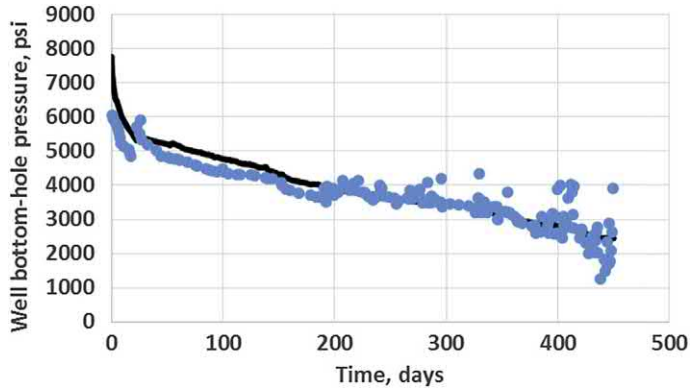

Figure 5.4 Well bottom-hole pressure (dot points are actual data, and line is simulated data).

During history matching of 1.2 years of production, the oil rate history is set in the model, the gas rate and well bottom-hole pressure data are matched by adjusting model parameters. The simulated well bottom-hole pressure (line) and the actual data (dotted points) are compared in Fig. 5.4. They are reasonably matched. The oil rate is exactly matched because it is input to the model. The gas rate from the model is lower than the actual data, but it follows the same trend of actual data. We believe it is caused by the imperfect representation of PVT data by the EOS model used. Therefore, the model is reasonably calibrated.

5.3 Optimization principles

An objective function or parameter needs to be defined for optimization. Although a net present value is a good parameter, many

parameters are needed such as equipment cost, operational cost, royalty tax, and interest rate. These parameters are very case-specific. It will be very difficult to use this parameter to work out general optimization criteria. Alternatively, oil recovery factor is chosen as the objective function.

Compared with gas flooding, huff time, puff time, and soaking time are important parameters. They are closely related to injection and production pressures, and injection and production rates. First, pressures and rates are addressed. As discussed in the preceding chapters, injection pressure should be as high as possible. Generally, this pressure is set to be the initial reservoir pressure which is 7800 psi in this model. A higher pressure may fracture the reservoir. This is a typical practice for pressure maintenance. The maximum injection rate for the whole fractured horizontal well is set to be 9 MMSCF/D. For this model, we only simulate a half-fracture for a 15-stage well. Thus, the maximum gas rate in the model is 300 MSCF/D. Sheng and Chen (2014) showed that a higher oil recovery is obtained if a lower bottom-hole flowing pressure (BHFP) is used, even though the flowing pressure is lower than the bubble point pressure. Thus, the minimum bottom-hole flowing pressure is set at 500 psi. The maximum producing oil rate is 1500 STB/D or 50 STB/D in the model. The maximum producing gas rate is 9 MMSCF/D or 300 MSCF/D in the model. Before gas injection, the primary depletion is extended from 1.2 years to about 3 years (1000 days) at the minimum flowing pressure of 500 psi. Huff-n-puff injection is continued until 10,950 days (total about 30 years). The injected gas is methane.

5.4 Optimization criteria

Based on the above principles, optimum huff time, puff time, and soaking time are determined, and the number of cycles is discussed.

5.4.1 Optimum huff time and puff time

In the literature, huff time, puff time, and soaking time in conventional and tight field projects range from days, months, to years (Kurtoglu, 2013; Shoaib and Hoffman, 2009; Wang et al., 2010). Oil recovery factors at different huff and puff times are presented in Table 5.4. When the huff time is increased from 100 days (Case H100P300) to 300 days (Case H300P300) but the same puff time of 300 days is kept, the oil recovery factor increases by 6.15% from 15.05% to 21.2%, indicating the oil recovery is very sensitive to the huff time. Note in the case name H100P300, H means

Table 5.4 Effect of huff-n-puff times.

Case	Huff, days	Puff, days	Oil RF, %
Primary	0	10,950	11.42
H100P100	100	100	15.12
H100P300	100	300	15.05
H300P300	300	300	21.20
H300P100	300	100	15.38
H300P200	300	200	19.49
H300P350	300	350	20.95
H300P450	300	450	20.57
H300P600	300	600	20.12
H100P100qx3	100	100	23.33
Primarytrans0.33	0	10,950	9.46
H100P100trans0.33	100	100	15.53

huff and the following number represents the huff time in days; P means puff and the following number presents the puff time in days. This naming applies to the subsequent case numbers. The block pressures at block (2,16,1) near the injection well at block (1,16,1) for 100 and 300 days of huff time are shown in Fig. 5.5. It shows that the pressure for 100-day huff time is raised to be less than 4000 psi, while the pressure for 300-day huff time reaches around the maximum allowable 7800 psi. Then the drawdown pressure to produce oil from the 100-day case is almost half of that from the 300-day case. 100-day huff time is not long enough to boost the pressure (energy).

For the same huff time of 100 days, when the puff time is increased from 100 days (Case H100P100) to 300 days (Case H100P300), the oil recovery factor decreases by 0.07% from 15.12% to 15.05%, indicating the puff time is not important. The near-wellbore block pressures are shown in Fig. 5.6. When the huff time is 100 days, the pressure near the well is relatively low (4000−5000 psi). Then the production drawdown and the oil rate will be low. Therefore, a longer puff (production) time may not be helpful to oil production. If it is too long, effective operation time is lost.

Comparing the two cases, H300P300 and H300P100, the oil recovery factor for H300P100 decreases by 5.82%, from 21.2% to 15.38%, for H300P300. The puff time is important in these two cases. The block pressure at block (2,16,1) near the well (fracture) block (1,16,1) in H300P100 is shown in Fig. 5.7. It shows that the pressure reaches the injection pressure during the huff period, but it cannot deplete to the set puff pressure of 500 psi at the end of 100 days of puff, before the well is

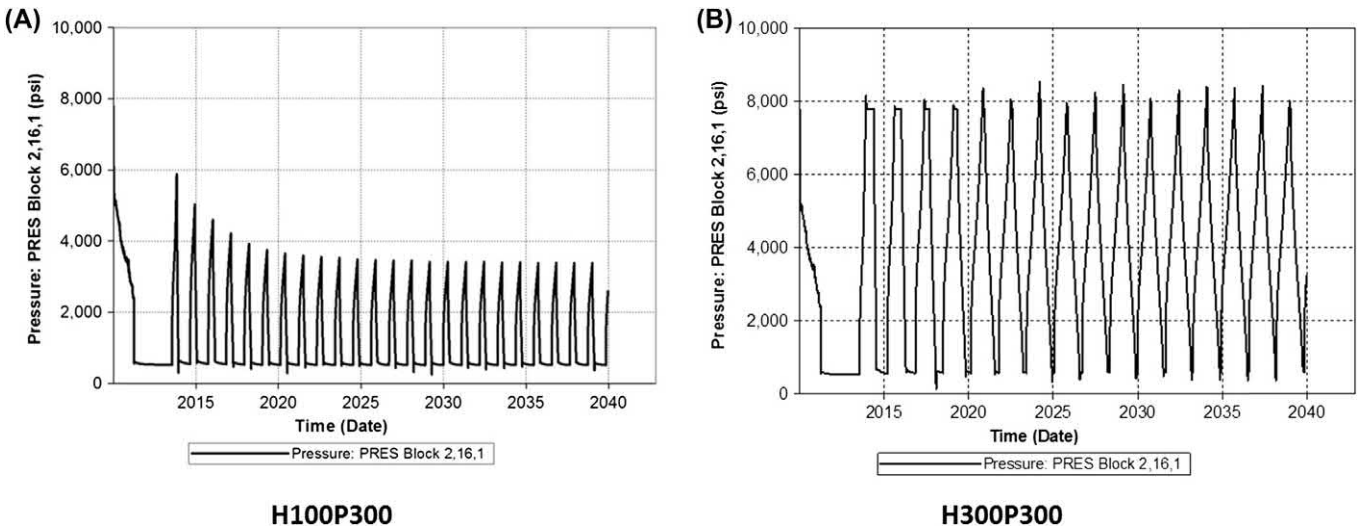

Figure 5.5 Near-wellbore block pressures for the huff time of (A) 100 days and (B) 300 days with the puff time of 300 days.

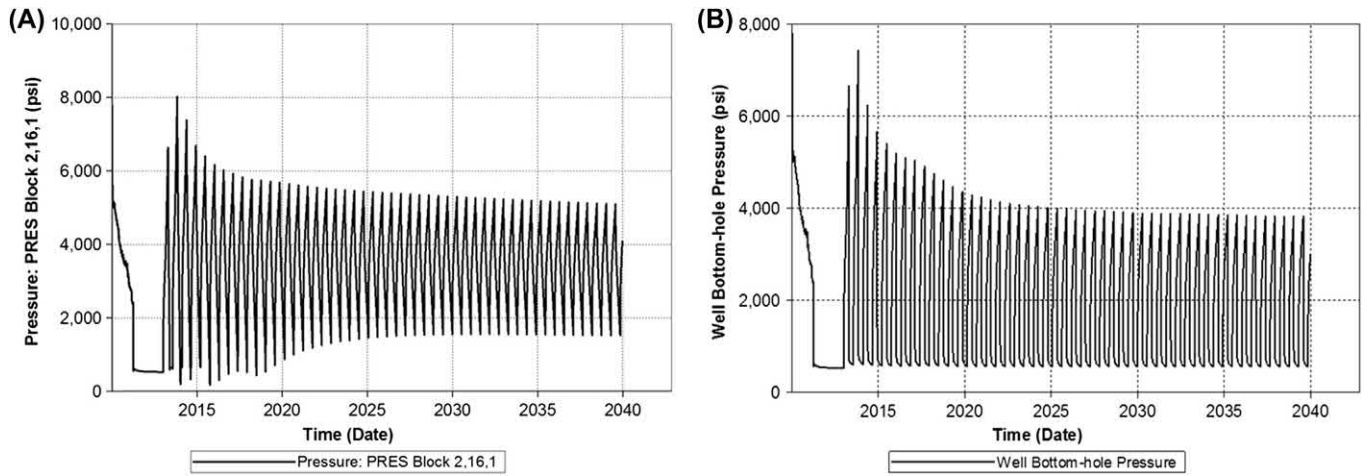

Figure 5.6 Near-wellbore block pressures for the puff time of (A) 100 days and (B) 300 days with the huff time of 100 days.

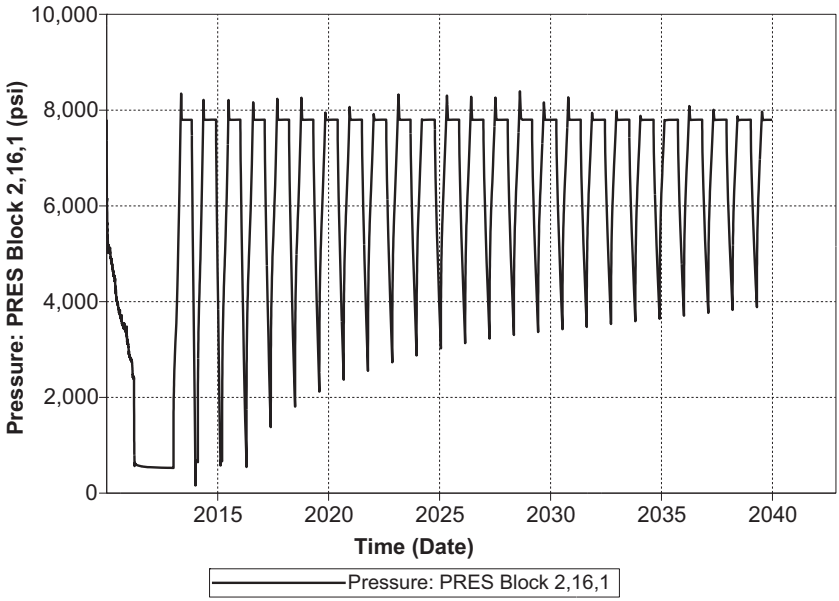

Figure 5.7 Near-well block pressure in H300P100.

switched to the huff mode. Thus, the effective production is lost. To support this statement, case H300P200 is simulated. The oil recovery factor is increased to 19.49%.

Will the oil recovery increase when the puff time is further increased from 300 days? Three more cases, H300P350, H300P450, and H300P600, where the puff time is extended to 350, 450, and 600 days are simulated. The oil recovery factors are 20.95%, 20.57%, and 20.12%, respectively (see Table 5.4), all lower than that from H300P300! The near-wellbore block pressures during the huff-n-puff are slightly lower than those in H300P300 (data not shown here to shorten the presentation). Also, the oil rate after 300 days is very low; thus the extended production is not effective.

From the above discussions, we may conclude that the optimum huff time is so long that the near-wellbore pressure reaches to the set maximum huff pressure, and the optimum puff time is so long that the near-wellbore pressure reaches to the set minimum puff pressure.

To support the above conclusion, based on the case H100P100, another case H100P100qx3 is simulated. In this case, both the maximum injection rate and the maximum production rate are increased by three times. By

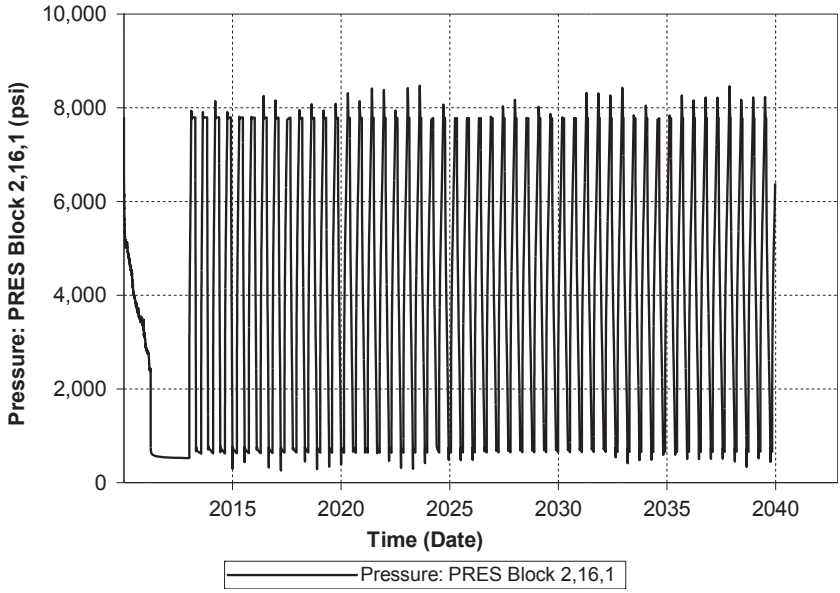

Figure 5.8 Near-wellbore block pressure when the huff-n-puff time are 100 days but high rate (H100P100qx3).

increasing the rates, higher huff pressures and lower puff pressures near the wellbore (fracture) will occur. Fig. 5.8 shows the near-wellbore pressure reaches both the set maximum huff pressure and the set minimum puff pressure. The oil recovery factor from this case is 23.3%, higher than that from the case H300P300 (21.2%).

Furthermore, additional models are used to support the conclusion. If the transmissibility is reduced, the near-wellbore block pressure will more easily reach the set maximum injection pressure (7800 psi) during the huff period and the set minimum production pressure (500 psi) during the puff period. Even the huff time and puff time are short such as 100 days; the oil recovery factor will be high or optimized. To prove that the transmissibilities in the primary case (Primary) and the huff-n-puff case (H100P100) are decreased by three times, the corresponding new cases, Primarytrans0.33 and H100P100trans0.33, are created. The near-wellbore block pressure in the huff-n-puff case H100P100trans0.33 is shown in Fig. 5.9. It shows that the pressure reaches the set maximum injection pressure during the huff period and the set minimum production pressure during the puff period. The oil recovery factors for the primary and huff-n-puff cases are 9.46% and 15.53%, respectively (see Table 5.4), resulting in the incremental oil recovery factor 6.07%.

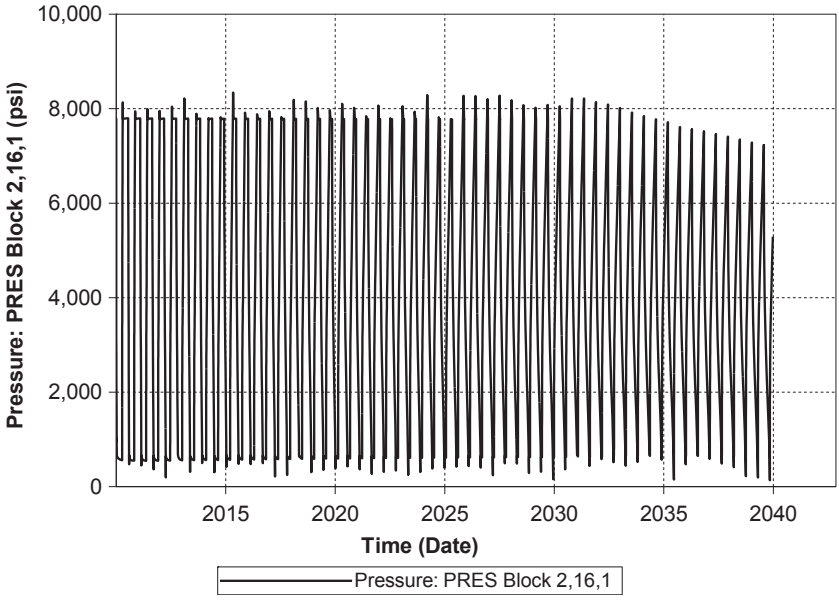

Figure 5.9 Near-wellbore block pressure in Case H100P100trans0.33 with its transmissibility reduced 3 times from Case H100P100.

Fragoso et al. (2018b) found that longer cycle time (longer huff and puff time) performs better than the shorter time, as more gas is injected, and long production time is allowed. Their result is consistent with the above discussion. They further found that the optimal schedule is such that the cycle time increases with cycle, as more gas is produced so that more gas is needed to supplement the voidage and a long time is needed to produce the oil deep in the reservoir. They also proposed that refracturing and huff-n-puff are combined to improve oil recovery.

Kong et al. (2016) found from simulation that the optimum huff-n-puff CO_2 injection for the Cardium tight oil reservoir (0.2 mD) is 1 month of huff time, 3 months of puff time, and selected 10 days of soaking time. They found 0.7% more oil is produced in 5 years, if the huff time and the puff time are increased by 5 days for each consecutive cycle.

Kong et al. (2016) also studied the interwell interference during huff-n-puff CO_2 injection by comparing an asynchronous huff-n-puff injection with the counterpart synchronous injection. In the synchronous injection, all the wells perform huff, soak, and puff operations at the same pace, while in the asynchronous injection, when a group of wells are in the huff mode, the rest of the wells are in the puff mode. They tested a three-well sector. When the middle well is in the huff mode, the two side wells are

in the puff mode, and vice versa. They found that the asynchronous injection outperforms the synchronous injection. This probably results from that the energy is more effectively used during the asynchronous injection.

5.4.2 Optimum soaking time

Experimental data show that the oil recovery will be higher within a single cycle if soaking time is added or a longer soaking time is used (Gamadi et al., 2013). However, if the total experimental time of huff, soak, and puff is the same, more oil can be recovered without soaking time or shorter soaking time (Yu and Sheng, 2015). The field tests reported by Monger and Coma (1988) used the soaking time of 18–52 days; the results did not show the sensitivity of soaking time. Their laboratory tests showed that soaking time improved recovery of waterflood residual oil in the cores. But the improved oil recovery was mainly from the subsequent waterflooding period. Sanchez-Rivera et al.'s (2015) simulation result shows a lower oil recovery at a longer soaking time; adding molecular diffusion does not change the result.

To find out the effect of soaking time, a new case H300S100P300 is created. In this case, 100 days of soaking time is added, and the total number of huff-n-puff cycles remains the same as H300P300. The total number of cycles for 10,950 days is about 17 for the two cases. But the total elapse time for H300S100P300 is increased to 12,650 days (=10,950 + 1700). Its oil recovery factor is 21.39%, higher than 21.2% from H300P300, as presented in Table 5.5. This result is consistent with the experimental observations mentioned above.

However, if the total operation time is fixed at 10,950 days, and the huff time of 300 days is split into 200 days of huff time and 100 days of soaking time in H200S100P300, the oil recovery factor becomes 17.7% that is lower than 21.2% in H300P300 (Table 5.5). This result is consistent with that in a condensate reservoir case (Sheng, 2015b).

Table 5.5 Effect of soaking time.

Case	Huff, days	Soak, days	Puff, days	Oil RF, %
Primary	0	0	10,950	11.42
H300P300	300	0	300	21.20
H300S100P300ext	300	100	300	21.39
H200S100P300	200	100	300	17.70
H300S5P300	300	5	300	21.01
H300S50P300	300	50	300	20.71
H300S100P300	300	100	300	20.33
H300P300Diff	300	0	300	23.40
H300S100P300Diff	300	100	300	22.71

Now keeping the total elapse time (10,950 days) and the huff time (300 days) unchanged, soaking times of 5, 50, and 100 days are added to H300P300 in the cases of H300S5P300, H300S50P300, and H300S100P300. The oil recovery factors for these cases are 20.01%, 20.71%, and 20.33%, respectively, as shown in Table 5.5. All these recovery factors are lower than 21.2% in H300P300 without soaking time. Therefore, soaking time was not added (Wan et al., 2013a, b; Wan et al., 2014a, b; Sheng and Chen, 2014; and Wan and Sheng, 2015b; Meng et al., 2015b).

In the above cases with soaking time, diffusion is not included. Soaking may help gas diffuse into oil phase. Therefore, to study the effect of soaking time, diffusion is added to create a case H300S100P300Diff. The oil recovery factor is 22.71% that is lower than that in H300P300Diff without soaking time (see Table 5.5). The total project time is the same in these two cases. This comparison shows that including diffusion does not make soaking time beneficial. Fragoso et al. (2018a) did not use soaking time in their simulation study as the highest oil recovery could be obtained without soaking time.

5.4.3 Number of cycles

More oil can be produced in each of early cycles than each of late cycle. There should be an optimum number of cycles. Artun et al.'s (2011) simulation work indicated that an optimum number of cycles were two to three based on net present value for a fractured conventional reservoir. Yu and Sheng (2015) did 10 cycles of huff-n-puff experiments and the cumulative oil recovered continued to increase with the cycle. Wan et al.'s (2015) history matched the Yu and Sheng's experiments and the models also predict the continuous increase with the cycle.

The case H300P300 is extended from 10,950 to 32,850 days (about 90 years) to create the case H300P300ext. The cumulative oil recovery factor keeps increasing as shown in Fig. 5.10; the oil rate decreases with time (Fig. 5.11). An economic analysis is needed to determine the optimum number of cycles for a real project.

5.4.4 Start time of huff-n-puff

Sanchez-Rivera et al.'s (2015) simulation data indicate that too early start of the first huff-n-puff gas injection from the primary depletion is detrimental to oil recovery, but too late start is disadvantageous to the net present value.

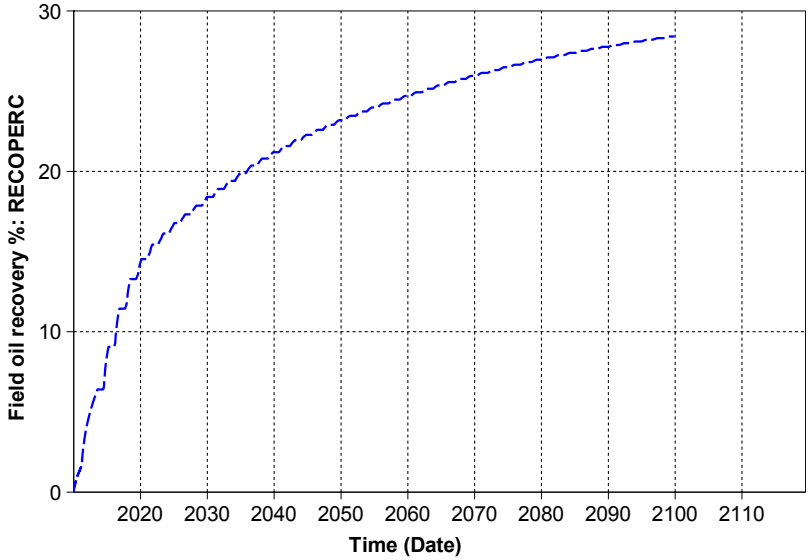

Figure 5.10 Oil recovery factor versus time in H300P300ext.

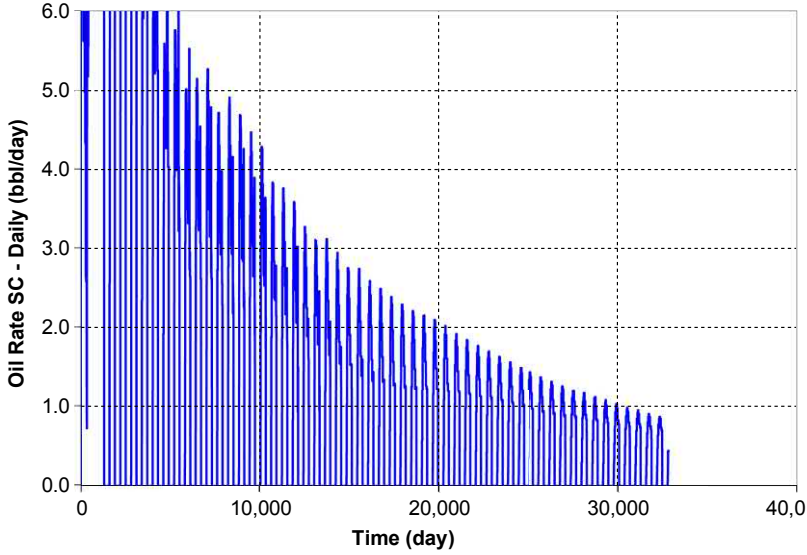

Figure 5.11 Oil rate versus time in H300P300ext.

According to the Sheng's (2015d) simulation results, some years of primary depletion assists the subsequent production of oil by gas flooding and huff-n-puff gas injection. Meng and Sheng (2016a) proposed that in the huff-n-puff gas injection in gas condensate reservoirs, the puff time should be started when the gas rate at the end of puff period should be 10% of the gas rate in the beginning. It suggests that the first huff-n-puff cycle should be started when the primary oil rate is depleted to a low enough rate, for example, 10% of the initial rate. There is no criterion proposed in the literature.

CHAPTER SIX

Gas flooding compared with huff-n-puff gas injection

Abstract

This chapter is to discuss gas flooding in shale and tight oil reservoirs and to compare the gas flooding with the corresponding huff-n-puff gas injection. A few field projects are presented. The feasibility of gas flooding is briefly cited from a reference.

Keywords: Feasibility; Field projects; Gas flooding; Huff-n-puff gas injection.

6.1 Introduction

Gas flooding is much more commonly used than huff-n-puff gas injection in conventional reservoirs. However, in shale or tight reservoirs, because of ultra-low permeability and the resulting significant pressure drop in the matrix, it is very difficult for the gas to drive oil from an injector to a producer. If a shale or tight reservoir has natural fracture networks or the hydraulic fractures connect an injector and a producer, gas will easily break through, resulting in very low sweep efficiency (Sheng and Chen, 2014). To avoid these problems, huff-n-puff gas injection is preferred. Regardless, gas flooding is still an important EOR method, particularly in tight reservoirs where the reservoir permeability is not as low as shale reservoirs. This chapter discusses gas flooding in shale and tight formations, and to compare with huff-n-puff gas injection. A few field projects are presented.

6.2 Research results on gas flooding

Yu and Sheng (2016a) used Eagle Ford outcrop cores to conduct nitrogen flooding tests. The core dimensions were 1.5 inches in diameter and 2 inches in length. The porosity was about 5% and the permeability was about 70 nD estimated using AutoLab 1000 developed by NER Inc., USA (however, the estimated gas permeability was 0.5 nD Core GF_6 and 5 nD for Core GF_7 if the steady-state Darcy equation is used and the data presented in the paper are used, indicating that different

Enhanced Oil Recovery in Shale and Tight Reservoirs
ISBN: 978-0-12-815905-7
https://doi.org/10.1016/B978-0-12-815905-7.00006-2

permeabilities may be calculated if different methods are used). The oil was a dead oil of the viscosity of 8.5 cP. The experimental setup is shown in Fig. 6.1. A gas mass flow meter (SmartTrak 100) with a readability of 0.02 SCCM was installed at the outlet to monitor the gas flow rate. An analytical balance with the readability of 0.0001 g was used to measure the dry weight (W_{dry}), oil-saturated weight (W_{sat}), and the weight of the core plug (W_{end}) at the end of each flood. The oil recovery (RF) was calculated by

$$RF = \frac{W_{sat} - W_{end}}{W_{sat} - W_{dry}} \tag{6.1}$$

A core plug had about 2.5 g oil when it was fully saturated, and the oil that could be produced at the end of a flood test was less than 1 g. During the test, the produced oil would be less than 1 g. Such a litter amount of oil could not be measured by a graduated collector or by a balance, as some of the produced oil would be in the tubing. Only the weight at the end of each test could be measured, and the RF was calculated by the above equation. However, the recovery factors at different times were needed. To achieve that, multiple tests of different flooding times were performed using the same core. All the tests were conducted at the room temperature of 71°F, at the same injection (inlet) pressure and the same outlet pressure (the atmospheric pressure).

Fig. 6.2 shows the oil recovery factors at different flow times and at different injection pressures using core GF_6. It shows that in the early hours, the recovery factors almost linearly increased with time; at later

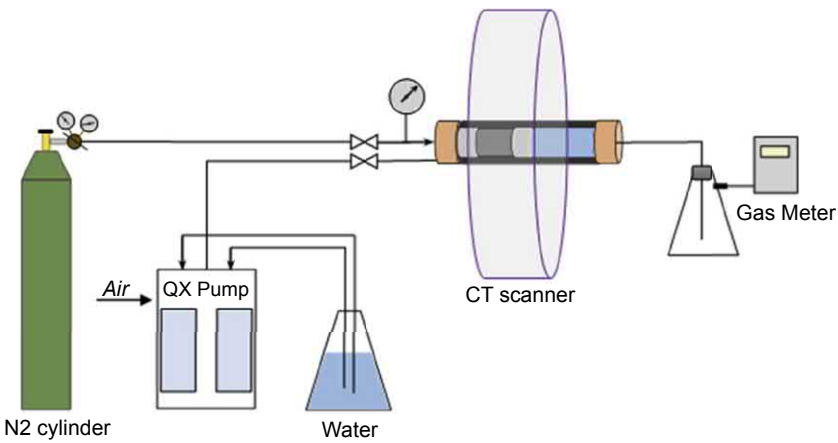

Figure 6.1 Schematic of experimental setup for gas flooding tests.

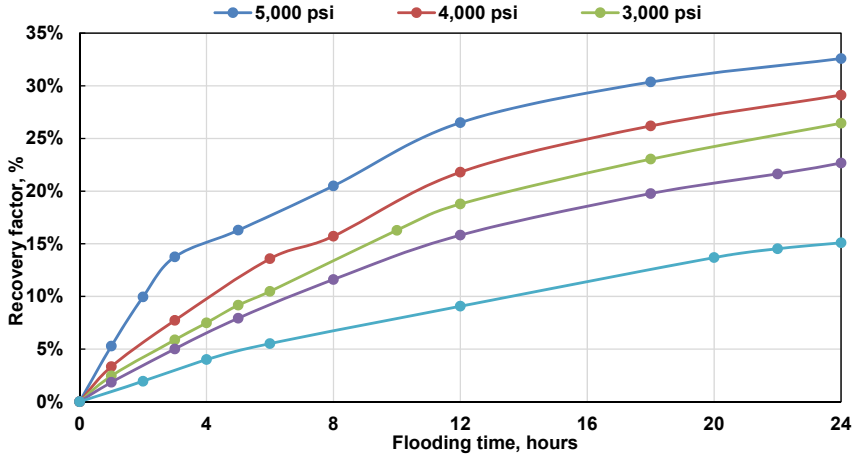

Figure 6.2 Oil recovery factors at different flooding pressures.

time, the recovery factors slowed down with time. Yu et al. (2016b) extended the work to 32 tests in longer flood time and more cores. These tests were able to be matched by simulation models. One example is shown in Fig. 6.3 where the experiments do show it is possible to produce oil from

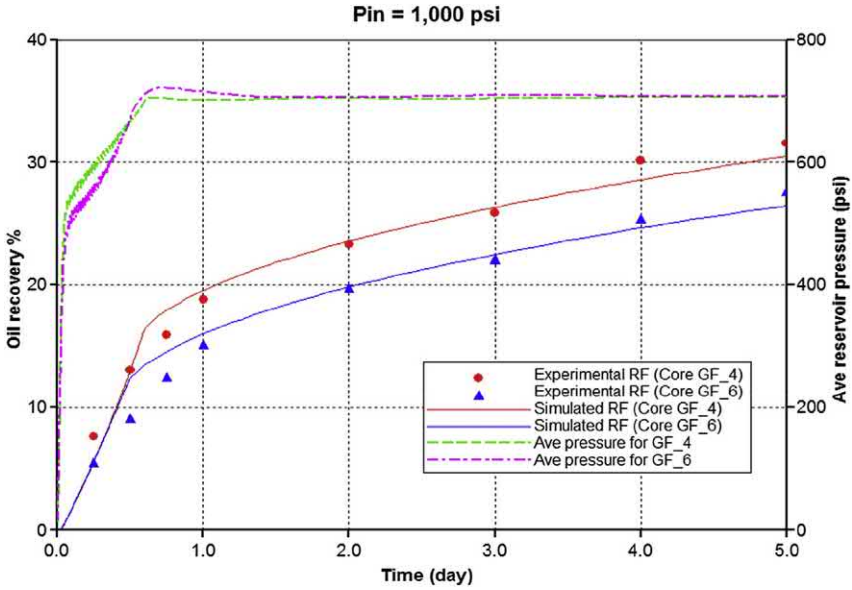

Figure 6.3 Oil recovery factors of the two flood tests at 1000 psi injection pressure and using two cores (experimental vs. simulation).

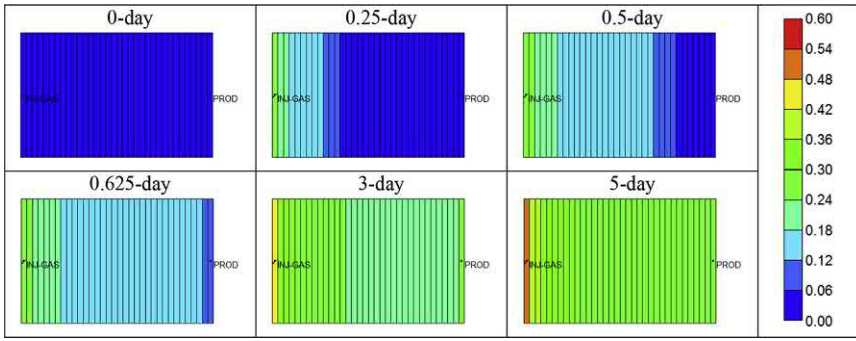

Figure 6.4 Gas saturation profiles during a nitrogen flooding test (GF_4) at different flood times.

gas flooding. Fig. 6.4 shows the gas saturation profiles for test GF_4 at different times which shows that gas broke through at about 0.625 days. By this time, the oil recovery was about half the total recovery by 5 days. Cross-checking the recovery factor in the previous figure, it can be seen after 0.625 days that the recovery factor curve decreased the increasing trend. In other words, after gas breakthrough, it will be more difficult to produce oil.

Early experimental data show that the oil recovery was very sensitive to the injection pressure in early time. However, extended simulation results from a model based on GF_6 core experiments show that the ultimate RF at the injection pressures of 1000, 3000, and 5000 psi are 80.5%, 82%, and 85%, respectively. The corresponding times that the ultimate RF is achieved are about 60, 140, and 220 days. The recovery factor is increased by 4.5% for the unrealistically long flood time in the small core scale, when the injection pressure is increased from 1000 psi to 5000 psi. The benefit of a high injection pressure is to increase the oil recovery rate at a higher injection volume or cost within the same time interval. The process should be optimized based on economic benefits.

Zhu et al. (2015) proposed injection of gas from a fracture and production of fluids from another adjacent fracture, with the injection fracture and the producing fracture alternating in the same horizontal well. They called it the fracture-to-fracture gas-flooding scheme. Such a scheme can mitigate the need of high pressure gradient or overcome a minimum threshold pressure gradient (Wang and Sheng, 2017a; 2017b) in a shale and tight formation. Their simulation results show that injection pressure is an important operation parameter with higher pressure leading to higher incremental oil recovery; formation heterogeneity reduces oil recovery; reducing the hydraulic fracture spacing increases early-time rates because

of higher pressure gradient, but it lowers late-time rate; higher mechanical dispersion slightly decreases the ultimate recovery. These results are expected. The main issue is the technical difficulties and economic return to complete the horizontal well so that two sets of alternate fractures can be used for injection and production. But the designs of such a downhole tool are available (Sharma et al., 2013; MacPhail et al., 2014).

6.3 Gas flooding versus huff-n-puff gas injection

Huff-n-puff gas injection has been studied by experiments and simulation work, and it has been found that it is an effective EOR method in shale and tight reservoirs. However, gas flooding is much more used method in conventional reservoirs. A very important question arises: which method should be a preferred method?

Sheng (2015d) compared these two methods by simulation. The dimensions of the base model are the same as that used by Sheng and Chen (2014), as shown in Fig. 6.5. Two half-fractures are included in the base model. For a flooding mode, one injector is located in the left half-fracture and one producer is located in the right half-fracture, as shown in the figure. For a huff-n-puff mode, two wells are located in the two half-fractures, and these two wells are injectors during the huff period and become producers during the puff period. Such setup makes the flow area and number of wells the same in the two modes. The fracture length is 1000 ft. The initial reservoir pressure is 6425 psi. The permeability is 100 nanoDarcy. The porosity is

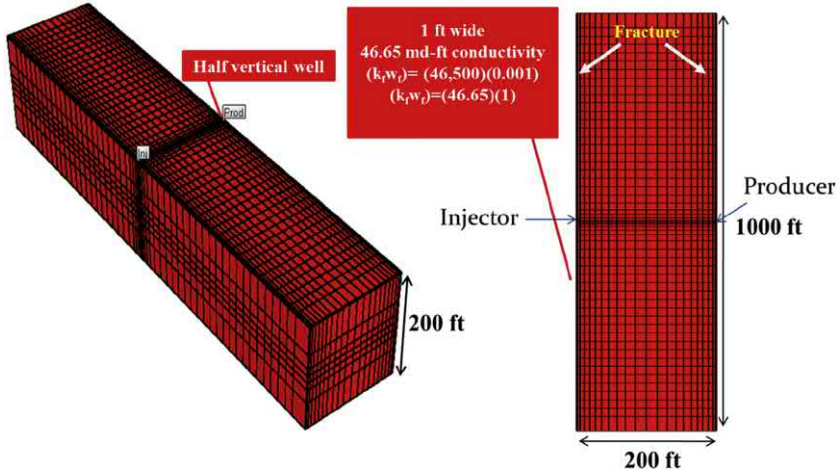

Figure 6.5 Dimensions and well locations in the base reservoir model.

0.06. The injection (huff) pressure is 7000 psi, and the production (puff) pressure is 2500 psi above the bubble point pressure of 2398 psi. The puff time and huff time are 200 days.

A black oil simulator, IMEX, developed by Computer Modeling Group (CMM) is used. The miscibility model uses the Todd and Longstaff (1972) mixing parameter ω. ω determines the degree of mixing between the miscible fluids within a grid block. $\omega = 0$ means immiscible displacement, and $\omega = 1$ complete mixing.

Using the above described model, both the flooding mode and the huff-n-puff mode are simulated. The oil recovery factor after 10 years of primary depletion is 5.75% which is representative to the typical field performance. The incremental oil recovery factors over the primary depletion after 20 years of the flooding and huff-n-puff injection are 2.59% and 16.69%, respectively. Thus, the huff-n-puff gas injection outperforms the gas flooding. If a net present value is used, the huff-n-puff performance is even better than the flooding performance, as the pressure built up near the injector needs a long time to transport to the producer to enhance oil production in the flooding mode, whereas oil will be produced immediately after the first huff period in the huff-n-puff mode. The details are presented as follows.

The oil saturation and pressure maps at different times of the gas flooding are shown in Figs. 6.6 and 6.7, respectively, from Sheng and Chen (2014). During the flood, oil is pushed away from the injection well, and the reservoir pressure builds up. Due to the ultralow permeability, pressure and fluid

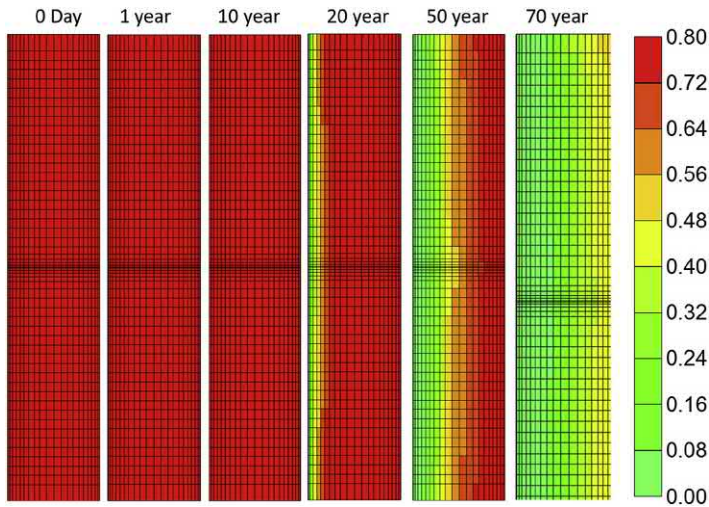

Figure 6.6 Oil saturation maps at different times in the gas flooding case.

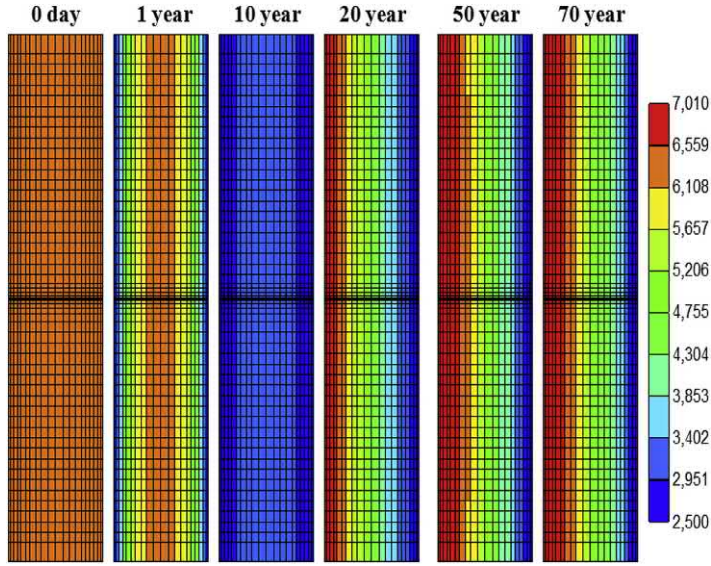

Figure 6.7 Reservoir pressure maps at different times in the gas flooding case.

transportation in the shale and tight reservoir are much more difficult than in a conventional reservoir. The saturation maps show that the gas is only in the injector side in the first 50 years. Gas could not reach the producer. Near the producer, it is oil only. The viscosity decreases, due to gas injection, occur near the injector but not near the producer. The pressure maps show that after 60 years of gas flooding from 10 years (at the end of primary depletion) to 70 years, the pressure in the middle of the model is about 5000 psi (the pressure at the injection side is 7000 psi). In other words, the high injection pressure cannot transmit to the area near the producer.

Sheng and Chen (2014) also compared nitrogen flooding with huff-n-puff. Wan et al. (2014b) compared the oil recovery from CO_2 flooding with that from huff-n-puff CO_2 injection. Both studies show that the huff-n-puff oil recovery is higher than from the flooding recovery.

Yu et al. (2017) did experiments to compare the oil recovery from gas flooding and huff-n-puff gas injection. Eagle Ford outcrops and Wolfcamp oil were used. The properties of two core plugs are presented in Table 6.1. The experimental setups for gas flooding and huff-n-puff are similar to that shown in Fig. 6.1 in this chapter and that in Fig. 2.4 in Chapter 2, respectively. The injection pressure was 1000 psi, and the puff pressure was at the atmospheric pressure for all the tests. The tests were done at 70°F. The test

Table 6.1 Core plug properties.

Core no.	Diameter (mm)	Length (mm)	Dry weight (g)	Saturation Porosity	Average permeability (nD)
CEF_1	38.5	50.9	152.099	4.4%	85
CEF_2	38.1	101.8	249.697	13.1%	400

Table 6.2 Test schedules.

Core no.	Gas injection mode	Test no.	Test schedule
CEF_1	Flooding	1	Flooding period: 48 hrs
	Huff-N-Puff	2	Huff and soaking 0.5 h, puff 1 h (32 cycles)
		3	Huff and soaking 2 h, puff 1 h (16 cycles)
		4	Huff and soaking 5 h, puff 1 h (8 cycles)
CEF_2	Flooding	5	Flooding period: 72 h
	Huff-N-Puff	6	Huff and soaking 1 h, puff 3 h (18 cycles)

schedules are presented in Table 6.2. Note that the total test times for flooding and huff-n-puff for each core plug were the same; for the huff-n-puff tests, huff time and soaking time were added together.

The recovery factors of tests #1 to #4 within 48 h using the core CEF_1 are shown in Fig. 6.8. The recovery factor of the flooding test was 17.9% at the end of 48 h of flooding. The recovery factors of the huff-n-puff tests depended on the huff and soaking time. When the huff and soaking time was shorter, more cycles could be performed within the same total test time, and the recovery factors at the end of test were higher. When it was 0.5 h, the recovery factor was the highest (22.5%). However, Yu et al. (2017) observed that little oil was produced when the huff and soaking time was too short (e.g., a few minutes). They thought soaking time was necessary for the pressure (or energy) to be transmitted to the inner area of the core and for gas to diffuse into the matrix, which is not consistent with simulation results presented in the preceding chapters. Note that in these experiments discussed here, the huff time and soaking time were added together. If this add time was a few minutes, the injected gas could not reach or even the pressure could not transmit to the inner area of a core. Therefore, litter could be produced. When the soaking time was 2 h, the recovery was almost the same as that from the flooding test. These results show two important points: (1) huff-n-puff performance strongly depends on

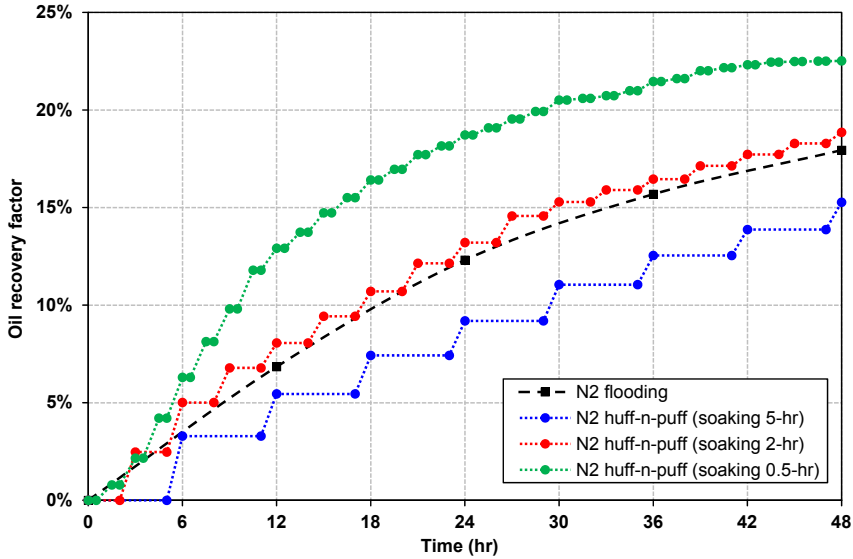

Figure 6.8 Recovery factors of nitrogen flooding and huff-n-puff injection within 48 h using core CEF_1.

operation parameters; (2) whether a huff-n-puff injection mode outperforms a flooding mode depends on whether the huff-n-puff is optimized or not.

Two more tests (#5 and #6) were conducted for nitrogen flooding and huff-n-puff nitrogen injection, respectively, using core CEF_2 for 72 h. The recovery factors from the flooding test and the huff-n-puff test (huff and soaking 1 h and puff 3 h) were 19.9% and 24.1%, respectively. The data are shown in Fig. 6.9 together with the corresponding simulation results. In the first 24 h, the oil recovery factors from the two injection modes were close. After 24 h, the difference between the flooding and the huff-n-puff tests started to show up and grew with time. The production rate in the flooding test decreased rapidly because the gas had broken through in 24 h. Most of injected gas flew through the established flow channels without bringing significant oil out. By comparison, the huff-n-puff test continued providing energy at later cycles, maintaining the effectiveness of the process. Extending the two tests to 15 days, the difference in the oil recovery factors increased from the second day and became stabilized after 6 days (see Fig. 6.10), as the huff-n-puff test became less effective as well in the later cycles. In these two tests, the huff-n-puff mode outperformed the flooding mode by about 11%.

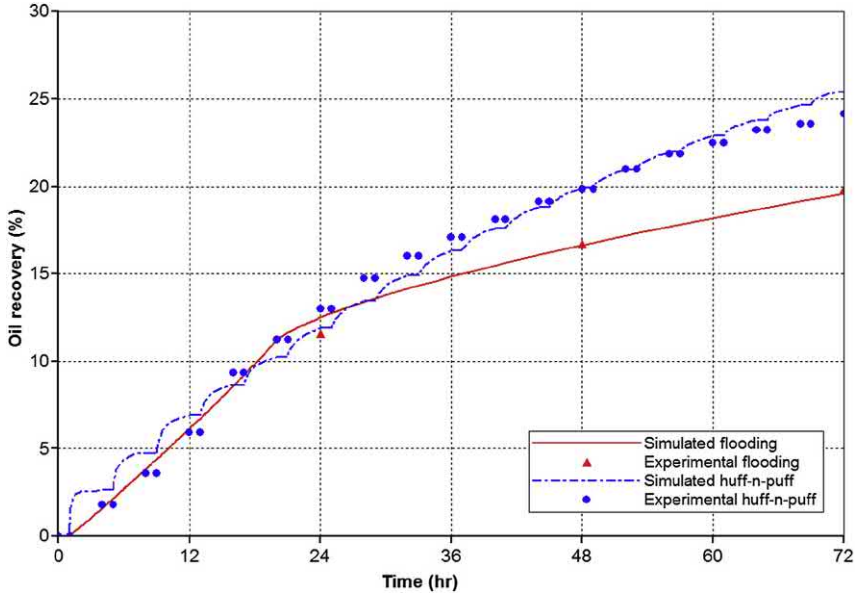

Figure 6.9 Experimental and simulated oil recovery histories by N_2 flooding and N_2 huff-n-puff in 72 h.

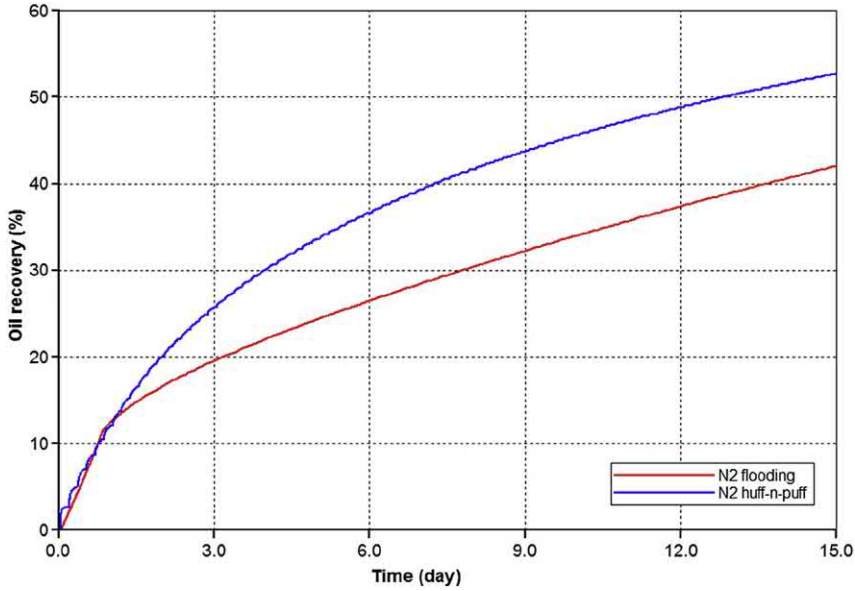

Figure 6.10 Simulated oil recovery factors by nitrogen flooding and huff-n-puff nitrogen injection.

Other researchers also compared huff-n-puff gas injection with gas flooding. Shoaib and Hoffman (2009) simulated CO_2 injection in different injection schemes (continuous injection or flooding and huff-n-puff) in the Elm Coulee field in Richland County, Montana. Oil is produced from the Bakken formation. The reservoir porosity is 7.5%, the permeability is 0.01−0.04 mD, and the oil viscosity in the reservoir is about 0.3 cP. The shale layers contain natural fractures that formed during the conversion process of kerogen followed by generation and expulsion of oil. The pressure buildup tests indicate a permeability of 2.5 mD in the upper shale region. For the huff-n-puff mode, a cycle of 9 months is used (3 months in each of injection, soaking, and production periods). The huff-n-puff injection increased recovery over primary production by 2.5% for 0.19 PV injection. The incremental oil recovery from the flooding ranges 13%−15% for about 0.2 PV injection. They found that the gas flooding is better than huff-n-puff. The good flooding performance may result from the relatively high permeability (2.5 mD from the buildup) because the injected gas and displaced oil can flow to the producers in the flooding mode (Sheng and Chen, 2014). The lower huff-n-puff performance in this case may be able to be improved by optimization of the huff, puff, and soaking time, for example, by reducing the soaking time, as the optimization can change the conclusion about the preference of huff-n-puff and flooding (Sheng, 2015b), as also discussed earlier in this section.

Wang et al. (2010) assessed the CO_2 potential in the Bakken formation in the Saskatchewan area. In their simulation model, the porosity is 7.5%, and the permeabilities in the upper three layers andlower five layers are 2.5 mD and 0.04 mD, respectively. The oil viscosity in the reservoir is about 0.3 cP. They claimed that continuous CO_2 injection is better than the huff-n-puff CO_2 injection. In their continuous mode, there are four injectors and nine producers. In their huff-n-puff mode, two wells are in 10 years of huff injection, while another group of two wells are in 5 years of soaking followed by 5 years of production, and the rest of nine wells are in continuous production mode. Three points may help understand why the continuous injection is better than the huff-n-puff injection in this case. (1) In the huff-n-puff mode, not all the wells are operated in such mode; (2) 5 years of soaking time is too long, and thus some operation time is lost; (3) the permeability from this model is not ultralow so that CO_2 is able to flood from an injector to a producer (Sheng and Chen, 2014).

Kurtoglu (2013) simulated a three-well pattern. The three horizontal wells are parallel with each other and produce in the first 450 days, the

central well is used as a CO_2 injection well. The performance of huff and puff is compared with that of CO_2 flooding. In gas flooding the central well injects CO_2 from 450 to 1450 days. In the huff-n-puff, the central well injects 60 days, soaks 10 days, then produces 120 days, and this process is repeated for six cycles until 1450 days for the huff and puff mode. The simulation results show that the incremental oil recovery over the primary depletion for the flooding mode is higher than for the huff and puff mode. The better flooding results are probably caused by her model in which only the center well is changed from primary depletion to huff and puff or continuous injection. For such model setup, the huff and puff benefit cannot be realized in the two side wells. But the benefit of continuous injection is well captured by the two side wells. Another reason may be the partial loss of soaking benefit, as her model does not include molecular diffusivity. The third reason may be that the injection volume by one well for 60 days is far not enough. Probably a more important reason is the small natural fracture spacing (2.27 ft) in her model. The matrix permeability is around 300 nD, and the effective permeability in the SRV is 31 mD. Such a high permeability model will make the gas flooding feasible.

Yu et al. (2014a) did a sensitivity study of CO_2 injection to enhance dry *gas* recovery in Barnett reservoirs. They found that CO_2 flooding is a good option to enhance gas recovery, but CO_2 huff and puff is not because most of the injected CO_2 quickly flows back during the puff period. In their simulation model, the wells were under primary production for 5 years, injected for 5 years, soaked for 5 years, and produced for the test of 15 years. Obviously, the soaking time and the subsequent puff time are too long. Such huff-n-puff operation is far from the optimized. Therefore, the huff-n-puff cannot be compared with the flooding mode for performance. Note this is a case to produce dry gas (methane).

Schepers et al. (2009) simulated CO_2 sequestration and its enhanced gas recovery in the Devonian gas shale of Eastern Kentucky, considering organic matter in the shale has a greater sorption affinity for CO_2 than natural gas (methane). They compared continuous CO_2 injection with huff-n-puff CO_2 injection. The average formation permeability is 18 μD. The simulated pattern is one injector and three producers in a 40-acre spacing. The gas recovery of huff-n-puff CO_2 injection is 2.0% compared with 2.2% without CO_2 injection. It is found that a significant amount of CO_2 is produced back during the puff period. The huff-n-puff parameters are 5 days of injection, 1 month of soaking, and 3 months of production. 300 tons of CO_2 are injected. However, the gas recovery factor for the continuous gas injection

(flooding) is 7.3%. These results show that the huff-n-puff does not perform as well as the gas flooding or the primary depletion without any CO_2 injection. Several factors may contribute to this result. (1) From the paper, it cannot be figured out whether all the four wells in the pattern are under the huff-n-puff injection. If all the wells are not under huff-n-puff injection, then the performance cannot be directly compared with the continuous injection. (2) The soaking time of 1 month is too long in the case of 5 days of injection. In other words, the huff-n-puff is not optimized. (3) The injected amount of CO_2 of 300 tons (or 5 days of injection) may be too small. (4) This huff-n-puff injection has only one cycle. One of the advantages of huff-n-puff injection is that it can have many cycles, and even late cycles may contribute to gas recovery. But for a gas flooding case, once the injected gas breaks through, addition recovery is significant, or a significant recovery takes a long time. (5) The permeability of 18 μD may be high for a gas reservoir so that huff-n-puff may not have the advantage.

Meng et al. (2017) conducted experiments to compare the liquid condensate recovery from the two modes as well. They found that the recovery from huff-n-puff was higher than that from gas flooding for the same operation time.

From the above discussion, we may conclude that huff-n-puff gas injection should outperform gas flooding in shale and tight reservoirs, if the huff-n-puff is well designed (optimized). In other words, for huff-n-puff to be better than flooding, the huff-n-puff scheme (e.g., huff, puff, and soaking times) needs to be optimized.

6.4 Field applications of gas flooding

In this section, four field cases of gas flooding are presented.

6.4.1 Gas flooding in Viewfield Bakken field, Saskatchewan (Schmidt and Sekar, 2014)

In this project, immiscible continuous gas injection was carried out through one central horizontal injection well (east-west orientation) that was perpendicular to nine horizontal production wells (north-south orientation). See Fig. 6.11. The pilot project covered 1280 acres and was developed on a combination of 80-acre and 160-acre spacing. The wells were about 1 mile long. The wells were multistage hydraulically fractured. The center injection well created a toe-to-heel injection pattern. The distances from the injector to the nearest hydraulic fracture of each offset producer were almost

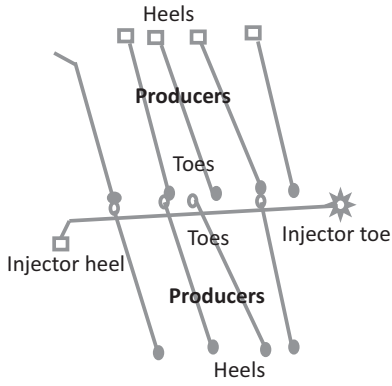

Figure 6.11 Viewfield gas injection pattern. *Modified based on Schmidt, M., Sekar, B.K., 2014. Innovative Unconventional2 EOR-A light EOR an unconventional Tertiary recovery approach to an unconventional Bakken reservoir in Southeast Saskatchewan. Paper WPC-21-1921 Presented at the 21st World Petroleum Congress Held in Moscow, Russia, 15–19 June.*

the same. When gas broke through at the toe end of a producer, the toe portion was plugged to alleviate gas cycling. The injected gas continued moving to the next portion. This pattern enabled one injector to serve the nine producers. For the producers with heels close to the injector, a straddle packer system called "scab-liner" technique was applied at the immediate heel port. Two packers were set, one in the upstream and the other in the downstream of the problem fracture port, with the tubing in between to allow flow through while still isolating port(s). This technique proved to work in the pilot. The porosity and permeability of the Bakken formation in the test area were 9%–10% and 0.01–0.1 mD, respectively. The median pore throat size was 0.1–0.2 microns. The oil viscosity was 2–3 cP. The initial water saturation was 55%–59%. The initial pressure was 2320 psi and the bubble point was 990 psi.

The project was initiated in December 2011. Initially, the injection rate was 300 MSCF/d at the injection pressure of 500 psi. When compression was added in March 2012, the injection rate was increased to 1 MMSCF/d at 1000 psi. Immediately, gas broke through two pattern wells. The oil production rate decreased to 53 bbl/d by July 2012. After workovers, oil rates consistently increased in all of nine producers and the total rate climbed to 295 bbl/d. The average decline rate of the pattern wells decreased from 20% before gas injection to 15% after gas injection. The project clearly demonstrated that alleviation of gas breakthrough made the gas flooding work. The gas utilization factor was 6.5–10 MSCF/bbl of oil.

This project also demonstrated that the injected lean gas could vaporize natural gas liquid (NGL) content. The original solution gas from the Bakken formation in the pilot area had an NGL content (C_2—C_7) of 225—250 bbl/MMSCF. The injected gas had NGL of 138—145 bbl/MMSCF. One well data showed that the NGL yield increased from 2.2 to 5.6 bbl/d. The oil production from this well increased by about 10%.

There are several important learning points from this pilot test. (1) An injector to producer well ratio of one to nine was a key factor in the economic success of this project. This ratio was much lower than a typical one to one ratio for waterflooding. This practice reduces surface infrastructure costs and increase production time. (2) Compared with water injection, gas injection required less capital investment and gas was a nondamaging injection fluid.

6.4.2 Gas flooding in Bakken formation in North Dakota (Hoffman and Evans, 2016)

One waterflooding pilot was performed in the Bakken formation in the North Dakota area in 2012—13. However, it was not successful. It was converted to gas injection in 2014. The horizontal injector was surrounded by four horizontal producers. Produced natural gas was used. Gas was reinjected for 55 days in the middle of 2014 at a rate of 1.6 MMSCF/d and at the surface injection pressure of 3500 psi. All the production from four producers increased in the months immediately after the gas injection. Because the wells further to the west producer were being hydraulically fractured, the production increase at the south and west wells might be caused by the fracture-hits. The other two wells (north and east) might not be hit by fractures. After 1 week of gas injection, gas rate was increased to 160 MSCF/d at the east offset well, or about 10% of the injected gas was being produced at this well. The well was subsequently closed for 1 month. After the well was reopened, the gas rate was high and the oil rate peaked for a short time and then went back to the normal decline. The north offset well had oil rate increased by three times, probably due to long-distance fracture-hit. Gas flooding improved oil production in this case.

6.4.3 CO_2 injection in Song-Fang-Dun Field, Daqing (Jiang et al., 2008)

A CO_2 flooding pilot was carried in the Fuyang Layer in the Fang-48 fault block, Song-Fang-Dun Field, Daqing, China, starting in March 2003. The porosity was 12%, and the air permeability was 0.79 mD. The oil viscosity

in the reservoir was 6.6 cP. There were one injector and five producers. The benefit was observed at the producers by August 2004. By the end of 2006, total 0.33 PV CO_2 was injected. The injector was not fractured. The CO_2 injectivity was about 6.3 times water injectivity. The pilot performance was positive. However, uneven CO_2 sweep to the producers were observed. This pilot was expanded to 14 injectors and 26 producers. CO_2 injection was started in November 2007 *before* oil production in April 2009. In the beginning, CO_2 injection rate was 22 tons/day, oil rate 0.2 tons/day. After the producers responded to CO_2 injection, oil rate increased to 0.6 tons/day. By 2014, water-alternate-gas injection was applied. By May 2015,204,000 tons of CO_2 had been injected, and 9000 tons of oil had been produced. The ratio of oil produced to CO_2 injected was 0.044 tons/ton which is equivalent to 53.75 MSCF/bbl oil if it is assumed that the oil density is 0.85 and 1 ton of CO_2 is approximately 17.5 MSCF. Such CO_2 injection performance was not good. The main reason was that the net-to-gross ratio was low (less than 0.5), and the formation was very heterogeneous.

6.4.4 CO_2 injection in Yu-Shu-Lin Field, Daqing (Wang, 2015)

The permeability in the Fuyang reservoir, Well-101 block, Yu-Shu-Lin field was 0.96 mD in the injection area. The reservoir oil viscosity was 3.6 cP. Before CO_2 injection, the field was under waterflooding. The injection pattern was 5-spot with well spacings of 300 and 500 m. There were total seven injectors and 17 producers. Two injectors started work in December 2007, and five injectors in July 2008. By September 2013,110,600 tons of CO_2 had been injected, and 55,300 tons of oil had been produced. The ratio of oil produced to CO_2 injected was 0.5 (tons of oil to tons of CO_2) which is equivalent to 4.73 MSCF/bbl. Several points are worth noting. CO_2 injection was half years ahead of production. CO_2 injectivity was more than four times water injectivity, making the pressure maintenance by CO_2 injection easier than water injection. The wells were not fractured. The estimated oil recovery was 21% compared with 12% from a waterflooding well pattern in the same field. This pilot area was expanded to 70 injectors and 140 producers.

6.4.5 Summary of gas flooding performance

The above discussed gas flooding projects may be briefly summarized in Table 6.3. These observations may be made.

Table 6.3 Gas flooding performance.

Field	Inj. gas	k, mD	μ_o, cP	# Inj	# Prod	Well spacing	Performance, MSCF/bbl	References
Viewfield, Bakken formation, Saskatchewan	Lean gas	0.01—0.1	2—3	1	9	80, 160 acres	Oil rate increased, 6.5—10	Schmidt and Sekar, 2014
Bakken formation, North Dakota	Natural gas			1	4		Oil rate improved	Hoffman and Evans, 2016
Song-Fang-Dun, Daqing	CO_2	0.79	6.6	14	26	200—300 m	53.75	Jiang et al., 2008
Fuyang Daqing	CO_2	0.96	3.6	7	17		4.73	Wang 2015

1. Three out of four projects that demonstrated gas injection were successful with more oil produced.
2. The formation permeabilities were less than 1 mD, but much higher than nanoDarcy.
3. The oil viscosities were low.
4. Tests showed there was no gas injectivity issue. Some cases rather showed gas breakthrough issue.

6.5 Feasibility of gas flooding

Joslin et al. (2017) used simulation approach to study the feasibility of flooding methods in a volatile oil reservoir. They found that when the matrix permeability is lower than 0.03 mD, any flooding method, nitrogen, CO_2, and water, will not be economical at the oil price of $40/bbl oil and the gas price of $2.5/MSCF. Nitrogen flooding is the best option when the matrix permeability is 0.03—0.1 mD in terms of incremental oil recovery. CO_2 is the best when the matrix permeability is higher than 0.1 mD. In terms of net present value (NPV), when the matrix permeability is higher than 0.1—0.3 mD, nitrogen flooding is profitable, but not for CO_2 flooding. When the matrix permeability is higher than 0.3 mD, both nitrogen and CO_2 flooding outperformed primary depletion. Waterflooding requires the matrix permeability greater than 1 mD to be profitable.

CHAPTER SEVEN

Water injection

Abstract

In this chapter, research results on experimental and simulation studies are presented to evaluate the EOR potential of water injection. Water can be injected in a huff-n-puff mode or a flooding mode. Their performance is compared. Water injection is also compared with gas injection. At the end, field performance of water injection is summarized. Other modes of water injection are also briefly mentioned.

Keywords: Field performance; Huff-n-puff; Waterflooding; Water injection; Water injection modes.

7.1 Introduction

Waterflooding is the most practiced method to produce oil in conventional reservoirs. One main concern for waterflooding in shale and tight reservoirs is injectivity. Therefore, there are not many water injection projects in the United States, but quite a few in Chinese tight formations. In this chapter, we present research results on experimental and simulation studies to evaluate the EOR potential of water injection. Water can be injected as a huff-n-puff mode or a flooding mode. Their performance is compared. At the end, field performance of water injection is summarized. Other modes of water injection are also briefly mentioned.

7.2 Waterflooding

Although there is a concern of water injectivity, field projects performed in US so far did not show the problem as serious as expected in shale reservoirs (Hoffman and Evans, 2016). Many tight reservoirs in China did not show injectivity problem either.

Song and Yang (2013) used Bakken cores to conduct a waterflooding experiment. The oil viscosity was 2.17 cP at 20°C and at an atmospheric pressure. The core permeability was 0.27 mD and the porosity was 0.23. The initial oil saturation was 0.55. The oil recovery factor at the breakthrough was 0.48 at 0.36 pore volumes of injection. The total oil

Enhanced Oil Recovery in Shale and Tight Reservoirs
ISBN: 978-0-12-815905-7
https://doi.org/10.1016/B978-0-12-815905-7.00007-4

recovery factor was 0.515, indicating not much oil produced after the breakthrough.

One may think that water preferentially invades into smaller pores, as the capillary pressure as a driving force is higher. However, the resistance in smaller pores is also higher. As a result, water imbibition velocity is higher in large pores (Sheng, 2017c). This can be explained as follows.

Based on Poiseuille's law, Washburn (1921) derived an equation to describe the imbibition velocity in a single capillary tube. The velocity equation can be restated as follows without including the coefficient of slip or a noncapillary drive force:

$$\frac{dl}{dt} = \frac{\sigma \cos\theta}{4\mu_w l} r \tag{7.1}$$

In the Eq 7.1, l is the imbibition distance, t is the imbibition time, σ is the interfacial tension, μ_w is the wetting phase viscosity, θ is the contact angle, and r is the capillary radius. We can see that the imbibition velocity into a larger pore is lower than that into a smaller pore. A small radius corresponds to a low permeability reservoir because r is proportional to $\sqrt{k/\varphi}$. Now we can understand that in the low-permeability rock, although the capillary force is higher, the viscous force is high as well; by considering these two forces, the imbibition velocity in the low-permeability rock is actually lower than that in the high-permeability rock. Note that the above ignores the slip flow. For the slip flow to take place, the capillary diameter needs to be smaller than approximately 3 nm (Sharp et al., 2001). This was confirmed by an experimental and theoretical study by Koo and Kleinstreuer (2003). Thus, the continuum theory is still applicable to fluid flow through nanopores in shale matrix in a practical sense.

The above theory is consistent with what was observed by Lin et al. (2016) as shown in Fig. 7.1. This figure also shows that when there was a fracture, the water could much more quickly imbibe into the neighbor matrix. Another important mechanism is the imbibed water increase reservoir pressure and local pressure so that the drive energy is boosted. From the imbibition point of view, water-wet formation is preferred. This conclusion is supported by experimental data by Huang and Xiang (2004). By the way, Sun et al. (2015) attributed their slower imbibition rate after the cores were dried in an oven to the fractures generated during the earlier water imbibition. They argued that the existence of fractures with openings in micrometers reduced capillary pressure; thus the imbibition rate was decreased. As discussed here, the resistance in fractures is lower and the resulting

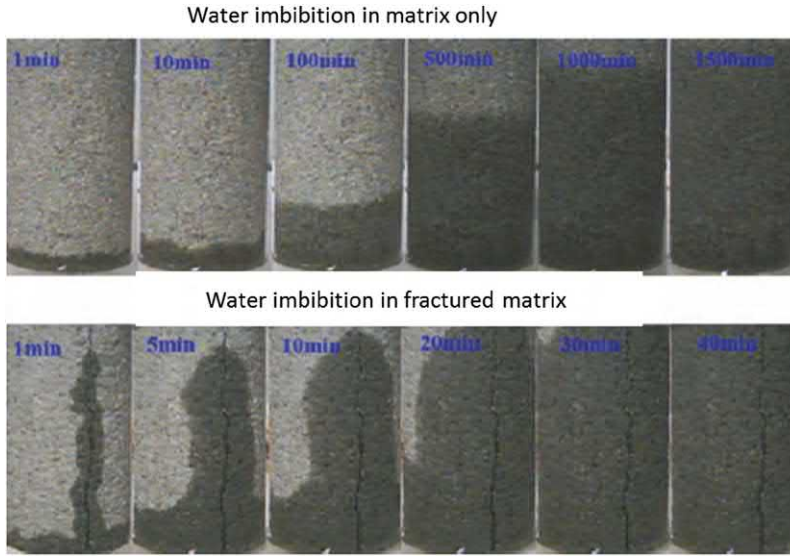

Figure 7.1 Comparison of water imbibition in matrix and fractured matrix (Lin et al., 2016).

imbibition rate should be higher. Their lower imbibition rate might result from other causes, for example, the core permeability might be reduced after the earlier imbibition. Now we review some of waterflooding field projects.

7.2.1 Waterflooding in Bakken and Lower Shaunavon, Saskatchewan

Waterflooding projects have been performed by Crescent Point Energy in its Bakken and Lower Shaunavon resources since 2006. Totally five patterns in the Bakken and three patterns in the Lower Shaunavon were sanctioned before 2011. For those trials, the first one in Bakken had a peak oil rate of 550 bbl/d from 50 to 100 bbl/d for four produces. The second pattern had less increase in oil rate. It was too early to see the responses for rest of the patterns by 2011. The injection patterns were such that horizontal injectors paralleled horizontal producers with their spacings of hundreds meters (Wood and Milne, 2011). Later a simulation study was conducted for a Lower Shaunavon of one injector and 18 producers. The pilot production and injection history were matched. At the end of history match, the recovery factor was 1.4%. After 50 years, the recovery factor was predicted to be

5.1%. The porosity in the pattern area was from 14% to 18% and the permeability was less than 1 mD (Thomas et al., 2014).

7.2.2 Waterflooding in Bakken formation in North Dakota

Meridian Oil injected water in NDIC 9660 in the Bicentennial Field in McKenzie County early in 1994. Approximately 13,200 barrels of freshwater were injected into a horizontal well in the Upper Bakken Shale in 50 days. The well was shut-in for 2 months. After that oil production remained below the rates before water injection for the rest of the well's operational life (Sorensen and Hamling, 2016).

One waterflooding pilot was performed in the Bakken formation in the North Dakota part. One horizontal injector was surrounded by four horizontal producers (Fig. 7.1). The east and west offset wells were 2300 ft away and the north and south offset wells were 900 and 1200 ft away from the injector. The injection rate was about 1350 bbl/day for 8 months in the middle of 2012. The bottom hole pressure at the injector increased to about 6000 psi, and the east and west producers' water rates increased. However, no incremental oil was observed. The injection was stopped for about 6 months at the end of 2012 and begun in 2013 again and continued for 8 months. During the second period of water injection, the injection rate was decreased, and the bottom hole pressure was maintained at 5500 psi. Again, no incremental oil was seen. About 444,000 STB of water was injected, but only 65,000 STB of additional water was produced. Later water injection was converted to gas injection (Hoffman and Evans, 2016). The gas injection performance is reviewed in the Gas Flooding section. The failure of this waterflooding pilot seemed to be caused by low water sweep efficiency, because much less water was produced than the water injected (water lost). Therefore, this case may not be used to generalize waterflooding performance in shale or tight formations. Another comment is about the well layout as shown in Fig. 7.2. The horizontal well pattern is similar to the inverted five-spot pattern for vertical wells. Whether such a pattern can have a good sweep efficiency and effectively displace oil to producers is the question.

7.2.3 Waterflooding in Bakken formation in Montana

The test was conducted in 2014. There was one injection well and several offset wells. In the first 3 months, the well injection rate was 1700 STB/d, and later reduced to 1000 STB/d because of breakthrough at a close offset

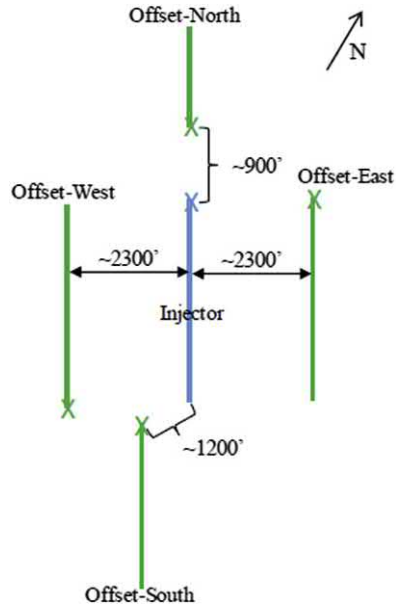

Figure 7.2 Well layout for one Bakken area in North Dakota (Hoffman and Evans, 2016).

well (Hoffman and Evans, 2016). The close offset well (about 880 feet away) had a huge increase in water production, but the oil rate did not increase during this time. The water broke after 1 week. Because of water breakthrough at some stages, the injection well was finally closed. In early 2015, the closest offset well was shut-in for a couple of months. When it was reopened, the oil rate increased. This test showed that one problem for waterflooding is water breakthrough.

7.2.4 Waterflooding in Bakken Viewfield in Saskatchewan

This formation is a low-permeability formation. Experience or performance from this formation may also be useful for developing shale and tight formations. Starting in 2006, waterflooding after 2–6 years of depletion by horizontal injectors with multistage fracturing was launched. Line-drive patterns were used. Before widespread waterflooding, several pilots were conducted. Most of the horizontal injectors had 1600 m length. The well spacing from a horizontal injector to a neighboring producer was about 200 m. Water broke through right after waterflooding, but the oil rate peaked in the first year, avoiding negative cash flow in early years. The oil decline rate was decreased from 43% to 45% per year for depletion to 25%–38%. Horizontal

injectors were found more economical than vertical injectors (Karpov et al., 2016).

7.2.5 Waterflooding in Pembina Cardium in Alberta

By July 2014, only 15 out of 1500 horizontal wells with multistage fracturing were switched to water injectors. The distances from injectors to producers were 200−450 m. An obvious increase in oil rate was not observed from waterflooding (Karpov et al., 2016).

7.2.6 Waterflooding in Vinogradova field in Russia

The field was produced by horizontal wells of 1000 m with multistage fracturing, and water was injected through vertical deviated wells. The well spacing from an injector to a producer was about 800 m. Low waterflood efficiency from vertical wells was observed (no significant oil rate increase but decreased decline rate). Horizontal injectors were better and planned for future development (Karpov et al., 2016).

7.2.7 Summary of waterflooding performance

The above three waterflooding projects were all conducted in Bakken formation. Their performance is summarized in Table 7.1. It can be seen that low sweep efficiency was a problem. However, there are a number of other fields where direct water breakthrough channels occurred, but higher oil recovery factors were still able to be reached (Baker et al., 2016).

7.3 Water huff-n-puff injection

Li (2015) summarized several favorable conditions for water huff-n-puff injection: (1) water-wet reservoirs, (2) well controlled volume (containment, low permeability reservoirs), (3) high natural fracture density, (4) lack of reservoir energy (low pressure). Yu and Sheng (2017) conducted water huff-n-puff experiments. The experimental setup is shown in Fig. 7.3. The Quizix pump (QX-6000) was used for water injection to provide huff pressure in the vessel through the accumulator. An oil-saturated core was put in the vessel. There was 1.0 cm space between the inside wall of the vessel and the core outer boundary; such an annular space represented fractures surrounding the matrix in a reservoir. The huff and puff pressures were achieved through the three-way valve. The pump was operated in the mode of constant pressure delivery. With the solution injected into the

Table 7.1 Waterflooding performance.

Field	k, mD	Performance	References
Bakken + lower Shaunavan	<1	Oil rate increase	Thomas et al., 2014, Wood and Milne, 2011
Bakken in ND		No oil rate increase, low sweep efficiency	Hoffman and Evans, 2016
Bakken in Montana		Water breakthrough	Hoffman and Evans, 2016
Bakken Viewfield in Saskatchewan	~1	Water broke through right after waterflooding, oil rate peaked in the first year, decline rate decreased	Karpov et al., 2016
Pembina Cardium in Alberta	0.1–5	Oil rate not increased	Karpov et al., 2016
Vinogradova in Russia	0.87	Decline in oil rate, low efficiency from vertical injectors	Karpov et al., 2016

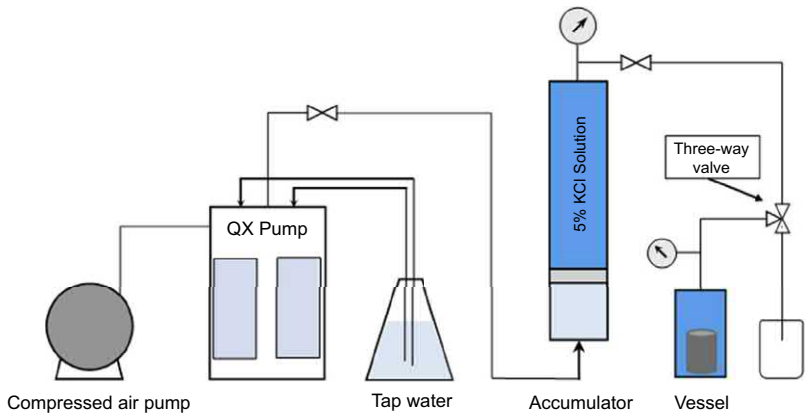

Figure 7.3 Schematic of setup for water huff-n-puff tests.

vessel, the pressure in the annulus was increased. Once the pressure reached a set pressure, the three-way valve and the pump were closed. After a set period of soaking time, the three-way valve was opened to allow the liquid flow out, and the pressure of the vessel was bled off. The core was kept in the

vessel for a set puff time. At the end of each cycle, the core was pull out of the vessel, the liquid on the core surface was wiped, and the core was weighted with the weight recorded as W_{exp}. That ended one cycle of huff-n-puff water injection. Then the core was placed back in the vessel for the next cycle.

Oil recovery factor (RF) during a water huff-n-puff test can be determined in the following. Based on the material balance, the weight of the core that is saturated with oil and water at the end of each cycle (W_{exp}) equals the weight of the original oil saturated core (W_{sat}) minus the weight of oil produced ($V_p \cdot RF \cdot \rho_o$) plus the weight of water imbibed ($V_p \cdot RF \cdot \rho_w$):

$$W_{exp} = W_{sat} - RF \cdot V_p \cdot \rho_o + RF \cdot V_p \cdot \rho_w \tag{7.2}$$

The pore volume in the above equation V_p can be calculated by

$$V_p = \frac{W_{sat} - W_{dry}}{\rho_o} \tag{7.3}$$

Then the oil recovery factor which is oil produced divided by the pore volume can be derived from the above equations:

$$RF = \frac{(W_{exp} - W_{sat}) \cdot \rho_o}{(W_{sat} - W_{dry}) \cdot (\rho_w - \rho_o)} \tag{7.4}$$

During the huff period, water may finger into the oil phase; water may also imbibe into the core through the countercurrent flow with oil; water preferentially invades in large pores and then imbibes into small pores to displace oil. During soaking the period, water may continue fingering into the oil phase in the early period as the pressure outside the core may still be higher than that inside; of course, water imbibes into the core. During the puff period, oil comes out of the core owing to the pressure difference between the inside core and the annulus and possibly by water imbibition. Probably, an important mechanism is that the invaded water and imbibed water increase reservoir pressure and local pressure so that the drive energy is boosted. From the imbibition point of view, water-wet formation is preferred. This conclusion is supported by experimental data by Huang and Xiang (2004).

Fig. 7.4 shows the effect of soaking time. As water is not as compressible as gas, when water was injected, the pressure in the vessel quickly reached the set pressure of 1000 psi. The huff time was short, and a relatively longer soaking period was needed. In the figure, the soaking time actually included the huff time. The puff time was 3 h. On increasing the huff and soaking

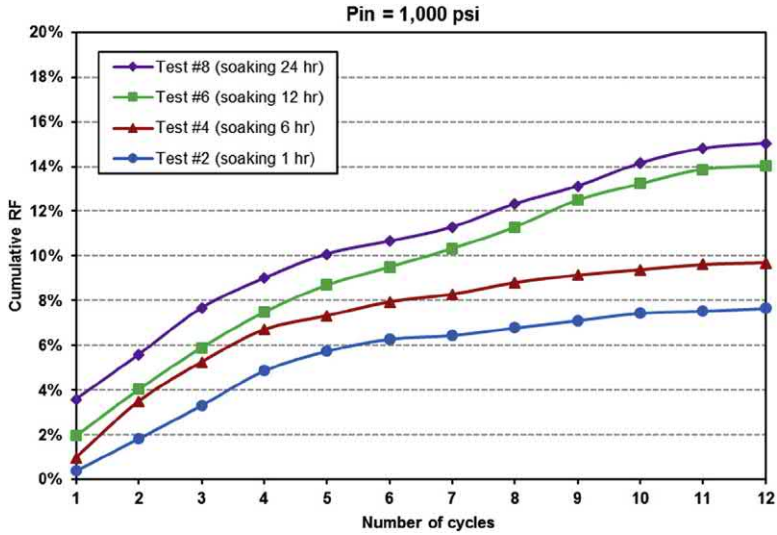

Figure 7.4 Oil recovery from water huff-n-puff at different huff and soaking times.

time from 1 to 12 h, there was an obvious improvement in cumulative oil recovery factor from 7.67% to 14.04%, respectively, after 12 cycles. But when the huff and soaking time was increased from 12 to 24 h, the oil recovery was increased less than 1%. It indicates that the oil recovery might not effectively benefit from a further longer soaking time. Since the pressure buildup in the experimental setup was very fast, a soaking period was necessary to transfer the surrounding pressure into the inside of the core. In a reservoir, there might be an optimum soaking time which was not studied. As the injection fluid might cause the change in the rock properties, and cores could not be totally cleaned to resume the original conditions before operating the tests, four cores from the same batch of cores which has similar rock properties were used, instead of using one core to repeat the four tests.

Fig. 7.5 shows the effect of injection (huff) pressure on huff-n-puff water injection. The huff and soaking time together was 12 h, and the puff time was 3 h. This figure shows that injection pressure significantly affected oil recovery.

Altawati (2016) did huff-n-puff experiments when cores initially had some water saturation. He observed that the liquid recovery factor (defined as the total produced water and oil divided by the total initial water and oil) was lower than the oil recovery under huff-n-puff when no water was

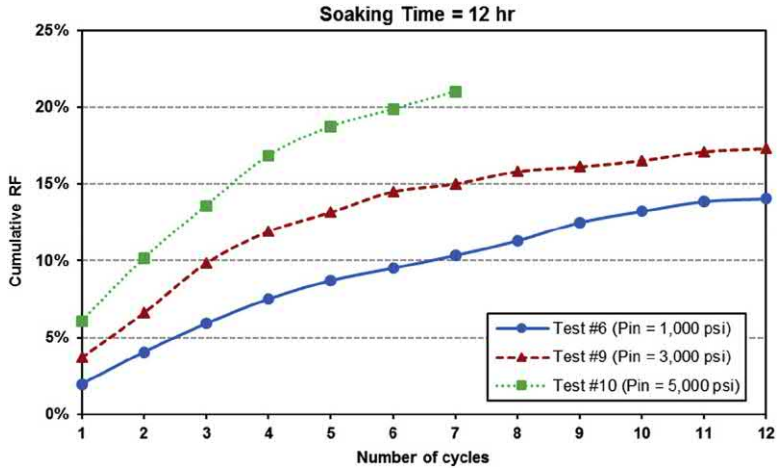

Figure 7.5 Oil recovery from water huff-n-puff at different injection pressures.

initially in the core. Shen and Chen (2014) simulation results show that the incremental oil recovery from water huff-n-puff over the primary depletion is less than 2% higher. Therefore, the EOR potential for water huff-n-puff is limited. Some of huff-n-puff water injection projects are briefed below.

7.3.1 Huff-n-puff water injection in Bakken formation in North Dakota

One water huff-n-puff pilot test was conducted in the North Dakota part of the Bakken formation in 2012. The injection time was just over 1 month, the soaking time was 2 weeks, and the production time was 3–4 months. The injection rate was 1200 bbl/d. No water injectivity problem was observed, but little to no oil rate was increased (Hoffman and Evans, 2016). Probably, 1 month of injection might not be long enough to inject a minimum gas volume.

7.3.2 Huff-n-puff water injection in Parshall Field

EOG conducted a produced water injection test in a well in the Parshall Field, the NDIC 17170. Injection began in the spring of 2012 with a plan to operate the well in a huff-n-puff scheme according to a 30-day injection and 10-day soak schedule. 10,000 barrels of water were injected in April and 29,000 barrels were injected in May 2012. There was no observable

incremental improvement in oil production attributable to water injection (Sorensen and Hamling, 2016).

7.3.3 Huff-n-puff water injection followed by huff-n-puff CO_2 injection in Parshall Field

A Parshall Field well operated by EOG, the NDIC 16986, has been the subject of both produced water and field gas injection testing. Water injection was conducted periodically from April 2012 to February 2014 in a "waterflood pilot." Nearly 439,000 barrels of water were injected before the well was returned to production in March 2014. No obvious increase in oil rate was observed (Sorensen and Hamling, 2016).

Starting in June 2014, EOG began injecting field gas mingled with produced water injection. Water was used to manage the effects of gas mobility in the fracture system, or if needed, to build system pressure with less gas volume. Through August 20, 2014, a total of 88.729 MMSCF had been injected. Changes in fluid production rates were observed in two offset wells, demonstrating that communication between wells can occur rapidly. No data showed the test was successful (Sorensen and Hamling, 2016).

7.3.4 Summary of water huff-n-puff performance

The above three water huff-n-puff project performances are summarized in Table 7.2. No oil production increase was observed from any of them. The results are consistent with the research results presented earlier: the water injection EOR potential is limited.

Table 7.2 Water huff-n-puff performance.

Field	Huff, days	Soak, days	Puff, days	Performance	References
Bakken, ND	30	15	90–120	Little or no oil increase, no injectivity issue	Hoffman and Evans, 2016
Parshall field	30	10		No oil increase	Sorensen and Hamling, 2016
Parshall field	439,000 bbls of water injected first then produced. Later water-alternate-gas tested			No oil increase	Sorensen and Hamling, 2016

Table 7.3 Incremental oil recovery from water and gas injection over primary depletion.

Scenario	Gas injection	Water injection
10 years of primary	5.73%	5.73%
20 years of flooding	2.39%	1.86%
20 years of huff-n-puff	16.69%	2.40%

7.4 Waterflooding versus huff-n-puff water injection

Sheng (2015d) compared waterflooding and huff-n-puff water injection by simulation. The base simulation model is similar to what is described in Section 6.3 of Chapter 6. The oil recovery factor after 10 years of primary depletion is 5.73% which is representative to the typical field performance. The incremental oil recovery factors over the primary depletion after 20 years of the flooding and huff-n-puff injection are 1.86% and 2.40%, respectively (see Table 7.3). Thus, the huff-n-puff water injection performs better than the water flooding. Sheng and Chen's (2014) simulation results show that water huff-n-puff oil recovery is slightly lower than that from waterflooding because the water huff-n-puff cases are not optimized.

7.5 Water injection versus gas injection

Sheng (2015d) also compared waterflooding and gas flooding by simulation. The results are presented in Table 7.3. It can be seen that gas injection is better than water injection, either by huff-n-puff mode or flooding mode. Because water viscosity is much higher than gas viscosity (Fai-Yengo et al., 2014) and because of ultralow shale permeability, the pressure near the injector cannot propagate to the producer. Figs. 7.6 and 7.7 show the pressure distribution from the injector to the producer at the end of 60 years of gas flooding and waterflooding, respectively, after 10 years of primary depletion. They show that it is much easier for the pressure to transmit from the injector to the producer for gas flooding than water flooding, indicating gas flooding is more efficient.

Wang et al. (2010) simulated the CO_2 EOR potential in the tight Bakken formation in Saskatchewan (0.04—2.5 mD). Their simulation results indicate that CO_2 injection performs much more effectively than waterflooding, because the sweep efficiency and pressure propagation in waterflooding were much worse than those in CO_2 flooding. Such result is consistent with those presented by Sheng and Chen (2014), by

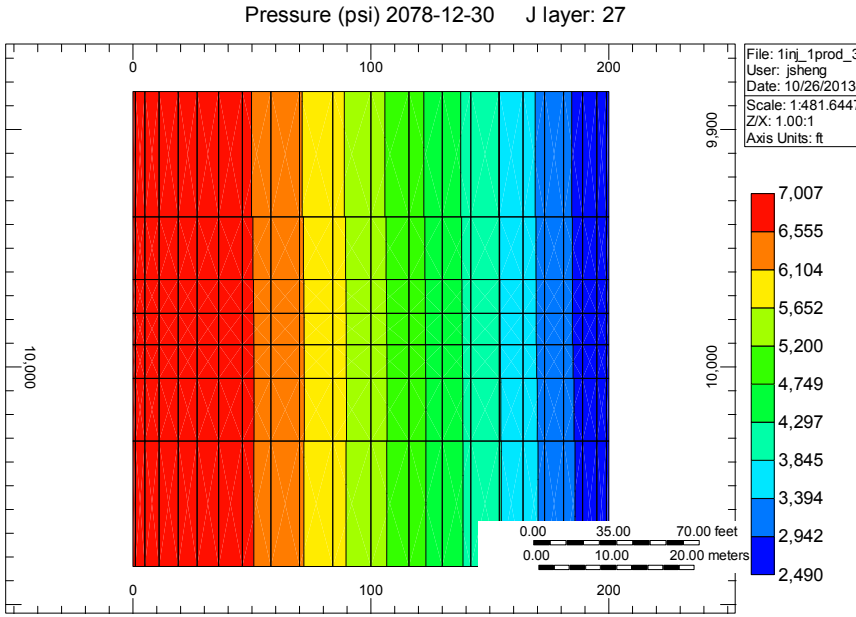

Figure 7.6 Pressure from the injector to the producer at the end of 60 years of gas flooding.

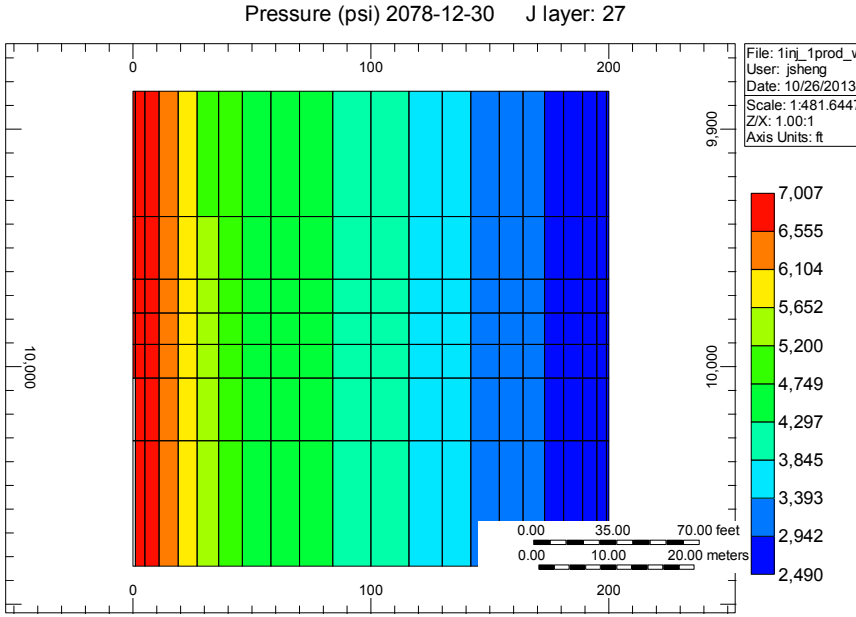

Figure 7.7 Pressure from the injector to the producer at the end of 60 years of water flooding.

Joslin et al. (2017), and by Dong and Hoffman (2013) for the Bakken formation in the Sanish field, North Dakota. Sheng and Chen's (2014) simulation results show that the average pressure during water injection cannot be increased much higher than that before water injection, as the high pressure is only near the injector. Their results also show that the oil recovery from waterflooding is lower than that from gas flooding. Dong and Hoffman's (2013) simulation results show that the oil recovery from their continuous CO_2 injection is four times higher than that from waterflooding in the Middle Bakken in the Sanish field (tight formation of 0.04 mD). Kurtoglu's (2013) simulation results also show that oil production from CO_2 injection outperforms waterflooding. However, water-rock interactions are not considered in the modeling work.

The above paragraphs compare the water and gas injection in the flooding mode. Yu and Sheng (2017) compared the huff-n-puff mode by experiments. The experimental setup for water injection has been presented earlier in this chapter. For the huff-n-puff gas injection tests, the KCl solution (water) was replaced by nitrogen as the injection medium. Nitrogen could be directly introduced into the vessel from the gas cylinder without using the accumulator.

Fig. 7.8 compares the oil recovery performance from water huff-n-puff and nitrogen huff-n-puff under different soaking times, with other conditions being the same. It presents consistent trends that the nitrogen huff-n-puff injection had much higher oil recovery than the water huff-n-puff injection. Under the same operating conditions, a similar amount of oil was produced in the first cycle from the two IOR processes. Their difference increased with the cycle. After 12 cycles, the cumulative oil recovery factors from water injection were all 10% higher than those from gas injection.

Kong et al. (2016) simulation results show that the CO_2 huff-n-puff performance is much better than waterflooding in the tight Cardium oil reservoir (0.2 mD).

However, Song and Yang (2013) compared waterflooding with huff-n-puff CO_2 injection. In the waterflooding case, a core of 0.27 mD and the initial oil saturation of 0.55 were flooded by 1.2 pore volumes of water until no more oil was produced. The ultimate oil recovery was 51.5%. In the huff-n-puff case, a core of 0.56 mD and the initial oil saturation of 0.43 were used. The oil viscosity was 2.17 cP at 20°C. CO_2 was injected for 1 h at a constant pressure of 7 MPa, soaked for 6 h and produced for 1 h. The oil recovery was 42.8% after six cycles. It was under an immiscible

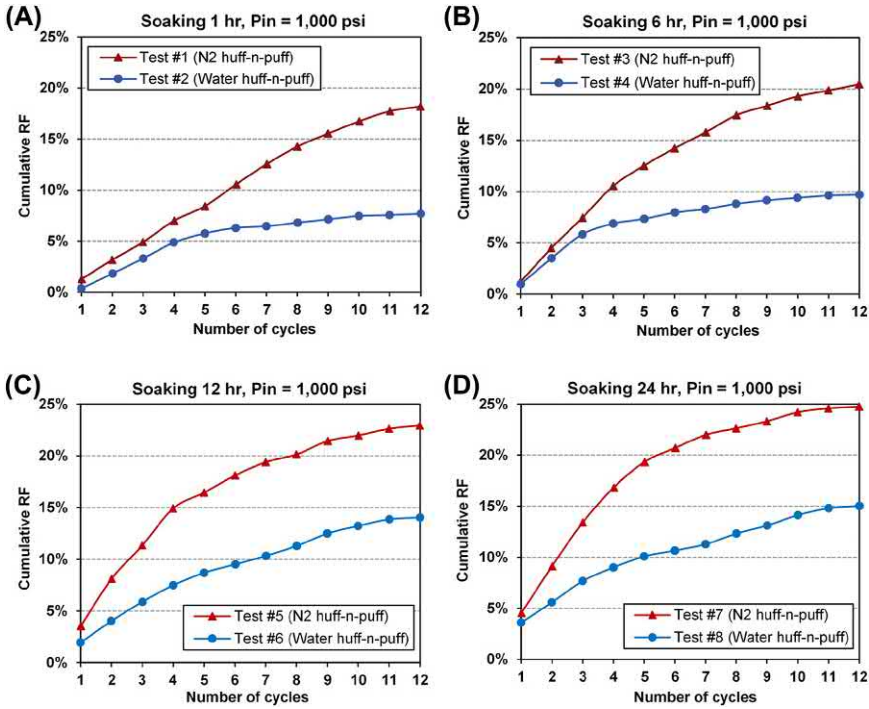

Figure 7.8 Comparison of oil recovery performance from water huff-n-puff and nitrogen huff-n-puff under different soaking times.

condition. From the oil recovery factors, they concluded that the waterflooding outperformed the huff-n-puff CO_2 injection. This conclusion is opposite to Sheng's (2015d) (see a table early in this chapter). The comparison or the conclusion might not be properly made for these reasons: (1) the huff-n-puff cycle could be performed more times to get more oil, but no more was able to be produced in the waterflooding; (2) the huff-n-puff might not be optimized; probably the puff time of 1 h was too short; (3) the comparison should be made based on the same operation time as it is the most important parameter, although a better comparison should be made based on the net present value (NPV). When it was under a near-miscible condition (9.3 MPa pressure, the MMP was 9.7 MPa), the oil recovery increased to 63%. When the injection pressure was at 14 MPa at a miscible condition, the oil recovery was 61%, slightly lower than that from the near-miscible condition. They stated that a pressure higher than the MMP was not necessary.

7.6 Water-alternating-gas (WAG)

To overcome the gravity override of gas and the gravity underride of water or to combine the benefits of water and gas, water-alternating-gas is widely used in conventional reservoirs. In shale and tight reservoirs, the gravity-related problem should be less severe. But Yang et al. (2015) evaluated the performance of water-alternating-CO_2 injection in laboratory with core permeability less than 0.5 mD, and the oil viscosity is 2.17 cP at 20°C and at atmospheric pressure. They observed that when the ratio of water to CO_2 slug sizes was decreased, the fluid injectivity was improved, but the recovery efficiency was decreased because sweep efficiency was decreased. In terms of the effect of the ratio on oil recovery efficiency, the result is consistent with the simulation result from Ghaderi et al. (2012). In their model, the horizontal reservoir permeability is 0.61 mD and the vertical permeability is 0.061 mD. The oil viscosity at the bubble point is 0.63 cP. Three horizontal wells (two edge producers and one middle injector) have transverse fractures in a staggered configuration. Such configuration helps to maximize the contact area with the formation and to maximize the distance between fractures to delay breakthrough and improve sweep efficiency. Their result shows that WAG performs better than continuous CO_2 injection, and higher water-to-gas ratio results in higher oil recovery; for example, after one pore volume of injection, the oil recovery factors for water-to-gas ratios of 0.5, 1.0, and 2.0 are 16.7%, 19.8%, and 21.7%, respectively. But tertiary recovery for CO_2 injection should be better as CO_2 contacts with oil, reducing residual oil saturation through miscible displacement. In a specific reservoir, there should exist an optimal water-to-gas ratio. Their results also show that when the water-to-gas ratio is identical, as the WAG cycle length becomes shorter, higher oil recovery is obtained. This is because more cycles can be performed within a fixed time interval. This result is consistent with that for a huff-n-puff gas injection.

7.7 Huff-n-puff water and surfactant injection

Water injection can build up reservoir pressure to a depleted reservoir. Zhang et al. (2019) used field-scale simulation models to demonstrate the potentials of water injection and surfactant solution injection. In the simulation models, the matrix permeability is 150 nD and the natural fracture spacing is 0.5 ft. The surfactants have the functions to change rock wettability to more water-wet and reduce IFT. The surfactants of two gpt

concentrations are added in the first cycle, and the next two cycles are water only. Each cycle has 6 months of injection and 12 months of production. Their results show that water injection of three cycles improves oil recovery by 43% and surfactant injection doubles the improvement.

7.8 Water injection in China

Because water injection modes in China are not simply huff-n-puff or flooding, and the permeability is generally higher than those cases presented in the previous sections, this section is allocated to discuss water injection in China. Typical tight formations in China are distributed in Ordos Basin (Chang 7, Chang 6, and Chang 8), Zhengger Basin, and Songliao Basin. The typical technologies to develop tight oil are long horizontal wells with multistage fracturing, primary depletion followed by water injection, production above the bubble point pressure, and other means to reduce production costs (Li et al., 2015a,b). Sometimes, water injection *proceeded* primary depletion. Different modes of water injection and their performance are summarized in Table 7.4 and discussed separately below. Some of them are further briefed next.

7.8.1 Pulsed water injection

Pulsed water injection is to change water injection rate at some cycles of time. Sometimes water injection is completely stopped for some time at the injectors, but the oil producers are kept flowing. The idea is to generate pulsed elastic energy. It is a flooding process. The mechanisms of pulsed water injection are believed to be as follows. (1) Oil is displaced out of lower-permeability zones by water imbibition. (2) During the high-rate injection period, high pressure drives water from high-permeability zones to lower-permeability zones to displace oil out. (3) Pulsed pressure pulses enhance elastic energy. Thus, the conditions to apply pulsed water injection are heterogeneous, water-wet, and low oil viscosity reservoirs, short normal injection history, and the facility can enable increase in water injection rate (Guo et al., 2004). A typical cycle is 30 days injection and 30 days shut in (Xie et al., 2016). Here is a field case of pulsed water injection.

The porosity and permeability of the An 83 zone in the Chang 7 formation were 8.9% and 0.17 mD. The rock was weakly water-wet to water-wet. The formation water salinity was 51 g/L and the water was $CaCl_2$ type. It was a thick formation but there were many separation layers. The oil viscosity was 1.01 cP in situ and 6.5 cP at the surface. The GOR was

Table 7.4 Water injection performance of Chinese projects.

Injection mode	Field	k, mD	μ_o, cP	Performance	References
Pulsed	An 83, Chang7	0.17	1.01	When shut in, P reduced sharply, f_w not reduced.	Wang et al., 2015a
Asynchronous	An 83, Chang7			q_o increased, f_w reduced.	Wang et al., 2015a
Huff-n-puff 1	An 83, Chang7			q_o increased.	Lin et al., 2016
Huff-n-puff 2	An 83, Chang7			Well interference, performance not as good as huff-n-puff 1.	Lin et al., 2016
Huff-n-puff 3	An 83, Chang7			6 wells had one cycle, and 2 wells had two cycles. Neighboring non-huff-n-puff wells outperformed huff-n-puff wells. The second cycle performed not as good as the first cycle.	Lin et al., 2016
Huff-n-puff 4	Chang 6	0.54	4.67	7 day soaking for most of wells, 3 days for the rest. Oil rate increased. Performance for 7 days better. Optimum well spacing 300 m.	Wei, 2016
Huff-n-puff 5	Duha Field, Xingjiang	0.1−1		7 days injection (2000 m^3 water injected), initial q_o increased from 0.9 to 5 tons/day, effective for 9 months, total incremental oil 155 tons.	Li, 2015

75.7 m^3/ton. Pulsed water injection was performed. It was found that after water injection was stopped, the reservoir pressure declined fast, and the water cut was not significantly reduced. It was not clear what optimal cycle time should be. Once water broke, the water cut sharply rose up (Wang et al., 2015a).

7.8.2 Asynchronous water injection

Asynchronous water injection is when injectors are open and producers are shut in, and vice versa. While the water is injected, injected water is prevented from breaking through producers. While the producers are shut-in, the water is promoted to enter matrix from fractures by high pressure difference and capillary pressure. During a short period of shut-in for both injectors and producers, the pressure is equilibrated among matrix and fractures. When the producers are open, oil is produced from the matrix to fractures. Such operation was practiced in the An 83 zone in the Chang 7 formation. The daily rate of oil from the producer An 18 increased from 3.6 to 5.4 tons/day, and the water cut decreased from 100% to 37.2% after five cycles of operation (Wang et al., 2015a). This method was also practiced in a metamorphic reservoir where the oil rate was increased from 21.8 to 42.5 tons/day after asynchronous water injection (Li, 2011).

7.8.3 Huff-n-puff water injection

Huff-n-puff water injection injects water and produces fluid at the same well. Two different huff-n-puff patterns were conducted in two An 83 zones in Chang 7 Field in 2014. In the first zone (Huff-n-puff 1), totally four wells were tested with one huff-n-puff well in the middle, while the other two wells in the two sides of the huff-n-puff well were continuous production wells. In the second zone (Huff-n-puff 2), all three wells were huff-n-puff wells.

In Huff-n-puff 1, the average daily water injection was 109 m^3 and cumulative water injection was 2177 m^3. The pressure was raised to 4.7 MPa. The incremental oil from the huff-n-puff well itself was 419 tons, and the decline rate decreased from 17.9% to 10.8%. The incremental oil from the neighboring continuous production wells was 2358 tons, and the decline rate decreased from 16.6% to 31%. These data show that oil production benefitted from the huff-n-puff water injection, and the benefit was better for the two continuous production wells than the huff-n-puff itself. In the second zone of all four huff-n-puff wells, the wells were interfered, and the performance was not as good as in the first zone (Lin et al., 2016).

Around the year of 2015, eight wells were put in huff-n-puff water injection in the An 83 zone (this zone is named huff-n-puff 3 in Table 7.4). Among these eight wells, 6 wells had one cycle, while the other two wells had two cycles. Seven wells benefitted from the water injection. The incremental oil from the huff-n-puff wells was 456 tons, but 1127 tons of oil from the neighbor wells. Among the 6 wells with one cycle injection, two wells, Well AP 53 and Well An 120, did not see pressure increase, but the neighbor wells had 497 tons of incremental oil. The rest of the four wells had injection pressure raised to 7.25 MPa and benefitted. For example, Well AP 83 had 5100 m^3 of water injection and 45 days of soaking. Injected water reached its two neighbor wells AP 48 and AP 84. By June 2016, Well AP 83 had daily incremental oil rate 2.71 tons, and cumulative incremental oil 361 tons, while its neighbor wells AP 48 and AP 84 had daily incremental oil 4.52 tons, and cumulative incremental oil 596 tons. A second cycle was put on the two wells AP 20 and AP 21 who performed well in 2014. Compared with their first cycle, the performance was not good.

Huff-n-puff water injection was also performed in the Chang 6 reservoir, Yanchang oil field near Qieli Village, Ordos Basin, China (Wei, 2016) (Huff-n-puff 4 in Table 7.4). The average porosity was 8%, and the average permeability was 0.54 mD in the reservoir. The oil viscosity at 50°C was 4.67 cP. The formation rock was weakly water-wet with the wettability index 0.17. The reservoir pressure was 4.25 MPa, and the bubble-point pressure was 1.12 MPa. The initial well oil daily rate was 0.74 tons. The rate declined very fast. The water flooding sweep efficiency and injectivity were low. Therefore, huff-n-puff water injection was proposed. Some surfactant was added in the water. But no details about the surfactant were reported. Nine wells in Block G and 20 wells in Block Z were selected in November 2015. These wells had produced for more than 10 years. The daily oil rate by March 2016 was less than 0.2 tons on average. The economic oil daily rate was 0.3 tons.

For 29 wells, the soaking time was 7 days for most of wells and 3 days for the rest. Test results showed that 7-day soaking outperformed 3-day soaking in terms of incremental oil rate. A longer soaking time helped water imbibition and pressure propagation from higher-permeability zones to low-permeability zones. Water injection volume was 50 m^3 for most of wells and 70 m^3 for the rest. Test results showed that higher volume injection was better. After water injection, the incremental daily oil rate was 0.1−0.4 tons on average.

Huff-n-puff water injection was also successfully tested in Toutai reservoir, Daqing. The permeability was 1.25 mD, and the huff-n-puff cycle was half to 1 year (Tian et al., 2003). Huff-n-puff water injection was tested in 2007 in Well Niu 15−5 in Niuquanhu reservoir, Tuha Field. The permeability in this area was 0.42−7.84 mD. The soaking time was 108 days. Two cycles were performed with incremental oil of 1816 tons (Yang et al., 2006; Tang and Li, 2010).

Huff-n-puff water injection was performed in Duha Field, Xingjiang, China (Huff-n-puff 5 in Table 7.4). Duha Field was an igneous reservoir. The porosity was 8.4%−19.1%, and the permeability was 0.1−1 mD. The initial reservoir pressure was 20.4 MPa (2958 psi) and the reservoir temperature was 60.9−70.7°C. Water was injected in Well Ma-55 from July 18 to July 24, 2014. The well was fractured. The injection pressure was 30−38 MPa (4350−5510 psi). The injection rate was 285 m^3/day. The total injected water volume was 2000 m^3. The oil rate before water injection was 0.9 tons/day and the water cut was 16%. After the huff-n-puff water injection, the oil rate was 5 tons/day and the water rate was kept constant until the reporting date (August 2015). The incremental oil was 155 tons (Li, 2015).

The above field cases show that huff-n-puff water injection generally worked. The injection, soaking, and production times were quite different from case to case. Huff-n-puff water injection was even practiced in conventional reservoirs, for example, in the Machang field where the permeability is 90 mD (Li et al., 2001). Some experimental work in high permeability cores (110−180 mD) was also carried out (Huang Xiang, 2004).

CHAPTER EIGHT

Fluid-rock interactions

Abstract

This chapter discusses the research results on the interactions between an aqueous solution and a clay-bearing rock. The effects of confining stress, bedding, existing natural fractures, low-pH and carbonated water, high-pH water and surfactants on the permeability changes from water-rock interactions are discussed. The effects of some of those factors on rock mechanical properties are also discussed. Some reactions which induce fractures are introduced.

Keywords: Confining stress; Fluid-rock interactions; Mechanical properties; Natural fractures; Permeability changes; pH; Reaction-induced fractures; Surfactants.

8.1 Introduction

The fluid-rock interactions to be discussed in this chapter are the interactions between an aqueous solution and a clay-bearing rock. There are three reasons we need to study the interactions in shale and tight reservoirs: (1) most of fracturing fluids are aqueous fluids; (2) most of chemicals are injected through aqueous fluids; (3) water injection may still be a practical EOR method. In conventional reservoirs, it is generally accepted that water-rock swelling may cause formation damage—reducing formation permeability. However, there are some discrepancies in shale reservoirs regarding the results of water-rock interactions. Some believe water-rock interactions also cause formation damage. Some argue that water-rock interactions, especially the interactions between water and shale, may generate microfractures or reopen existing natural fractures; therefore, formation may not be damaged, instead, it may be stimulated. This chapter is to discuss the research results on the interactions between water and a clay-bearing rock.

8.2 Evidences of microfractures generated or existing natural fractures reopened

Many papers have been published on water-rock interaction. It is commonly accepted that water-rock interaction causes formation damage

Enhanced Oil Recovery in Shale and Tight Reservoirs
ISBN: 978-0-12-815905-7
https://doi.org/10.1016/B978-0-12-815905-7.00008-6

(reduce formation permeability). However, it was observed that the water may help to generate microfractures or open existing microfractures in shale formations if no confining pressure is applied (Dehghanpour et al., 2013; Morsy et al., 2013a-c, 2014a-b, Morsy and Sheng, 2014a).

We studied the effect of water hydration swelling on microfracture generation without confining pressure and observed that shale rocks could be fragmented or cracked. Fig. 8.1 shows that Mancos shale samples had cracks and became fragmented by different degrees depending on the salinity. At 5% and 10% NaCl, the rock samples were fragmented; however, when the concentration was above 15%, the sample had fewer cracks. Imbibition tests showed that higher oil recovery was obtained as the salinity concentration decreased (Morsy and Sheng, 2014a).

In Fig. 8.2, Barnett shale samples showed clear fractures parallel to the bedding when immersed in distilled water. The imbibition oil recovery was enhanced, and the measured permeability was significantly increased owing to the fractures generated.

Fig. 8.3 shows that the Mancos sample exposed to fresh water during spontaneous imbibition was most sensitive to fresh water as it was highly damaged due to severe hydration; the Barnett sample showed several cracks when exposed to fresh water (distilled water); there were cracks on the Marcellus shale, although they are not clearly seen in the figure; the Eagle Ford sample was least sensitive to water salinity with no cracks seen (Morsy and Sheng, 2014a).

Figure 8.1 Mancos rock samples in 5%, 10%, and 15% NaCl solutions.

Figure 8.2 Barnett Shale with clear fractures parallel to the bedding after immersion in distilled water.

Figure 8.3 What Mancos, Barnett, Marcellus, and Eagle Ford samples looked like in water.

The oil recoveries from the Mancos, Barnett, Marcellus, and Eagle Ford samples exposed to fresh water are presented in Fig. 8.4. The recovery factor of Mancos was the highest (59%) among all the samples, because the samples were fragmented, and it was easier for oil to come out of the shale sample.

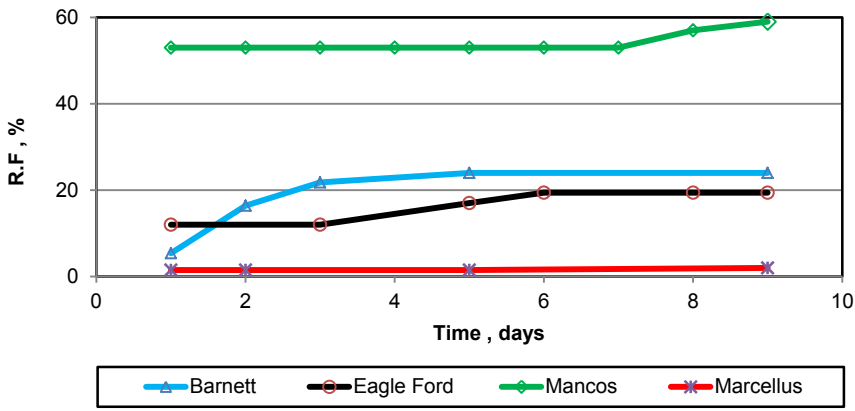

Figure 8.4 Oil recovery factors (RF) in spontaneous imbibition in fresh water from the Barnett, Eagle Ford, Mancos, and Marcellus shale samples.

Eagle Ford and Barnett recovered 20% and 24%, respectively. The cracks were induced over time in Barnett samples when exposed to the distilled water. As a result, more oil was recovered. Although no fractures were visually seen in the Eagle Ford sample, the high oil recovery factor was obtained. It is believed that the Eagle Ford sample had better-connected pores. Marcellus sample showed the lowest recovery of about 2% somehow. It can be seen that the imbibition oil recovery was closely related to the degree of hydration. More hydration led to higher oil recovery.

Other researchers also observed microfractures generated by hydration. Dehghanpour et al. (2012) observed that water did not physically damage organic shales. Water altered shale samples much more than oil (Dehghanpour et al., 2013). Gomaz and He (2012) observed secondary fractures generated along bedding, and more fractures observed in fresh water than saturated salt mud. Ji and Geehan (2013) conducted studies on shale samples immersed in fresh water and saturated with salt water and found that shale hydration swelling stress could cause formation of secondary fractures that enhance shale oil and gas recovery.

Actually, a few operators have suggested that water adsorbed by minerals in the rock creates localized clay swelling that may serve to hold open small fractures and fissures (Hu et al., 2013). In contrast to conventional propped hydraulic fracture treatments, slick water fracturing relies on the reactivation of natural fractures to induce permanent shear-induced dilation, which enhances reservoir permeability (Zoback et al., 2012; Weng et al., 2015). Sharma and Manchandra (2015) listed five evidences of the existence of induced unpropped fractures. Although the conductivity of unpropped, shear-induced fractures is relatively low compared to that of propped fractures, such conductivity has played an important role in enhancing the productivity of ultralow-permeability rocks like shale (Weng et al., 2015; Jansen et al., 2015).

Water absorption in shale is often accompanied by a change in the crystal dimension of clay minerals: this manifests as a swelling of the rock and leads to cracks and fractures. The swelling pressure may break the natural cementation of shale and thus secondary fractures may be formed (Ji and Geehan, 2013).

Generally, shale reservoirs have laminated beddings in the form of heavy disklike cores from vertical wells and small broken cores from deviated wells. Beside dominant bedding planes, shale also shows networks of smaller weak planes and natural fractures (Abousleiman et al., 2010). These weak planes could serve as the sites for secondary fracture creation.

Xue et al. (2018) found that the organic matter and organic pores in shale samples were unchanged after hydration, but the fractures were likely to form between organic matter and inorganic minerals, and microfractures could probably be generated or induced in inorganic minerals. The cohesive force between mineral particles became weak after hydration. The nonclay mineral particles fell off to form inorganic pores, and these pores gradually developed into microfractures between nonclay and clay mineral particles. In their experiments, shale samples were not confined during hydration.

Yuan et al. (2018) measured the shale permeability during hydration. They found that the permeability decreased first, then recovered with increasing immersion time, as shown in Fig. 8.5. The permeability decrease was caused by the fact that flowing channels were narrowed byclay swelling. At later time, the permeability recovery was caused by the wettability toward more water-wet and by the connection and expansion of induced microfractures. Again, the shale samples were not confined during hydration.

Shen et al. (2017) measured shale permeability as water imbibed into the shale sample. The measured permeability was actually effective gas permeability (not absolute permeability) at different imbibition volume (at different water saturation). Fig. 8.6 shows the permeability changes with water imbibition time for different shale samples. In the beginning, the permeability was decreased owing to water blockage; then the permeability increased owing to some cracks created by water swelling; at later time, the permeability decreased again except Sample Y4 because more water blockage occurred as more water imbibed. Note that samples were taken out from the imbibition

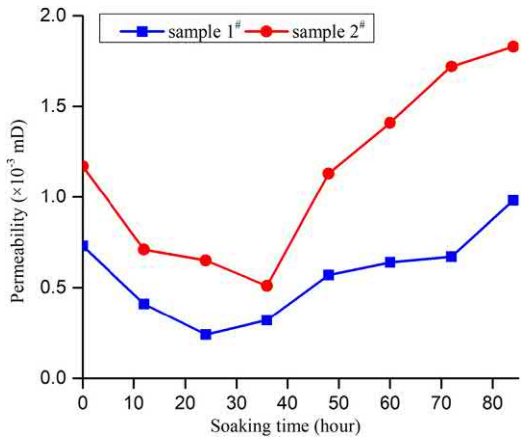

Figure 8.5 Shale permeability changes with immersion time (Yuan et al., 2018).

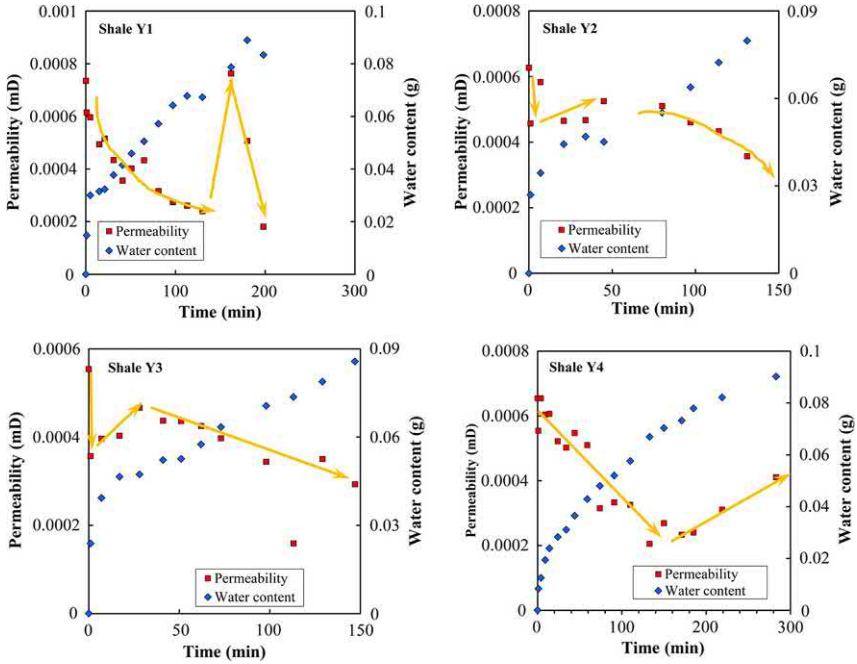

Figure 8.6 Effective gas permeability at different water imbibition times (Shen et al., 2017).

cells and the gas permeability was quickly measured; after that the shale samples were put back to the imbibition cells for continued imbibition. And the shale samples were not confined during imbibition. They also used sandstone samples and volcanic samples to do the same type of experiments for comparison. The permeabilities from sandstone and volcanic samples were continuously decreased as more water was imbibed.

Santos et al. (1997a) studied the water-shale interactions and found that the reaction depended on the moisture of rock samples. The evidence of reactions (core disintegration or created microfractures) was not noticeable for preserved shale samples even at atmospheric conditions without confinement, but only noticeable for dry samples. Therefore, they concluded that the shale instability problem was mainly caused by mechanical failure (mud weight), rather than by chemical interaction between the rock and drilling fluid, as opposed to their initial hypothesis. Makhanov et al. (2014) observed that swelling of clay was not the only mechanism that creates microfractures, because some microfractures are also created with the imbibition of oil despite having no affinity for absorption in clays. This suggests that some pore pressure is developed due to imbibition of fluid (water or oil) or called mechanical

failure, even without clay swelling inside the rock that initiates the creation of microfractures.

8.3 Effect of confining stress

The above reported lab results were observed at ambient conditions (without a confining pressure). Based on the reports in the literature and our work, no doubt, microfractures can be generated when a clay-bearing rock contacts with water without confinement. During hydraulic fracturing the shale reservoir matrix is in contact with the fracturing fluid under confining conditions, and the shale rock interaction with fracturing fluid will be influenced by in situ stresses. Therefore, we are more interested whether microfractures can be formed under confining stresses.

It can be understood that when water enters the inner structure of rock grains, swelling causes the rock grains to be disintegrated without confinement; with confinement, the swelling pressure increases. Behnsen and Faulkner (2011), Duan and Yang (2014), and Faulkner and Rutter (2000) reported that with isotropic confining pressure, significant reduction was observed on clay-bearing rocks or montmorillonite sample permeability measured with water. Whether or not fractures can be induced to increase permeability during water imbibition in shale under an isotropic compressive stress remains controversial.

Onaisi et al. (1993) studied the swelling and swelling-induced fracturing of cylindrical drained Pierre shale samples in contact with water-based mud placed in a central cylindrical borehole. When the water activity of the mud was greater than that of the shale, swelling, large deformation of the wellbore and fractures appeared, the fracture pattern depending on the confinement conditions. When a sample was not confined, fractures were mainly radial; and when a sample was confined, fractures were mainly circular, with some well-developed slip lines around the borehole. When water activities of mud and shale were in balance, virtually no alteration of the wellbore was seen. Their borehole configuration can be considered equivalent to the fractured shale condition.

Santos and da Fontoura (1997) also stated that swelling only occurs if the water equilibrium inside the rock is disturbed, being subsequently contacted by different fluids. Santos et al. (1997a) observed that dehydrated shale cores were more reactive to water than preserved cores; wellbore instability was more caused mechanically (mud weight) than chemical reaction.

Similarly, Chenevert (1969) found that the swelling pressure induced by water adsorption on clay minerals could be extremely high. This was the case of crystalline swelling for the first layers of water adsorbed on the surface. Equations to estimate the potential swelling pressure of shale were suggested as a function of the activity of the water in the shale. The adsorption of water by clay platelets induces large internal stresses in confined samples or expands the unconfined samples (Chenevert, 1970). Adsorption of water on the surface of negatively charged clay platelets develops internal expansive stresses, and in turn expands and disintegrates the unconfined shale samples (Hensen and Smit, 2002; Steiger, 1982).

When Sun et al. (2015) did imbibition tests, core surfaces were sealed with epoxy except the two end surfaces were open. They observed microfractures generated during imbibition. The epoxy prevented the cores from falling apart owing to fracturing.

Zhang and Sheng (2018) studied the effect of water imbibition on fracture generation in Mancos shale cores under isotropic stress conditions using an isotropically confined core holder. Slices along the axial direction of the shale core were obtained by CT scanning. An NL3000 CereTom X-ray CT scanner made by NeuroLogica Company was used to conduct the CT tests. The CT scanner's minimum recognizable slice volume was 0.1225 mm^3 (with a slice thickness of 1 mm) and spatial resolution was 0.35 × 0.35 mm. The relative density resolution for the CT machine was 0.3% Hu. To improve the contrast, an adaptive pseudocolor enhancement method (Li et al., 2011) based upon gray scale-color transformation and Otsu thresholding segmentation (Otsu, 1979) was adopted to create color images.

Fig. 8.7 shows the two-dimensional cross-sectional images from CT scanning and those after adaptive pseudocolor enhancement. In the figure, po denotes injecting fluid pressure or pore pressure, icp means isotropic confining pressure. In these three tests, po is the same (0.03 MPa). Each fracture is circled with a red line. The image shown in the figure is taken at the middle of the inlet surface (far left line) and the red vertical line (approximately 1.25 mm distance from the inlet surface). This location should be fully water-saturated at each time except the initial time. For the Mancos shale under 0.1 MPa confining pressure (a), during the 72 h of water imbibition, among the initial 11 fractures, two fractures propagated to become two large fractures across the whole core. Under the 2.0 MPa confining pressure (b), during water imbibition seven fractures were popped up, but only one existed on the cross-section at the end of the test. Under the 20.0 MPa confining pressure (c), 12 obvious fractures were observed to pop up during water imbibition, but only four new generated small fractures were observed on the cross-section by 72 h.

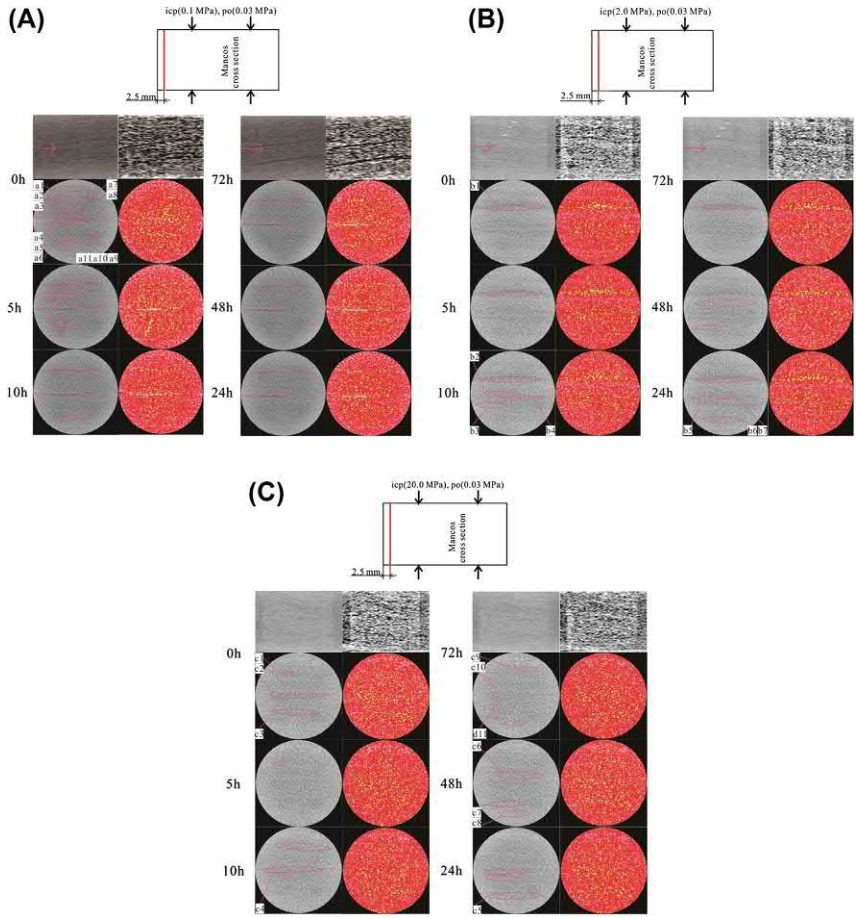

Figure 8.7 CT images of Mancos shale core under various icps (the CT cut face image at 72 h was reconstructed using the all cross-section images).

From these three tests, the following observations can be made.

(1) Under a lower confining pressure, more fractures were generated during the initial water imbibition.

(2) Generated fractures could be closed, reopened, closed and reopened … In other words, opening or closing of a fracture was dynamic, depending on the water concentration change rate and stress conditions (Zhang and Sheng, 2017a; 2017b, 2017c, 2018).

(3) At the end of each test, very few fractures remained open, regardless of the magnitude of confining pressure, which were also observed earlier (Zhang and Sheng, 2017a; 2017c).

Zhang and Sheng (2018) also measured shale (Mancos) strain changes during water imbibition under isotropic confining pressures. Cylindrical samples of 38 mm diameter and 76 mm length were used during the shale swelling experiments. Shale swelling strain was tested. The strain gauges (1.78 mm width and 3.18 mm length) were cemented to the surface of the samples to measure strain in axial and lateral directions. A waterproof silicone rubber (an excellent electrical insulator, even in brine) was used as a protective coating for the strain gauges and connections. All measurements were carried out at room temperature, which was kept largely constant and was recorded for control. The sample with the strain gauge frame was then placed in a beaker and the core inlet surface was immersed in the distilled water. The strain was recorded continuously for nearly 2 days until the value remained constant. The Hoek triaxial cell shown in Fig. 8.8 was used to apply confining pressure, and an HCM-0032 compression machine (Humboldt Mfg., Elgin, Illinois) could be used to apply an axial load.

During water imbibition, with the confining pressure increasing from 0 to 20.0 MPa, the radial and the axial swelling strains are shown in Fig. 8.9. Hydration swelling stress acts as the volume stress to induce plastic swelling strain (Heidug and Wong, 1996). Although the hydration-induced fractures experienced a dynamic process of opening and closing locally, the swelling

Figure 8.8 Cutaway view of Hoek triaxial cell.

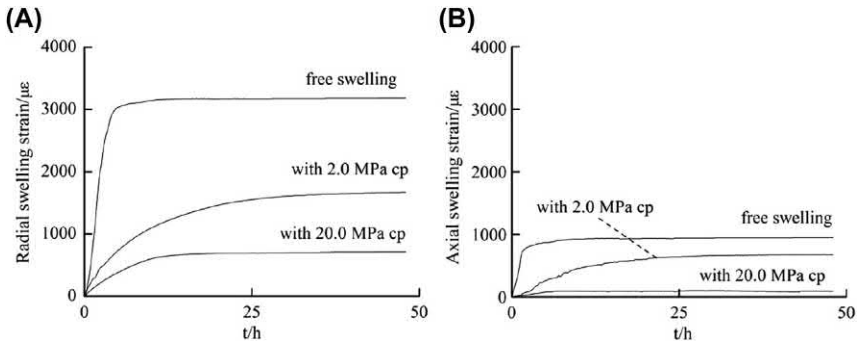

Figure 8.9 Swelling strain of Mancos shale cores during water imbibition under different isotropic confining pressures.

strain that was considered the total core swelling increased significantly first and then gradually stabilized. Swelling strain reduced due to compressive stress as the confining pressure was increased. It can be understood that a shale core can expand with water imbibition without confining pressure, probably resulting in larger pores or higher permeability. However, with a high confining pressure but the rock expanding, pores must shrink. The confining pressure has a significant effect on the water-rock interaction. These results are consistent with the observation from Ewy and Stankovic (2010) that confining pressure can significantly prevent induced swelling from occurring; there exists a threshold confining pressure below which swelling decreases with confining pressure.

Roshan et al. (2015) studied fracturing under isotropically confined conditions (by hydraulic pressure). A fracture was observed on a bedding plane when a shale core was immersed in deionized water for 40 h under 1000 psi, but the fracture formation took a longer time than the case without confinement. Note that the core could still expand under such hydraulic confinement.

To study the effect of anisotropic stresses, an anisotropic core holder was needed by Liu and Sheng (2019). Fig. 8.10 is the schematic of an anisotropic core holder which can be used under CT scan. The part 7 controls the confining pressure in the radial direction of the core, while the part 9 controls the axial pressure.

For water to be able to contact a core quickly, a hole of 13 mm diameter and 15 mm in length was drilled in a core of ~38 mm in diameter and ~51 mm in length, as shown in Fig. 8.11 (Liu and Sheng, 2019). The sample was put in an FCH aluminum wrapped triaxial core holder. A fluid could flow into the core sample through the hole and the core end face. An axial

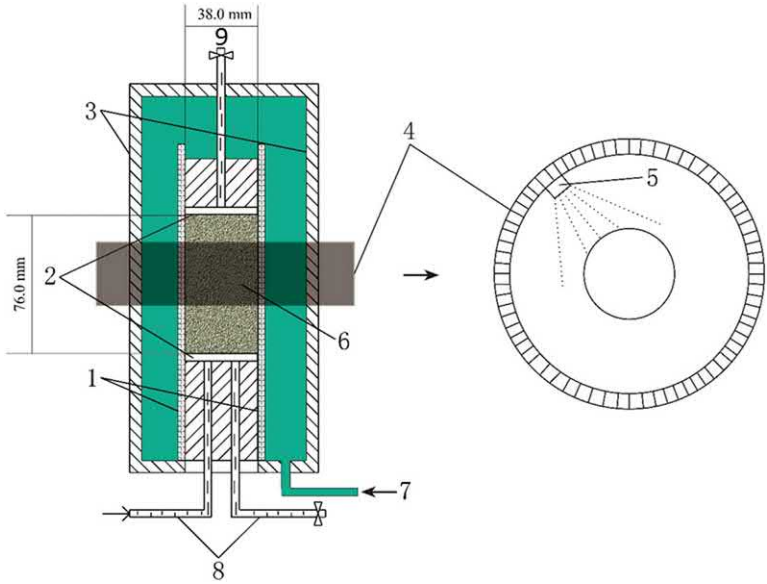

Figure 8.10 Schematic of anisotropic core holder and related CT parts: 1 — Rubber sleeve, 2 — Load block, 3 — Steel sleeve, 4 — CT scanner, 5 — X-ray source, 6 — Shale core, 7 — Fluid for radial confining pressure application, 8 — Test solution injected into shale, and 9 — Fluid for axial confining pressure application.

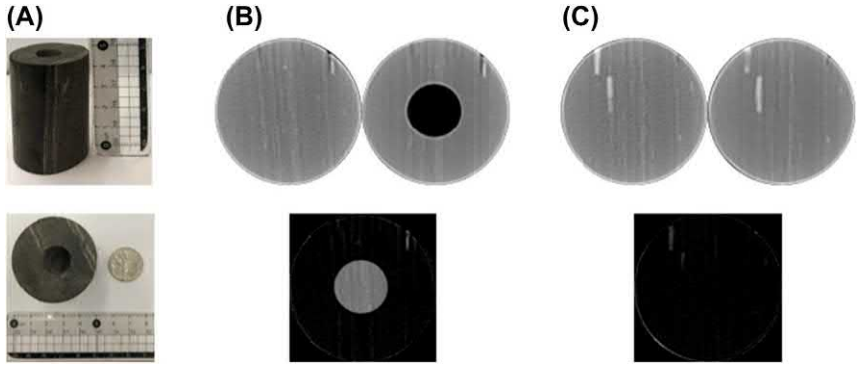

Figure 8.11 (1) An example core used in the experiment, a hole with dimensions of 15 mm length and 13 mm diameter was drilled from the core inlet surface; (2) images near the hole; (3) images far away from the hole.

pressure could be set different from the confining pressure. For the CT images, darker color represents pores and fractures.

Three Eagle Ford core samples were used to conduct oil imbibition tests for 48 h first; after drying, water imbibition tests were conducted for 48 h. The test conditions and masses after imbibition are listed in Table 8.1.

Fig. 8.12 shows the images after the sequential imbibition tests. All the images were parallel to the core axial through the middle of core. The

Table 8.1 Test conditions and masses after imbibition.

Label	Axial stress (psi)	Confining stress (psi)	Pore pressure (psi)	Imbibition fluid	Mass after oil imbibition test (g)	Mass after water imbibition test (g)
EF-1	500	500	100	Oil, water	127.686	124.91
EF-2	1350	500	100	Oil, water	133.49	135.263
EF-4	3000	500	100	Oil, water	132.633	132.4
EF-7	3000	3000	100	water		126.45

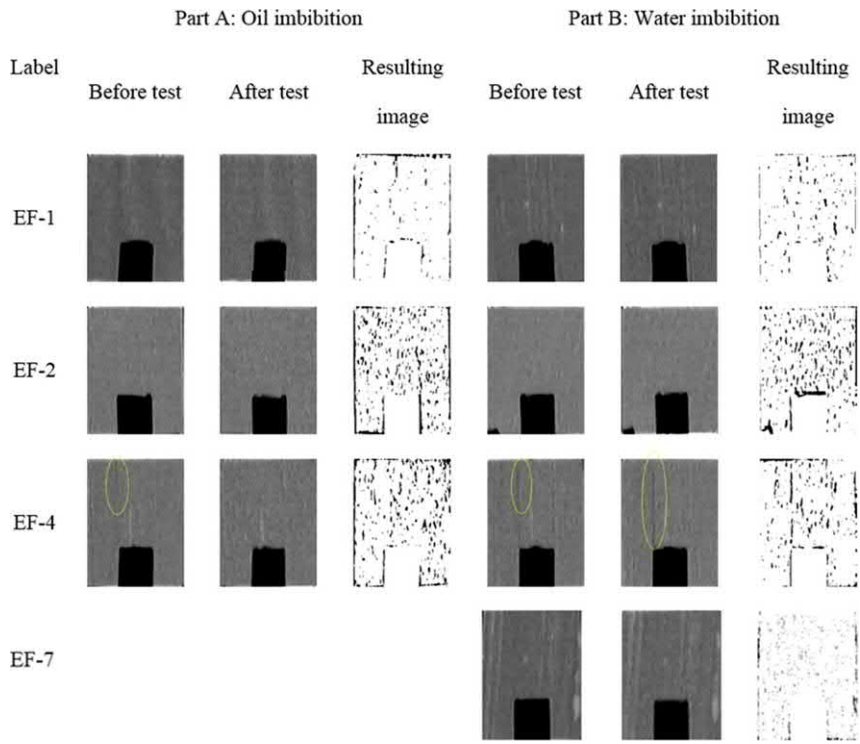

Figure 8.12 CT images after oil and water imbibition tests.

resulting images are the subtraction of the CT numbers after and before test. For EF-1, it was under isotropic stresses. No fractures were visible for both oil and water imbibition tests. For EF-2, it was under anisotropic stresses, no fractures were visible either, probably because the stress difference was not large enough. Compared with EF-1, there were more darker points indicating more pore space. For EF-4, the difference between two stresses was larger. One visible fracture was closed during the oil imbibition test, but it reopened and grew during the water imbibition test. For EF-7, although the axial stress and the confining stress were the highest, they had the same value, and no fracture was visible at the end of water imbibition. Two conclusions can be made from these tests: (1) it is easier to generate fractures by water than oil; (2) it is easier to generate fractures under anisotropic stress conditions than isotropic stress conditions.

8.4 Effect of bedding

Bedding or lamination is ubiquitous in shale rocks. It has been observed that fractures prefer to form along the beddings (Moradian et al., 2017; Liu and Sheng, 2019). Fluid imbibition is faster in the direction parallel to the lamination than that is perpendicular (Ghanbari and Dehghanpour, 2015). Guo et.al. (2012) analyzed the drilling performance of more than 200 Eagle Ford shale wells drilled by 31 operators in 22 countries from 2008 to early 2011. They found that the water-based mud-shale interaction resulted in fracturing and delamination along the bedding and enlargement of preexisting fractures.

8.5 Effect of existing natural fractures

In contrast to conventional propped hydraulic fracture treatments, water fractures rely on reactivation of natural fractures to induce permanent shear induced dilation, which enhances reservoir permeability (Chen et al., 2000; Weng et al., 2015). Hydraulic fracturing is performed where shear failure is anticipated to dominate (Zoback et al., 2012) in shale under anisotropic stress.

In the core EF-4 in Fig. 8.12, the existing fractures after water imbibition were propagated and connected to form a longer fracture. Lei et al. (2017) also observed that new fractures could propagate from the tips of natural fractures driven by tensile failure and connection between other small fractures nearby.

8.6 Permeability changes from water-rock interactions

If microfractures are generated, the flow capacity near fractures may be improved. If the fractures can be connected to form a network, then permeability would be improved in a large scale. Zhang et al. (2017) and Zhang and Sheng (2017c) measured the permeability after hydration under isotropic compressive stress using an Autolab-1000 servo-hydraulic operated system (New England Research Company, USA). The measurement principle is based on a pulse decay method. The higher upstream is imposed, and the downstream pressure is recorded. They found that the permeability was higher using a higher KCl concentration. It implied that the hydration or swelling caused formation damage.

Zhou et al. (2016) measured shale gas permeability during water imbibition. Although they concluded that the shale matrix permeability and fracture permeability were reduced, the permeability reduction was actually the reduction in the effective gas permeability. The causes of the reduction were not supported by data, although they claimed rock swelling. But one main reason is the increased water saturation that blocked gas flow. They also found that shale permeability was increased if there initially existed microfractures, because water imbibition reopened those microfractures because of shear and tensile failure.

Behnsen and Faulkner (2011) compared the permeability of compacted and confined phyllosilicate powders measured using argon and that using water. The argon permeability was always higher than water permeability (up to 1.8 orders of magnitude). They attributed the difference to the hydrophilicity of tested minerals and hydrogen-bonding surface properties. They did not report the generation of fractures. Moghadam and Chalaturnyk (2015) also reported that measured gas permeability is higher than the liquid permeability.

Duan and Yang (2014) measured the permeabilities of fault rocks from the rupture of Wenchuan earthquake using nitrogen gas and distilled water under the confining pressure ranging from 20 to 180 MPa at a room temperature. The water permeability was about half order smaller than the gas permeability corrected by the Klinkenberg effect. They attributed the difference to the reduction of effective pore size caused by the adhesion of water molecules to clay particle surface and water-swelling of expandable clay minerals.

Faulkner and Rutter (2000) also attributed the permeability reduction to the water adsorption on mineral surfaces so that the pores became smaller; the permeability reduction might not be caused by clay swelling. In other words, nonswelling minerals could also have lower water permeability. For this liquid adsorption mechanism to inhibit flow, the pores must be very small, probably few nanometers. Zhang and Sheng (2017a, 2018) also observed that the shale core permeability measured using water is several times up to 100 times lower than that measured using nitrogen, after the cores were hydrated. However, in their original paper, they attributed this difference to clay swelling, which is not. It is caused by liquid adsorption in small pores.

Roshan et al. (2015) measured the upstream pressure (with the downstream being atmospheric), when a fractured core (split into two halves) was flooded. The core was under 1000 psi (6.9 MPa) confining pressure. A 10 wt.% NaCl solution, followed by deionized (DI) water, was injected into the core for approximately 4 h. Fig. 8.13 shows the upstream pressures of the core when 10 wt.% NaCl solution and DI water were flooded. The upstream pressure maintained almost constant in the case of 10 wt.% NaCl

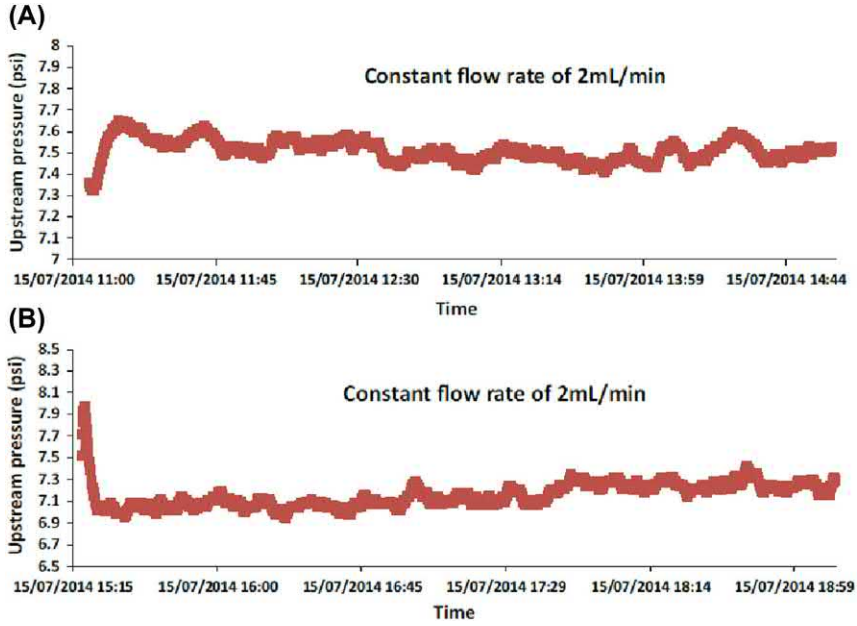

Figure 8.13 Upstream pressure measurements versus time during the fracture permeability test when (A) 10 wt.% NaCl solution was used, and (B) deionized water was used (Roshan et al., 2015).

solution, while it reduced from 8 psi to almost 7 psi when flooded by DI water, indicating the fractured core permeability was increased. In their experiment, the core was not confined in the axial direction. They found that rock particles had been detached from the fracture surface due to hydration (see Fig. 8.14). The surface hydration increased the internal forces within clay minerals mostly through crystalline swelling and caused the clay or surrounding particles to detach from the fracture surfaces to be subsequently washed out by water flowing through the fracture. As the effective aperture of the fracture became wider, the permeability was

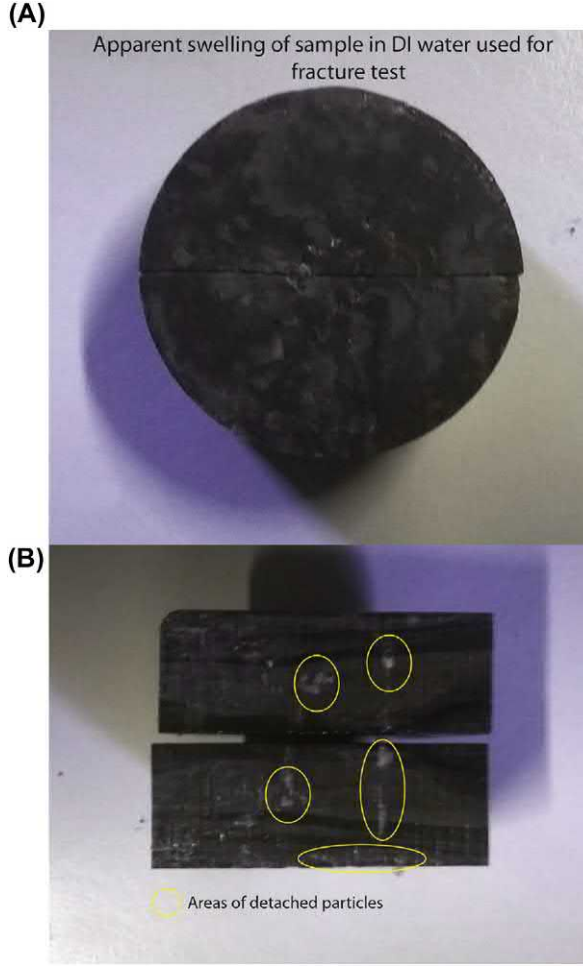

Figure 8.14 (A) Swelling of the sample with deionized water injection, (B) the disintegration of the rock particles on the fracture surface (Roshan et al., 2015).

increased. However, particle detachment may clog the pores depending on the mass of solids being mobilized and the fracture network structure.

By the way, Fig. 8.15 shows the axial displacements of the core measured by LVDT when flooded by the 10 wt.% NaCl solution and DI water, respectively. The sample shrank slightly when exposed to the NaCl solution (Fig. 8.15A), while relatively larger axial swelling of 0.03% is observed in the test with DI water (Fig. 8.15B).

Improvements to microfracture generation from water-shale interactions could lead to improved rates and recoveries. However, Kurtoglue (2013) reported that for all the Bailey shale cores, a higher oil volume was displaced than the water imbibed in the core. The water used was fracturing fluid and 2% KCl water. That means the swelling reduced pore volume; the pores became smaller; and the permeability became lower. In other words, swelling reduced core permeability. She also reported that the average oil recovery was 50%–60% from high permeability laminated clay-rich samples (samples 1–3), and 23% from low permeability calcite-rich sample (sample 4). Those samples were more oil-wet, but water imbibition took place

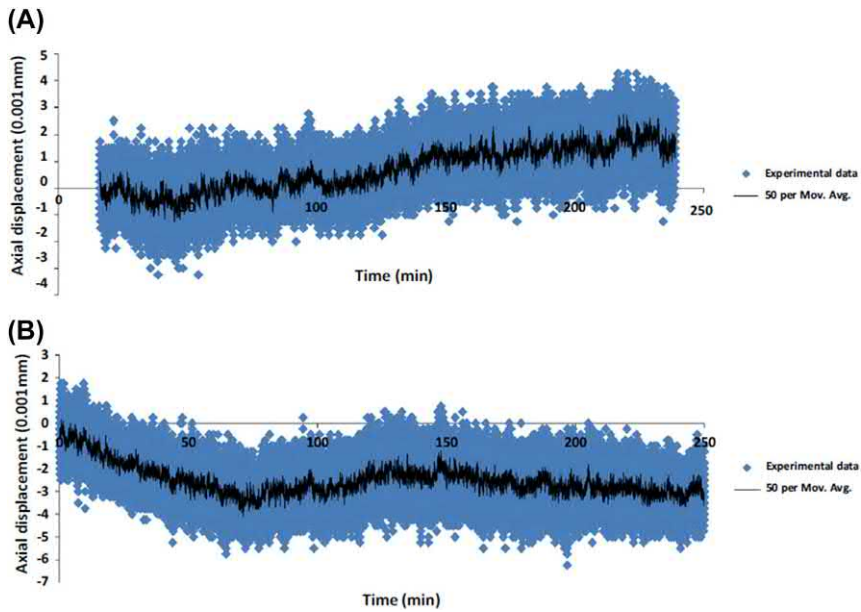

Figure 8.15 Axial displacement measurements show (A) slight shrinkage (positive displacement) of the shale core when a 10 wt.% NaCl solution was flooded, and (B) swelling (negative displacement) when deionized water was flooded (Roshan et al., 2015).

through some water-wet pores. In addition, she reported higher imbibition oil recovery in low-salinity water than in high-salinity water. Low-salinity water will have higher reactivity, resulting in more swelling. Then most likely, more fractures would be created, if swelling could. But her data did not indicate swelling created fractures or resulted in higher permeability.

Clay swelling may decrease matrix permeability and natural fracture permeability, but induced fracture may result in permeability increase. Whether the permeability is increased or decreased depends on the balance between the two factors, as Singh (2016) described in Fig. 8.16.

8.7 Effect on rock mechanical properties

Hydration swelling due to water imbibition can weaken the mechanical strength of shale (even more than 60%) (Wong, 1998; Al-Bazali, 2013; Cheng et al., 2015), and it can reduce the shear-induced fracture conductivity (Pedlow and Sharma, 2014; Jansen et al., 2015).

Zhang and Sheng (2018) used experimental setup shown in Fig. 8.8 to find the stress difference ($\sigma_1 - \sigma_2$) required to generate shear-induced fractures in a shale rock before and after water imbibition under some isotropic pressure. The stress differences required were 58.7, 40, and 24.4 MPa, respectively, for Mancos cores after water imbibition without confining pressure, at the confining pressure of 20 and 2 MPa. When the isotropic confining is zero (at an atmospheric condition), no stress difference was required. See Fig. 8.17. The data show that the rock was more difficult to fracture under water imbibition at a higher isotropic confining pressure. These data also suggest that refracturing would be easier as the rock was already imbibing water.

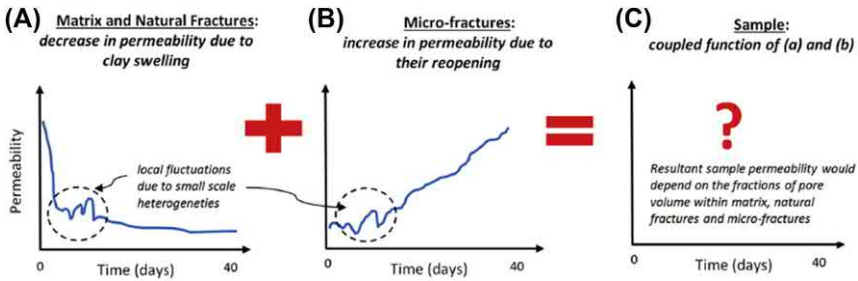

Figure 8.16 Schematic to describe permeability change due to water imbibition for (A) matrix and natural fractures, (B) microfractures, and (C) the whole rock sample (Singh, 2016).

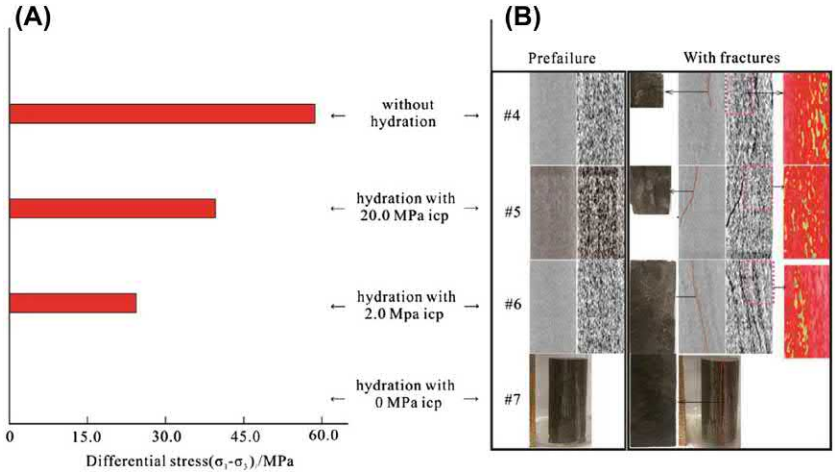

Figure 8.17 (A) Stress ($\sigma_1 - \sigma_3$) required to generate shear-induced fractures in Mancos after being hydrated, (B) CT images before and after being fractured.

Akrad et al. (2011) measured the shale rock strength before and after they exposed to 2% KCl slick water and fresh water. Fig. 8.18 shows that 2% KCl slick water weakened the shale rocks by reducing Young's modulus. The rock was defined a soft rock if the Young's modulus was <30 GPa, and

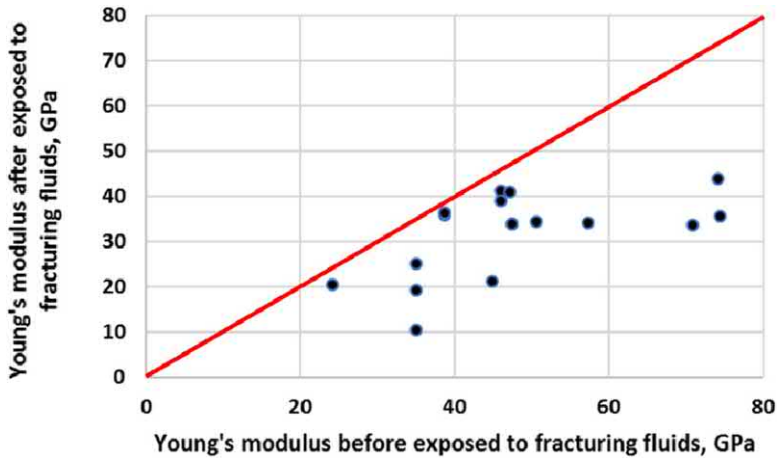

Figure 8.18 Young's moduli for different shale rocks before exposure to slick water at the room temperature (X-axis) and after (Y-axis) exposure to slick water at 300°F for 48 h. *Data from Akrad, O.M., Miskimins, J.L., Prasad, M., 2011. The effects of fracturing fluids on shale rock mechanical properties and Proppant Embedment. Paper SPE 146658 Presented at the SPE Annual Technical Conference and Exhibition, Denver, Colorado, USA, 30 October-2 November. doi:10.2118/146658-MS.*

hard rock if >30 GPa. Under the same conditions (300°F for 48 h), the Young's modulus of a middle Bakken core reduced by 52.39% and 51.97% when exposed to 2% KCl water and fresh water, respectively; the Young's modulus of a Bakken core reduced by 32.88% and 40.61% when exposed to 2% KCl water and fresh water, respectively. When the Young's modulus was reduced, the fracture conductivity was decreased (see Fig. 8.19). Morsy et al. (2013a) reported 5% NaCl and HCl solutions also weakened Eagle Ford shale samples.

Abousleiman et al. (2010) found that Middle Woodford shale was weakened when exposed to the oil-based mud with low-salinity (50,000 ppm $CaCl_2$). But the ultimate strength of the shale increased when exposed to the high salinity oil-based mud, indicating that shale strengthening by appropriate fluid chemistry is possible. Interestingly, their experimental data even showed that shale strength was increased with longer exposure time to two water-based mud. Generally, water would weaken the shale strength. Younane Abousleiman (personal communication on February 20, 2019) explained that those fluids were emulsified (different additives added to water-based muds and intended to minimize water-shale invasion effects). Apparently, those mixes increased shale strength. However, detailed additives were not unknown.

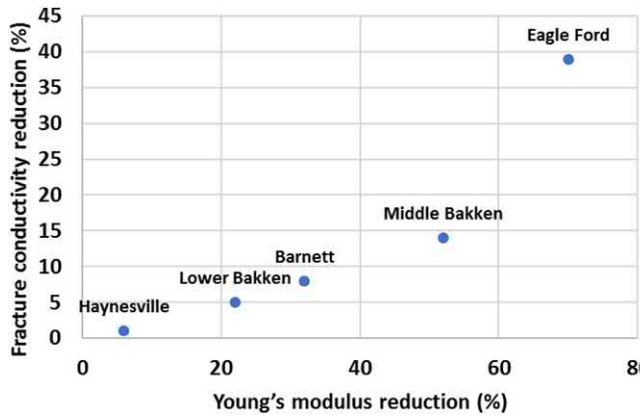

Figure 8.19 Fracture conductivity reduction corresponding to Young's modulus reduction for different shale cores exposed to 2% KCl slick water at 300°F for 48 h. *Data from Akrad, O.M., Miskimins, J.L., Prasad, M., 2011. The effects of fracturing fluids on shale rock mechanical properties and Proppant Embedment. Paper SPE 146658 Presented at the SPE Annual Technical Conference and Exhibition, Denver, Colorado, USA, 30 October-2 November. doi:10.2118/146658-MS.*

8.8 Further discussions and summary of views and hypotheses

From the above discussions, we can conclude that if a clay-bearing rock is not confined, microfractures may be generated. More microfractures may be generated owing to shear failures under anisotropic stress conditions than under isotropic stress conditions. Fracture opening, closing, reopening, and reclosing are a dynamic process, as the hydration conditions are changed.

The views on the interactions of water-clay bearing rock are not agreed in terms of microfractures or permeability. Clays are fine crystalline particles with two-dimensional arrays of either silicon/oxygen tetrahedral or aluminum (or magnesium)/oxygen hydroxyl octahedral. Clays can be classified into five categories: montmorillonite, illite, kaolinite, chlorite, and attapulgite (van Olphen, 1977). All natural clays have hydrophilic surfaces that can adsorb water and some ion species. Hydration of clays in a suspension brings about a repulsive force between particles. In addition, the water being adsorbed on clays in a formation dissolves the existing salts and results in the increase of swelling pressure, which causes the particles clusters to be dispersed in the water medium. Therefore, when water contacts swelling clay, the rock will swell. But whether the swelling will generate microfractures or reopen existing natural fractures remains unconfirmed. Groisman and Kaplan (1994) studied the influence of the bottom friction on the size and pattern of created fractures during desiccation experiments. Fig. 8.20 shows the formed fractures. In their experiment, rock samples lost water and contracted, so that tension was reduced, and fractures were created. Such experiments are opposite to water imbibition and rock swelling. From their experiments, swelling may not create microfractures.

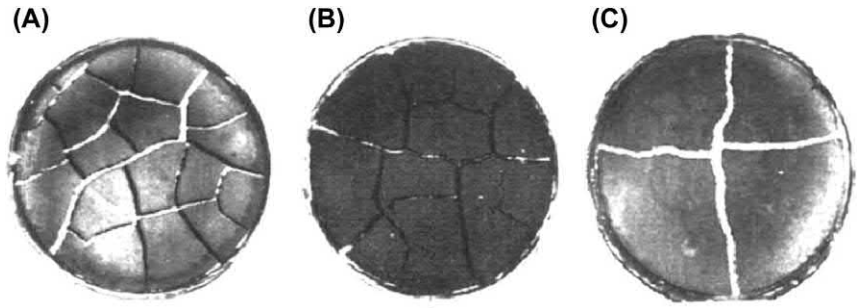

Figure 8.20 Pictures of experiment showing fracture creation during desiccation: (A) glass plate uncoated, (B) bottom coated with 2 mm of grease, and (C) bottom coated with 6 mm of Vaseline (Groisman and Kaplan, 1994).

However, water adsorption by clay minerals generates swelling pressure that can be extremely high if water equilibrium inside the rock is disturbed by its subsequent contact with different fluids (Chenevert, 1969; Santos et al., 1997b). Liquid water or some reactive species in the crack tip environment can facilitate crack propagation by promoting weakening reactions. For the quartz/water system, reactions of the form

$$(\text{– Si} - \text{O} - \text{Si} -) + \text{H}_2\text{O} \rightarrow (\text{– Si} - \text{OH} \cdot \text{HO} - \text{Si} -)$$

may occur. The strong silicon-oxygen bonds are replaced with much weaker hydrogen bonds (Scholz, 1972; Martin, 1972; Swain et al., 1973; Atkinson, 1979; Atkinson and Meredith, 1981). This phenomenon is termed "stress corrosion" in the literature (Atkinson, 1982). To prevent this problem, nonaqueous fluids based on diesel oil or mineral oil is used (Mehtar et al., 2010). All of the rock-chemical solution combinations from Karfakis and Akram (1993) show a statistically significant decrease in fracture toughness, as well as a decrease in the work of fracture required in crack initiation when compared to dry samples. If the chemical environment contains species which can undergo ion exchange with species in the solid phase, lattice strains may result from ion exchange which can facilitate crack extension, for example, exchange of H^- for Na^+ in silicate glasses (Wiederhorn, 1978). Other studies (e.g., Dunning et al., 1980) show that surfactants cause a reduction in the bonding forces across the crack or fracture, and that zeta potential of the fluid environment and chemical interaction between a fluid and rock surface, such as ion exchange, also affected microfracture propagation and growth.

Some solids contain dissolved chemical impurities, such as structurally bound water in quartz, which if present in sufficient quantities can have a degrading effect on strength. During crack propagation, stress-directed diffusion of these chemical impurities to crack tips may occur, resulting in weakening reactions and facilitating crack extension (Schwart and Mukherjee, 1974). On the other hand, Abousleiman et al. (2010) found that the shale strength was increased when the shale was exposed to the high salinity oil-based mud, confirming that shale strengthening by appropriate fluid chemistry was possible (Hemphill, 2008). Bol et al. (1994) concluded that salt and certain organic solvents were effective inhibitors of shale instability if the concentrations were high enough. Carminati et al. (1999) studied the effect of anions on shale stability, and Lu (1988) studied the effect of polymeric drilling fluid on shale stability.

Inducing fractures in shale depends upon whether the swelling stress can be larger than the fracture closure stress. Smectite clays formed in a "T–O–T"

layered pattern made from tetrahedral (T) silicate sheets surrounding octahedral (O) aluminum sheets have layers approximately 10 Å thick. The clays have the tendency to expand up to 20 times their original volume (Park et al., 2016) and a high swelling pressure exists due to water adsorption on smectite clays. The amount of smectite clays in shale is the major factor influencing swelling stress. Wang and Rahman's (2015) water leak-off model shows that the total water flux into shale matrix during a hydraulic fracturing treatment is controlled by capillary pressure, osmotic pressure, and hydraulic pressure of different solid components. The invaded water volume increases with the increase of clay content and the decrease of organic matter.

As reported by Wong (1998), Zhang et al. (2016), Al-Bazali et al. (2007), and Al-Bazali (2013), hydration swelling due to water imbibition can weaken the mechanical strength of shale (i.e., water-weakening effect). Therefore, hydration softening of shale can possibly be used to enhance the shear failure of shale rocks and the generation of fractures.

Fu et al. (2004) studied the heterogeneity effect on fracture generation when the temperature was elevated. They observed that heterogeneity promoted fracture generation during temperature alterations (Fig. 8.21). Different materials have different thermal expansion behaviors. Raising or reducing temperature creates strain contrasts between the two adjacent materials. The difference in strain may create internal shear stresses and promote fracture generation. Shale is typically heterogeneous and laminated and contacts clays which have different swelling properties from other minerals. Based on the

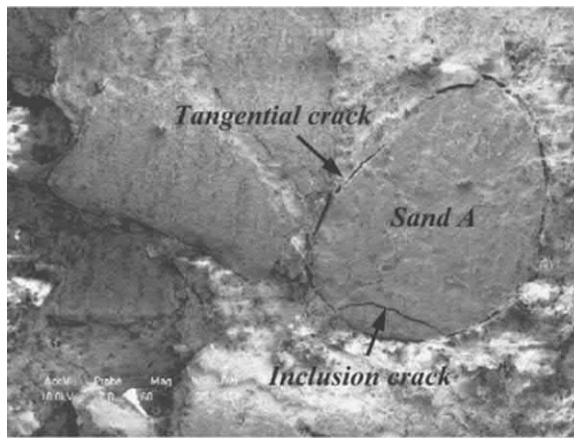

Figure 8.21 Fractures formed between two adjacent materials because the difference in their strains created internal shear stress and promoted fracture creation (Fu et al., 2004).

Schmitt et al. (1994) laboratory analysis and the numerical results of Wang and Rahman (2015) water leak-off model, the first shale microfailure mode is the tension crack mode. Another failure mode is the sliding crack between the interfaces of different solid components, which can be represented similarly by Fig. 8.21. Before fracture treatment, the stress state of shale is in equilibrium. After water leak-off into the shale matrix, an additional pressure is induced to the pore in each component. Because the pore pressures are different now in each component, the effective stress of each component is different, and this difference will result in a slip at the interface (shear failure); thus microcracks or fractures are generated. Rahman et al. (2002) also stated that the offset of two rough interfaces due to shear stress perturbation can greatly increase the permeability of the reservoir. From this point of view, swelling due to water imbibition may create microfractures.

As mentioned earlier, it has been observed that fractures can be created without confinement in laboratory. In an organic-rich shale reservoir, the tensile fractures induced by water imbibition are possible, because the organic matter may provide the displacement space, and the capillary pressure and clay swelling pressure may lead to tensile stresses to exceed the tensile strength to grow the fractures (Yang et al., 2015). They further used a discrete particle model to explain the fracturing mechanisms in different boundary conditions. Without confinement, shale matrix expands freely, and disordered microscopic failures occur (Fig. 8.22A). The fracture networks will be able to grow and cause macroscopic failures. Under confinement, the displacement space is provided by organic materials, but tensile failures or created fractures will be smaller (Fig. 8.22B). Under confinement in a standard triaxial test, the cracks will grow in the direction of maximum stress S_1, leading to the global failure plane (Fig. 8.22C). This feature differs largely from conventional rocks.

Even if microfractures are formed, these microfractures may not form a network; therefore, whether the rock permeability is enhanced remains questionable. Apparently, using clay stabilizers in fracturing fluids is more practiced in the oil industry. Typical clay stabilizers are choline chlorite ($(CH_3)_3NCH_2CH_2OHCl$), KCl, and TMAC ($(CH_3)_4N^+Cl^-$ often abbreviated further as $Me_4N^+Cl^-$, tetramethyl ammonium chloride).

8.9 Effect of low-pH and carbonated water

Shale is generally considered to be composed of material that has little or no acid solubility. Clay, fine quartz, and organic material make up the "default"

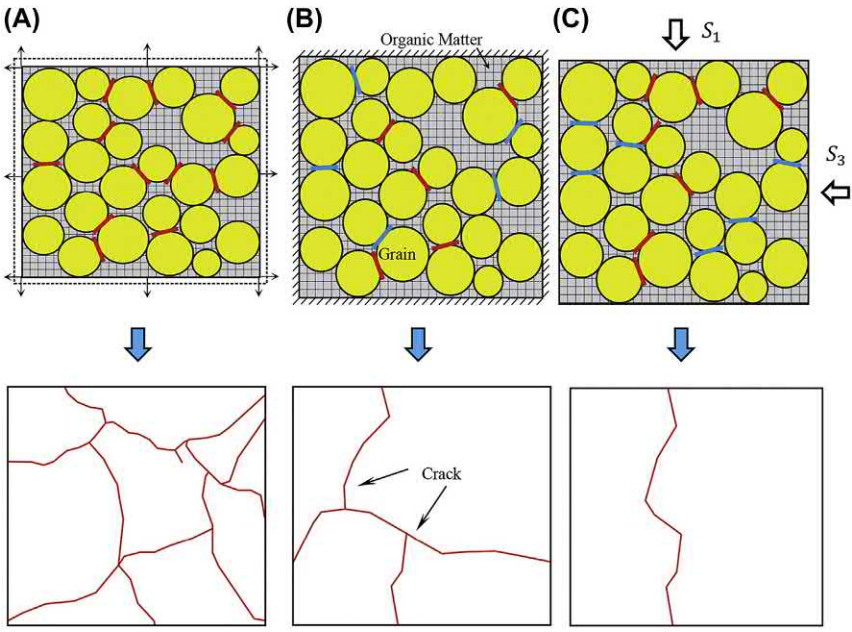

Figure 8.22 Tensile fractures in organic-rich shale with different boundary conditions: (A) no confinement, (B) displacement confinement, and (C) stress confinement. The red lines (black lines in print version) represent tensile failures, whereas the blue lines (dark gray lines in print version) show shear failures (Yang et al., 2015).

shale specimen. However, lab data shows that most shales are very heterogeneous at the microscopic scale; they have some acid-soluble minerals. Some shales like Caney have high content of calcite (Grieser et al., 2007).

In a hydraulic fracturing operation, an acid (HCl) preflush is commonly practiced to low the rock compressive strength near the wellbore, to remove drilling and completion damage, and to enhance microfracture connectivity by removing calcite (Fontaine et al., 2008). Typical acid concentrations are 0.08%–2.1% of the total fluid pumped in shale formations (McCurdy, 2011). Morsy et al. (2015) observed that the shale rock mechanical strength (Young's modulus and breakdown pressure under uniaxial compressive tests) was decreased, and the porosity became higher, when shale rock samples were immersed in low-concentration (up to 2%) HCl solutions. The oil recovery from spontaneous imbibition increased with HCl concentration.

Grieser et al. (2007) reported that when acid pads and sand slugs were alternatively injected in an S.E. Oklahoma Woodford frac job, unexpected pressure drop was observed when the acid pads hit the perforations, and gas rate was increased. Table 8.2 shows the pump schedule in the Woodford

Table 8.2 Pump schedule in a Woodford shale frac. job (Grieser et al., 2007).

Stage	Vol., gal	Fluid	Conc., lbm/gal	Proppant
1 Acid spearhead	4,000	15% HCl acid		
2 Pad	26,400	Pad and flush		
3 Sand slug	5,000	Treated water	0.1	Premium Brown-30/70
4 Pad	26,400	Pad and flush		
5 Sand slug	5,000	Treated water	0.15	Premium Brown-30/70
6 Pad	26,400	Pad and flush		
7 Sand slug	5,000	Treated water	0.2	Premium Brown-30/70
8 Pad	26,400	Pad and flush		
9 Sand slug	5,000	Treated water	0.25	Premium Brown-30/70
10 Pad	26,400	Pad and flush		
11 Sand slug	14,240	Treated water	0.1	Premium Brown-30/70
12 Acid	7,120	28% HCl acid cut on the fly to 3%		
13 Sand slug	14,240	Treated water	0.19	Premium Brown-30/70
14 Acid	7,120	28% HCl acid cut on the fly to 3%		
15 Sand slug	14,240	Treated water	0.28	Premium Brown-30/70
16 Acid	7,120	28% HCl acid cut on the fly to 3%		
17 Sand slug	14,240	Treated water	0.37	Premium Brown-30/70
18 Acid	7,120	28% HCl acid cut on the fly to 3%		
19 Sand slug	14,240	Treated water	0.46	Premium Brown-30/70
20 Acid	7,120	28% HCl acid cut on the fly to 3%		
21 Sand slug	14,240	Treated water	0.55	Premium Brown-30/70

(*Continued*)

Table 8.2 Pump schedule in a Woodford shale frac. job (Grieser et al., 2007).—cont'd

Stage	Vol., gal	Fluid	Conc., lbm/gal	Proppant
22 Sand slug	14,240	Treated water	0.64	Premium Brown-30/70
23 Sand slug	14,240	Treated water	0.73	Premium Brown-30/70
24 Sand slug	14,240	Treated water	0.82	Premium Brown-30/70
25 Sand slug	14,240	Treated water	0.9	Premium Brown-30/70
26 Flush	3,655	Pad and flush		

shale frac job. About 3% HCl was used in the acid pad. The total acid pad volume was about one-third of the total fracturing fluid volume.

Carbon dioxide (CO_2) EOR is a popular EOR method. CO_2 injection results in carbonate water because there is generally water in reservoirs. Carbonated water is a low-pH solution. Takahashi and Kovscek's (2009) experiments showed that the oil recovery factors of spontaneous countercurrent imbibition from carbonated water and HCl (low-pH) are similar (Fig. 8.23). The oil recovery factors from neutral pH brine and a high-pH

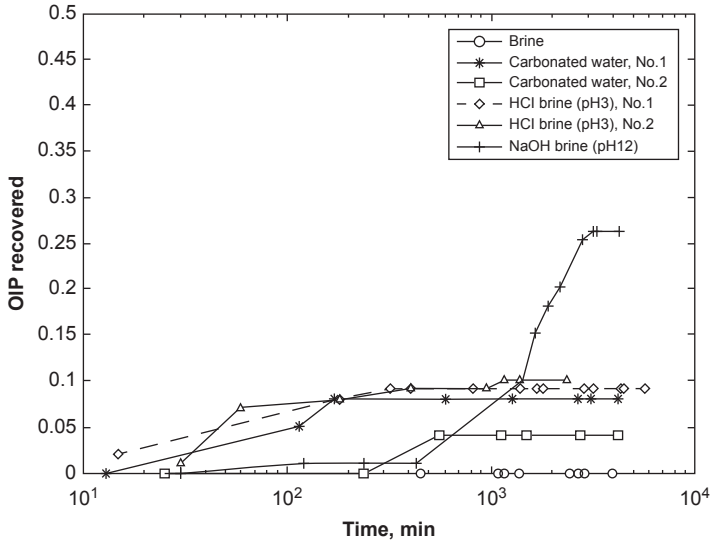

Figure 8.23 Oil recovery of spontaneous countercurrent imbibition of different pH brines (Takahashi and Kovscek, 2009).

solution (NaOH) are also presented in this figure. It shows that no oil was recovered from the brine, indicating the core was non-water-wet; the oil recovery was the highest for the high-pH solution, probably the NaOH solution reacted with the crude to have generated some surfactant. The initial low rate of oil recovery from the high-pH brine was due to the lower interfacial tension which resulted in lower capillary pressure as a main drive force.

Takahashi and Kovscek (2009) also conducted forced displacement experiments. The final oil recovery factors were 65%, 70%–80%, and 95% for the neutral pH brine, low-pH and carbonated water, and high-pH brine, respectively, as shown in Fig. 8.24. The highest oil recovery for the high-pH brine was attributed to the lower interfacial tension.

Moore et al. (2017) studied the fracture permeability of a fractured Bakken shale sample and a fractured Marcellus shale sample exposed to liquid CO_2 flow. The confining pressure was 3000 psi (20.68 MPa) and the pore pressure was 1000 psi (13.79 MPa). They observed that the fracture permeability was reduced several times to tens of times as the cores were exposed to the liquid CO_2 for up to over 300 h. However, they concluded: "CO_2 does not appear to reduce intrinsic fracture permeability significantly." Those shale samples did not have a high account of swelling minerals. It was implied that swelling minerals would reduce matrix and fracture permeabilities.

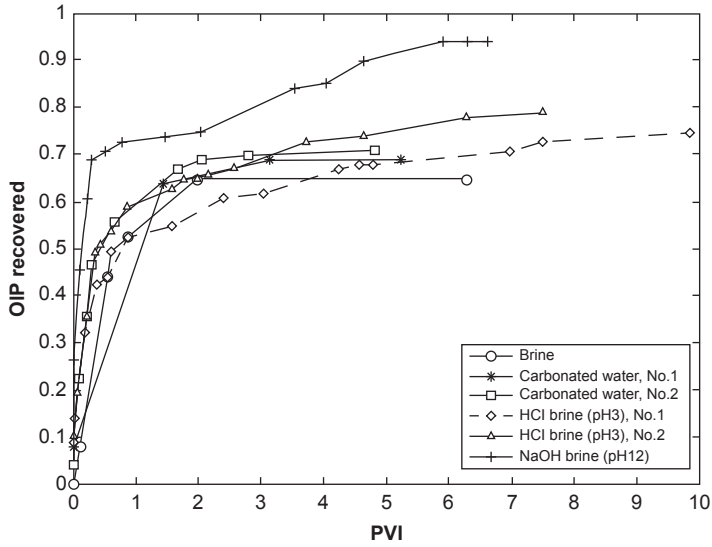

Figure 8.24 Oil recovery of forced displacement using different pH brines (Takahashi and Kovscek, 2009).

8.10 Effect of high-pH water

High-pH water is typically sodium hydroxide and sodium carbonate solution used in conventional EOR projects. Several EOR mechanisms are proposed in the literature.

(1) A high-pH solution reacts with crude oil to generate surfactant in situ so that surfactant-related mechanisms can be expected (Sheng, 2011).

(2) Emulsification and entrapment of oil improves the sweep efficiency of the high-pH solution (Johnson, 1976).

(3) Emulsification and entrainment of oil improves the recovery of residual oil (Johnson, 1976).

(4) Wettability is altered from oil-wet to water-wet or water-wet to oil-wet (Johnson, 1976).

(5) When alkaline and surfactants are injected together, their synergy will reduce surfactant adsorption and the microemulsion phase behavior of the in-situ generated surfactant is improved (Sheng, 2011).

(6) Alkalies also react with divalents like calcium and magnesium to give precipitates and deposit on higher-permeability channels, switching the subsequent water to lower-permeability zones where more oil remains.

As mentioned earlier, the high-pH solutions resulted in the highest recovery in spontaneous imbibition and forced displacement in tight siliceous reservoirs, probably due to lower interfacial tension and wettability alteration to more water-wet. In this section, we focus on the interactions of alkaline solutions with shale or tight rocks.

Fig. 8.25 shows the Barnett shales after being immersed in alkaline solutions of different NaOH concentrations. With higher NaOH concentrations, the samples became more dissolved and more fragmented. These results

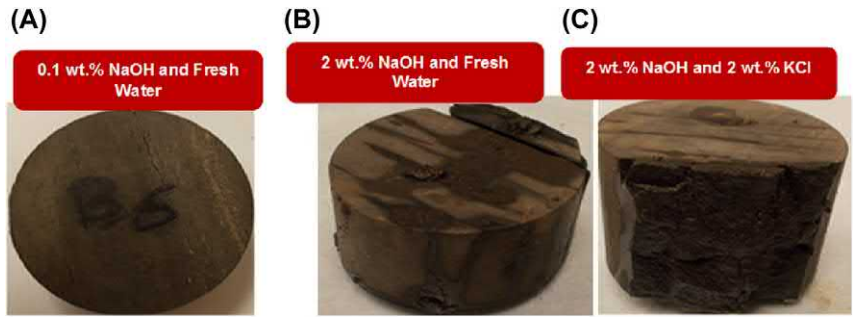

Figure 8.25 Barnett shale samples after being immersed in (A) 0.1 wt% NaOH water, (B) 2 wt.% NaOH water, and (C) 2 wt.% NaOH and 2 wt.% of KCl water.

showed that water at different alkaline solutions had different degree of reactions with shale rocks. The spontaneous oil recovery from cores (a), (b), and (c) were 17%, 15%, and 20%, respectively (Morsy and Sheng, 2013c). The core (c) had the highest oil recovery with it being most damaged or reacted.

Fig. 8.26 presents the oil recovery factors of spontaneous imbibition of different solutions (Morsy et al., 2016). It shows that the oil recovery from the 30 wt.% KCl solution was 9.4%, and 31%–40% from high-pH solutions (pH from 11.7 to 13). The oil recovery factors did not show a clear trend with pH, probably caused by the difference in Mancos core quality. A trend between oil recovery and pH was not established for other shale core samples (Morsy et al., 2016). Interestingly, the distilled water's oil recovery was 59% higher than alkaline solutions. They observed that the core immersed in the distilled water was more fragmented than that in high-pH solutions. Morsy et al. (2016) suspected that the lower oil recovery from high-pH solutions might also be caused by the precipitation occurring when the pH solutions reacted with the rocks. Such a result was observed for a Barnett core but not for a Marcellus core. It was observed that alkaline solution changed the core wettability to more water-wet, but the water contact angles were reduced only a few degrees in Morsy et al.'s (2016) experiments. Kim et al. (2009) referred several papers which show that increasing aqueous pH can significantly accelerate the crack growth rate in bulk glasses and organosilicate thin films.

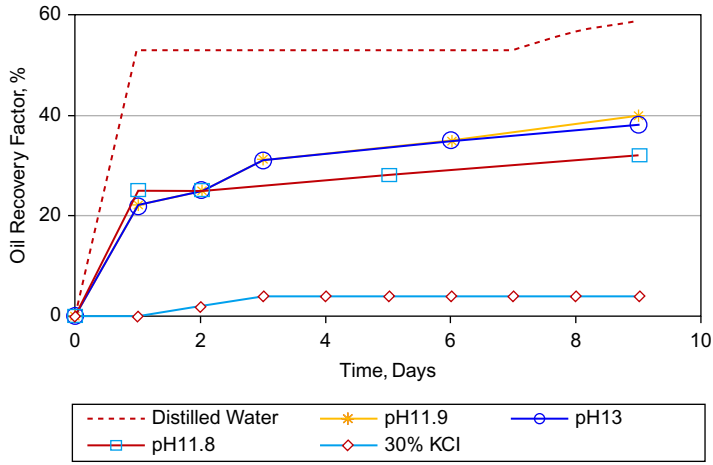

Figure 8.26 Spontaneous oil recovery factors for Mancos samples immersed in different solutions.

8.11 Cooling effect of injected water

When cold water is injected into a shale reservoir, the increase in pore pressure results in the decrease in effective stress, and the decrease in the reservoir temperature leads to the contract of matrix leading to the decrease in effective stress as well. Such technique is called thermal stimulation applied in geothermal reservoirs. Siratovich et al. (2011) conducted experiments to verify that temperature-induced stress can create fractures in a volcanic rock sample. A typical example was to submerge a sample of 300–650°F into a 68°F water bath. New fractures were created. Numerical studies also confirm that temperature-induced stress can form new fractures. Cold water injection in a hot fractured rock induces thermal contraction and creates tension near the main fracture. If the induced stress exceeds the rock strength, secondary fractures can propagate from the main fractures (likely perpendicular to the main fracture) in the matrix (Ghassemi, 2012). Groisman and Kaplan (1994) studied the formation of fractures during desiccation. During the process, the samples lost water and contracted, creating tension and forming fractures. This process has some similarity to the cooling effect.

Fakcharoenphol et al. (2013) used a 5-spot pattern model to simulate the cooling effect. We may use their result to explain the mechanisms. Fig. 8.27A shows the stress profiles plotted as the Mohr circle including the failure envelope with a 100 psi cohesion and a fraction angle of 30 degree for healed natural fractures. On the plot, the maximum stress reduction is near the injector where the maximum temperature occurs. The intersection of the stress profile with the failure envelope shows a possible reactivation of healed natural fractures. Fig. 8.27B compares the pore pressure-induced stress

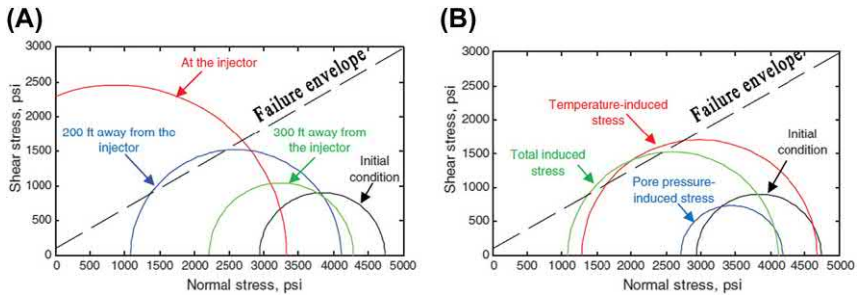

Figure 8.27 (A) Simulated effective stress profiles at the initial condition, 200 and 300 ft from the injector, (B) temperature- and pore pressure-induced stress profiles at 200 ft from the injector, after 1 years of injection (Fakcharoenphol et al., 2013).

change with temperature-induced stress change at 200 ft from the injector. The pore pressure increases decreases the effective stress and shifts the Mohr circle to the left. The temperature decrease causes negative strain or tension in the system, and it creates significant shear stress due to the mechanical strain contrast in the vertical and horizontal directions. As a result, the Mohr circle is shifted to the left. Thus, both the increase in pore pressure and the decrease in temperature shift the Mohr circle toward the failure envelope, synergistically leading to rock failure. However, the effect of temperature decrease is more important than that of pore pressure increase in a typical water injection case, because the pressure is generally maintained as injection and production continues, but the temperature keeps declining as more cold water is injected and hot reservoir fluids are produced.

The above paragraph discusses the concept of water-cooling effect. More meaningfully, we want to know whether such effect is significant in a typical shale and tight reservoir, and how much more oil can be produced from such effect. Fakcharoenphol et al. (2013) used a sector model of Bakken shale to study the effect. Fig. 8.28 shows the rock failure indicator. The positive value indicates the rock failure potential. From this figure, there does not appear to be extensive rock failure sites. Probably cooling the reservoir in a high temperature drop requires a huge amount of water.

Taghani et al. (2014) studied reactivation of existing microfractures by the difference between the fracturing fluid and the reservoir fluid. Owing to the fracture fluid leak-off, the increased pore pressure and decreased fracture pressure reduce the formation of effective stresses; and the cooling effect induced the rock tensile stresses. Collectively, these phenomena may open existing natural microfractures and increase the fracture complexity. The effect of such reactivated fractures depends on the number of existing fractures. If the number is large, the increased area open to flow is large and the productivity or injectivity could be significantly increased. However, the changes in reservoir pressure may close or reopen microcracks; hence the effectiveness of these microcracks could be dynamic.

8.12 Reaction-induced fractures

Kelemen et al. (2017) filed a US patent that fluids are chemically reacted within pores. Crystallization of solid minerals in pore space will lead to compressive stresses and fracturing of rocks with crack spacing close to the pore scale. Examples of fluids may be: (1) dissolved lime (CaO, as $Ca(OH)_2$, in solution) and carbon dioxide (CO_2, as HCO_3 in solution) to

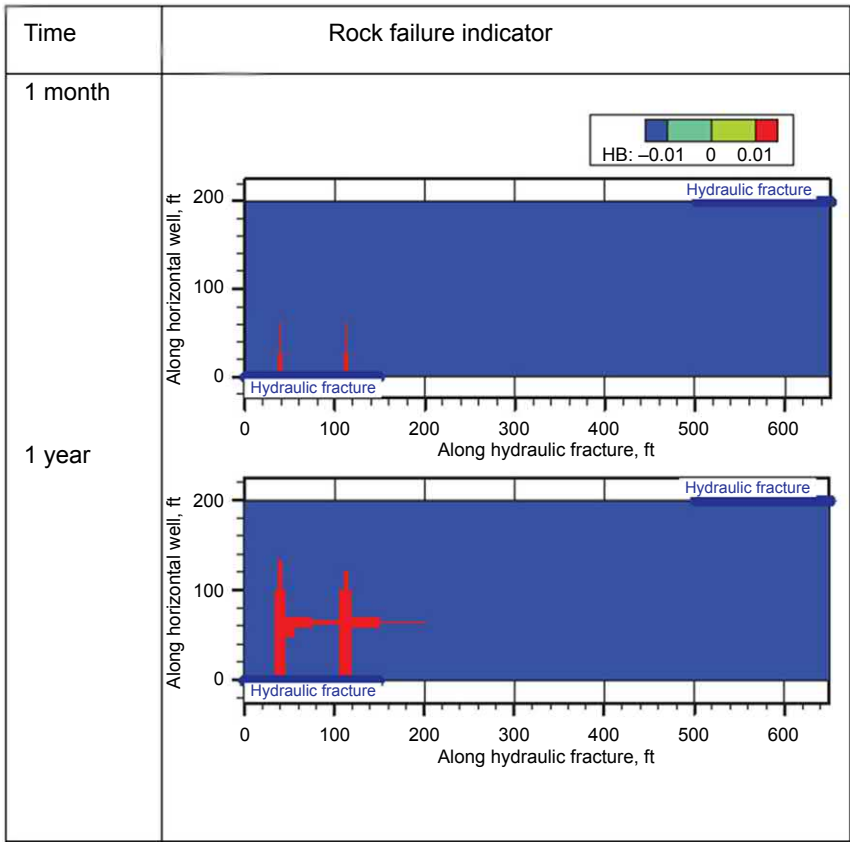

Figure 8.28 Likely rock failure sites 1 month and 1 year after cold water injection (Fakcharoenphol et al., 2013).

precipitate calcite or aragonite ($CaCO_3$), (2) dissolved periclase (MgO) and CO_2 to precipitate magnesite ($MgCO_3$), (3) Na_2O and HCl to precipitate salt (NaCl); or Na_2O and SO_4 to precipitate a range of sodium sulfate salts. Sometimes, dehydration reactions occur. Large volume changes in the rock formation result in cracking and fracturing of the rock formation.

Chen et al. (2017) reported that oxidative reagents, such as sodium hypochlorite (NaOCl), hydrogen peroxide (H_2O_2), and sodium peroxydisulfate ($Na_2S_2O_8$), had been widely applied in the removal of organic matter; undoubtedly, H_2O_2 was the most widely used oxidant to organic matter because of its high removal efficiency and relatively low price. They used 15 wt.% H_2O_2 to investigate the oxidative dissolution of organic-rich shale and its effect on pore structure.

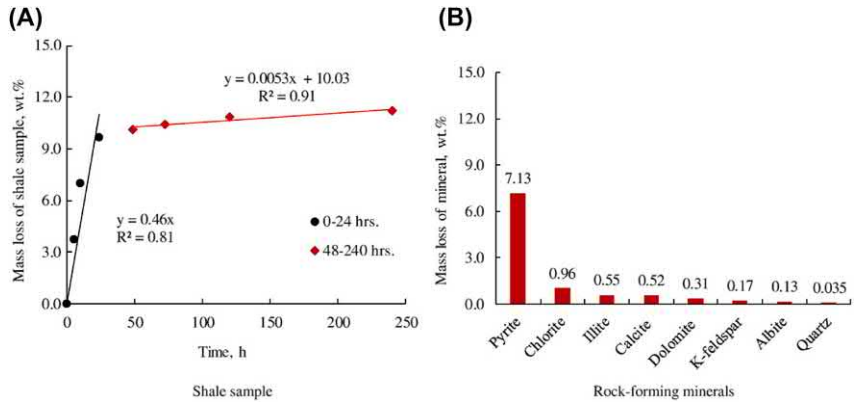

Figure 8.29 Mass loss of shale sample (A) and eight rock-forming minerals (B) by the H_2O_2 oxidation (Chen et al., 2017).

Chen et al. (2017) first tested the reactivity of shale samples and pure inorganic mineral particles by measuring their mass loss. Fig. 8.29A shows the mass loss of shale samples and inorganic minerals at different times. For the crushed shale sample with particle size ranging from 380 to 830 μm, the mass loss was 9.7 wt.% and 11.2 wt.% by 24 and 240 h, respectively. After 24 h of exposure to the hydrogen peroxide solution, pyrite's mass loss was 7.13 wt.%, and the mass losses of other minerals were <1.0 wt.%. The significance order of their mass loss was: pyrite ≫ chlorite > illite ≈ calcite > dolomite > feldspar (K-feldspar and albite) ≫ quartz, as shown in Fig. 8.29B. The mass was measured at each time by drying the samples for 48 h at 60°C. Although pyrite's mass loss percentage was much higher than other minerals, its mass percentage in a whole shale sample was not high. Therefore, the more meaningful data from this figure is the mass loss of 9.7 wt.% for the whole shale sample by 24 h. Corresponding to this 9.7 wt.% mass loss, the TOC content decreased from 4 wt.% of the untreated sample to 0.6 wt.% after the treatment, with the removal efficiency of organic matter being 85%. Compared to inorganic minerals, the mass loss percentage of organic matter was much higher. As organic matter is generally surrounded by inorganic matrix, removal of organic matter indicates there is pore connectivity in the inorganic matrix which uptakes hydrogen peroxide. Therefore, it can be predicted that oxidation dissolution may improve pore connectivity in shale matrix.

Fig. 8.30 shows the pH changes with time for the shale samples and the eight rock-forming minerals. The pH value of 15 wt.% H_2O_2 was 5.76. During the shale sample oxidation, the pH was slightly reduced from 6.93 to 5.76;

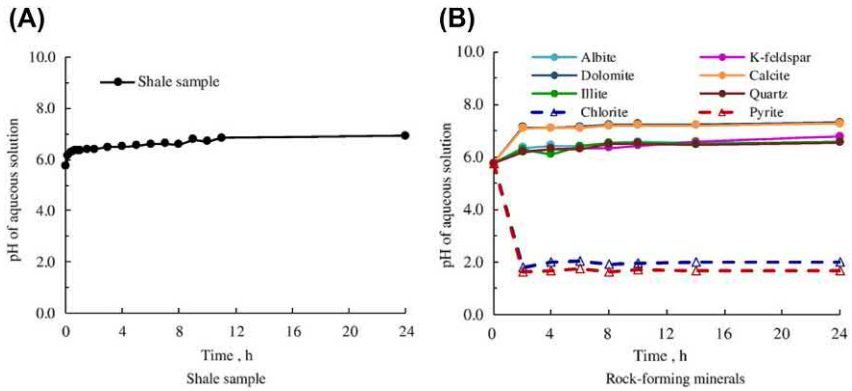

Figure 8.30 pH changes with time for shale samples (A) and for the eight rock-forming minerals (B) (Chen et al., 2017).

however, the oxidation of pyrite and chlorite generated large amount of acid, leading to a rapid decrease in pH from 5.76 to 1.67 and 2.0, respectively; the other six minerals pH's were slightly increased from 5.76 to 7.50. This figure also shows that quartz and dolomite cannot be oxidized to generate acid. However, in the analysis of another shale sample, dolomite was consumed; this was because the pyrite oxidation generated some acid and the dolomite reacted with the acid so that it was consumed (Chen et al., 2017).

Similarly, to the discussion applied to the preceding figure, as the pyrite and chlorite generally have a small mass fraction in a whole shale sample, their high reactivity does not mean the high effect on the whole sample. Actually, for the whole sample in this example, the pH was slightly reduced from 6.93 to 5.76, indicating the reaction was not significant.

Fig. 8.31 shows the pictures of samples D and H before and after exposure to deionized water and 15 wt.% H_2O_2. Before exposure, no fractures were visible. After exposure to deionized water, sample D had two induced fractures; after exposure to H_2O_2, sample H had quite a few induced fractures parallel to the bedding, indicating the shale sample reaction to H_2O_2 was much stronger. The mechanisms of fracture initiation and propagation are complicated by the dissolution of inorganic minerals and organic matter content. The dissolution may weaken the structures of clay minerals in shale, and lower the barriers to crack propagation, and then the swelling stress of clay minerals trigger the growth of dissolution-induced fracture much more easily. It should also be emphasized that the samples were not confined.

Hydrogen peroxide is a strong oxidant; pyrite is oxidized by the following reaction (McKibben and Barnes, 1986):

$$FeS_2 + 7.5H_2O_2 = Fe^{3+} + 2SO_4^{2-} + H^+ + 7H_2O \quad (8.1)$$

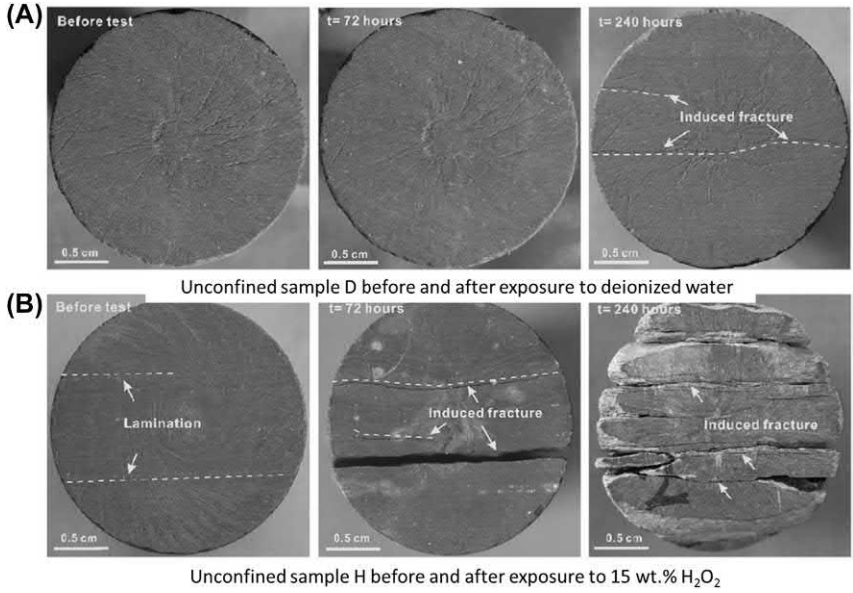

Figure 8.31 Pictures of shale samples before and after exposure to deionized water (A) and 15 wt.% H_2O_2 (B).

The above reaction shows that Fe^{2+} is oxidized to Fe^{3+}; in addition, H^+ and SO_4^{2-} are also released. This reaction is much stronger than the weathering of pyrite. The oxidation reaction of pyrite with oxygen and water is generally represented by these reactions (Garrels and Thompson, 1960; Singer and Stumm, 1970):

$$FeS_2 + 3.5O_2 + H_2O = Fe^{2+} + 2SO_4^{2-} + 2H^+ \tag{8.2}$$

$$Fe^{2+} + 0.25O_2 + H^+ = Fe^{3+} + 0.5H_2O \tag{8.3}$$

$$FeS_2 + 14Fe^{3+} + 8H_2O = 15Fe^{2+} + 2SO_4^{2-} + 16H^+ \tag{8.4}$$

The above three-step reactions indicate that during the FeS_2 oxidation process, S^{-1} is first oxidized, then Fe^{2+} is oxidized by O_2 and Fe^{3+} (Qiang Chen, personal communication, March 4, 2019).

Microfractures may also be created by mineral crystallization or growth by volume-increasing mineral replacement reactions. Chen et al. (2018) used 10% sulfuric acid (H_2SO_4) and 10 wt.% ammonium persulfate ($(NH_4)_2S_2O_8$) solutions to react with a mineral of calcite ($CaCO_3$) and

dolomite ($CaMg(CO_3)_2$) and pyrite (FeS_2). Pyrite in shale reacts with persulfate to generate sulfuric acid by the following oxidation reaction:

$$2FeS_2 + 15S_2O_8^{2-} + 16H_2O = 2Fe^{3+} + 34SO_4^{2-} + 32H^+ \quad (8.5)$$

Ammonium persulfate is a very strong oxidizer that is commonly used to decompose the gelling agent in hydraulic fracturing. The resultant sulfuric acid is a strong acid whose solution pH can be less than 2. Then this acid reacts with calcite and dolomite to precipitate gypsum crystal:

$$CaCO_3 + 2H^+ + SO_4^{2-} + H_2O = CaSO_4 \cdot 2H_2O + CO_2\uparrow \quad (8.6)$$

$$CaMg(CO_3)_2 + 2H^+ + SO_4^{2-} + H_2O = CaSO_4 \cdot 2H_2O + MgSO_4 + 2CO_2\uparrow \quad (8.7)$$

The above reactions (processes) are called replacement reactions (processes), as the calcite and dolomite are dissolved by the acid and a new replacing mineral, gypsum, is precipitated in the immediate vicinity of the dissolved carbonate mineral surfaces. As gypsum has a higher molar volume (74.4 mL/mol) than calcite (36.9 mL/mol) and dolomite (64.3 mL/mol), the local replacement reactions can generate internal swelling stress that may fracture the surrounding shale matrix. The reaction-induced stress from crystallization pressure is on the grain scale. The crystallization pressure can easily exceed 30 MPa, which sufficiently causes intensive shale microfracturing.

Fig. 8.32 shows the induced fractures when unconfined cylindrical shale samples were exposed to deionized water (a), H_2SO_4 solution (b), and $(NH_4)_2S_2O_8$ solution (c). Few fractures were seen on shale samples exposed to deionized water. In contrast, many fractures could be seen when the samples were exposed to the chemical solutions. These induced fractures propagated parallel to the lamination. It took 3 and 5 days for those fractures to form for H_2SO_4 solution (b) and $(NH_4)_2S_2O_8$ solution (c), respectively, indicating the H_2SO_4 solution reaction was faster than the $(NH_4)_2S_2O_8$ solution. Interestingly, the gypsum deposited in the induced fractures, and not on sample surfaces, indicating that those fractures were caused by the increased gypsum volume.

$(NH_4)_2S_2O_8$ is a very strong oxidizer, whereas the dilute sulfuric acid solution is only a strong dibasic acid not an oxidizer. Oxidation reaction may significantly change the organic fraction and the color of black shale. Their experiments did not show obvious color change, and the fracture-generation behavior is similar in both the H_2SO_4 solution and

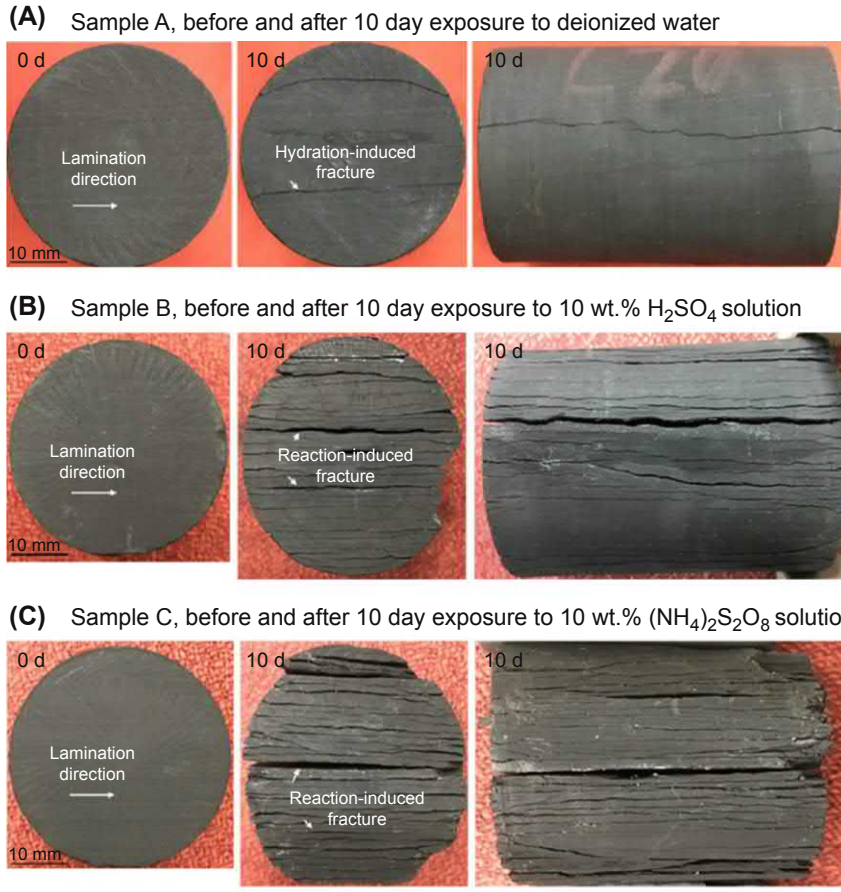

Figure 8.32 Macroscopic observations of fractures induced by (A) clay hydration and (B) H_2SO_4 solution and (C) by $(NH_4)_2S_2O_8$ solution in the unconfined shale samples (Chen et al., 2018).

the $(NH_4)_2S_2O_8$ solution, suggesting that the fractures were induced by the above reactions, and they were not affected by the organic fraction at the experimental time scale.

Note that from the first of the above three reaction equations, pyrite reacts with ammonium persulfate ($(NH_4)_2S_2O_8$) to produce the acid solution of $H^+ + SO_4^{2-}$. In an anoxic depositional environment, pyrite commonly exists in a shale formation. Even if there is no pyrite, a sulfate-bearing acid solution like H_2SO_4 can react with carbonate minerals to precipitate gypsum, and the above volume increase-induced fractures should be created. However, the above experiments were conducted without confinement.

8.13 Surfactant effects

Surfactants are typically added in fracturing fluids to assist flowback, enhance water imbibition, and enhance oil and gas recovery through other mechanisms such as wettability alteration and IFT reduction. Kim et al. (2009) studied the effects of surfactants on the crack growth rate in nanoporous organosilicate thin films. They found that the C_mE_n surfactant significantly retarded crack growth rates, whereas dimeric surfactants accelerated the crack growth process. The dimeric surfactants were shown to accelerate growth rates by lowering the surface energy of the fracture surface. The C_mE_n surfactant is polyoxyethylene alkyl ether, $CH_3(CH_2)_{m-1}(OCH_2CH_2)_nOH$, with various hydrophobic alkyl tail lengths, m, and hydrophilic ethylene oxide (EO) head lengths, n. The suppression of crack growth rates in C_mE_n surfactant solutions was attributed to bridging of the crack surfaces by surfactant molecules or the formation of nanobubbles in the surfactant-containing solution. Their work indicates that surfactants may affect crack growth.

Aderibigbe and Lane (2013) conducted unconfined compression and Brazilian tests after Mancos shale samples were exposed to water and surfactant solutions. In their uniaxial compressive strength tests and the Brazilian tests, the strength of the samples was the weakest when exposed to water, a similar (slightly lower) reduction was observed with the samples exposed to 0.1% w/v DTAB (dodecyl trimethylammonium bromide) and 0.1% w/v SDBS (sodium dodecyl benzenesulfonate) solutions. In other words, the surfactant addition did not significantly change the rock strength compared with water. The rock strength in 4% KCl solutions was higher than in water or in surfactant-only solutions.

CHAPTER NINE

EOR mechanisms of wettability alteration and its comparison with IFT

Abstract

A surfactant has two functions: interfacial tension (IFT) reduction and wettability alteration. The function of wettability (alteration) may be more important in shale and tight formations. This chapter focuses on the discussions related to wettability alteration and a brief discussion of IFT related to wettability alteration. The discussions include the EOR mechanisms of wettability alteration and IFT, formulation of these two functions, IFT reduction versus wettability alteration, surfactants used to alter wettability, determination of wettability, and conversion of wetting angles.

Keywords: Conversion of wetting angles; Determination of wetting angles; Formulation; IFT; Wettability alteration; Wetting angles.

9.1 Introduction

Although chemical methods like surfactant injection are important methods to enhance oil recovery in conventional reservoirs (Samanta et al., 2012; Rai et al., 2015; Mandal, 2015), very limited applications were reported in shale and tight reservoirs. More often, surfactants are added as an additive in the fracturing fluid or completion fluid to improve oil and gas production. When surfactants are added for the EOR purpose, water-oil interfacial tension reduction results in the increase in capillary number so that residual oil saturation is reduced. This mechanism related to IFT reduction has dominated the literature. Sheng (2013b) explicitly explained that a surfactant has two functions: interfacial tension (IFT) reduction and wettability alteration, and he quantified the two mechanisms using simulation. Chen and Mohanty (2015) subsequently experimentally studied the two functions. As the function of wettability (alteration) becomes more important in EOR in shale and tight formations, more research has been focusing on this mechanism recently. This chapter focusses on the discussions related to wettability and brief discussion of IFT related to wettability alteration. The discussions

Enhanced Oil Recovery in Shale and Tight Reservoirs
ISBN: 978-0-12-815905-7
https://doi.org/10.1016/B978-0-12-815905-7.00009-8

include the EOR mechanisms of wettability alteration and IFT reduction, formulation of these two functions, IFT reduction versus wettability alteration, surfactants used to alter wettability, determination of wettability, and conversion of wetting angles.

9.2 Mechanisms of interfacial tension (IFT) reduction

To understand mechanisms of interfacial tension reduction, first review the concept of capillary number. The dimensionless capillary number, N_C, is defined by the ratio of the viscous to capillary force:

$$N_C = \frac{F_v}{F_c} = \frac{v\mu}{\sigma cos\theta} \tag{9.1}$$

where F_v and F_c are viscous and capillary forces, respectively, μ is the *displacing* fluid viscosity, v is the pore flow velocity of the *displacing* fluid, σ is the interfacial tension (IFT) between the displacing and displaced phases, and θ is the contacting angle defined by the displacing fluid. A set of consistent units are used so that the dimensionless group is dimensionless. For example, v is in m/s, μ in mPa·s, σ in mN/m or dyne/cm.

Let us first use the above equation to calculate the waterflooding capillary number in a conventional reservoir. A typical injection velocity may be 1 ft/day (3.528×10^{-6} m/s), the water viscosity is close to 1 mPa·s, the oil-water interfacial tension is assumed to be 30 mN/m, and the contact angle is assumed zero. Then the corresponding capillary number is

$$N_C = \frac{u\mu}{\sigma} = \frac{(3.528 \times 10^{-6}\,\mathrm{m/s})(1\,\mathrm{mPa\cdot s})}{(30\,\mathrm{mN/m})} \approx 10^{-7}$$

It has been established that as the capillary number is increased, the residual oil saturation is decreased, thus the oil recovery will be improved. The relationship between the capillary number and the residual oil saturation is the capillary desaturation curve (CDC), as shown in the solid curve and square points in Fig. 9.1. It is also known that as the capillary number is increased, the residual water saturation and residual microemulsion saturation are also decreased. The CDCs for them are also presented in this figure. In the figure, the discrete data points are experimental data and the smooth curves are fitted curves.

The presented CDC curves show that when the capillary number is less than 0.00,001, even though it is increased from 0.000,001 to 0.00,001, the residual oil saturations are barely decreased. It means that for a residual saturation to be decreased, a minimum capillary number is required; in this case

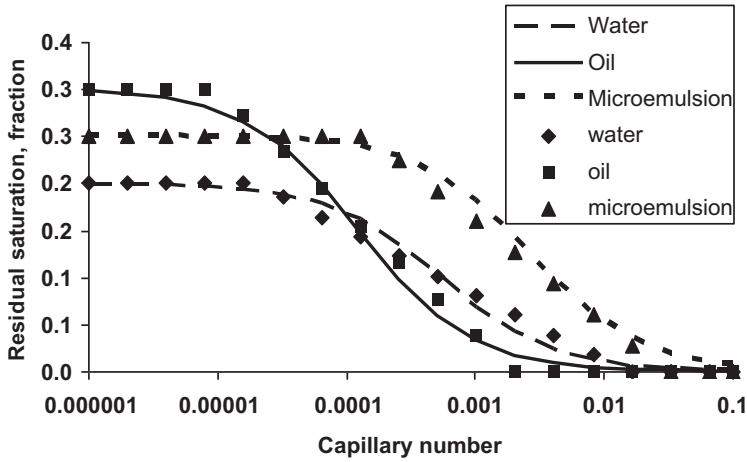

Figure 9.1 Capillary desaturation curves for water, oil, and microemulsion phases.

it is 0.00,001. This minimum capillary number is called critical capillary number $(N_C)_c$. When the capillary number is greater than 0.01, even though it is increased, the residual oil saturation does not decrease significantly any more. This capillary number is called the maximum capillary number $(N_C)_{max}$. Between $(N_C)_c$ and $(N_C)_{max}$, the change of residual oil saturation may be described by this equation:

$$S_{or} = S_{or}^{(N_C)_{max}} + \left(S_{or}^{(N_C)_C} - S_{or}^{(N_C)_{max}}\right)\frac{1}{1 + T_p N_C} \tag{9.2}$$

where T_p is the parameter used to fitting the laboratory measurements. The subscript o means oil phase; it can be substituted by w for water, me for microemulsion phase, or p for any phase p in general.

The CDC for oil in this figure shows when the capillary number is increased to 0.0001, the residual oil saturation is decreased from 0.3 to 0.2. In other words, to decrease residual oil saturation by 0.1, the capillary number needs to be increased by 1000 times from 10^{-7} to 10^{-4}.

According to the definition, the capillary number can be increased by one of three methods: increasing v or μ, or decreasing σ, if the contact angle is not changed. It is easy to understand that it is not practical to increase v or μ by 1000 times in a real reservoir. However, it is well known that it is feasible to reduce the oil-water interfacial tension 1000 times by adding surfactants.

Similarly, by adding surfactants and reducing interfacial tensions, residual water and residual microemulsion saturations can also be decreased.

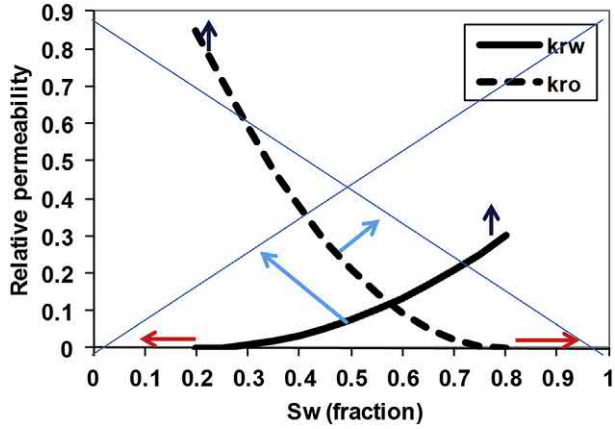

Figure 9.2 Oil and water relative permeability curves change as the residual water and oil saturations are reduced.

For a simple description, Fig. 9.2 schematically shows how oil and water relative permeability curves change as the residual water and oil saturations are reduced. Particularly, as the residual water saturation (connate water saturation) is decreased, the water and oil relative permeability curves, k_{rw} and k_{ro}, move to the left; meanwhile, these two curves must also move up as well. Similarly, as the residual oil saturation is decreased, the water and oil relative permeability curves, k_{rw} and k_{ro}, move to the right; and these two curves must also move up. As a result, both the curves cover wider saturation ranges and their relative permeabilities are increased. In the extreme case, the two curves become two straight diagonal lines.

To formulate the capillary-dependent relative permeability curves, assume that the relative permeability k_{rw} for water phase w can be described by

$$k_{rw} = k_{rw}^{e}\left(\overline{S}_w\right)^{n_w} \tag{9.3}$$

where

$$\overline{S}_w = \frac{S_w - S_{wr}}{1 - S_{wr} - S_{or}} \tag{9.4}$$

where k_{rw}^{e} is the end point relative permeability of water phase at its maximum saturation (the superscript e means end-point), n_w is the exponent of water phase, $\overline{S}_w$ is the normalized saturation. Those equations are applied at a specific capillary number. At different capillary numbers, a linear interpolation may be used between the minimum and maximum capillary

numbers. For the ease of description and understanding, we describe water-oil two phase flow.

From the above description, it can be understood that as the capillary number is increased, residual oil saturation is decreased, the end-point water relative permeability at any N_C, k_{rw}^{e,N_C} is increased following this equation:

$$k_{rw}^{e,N_C} = \left(k_{rw}^{e}\right)^{(N_C)_c} + \frac{(S_{or})^{(N_C)_c} - (S_{or})^{N_C}}{(S_{or})^{(N_C)_c} - (S_{or})^{(N_C)_{max}}} \left[\left(k_{rw}^{e}\right)^{(N_C)_{max}} - \left(k_{rw}^{e}\right)^{(N_C)_c}\right] \tag{9.5}$$

Similarly, for the exponent of water $n_w^{N_C}$ at any N_C, we have

$$n_w^{N_C} = n_w^{(N_C)_c} + \frac{(S_{or})^{(N_C)_c} - (S_{or})^{N_C}}{(S_{or})^{(N_C)_c} - (S_{or})^{(N_C)_{max}}} \left[(n_w)^{(N_C)_{max}} - (n_w)^{(N_C)_c}\right] \tag{9.6}$$

In the above equations, if the subscripts w and o are exchanged for their positions, the parameters for the oil phase can be written similarly. Furthermore, three-phase relative permeabilities can be written similarly as well. For detailed formulation, see Chapter 7 in Sheng (2011).

In summary, when surfactants are added, the oil-water interfacial tension is reduced greatly, the residual oil saturation is decreased, and the oil recovery is improved.

9.3 Mechanisms of wettability alteration on oil recovery

In an oil-water-rock system, the water-oil capillary pressure p_{cwo} is defined as

$$p_{cwo} = p_o - p_w = \frac{2\sigma_{wo}cos\theta_w}{r} \tag{9.7}$$

where p_o and p_w are the oil phase pressure and water phase pressure, respectively, r is the pore radius, σ_{wo} is the water-oil interfacial tension, and θ_w is the water contact angle. When the rock is water-wet, θ_w is less than 90°, and the oil phase pressure p_o is higher than the water phase pressure p_w so that oil will flow out of the pores, meanwhile water will imbibe into the pores, resulting in countercurrent flow of oil and water. The countercurrent flow will drive oil out of the rock system. This is the fundamental principle to use wettability to produce oil.

When the rock is oil-wet, θ_w is greater than 90°, and the oil phase pressure p_o is lower than the water phase pressure p_w. The water cannot imbibe into the

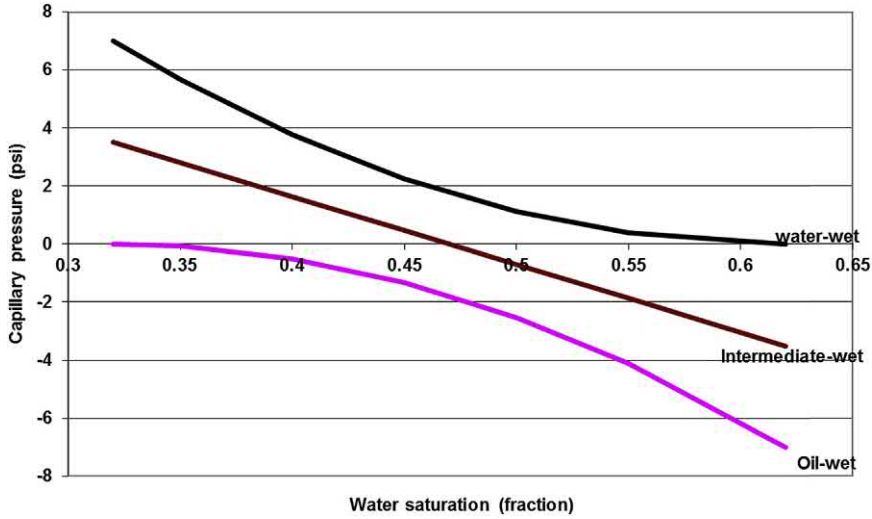

Figure 9.3 Example capillary pressure curves for different wettabilities.

rock or oil cannot come out of the pores. When the rock is intermediate wet, some oil may come out of the pores. Example capillary curves for different wettabilities are shown in Fig. 9.3.

Fig. 9.4 shows the wettability effect on water and oil-relative permeabilities. It can be seen that at water saturation, the oil relative permeability in the

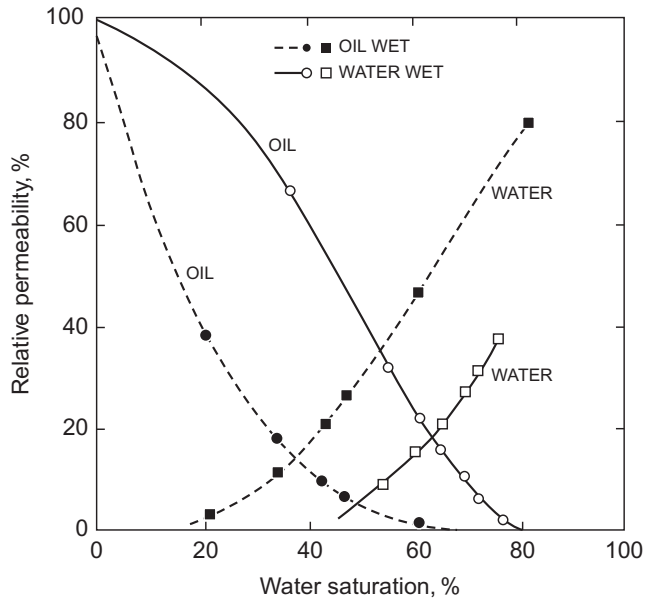

Figure 9.4 Steady-state oil/water relative permeabilities measured with heptane and brine in water- and oil-wet synthetic alundum core. The oil-wet core was treated with organi-chlorosilanes (Jennings, 1957).

water-wet case is higher than that in the oil-wet case; the water relative permeability has the opposite behavior. Therefore, a water-wet system is more favorable to oil recovery than an oil-wet system. This is another mechanism of wettability on oil recovery.

From the above listed mechanisms, a strongly water-wet system should be preferred for oil recovery. However, early researchers found that the highest waterflooding oil recovery occurs at intermediate wetting conditions (Moore and Slobod, 1956; von Engelhardt and Lubben, 1957; Kennedy et al., 1955; Loomis and Growell, 1962; Morrow and McCaffery, 1978), as presented by Tiab and Donarld (2004) in Fig. 9.5.

Alhammadi et al.'s (2017) microscale study of waterflooding performance showed that the optimal recovery was obtained for a rock that appeared neither strongly water-wet nor strongly oil-wet at the pore scale. In strongly water-wet pores, snapoff in small pores traps oil; in strongly oil-wet pores, oil is confined to layers which flow too slowly to provide significant oil recovery. Jadhunandan and Morrow (1995) core-scale experiments also showed such result. More generally, how wettability affects oil recovery or gas recovery is process-dependent. For example, in depleting condensate reservoirs, one may think gas wetting is not preferred to maximum gas production. However, fluorocarbon surfactants are used to alter the rock wettability from liquid wetting to favorably gas-wetting condition, because the condensate saturation trapped in the near wellbore region can be reduced to mitigate the condensate blockage (Sharma et al., 2018).

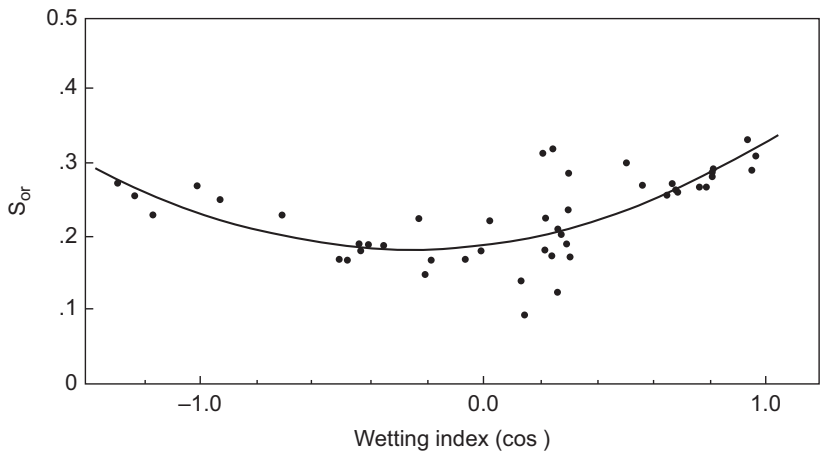

Figure 9.5 Ultimate oil recovery as a function of wettability index (Tiab and Donarld, 2004).

9.4 Mathematical treatments of wettability alteration and IFT effect

The mechanisms of IFT reduction are more discussed and formulated in the literature, but not for the mechanisms of wettability alteration. Therefore, a special section is dedicated to present the mathematical treatments. Four models are presented in this section: UTCHEM model, Adibhatla et al. (2005) model, a proposed simple model and a CMG model.

9.4.1 UTCHEM model

A common practice to consider wettability alteration is to modify the relative permeability term and capillary pressure term of mixed wettability based on strongly wetting and strongly nonwetting relative permeability and capillary pressure curves (Delshad et al., 2009):

$$k_r = \omega k_r^{ww} + (1-\omega) k_r^{ow} \tag{9.8}$$

$$p_c = \omega p_c^{ww} + (1-\omega) p_c^{ow} \tag{9.9}$$

where the superscript *ww* and *ow* mean water-wet and oil-wet, respectively, k_r is the relative permeability, and p_c is the capillary pressure. ω is the interpolation scaling factor to describe the effect of wettability and depends on surfactant adsorption:

$$\omega = \frac{\widehat{C}_{surf}}{C_{surf} + \widehat{C}_{surf}} \tag{9.10}$$

where $\widehat{C}_{surf}$ and C_{surf} are the adsorbed and equilibrium concentrations of surfactant, respectively. Those equations assume that surfactant adsorption on rock surfaces increases water-wetness. If surfactant adsorption increases oil-wetness, those equations can be modified accordingly. This model is implemented in UTCHEM version 9.95 (UT Austin, 2009).

The capillary pressure p_{Cwo} is scaled with the interfacial tension and rock properties:

$$p_{Cwo}^{ww} = C_{pc}\sqrt{\frac{\phi}{k}}\,\frac{\sigma_{wo}^{ww}\cos\theta^{ww}}{\sigma_{wo}^{ow}\cos\theta^{ow}}\left(1 - \frac{S_w - S_{wr}}{1 - S_{wr} - S_{or}}\right)^{E_{pc}} \tag{9.11}$$

where $C_{pc}\sqrt{\phi/k}$ takes also into account the effect of permeability and porosity using the Leverett-J function (Leverett, 1941), ϕ is the porosity and k is the permeability, σ_{wo} is the water-oil interfacial tension, S is the

saturation with the subscript *wr* and *or* for residual water and oil saturation, respectively, θ is the water contact angle with the superscript *ww* and *ow* for water-wet and oil-wet, respectively, E_{pc} is the capillary exponent. The effect of IFT is treated according to Eqs. (9.2)–(9.6).

9.4.2 Adibhatla et al. (2005) model

Adibhatla et al. (2005) proposed another model explicitly including the effect of wetting angle on residual saturations and the trapping number. The trapping number is the capillary number including gravity effect which is discussed in detail by Sheng (2015a). According to the existing definition of trapping number, it does not *generally* include the wettability effect, although it can *theoretically* with *cosθ* term combined with the interfacial tension σ. However, such model has not been proposed or described in detail in the literature.

Adibhatla et al.'s (2005) model requires these data: residual saturations at two wetting angles and at low trapping number $\left(S_{rj}^{\text{low}}\right)$; relative permeability curves at trapping number N_{T0}. The two wetting angles are θ_0 and $\pi - \theta_0$ corresponding to two base phases *b*1 and *b*2. In principle, these two angles can be arbitrary. Practically, if one is strongly wetting (wetting angle close to 0), the other one is strongly nonwetting (wetting angle close to π). We use their notation. More generally, θ_0 can be replaced by θ_{b1}, and π-θ_0 can be replaced by θ_{b2}. A simple interpolation technique is used to consider the wettability effect on a residual saturation at low trapping number:

$$\frac{S_{rj}^{\text{low}} - S_{r,b1}^{\text{low}}}{cos\theta - cos\theta_0} = \frac{S_{r,b2}^{\text{low}} - S_{r,b1}^{\text{low}}}{cos(\pi - \theta_0) - cos\theta_0} \tag{9.12}$$

Note that oil and aqueous phases are not distinguished (a dummy phase *j* is used). To find S_{rj} at any trapping number, we also need S_{rj}^{high} at two wetting angles. Alternatively, Adibhatla et al. (2005) defined the trapping parameter T_j as a function of wetting angle:

$$\frac{\ln T_j - lnT_{b1}}{cos\theta - cos\theta_0} = \frac{\ln T_{b2} - lnT_{b1}}{cos(\pi - \theta_o) - cos\theta_0} \tag{9.13}$$

Using this new defined T_j, the residual saturation at any wetting angle and any trapping number N_T is estimated from this equation:

$$S_{rj} = S_{rj}^{\text{high}} + \frac{S_{rj}^{\text{low}} - S_{rj}^{\text{high}}}{1 + T_j N_{Tj}} \tag{9.14}$$

The superscript "low" and "high" refer to low and high trapping numbers, respectively. Using the above equation, we still need S_{rj}^{high} that is generally assumed zero. Following the above procedures, both effects of wettability alteration and IFT reduction (through trapping number) on the residual saturation are considered.

From the discussion of the preceding section, it can be seen that the end-point k_{rj}^{e} of a phase increases when the residual saturation of its conjugate phase is decreased. Therefore, the end-point k_{rj}^{e} of a phase may be linearly interpolated according to the residual saturation of its conjugate phase:

$$\frac{k_{rj}^{e,\text{NT}} - k_{rj}^{e,\text{high}}}{k_{rj}^{e,\text{high}} - k_{rj}^{e,\text{low}}} = \frac{S_{j'r} - S_{j'r}^{\text{high}}}{S_{j'r}^{\text{low}} - S_{j'r}^{\text{high}}} \tag{9.15}$$

In the above equation, the subscript j' denotes the conjugate phase of phase j.

Combining the above two equations results in

$$\frac{k_{rj}^{e,N_T} - k_{rj}^{e,\text{high}}}{k_{rj}^{e,\text{high}} - k_{rj}^{e,\text{low}}} = \frac{1}{1 + T_{j'}N_{Tj'}} \tag{9.16}$$

If the end-point relative permeability at trapping number N_{T0} is known, the end-point relative permeability at any trapping number can be estimated from the following equation, according to the preceding equation:

$$\frac{k_{rj}^{e,N_T} - k_{rj}^{e,\text{high}}}{k_{rj}^{e,N_{T0}} - k_{rj}^{e,\text{high}}} = \frac{1 + T_{j'}N_{T0j'}}{1 + T_{j'}N_{Tj'}} \tag{9.17}$$

where k_{rj}^{e,N_T}, $k_{rj}^{e,N_{T0}}$,$k_{rj}^{e,\text{high}}$ correspond to the end-point relative permeabilities at N_T, N_{T0} and a very high trapping number. Note $T_{j'}$ is the trapping parameter of the conjugate phase of phase j.

To include the effect of wettability on the end-point relative permeability at N_{T0}, following Eq. 9.12, we may have

$$k_{rj}^{e,N_{T0}} - k_{r,b1}^{e,N_{T0}} = \frac{cos\theta - cos\theta_0}{cos(\pi - \theta_0) - cos\theta_0}\left(k_{r,b2}^{e,N_{T0}} - k_{r,b1}^{e,N_{T_o}}\right) \tag{9.18}$$

Here it is assumed that we have the relative permeability curves measured at a certain trapping number N_{T0} for a pair of base phases with the contact angle θ_0 for the phase $b1$ and $\pi - \theta_0$ for the phase $b2$. Combining

the above two equations, we have the relative permeability curves with the trapping number N_T and the contact angle θ:

$$k_{rj}^{e,N_T} = k_{rj}^{e,\text{high}} + \left[k_{r,b1}^{e,N_{T0}} + \frac{cos\theta - cos\theta_0}{cos(\pi - \theta_0) - cos\theta_0} \left(k_{r,b2}^{e,N_{T0}} - k_{r,b1}^{e,N_{To}} \right) - k_{rj}^{e,\text{high}} \right] \frac{1 + T_{j'} N_{T0}}{1 + T_{j'} N_T} \tag{9.19}$$

Similarly, the exponents of relative permeabilities are

$$n_j^{N_T} = n_j^{\text{high}} + \left[n_{b1}^{N_{T0}} + \frac{cos\theta - cos\theta_0}{cos(\pi - \theta_0) - cos\theta_0} \left(n_{b2}^{N_{T0}} - n_{b1}^{N_{To}} \right) - n_{rj}^{\text{high}} \right] \frac{1 + T_{j\prime} N_{T0}}{1 + T_{j\prime} N_T} \tag{9.20}$$

Again, we assume that the end-point value, k_{rj}^e, and the exponent n_j, for the phase j are correlated to the residual saturation of the conjugate phase j' through linear interpolation. Actually, the above two equations double count the effect of wettability, as T_j already considers the effect.

After the end-point relative permeabilities and the exponents are defined, the Brooks-Corey model is used to describe the relative permeability

$$k_{rj} = k_{rj}^e \left(\overline{S}_j \right)^{n_j} \tag{9.21}$$

$$\overline{S}_j = \frac{S_j - S_{jr}}{1 - S_{jr} - S_{j\prime r}} \tag{9.22}$$

The effects of IFT and contact angle on capillary pressure are described with the following equation:

$$p_{cjj'} = p_{c0jj'} \frac{\sigma_{jj'} cos\theta}{\sigma_{jj'} cos\theta_0} \tag{9.23}$$

where $p_{cjj'}$ and $p_{c0jj'}$ are the capillary pressures, and $\sigma_{jj'}$ and $\sigma_{0jj'}$ are the interfacial tensions at the contact angle θ and θ_0, respectively.

9.4.3 A proposed simply model

The above Adibhatla et al. (2005) model double counts the effect of wettability, and it is complex. Here we propose a new model that sequentially considers both effects of wettability alteration and IFT reduction (trapping number);

the effects of wettability and IFT reduction on end-point relative permeabilities and exponents are based on their effects on residual saturations.

First, a simple interpolation technique is used to consider the wettability effect only (no IFT or capillary number effect) on a residual saturation:

$$\frac{S_{rj}^{WA} - S_{r,b1}^{WA}}{\cos\theta - cos\theta_{b1}} = \frac{S_{r,b2}^{WA} - S_{r,b1}^{WA}}{cos\theta_{b2} - cos\theta_{b1}} \tag{9.24}$$

In the above equation, the superscript "WA" refers to the parameter value when only wettability alteration is considered. The subscripts $b1$ and $b2$ represent two wetting cases that correspond to the two wetting angles θ_{b1} and θ_{b2}. Then the effect of IFT or capillary number (trapping number) on the residual saturation is considered using Eq. (9.14).

The above two procedures generate one conventional (without effect of wettability) capillary desaturation curve (CDC) for one wetting angle, and the effect of wettability will be reflected by a series of CDC curves with each CDC corresponding to one wetting angle. Practically, two CDC curves for each phase are defined; one corresponds to the strongly water-wetting case, and the other the strongly oil-wetting case.

Once the residual saturations are defined in terms of the effects of wettability alteration and IFT, the end-point relative permeabilities are estimated directly from the residual saturations, following Eq. (9.15); and the exponents are estimated similarly.

9.4.4 CMG-STARS model

The above mathematical models may not readily be available to a practical engineer or it may not be convenient for the engineer to code the models. Instead, a commercial simulator is more convenient. In this section, a CMG-STARS model is presented.

In the CMG-STARS (Computer Modeling Group, 2016) model, it is assumed that the degree of wettability alteration is scaled by the amount of surfactant adsorbed. The surfactant adsorption isotherm is described by the Langmuir-type isotherm:

$$\Gamma_s = \frac{ax_{sw}}{1 + bx_{sw}} \tag{9.25}$$

where Γ_s is the adsorbed surfactant, a and b are adsorbing constants for Langmuir-type isotherm obtained by matching adsorption experiments, and x_{sw} is the surfactant mole fraction in the aqueous surfactant solution. The above equation assumes that the adsorbed surfactant is much less than the

surfactant in the solution. In building a model, the user directly inputs a table of adsorption Γ_s versus surfactant concentration x_{sw}. The upper boundary (Γ_s^U) and lower boundary (Γ_s^L) are set and they correspond to the adsorbed surfactant at the completely water-wetness and the completely oil-wetness. At any intermediate wetness, k_r and p_c are interpolated:

$$k_{\mathrm{r}} = k_r^{\Gamma_s^L} + \left(\frac{\Gamma_s - \Gamma_s^L}{\Gamma_s^U - \Gamma_s^L}\right)\left(k_r^{\Gamma_s^U} - k_r^{\Gamma_s^L}\right) \tag{9.26}$$

$$p_{\mathrm{c}} = p_c^{\Gamma_s^L} + \left(\frac{\Gamma_s - \Gamma_s^L}{\Gamma_s^U - \Gamma_s^L}\right)\left(p_c^{\Gamma_s^U} - p_c^{\Gamma_s^L}\right) \tag{9.27}$$

Water-oil IFT is required to define the capillary number that is used to calculate residual saturations and to scale capillary pressure. One of the simplest ways is to input IFT versus surfactant concentration.

To include the effect of IFT in CMG-STARS, the IFT (σ) is calculated from Huh's (1979) equation:

$$\sigma = \frac{C_H}{\left(\frac{V_{om}}{V_{sm}}\right)^2} \tag{9.28}$$

where V_{om} and V_{sm} are the volumes of oil and surfactant, respectively, in the microemulsion phase, C_H is an empirical constant obtained by fitting experimental data of σ versus V_{om}/V_{sm}. The volumes of oil and surfactant need to be converted to the liquid-liquid K-values required in CMG-STARS.

The K-value for a component c is defined as

$$K_c^{AB} = \frac{\text{mole fraction of component } c \text{ in Phase } A}{\text{mole fraction of component } c \text{ in Phase } B} \tag{9.29}$$

If the microemulsion is type I (oil-in-water microemulsion), the microemulsion phase is actually the water phase solubilized with oil and surfactant.

$$K_{\mathrm{o}}^{WO} = \frac{\chi_o^W}{\chi_o^O} = \chi_o^W \tag{9.30}$$

$$K_{\mathrm{w}}^{OW} = \frac{\chi_w^O}{\chi_w^W} = 0 \tag{9.31}$$

$$K_s^{OW} = \frac{\chi_s^O}{\chi_s^W} = 0 \tag{9.32}$$

where χ_o^W is the mole fraction of oil in the aqueous phase (microemulsion phase), χ_o^O is the mole fraction of oil in the oleic phase, χ_w^O is the mole fraction of water in the oleic phase, χ_w^W is the mole fraction of water in the aqueous phase, χ_s^O is the mole fraction of surfactant in the oleic phase, χ_s^W is the mole fraction of surfactant in the aqueous phase.

The volume solubilization ratio has the following relationship with the mole fractions:

$$\frac{V_{om}}{V_{sm}} = \frac{x_o^W M_o/\rho_o}{x_s^W M_s/\rho_s} = \frac{K_o^{WO} M_o/\rho_o}{x_s^W M_s/\rho_s} \tag{9.33}$$

Here M and ρ are the molecular weight and density, respectively. From the experimental data of the solubilization ratio versus surfactant concentration χ_s^W, we can define a table of K_o^{WO} versus χ_s^W. If a type II microemulsion phase is defined in the oil phase, the water solubilized in the oil phase (now becoming an oleic phase) can be defined through another liquid-liquid K-value.

Once the IFT is calculated, the capillary number (N_c) is calculated. Then interpolation parameter γ is defined:

$$\gamma = \frac{N_c - (N_c)_c}{(N_c)_{max} - (N_c)_c} \tag{9.34}$$

At any IFT, the k_r and p_c are obtained from the following equations:

$$k_r = \gamma k_r^{(N_c)_{max}} + (1-\gamma) k_r^{(N_c)_c} \tag{9.35}$$

$$p_C = \gamma p_c^{(N_c)_{max}} + (1-\gamma) p_c^{(N_c)_c} \tag{9.36}$$

Looking different, the above Eq. (9.35) is actually same as the combination of Eqs. (9.2) and (9.5).

9.5 IFT reduction versus wettability alteration

As discussed in the preceding sections, the EOR mechanisms for wettability alteration and IFT reduction are different. The fundamental mechanism of IFT reduction is to decrease residual oil and water saturations and increase relative permeabilities of oil and water. When the wettability is changed from oil-wet to water-wet, the capillary pressure is changed from flow resistance to drive force, so that oil will flow out of the core and water will imbibe into the core (spontaneous imbibition). However, a surfactant

may have both functions, and it is difficult to split these two functions by experiments. Sheng (2013b) used the simulator, UTCHEM version 9.95 (UT Austin, 2009), to study these two mechanisms.

Hirasaki and Zhang (2004) conducted spontaneous imbibition experiments using the formation brine, stock-tank crude oil, and core samples of the dolomite formation from the Yates field. A core was saturated with the oil and connate water first, and then immersed in an imbibition cell. The imbibition cell was filled with either the formation brine or an alkaline surfactant solution. The formation brine had 5815 mg/L NaCl, 2942 mg/L $CaCl_2 \cdot H_2O$, 2032 mg/L $MgCl_2 \cdot H_2O$, 237 Na_2SO_4, and 7 $Fe(NH_4)_2(SO_4)_2 \cdot 6H_2O$. The alkali used was 0.3 M Na_2CO_3. The surfactants were 0.025% CS-330 (C_{12}-3EO-sulfate) and 0.025% TDA-4PO (C_{13}−4PO-sulfate). The cores were aged 24 h at 80°C. The spontaneous imbibition tests in the formation brine did not drive oil out of the cores, confirming the cores were oil-wet. The imbibition test in the alkaline surfactant solution lasted 138 days, and 44% oil was driven out.

Delshad et al. (2009) used a 3D simulation model to have successfully history matched the Hirasaki and Zhang (2004) experiments. Sheng (2013b) used their model as the base model for the study. The simulation model is a homogenous Cartesian grid with 7 × 7 × 7 grid blocks. 5 × 5 × 5 grid blocks in the middle of the model represent the core, and the remaining grid blocks represent the imbibition cell of aqueous solution or brine, as shown in Fig. 9.6. In the imbibition cells (lighter red in the figure), the initial surfactant concentration is 0.05%, the porosity is 1.0, the capillary pressure is 0.0 kPa, and the permeability is 1000 μm^2. In the matrix core (darker red), the initial surfactant concentration is zero, the porosity is 0.24, the permeability is 0.122 μm^2, and the initial oil saturation is 0.68. The relative permeability and capillary pressure are described by Eqs. (9.8)−(9.11), and their parameters in the Brooks and Corey (1966) model are shown in Table 9.1. Using this model, the alkaline surfactant imbibition test in Core B conducted by Hirasaki and Zhang (2004) is history matched. This history-match model is used to quantify the mechanisms of IFT reduction and wettability alteration in different cases below.

9.5.1 Effect of combined wettability alteration and IFT reduction

Fig. 9.7 presents the oil recovery factors in different scenarios. "OW + IFT" is the oil-wet case without wettability alteration with ω set 0; "WW + IFT" is the water-wet case with ω set 1; "IW + IFT"

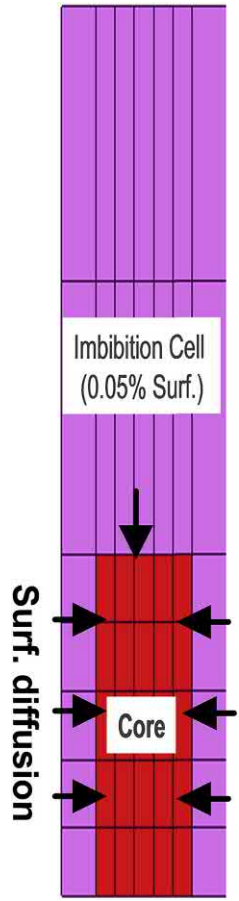

Figure 9.6 Simulation grids and the initial surfactant concentration.

Table 9.1 Relative permeability and capillary pressure parameters in the base model.

	Initial oil wettability (OW)		Altered water wettability (WW)	
	Oil	**Water**	**Oil**	**Water**
S_{or}	0.38	0.32	0.38	0.32
End point k_r	0.59	0.23	0.59	0.23
k_r exponent	3.3	2.9	2	2
C_{pc}, psi·Darcy$^{0.5}$	5		5	
Contact angle	180		0	
E_{pc}	2		2	

is the intermediately wet case with ω set 0.5. These ω values are presented in Table 9.2. The IFT in these cases is the same, 0.0088 mN/m. From this figure, we can see that the oil recovery factors are: WW + IFT case -> IW + IFT case > OW + IFT case, indicating that wettability alteration improves oil recovery.

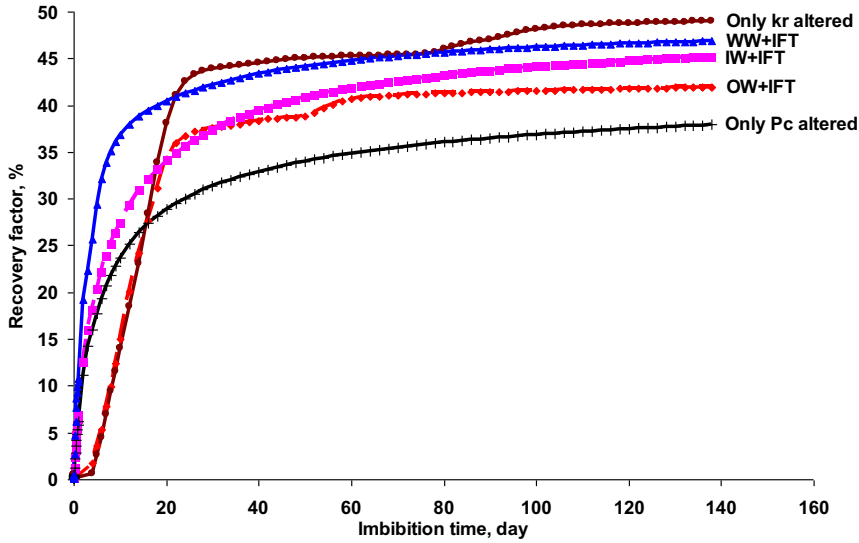

Figure 9.7 Effect of the combined wettability alteration and IFT reduction in spontaneous imbibition.

Table 9.2 ω in difference cases.

Case	ω for k_r	ω for p_c
OW + IFT	0	0
WW + IFT	1	1
IW + IFT	0.5	0.5
Only pc altered	0	0.5
Only k_r altered	0.5	0

As discussed earlier, wettability alteration can result in the changes in p_c and k_r. To quantify the effects of p_c and k_r, two extra cases are compared. One case is "Only Pc altered," in which the oil-wet p_c is changed to the intermediately wet p_c, but k_r is assumed not changed. Correspondingly, the interpolation parameter ω for p_c is 0.5, and ω for k_r is 0. Compare the cases of "OW + IFT" and "Only Pc altered." When only p_c is changed from the oil-wet p_c to the intermediately wet p_c, the oil recovery is higher in the early days, but the ultimate recovery is lower than that in the oil-wet case with IFT reduction. The result indicates that the capillary imbibition only improves the recovery in the early time.

The other case is "Only kr altered" in which the oil-wet k_r is changed to the intermediately wet k_r, but p_c is assumed not changed. Correspondingly, ω for p_c is 0, and ω for k_r is 0.5. When only k_r is partially changed from the

oil-wet k_r to the intermediately wet k_r, the oil recovery is almost unchanged because no p_c is changed; but the ultimate recovery is higher than that in the oil-wet case with IFT reduction. These results indicate that the relative permeability dominates the oil recovery in the later stage.

One may ask why the oil recovery from the case "Only Pc altered" with p_c is even lower than that from the case "OW + IFT" without p_c. Refer to Fig. 9.3, water saturation becomes higher at the later time, then the capillary pressure becomes negative. Therefore, the capillary pressure becomes resistant to flow at the later time, thus reducing oil flow. In the case of "WW + IFT", a positive capillary pressure and beneficial (increased) k_r effect must be effective only when some block wettability has been changed from oil-wet to water-wet in the early time, as indicated in the figure that the oil recovery in the early time is higher than the case of "Only kr altered." At a later time, relatively higher water saturation may lead to lower k_r in "WW + IFT" than that in the "Only kr altered." Also, because of ultralow IFT, the capillary effect is minimum, and the oil recovery is dominated by k_r.

9.5.2 Relative importance of wettability alteration and IFT reduction

Wettability alteration may be caused by surfactant adsorption; with more adsorption, wettability is altered more significantly. For a fixed amount of surfactant injected, more surfactant adsorption leaves less surfactant available for IFT reduction. Fig. 9.8 shows the effect of the adsorption on oil recovery using the model in the preceding section. There are three cases: a base adsorption, twice the base adsorption, and half the base adsorption. It shows that when the adsorption is higher, the oil recovery factor becomes lower. It is implied that the decreased IFT effect is more significant than the increased effect of wettability alteration, owing to higher adsorption. Here the surfactant assumption is assumed as the mechanism of wettability alteration. It implies that the effect of IFT is more significant than that of wettability alteration. This observation may be specific from this model. It also holds from the discussions presented in the following section. However, for this observation or conclusion to hold, the core permeability must be high enough so that oil can move by gravity (for example). Capillary pressure should not be the dominant driving force. Therefore, this conclusion may not hold in formations with ultralow permeability.

Actually, Zhang et al. (2018) collected the 35 experimental data on surfactant solution imbibition in Wolfcamp and Eagle Ford cores. They correlated the oil recovery factors with the contact angles, IFTs, and capillary

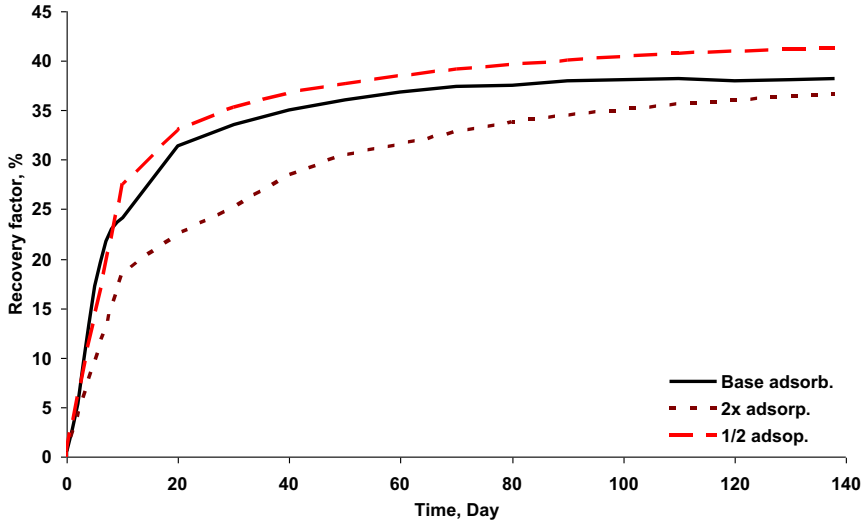

Figure 9.8 Effect of surfactant adsorption.

pressures, as shown in Fig. 9.9. It shows that the oil recovery factors correlated with contact angles better than with IFTs; with a lower contact angle, the recovery factor was higher; but the recovery factors did not show a correlation with the IFTs. It implies that the wettability alteration effect of a surfactant solution is more important than the IFT reduction effect.

9.5.3 Effect of IFT on spontaneous oil recovery with and without wettability alteration

As discussed earlier, the dominant mechanism of wettability alteration is to change the capillary pressure. The capillary pressure is directly proportional to IFT. Therefore, the IFT reduction actually mitigates the effect of wettability alteration, and the oil rate or oil recovery is reduced, as shown in Fig. 9.10. In the figure, the incremental oil recovery is defined by the oil recovery with wettability alteration minus the oil recovery without wettability alteration for the same IFT value. Thus, the incremental oil recovery represents the oil recovery due to the wettability alteration mechanism only. As the IFT becomes lower, the oil recovery due to wettability alteration is lower.

Fig. 9.11 shows that a high IFT does increase oil recovery without wettability alteration. This result is consistent with the theory and it also confirms that the used simulation model correctly captures the mechanisms. A surfactant may reduce IFT and change wettability. IFT reduction can increase oil

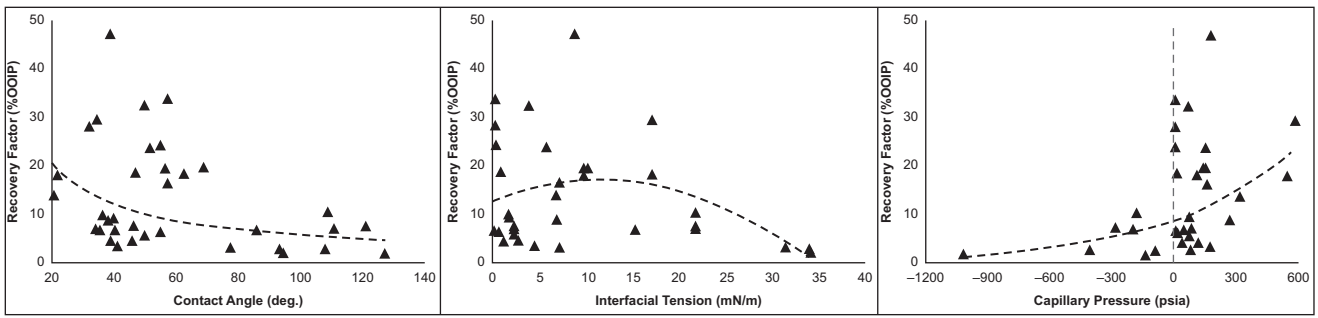

Figure 9.9 Oil recovery factors versus contact angles, IFTs, and capillary pressures for Wolfcamp and Eagle Ford cores (Zhang et al., 2018). *The following URTeC paper, Zhang, F., Saputra, I. W. R., Adel, I. A., & Schechter, D. S. (2018, August 9). Scaling for Wettability Alteration Induced by the Addition of Surfactants in Completion Fluids: Surfactant Selection for Optimum Performance. Unconventional Resources Technology Conference. http://doi.org/10.15530/URTEC-2018-2889308, is reprinted with permission from the Unconventional Resources Technology Conference, whose permission is required for further use.*

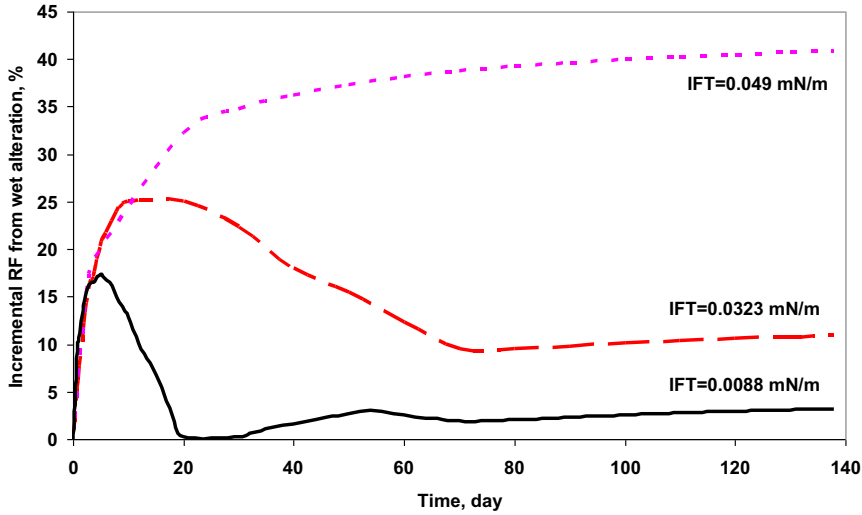

Figure 9.10 Effect of wettability alteration on oil recovery by spontaneous imbibition at different IFT values.

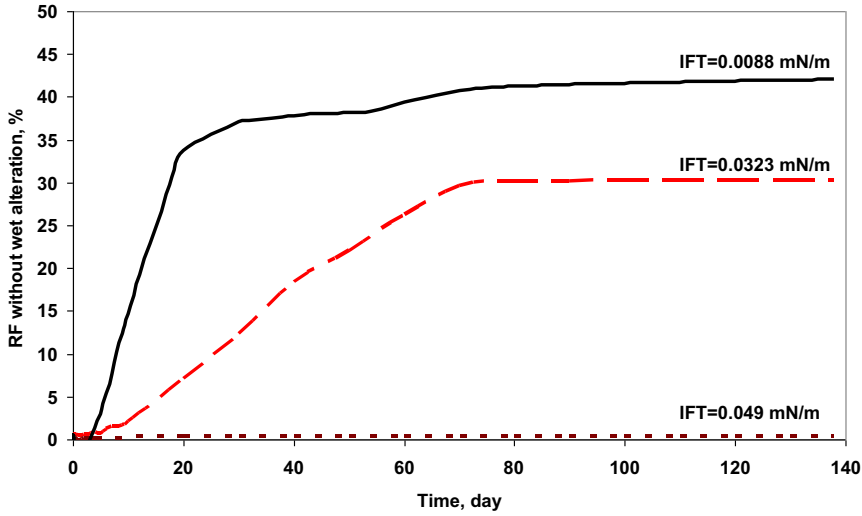

Figure 9.11 Effect of IFT without wettability alteration.

recovery but mitigate wettability alteration mechanism. The resultant effect will be the balance of the two negative and positive effects.

Xie et al. (2005) compared the spontaneous imbibition rates using nonionic poly-oxyethylene alcohol (POA) and cationics (CAC). The IFT of POA solution was 19 times higher than of CAC solution (5.7 vs.

0.3 mN/m). Therefore, the additional oil recovery from POA was higher and faster than that from CAC. Austad and Milter (1997) had the same observation. To make use of wettability alteration, IFT should not be too low. But IFT should not be high either, as high IFT cannot reduce residual oil saturation (thus cannot increase relative permeabilities). There may exist an optimum combination of IFT reduction and wettability alteration. In principle, IFT affects the oil rate because it determines the magnitude of capillary pressure (drive force), and it also affects the ultimate oil recovery because it determines the capillary number which determines the residual oil saturation (thus oil recovery).

Chen and Mohanty (2015) studied the synergy of wettability alteration and IFT reduction on spontaneous imbibition oil recovery by simulation. They concluded that the effect of low IFT on imbibition oil recovery in the presence of wettability alteration is not significant, and the low IFT becomes extremely important when the wettability alteration is not involved in oil recovery, based on their simulation results shown in Fig. 9.12. However, low IFT should be important, if any, despite whether the wettability alteration exists or not. As shown in the figure the oil recovery is about 70% when the IFT is 0.003 mN/m with and without wettability alteration. In Fig. 9.12A, as the IFT becomes higher, the oil recovery becomes lower, although the wettability alteration is included, indicating the positive effect or the assistance to IFT provided by wettability alteration is not significant. This is probably if the IFT values in this case are not high. In Fig. 9.12B, as there is no wettability alteration, the only effect is from IFT. As the IFT becomes higher, the oil recovery

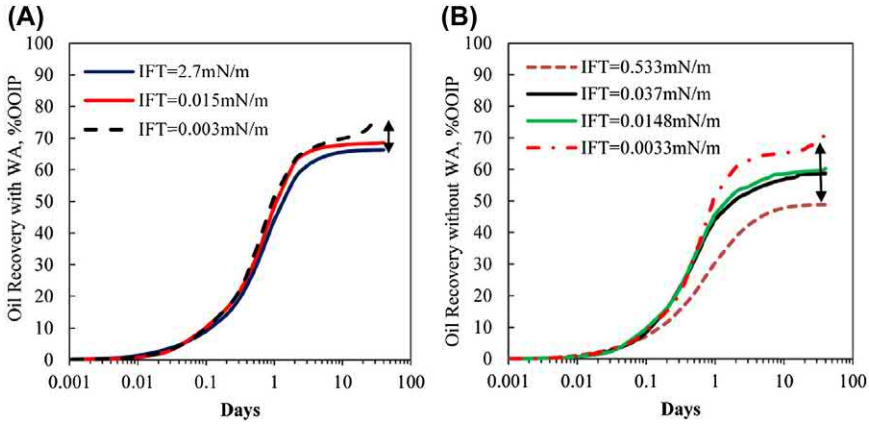

Figure 9.12 Effects of IFT on oil recovery with (A) wettability alteration or (B) without wettability alteration (Chen and Mohanty, 2015).

decreases more significantly. Fig. 9.12 shows that oil recovery will always be high, or it does not matter whether the wettability is altered or not, as long as the IFT is low (as shown in the figure when IFT = 0.003 mN/m); Fig. 9.11A also shows that when the IFT is low, the effect of wettability alteration is not important any more. Note their core permeability was over 100 mD.

More likely, anionic surfactants reduce IFT, while cationic surfactants change wettability. While studying imbibition oil recovery in Silurian dolomite cores using surfactants, Chen and Mohanty (2015) combined cationic surfactants and anionic surfactants. Their experimental data are shown in Fig. 9.13. The properties of those surfactants are summarized in Table 9.3. Fig. 9.13A shows that when the 0.2% cationic surfactant BTC 8358 had spontaneous imbibition oil recovery of 31%. After that, adding 0.02% anionic surfactant A092 to 0.2% BTC 8358 resulted in 10% incremental oil recovery to 41.6%. Fig. 9.13B shows that a combination of 0.1% cationic surfactant BTC 8358 and 0.5% anionic surfactant AS-3 had oil recovery of 46%, 13% higher than that (33%) from 1% anionic surfactant. They claimed the incremental oil recovery resulted from the synergy of cationic and

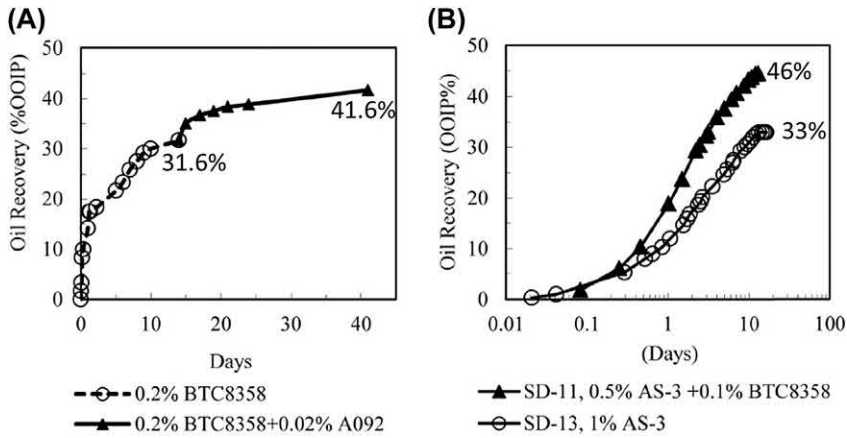

Figure 9.13 Synergy of wettability alteration and IFT reduction (Chen and Mohanty, 2015).

Table 9.3 Property data of surfactants.

Surfactant	Type	IFT, mN/m	Wettability alteration
BTC8358	Cationic	3	Oil-wet to water-wet
A092	Anionic	0.03	No
AS-3	Anionic	0.05	No

anionic surfactants. An additional benefit of combining anionic and cationic surfactants was the reduction of adsorption of anionic surfactant on the positively charged carbonate rock surface. However, it should be aware that a mixture of opposite charge surfactants may tend to precipitate.

Although Chen and Mohanty (2015) presented the property data of each surfactant, the property data of the mixed surfactant solutions were not provided. It could be possible that the properties of the mixed surfactant solutions were very different from their counterparts of each individual surfactant. To understand or confirm the real mechanisms or synergy of those surfactants, the properties of the mixed surfactant solutions should have been measured, so that it became more clear what properties had made the mixed surfactant solutions more effective in improving spontaneous oil recovery.

To have such synergy for incremental oil recovery from spontaneous imbibition, at least two properties of a mixed surfactant solution must be met: (1) wettability alteration to water-wet, (2) the interfacial tension may be intermediately high (it cannot be ultralow or too high). These properties will make sure that the surfactant solution can enter the porous medium to displace oil out, and the solution also has the favorable flow properties like improved relative permeability.

9.6 Specific surfactant EOR mechanisms related to shale and tight formations

Some surfactant EOR mechanisms specifically related to wettability alteration are reviewed in this section.

9.6.1 Bilayer mechanism by anionic surfactants

The mechanism of bilayer formation is shown schematically in Fig. 9.14. The negative EO-surfactant adsorbs onto the positive surface of the chalk through hydrophobic interactions with the adsorbed crude oil components to form a monolayer as Chen and Mohanty (2015) called it. The water-soluble head-group of the surfactant, the EO-group, and the anionic sulfonate group may decrease the contact angle below 90° by forming a small water zone between the organic coated surface and the oil. The formation of the bilayer must not be regarded as a permanent wettability alteration of the chalk. In fact, it will probably be fully reversible due to the weak hydrophobic bond between the surfactant and the hydrophobic surface (Standnes and Austad, 2000).

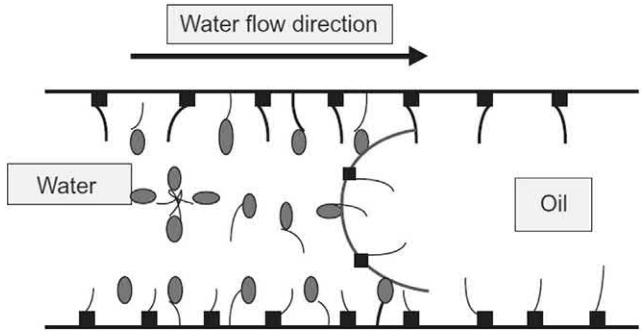

Figure 9.14 Bilayer mechanism of EO-sulfonates, the *eclipses* represent EO-sulfonates, and the *squares* represent the carboxylates in the oil (Stadnes and Austad, 2000).

To make anionic surfactants work in hard brine conditions, divalent cation scavengers like EDTA.4Na and NaPA need to be added to remove divalent cations such as Mg^{2+} and Ca^{2+} (Chen and Mohanty, 2014; 2015). Without the intervention by divalent cations, the micelles of anionic surfactant are the source of monomers. In the presence of divalent cations, the divalent ions will bind to micelles (Talens et al., 1998), form precipitates with surfactants, and act as a clamp between two surfactant ions, thus inducing properties commonly associated with dimeric surfactants. By the way, the ionic bonding between calcium and surfactant micelles does not change micelles-induced IFT reduction, as the micelles are still able to solubilize oil (Chen and Mohanty, 2015). Divalent ions do reduce optimum salinity.

9.6.2 Micellar solubilization of organic component by anionic surfactants

During surfactant solution imbibition, anionic surfactants (Sasol's Alf-38 and Alf-69 (propoxylated sulfates-8PO)) lowered the interfacial tension, the gravitational force exceeded the capillary pressure, and surfactant solutions invaded the gap between the rock surfaces, but left a thin oil film. The surfactants solubilized the oil film slowly, leading to the wettability altered toward water-wet. The time-scale for the wettability alteration appeared to be much longer than the time-scale of the movement of oil/water meniscus caused by IFT.

9.6.3 Ion-pair mechanism

When the head groups of a surfactant and polar compounds of crude oil have opposite charges, ion-pairs form by electrostatic interactions. These ion-pairs strip the adsorbed oil components away, resulting in more water-wet surfaces

(Feng and Xu, 2015). In carbonate reservoirs, the adsorbed negative compounds of carboxylic acids and positive heads of cationic surfactant form ion-pairs and the carboxylic acids are carried away by ion-pairs.

Austad and his workers (e.g., Standnes and Austad, 2000; Austad and Standnes, 2003) believed that cationic surfactants form ion-pairs with adsorbed organic carboxylates of crude oil and stabilize them into the oil, thus they were able to desorb organic carboxylates from the carbonate rock surface and change the rock surface to more water-wet. The mechanism of ion-pair formation is schematically described in Fig. 9.15. Due to electrostatic forces, the cationic monomers will interact with adsorbed anionic materials from the crude oil. Some of the adsorbed material at the interface between oil, water, and rock will be desorbed by forming an ion-pair by the cationic surfactant and the negatively charged adsorbed material, mostly carboxylic groups. This ion-pair complex is termed "cat-anionic surfactant," and it is regarded as a stable unit. In addition to electrostatic interactions, the ion-pairs are stabilized by hydrophobic interactions. The ion-pairs are not soluble in the water phase but can be dissolved in the oil phase or in the micelles. As a result, water will penetrate the pore system, and oil will be expelled from the core through connected pores with high oil saturation in a so-called countercurrent flow mode. Thus, once the adsorbed organic material has been released from the surface, the chalk becomes more water-wet. As the wettability alteration step was slow and was the dominant mechanism, the movement of the altered water-wet front was slow using the cationic surfactant (Kumar et al., 2008).

When positively charged organic matter adsorbs to the siliceous surface, it will interact with negatively charged heads of anionic surfactant to form ion-pairs; then the wettability is altered from oil-wet to water-wet (Alvarez and Schechter, 2017). They reported that anionic surfactants changed the wettability of negatively charged siliceous cores to water-wet better than

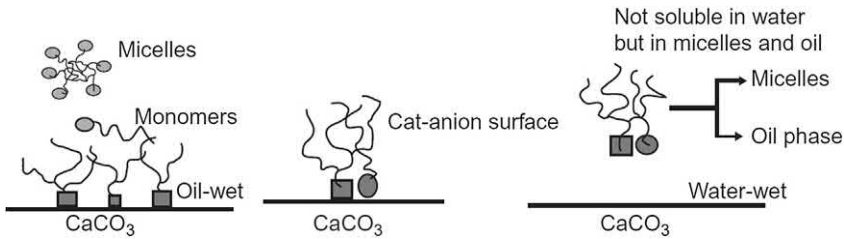

Figure 9.15 Mechanism of wettability alteration from oil-wet to water-wet by ion-pairs. Large *squares* represent carboxylate groups, $-COO^-$, small *squares* represent other polar components, and *circles* represent cationic ammonium group, $-N^+(CH_3)_3$ (Austad and Standnes, 2003).

positively charged surfactants, because anionic surfactants interact with the positively charged oil molecules, mostly carbon-based compounds adsorbed to the siliceous rock surface, forming ion-pairs. The layer of oil in the rock surface is desorbed as ion-pairs forming micelles and transported due to their hydrophobicity to the bulk oil phase in the pores. Liu et al. (2019) also observed that organic material and oil film are detached from rock surface in anionic surfactant solutions. That is an example of ion-pair mechanism. The mechanism is schematically shown in Fig. 9.16. Salehi et al. (2008) found that the wettability alteration by forming ion-pairs was more effective than by the surfactant adsorption.

9.6.4 Surfactant adsorption mechanism

When an anionic surfactant solution is placed in a carbonate formation, the charged hydrophobic heads of the surfactant are adsorbed on those surface places (positively charged) unoccupied by counter ions via electrostatic interactions. If the adsorption is sparse, the interactions between adsorbed surfactant molecules are negligible (Atkin et al., 2003; Paria and Khilar, 2004). The rock surface becomes more oil-wet, as shown in Fig. 9.17. However, if the carbonate surface is originally intensely occupied by negative oil components, and anionic surfactant molecules adsorb on the rock surface via competition adsorption, then the rock surface is less occupied by the oil components, leading to less oil-wet.

Similarly, for a cationic surfactant, the positively charged head groups adsorb onto the negatively charged surfaces of siliceous minerals by electrostatic interactions. This could cause the mineral surface to become more

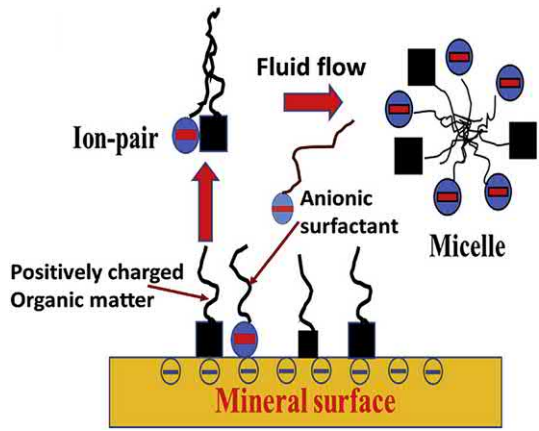

Figure 9.16 Schematic of ion-pair mechanism of an anionic surfactant in a siliceous rock.

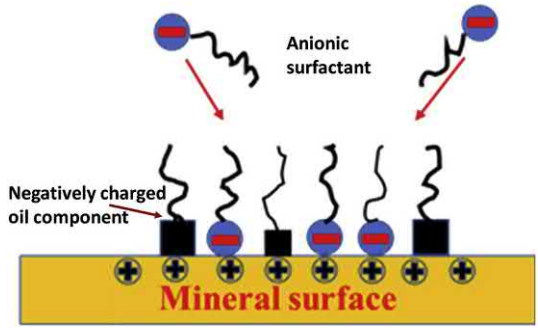

Figure 9.17 Schematic of wettability alteration of an anionic surfactant in a carbonate rock.

oil-wet as shown in Fig. 9.18 (Liu et al., 2019). Bi et al. (2004) called this process as the first adsorption of surfactant to form a monolayer when the cationic surfactant concentration is low. When the surfactant concentration is high, the second adsorption takes place to form a bylayer where the hydrophilic parts of the surfactant expose to the water phase so that the rock becomes more water-wet.

If the siliceous surface is originally intensely occupied by negative oil components, and cationic surfactant molecules adsorb onto the rock surface via competition adsorption, then the rock surface is less occupied by the positively charged oil components, probably being able to lead to less oil-wet.

9.6.5 Monolayer adsorption by nonionic surfactants

Nonionic surfactants adsorb onto rock surfaces (either carbonate or siliceous rocks) physically by hydrophobic bonding, rather than electrostatically or chemisorbed, forming a surfactant monolayer on the oil-wet surface. The oil wetness may be changed to less oil-wet or intermediate-wet, as shown

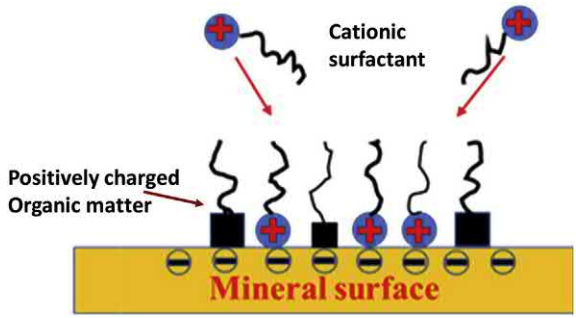

Figure 9.18 Schematic of wettability alteration of a cationic surfactant in a siliceous rock.

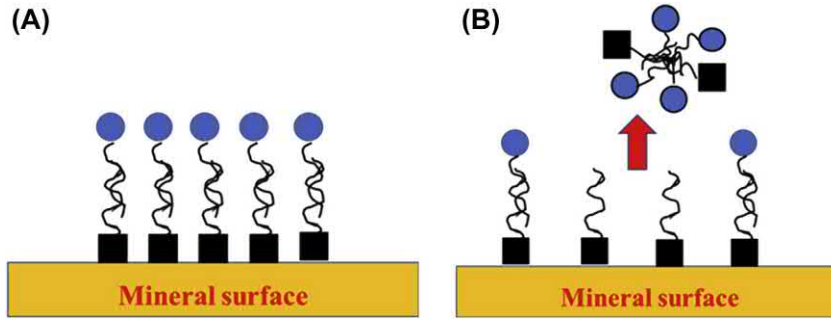

Figure 9.19 Schematic of monolayer mechanism of wettability alteration.

in Fig. 9.19A. This process is reversible because of the week hydrophobic interactions (Salehi et al., 2008; Standnes et al., 2002). When the surfactant is added, surfactant molecules tend to diffuse to the interfaces between isolated oil droplets and water due to the surface tension gradient or the Gibbs-Marangoni effect (Sheng, 2013d). The surfactant molecules displace the oil attached to the rock surface, and the isolated oil droplets tend to roll up slowly and eventually detach from the surface, as shown in Fig. 9.19B.

9.6.6 Effect of IFT reduction on wettability alteration

Liu et al. (2019) found that the wettability of shale surface was more water-wet when the IFT decreased in the anionic surfactant solutions, because both water-wetting angle and the IFT decreased with the surfactant concentration as shown in Figs. 9.20 and 9.21, while it was hardly changed for low

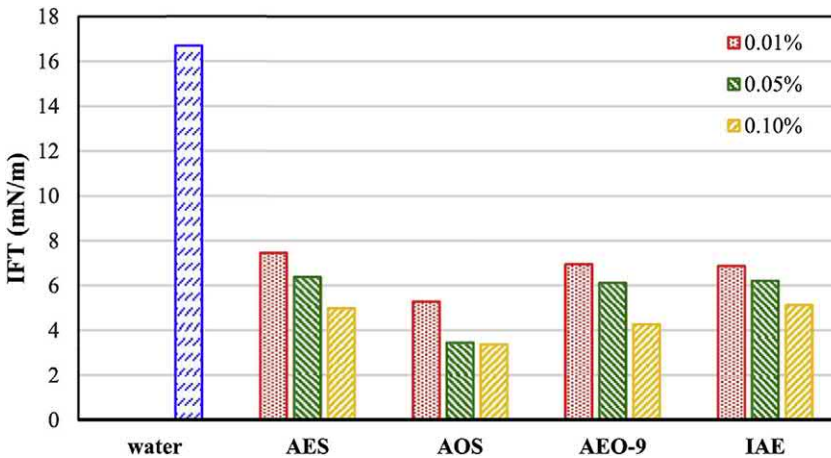

Figure 9.20 Measured IFT values of shale cores in different surfactants with different concentrations.

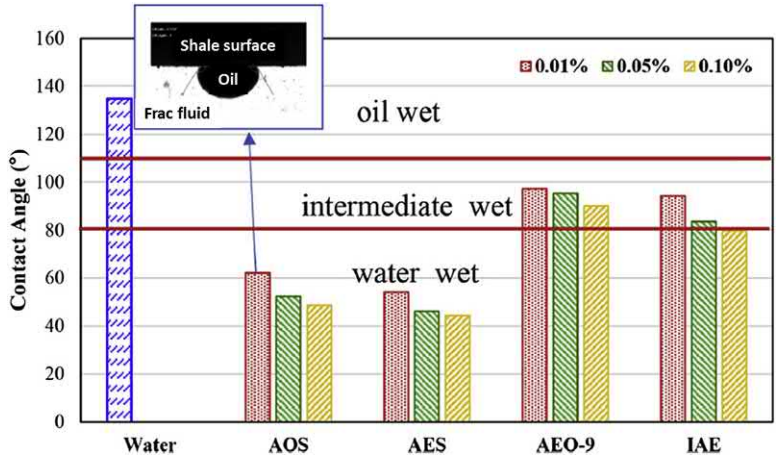

Figure 9.21 Contact angles when the shale cores were soaked in different surfactant concentrations for 48 h.

IFT conditions in nonionic surfactants. As σ_{ow} decreases, the oil film desorption does not significantly increase the adhesion work (W) as Fig. 9.22 shows and as the following equation indicates:

$$W = (\sigma_{ow} + \sigma_{ws})A - \sigma_{os}A \tag{9.37}$$

Therefore, the IFT reduction is beneficial to the desorption of oil film or organic matter from the rock surfaces. In nonionic surfactant solutions, the oil film or organic matter does not have electrostatic forces to be stripped off. The shale wettability is altered by adsorption, rather than by the stripping process through ion-pairs. Thus, the effect of IFT reduction on wettability alteration is not as effective as in anionic surfactant.

9.7 Surfactant selection for wettability alteration

There are many surfactants that are used to reduce IFT in the surfactant flooding literature. Less discussions have been allocated to surfactants that are used to change wettability. These surfactants could be nonionic surfactants (Standnes et al., 2002; Vijapurapu and Rao, 2004; Xie et al., 2005),

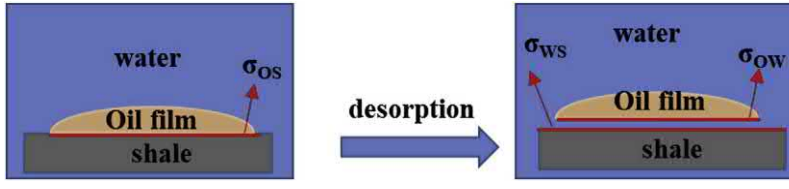

Figure 9.22 Schematic of the stripping process of oil film.

cationic surfactants (Austad et al., 1998; Standnes et al., 2002), and anionic surfactants (Sharma and Mohanty, 2013; Seethepalli et al., 2004; Chen and Mohanty, 2013). Nonionic fluorinated polymeric surfactants were proposed to treat gas condensate reservoirs to mitigate condensate dropout by altering wettability to more gas-wetting conditions (Li and Firoozabadi, 2000; Kumar et al., 2006; Sharma et al., 2018). Ethoxylate sulfates could change carbonate surfaces from more oil-wet to more water-wet, but they are not stable at high temperature (e.g., 60°C). At room temperature, Hirasaki and Zhang (2004) showed that the ethoxy and propoxy sulfates had high performance in imbibition oil recovery in carbonate cores, when Na_2CO_3 was added. Sulfonates and carboxylates are thermally stable, but they are generally poor in altering wettability (Chen and Mohanty, 2015). Sharma and Mohanty (2013) tested ethoxylate sulfonates for wettability alteration in hard brine at 100°C and found that water contact angles were reduced to around 90°C in the best case. Chen and Mohanty (2013, 2014) found that the divalent scavengers (e.g., EDTA.4Na, Sodium polyacrymide (NaPA)) sequestered divalent ions in hard brine to free anionic surfactants to react at the solid-fluid interface to alter wettability of carbonates from oil-wet to more water-wet. Generally, anionic surfactants are cheaper than cationic surfactants. A quaternary amine surfactant, BTC 8358 (n-alkyl dimethyl benzyl ammonium chloride) was found to be effective in wettability alteration on oil-wet calcite surfaces. A combination of two Guerbet alkoxy sulfate and one internal olefin sulfonate (IOS) was found be a strong wettability modifier at a salinity below the optimum salinity. A mixture of cationic surfactant BTC 8358 and an anionic surfactant Enordet A092 ($C_{16,17}$ branched IOS to reduce IFT) was also found to have a good imbibition oil recovery (Chen and Mohanty, 2015).

Liu et al. (2019) compared anionic surfactants and nonionic surfactants in terms of their capability of wettability alteration. Fig. 9.23 shows the ζ-potential in these surfactant solutions. It shows that for the same surfactant, the absolute values of the ζ-potential increased with surfactant concentration. The increase for anionic surfactants (sodium alcohol ether sulfate (AES) and sodium C14-16 alpha olefin sulfonate (AOS)) was much greater than in nonionic surfactants. At the same concentration, the ζ-potential (absolute value) in the anionic surfactant solutions was higher than that in the nonionic surfactant solutions (alcohol ethoxylate (AEO-9) and isomeric alcohol ethoxylates (IAE)). The absolute values of the ζ-potential for the nonionic surfactant solutions at concentrations of 0.01 wt.%, 0.05 wt.%, and 0.1 wt.% were less than 20 mV which is close to water's ζ-potential.

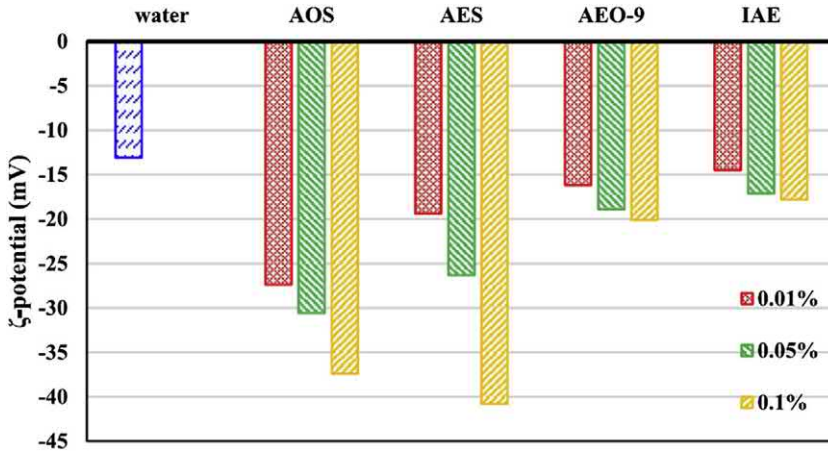

Figure 9.23 ζ-potential for shale cores at different surfactant concentrations.

These data indicate the anionic surfactants were better than the nonionic surfactants in terms of wettability alteration, as the higher the ζ-potential, the more water-wet the cores are. It is confirmed by direct angle measurements after 48 h of soaking in the surfactant solutions shown in Fig. 9.21 and by visual oil shown in Fig. 9.24 coming out of the cores by spontaneous imbibition of different surfactant solutions for 48 h. However, the mechanism of wettability alteration by forming ion-pairs for anionic surfactants took some time, while the mechanism by surfactant adsorption made the contact angle decrease immediately. For example, the time-dependent wettability alteration for AOE and AES anionic surfactants are shown in Fig. 9.25. However, the effectiveness of a surfactant to alter wettability

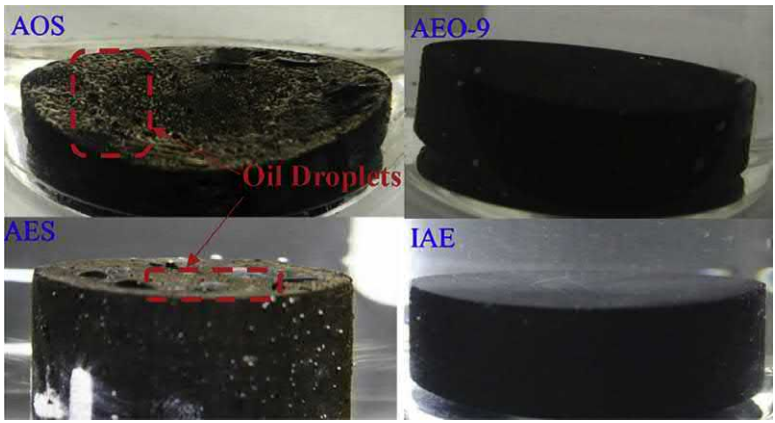

Figure 9.24 Oil seen when the shale cores were soaked in different surfactant concentrations for 48 h.

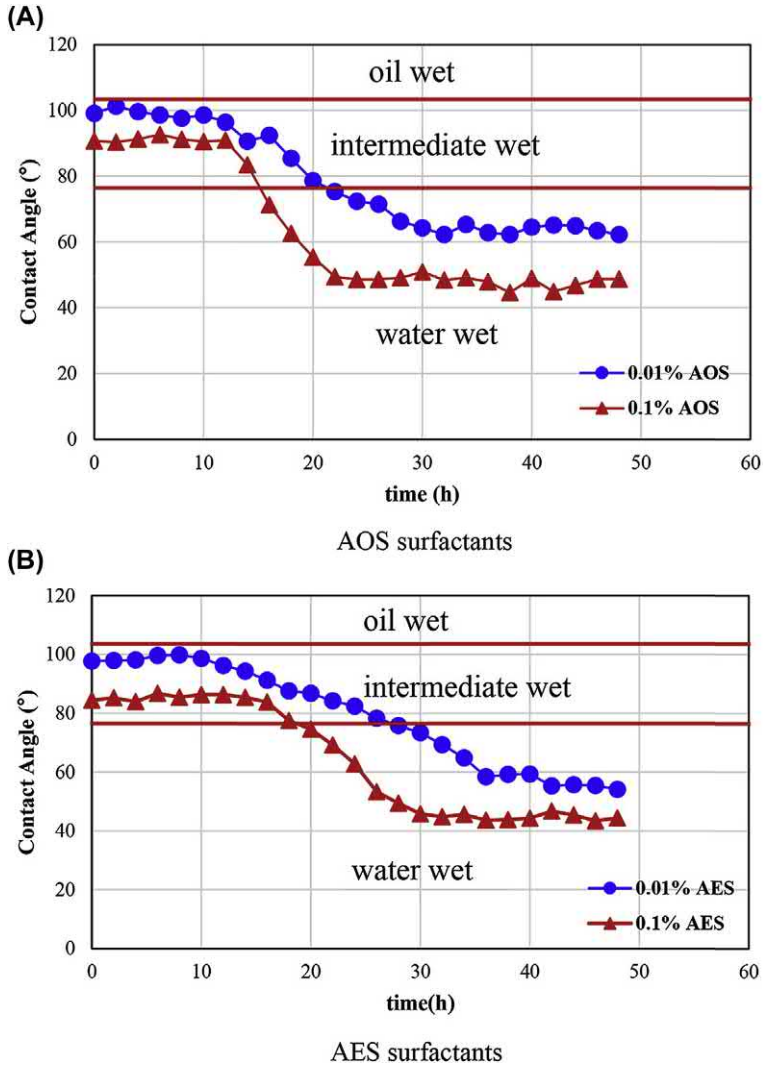

Figure 9.25 Contact angle changes with time for anionic surfactants AOS and AES.

depends on the rock type. Chen and Mohanty (2014) reported Adibhatla and Mohanty's (2008) work that the tested carbonate rock wettability was not altered by either property alpha olefin sulfonate (AOS) or alkyl aryl sulfonate in softened brine, although such data are not found in the original Adibhatla and Mohanty (2008) paper.

Nonionic surfactants have excellent solubility, high chemical stability, and high tolerance to hard brine, but their cloud points are low. Chen

and Mohanty (2014) tested surfactants called ethoxylated aliphatic amine, trade name Ethomeen by AkzoNobel. At neutral to high pH, Ethomeen is a triamine with ethoxylate (EO) groups. In acidic brine, it may be protonated and become a cationic surfactant. EO group usually increases the hydrophilicity of a surfactant at high temperatures. Tests showed that Ethomeen T/25 is a good candidate for wettability alteration in harsh dolomite conditions.

Rock type may affect selection of surfactants. Feng and Xu (2015) showed that for carbonates with shale oil with a higher total acid number (TAN), a cationic surfactant is better than an anionic surfactant; for sandstones with shale oil having a higher total base number (TBN), an anionic surfactant is better than a cationic surfactant.

Alvarez et al. (2018) reported that the cationic surfactants changed the oil wetness of *carbonate* surfaces of Wolfcamp and Eagle Ford rocks to water-wetness more than anionic surfactants, due to the electrostatic interactions between its positively charged heads and the negatively charged oil compounds, mostly acid compounds, attached to positively charged carbonate surfaces present in both Wolfcamp and Eagle Ford rocks. Oil molecules attached to the rock surface are stripped and moved to the oil phase, so that the rock wettability is changed to less oil-wet. Table 9.4 presents the data of IFT reduction and wettability alteration by different surfactants used in the different cores. When the anionic, nonionic, and cationic surfactants were used, the *carbonate* cores (both Wolfcamp and Eagle Ford) had highest oil recovery factors (47.3% and 9.0%, respectively), when the *cationic* surfactant solution had lowest final contact angles (38.1 and 34.3°, respectively). A separate set of measurements of contact angles, zeta potentials, and IFTs of the surfactant solutions are shown in Figs. 9.26–9.28, respectively. Interestingly, the absolute values of zeta potential for the cationic solution are lower than those for the anionic one and anionic/nonionic solutions, not consistent with the contact angle values (if consistent, the absolute values should be higher, as others reported (Liu and Sheng, 2019)). The IFTs of cationic solution are higher than those of anionic and anionic/nonionic solutions, resulting in the highest final capillary pressures, and the cationic solution had higher oil recovery. It seems that a low wetting angle and an intermediately high IFT, which leads to the high positive capillary pressure, are favorable to oil recovery spontaneous imbibition.

However, the Wolfcamp *siliceous* cores had higher oil recovery factors by spontaneous imbibition (33.9% and 28.5% in Table 9.4), when the *anionic* surfactant solution had lower final contact angles (57.4 and 32.4°), as shown

Table 9.4 Capabilities of IFT reduction and wettability alteration of different surfactants on different cores.

Core	Surfactant	Surfactant components	IFT, mN/m	Final contact angle	Final p_c, psi	RF, %
Wolfcamp carbonate cores (quartz 13%, clays 15%, calcite 46%, dolomiate 19%, feldspar 4%, pyrite 3%) (Alvarez et al., 2018)						
1	Anionic 1	Methyl alcohol, proprietary sulfonate	0.4	45.6	16	24.3
2	Anionic/nonionic	Methyl alcohol, sulfonate A, sulfonate B, ethoxylated alcohol	0.9	47.4	35	18.9
3	Anionic 2	Isopropyl alcohol, citrus terpenes, proprietary	3.9	48.7	149	32.6
4	Cationic	Isopropyl alcohol, ethoxylated alcohol, quaternary ammonia compound, citrus terpenes	8.9	38.1	406	47.3
5	Water		21.8	89.9	2	7.6
Eagle ford carbonate cores (quartz 17%, clays 35%, calcite 40%, dolomiate 1%, feldspar 3%, pyrite 4%) (Alvarez et al., 2018)						
6	Anionic 1	Same as above Wolfcamp	0.7	47.2	20	6.5
7	Anionic/nonionic	Same as above Wolfcamp	1.2	53.4	30	4.5
8	Anionic 2	Same as above Wolfcamp	2.3	48.3	63	5.8
9	Cationic	Same as above Wolfcamp	6.9	34.3	236	9
10	Water		34.4	89.5	12	2.1
Wolfcamp siliceous cores (quartz 40%, clays 40%, calcite 4%, dolomite 2%, feldspar 7%, pyrite 7%) (Alvarez and Schechter, 2017)						
	Nonionic	Branched alcohol oxyalkylate	9.8	62		

(*Continued*)

Table 9.4 Capabilities of IFT reduction and wettability alteration of different surfactants on different cores.—cont'd

Core	Surfactant	Surfactant components	IFT, mN/m	Final contact angle	Final p_c, psi	RF, %
3	Nonionic/cationic	Ethoxylated isodecyl alcohol, quaternary ammonium compound, quaternary ammonium salt	9.8	62.6	327	18.4
4	Nonionic/cationic	Ethoxylated isodecyl alcohol, quaternary ammonium compound, quaternary ammonium salt	9.8	56.6	391	19.7
1	Anionic	Methyl alcohol, proprietary sulfonate	0.4	57.4	16	33.9
2	Anionic	Methyl alcohol, proprietary sulfonate	0.4	32.4	24	28.5
	Nonionic/anionic	Methyl alcohol, proprietary ethoxylated, proprietary sulfonate	4	46		
5	Water		21.8	110.9	−564.0	7.1
6	Water		21.8	108.7	−507.0	10.5

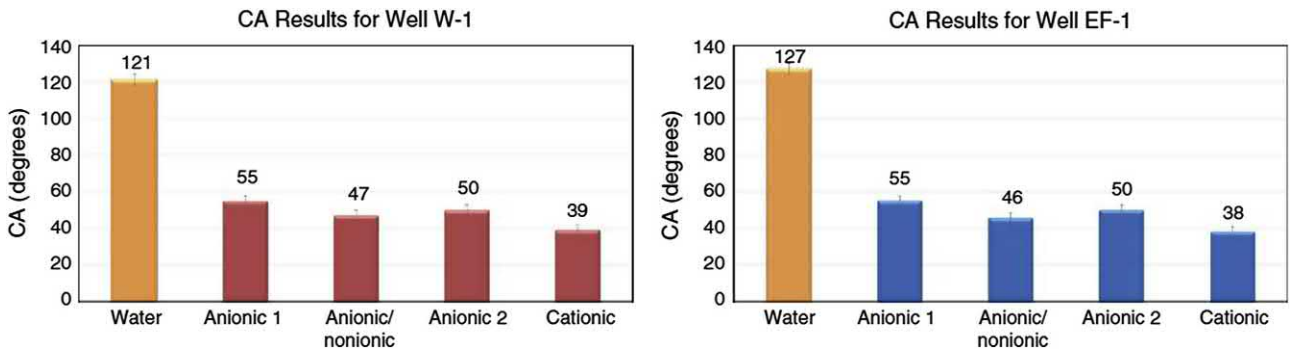

Figure 9.26 Contact angles of different surfactant solutions of a concentration of 2 gpt on Wolfcamp carbonate cores from Well W-1 and on Eagle Ford carbonate cores from Well EF-1 (Alvarez et al., 2018).

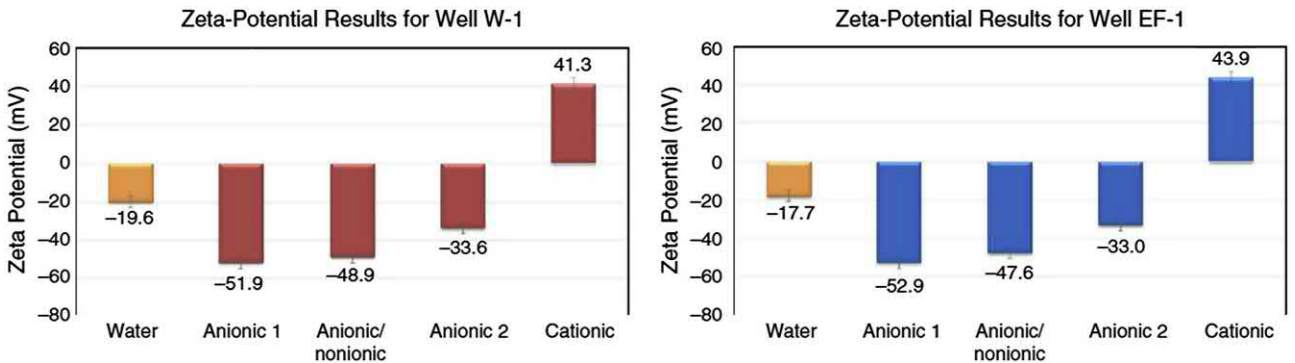

Figure 9.27 Zeta potentials of different surfactant solutions of a concentration of 2 gpt on Wolfcamp carbonate cores from Well W-1 and on Eagle Ford carbonate cores from Well EF-1 (Alvarez et al., 2018).

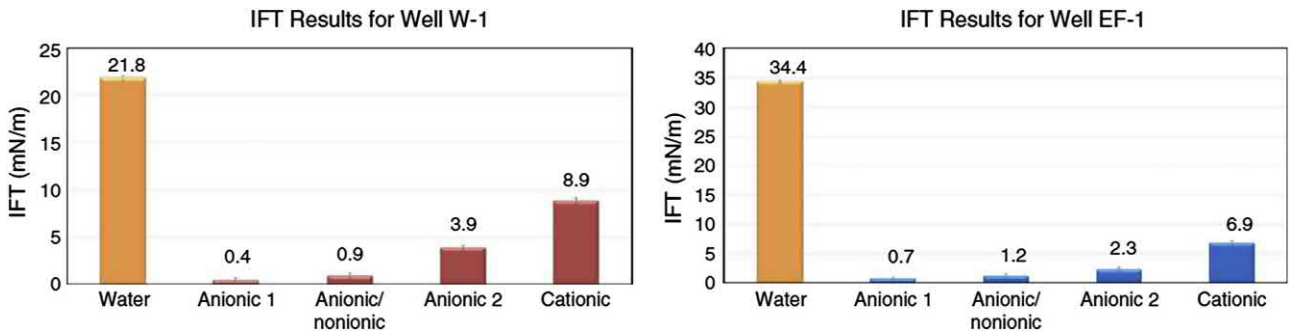

Figure 9.28 IFTs of different surfactant solutions of a concentration of 2 gpt on Wolfcamp carbonate cores from Well W-1 and on Eagle Ford carbonate cores from Well EF-1 (Alvarez et al., 2018).

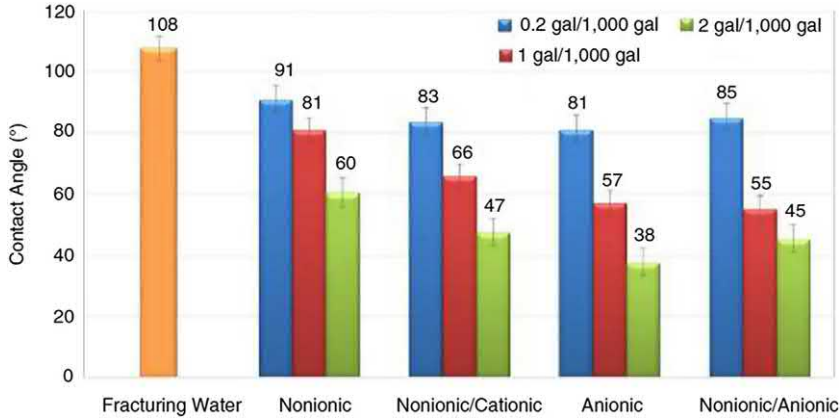

Figure 9.29 Contact angles of surfactant solutions on Wolfcamp siliceous cores from the same well depth (Alvarez and Schechter, 2017).

in a separate set of contact angle measurements in Fig. 9.29. Similarly, to the above carbonate cores, the absolute values of zeta potential for the anionic solutions were lower than those for the nonionic/cationic solutions for the siliceous cores as shown in Fig. 9.30, not consistent with their contact angle values. The IFT of the nonionic/cationic solution is higher than that of the anionic solution, resulting in the much higher final capillary pressures, but the nonionic/cationic solution had lower oil recovery. This indicates that the lower wetting angle is more favorable to oil recovery than the higher IFT. Generally, anionic surfactants have lower IFT than nonionic or cationic surfactants.

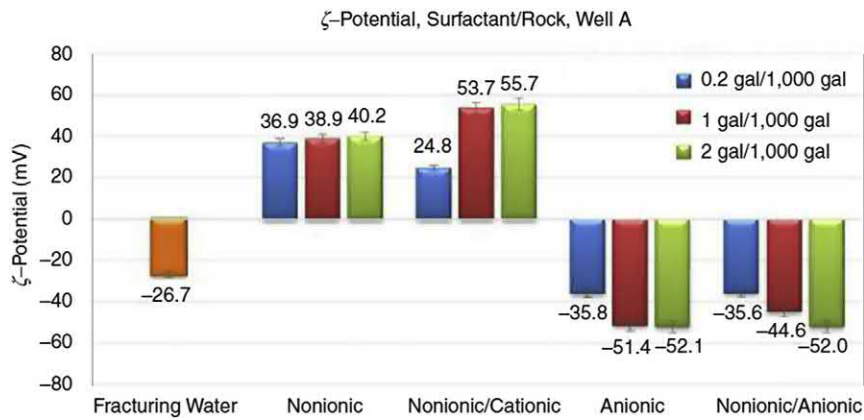

Figure 9.30 Zeta potentials of different surfactant solutions of a concentration of 2 gpt on Wolfcamp siliceous cores (Alvarez and Schechter, 2017).

Table 9.5 A guideline to select surfactants.

	Sandstone	Carbonate
Rock surface charge	−	+
Adsorbed oil compounds	Weakly acidic, e.g., alkylated quinolones pyridines	Weakly basic, e.g., organic carboxylic acids
Preferred surfactants	Anionic	Cationic

The above discussions may be summarized in Table 9.5.

Fluorocarbon surfactants are used to alter the wettability to less liquid-wet or more gas-wet in gas condensate reservoirs. This has been discussed in Chapter 4.

9.8 Determination of wettability

Since wettability alteration is very important in shale and tight reservoirs, the wettability must be correctly measured or determined. Before discussing the methods to determine the wettability of a shale or tight core, the methods including those used in conventional cores are reviewed.

9.8.1 Commonly used methods

First clarify the terminology about intermediate wet, fractional wet, and mixed wet. Anderson (1986, 1987) define the system as neutrally wet, if the contact angles (measured through the water phase) are 60−75 to 105−120°, it is water-wet below 60−75°, and it is oil-wet above 105−120°. It is implied that neutrally wet was synonymous to intermediate wet. Strictly speaking, being neutrally wet, the contact angle should be close to 90° (Dandekar, 2013). Fractional wettability refers to the system where some of the pores are water-wet, while others are oil-wet. Jerauld and Rathmell (1997) state that fractional wettability is when there are oil-wet and water-wet regions in the same pore. Although mixed wettability was proposed by Salathiel in 1973, referring to a special type of fractional wettability in which the oil-wet surfaces form continuous paths through the larger pores, mixed wettability is widely used, and it actually refers to fractional wettability. In the modern literature, mixed wettability is more often used than fractional wettability.

Typical methods to determine wettability are contact angle measurement, Amott method (often called Amott−Harvey method), U.S. Bureau of Mines (USBM) method, and combined Amott-USBM method. The method to measure contact angles is affected by the rock heterogeneity in wettability

and the surface roughness. The Amott method (Amott, 1959) or the Amott-Harvey method (Boneau and Clampitt, 1977) measures the "overall or average" wettability of a core. Although the formulas vary, the common principle is that the wetting fluid will imbibe into the core more than the nonwetting fluid. For the Amott-Harvey method, at the end of spontaneous imbibition, forced imbibition is continued. One problem for the Amott method and Amott-Harvey method is that spontaneous imbibition in shale or tight cores is very slow; therefore, a long test time is needed. This method may have its limited use in shale and tight cores.

In the US Bureau of Mines (USBM) method (Donaldson et al., 1969), a core sample is spun in a water-filled centrifuge tube. After several spin rates, the sample reaches residual oil saturation, S_{or}, and then it is placed into an oil-filled tube for another series of measurements. This method consists of two stages: the primary forced imbibition and the secondary forced drainage. The centrifuge force represents capillary pressure. If the capillary pressure in the forced water imbibition process is lower than that in the oil drainage process, the core is more water-wet, and vice versa. For the currently available centrifuge instruments, the centrifuge force is not high enough to displace out the fluids in a shale or tight core. Therefore, this method cannot be used in shale or very tight cores.

In the USBM tests, spontaneous imbibition is not measured, but it occurs during initial centrifugation at low pressures. Consequently, the combined Amott-USBM method (Sharma and Wunderlich, 1987; Anderson, 1986) is preferred. In the test, spontaneous imbibition is carried out in an Amott cell, while forced imbibition is carried out in a high-speed centrifuge using the same multiple speeds as those used for the USBM test.

9.8.2 Capillary rise method and thin layer wicking method

The height h of a wetting phase in a capillary tube is calculated by

$$h = \frac{p_c}{\Delta\rho g} \tag{9.38}$$

The capillary pressure p_c is calculated by

$$p_c = \frac{2\sigma cos\theta}{r} \tag{9.39}$$

where $\Delta\rho$ is the density difference between the wetting and nonwetting fluids, σ is the interfacial tension, θ is the contact angle, r is the radius of the capillary tube, and g is the gravity constant. The contact angle is estimated

from the above equations (Siebold et al., 1997). The thin layer wicking method is also based on the same principle. In this method, glass slides covered with particles are vertically immersed in a liquid and the height of the rising liquid is measured using a video camera (Van Oss et al., 1992).

9.8.3 Spontaneous imbibition method

For shale and tight rocks, the wettability is commonly determined by measuring contact angles and spontaneous imbibition volumes of water and oil. The principle is that water imbibition volume will be higher if one rock is more water-wet than the other (Zhou et al., 2000). The rock is more water-wet if more water is imbibed than oil. Similarly, if the water-wetting (contact) angle is smaller, it is more water-wet. But wetting angle must be measured in a system of liquid-liquid not liquid-gas, as discussed later. Lan et al. (2015a) defined the wettability index of water (WI_w) and the wettability index of oil (WI_o):

$$WI_w = \frac{V_{w1}}{V_{w1} + V_{o2}} \tag{9.40}$$

$$WI_o = \frac{V_{o2}}{V_{w1} + V_{o2}} \tag{9.41}$$

where V_{w1} is the normalized water volume imbibed into the dry plug 1, and V_{o2} is the normalized oil volume imbibed into the dry plug 2; the plug 1 and plug 2 are twin plugs. The normalized volumes are calculated by dividing the final equilibrium volumes of water and oil by their plug pore volumes, respectively. These normalized volumes V_{w1} and V_{o2} are actually imbibition saturations S_{w1} and S_{o2}, respectively. In their experiments, the core plugs were set vertically, and the bottom face of each plug contacted with imbibing water or oil. Then the water gravity and oil gravity are different in the experiments. Strictly speaking, the plugs should be set horizontally.

Note that it is implied in the literature that a higher imbibition volume corresponds to a higher imbibition rate when the wettability is evaluated using water and oil for imbibition. This may not be necessarily true. When the imbibition rate is compared, we need to consider the differences of fluid viscosities and surface tensions of water and oil. Therefore, we propose to conduct countercurrent imbibition experiments. For a twin plug initially saturated oil, measure the imbibed water volume (saturation); for the other

twin plug initially saturated with water, measure the imbibed oil volume (saturation). The wettability indices are defined as follows.

$$WI_w = \frac{S_{w1}}{S_{w1} + S_{o2}} \tag{9.42}$$

$$WI_o = \frac{S_{o2}}{S_{w1} + S_{o2}} \tag{9.43}$$

The plugs must be set horizontally, especially when the interfacial tension is low because gravity is relatively more important.

9.8.4 Pore-space imaging methods

Recent advances in microtomography have allowed the noninvasive imaging of fluid distributions in rocks at reservoir conditions. Andrew et al. (2014) characterized the effective contact angle directly in a carbonate-brine-scCO_2 system at reservoir conditions using the microtomography (micro-CT imaging) technology, as shown in Fig. 9.31. The micro-CT

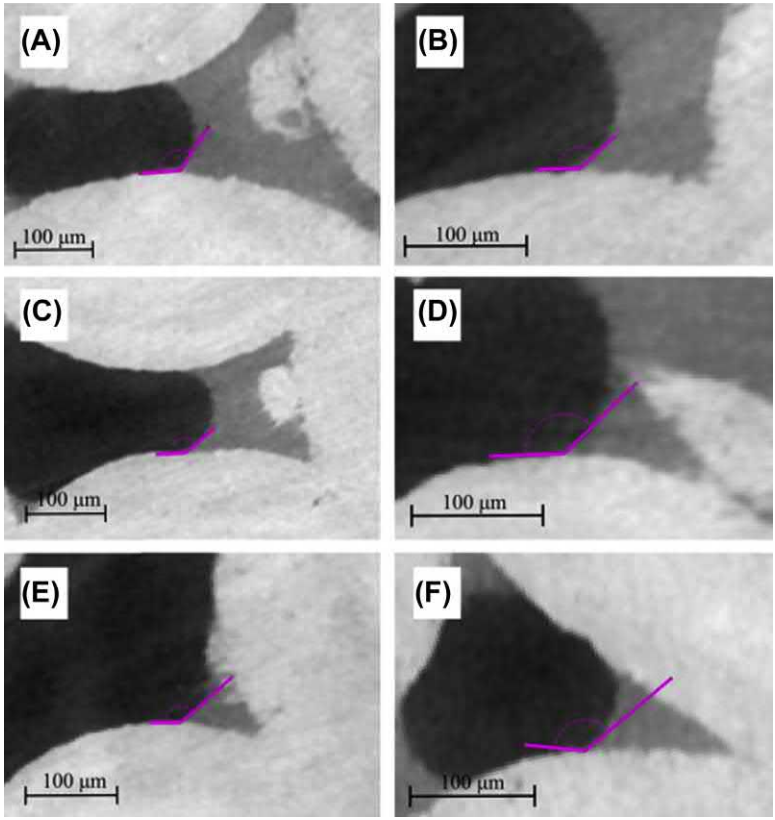

Figure 9.31 Contact angles measured directly in a rock sample (Andrew et al., 2014).

data are resampled onto a plane perpendicular to the contact line, and the contact angle is measured manually by tracing vectors tangential to the solid surface and the $scCO_2$–brine interface. Although this technology requires detailed imaging and sophisticated experimental methods, it can image multiphase fluid configurations at reservoir conditions. The images can be taken at many locations and a statistical analysis can be conducted. This direct approach has been used successfully to predict fluid configurations and multiphase properties using contact angles measured using a combination of micro-CT scanning, high-resolution SEM images and imaging to determine the chemical composition of the rock surface (Idowu et al., 2015). However, for nanopore systems, the resolution is an issue. Kumar et al. (2008) used atomic force microscope to study wettability alteration by surfactants.

Akbarabadi et al. (2017) used nano-CT to directly study fluid occupancy inside nanopores of ultratight reservoir rock samples, and to investigate spontaneous imbibition and pore-scale wettability.

9.8.5 Nuclear magnetic resonance (NMR) method

Nuclear magnetic resonance (NMR) method is a fast and nondestructive method to study wettability. NMR occurs in a nuclear system. In a porous medium, the amplitude of NMR signal is proportional to the number of hydrogen atoms in the hydrogenous fluid. Thus, this technology can be used to study the hydrocarbon and water distribution in the porous medium. Thereare two kinds of NMR relaxations during the dipole moment time evolution: longitudinal relaxations (T_1), transverse relaxations (T_2). T_2 spectrum is more widely used than T_1 because it requires less measured time and can provide the same pore information. At the solid-liquid interface, molecular motion is slower than that in the bulk liquid (Brown and Fatt, 1956). The solid surface slows down the molecular spin; longer relaxation time is needed to adjust to a new magnetic field. The relaxation rate is reflected on the transverse relaxation time T_2, with higher rate (v) corresponding to longer T_2 (v proportional to $exp(-t/T_2)$. The magnitude of this effect depends on the solid area covered by the liquid which is related to the wettability characteristics of the solid with respect to the liquid. The wettability of the surface can reduce the relaxation time. Oil-wet surfaces cause a smaller reduction in relaxation time than water-wet surfaces. In other words, if the rock is more water-wet, T_2 will be smaller.

The relationship among the transverse relaxation time T_2 in porous media, the transverse relaxation time of the bulk liquid $T_{2,\text{bulk}}$, the surface area A of the pore, the surface relativity ρ, and the volume of the pore is (Looyestijn and Hofman, 2006)

$$\frac{1}{T_2} = \frac{1}{T_{2,\text{bulk}}} + \rho\frac{A}{V} \tag{9.44}$$

The effect of fluid diffusion ($DGT_E\gamma/12$) can be added in the above equation, D is the fluid diffusion coefficient (cm^2/s), G is the magnetic gradient, T_E is the echo spacing of measurement sequence (ms), and γ is the gyromagnetic ratio. In the experiment conditions where the magnetic-field of the NMR apparatus is relatively uniform, and the magnetic gradient G is too small, the diffusion relaxation can be ignored. The bulk relaxation $T_{2,\text{bulk}}$ may not be considered because it takes much longer time than the surface relaxation in a tight porous medium. Thus, the T_2 relaxation time measured is mainly determined by the surface relaxation. If the pores are smaller, the area-volume ratio is larger, T_2 will be shorter. A fluid in large pores has higher T_2 value because more nuclei are available to exhibit the NMR effect, and the fluid in small pores has lower T_2 value. T_2 relaxation time is in inverse proportion to specific surface of samples (Appel, 2004). In other words, the pore radius r is proportional to T_2 (Zhao et al., 2015):

$$T_2 = Cr \tag{9.45}$$

where C is the conversion constant.

The above equation can be applied to the system of oil and water that covers different areas of the solid A_o and A_w, respectively:

$$\frac{1}{T_{2,w}} = \frac{1}{T_{2,\text{bulk},w}} + \rho_w\frac{A_w}{VS_w} \tag{9.46}$$

$$\frac{1}{T_{2,o}} = \frac{1}{T_{2,\text{bulk},o}} + \rho_o\frac{A_o}{VS_o} \tag{9.47}$$

where the subscript w and o refer to water and oil, respectively, and S denotes the saturation. It can be understood that if the solid is more water-wet, water will cover more of the solid surface. Therefore, the wetting index I_w may be defined as

$$I_w = \frac{\text{surface wetted by water} - \text{surface wetted by oil}}{\text{total surface}} \tag{9.48}$$

Looyestijn and Hofman (2006) found that the quantitative NMR wettability index I_w shows a good agreement with the USBM index, as shown in Fig. 9.32.

Liu and Sheng (2019) used the NMR technique to study the effect of surfactant on wettability alteration. The cores were initially saturated with oil. Heavy water imbibed into the cores. Since heavy water did not have NMR signal but oil had some signal strength, the NMR signal amplitude decreased as more heavy water imbibed. Fig. 9.33 shows the NMR amplitude at different imbibition time for heavy water and the heavy oil of different surfactants at two surfactant concentrations of 0.01% and 0.1%. The following observations can be made.

First, those subfigures all show that the cores have two T_2 peaks, first one representing small radius pores, and the second large radius pores. The subfigure a shows that heavy water could hardly imbibe the small pores; as more heavy oil imbibed into large pores, more oil with NMR signal was displaced out, and the T_2 amplitude decreased with time.

The subfigures b and c show the T_2 amplitude when heavy water with surfactant IAE at 0.01% and 0.1% imbibed into the cores, respectively. Because the surfactant could change the wettability from oil-wet to

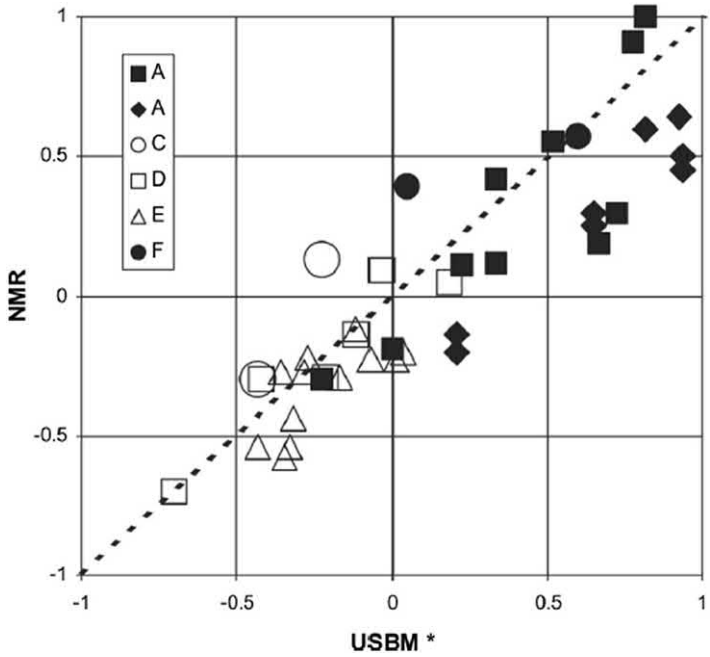

Figure 9.32 Comparison of NMR wettability index and USBM index (Looyestijn and Hofman, 2006).

water-wet, it could imbibe into small pores (indicated by the left peak). Similarly to the heavy water case, more heavy water with the surfactant imbibed into the cores, and T_2 decreased.

Comparing the subfigure b and the subfigure c, the T_2 spectrum curves became lower at the higher concentration, indicating higher concentration resulted in more wettability alteration from oil-wet to water-wet; therefore,

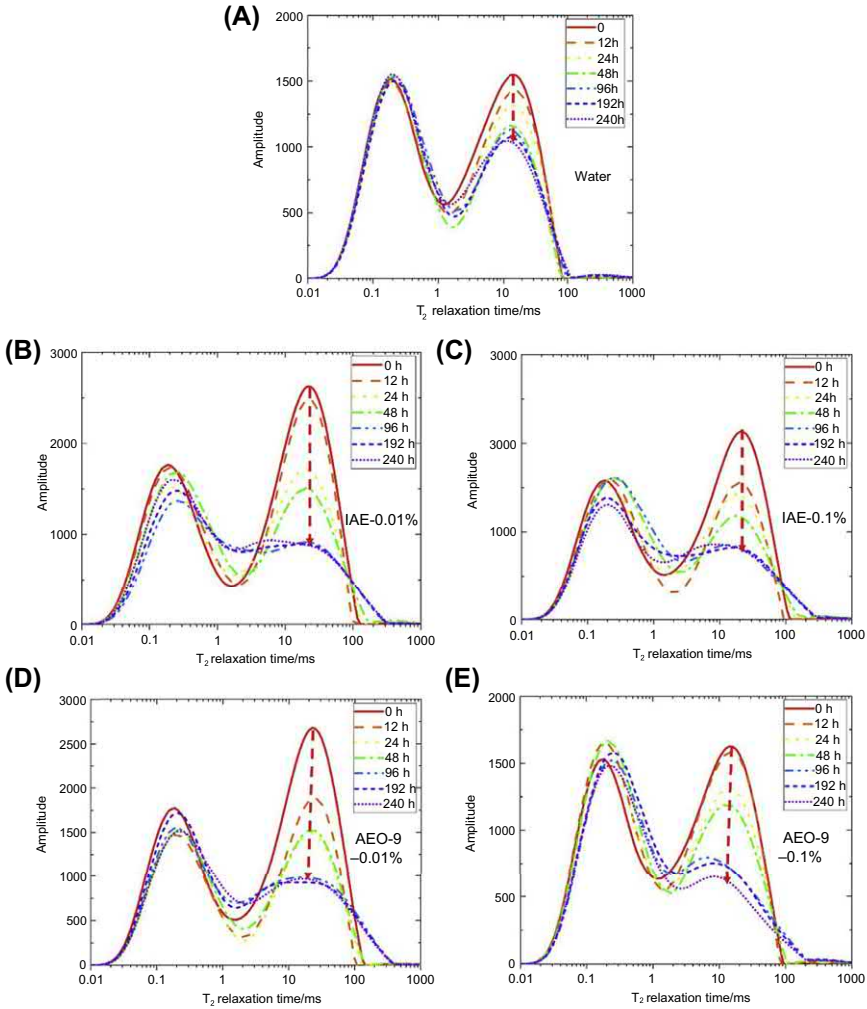

Figure 9.33 T_2 spectrum curves during the process of spontaneous imbibition in heavy oil and heavy water of different surfactants at two concentrations of 0.01% and 0.1%.

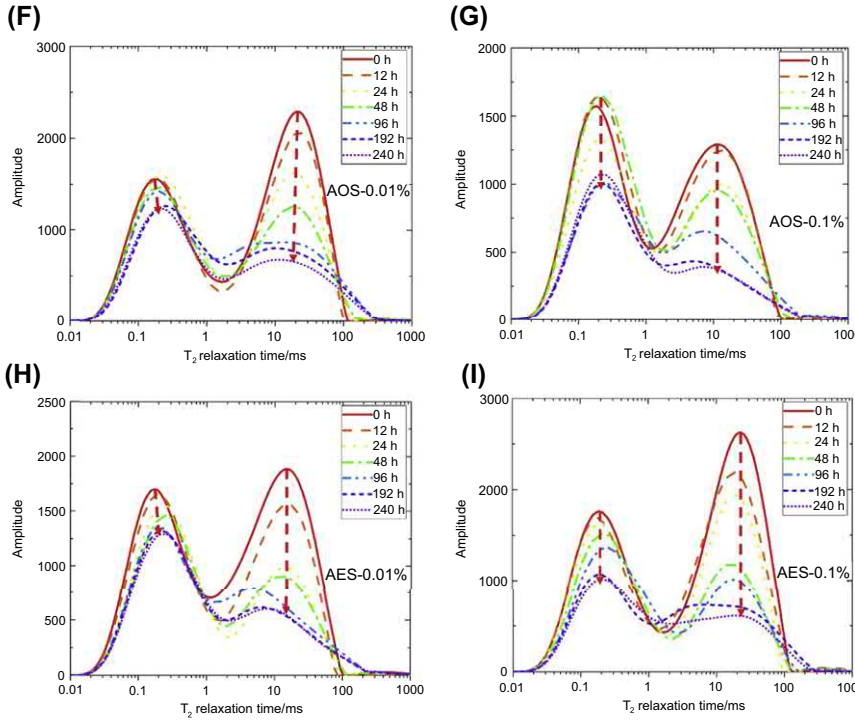

Figure 9.33 (*continued*).

more heavy water surfactant solution imbibed into the pores. Those observations also applied to the other surfactant solutions, except AEO-9 showed lower right peak at 0.1% than 0.01% which might be caused by the different cores.

Comparing the T_2 spectrums from the anionic surfactant solutions and nonionic surfactant solutions, the oil recovery from small pores were more improved by anionic surfactants than by nonionic surfactants, which was caused by the more wettability alteration by anionic surfactants.

9.8.6 Zeta potential (ζ-potential) measurements

Refer to Fig. 9.34, when a particle is surrounded by a liquid, two layers are formed. One is the stern layer where ions are attracted near the particle surface due to the surface charge. The other layer is the diffuse layer that is composed of ions attracted to the surface charge via the coulomb force, electrically screening the first layer. This diffuse layer is loosely associated with the particle because ions can move freely owing to electric attraction and thermal motion. Between the two layers, there is a slipping plane that divides the moving fluid

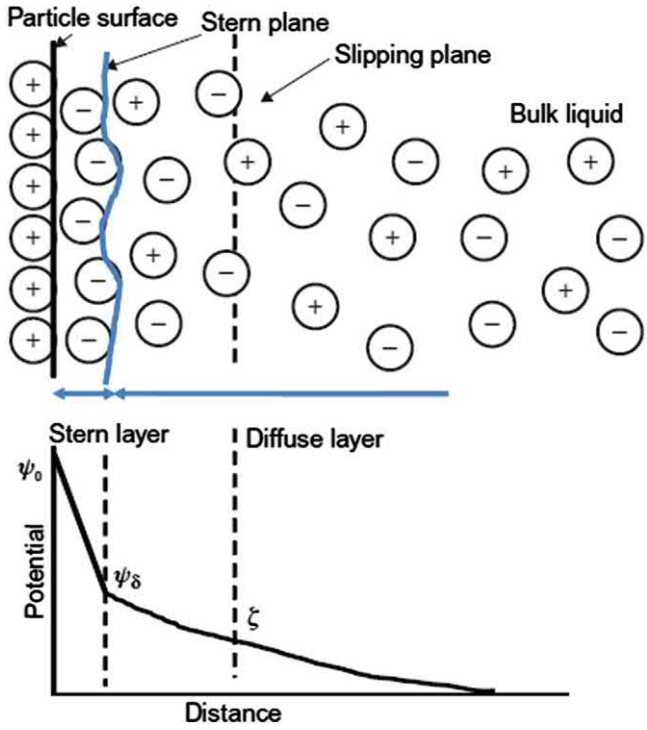

Figure 9.34 Schematic of electric double layer.

and the fluid attached to the particle. The ζ-potential is the electrokinetic potential at the slipping plane.

The surface charges at the rock/brine interface determine the magnitude of the ζ-potential. When the absolute value of the ζ-potential is great, the repulsion between the rock/brine interface and the brine/oil interface is stronger, which makes the water film more stable and makes it easier for oil film to be detached from the rock surface, thus, the rock surface is more water-wet.

9.8.7 Discussion of methods to determine wettability

Refer to Fig. 9.35, the interfacial tensions σ and the wettability indices $cos\theta_{ws}$ and cos θ_{os} at equilibrium in an oil-water-solid system have the following relationships:

$$cos\theta_{ws} = \frac{\sigma_{os} - \sigma_{ws}}{\sigma_{wo}} \tag{9.49}$$

$$cos\theta_{os} = \frac{\sigma_{ws} - \sigma_{os}}{\sigma_{wo}} \tag{9.50}$$

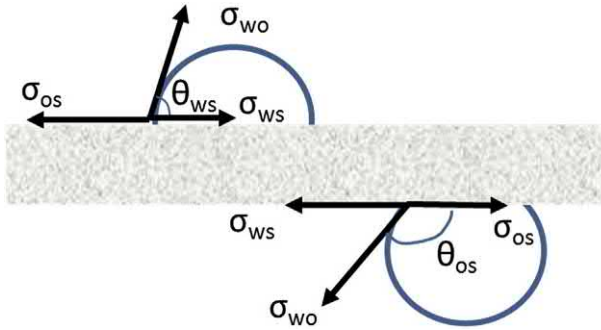

Figure 9.35 Interfacial tensions and wetting angles at equilibrium.

where the subscripts *s*, *w*, and *o* represent solid phase, water phase, and oil phase, respectively. According to Eqs. (9.49) and (9.50), $cos\theta_{ws} = -cos\,\theta_{os}$. So, the oil contact angle $\theta_{os} = \pi - \theta_{ws}$. For a water-wet rock, the water-wetting angle is less than 90°, and the oil-wetting angle is higher than 90°. Therefore, we have **Conclusion 1**:

In a water-oil-solid system (a liquid-liquid-solid system), a water-wetting angle or an oil-wetting angle on a core can be used to determine the wettability.

In an air-liquid-solid system, the preceding two equations become

$$cos\theta_{wsa} = \frac{\sigma_{as} - \sigma_{ws}}{\sigma_{wa}} \tag{9.51}$$

$$cos\theta_{osa} = \frac{\sigma_{as} - \sigma_{os}}{\sigma_{oa}} \tag{9.52}$$

by replacing *o* by *a* and replacing *w* by *a*, respectively in those two equations. The subscript "*a*" is added to represent the presence of air. Generally, a rock is more liquid-wet than gas-wet. Thus, both $cos\theta_{wsa}$ and $cos\theta_{osa}$ are positive. From the preceding two equations, we have

$$\begin{aligned} cos\theta_{wsa} - cos\theta_{osa} &= \frac{\sigma_{as} - \sigma_{ws}}{\sigma_{wa}} - \frac{\sigma_{as} - \sigma_{os}}{\sigma_{oa}} = \frac{\sigma_{as}(\sigma_{oa} - \sigma_{wa}) - \sigma_{ws}\sigma_{oa} + \sigma_{wa}\sigma_{os}}{\sigma_{wa}\sigma_{oa}} \\ &= \frac{\sigma_{as}(\sigma_{oa} - \sigma_{wa}) - \sigma_{ws}(\sigma_{oa} - \sigma_{wa}) + \sigma_{wa}(\sigma_{os} - \sigma_{ws})}{\sigma_{wa}\sigma_{oa}} \\ &= \frac{(\sigma_{oa} - \sigma_{wa})(\sigma_{as} - \sigma_{ws}) + \sigma_{wa}(\sigma_{os} - \sigma_{ws})}{\sigma_{wa}\sigma_{oa}}. \end{aligned} \tag{9.53}$$

Now we consider a water-wet rock. Refer to Eq. (9.49), $\sigma_{os} > \sigma_{ws}$ for a water-wet rock because the cosine term should be positive. Then the second term of the above numerator is positive. Similarly, for the first term of the above numerator, $\sigma_{as} > \sigma_{ws}$ because a rock generally prefers water-wet to air-wet; and generally, $\sigma_{oa} < \sigma_{wa}$; Thus, the first term is negative. Now the numerator has one positive value and one negative value. Then $cos\theta_{wsa} - cos\theta_{osa}$ could be negative or positive. Therefore, the θ_{wsa} measured on a water-wet rock may not necessarily be smaller than θ_{osa}. That means, even θ_{wsa} is greater than θ_{osa}, the rock may still be possibly water-wet. Therefore, we have **Conclusion 2**:

In a gas-water-solid system (a gas-liquid system), the water-wetting angle cannot be used to determine the wettability; similarly, in a gas-oil-solid system (a gas-liquid system), the oil-wetting angle cannot be used to determine the wettability.

One may think that if the volume of water imbibed into a dry core is higher than the oil volume, the rock is water-wet. According to Washburn's (1921) equation, the imbibition velocity of a fluid into a capillary tube of radius r is:

$$\frac{dl}{dt} = \frac{\left(\Delta\Phi + \frac{2\sigma cos\theta}{r}\right) r^2}{8\mu l} \tag{9.54}$$

where l is the imbibition distance, Φ is the potential, t is the imbibition time, σ is the interfacial tension, μ is the phase viscosity, and θ is the contact angle. For spontaneous imbibition, $\Delta\Phi$ is zero. The imbibition volume can be obtained by integrating the preceding equation:

$$V^2 = \frac{\pi^2 \sigma cos\theta r^5}{2\mu} t \tag{9.55}$$

Then the ratio of spontaneous imbibition volume of water to that of oil is

$$\frac{V_w}{V_o} = \sqrt{\frac{\sigma_{wa} cos\theta_{wa} \mu_o}{\sigma_{oa} cos\theta_{oa} \mu_w}} \tag{9.56}$$

If $V_w > V_o$, $\sigma_{wa}\mu_o cos\theta_{wa} > \sigma_{oa}\mu_w cos\theta_{oa}$. Since $\sigma_{wa} > \sigma_{oa}$, and $\mu_o > \mu_w$, generally, $cos\theta_{wa}$ may not necessarily greater than $cos\theta_{oa}$. Thus, the rock is not necessarily water-wet. If $V_w < V_o$, $\sigma_{wa}\mu_o cos\theta_{wa} < \sigma_{oa}\mu_w cos\theta_{oa}$. Since $\sigma_{wa} > \sigma_{oa}$, and $\mu_o > \mu_w$, generally, $cos\theta_{wa}$ must be smaller than $cos\theta_{oa}$. Thus, the rock is oil-wet.

Thus, if $\sigma_{wa} > \sigma_{oa}$, and $\mu_o > \mu_w$, we have **Conclusion 3**:

If the volume of water imbibed into a dry core is lower than the oil volume imbibed into the same dry core (gas-liquid systems), the rock is oil-wet; but if the volume of water imbibed into a dry core is larger than the oil volume imbibed into the same dry core (gas-liquid systems), the rock is not necessarily water-wet (the water-wetness cannot be determined by comparing the imbibition volumes).

Conclusions 2 and 3 can be used to explain the paradoxical wettability data of Montney and Horn River shale samples reported by Lan et al. (2015b). For the Montney shale samples, the water-wetting angle and oil-wetting angle on the dry cores were 45 and 0° (shown in Table 9.6 later), indicating oil-wet. The wetting indices for water were 0.26—0.42 (<0.5), indicating oil-wet. And the water volumes imbibed into similar Montney cores were lower than the imbibed oil volumes, as shown in their Fig. 9.36, indicating oil-wet. All the above data consistently showed that the Montney cores were oil-wet.

For the Horn River shale samples, the water contact angles were 37—73° (not higher than 90°) and the oil contact angles were 0° (see Table 9.6 later), indicating oil-wet. But the water wetting indices were 0.67—0.77 (>0.5), indicating water-wet. According to Conclusion 2, these wetting angles cannot be used to determine the wettability. Actually, according to the estimated wetting angles in the corresponding water-oil-solid systems, those shale samples were likely to be water-wet (see Table 9.6 later). The imbibed water volumes into Horn River samples were higher than the imbibed oil volumes, as shown in Fig. 9.37, indicating water-wet. According to Conclusion 3, the shale samples were not necessarily water-wet. Therefore, their data cannot consistently determine the wettability without using the Conclusions 2 and 3. However, Lan et al. (2015b) hypothesized that the higher water imbibition volumes were due to imbibition-induced microfractures, poor hydrophobic pore connection, and/or osmotic potential.

Liang et al. (2016) had similar observations for shale samples from Lower Longmaxi formation in China. The contact angles for water were 12—37° at elevated and normal temperatures, but the contact angles for oil were also 0°, indicating oil-wet. Actually, according to the estimated wetting angles in the corresponding water-oil-solid systems, those shale samples were likely to be water-wet (see Table 9.6 later). However, the water imbibition volumes were higher than oil imbibition volumes, indicating water-wet by the conventional misconception. Actually, according to Conclusion 3, the samples were not necessarily water-wet.

Table 9.6 Estimated water and oil contacting angles in oil-water-solid systems from their angles measured in air-liquid-solid systems.

References	Sample ID	θ_{wa} Deg	θ_{oa} Deg	σ_{wa} mN/m	σ_{oa} mN/m	σ_{wo} mN/m	θ_{os} Deg	θ_{ws} Deg	Comments
Roshan et al. (2016)	New South Wales CO_2 storage site	25	3	73.7	19.7	51.1	157.2	22.8	Although $\theta_{wa} > \theta_{oa}$, $\theta_{ws} < \theta_{os}$, WW
Roshan et al. (2015)	Evergreen sample _ DI, Surat basin, Australia	26	0	72	30	48	136.3	43.7	WW
	Evergreen sample _ 5% NaCl	30	0	72	30	48	132.6	47.4	WW
	Evergreen sample _ 10% NaCl	48	0	76	30	48	115.8	64.2	WW
Yassin et al. (2017)	Duvemay MIN1, Canada	103	0	47.8	23.3	35	13.4	166.6	$\sigma_{wo} = 35$ assumed to make $-1 \leq cos\theta \leq 1$. OW
	Duvemay MIN2	66	0	47.8	23.3	20	78.9	101.1	$\sigma_{wo} = 20$ assumed. OW
	Duvemay WAH1	78	0	62.5	23.5	20	58.3	121.7	$\sigma_{wo} = 20$ assumed. OW
	Duvemay WAH2	80	0	62.5	23.5	20	50.8	129.2	$\sigma_{wo} = 20$ assumed. OW
	Duvemay FER1	90	0	51.9	23.2	25	21.9	158.1	$\sigma_{wo} = 35$ assumed to make $-1 \leq cos\theta \leq 1$. OW
	Duvemay FER2	74	0	51.9	23.2	20	63.6	116.4	$\sigma_{wo} = 20$ assumed. OW
	Duvemay SAX1	74	0	46.5	22.3	20	61.7	118.3	$\sigma_{wo} = 20$ assumed. OW

	Duvemay CEC1	82	0	51.9	23.2	20	37.0	143.0	σ_{wo} = 20 assumed. OW
	Duvemay CEC2	65	0	51.9	23.2	20	86.4	93.6	σ_{wo} = 20 assumed. OW
Dehghanpour et al. (2012)	Horn River FS, Canada	27	0	72	30	35	167.4	12.6	σ_{wo} = 35 assumed to make $-1 \leq cos\theta \leq 1$. WW
	Horn River Muskwa	38	0	72	30	35	139.8	40.2	σ_{wo} = 35 assumed to make $-1 \leq cos\theta \leq 1$. WW
	Horn River Muskwa	45	0	72	30	25	146.8	33.2	σ_{wo} = 25 assumed. WW
	Horn River Otter Park	46	0	72	30	25	143.2	36.8	σ_{wo} = 25 assumed. WW
	Horn River Otter Park	50	0	72	30	25	130.6	49.4	σ_{wo} = 25 assumed. WW
Lan et al. (2015b)	Montney, Canada	45	0						WI_w = 0.26 to 0.42, OW
	Horn River Muskwa	58	0	73.6	20.7	20	156.2	23.8	σ_{wo} = 20 assumed, WW. WI_w = 0.67, WW
	Horn River Otter Park	73	0	73.6	20.7	20	92.3	87.7	σ_{wo} = 20 assumed, IW. WI_w = 0.77 (WW)
	Horn River Evie	37	0	73.6	20.7	40	162.2	17.8	σ_{wo} = 40 assumed to make $-1 \leq cos\theta \leq 1$, WW. WI_w = 0.68, WW

(*Continued*)

Table 9.6 Estimated water and oil contacting angles in oil-water-solid systems from their angles measured in air-liquid-solid systems.—cont'd

References	Sample ID	θ_{wa} Deg	θ_{oa} Deg	σ_{wa} mN/m	σ_{oa} mN/m	σ_{wo} mN/m	θ_{os} Deg	θ_{ws} Deg	Comments
Liang et al. (2016)	Lower Silurian Longmaxi, China	33	0	72	28	35	157.1	22.9	$\sigma_{wo} = 35$ assumed (but 14.5 reported) to make $-1 \leq cos\theta \leq 1$. WW
	Lower Silurian Longmaxi	37	0	72	28	35	148.4	31.6	$\sigma_{wo} = 35$ assumed (but 11.7 reported) to make $-1 \leq cos\theta \leq 1$. WW
	Lower Silurian Longmaxi	33	0	72	28	35	159.2	20.8	$\sigma_{wo} = 35$ assumed (but 11.6 reported) to make $-1 \leq cos\theta \leq 1$. WW
Liang et al. (2015)	Lower Silurian Longmaxi	11	0	72	28	48	152.9	27.1	$\sigma_{wo} = 48$ assumed to make $-1 \leq cos\theta \leq 1$. WW
	Lower Silurian Longmaxi	13	0	72	28	48	151.8	28.2	$\sigma_{wo} = 48$ assumed to make $-1 \leq cos\theta \leq 1$. WW
	Lower Silurian Longmaxi	20	0	72	28	48	145.3	34.7	$\sigma_{wo} = 48$ assumed to make $-1 \leq cos\theta \leq 1$. WW

	Lower Silurian Longmaxi	20	0	72	28	48	146.1	33.9	σ_{wo} = 48 assumed to make $-1 \leq cos\theta \leq 1$. WW
	Lower Silurian Longmaxi	36	0	72	28	48	128.6	51.4	σ_{wo} = 48 assumed to make $-1 \leq cos\theta \leq 1$. WW
	Lower Silurian Longmaxi 3	39	0	72	28	48	126.0	54.0	σ_{wo} = 48 assumed to make $-1 \leq cos\theta \leq 1$. WW
Ksiezniak et al. (2015)	Baltic Basin, Poland	85	44	72	28.4	25	55.5	124.5	OW consistent with the authors claim
Engelder et al. (2014)	Haynesville	51	10	72	31	25	127.1	52.9	σ_{wo} = 25 assumed. WW
Teklu et al. (2015)	Three forks						146.2	33.8	Oil/formation water angle, directly measured, WW
Peng and Xiao (2017)	Eagle Ford	82	46	72	50.8	40	52.2	127.8	σ_{wo} = 40 assumed to make $-1 \leq cos\theta \leq 1$. OW
	Barnett	90	41	72	50.8	40	18.7	161.3	σ_{wo} = 48 assumed to make $-1 \leq cos\theta \leq 1$. OW
Mirchi et al. (2014)	A shale					20.3	107.4	72.6	Weekly WW

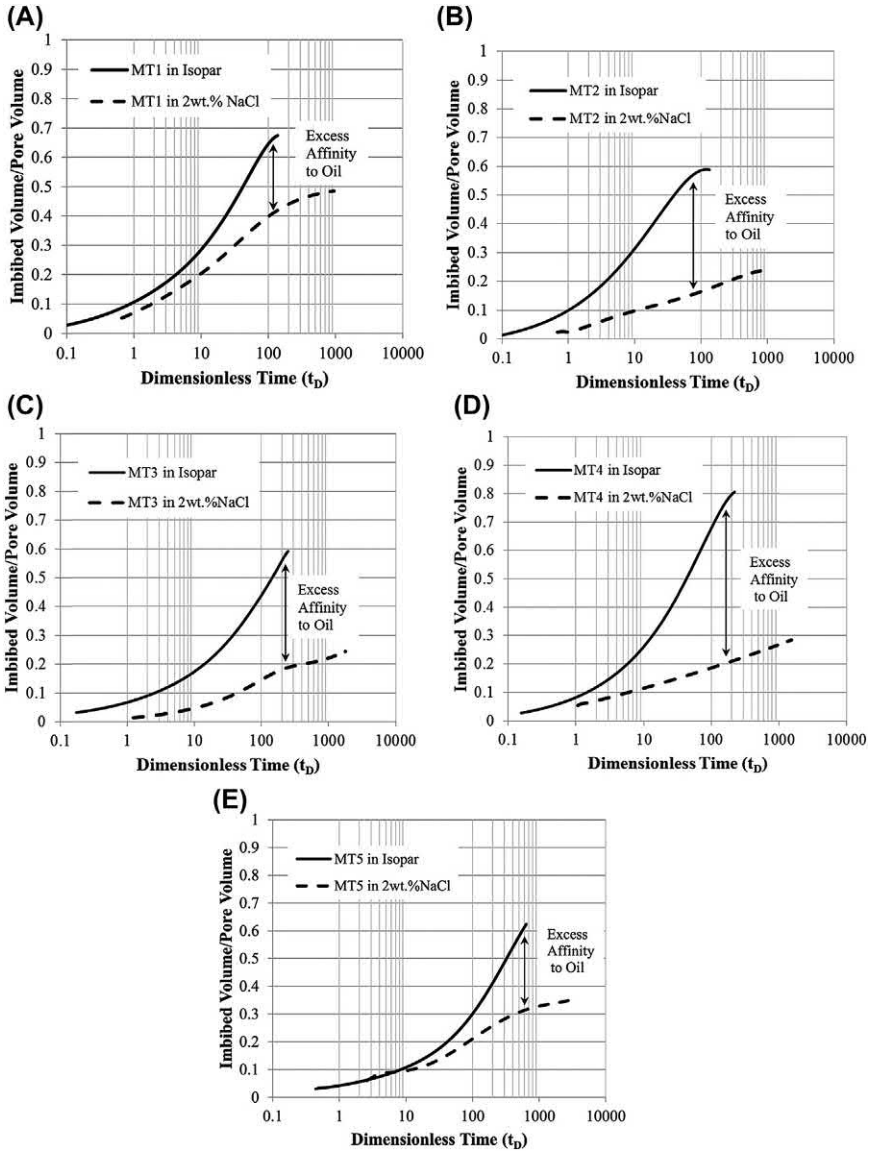

Figure 9.36 Normalized imbibed oil and brine volumes versus dimensionless time for intact Montney samples (Lan et al., 2015b).

Javaheri et al. (2017) did four different types of experiments: (1) a liquid contact angle measured on a system of air-liquid-flat surface system (air-liquid contact angle); (2) a water contact angle measured on a system of water-oil-flat surface system or an oil contact angle measured in a system

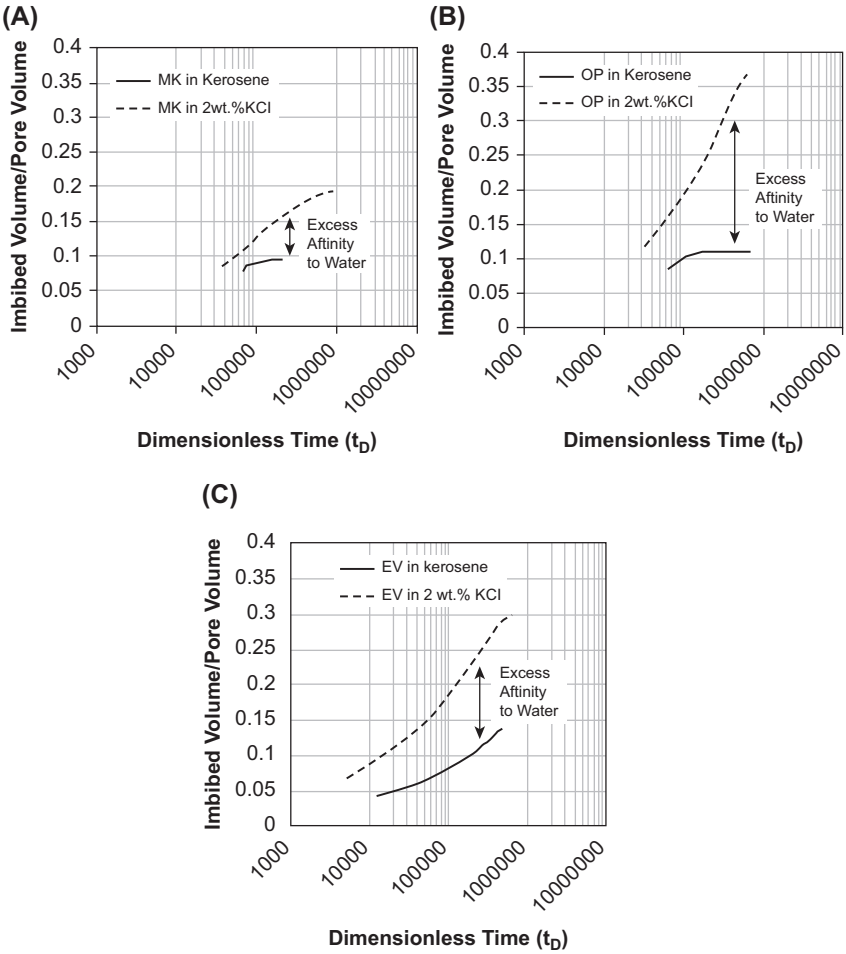

Figure 9.37 Normalized imbibed oil and brine volumes versus dimensionless time for intact Horn River samples (Lan et al., 2015b).

of oil-water-flat surface system (liquid-liquid contact angle); (3) Spontaneous imbibition of a liquid into a dry rock sample (initially air saturated), and (4) water imbibition into an oil-saturated rock sample (an Amott-type imbibition system). They found that the air-oil contact angles were smaller (e.g., as shown in Fig. 9.38A). According to Conclusion 2, such wetting angle cannot determine oil-wetness. They also observed that the oil volume by spontaneous imbibition into the dry rock sample (Fig. 9.39) was higher. According to Conclusion 3, it should be oil-wet. Without using Conclusions 2 and 3, one may think the oil-wetness can be determined, as Yassin

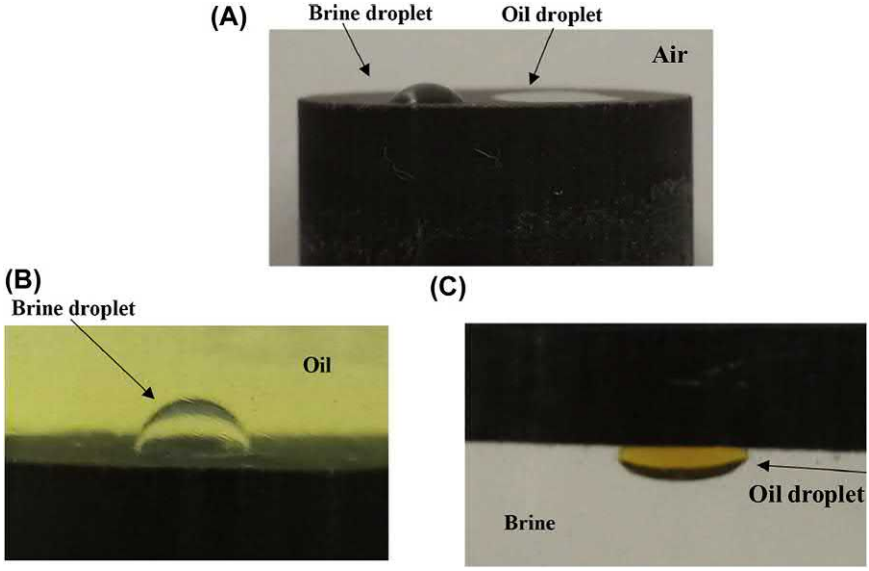

Figure 9.38 (A) air-liquid contact angles, (B) brine contact angle in the oil phase, (C) oil contact angle in the brine phase (Javaheri et al., 2017).

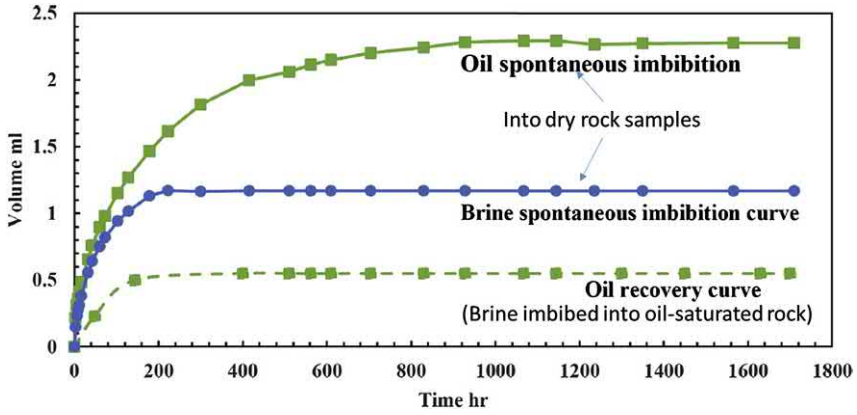

Figure 9.39 Oil and water imbibition volumes in dry rock samples and oil recovered from the Amott-type imbibition test (Javaheri et al., 2017).

et al. (2017) did for Duvernay cores. Fig. 9.40 shows that the brine contact angles for the same batch of rocks were higher, indicating oil-wet; but oil was recovered from the Amott-type imbibition tests as shown in Fig. 9.39, indicating water-wet. They interpreted water-wetness because the brine was able to imbibe into the oil-saturated rock samples in the Amott-type imbibition tests. Such interpretation may not be valid, because

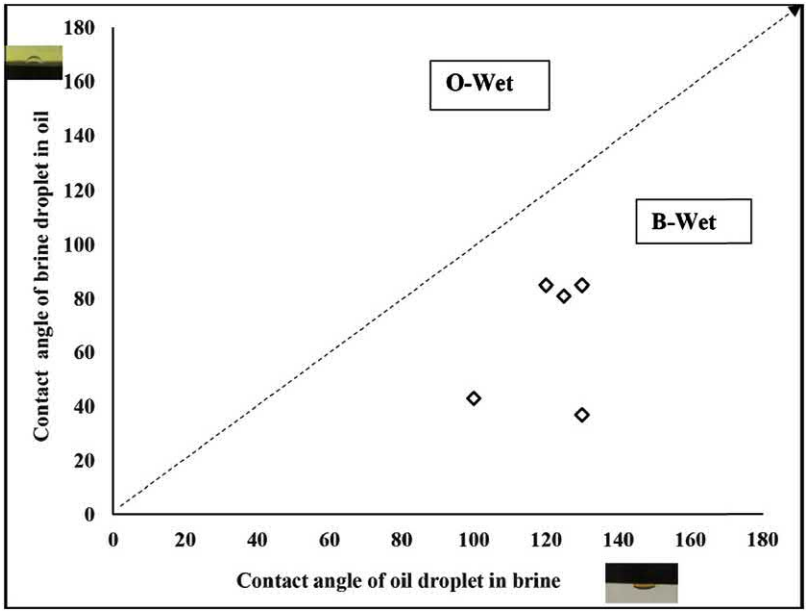

Figure 9.40 Oil and brine contact angles in the liquid-liquid systems (Javaheri et al., 2017).

oil might be able to imbibe in brine-saturated rock samples as well. Unfortunately, they did not do such imbibition tests. According to Conclusion 2, the water-wetting angle cannot be used to determine the wettability. In a separate study, Dehghanpour et al. (2012) observed higher water imbibition than oil imbibition into the core samples taken from the Horn River basin. According to Conclusion 3, the water-wetness cannot be determined.

Habibi et al. (2016) reported similar results or observations for Montney samples. The contact angles on dry, oil-, or water-saturated Montney samples showed oil-wetness; oil or water volumes imbibing in dry (fresh) samples also showed oil-wet; but the oil recovery by spontaneous water imbibition was about 25%—45%, whereas the water recovery by spontaneous oil imbibition was negligible, indicating water-wetness. We can see that different methods led to different conclusions about the wettability of the same rocks, without using Conclusions 2 and 3!

In a rock initially saturated with oil, by considering the effect of oil viscosity, the water volume by spontaneous imbibition is proportional to $t\sqrt{\frac{k}{\varphi}}\ \frac{\sigma_{wo}cos\theta_{wsi}}{\sqrt{\mu_o\mu_w}L_c^2}$, L_c is the characteristic length (Ma et al., 1997). The oil volume by spontaneous imbibition into an initially water saturated core should

be proportional to $t\sqrt{\frac{k}{\varphi}}\ \frac{\sigma_{wo}cos\theta_{osi}}{\sqrt{\mu_o\mu_w}L_c^2}$. The ratio of water volume (V_{wsi}) to oil volume (V_{osi}) by spontaneous imbibition is

$$\frac{V_{wsi}}{V_{osi}} = \frac{cos\theta_{wsi}}{cos\theta_{osi}} \tag{9.57}$$

θ_{wsi} and θ_{osi} are the water-wetting angle and oil-wetting angle during spontaneous imbibition, respectively. If $V_{wsi} > V_{osi}$, $cos\theta_{wsi} > cos\theta_{osi}$. Then $\theta_{wsi} < \theta_{osi}$, the core is more water-wet, and vice versa. Therefore, we have **Conclusion 4**:

The rock wettability can be determined by comparing the water and oil spontaneous volumes, if the core is initially saturated with oil or water; with higher water imbibition volume, the rock is water-wet.

During the forced imbibition, the water volume imbibed into the initially oil-saturated core is

$$V_{w,FI}^2 = \frac{\pi^2\left(\Delta\Phi_w + \frac{2\sigma_{wo}cos\theta_{ws}}{r}\right)r^6}{4\mu_w}t_{w,FI} \tag{9.58}$$

The oil volume imbibed into the initially water-saturated core is

$$V_{o,FI}^2 = \frac{\pi^2\left(\Delta\Phi_o + \frac{2\sigma_{wo}cos\theta_{os}}{r}\right)r^6}{4\mu_o}t_{o,FI} \tag{9.59}$$

The fraction of water volume by spontaneous imbibition in the total water imbibition volume, $\delta_{w,SI}$, is

$$\delta_{w,SI} = \frac{V_{w,SI}}{V_{w,SI}+V_{w,FI}} = \frac{\sqrt{\frac{2\sigma_{wo}cos\theta_{ws}}{r}t_{w,SI}}}{\sqrt{\frac{2\sigma_{wo}cos\theta_{ws}}{r}t_{w,SI}} + \sqrt{\left(\Delta\Phi_w + \frac{2\sigma_{wo}cos\theta_{ws}}{r}\right)t_{w,FI}}}$$

$$= \frac{1}{1+\sqrt{\left(1+\frac{\Delta\Phi_w}{p_{cw}}\right)\frac{t_{w,FI}}{t_{w,SI}}}}. \tag{9.60}$$

The fraction of oil volume by spontaneous imbibition in the total oil imbibition volume, $\delta_{o,SI}$, is

$$\delta_{o,SI} = \frac{V_{o,SI}}{V_{o,SI} + V_{o,FI}} = \frac{\sqrt{\frac{2\sigma_{wo}cos\theta_{os}}{r} t_{o,SI}}}{\sqrt{\frac{2\sigma_{wo}cos\theta_{os}}{r} t_{o,SI}} + \sqrt{\left(\Delta\Phi_o + \frac{2\sigma_{wo}cos\theta_{os}}{r}\right) t_{o,FI}}}$$

$$= \frac{1}{1 + \sqrt{\left(1 + \frac{\Delta\Phi_o}{p_{co}}\right) \frac{t_{o,FI}}{t_{o,SI}}}}. \tag{9.61}$$

In the above equations, p_{cw} and p_{co} are the water-oil capillary pressure, when respective water or oil imbibes; Φ_w and Φ_o are applied water and oil potentials, respectively.

For the Amott-Harvey method, the wettability is determined by the difference of $\delta_{w,SI}$ and $\delta_{w,SI}$.

In shale and tight cores, the spontaneous imbibition times and forced imbibition times are very long. It is not practical to use the Amott-Harvey method.

Recently, Siddiqui et al. (2018) raised three critical questions about wettability:

1. Which contact angle measurements represent in-situ reservoir wettability, air/water/rock, air/oil/rock, or oil/water/rock?
2. If oil/water/rock contact angle measurements represent actual reservoir wettability, can it really be reliable if it does not behave similarly in imbibition tests?
3. The electrostatic and chemical forces can significantly contribute to water and oil imbibition volumes in shales, and they are also very active in controlling contact angles on the rock surface. Why does the imbibition volume measurement lead to different wettability than that reached by contact angle measurements?

The above question 1 is answered by Conclusions 1 and 2 earlier in this chapter. Put it simply, the wettability cannot be determined by contact angles in a gas-liquid-solid system, and it must be determined in a liquid-liquid-solid system.

The above question 2 is answered by Conclusion 3: the water and oil volumes by spontaneous imbibition in two same dry cores cannot be used to determine the wettability.

The above question 3 is answered by Conclusions 3 and 4. In a water-oil-solid (liquid-liquid-solid) system, these two types of measurements are consistent. However, if two systems, air-oil-solid and air-water-solid (gas-liquid-solid system), are used, these two types of measurements may lead to different wettabilities.

9.9 Conversion of wetting angles

The preceding section explains why the wetting angles cannot be used to determine rock wettability if measured in gas-liquid-solid systems; but the water and oil wetting angles can be compared to determine the wettability in a water-oil-solid system according to Conclusion 1 discussed earlier. Logically, if the wetting angles in gas-liquid-solid systems can be converted to the wetting angles in the corresponding water-oil-solid system, then the wetting angle measurements can be used to determine the wettability.

From Eqs. (9.51) and (9.52),

$$\sigma_{ws} = \sigma_{as} - \sigma_{wa} cos\theta_{wsa} \tag{9.62}$$

$$\sigma_{os} = \sigma_{as} - \sigma_{oa} cos\theta_{osa} \tag{9.63}$$

Refer to Fig. 9.35

$$cos\theta_{ws} = \frac{\sigma_{os} - \sigma_{ws}}{\sigma_{wo}} = \frac{\sigma_{wa} cos\theta_{wsa} - \sigma_{oa} cos\theta_{osa}}{\sigma_{wo}} \tag{9.64}$$

Then the water and oil wetting angles can be calculated from the water and oil contacting angles in dry cores by the following equations:

$$\theta_{ws} = cos^{-1}\left(\frac{\sigma_{os} - \sigma_{ws}}{\sigma_{wo}}\right) = cos^{-1}\left(\frac{\sigma_{wa} cos\theta_{wsa} - \sigma_{oa} cos\theta_{osa}}{\sigma_{wo}}\right) \tag{9.65}$$

$$\theta_{os} = cos^{-1}\left(\frac{\sigma_{ws} - \sigma_{os}}{\sigma_{wo}}\right) = cos^{-1}\left(\frac{\sigma_{oa} cos\theta_{osa} - \sigma_{wa} cos\theta_{wsa}}{\sigma_{wo}}\right) \tag{9.66}$$

It is easier to measure wetting angles on dry cores. But they cannot be used directly to determine wettability. Instead, the water and oil wetting angles in water-oil-solid systems are estimated using the above equations. Some of the estimated wetting angles are summarized in Table 9.6.

In this table, if the oil/water interfacial tension σ_{wo} was not provided by the references, typical values of 20–30 mN/m are used. When these typical values are used, $cos\theta$ is outside the range of −1 to +1 in some cases. So other values are used. When nontypical values of σ_{wo} are used, sensitivities are

conducted to ensure that these values do not change the conclusions regarding the wettability for each of shale samples.

This table shows that both water and oil contact angles were less than 90° (except two water angles) and the oil contact angles were smaller (zero in most of the cases) than the water contact angles. By the conventional intuition or misconception, those shale rocks are believed to be oil-wet. However, as the table shows, the estimated water wetting angles are less than 90°, indicating water-wetness. It seems that more shale samples are water-wet. The author of this book also observed that when the IFT is low, the liquid drop is gradually collapsing into the rock or at least the drop is becoming smaller and smaller. When this observation is made, one may believe the shale samples are oil-wet; They may not, actually!

The conversion of wetting angle enables some paradoxical data about wettability. For example, Lan et al. (2015b) observed stronger oil uptake than water update by their tight siltstone rock samples, indicating strong oil-wet, but the water contact angle was greater than 37° (supposed to be higher than 90° if oil-wet). They believed that this phenomenon was caused by oil sorption onto the organic materials (primarily solid bitumen). However, as indicated by the estimated results in the above table, the sample might be water-wet. Liang et al. (2016) observed the similar behavior for shale samples from the Lower Longmaxi formation in China, but the water wetting angles were 12—37° at elevated and normal temperatures; but the estimated results in the above table indicate that the sample might be water-wet.

9.10 More on wettability of shale and tight formations

Overall, the wettability of shale rocks is mixed (possibly oil-wet and water-wet), similar to conventional sandstone rocks. It may not be dominantly oil-wet as one believes. Adsorption of asphaltenic components controls the wettability in conventional reservoirs (Kumar et al., 2008). Shale wettability depends on the total organic carbon (TOC) (Odusina et al., 2011). The mixed wettability results from the fact that different rock types have different wettabilities, as inorganic shale rocks are more likely water-wet, whereas the organic parts are more likely oil-wet.

From the measurements of contact angle and zeta potential, Wolfcamp cores and Eagle Ford cores demonstrated intermediate wet to oil-wet

(Alvarez et al., 2018). But those cores were aged for 4 weeks or 6 months. Eagle Ford shale cores were also found oil-wet (179°), after 1 day of aging in brine followed by 7 days of aging in oil at 80°C (Mohanty et al., 2017). Apparently, shale rocks were reported oil-wet or mixed wet (Odusina et al., 2011; Akbarabadi et al., 2017). However, it is possible that data were misinterpreted, as discussed in the preceding section.

Some authors stated that the wettability cannot be determined by measuring contact angles, because the measured contact angles are not consistent with imbibition experiments (Xu and Dehghanpour, 2014; Ghanbari and Dehghanpour, 2015). The inconsistency can be explained by the preceding discussions in this chapter.

Several authors (Odusina et al., 2011; Dehghanpour et al., 2013; Makhanov et al., 2014) observed that more water than oil imbibed into shales. They ascribed this phenomenon to absorption of water molecules by clays, as water adsorption may generate microfractures and thus increase sample permeability. But, those microfractures are generally generated in experiments when no confining pressure is applied. Under confinement, created microfractures may not be generated or may be closed later (Zhang and Sheng, 2017a,b; Zhang et al., 2017). However, it has been observed that more microfractures are generated under water imbibition than under oil imbibition (Makhanov, 2013). It is possible that more water imbibed may be caused by more microfractures generated under the experiments without confinement. Of course, it can be caused by water-wetness. Singh (2016) reviewed some theories that discuss the effect of liquid droplet size, and he stated this effect must be considered to determine wettability. Marmur (1988) proposed that if the water drop radius r_w satisfies the following condition, water can imbibe into oil-wet shares:

$$r_w < \frac{-r_c}{cos\theta} \tag{9.67}$$

where r_c is the capillary radius, and θ is the macroscopic contact angle.

Several researchers (Habibi et al., 2016; Yassin et al., 2017) including us observed that oil spread on shale rock surfaces in the presence of air, indicating oil-wetness. However, for the same rock samples, it was observed that the water contact angles in the presence of air could be acute, indicating water-wetness. The actual wettability could be opposite!

CHAPTER TEN

Spontaneous imbibition

Abstract

In shale and tight formations, imbibition, especially water imbibition, plays a very important role during fracturing and in enhancing oil and gas recovery. In this chapter, fundamentals of spontaneous imbibition and upscaling theories are first reviewed. Then the main factors which affect spontaneous imbibition are discussed. These factors include permeability and porosity, initial wettability, wettability alteration, interfacial tension diffusion, gravity, viscosity ratio, and initial water content. Countercurrent flow is compared with cocurrent flow. Finally, behaviors of different surfactants are discussed.

Keywords: Cocurrent flow; Countercurrent flow; Diffusion; Gravity; Initial wettability; Spontaneous imbibition; Surfactants; Upscaling; Viscosity ratio.

10.1 Introduction

Spontaneous imbibition is defined as the process in which a wetting phase imbibes into the rock (matrix). During the spontaneous imbibition, one fluid displaces another in a porous medium by capillary pressure. In shale and tight formations, imbibition, especially water imbibition, plays a very important role during fracturing and in enhancing oil and gas recovery. In this chapter, imbibition fundamentals and upscaling theories are first reviewed. Then the main factors which affect imbibition are discussed. These factors include permeability and porosity, initial wettability, wettability alteration, interfacial tension (IFT), diffusion, gravity, viscosity ratio, and initial water content. Countercurrent flow is compared with cocurrent flow. Finally, behaviors of different surfactants are discussed.

10.2 Discussion of some theoretical equations on spontaneous imbibition

McWhorter and Sunada (1990) derived a general two-phase Darcy equation for countercurrent imbibition. Schmid and Geiger (2013) demonstrated that the solution can be viewed as the capillary analog to the

Enhanced Oil Recovery in Shale and Tight Reservoirs
ISBN: 978-0-12-815905-7
https://doi.org/10.1016/B978-0-12-815905-7.00010-4

Buckley–Leverett (1942) solution for the viscous dominated flow. They derived one general scaling group that can represent many of the previously defined scaling groups with a different proportionality constant. No assumption is needed to derive such scaling groups other than those needed for Darcy's model. No fitting parameter needs to be introduced. Schmid and Geiger (2013) also showed that spontaneous imbibition can be better characterized by the total volume of the wetting phase imbibed than by the frontal movement of the wetting phase. Cai and Yu (2012) reviewed many imbibition equations. Here are listed a few for the convenience of later discussions. Some of the equations are used to upscale the relationship between the imbibition recovery and dimensionless time t_D in a laboratory-scale to that in a field scale.

10.2.1 Washburn's equation

Based on Poiseuille's law, Washburn (1921) derived an equation to describe imbibition velocity in a single capillary tube. The velocity equation can be restated as follows without including the coefficient of slip:

$$\frac{dl}{dt} = \frac{\left(\Delta\Phi + \frac{2\sigma\cos\theta}{r}\right)r^2}{8\mu l} \tag{9.54}$$

In the above equation, l is the imbibition distance, t is the imbibition time, Φ is the potential, σ is the interfacial tension, μ is the wetting phase viscosity, θ is the contact angle, and r is the capillary radius. For spontaneous imbibition, $\Delta\Phi$ is zero. The above equation becomes:

$$\frac{dl}{dt} = \frac{\sigma\cos\theta r}{4\mu l} \tag{10.1}$$

The velocity multiplied by πr^2 becomes the imbibition volume in a unit time. The integration results in an equation to describe imbibed volume versus time:

$$V^2 = \frac{\pi^2\sigma\cos\theta r^5}{2\mu}t \tag{9.55}$$

The equation shows that the volume of imbibition of a wetting phase versus the square root of imbibition time has a linear relationship. However, as early as 1920, Cude and Hulett (1920) observed that the volume curve becomes flat at later time. This is because in a porous medium, the pores have different radii, and the imbibition velocity is proportional to the radius

according to Eq. (10.1); initially the fluid imbibes into larger pores and later into smaller pores; therefore, the imbibition velocity becomes slower at late time. Another fact that can cause slow imbibition rate at late time is that the pressure inside the core builds up; this built pressure serves as a resistance to the imbibition. The late flat portion of the curve is not caused or represented by diffusion as Shen et al. (2016) interpreted.

Again from Eq. (10.1), we can see that the imbibition velocity into a smaller pore is lower than that into a larger pore; as the imbibition takes a longer time (longer l), the imbibition velocity becomes lower. Tagavifar et al.'s (2019) simulation results also approve this fact. Yang et al.'s (2016) experimental data showed that imbibition velocities were lower for lower porosity and permeability cores; their experimental velocities were lower than what the theory (Eq. 10.1) predicted; the lower their porosity and permeability, the lower their experimental velocity was, compared with the theoretical velocity.

Real experimental data in log(V) versus log(t) may not show the slope of 0.5. Hu et al. (2012) suggested the change of the slope of the curve represented the change in pore connectivity. Cai and Yu (2011) suggested the slope change was caused by pore tortuosity. Yang et al. (2016) suggested that the slopes reflected the pore distribution and pore connectivity, with the early slope reflected macropores (>50 nm), the middle and late slopes reflected meso- and micropores, as shown in Fig. 10.1.

For type "B," the linearity appears in the early time, suggesting relatively high permeability and good pore connectivity. The macropores are well-developed, and the pore size distribution is of a single-peak type. For type "S," the initial position has an "arc-shaped tail" which suggests $n_i > 0.5$ at the early imbibition stage and good pore connectivity. The macropores and mesopores are well developed, and the pore size distribution is of the two-peak-type. For type "A," the arc-shaped and convex behavior suggests a low initial time exponent ($n_i < 0.5$) and poor pore connectivity; the late time exponent (n_L) appears to be above 0.1 which suggests well-developed meso/micropores. The pores are narrowly distributed. For type "M," with complex multiporosity feature, the initial imbibition rate becomes lower, which suggests microfractures are embedded in the rock matrix, representing good-connected microfractures to poor-connected matrix pores. The macropores, mesopores, and micropores are developed, and the pore size distribution is of the multipeak type. Here macropores are >50 nm diameter, mesopores are between 2 and 50 nm, and micropores are <2 nm, according

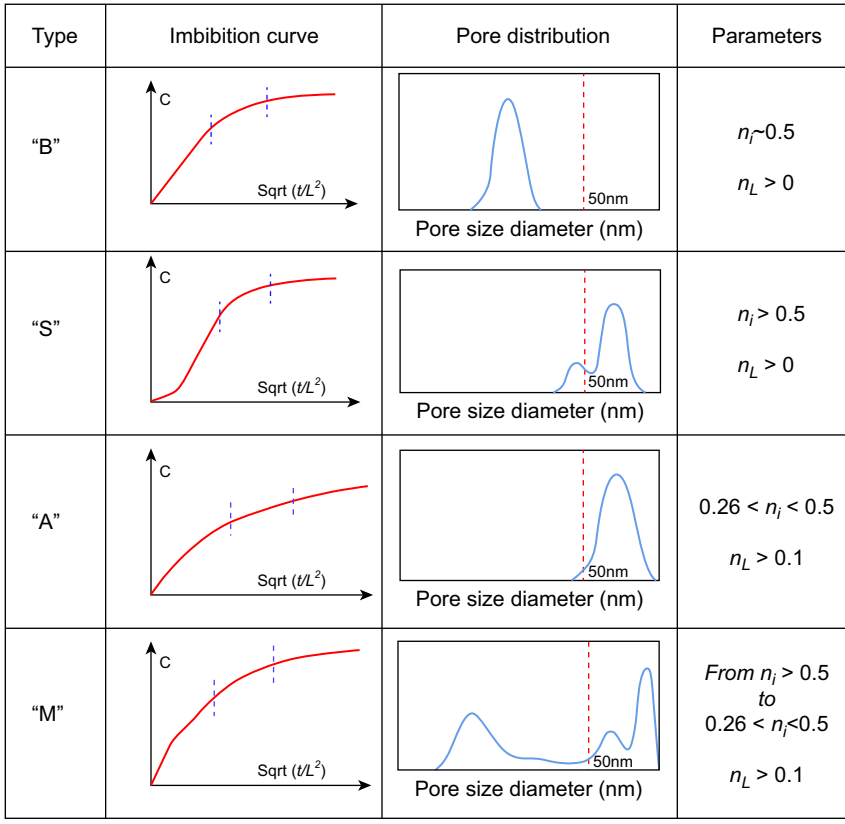

Figure 10.1 Imbibition characteristics of tight gas rocks, n_i is the early (initial) exponent, n_L is the late time exponent (Yang et al., 2016). Note that large pore sizes are in the left side of the axis.

to the International Union of Pure and Applied Chemistry (IUPAC) pore classification (Ross and Bustin, 2009).

10.2.2 Handy (1960) method

Assuming a pistonlike spontaneous imbibition, Handy (1960) derived an equation to predict that water imbibition volume (V_w) increases with the square root of imbibition time (t):

$$V_w^2 = \frac{2p_c k_w \varphi A^2 S_w}{\mu_w} t \tag{10.2}$$

In the above equation, p_c is the water-air capillary pressure at the front water saturation S_{wf}; S_w is the *average* water saturation behind the front

according to the Handy derivation; k_w is the effective water permeability at S_w; φ is the porosity; A is the flow cross-section area; and μ_w is the water viscosity. It is assumed that water displaces air in a pistonlike manner. No gravity is assumed to play the role in the process. Only the capillary force overcomes the viscous force within the imbibition zone. As more water is imbibed, water saturation S_w is increased and k_w is increased, but p_c is declined exponentially with S_w. Handy's experimental data through cores confirmed the above linear relationship. Makhanov's (2013) experimental data also demonstrated the above relationship, but some imbibition data showed that the imbibition rate slowed at later time.

10.2.3 Mattax and Kyte (1962) method

The imbibition oil recovery in laboratory needs to be converted to the field scale. Based on the Rapoport (1955) scaling work, Mattax and Kyte (1962) verified that the spontaneous imbibition behavior (resultant oil recovery) is determined by the dimensionless time t_D:

$$t_D = t\sqrt{\frac{k}{\varphi}}\,\frac{\sigma}{\mu_w L_c^2} \tag{10.3}$$

Their equation does not consider gravity, matrix shape, wettability, relative permeability functions, boundary conditions, fluid viscosity ratios, or initial fluid distributions. L_c is the characteristic linear dimension of the block.

Based on the Mattax and Kyte (1962) equation, Ma et al. (1997) considered viscosity ratio by replacing μ_w with $\sqrt{\mu_w \mu_{nw}}$:

$$t_D = t\sqrt{\frac{k}{\varphi}}\,\frac{\sigma}{(\mu_w \mu_{nw})^{0.5} L_c^2} \tag{10.4}$$

Gupta and Civan (1994) introduced the wettability effect in the Ma et al. equation by multiplying σ by $cos\theta$:

$$t_D = t\sqrt{\frac{k}{\varphi}}\,\frac{\sigma cos\theta}{(\mu_w \mu_{nw})^{0.5} L_c^2} \tag{10.5}$$

θ is the contact angle. Zhang et al. (2018) observed that, from the experimental data of their research group, the imbibition recovery was not strongly dependent on the interfacial tension σ but inversely proportional to porosity. They further modified the above dimensionless time as follows:

$$t_D = t\sqrt{\frac{k}{\varphi}}\,\frac{abs(\log\sigma)cos\theta}{(\mu_w\mu_{nw})^{0.5}L_c^2}\varphi^2 \tag{10.6}$$

10.2.4 Li and Horne (2006) method

Our objective to study imbibition is to study the oil recovery by imbibition. Li and Horne (2006) derived a spontaneous imbibition equation which relates to almost all the parameters: gravity, initial fluid saturation, capillary pressure, and relative permeability of the wetting and nonwetting phases. Their equation is

$$t_D = -R^* - \ln\left(1-R^*\right) \tag{10.7}$$

where R^* is the normalized oil recovery:

$$R^* = cV_w \tag{10.8}$$

V_w is the pore volumes of imbibed wetting phase:

$$V_w = \frac{Ax\varphi\left(\overline{S}_{wf} - S_{wi}\right)}{V_p} \tag{10.9}$$

t_D is the dimensionless time:

$$t_D = c^2\frac{M_e p_c\left(\overline{S}_{wf} - S_{wi}\right)}{\varphi L_c^2}\,t \tag{10.10}$$

V_p is the pore volume. A is the cross-sectional area of the core perpendicular to the flow direction. x is the distance the front transports. φ is the porosity. L_c is the characteristic length equal to core length. $\overline{S}_{wf}$ is the average wetting phase saturation behind the imbibition front. S_{wi} is the initial water saturation in the core sample. M_e and p_c are the effective mobility and capillary pressure at the front wetting phase saturation S_{wf}. The effective mobility for cocurrent flow is defined as:

$$M_e = \frac{M_w M_{nw}}{M_{nw} - M_w} \tag{10.11}$$

The effective mobility for countercurrent flow is defined as:

$$M_e = \frac{M_w M_{nw}}{M_{nw} + M_w} \tag{10.12}$$

Here the subscripts w and nw represent wetting and nonwetting phases, respectively. The mobility M is defined as k/μ, and k is the permeability, and μ is the viscosity. c is the ratio of the gravity force to the capillary force:

$$c = \frac{b_0}{a_0} \tag{10.13}$$

$$a_0 = \frac{AM_e\left(\overline{S}_{wf} - S_{wi}\right)}{L} p_c \tag{10.14}$$

$$b_0 = AM_e \Delta\rho g \tag{10.15}$$

where $\Delta\rho = \rho_w - \rho_{nw}$, $p_c = p_{nw} - p_w$.

Several conditions for the above equations need to be emphasized. For the cocurrent flow, it is assumed that wetting phase velocity is equal to the nonwetting phase velocity:

$$v_w = v_{nw} \tag{10.16}$$

For the countercurrent flow, those two velocities have the following relationship:

$$v_w = -v_{nw} \tag{10.17}$$

And the fluids are incompressible and immiscible. Another condition is

$$\frac{\partial p_c}{\partial x} = \frac{p_c}{x} \tag{10.18}$$

The above equation assumes a pistonlike spontaneous imbibition (Handy, 1960). Different factors that affect spontaneous imbibition are discussed next.

10.3 Effect of permeability and porosity

The effect of permeability and porosity is discussed using simulation data, experimental data, and theories.

10.3.1 Simulation results

When comparing the mechanisms of IFT reduction and wettability alteration in Section 9.5, a base sand model is introduced. The model matrix core has the porosity of 0.24 and the permeability of 0.122 μm^2. The model initially is oil-wet, and water cannot imbibe into it. A surfactant solution is added to imbibe the water into the core. To study the effect of

ultralow permeability and porosity, the base sand model is converted to a base shale model which has 0.1 porosity and 300 nD ($\sim 3 \times 10^{-19}$ m^2) horizontal permeability. The maximum pressure increases 412 times from seven psi for 122 mD permeability and 0.24 porosity to 2887 psi for 300 nD permeability and 0.1 porosity, scaled according to permeability and porosity using $\left(\frac{\sqrt{(k/\phi)_{\text{high}}}}{\sqrt{(k/\phi)_{\text{low}}}} = \frac{\sqrt{122e-3/0.24}}{\sqrt{3e-7/0.1}}\right) = 412$, according to Eq. 9.11. The imbibition recovery factors (RF) for the base sand model and the base shale model are shown in Fig. 10.2. One may think the high capillary pressure in the base shale model will quickly drive water in the core to displace oil out. However, the imbibition oil recovery factor is only 26.8% by more than 2 million days, indicating a very slow imbibition process. To find the cause(s), the surfactant phase saturation profile shown in Fig. 10.3 for the 122 mD model is compared with that shown in Fig. 10.4 for the 300 nD model. The saturation profiles are in the middle layer of the models by 20 days of imbibition of a surfactant solution. The surfactant phase saturations in the middle blocks are 0.47 and 0.32 for the 122 mD and 300 nD models, respectively. That means when the permeability is low, the

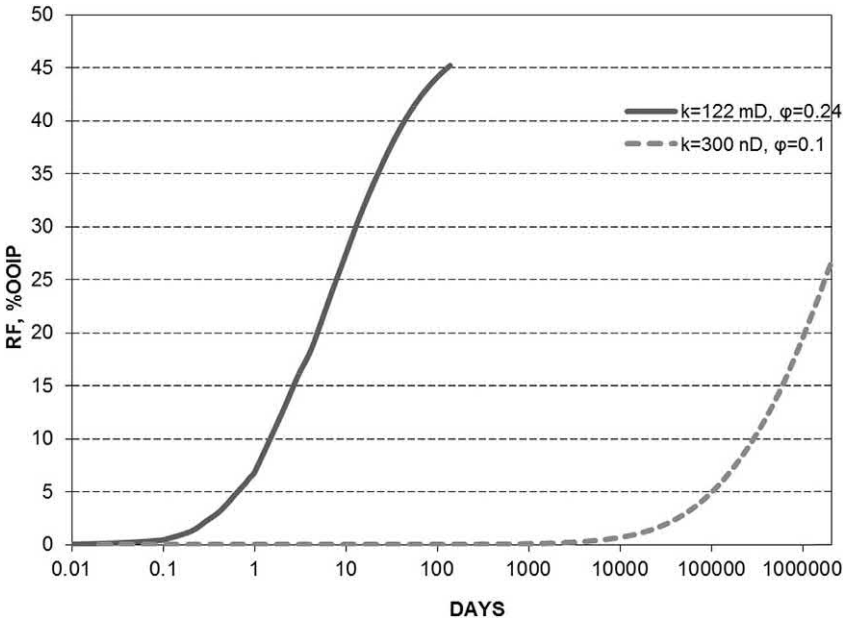

Figure 10.2 Effect of permeability and porosity on imbibition oil recovery.

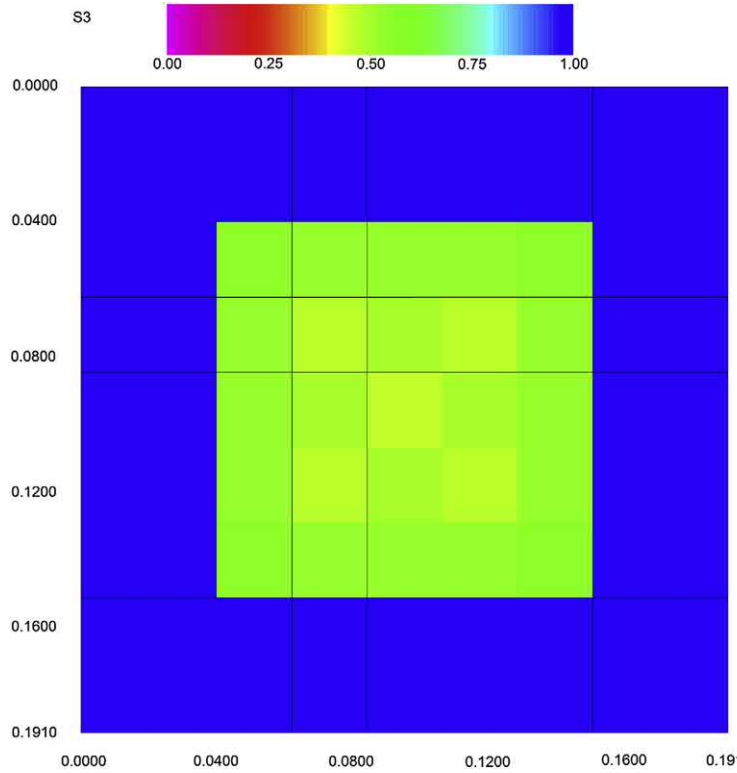

Figure 10.3 Surfactant phase saturation for 122 mD and 0.24 porosity at 20 days.

surfactant cannot diffuse into the low-permeability rock as fast as in the high-permeability rock, although the capillary pressure is 412 times higher. A higher capillary pressure means higher imbibition force, and thus higher imbibition rate. However, there is another force: viscous force. We need to consider these two forces together.

10.3.2 Theoretical considerations

According to Eq. (10.1), the imbibition velocity into a smaller pore is lower than that into a larger pore. A core of smaller radii has lower permeability as r is proportional to $\sqrt{k/\phi}$. Although the capillary force is high in a shale core, the viscous force is also high; the resultant effect of two forces makes the imbibition velocity in a low-permeability rock lower than that in a high-permeability rock.

Note that Eq. (10.1) ignores the slip flow. For the slip flow to take place, the capillary diameter needs to be smaller than approximately 3 nm (Sharp

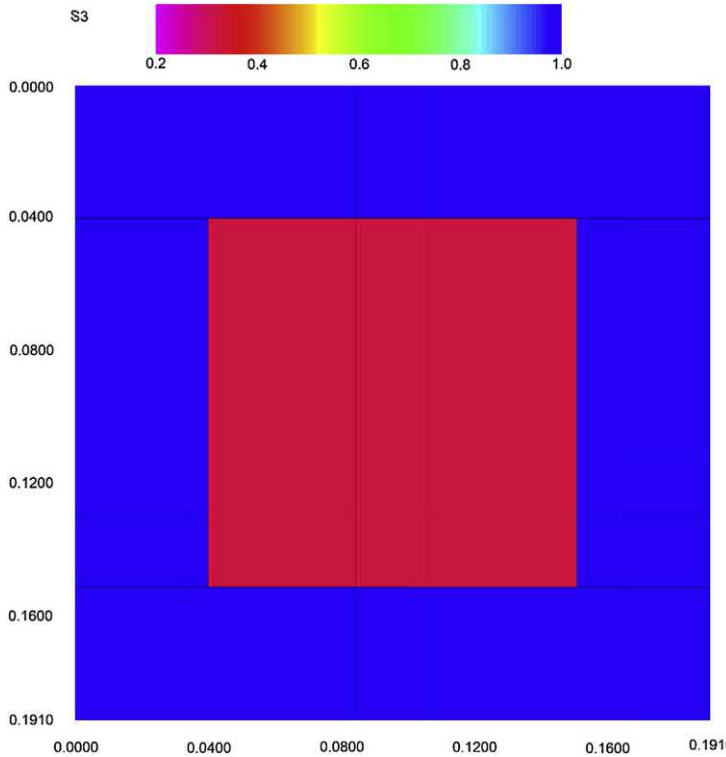

Figure 10.4 Surfactant phase saturation for 300 nD and 0.1 porosity at 20 days.

et al., 2001). This was confirmed by an experimental and theoretical study by Koo and Kleinstreuer (2003). Thus, the continuum theory is still applicable to fluid flow through nanopores in shale matrix in a practical sense.

From the above discussion, the imbibition velocity in the low-permeability rock should be one-412nd of that in the high-permeability rock. In other words, the oil recovery factor (RF) in the low-permeability rock should be close to that (45.2%) in the high-permeability rock by $412 \times 138 = 56{,}856$ days, since the RF in the high-permeability rock is 45.2% by 138 days of imbibition. However, the simulation data shows that the RF is only 26.8% by more than 2 million days. Why? There must exist other forces in addition to capillary force and viscous force, and/or other reasons. We now discuss the possible causes as follows.

First, Eq. (10.1) describes the wetting phase (water) imbibition into an air capillary tube. The resistance of air is neglected; water "freely" imbibes into the capillary tube of air. In the water-oil system, the oil resistance must be considered. In addition, water and oil are slightly compressible. For water

to enter the rock, oil must flow out in the same time through countercurrent flow. These factors make the water imbibition velocity in an oil-water-rock system lower than what is predicted by Eq. (10.1).

Second, in an oil-wet system, a surfactant must enter the system to alter the wettability. Surfactant has adsorption. The surfactant has higher adsorption in a low-permeability rock than in a high-permeability rock. The adsorption causes the retardation of surfactant transport (Sheng, 2011). The retardation is higher in the low-permeability rock than in the high-permeability rock. Therefore, the imbibition velocity of a surfactant solution will be lower than that predicted by Eq. (10.1).

Third, a surfactant enters the oil-wet system through diffusion and dispersion. The diffusion coefficient in a tortuous pore system is proportional to the pore porosity (Sheng, 2011). Then the diffusion in a low-porosity (low-permeability) rock will be lower than that in a high-permeability rock. The dispersion coefficient is proportional to the fluid velocity (Sheng, 2011). Thus the dispersion in a low-permeability rock is lower than that in a high-permeability rock as well. Therefore, both diffusion and dispersion will be lower in a low-permeability rock than in a high-permeability rock. As a result, the surfactant imbibition velocity in the low-permeability will be lower than that in the high-permeability rock.

Fourth, according to scaling theories, if the imbibition time is scaled by $\sqrt{k}$ or $\sqrt{k/\phi}$, the oil recovery from water imbibition should be same from a high-permeability formation and a low-permeability formation (Schmid and Geiger, 2013). But the simulation result does not show that. This is because the water imbibition into the oil-wet formation cannot occur before the wettability is altered by surfactant. The wettability alteration is controlled by surfactant diffusion and dispersion which are very slow in a tight formation. Therefore, this invasion is very slow and is not scaled by $\sqrt{k}$ or $\sqrt{k/\phi}$.

10.3.3 Experimental observation

Now we cite some experimental data of water imbibition in rocks of different permeabilities. Dutta et al. (2014) visualized the water imbibition profile in about 5−7 mD and about 100 mD cores. They observed that the imbibition velocities were lower in the lower-permeability cores than those in the higher-permeability cores. Yang et al. (2016) made the same observation; their experimental velocities were lower than that predicted by the theory; according to the theory, the cumulative imbibed volume increases with the square root of imbibition time (Handy, 1960); the lower

their porosity and permeability, the lower their experimental velocity was compared with the theoretical velocity.

Yang et al. (2016) studied water imbibition in pores of difference sizes by nuclear magnetic resonance (NMR). According to the NMR theory, the transverse relaxation (T_2) is inversely proportional to the surface-to-volume ratio (S/V) of a porous medium (core), because the bulk relaxation and diffusion relaxation can be negligible in porous media. As the pores become smaller, the S/V becomes larger, and then T_2 will be smaller. Yang et al.'s experimental data show that T_2 became smaller as more water imbibed, indicating that water imbibed into the core initially into larger pores and later into smaller pores. This is consistent with the Washburn (1921) equation, and it is also consistent with Mirzaei and DiCarlo's (2013) work. Imbibition in larger pores is higher than that in smaller pores, because smaller pores have higher friction, although they have higher capillary force. However, an earlier paper (Meng et al., 2015) from the same research group showed that T_2 becomes larger as the water imbibition time became longer. The data, which were not consistent with the spontaneous imbibition theory by capillary pressure (Washburn, 1921), might be affected by other unexplained factors. Furthermore, Wang et al. (2015b) observed in laboratory that as the core permeability was higher, or equivalently, as the oil viscosity was lower, the oil recovery from spontaneous imbibition was higher.

10.4 Effect of initial wettability and wettability alteration

In the base shale model discussed earlier, the rock is initially oil-wet. If no surfactant is added in the water solution, the rock remains oil-wet, and no oil can be recovered by the countercurrent oil-water flow. The preceding section shows that wettability alteration is a very slow process, especially in a shale or tight reservoir. Some reservoirs are initially water-wet. Then let us see how fast and how much oil can be produced from a shale reservoir. Table 10.1 shows that the oil recovery factor by spontaneous water imbibition from the shale rock being initially water-wet is 38% for 138 days. For comparison, the oil recovery factor from the conventional rock is also shown in the table which is 42.6%. For both the conventional rock and the shale rock, the recovery factors are zero if they are initially oil-wet and no surfactant is added to alter the wettability. These results indicate that the initial wettability is very important, which is consistent with Bourbiaux and Kalaydjian's (1990) experimental data; if the rock is initially water-wet,

Table 10.1 Oil recovery factors (RF, %) by 138 days at different initial wettabilities.

	Conventional rock	Shale rock
Permeability, mD	120	3.3E-04
Porosity	0.24	0.1
RF, initially oil-wet rock (no surfactant added)	0.0	0.0
RF, initially water-wet rock (no surfactant needed)	42.6	38
RF, initially oil-wet changed to intermediately wet (IFT = 0.008 mN/m)	45.0	0.01
RF, initially oil-wet changed to water-wet (IFT = 0.008 mN/m)	46.9	13.0
RF, initially oil-wet changed to intermediately wet (IFT = 20 mN/m)	41.2	5.0
RF, initially oil-wet changed to water-wet (IFT = 20 mN/m)	44.9	41.1

the oil recovery factors from spontaneous imbibition are similar for the conventional rock and the shale rock. Recall from the preceding section that when the rock is initially oil-wet, the oil recovery factors are very different as shown in Fig. 10.2.

To further explain our point, the oil recovery versus time is plotted in Fig. 10.5 for the two cases: initially water-wet rock and oil-wet rock but slowly altered to water-wet by surfactant. It shows that the oil recovery factor in the former case quickly reaches to the maximum recovery factor of 42.6%, while in the latter case, the oil recovery is very slow because it takes

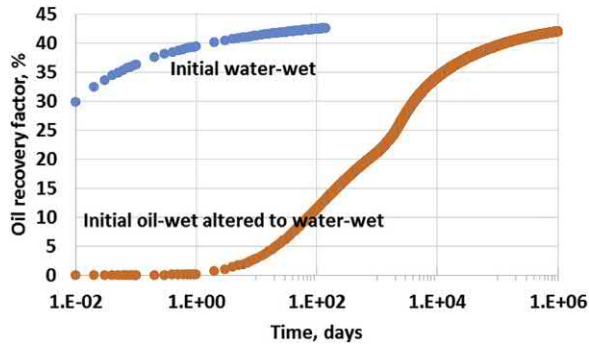

Figure 10.5 Comparison of oil recovery curve of the initial water-wet case with that of the case of initially oil-wet slowly altered to water-wet by surfactant.

time for the surfactant imbibition to alter wettability; it takes 1 million days to reach 42.2%.

The above table also shows that if the oil-wetness is gradually altered to completely water-wetness by surfactant, the shale rock can have an oil recovery of 13%, whereas the conventional rock has 46.9%. The former case has much lower oil recovery because the surfactant solution has to slowly imbibe into the rock to change the wettability. In other words, if a shale or tight reservoir is initially oil-wet, it is not an effective method to use surfactant to change wettability. Note that the water-oil interfacial tension (IFT) is ultralow (0.008 mN/m).

A surfactant may only change wettability but not reduce IFT. Such surfactants are generally cationic and nonionic surfactants (Sheng, 2013a). In such a situation, the water-oil IFT is maintained at 20 mN/m, but the wettability is altered to intermediately water-wet and water-wet completely by the surfactant. The simulation results for these two cases are also shown in the above table. When the oil-wetness is changed to intermediate water-wetness, the oil recovery from the shale core is 0.01% when the IFT equal to 0.008 mN/m, but it is 5% when the IFT is 20 mN/m. When the oil-wetness is changed to complete water-wetness, the oil recovery from the shale rock is 13% when the IFT is equal to 0.008 mN/m, but it is 41.1% when the IFT is 20 mN/m. These results show that when the wettability is altered, the IFT should be higher for a shale rock. To make this conclusion visually clear, the oil recovery curves for the case of IFT = 0.008 mN/m by 1 million days and for the case of IFT = 20 mN/m by 138 days are compared in Fig. 10.6, when the shale rock wettability is changed from initially oil-wet to water-wet by surfactant. Such results are consistent

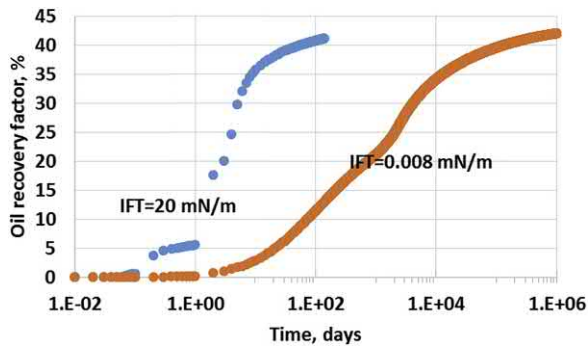

Figure 10.6 Comparison of oil recovery curves of different IFT values when the shale wettability is changed from initially oil-wet to water-wet by surfactant.

with those from an earlier work (Sheng, 2013b). Kathel and Mohanty's (2013) experimental data also showed that the rate of oil recovery in tight (10 μD) oil-wet or mixed wet sandstone cores increased with high IFT by spontaneous imbibition.

Generally, cationics and nonionics can change wettability by maintaining the IFT higher. Particularly, cationic surfactants can form ion pairs with adsorbed organic carboxylates of the crude oil and stabilize them into the oil thereby changing the rock surface to water-wet (Tabatabal et al., 1993; Stadnes and Austad, 2000; Austad and Standnes, 2003; Xie et al., 2005). Generally, the IFT between such surfactant solution and oil is not low (>0.1 mN/m) (Adibhatla and Mohanty, 2008).

However, for the conventional rock, the preceding table shows that the oil recovery factors for the 20 mN/m IFT cases are not as high as those in their respective 0.008 mN/m IFT cases, when the wettability is changed from oil-wet to intermediately water-wet and completely water-wet.

10.5 Effect of interfacial tension (IFT)

It can be seen from the preceding section that the IFT plays an important role in imbibition and in wettability alteration. This section further discusses its role in spontaneous imbibition.

10.5.1 Theoretical and experimental analysis

Capillary pressure (p_c) can be calculated from

$$p_c = \frac{2\sigma \cos\theta}{r} \tag{10.19}$$

Here θ is the contacting angle, r is the pore radius, and σ is the IFT between a wetting phase and a non-wetting phase. When σ is higher, p_c is higher. Then the imbibition becomes stronger, and the imbibition rate becomes higher, which generally corresponds to a higher recovery of the non-wetting phase (oil if the rock is water-wet). This claim can be verified experimentally by Mattax and Kyte (1962), for example.

Cuiec et al. (1994) reported that the average recovery curves versus time at different IFTs from oil recovery was higher in the early time as shown in Fig. 10.7, which is consistent with the simulation results by Sheng (2013b) who showed that the wettability alteration with higher capillary pressure is effective in the early time of imbibition. But the oil recovery factors during late time became lower than those from lower IFT experiments. This is

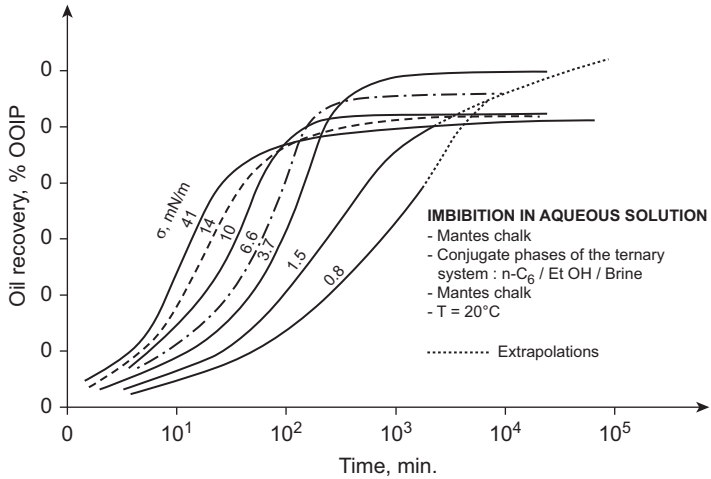

Figure 10.7 Average recovery curves for various IFTs (Cuiec et al., 1994).

because the gravity segregation played an important role at a longer time when the IFT was low. This also implies that the gravity effect is slower than the capillary effect in low-permeability porous media. Such results are in agreement with those from Schechter et al. (1991) for low-permeability samples. Austad and Milter (1997) used surfactants to reduce the oil-water IFT to conduct imbibition tests on chalk. The imbibition rate was lower than that of water.

Cuiec et al. (1994) also showed that after a higher IFT fluid system was used, a subsequent lower IFT fluid system resulted in an increase in oil recovery. Their interpretation was that there was a capillary pressure threshold caused by the contact angle hysteresis and short oil ganglia. A high IFT system caused the raised threshold and at some time, oil ganglia movement stopped, and no further oil could be recovered. Note that in Cuiec et al.'s experiments, the low IFT values of 0.8 and 1.5 mN/m might not be low enough to cause the significant increase in capillary number or the significant decrease in residual oil saturation. In other words, the increase in oil recovery may not be caused by capillary desaturation.

Wang et al. (2015b) reported that the imbibition oil recovery increased as the IFT became lower, but decreased as the IFT became further lower, as shown in Fig. 10.8. They interpreted that the increase of the interfacial tension enlarged the emulsified oil droplets, which increased the resistance to displace oil by gravity segregation. They concluded that there existed an optimal IFT that led to the highest imbibition recovery. The exact core

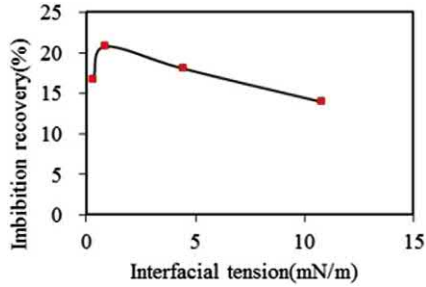

Figure 10.8 Imbibition oil recovery versus interfacial tension for an Ordos Basin core (Wang et al., 2015b).

permeability and other experimental details, for example, the surfactant used, were not reported in their paper. Their conclusion might not universally hold as there was only one data point that deviated from the thread of the rest of the data points.

10.5.2 Simulation analysis

Some surfactants like anionic surfactants can reduce water-oil IFT but may not change rock wettability (Sheng, 2013a). Table 10.2 shows the effect of IFT reduction by such type of surfactants. The simulation base shale model was referred earlier. For the conventional rock, when the IFT is higher than 0.049 mN/m, oil cannot be recovered by water imbibition without changing oil-wetness to water-wetness by surfactant. The capillary number in the simulation model is in the order of 10^{-9}. Such low capillary number cannot reduce residual saturations or increase relative permeabilities. Also, such intermediate IFT makes the capillary pressure negatively too large so that oil cannot flow out of the oil-wet rock.

For the case of initially oil-wet shale rock, no matter what values of the IFT, no oil can be recovered because of the very low permeability, in addition to the reasons mentioned above for the conventional rock. This is a very

Table 10.2 Oil recovery factors (RF, %) at different IFTs (no wettability alteration).

	Conventional rock	Shale rock
Permeability, mD	120	3.3E-04
Porosity	0.24	0.1
RF at 20 mN/m (initially oil-wet rock)	0	0
RF at IFT = 0.049 mN/m	0	0
RF at IFT = 0.0323 mN/m	20	0
RF at IFT = 0.008 mN/m	42	0

important observation. It means that conventional IFT reduction mechanism by surfactants may not be effective in shale or tight reservoirs for spontaneous imbibition. It should be mentioned that in those simulation models, the residual saturations (oil, water surfactant phases) are all assumed zero, and the maximum relative permeabilities of oil, water, and surfactant phases are all assumed one, and their exponents of relative permeabilities are also assumed one as well at their high capillary numbers. These values of the parameters represent the best benefits a surfactant can provide in terms of IFT reduction. In other words, although the models have made the best use of IFT reduction mechanism, oil cannot be recovered from the shale rock. The discussion here demonstrates that wettability alteration is fundamental in shale reservoirs in terms of oil recovery by spontaneous imbibition.

10.6 Effect of diffusion

In the base shale model, the effective molecular diffusion coefficient is 7×10^{-11} m^2/s (6.5×10^{-5} ft^2/day). The value is in line with typical surfactant diffusion coefficients on the order of 10^{-11}–10^{-10} m^2/s (Lindman et al., 1980; Cazabat et al., 1980; Chou and Shah, 1980; Weinheimeret et al., 1981). When the diffusion coefficient is of 0.1, 1, 10, and 100 times 7×10^{-11} m^2/s, their oil recovery factors are represented in Table 10.3. It is assumed that surfactant changes the oil-wetness to intermediate wetness ($\omega = 0.5$). First, it is assumed that the IFT is reduced to 0.008 mN/m by surfactant. Oil can hardly be recovered by 138 days of imbibition, no matter

Table 10.3 Recovery factors at different diffusion coefficients.

	By 138 days	By ~1.3 million days
IFT = 0.008 mN/m, the base diffusion coefficient D = 7E-11 m^2/s		
0.1D	0.01	21.8
Base D	0.01	21.9
10D	0.01	22.0
100D	0.01	22.1
IFT = 20 mN/m		
0.1D	4.7	
Base D	4.9	
10D	5.03	
100D	5.04	

what value of the diffusion coefficient is used. About 22% oil is recovered by ~1.3 million days of imbibition, indicating diffusion is a very slow process. Reducing and increasing the diffusion coefficient by 10 and increasing it by 100 times result in about (0.1–0.2)% difference in the oil recovery factor, showing the oil recovery is not sensitive to the diffusion coefficient. In other words, the diffusion cannot be a dominant mechanism.

When the IFT is 20 mN/m, the oil recovered is about 5% by 138 days of spontaneous imbibition, much higher than those when the IFT is 0.008 mN/m. The discussion in this section shows that a high IFT is needed for the capillary pressure to help diffusion play the role. When the IFT is low, capillary pressure as a driving force will be low, leading to low diffusion.

10.7 Effect of gravity

When the rock permeability is *high*, the gravity force and the capillary pressure together determine the fluid distribution through imbibition. In the case of initial oil-wetness and the wettability is altered by a surfactant solution, the imbibition rate and the oil recovery become higher as the IFT is lower. This has been verified by some experiments (e.g., Schechter et al., 1991) and by a numerical simulation study, as shown in Fig. 10.9 (Sheng, 2013b). The figure shows that when the IFT is 0.049 mN/m, oil can barely be recovered by water imbibition because the core is initially oil-wet, and the capillary force is resistant to the surfactant solution imbibition into the core to displace oil out. When the IFT becomes lower (0.0323 or 0.0088 mN/m), oil is driven out by gravity which overcomes the capillary

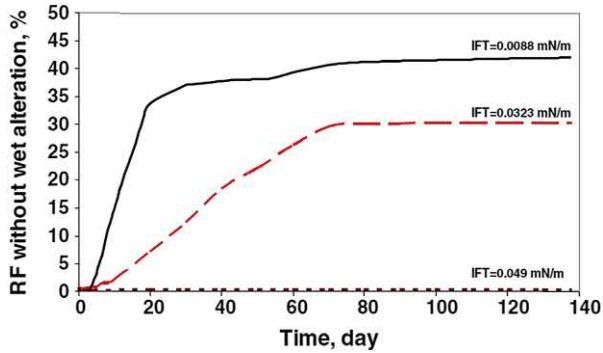

Figure 10.9 Effect of IFT on oil recovery by surfactant solution imbibition (Sheng, 2013b).

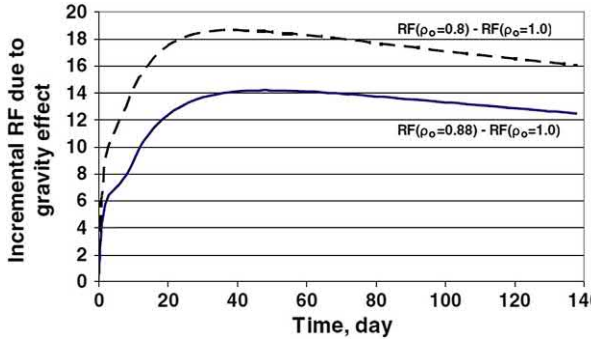

Figure 10.10 Effect of gravity on incremental recovery factor (Sheng, 2013b).

resistance. Fig. 10.10 shows as the density difference between oil and water (1 g/cm^3) is large, the incremental oil recovery due to gravity effect is higher. The incremental oil recovery is the oil recovered over that recovered when the oil density is equal to the water density.

When the gravity dominates an imbibition process, Cuiec et al. (1994) proposed a scaled or normalized time which is defined as the real imbibition time divided by the reference time (t_g):

$$t_g = \frac{L_c \mu_o}{k(\Delta\rho)g} \tag{10.20}$$

where t_g is the ratio of viscous force to gravity force, μ_o is the oil viscosity, k is the permeability, L_c is the characteristic length, and $\Delta\rho$ is the density difference between water and oil. When the normalized time is used to plot the oil recovery factors from the simulation models of different scales (different L_c), the recovery factor curves overlap each other, as shown in Fig. 10.11 (Sheng, 2013b). This indicates that the gravity is the dominant mechanism.

In a practical case, both capillary force and gravity force act in the imbibition process. To define the relative importance of the two forces, the Bond number is defined:

$$N_B = \frac{k(\Delta\rho)g}{\sigma} \tag{10.21}$$

A higher Bond number represents a higher gravity force. Morrow and Songkran's (1981) data showed that as the Bond number was increased (higher dip angle), the trapped oil saturation became lower (higher oil recovery) (See Fig. 10.12). A higher Bond number can also be achieved by lower IFT, higher permeability, and high density-difference. In the case of ultralow IFT, the flow is dominated by gravity segregation. The flow is

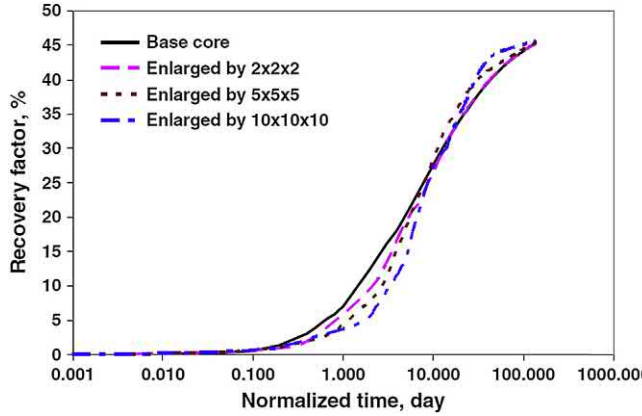

Figure 10.11 Oil recovery factor versus the scaled or normalized time (Sheng, 2013b).

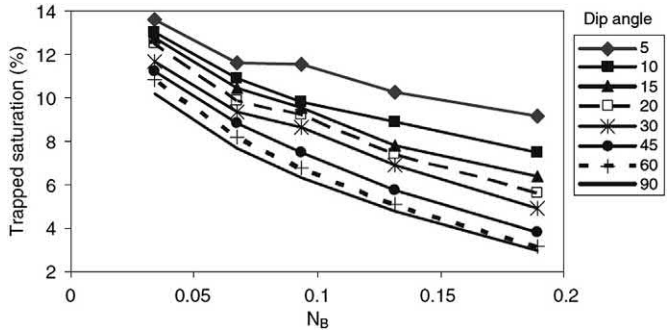

Figure 10.12 Effect of Bond number on trapping of residual oil saturation. *Data from Morrow, N.R., Songkran, B., 1981. Effect of viscous and buoyancy forces on nonwetting phase trapping in porous media. In: Shah, D.O. (Ed.), Surface Phenomena in Enhanced Oil Recovery. Plenum Press, 387–411.*

cocurrent for the two phases. Bourbiaux and Kalaydjian's (1990) relative permeability data showed that cocurrent relative permeabilities were higher than countercurrent values for capillary-dominated flow. For intermediate values of the bond number (0.5 − 5 according to Schechter et al. (1994)), the gravity contribution is strong enough to cause considerable segregation of the flow, and the capillary force is also strong enough. Schechter et al.'s (1994) experimental data showed that the combined effects of gravity and IFT led to faster recovery of the nonwetting phase than that observed by either gravity-dominated or capillary-dominated flow. The above discussions apply to conventional reservoirs.

Using the base shale model, the effect of gravity is also investigated by changing oil density. The oil and water densities in the base model are 0.88 and 1.0 g/cm^3, respectively. A low IFT of 0.008 mN/m and a high IFT of 20 mN/m are studied. Table 10.4 shows that at the IFT of 0.008 mN/m, no oil can be recovered by 138 days, when the oil density is 0.88 or 1.0 g/cm^3; and the incremental oil recovered from the gravity is about 8.7% (= 22−13.3) by 1.33 million days. At the IFT of 20 mN/m, the oil recovered is 5% by 138 days, when the oil density is 0.88 or 1.0 g/cm^3; the incremental oil recovered is 5.5% (= 33.5−28) by 1.33 million days. From these data, we can see that within a realistic time, the gravity cannot play an important role in increasing oil recovery. To realize the gravity effect on improving oil recovery, a very long time is needed (millions of days for the small shale core).

Using the parameter values for the small shale core, the calculated Bond number is 4.41×10^{-11} for the IFT equal to 0.008 mN/m:

$$N_B = \frac{\Delta\rho g k}{\sigma} = \frac{\left(120\text{kg/m}^3\right)\left(9.8\text{m/s}^2\right)\left(3 \times 10^{-19}\right)}{\left(8 \times 10^{-6}\right)} = 4.41 \times 10^{-11}$$

And it is 1.764×10^{-14} if the IFT is 20 mN/m. These data imply that in a shale reservoir, the gravity cannot play an important role in fluid flow compared with the capillary force. When the permeability is too low in shale and tight formations, the gravity cannot overcome the flow resistance (viscous force); a high IFT and water-wetness are needed to lead a high capillary drive force to displace oil out. In such a situation, the gravity is not a dominant factor; and the higher the IFT, the higher the oil recovery by spontaneous imbibition will be.

Table 10.4 Effect of gravity on RF.

	By 138 days	By 1.33 million days
IFT = 0.008 mN/m		
RF at oil density 0.88	0.01	22
RF at oil density 1.0	0.01	13.3
IFT = 20 mN/m		
RF at oil density 0.88	5.0	33.5
RF at oil density 1.0	5.0	28

10.8 Effect of viscosity ratio

Generally, the wetting phase viscosity (μ_w) is used and the nonwetting phase viscosity is ignored. Ma et al. (1997) included the effect of nonwetting phase (oil) viscosity (μ_{nw}) by using $\sqrt{\mu_w \mu_{nw}}$. However, many experimental studies (Behbahani and Blunt, 2005; Fischer and Morrow, 2006; Fischer et al., 2006) and numerical results (Behbahani and Blunt, 2005) did not support that such treatment could be general. Wang et al. (2015b) observed in laboratory that as the oil viscosity was lower, the oil recovery from spontaneous imbibition was higher. Makhanov et al. (2014) found that the imbibition rate of xanthan gum solution was significant despite its high viscosity. This suggests that water uptake is mainly controlled through preferential adsorption of water molecules by the clay particles, and high viscosity of the solution can only partly reduce the imbibition rate.

10.9 Effect of initial water content

If the initial water saturation S_{wi} is higher than the connate (immobile) water saturation S_{wc}, the capillary pressure will be lower but the water (wetting) phase mobility will be higher. They affect the imbibition in different directions. Most of experiments were done at S_{wc} or $S_{wi} = 0$ so far.

10.10 Countercurrent flow versus cocurrent flow

In a case of water-wet core which has a high initial oil saturation, the space between the outside core and the wall of the imbibition cell is full of water. The water and oil phase pressures in the imbibition cell is the same, but the oil phase pressure inside the core is higher because the capillary pressure is positive. Then oil will flow from the inside of the core to the outside. Meanwhile the water outside the core will flow toward the inside. Thus countercurrent flow occurs by the capillary force. In laboratory, oil can be seen to flow out of the core from all the faces of the core.

In the above system, if chemicals, a surfactant as an example, are added in the water so that the water-oil interfacial tension is reduced, the water-oil capillary pressure is significantly reduced, and the gravity force can overcome the capillary force. Then water will push oil from the bottom of the core. Both oil and water will flow out of the top face of the core in the same vertical direction. This flow is called cocurrent flow.

The countercurrent flow and cocurrent flow described above can occur in spontaneous imbibition for any pair of wetting and nonwetting phases, for example, in a gas-liquid system.

It has been observed that oil comes from all the faces of the core in the early time, then comes from the top face of the core only at later time (Schechter et al., 1994; Chen and Mohanty, 2015). In other words, the capillary force dominates in the early phase, while the gravity plays the dominant role in the late phase. The gravity works all the time, but the capillary force is higher in the early time than in the late time, because the capillary pressure gradient becomes lower in the late time because the imbibition distance becomes longer, while the capillary pressure at the imbibition front remains the same. The fact that the capillary pressure plays the important role in the early time has been verified by the simulation work by Sheng (2013b) which is represented in Fig. 10.13. Look at the two oil recovery curves marked by OW + IFT and WW + IFT. The OW + IFT curve represents the imbibition oil recovery when the wettability is kept oil-wet but a low water-oil IFT is maintained; the WW + IFT curve represents the oil recovery when the wettability is changed from oil-wet to water-wet and a low water-oil IFT is maintained. It can be seen that the oil recovery from WW + IFT is much higher than that from OW + IFT in the early time

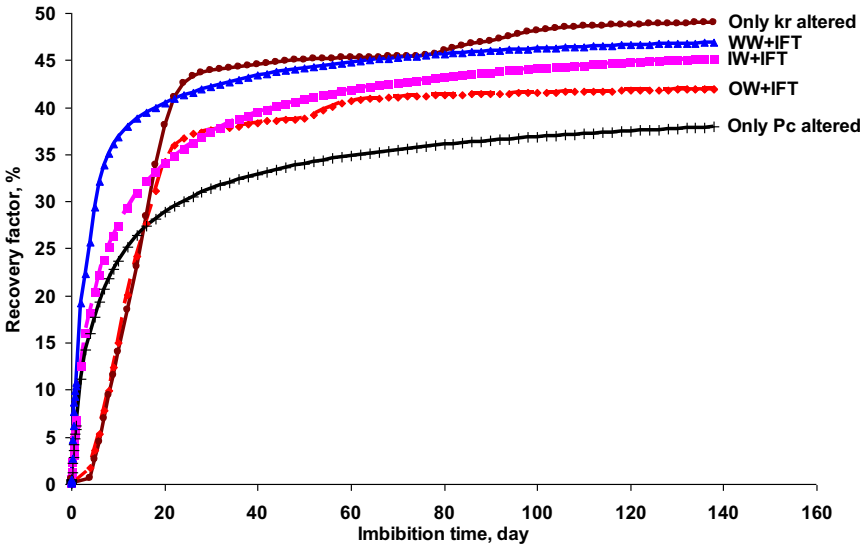

Figure 10.13 Effect of the combined wettability alteration and IFT reduction in spontaneous imbibition.

(less than 5 days), but in the late time, the two curves rise similarly and become almost parallel during the very late time. The difference between the two curves is that WW + IFT has additional wettability alteration which makes the capillary pressure work to improve oil recovery in the early time. In other words, the capillary force dominates in the early time. In these simulation cases, the IFT is low at 0.0088 mN/m. When the IFT is low, the capillary number becomes high, resulting in improved relative permeabilities, and the gravity can play its role to produce oil. Note the permeability in the model is 122 mD.

10.11 Behaviors of different surfactants

Alvarez et al. (2014) as well as Alvarez and Schechter (2017) performed spontaneous imbibition experiments monitored by CT in shale reservoirs to compare the effects of anionic surfactants and nonionic surfactants. They concluded that anionic surfactants show superior effect on wettability alteration and oil recovery during spontaneous imbibition.

Liu et al. (2019) compared the capability of wettability alteration of anionic surfactants and nonionic surfactants. They observed that anionic surfactants (sodium alcohol ether sulfate (AES) and sodium C14-16 olefin sulfonate (AOS)) more significantly altered core wettability toward more water-wet than nonionic surfactants (alcohol ethoxylate (AEO-9) and isomeric alcohol ethoxylates (IAE)). Those anionic and nonionic surfactants reduced the IFT to the similar level as shown in Fig. 10.14. Because the anionic surfactants have higher capability of wettability alteration, they

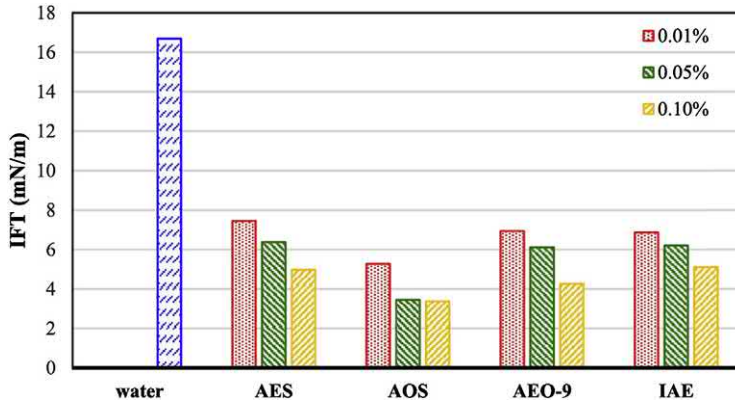

Figure 10.14 Measured water-oil IFT values in different surfactant solutions.

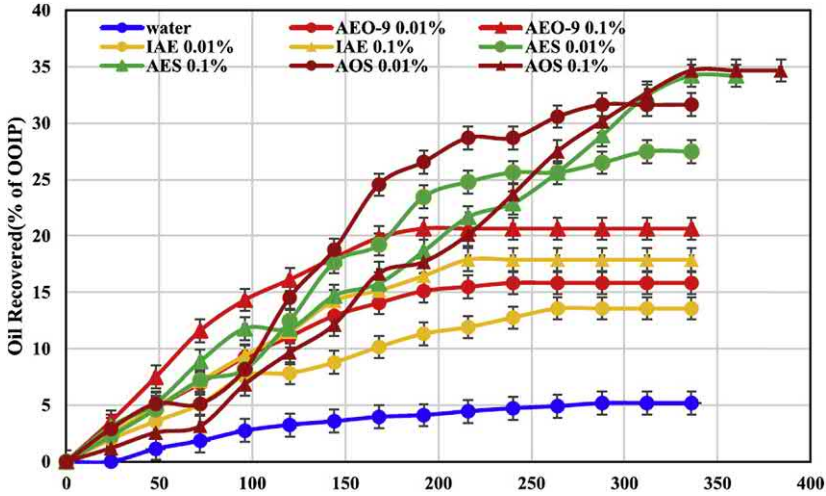

Figure 10.15 Imbibition oil recovery from anionic and nonionic surfactant solutions.

offered high imbibition oil recovery as shown in Fig. 10.15. This figure also shows that the imbibition rates of anionic surfactant solutions decreased with the concentration as the IFT was more significantly reduced.

The NMR T_2 spectrum curves before and after spontaneous imbibition of these four surfactant solutions and heavy water are shown in Fig. 10.16. Spontaneous imbibition took 10 days. The cores were initially saturated with oil. Heavy water imbibed into the cores. Since heavy water did not have NMR signal but oil had some signal strength, the NMR signal amplitude decreased as more heavy water imbibed. This figure shows that most of heavy water imbibed into the cores at T_2 longer than 2.5 ms. Since T_2 is proportional to the pore size (Zhao et al., 2015), calibrating measured pore size distribution with the T_2 curve, we found $T_2 = 0.05r_p$, r_p is in nm. According to this relationship and based on the International Union of Pure and Applied Chemistry (IUPAC) pore classification (Ross and Bustin, 2009), the pore types and T_2 have the relationship described in Table 10.5. From this figure and table, we can see that heavy water and surfactant solutions mainly entered macropores; anionic surfactant solutions could enter some pores smaller than those entered by nonionic surfactant solutions.

Nguyen et al. (2014) conducted spontaneous imbibition experiments on reservoir cores of Bakken shale and outcrops of Eagle Ford shale. The results showed that the nonionic surfactant performed best while the anionic surfactant came second and cationic surfactant (ethoxylated tallow amine) came last. Actual reservoir brines were used. Alkali sodium metaborate

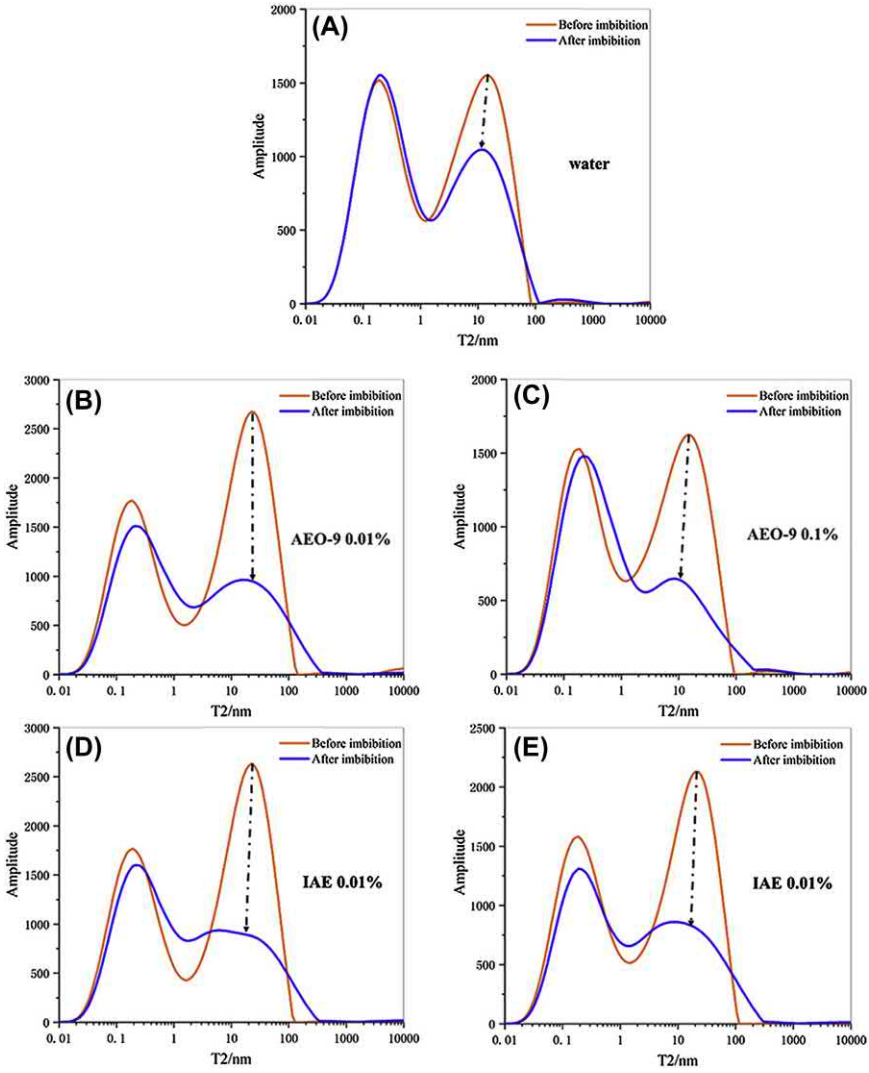

Figure 10.16 T_2 spectrum curves in initially saturated cores before and after spontaneous imbibition of heavy water and four surfactant solutions.

($NaBO_2 \cdot 4H_2O$) was added to generate soap (in situ generated surfactant), so that this soap may have a synergy with a synthetic surfactant, and alkali may reduce surfactant adsorption. These mechanisms are discussed in Sheng (2011) for alkali-surfactant flooding. Alkali may also change wettability (Johnson, 1976). For Bakken cores aged with Bakken crude with high resin content, Nguyen et al. (2014) found increase in alkali decreased oil recovery

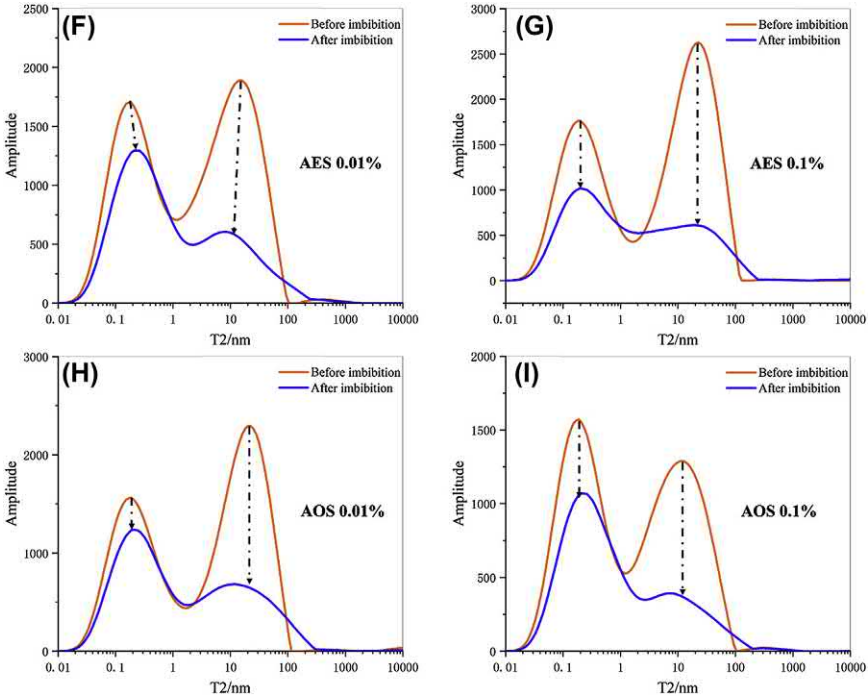

Figure 10.16 (***continued***).

Table 10.5 Relationship among T_2, pore size, IUPAC pore classification.

T_2 Relaxation time, ms	Pore radius (r), nm	Pore type
$0.01 \leq T_2 \leq 0.1$	$r_p < 2$	Micropores
$0.1 < T_2 \leq 2.5$	$2 < r_p \leq 50$	Mesopore
$T_2 > 2.5$	$r_p > 50$	Macropore

by an anionic surfactant and an amphoteric surfactant, but increased oil recovery by the cationic surfactant tallow amine. They suspected that increased alkali may change the optimum salinities of the anionic and amphoteric surfactants. However, they presented another experimental data showing adding alkali decreased oil recovery from a cationic surfactant solution. They explained that the soap and the cationic surfactant had opposite charges resulting in a much more hydrophobic mixture and altering the wettability and/or IFT in an unfavorable way. Alkaline precipitation was observed as the imbibition progressed for the cationic surfactant with alkali added in the 30% TDS brine (total dissolved salt). Their experimental data showed the nonionic

surfactant with the alkali additive behaved best in oil recovery. There was no alkaline precipitation observed, as the interaction between the soap and the nonionic surfactant is mainly a hydrophobic interaction of the hydrocarbon tails, not like the interaction between the opposite head groups of the soap and the cationic surfactant.

However, Nguyen et al. (2014) observed that a cationic surfactant (0.2% concentration, no alkali additive) produced the highest oil recovery (27% after 600 h of imbibition) from an Eagle Ford core aged with Bakken oil. The cationic surfactant altered the oil-wetness to water-wetness. The Eagle Ford core is carbonate dominated (47%). This result is consistent with that from Alvarez et al. (2018) that a cation works better with a carbonate core, as discussed in the last chapter of this book.

CHAPTER ELEVEN

Forced imbibition

Abstract

This chapter discusses the imbibition by pressure gradient that is sometimes called forced imbibition. Forced imbibition occurs in flooding and soaking. Numerical simulation approach is used to analyze the performance of forced imbibition in fractured shale and tight rocks. The effects of permeability and porosity, wettability alteration, interfacial tension, capillary pressure, and pressure gradients on fractured shale and tight rock system are investigated. At the end, experimental results are discussed, and field tests of surfactant EOR are presented.

Keywords: Forced imbibition; Fractured reservoirs; IFT; Pressure gradient; Surfactant EOR; Wettability alteration.

11.1 Introduction

In terms of EOR methods, water injection has not been studied as extensively as gas injection, probably because the former may not be as effective as the latter (Sheng and Chen, 2014; Yu and Sheng, 2017). To improve water injection performance, many efforts have been made to add surfactants or chemicals. Once water is injected, water may imbibe into rocks through capillarity or by pressure. The capillary imbibition is called spontaneous imbibition which was discussed in Chapter 10. The imbibition by pressure gradient is sometimes called *forced imbibition* which is discussed in this chapter. Forced imbibition occurs in flooding and soaking. Numerical simulation approach is used to analyze the performance of forced imbibition in fractured shale and tight rocks. The effects of permeability and porosity, wettability alteration, interfacial tension, capillary pressure, and pressure gradients on fractured shale and tight rock system are investigated. At the end, experimental results are discussed, and field tests of surfactant EOR are presented.

Enhanced Oil Recovery in Shale and Tight Reservoirs
ISBN: 978-0-12-815905-7
https://doi.org/10.1016/B978-0-12-815905-7.00011-6

11.2 Description of a base shale model

Compared with spontaneous imbibition, much less work has been done for forced imbibition in shale and tight reservoirs. To study the forced imbibition EOR performance, relatively more numerical simulation work will be discussed. To facilitate the discussion, a base simulation model is first described.

In the Najafabadi et al. (2008) experiment, a system of matrix and fractures was flooded sequentially by water, an alkaline solution, and an alkaline-surfactant solution. Nine Texas cream cores $1'' \times 1'' \times 1''$ each core were put together to form a fractured system with the apertures between neighboring blocks representing fractures, as shown in Fig. 11.1 by simulation grids. There were two fractures parallel to the flow direction and four fractures perpendicular. The fracture width was about 1 mm (0.003281 ft). The model grid parameters are reported in Table 11.1. The initial water saturation is 0.14. The oil viscosity is 10.5 cP.

The estimated pore volume of the core was 120 mL. The injection scheme in the experiment was: 0.71 PV water injection with 4.8 wt.% NaCl, 1.6 PV (from 0.71 to 2.4 PV) alkali injection with 1 wt.% sodium metaborate and 3.8 wt.% NaCl followed by 0.97 PV (from 2.4 PV to 3.37 PV) alkaline-surfactant injection with 1.5 wt.% PetroStep S-1 and

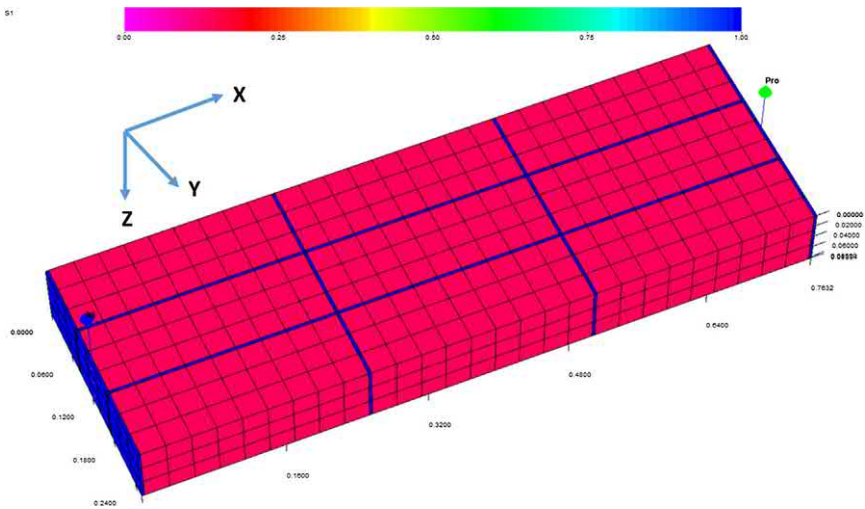

Figure 11.1 Model grid with initial water saturation, fractures, an injector (Inj), and a producer (pro).

Table 11.1 Grid parameters of the simulation model.

Parameter	Matrix	Fracture
Number of grids	31 × 11 × 3	
Grid size in the X direction, ft	0.02778	0.003281
Porosity	0.298	1
Permeability, mD	34	2000

0.5 wt.% PetroStep S-2, 2 wt.% secondary butanol as cosolvent, 1 wt.% sodium metaborate, and 3.8 wt.% NaCl. The injection rate in the experiment was 0.002 ft^3/day. The pressure gradient was 0.8 psi/ft. For more detailed experimental description, see Najafabadi et al. (2008).

Delshad et al. (2009) history matched the experiment using a UTCHEM model (version 9.95, 2009). The capillary pressure of the initial mixed-wet rock is described in Fig. 11.2, with positive and negative capillary pressures depending on water saturation. The negative pressure is responsible for trapping a large amount of oil in the matrix. After the wettability of the matrix is altered toward water-wet conditions, capillary pressures become positive as also shown in the figure. The wettability alteration is achieved if the surfactant concentration is above the input critical micelle concentration, or the alkaline concentration is above zero. As is well known, relative permeability depends on wettability. If the rock wettability is changed, the relative permeability curves will be changed. The parameters of relative permeability and capillary pressure at the initial wettability and altered wettability are

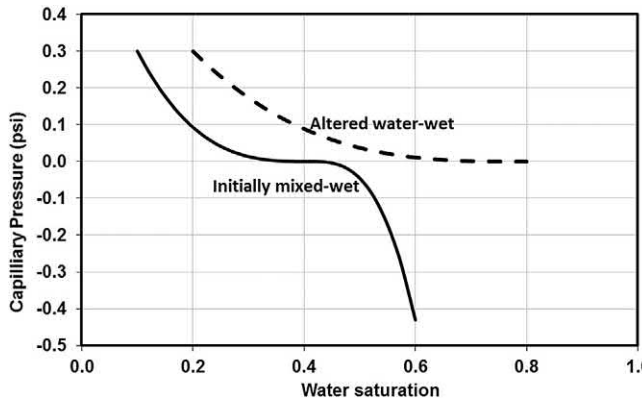

Figure 11.2 Capillary pressure curves at the initially mixed-wet and at altered water-wet.

Table 11.2 Model parameters of the relative permeabilities and capillary pressure at the initial mixed wettability and altered water-wet wettability for matrix and fracture at $(N_C)_C$.

	At initial wettability		At altered wettability	
Parameter	**Matrix**	**Fracture**	**Matrix**	**Fracture**
Residual water saturation	0.1	0.05	0.2	0.1
Residual oil saturation	0.4	0.35	0.2	0.05
Water rel. perm. endpoint	0.3	0.4	0.2	0.3
Oil rel. perm. endpoint	0.4	0.6	0.7	1
Water rel. perm. exponent	2	1.5	2.5	2
Oil rel. perm. exponent	3	1.8	2	1.5
Wettability	Mixed-wet	Mixed-wet	Water-wet	Water-wet
Positive capillary pressure endpoint, psia $(\text{Darcy})^{1/2}$	0.10133	0	0.10133	0
Negative capillary pressure endpoint, psia $(\text{Darcy})^{1/2}$	−0.14524	0	N/A	N/A
Capillary pressure exponent	3	0	3	0
Water saturation at zero capillary pressure	0.41	0	N/A	N/A

reported in Table 11.2, and the relative permeability curves are presented in Figs. 11.2–11.4. The relative permeability curves are described using the Corey-type of equation (Brooks and Corey, 1966). The parameters about the capillary pressure will be described later.

During the surfactant injection, the IFTs of water/microemulsion and oil/microemulsion are reduced, and they are functions of salinity as shown in Fig. 11.5. For the base model, the IFT is close to 0.001 mN/m at the optimum salinity of 0.96 meq/mL. When IFTs are reduced, residual saturations are reduced, and their relative permeabilities are increased. This mechanism is described by the capillary desaturation curves (CDC), such as Eq. 9.2 for the oil phase. The CDC parameters for water, oil, and microemulsion phases in the matrix blocks used in the base model are presented in Table 11.3, with the subscript dummy p being o, w, or m for oil, water, and microemulsion phase, respectively.

Note that two sets of relative permeability curves are required in simulation. One set describes the effect of wettability alteration in Table 11.2, and the other set describes the effect of capillary number in Table 11.3

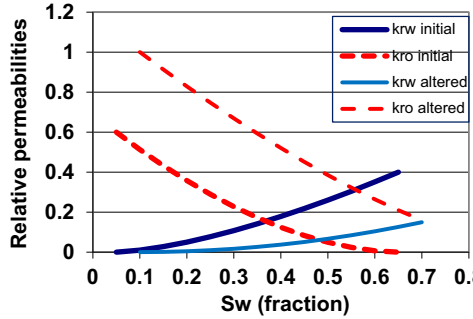

Figure 11.3 Relative permeability curves for the matrix at the initially mixed-wet and at altered water-wet.

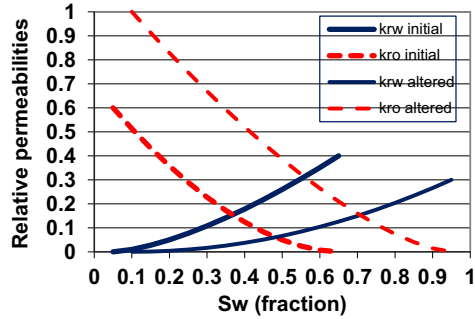

Figure 11.4 Relative permeability curves for the fractures at the initially mixed-wet and at altered water-wet.

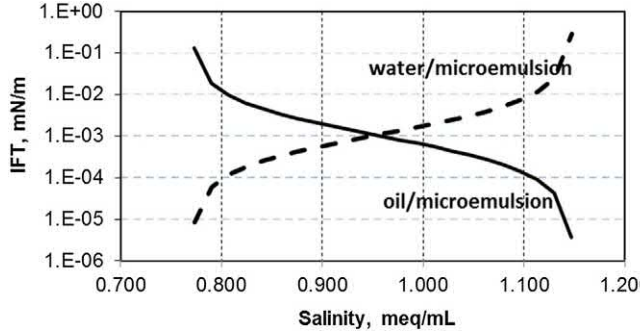

Figure 11.5 IFT changes with salinity in the base model.

which is for the matrix. The parameters for the capillary desaturation curves used in the base model for the fracture at $(N_C)_C$ are reported in Table 11.2, and the parameters for the fracture at $(N_C)_{max}$ are the same as those for the matrix in Table 11.3. The same values of T_p in Table 11.3 are used for the matrix and the fracture.

The model is symmetric along the Y direction. To cut the simulation running time, the model is cut into two halves along the Y direction. Furthermore, 1″ of matrix in the X direction (1/3 of model in the X direction) and one fracture (half model in the Y direction) are included in the model. The final model sizes become 1″ × 1.5″ × 1″. The grids are 11 × 6 × 3. The injection rate is changed to one-sixth of that of the experiment, that is, 0.00033 ft^3/day. Based on this smaller model, the permeability and porosity in the base model are replaced by shale properties which are 300 nD ($\sim 3 \times 10^{-19}$ m^2) and 0.1 for the permeability and porosity, respectively.

In general, a surfactant may change wettability and reduce IFT. Since the surfactant is injected with the alkali, the model assumes the surfactant reduces IFT and the alkali changes wettability. The degree of wettability alteration is controlled by interpolation scaling factor parameters ω_{kr} to represent the changes in relative permeability and ω_{pc} to represent the changes in capillary pressure:

$$k_r = \omega_{kr} k_r^{ww} + (1 - \omega_{kr}) k_r^{mw} \tag{11.1}$$

$$p_C = \omega_{pc} p_C^{ww} + (1 - \omega_{pc}) p_C^{mw} \tag{11.2}$$

where the superscript *ww* and *mw* denote water-wet and initially mixed-wet conditions. The capillary pressure p_C is a scaled with IFT, porosity, and permeability as follows:

$$p_{Cjj'}^{ww} = C_{pc} \sqrt{\frac{\varphi}{k}} \frac{\sigma_{jj'}^{ww}}{\sigma_{jj'}^{ow}} \left(1 - \frac{S_j - S_{jr}}{1 - \sum_{j=1}^{3} S_{jr}} \right)^{E_{pc}} j', j = 1, 2, 3 \tag{11.3}$$

where $C_{pc}\sqrt{\phi/k}$ takes also into account the effect of permeability and porosity using the Leverett-J function (1941), ϕ is the porosity and k is the permeability, σ is the interfacial tension, S is the saturation at the water-wet condition, the subscripts $j, j\prime$ denote phases with j being the wetting phase, and S_{jr} denotes the residual saturation of phase j. Phases 1, 2, and 3 represent water phase, oil phase, and microemulsion phase, respectively. The capillary pressure endpoints in Table 11.2 are C_{pc} here. Assume the same C_{pc}

Table 11.3 Parameters for capillary desaturation curves used in the base model for the matrix.

Phase	T_p	S_{pr} at $(N_C)_C$	S_{pr} at $(N_C)_{max}$	k_r end point at $(N_C)_C$	k_r end point at $(N_C)_{max}$	k_r exponent at $(N_C)_C$	k_r exponent at $(N_C)_{max}$
Water	30,000	0.1	0	0.3	1	2	1
Oil	1,868	0.4	0	0.4	1	3	1
Microemulsion	342	0.1	0	0.3	1	2	1

value can be used in the experimental sand rock and the shale rock; the maximum capillary pressure for the shale becomes $\left(= 0.3\frac{\sqrt{(k/\varphi)_{\text{high}}}}{\sqrt{(k/\varphi)_{\text{low}}}} = 0.3\frac{\sqrt{34/0.298}}{\sqrt{3e{-}4/0.1}} \right) = 58.5$ psia. Such pressure is unrealistically low for a shale rock. We leave it in the base model and will discuss about it later. Next the performance from the shale rock is compared with that from the sand rock. After that, the effects of capillary pressure and pressure gradient are investigated.

11.3 Shale rock versus sand rock

The performance of the shale rock is compared with that of the sand rock in terms of oil recovery factor, oil saturation, and oil cut. The oil recovery factors for the water injection only, surfactant injection only, alkali injection only, and their sequential injection for the *sand* rock are shown in Fig. 11.6. The oil recovery factor for the water injection only has the lowest oil recovery factor as expected, followed by surfactant injection only and alkali injection only. Interestingly, the sequential injection of water, alkali, and surfactant has the highest recovery factor (marked in W-A-S in the figure), even higher than those from alkali and surfactant injection. It is also interesting to notice that the oil recovery factor from the alkali injection only is higher than that from the surfactant injection only. Such a result cannot be universal, as alkali cannot perform so well (Sheng, 2011; 2015c). The specific conditions here are: the alkaline concentration is 1%, and the surfactant concentration is 2%; the alkali changes the initially mixed wet to intermediate wet (ω_{kr} and $\omega_{pc} = 0.5$); the surfactant reduces the oil-microemulsion IFT from the initially 20 mN/m (oil-water) to about 10^{-3} mN/m. Since the wettability alteration can be achieved by alkali

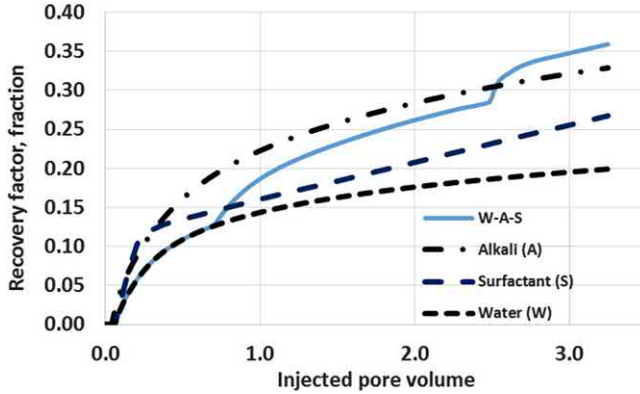

Figure 11.6 Oil recovery factors from water injection only, surfactant injection only, alkali injection only, and their sequential injection for the sand rock.

injection or surfactant injection (Sheng, 2012; 2013a), these results indicate that wettability alteration could be more important than IFT reduction.

The oil recovery factors from the water injection only, surfactant injection only, alkali injection only, and their sequential injection for the *shale* rock are shown in Fig. 11.7. No oil can be produced from the water injection only, because the shale rock is oil wet; once litter invaded water leads to a higher water saturation in the invaded blocks, the capillary pressure becomes negative (refer to Fig. 11.2), so oil can hardly flow out. For the surfactant injection only, the IFTs are reduced and the relative permeabilities are increased. The high permeabilities in the fracture make the injected surfactant solution break through the producer, so that the oil in the matrix

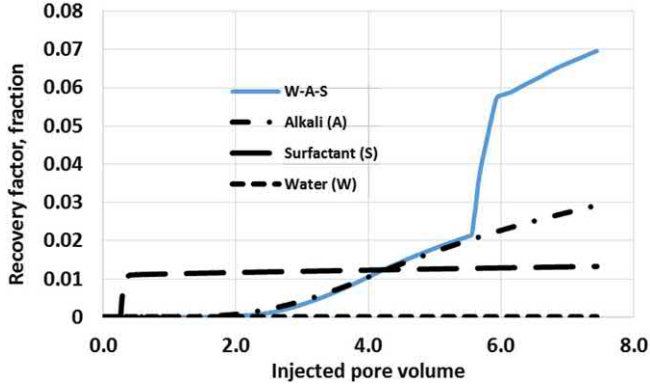

Figure 11.7 Oil recovery factors from water only, surfactant only, alkali only injection, and their sequential injection for shale rock.

blocks is bypassed, resulting in a very low oil recovery factor (~0.01). Oil can hardly be produced after 0.4 days of injection. Figs. 11.8A, 11.8B show the oil saturations at 0.4 and 9 days of injection, respectively in the matrix, almost unchanged, especially near the producer which is in the right-hand side. The oil saturation in the fractures is zero.

For comparison, the oil saturations at 0.4 and 9 days in the case of surfactant injection only for the sand model are shown in Figs. 11.9A, 11.9B, respectively. It can be seen that the saturation changes significantly

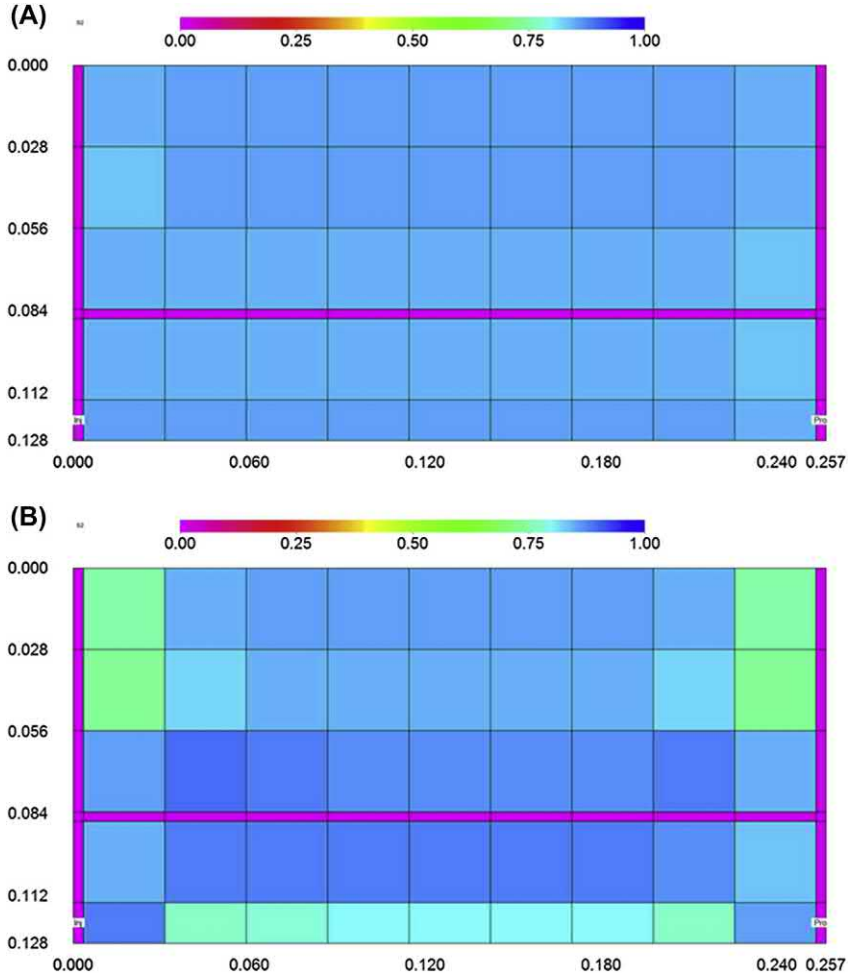

Figure 11.8 Oil saturation at 0.4 days (A) and 9 days (B) in the case of surfactant injection only (shale rock).

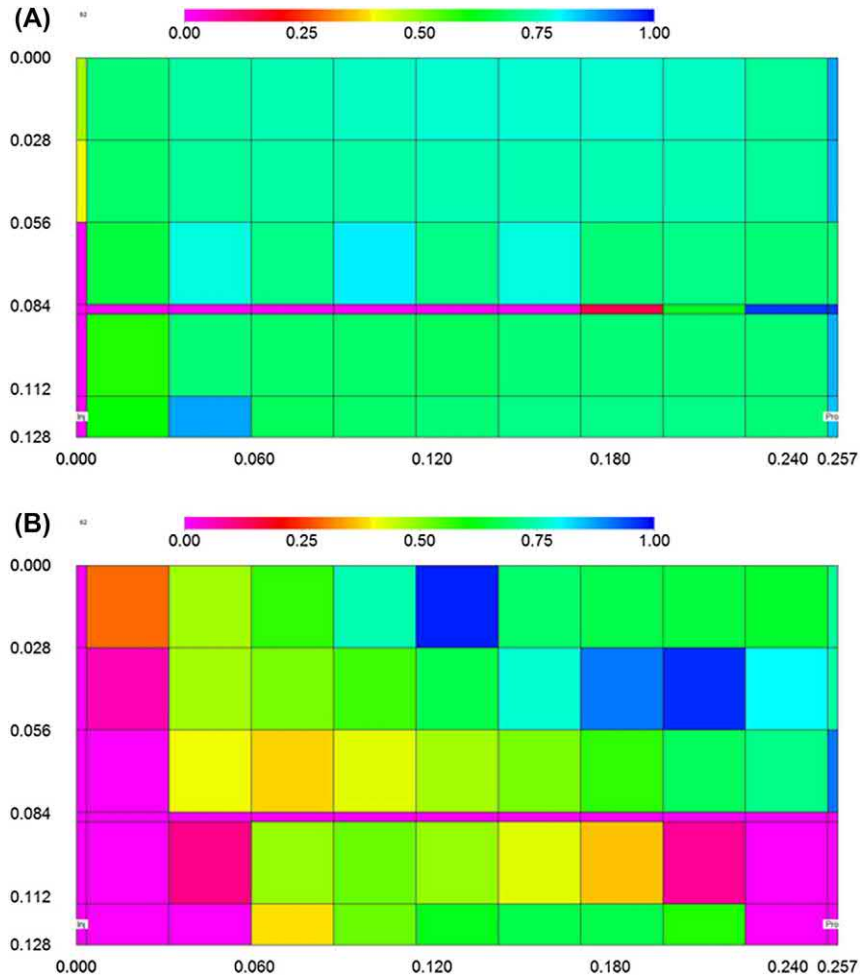

Figure 11.9 Oil saturation at 0.4 days (A) and 9 days (B) in the case of surfactant injection only (sand rock).

in the matrix, especially near the producer. In the sand rock, the permeability is not low, so that surfactant solution can partially enter the matrix instead of breaking through the fracture only.

For further comparison, the oil saturations at 0.4 and 9 days for the case of alkali injection only in the shale rock are shown in Figs. 11.10A, 11.10B, respectively. It can be seen the saturation changes significantly in the matrix from 0.4 to 9 days. More interesting, the oil saturations by 9 days at the two

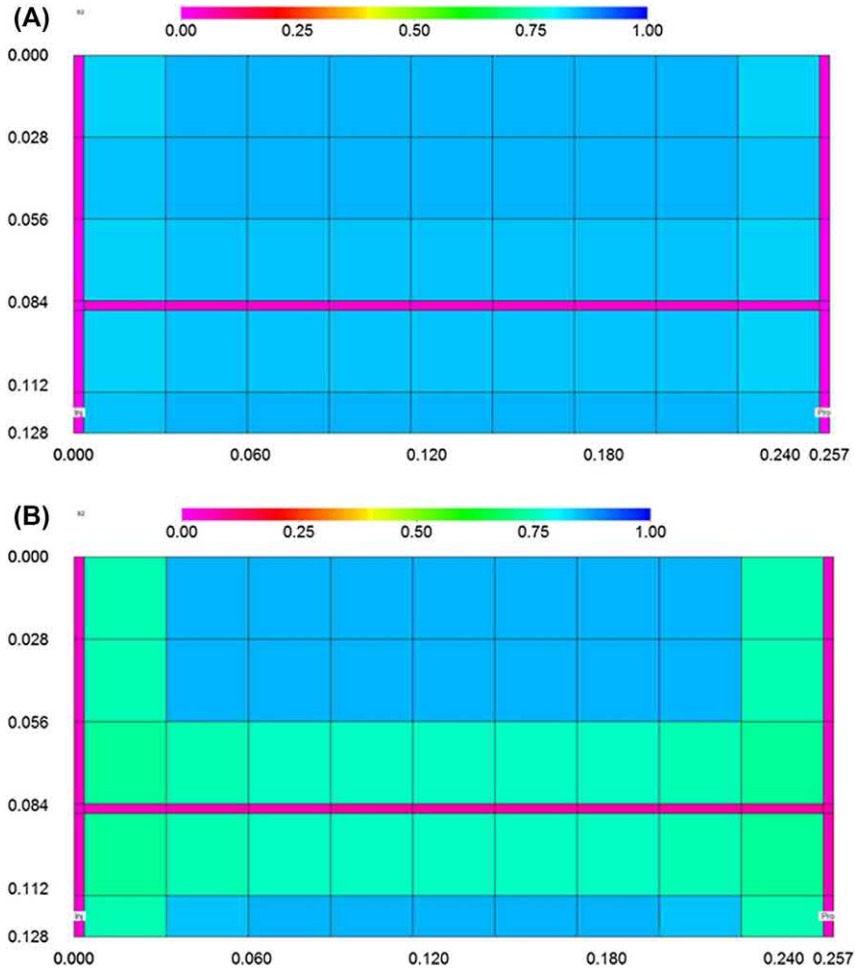

Figure 11.10 Oil saturation at 0.4 days (A) and 9 days (B) in the case of alkali injection only (shale rock).

sides of the fracture are uniformly distributed, indicating the alkaline solution enters the matrix uniformly by imbibition. And the oil saturation near the fractures is reduced, indicating that countercurrent flow of alkaline solution and oil occurs. Comparing to Fig. 11.9 for the surfactant injection only, the oil production in the alkali injection only is later, because the imbibition needs some time to effectively displace oil. The results from this model seem to indicate that wettability alteration is more effective than IFT reduction.

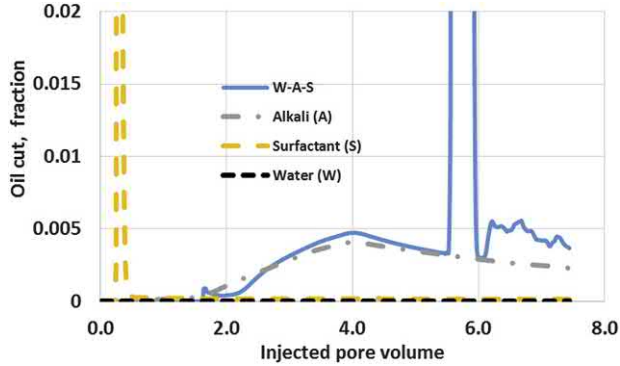

Figure 11.11 Oil cut for water injection only, surfactant injection only, alkali injection only, and the sequential injection for shale rock.

Fig. 11.11 shows the oil cut for water injection only, surfactant injection only, alkali injection only, and their sequential injection into the shale rock. The oil cut for the water injection only is almost zero in the entire injection history. The oil cut for the surfactant injection only has high oil cut (maximum 0.1 outside the scale in the figure) in a very short time and almost zero in the rest of injection history. The oil cut in the alkali injection only has oil cut about 0.005. The oil cut in the sequential injection has the oil cut similar to that in the alkali injection only, except there is short peak (maximum 0.12 outside the scale in the figure). This figure shows that the injected fluids break through at the producer through fractures, and very little oil can be displaced out.

For comparison, the oil cuts for water injection only, surfactant injection only, alkali injection only, and their sequential injection for the sand rock are presented in Fig. 11.12. It shows that there is a high oil-cut peak in every fluid injection in the early time, although the high oil-cut cannot be maintained. The contrast in performance between the sand rock and the shale rock is that some oil can be produced in the early time from the sand rock, whereas it is very difficult from the shale rock. Channeling is a well-known problem in fractured reservoirs. It can be seen that this problem is even worse in shale reservoirs from analyzing these simulation results. Such problem has been reported in the gas flooding in the Viewfield Bakken Field, Saskatchewan (Schmidt and Sekar, 2014), in the huff-n-puff CO_2 injection in the Parshall Field (Sorensen and Hamling, 2016), and the water-flooding in the Bakken formation in Montana (Hoffman and Evans, 2016).

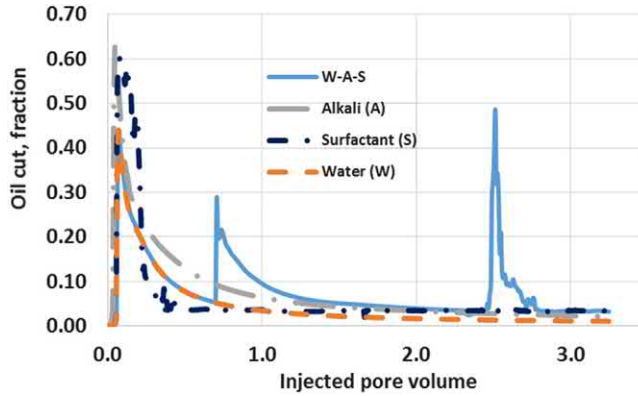

Figure 11.12 Oil cut for water injection only, surfactant injection only, alkali injection only, and the sequential injection for sand rock.

In the above discussions, the simulation time is limited to 9 days consistent with the experimental time done by Najafabadi et al. (2008). By 9 days, the total pore volumes injected for the sand and shale cases are 3.25 and 7.44, respectively. Such pore volumes injected are large for a field project, although 9 days sounds very short. Therefore, subsequent simulation runs are limited to 9 days, if not explicitly mentioned.

11.4 Relative permeability change versus capillary pressure change

In the base simulation models (sand and shale), alkali injection changes both relative permeability and capillary pressure. It will be interesting to see which change is more effective. For this purpose, two models are built for the sand rock. One is to assume only k_r changes in which $\omega_{kr} = 0.5$ and $\omega_{pc} = 0$ in Eqs. (11.1) and (11.2), and the other is to assume only p_c changes in which $\omega_{kr} = 0$ and $\omega_{pc} = 0.5$. The oil recovery factors are shown in Table 11.4. The recovery factor (0.333) in the former is 71% higher than that (0.195) in the latter. Another pair of two models is built for the shale rock and the oil recovery factors are also shown in the table. When only p_c is changed, no oil can be produced. When only k_r is changed, the recovery factor is 0.043. Both the sand model and shale model show that the change in k_r is more effective. Such a result is consistent with that for spontaneous imbibition (Sheng, 2013b).

Table 11.4 Effect of permeability change versus effect of capillary pressure change by alkali injection (initially mixed-wet).

	Sand	Shale
k_r changed only: $\omega_{kr} = 0.5$ and $\omega_{pc} = 0$	0.333	0.043
p_c changed only: $\omega_{kr} = 0$ and $\omega_{pc} = 0.5$	0.195	0.000

11.5 Effect of capillary pressure

The preceding section shows that capillary pressure change due to wettability alteration is not as effective as the k_r changes. Look at Fig. 11.2 again which shows that the maximum pressures are 0.3 psi and −0.43 psia. If Eq. (11.3) is used to estimate the maximum capillary pressure in the shale rock, they are 58.5 and −83.9 psia, respectively. One may argue that the capillary pressures used are too low to be effective. When the maximum capillary pressure is raised up to 100 times, the oil recovery factors are still insensitive to the value of capillary pressure, for both the sand model and the shale model! This clearly demonstrates that the flow is dominated by the viscous flow in the fracture. As it will be clear later in this chapter, the pressure gradient required for flow in the fracture is too small so that fluid may bypass the matrix.

In these models, the running time is 9 days. Probably it is too short to see the capillary effect. To check this hypothesis, the simulation time is extended to 90 days. Some of results by the end of 90 days are presented in Table 11.5. It is surprising to see that the oil recovery factor (0.404) for the sand model is

Table 11.5 Effect of capillary pressure in initially mixed-wet cores for 90 days.

Sand	Recovery factor	Alkali concentration at block (6 3 2), %
Max. $p_c = 0.3$ and −0.43 psia	0.404	0.496
Max. $p_c = 30$ and −43 psia	0.326	0.429
Shale	**Recovery factor**	**Alkali concentration at block (6 3 2), %**
Max. $p_c = 58.5$ and −83.9 psia	0.100	0.189
Max. $p_c = 5850$ and −8390 psia	0.228	0.361

higher at the lower capillary pressure than that (0.326) at the higher capillary pressure. But the oil recovery factors for the shale model do not show such result. This result demonstrates that the capillary drive in tight formation is more important.

To explain that result for the sand model, the alkaline concentration maps for the high and low capillary pressures in Figs. 11.13 and 11.14 at 90 days are compared. The alkaline concentrations in the high-p_c case are overall lower than those in the low-p_c case. For example, the concentrations at the model middle block (6 3 2) are 0.496% and 0.429% presented in Table 11.5, respectively, for the low-p_c and high-p_c. In these models, the initial wettability is mixed-wet, and the final altered wettability is not completely water-wet. Referring to Fig. 11.2, the capillary pressure is positive (drive force) in the beginning when the alkaline solution saturation is low; however, the capillary pressure becomes negative (resistance) when the saturation is high. Although the initial drive force is high, the later resistance is high as well for the high-p_c case. As a result, the high-p_c may not be an advantage.

For the shale models, the alkaline concentration maps at 90 days are shown in Figs. 11.15 and 11.16. The alkaline concentrations in the high-p_c case are higher than those in the low-p_c case. For the shale model compared with the sand model, there are two advantages for the high-p_c case. One is the fluid imbibition distance is lower, so the capillary pressure

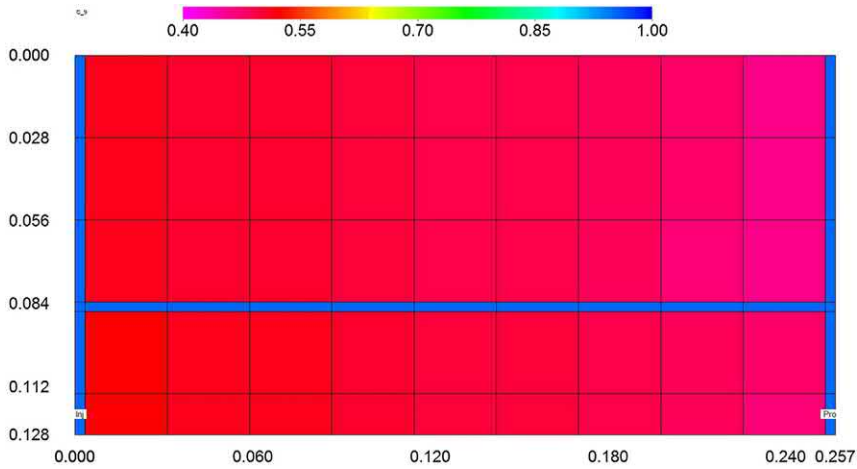

Figure 11.13 Alkaline concentration map in the middle layer at 90 days in the low-p_c sand model.

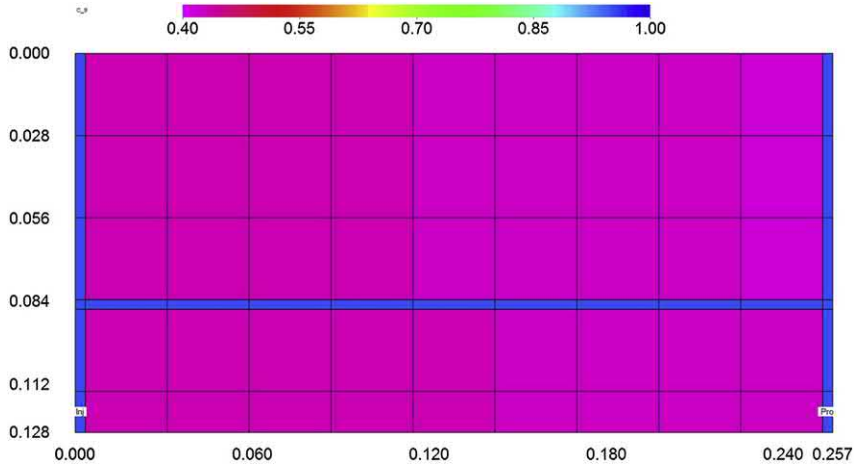

Figure 11.14 Alkaline concentration map in the middle layer at 90 days in the high-p_c sand model.

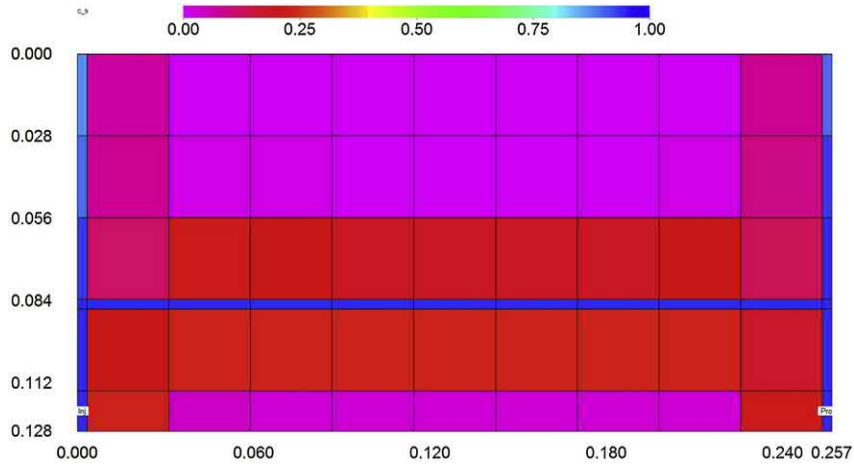

Figure 11.15 Alkaline concentration map in the middle layer at 90 days in the low-p_c shale model.

gradient is higher. The other one is that capillary pressure is higher. The resultant higher capillary gradient drives more alkaline solution into the matrix.

Note that 90 days of injection is modeled in such small cores. Upscaling such small models to a field model will result in unrealistically long injection time. For such a long time, capillary pressure has the mechanism in

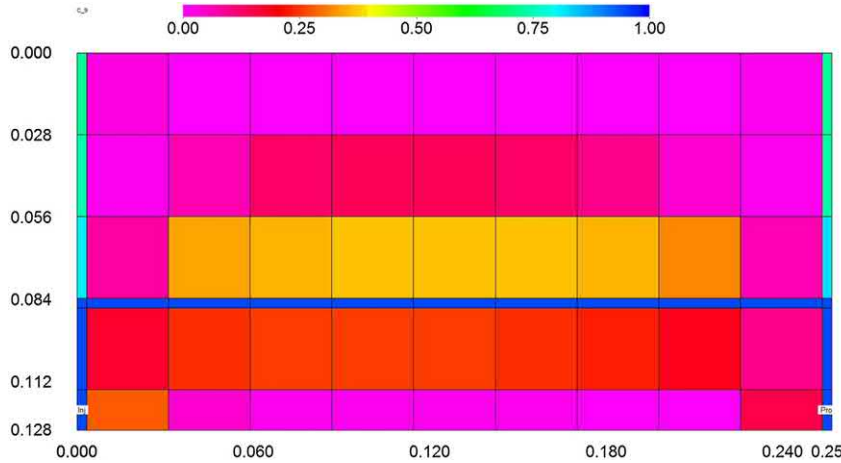

Figure 11.16 Alkaline concentration map in the middle layer at 90 days in the high-p_c shale model.

spontaneous imbibition. Such result may not be applicable to the forced imbibition (flooding) in a field scale. Therefore, we further investigate the effect of capillary pressure in small models for 9 days of injection.

Let us further check the sensitivity of capillary pressure when the initial wettability is oil-wet. The detailed parameters and results are presented in Table 11.6. In these models, the function to change relative permeabilities is removed. As the capillary pressures (both initial and altered) are increased by the same factors of 10 and 100, the oil recovery factor decreases from 0.067 to 0.025 and 0.001, respectively. The oil recovery is sensitive to the value of capillary pressure. For the shale model, because of the high resistance from the initially oil-wet cores, the alkaline solution cannot enter the matrix and the resulting oil recovery factors are null, regardless of the values of capillary pressure.

Table 11.6 Effect of capillary pressure in initially oil-wet cores for 9 days.

Capillary pressure endpoint, psia (Darcy)$^{1/2}$		Recovery factor	
Initially	**Altered**	**Sand**	**Shale**
−0.1452	0.1033	0.067	0.0
−1.452	**1.033**	**0.025**	**0.0**
−14.52	10.33	0.001	0.0
−1.452	**0.1033**	**0.0246**	**0.0**
−1.452	**10.33**	**0.0246**	**0.0**

From the sand models, when the initially wettability is changed from mixed-wet to oil wet, the oil recovery factor is changed from 0.195 (in Table 11.4) to 0.067 (in Table 11.6). This indicates that initial wettability is very important, which is consistent with Bourbiaux and Kalaydjian (1990) experimental data for spontaneous imbibition.

These models assume the magnitudes of maximum positive and negative p_c are increased at the same proportion. Now keep the initial oil-wet capillary pressure unchanged and the capillary pressure endpoint parameter is −1.452 psia (Darcy)$^{0.5}$. After wettability alteration, the parameter is changed to 0.1033, 1.033, and 10.33 psia (Darcy)$^{0.5}$ (the cases presented in bold in Table 11.6). For the sand models, the changes in oil recovery factors are not noticeable (close to 0.025). For the shale models, the oil recovery factors remain zero. These results confirm the conclusion that the oil recovery is insensitive to the *absolute value* of altered capillary pressure, if the rock is initially *oil-wet*. This is because when the rock is oil-wet, it is very slow for a chemical to diffuse into the rock to alter its wettability, then the subsequent high capillary pressure of water-wet nature cannot play its role. The p_c value is proportional to IFT. If the p_c value is not important, then the IFT is not important during wettability alteration from oil-wetness.

11.6 Effect of pressure gradient (injection rate)

The oil recovery factors during alkaline injection into the sand models and shale models at different injection rates (pressure gradients) are presented in Table 11.7. The pressure gradient is calculated using the injection well block (I = 1) pressure minus the production well block (I = 11) pressure divided by the distance between these blocks in the middle layer (K = 2). In the models, because the injector and the producer are directly connected

Table 11.7 Effect of pressure gradient in alkali injection.

	Sand		Shale	
Injection rate, ft^3/day	$(dp/dl)_f$, psi/ft	RF, fraction	$(dp/dl)_f$, psi/ft	RF, fraction
0.00011	0.117700	0.262	0.074297465	0.0145
0.00033	0.266507	0.328	0.214008893	0.0300
0.001	0.657965	0.424	0.624348985	0.0368
0.0033	1.857369	0.521	2.004676737	0.0406

through a fracture, the pressure gradient between the wells are the pressure gradient in the fracture $(dp/dl)_f$. Since the pressure gradient varies with time, the values presented in Table 11.7 and the subsequent tables are the average pressure gradient during the injection. It is shown that as the injection rate or pressure gradient $(dp/dl)_f$ is increased, the oil recovery factor is higher, both from sand and shale models. The higher pressure gradient provides a higher force to drive the injected alkaline solution into matrix, resulting in higher oil recovery. Such result has been presented for surfactant injection in laboratory by Parra et al. (2016).

Now we look at the surfactant injection. The oil recovery factors from the sand models and shale models at different injection rates (pressure gradients) are presented in Table 11.8. From the sand models, it is clear that as the injection rate or pressure gradient is increased, the oil recovery factor increases. If the first (very low rate) and last (very high rate) pair of data are removed, oil recovery factor versus pressure gradient is shown in Fig. 11.17. An approximately linear relationship can be observed. For the shale models, the oil recovery factors are very low with the maximum 0.0261. When the rates are low, as the pressure gradient is increased, the oil recovery factor increases. However, in the higher rate range, as the pressure gradient is increased, the oil recovery factor even decreases. The relationship between oil recovery factor and pressure gradient is not clear. This may be caused by numerical errors in simulation because of too low oil recovery factors. These results also show that even if a high pressure gradient is imposed, the ultralow IFT surfactant solution cannot enter the ultralow permeability matrix. It indicates that a surfactant solution of ultralow IFT with oil will not be beneficial to oil recovery, if there is the

Table 11.8 Effect of pressure gradient in surfactant injection.

	Sand		Shale	
Injection rate, ft^3/day	$(dp/dl)_f$, psi/ft	RF, fraction	$(dp/dl)_f$, psi/ft	RF, fraction
0.0000033	0.012295868	0.040	0.001733818	0.0000
0.00000165	0.044261351	0.126	0.012411145	0.0055
0.000033	0.061503113	0.166	0.02336886	0.0261
0.00011	0.115751967	0.198	0.049332963	0.0201
0.00033	0.260944796	0.267	0.132130724	0.0132
0.001	0.693085916	0.619	0.389119313	0.0107
0.0033	1.427742839	0.971	1.271664234	0.0096
0.033	8.71952236	1.000	12.67878541	0.0097

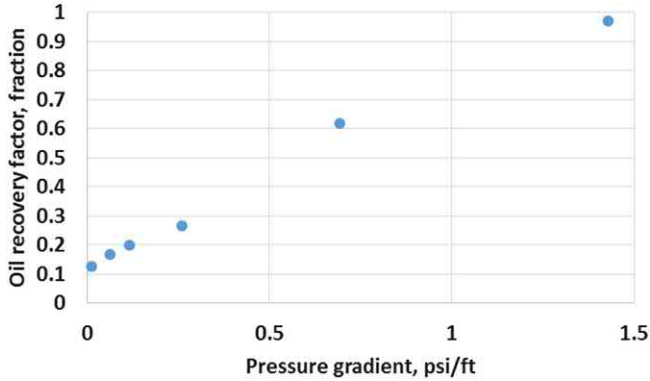

Figure 11.17 Oil recovery factor versus pressure gradient from surfactant flooding sand models.

existence of high-permeability fractures between the injector and the producer.

For comparison, the oil recovery factor versus pressure gradient for alkaline flooding from shale and sand models is plotted in Fig. 11.18. The relationship shows less linearity, indicating that the relationship is more complex than that in surfactant flooding. In addition to the pressure gradient effect, wettability alteration plays an important role.

In the above shale models, the fracture permeability is 2000 mD. This results in such high permeability ratio between the fracture and matrix that the injected fluid channels through the fracture, and surfactants or any chemicals added in the injected fluid may not function. To check this

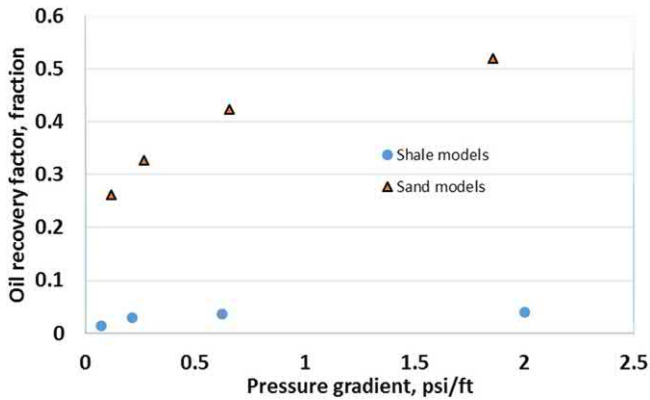

Figure 11.18 Oil recovery factor versus pressure gradient for alkali flooding from shale and sand models.

Table 11.9 Effect of pressure gradient by changing fracture permeability and injected water viscosity.

	Surfactant		Alkali	
Fracture permeability, mD	**$(dp/dl)_f$, psi/ft**	**RF, fraction**	**$(dp/dl)_f$, psi/ft**	**RF, fraction**
2000	0.132	0.0132	0.214	0.0300
20	13.209	0.0135	21.683	0.0263
2	134.281	0.0178	215.826	0.0284
Injected water viscosity, cP	**dp/dl, psi/ft**	**RF, fraction**		
1	0.132	0.0132		
10	1.274	0.0143		
100	12.681	0.0105		

effect, the fracture permeability is reduced in shale models with surfactant and alkaline flooding. Table 11.9 shows that as the fracture permeability is reduced to 2 mD, the pressure gradient is increased to 134.281 psi/ft in surfactant flooding. Such pressure gradient is too high in actual flooding cases in reservoirs. Even so, the oil recovery factors by 9 days of flooding are increased from 0.0132 to 0.0178 only, with the absolute recovery being practically insignificant. A similar observation can be made for the alkaline flooding from this table. Parra et al. (2016) proposed to increase microemulsion viscosity to increase the transverse pressure gradient from fracture to matrix for improved oil recovery in fractured reservoirs. This idea is tested in the shale models here. In the base case, the injected water viscosity is 1 cP. The viscosity is increased to 10 and 100 cP so that the pressure gradient is increased to 1.274 and 12.681, respectively. However, the absolute oil recovery factors shown in Table 11.9 are practically insignificant.

Parra et al. (2016) experimentally demonstrated that when the microemulsion viscosity was increased, the resulting higher pressure gradient improved oil recovery. In their experiments, the matrix permeability was 100−320 mD. Now we use our simulation models to verify their observation. By doing so, we can also verify whether our simulation models can predict actual performance in chemical flooding. The base shale model is used to change the matrix permeability to 100 mD, and increase the water viscosity from 1 cP in the base model to 10 cP. The results are presented in Table 11.10. When the water viscosity is increased from 1 to 10 cP, the resulting pressure gradient is increased from 0.145 to 0.675 psi/ft, and the oil recovery factor is increased from 0.766 to 0.999. The incremental oil

Table 11.10 Effect of pressure gradient by changing matrix permeability and injected water viscosity in surfactant only flooding.

Matrix permeability, mD	Injected water viscosity, cP	$(dp/dl)_f$, psi/ft	$(dp/dl)_{fm}$, psi/ft	RF, fraction
0.0003	1	0.132	−1.920	0.0132
100	1	0.145	0.000	0.766
100	10	0.675	−0.048	0.999
0.1	1	0.146	−0.384	0.060
0.1	10	1.284	−0.048	0.056

recovery factor is significant. This verifies Parra et al.'s experimental observation and our simulation models as well. To check whether oil recovery factor in tight oil reservoirs could be increased by increasing pressure gradient, two additional models are run. In these models, the matrix permeability is 0.1 mD, and the water viscosity is increased from 1 to 10 cP. The results are presented in Table 11.10 as well. Although the pressure gradient is increased from 0.146 to 1.284 psi/ft when the water viscosity is increased from 1 to 10 cP, the oil recovery factor is almost unchanged.

For comparison, the microemulsion phase pressure gradient $(dp/dl)_{fm}$ from the fracture block (6 4 2) to the matrix block (6 3 2) at the middle of injection process (4.4 days) for each case is also presented in Table 11.10. These data show that for the base shale model with the matrix permeability of 0.0003 mD, the pressure gradient from the fracture block to the matrix block is −1.920 psi/ft (negative!), indicating that the microemulsion phase in the fracture cannot enter the matrix. When the matrix permeability is 100 mD, the pressure gradient from the fracture block to the matrix block is zero for the injected water viscosity of 1 cP, and −0.048 psi/ft (close to zero) for the injected water viscosity of 10 cP. Compared with the pressure gradient for the 0.0003 mD case, these pressure gradients (absolute value) are much smaller. For the tight model with the matrix permeability of 0.1 mD and the injected water viscosity of 1 cP, the $(dp/dl)_{fm}$ is −0.384 psi/ft, while the pressure gradient in the fracture $(dp/dl)_f$ is +0.146 psi/ft. The fluid in the fracture block cannot enter the matrix block. For the tight model with the injected water viscosity of 10 cP, although the $(dp/dl)_{fm}$ is equal to −0.048 psi/ft (close to zero), the $(dp/dl)_f$ is +1.284 psi/ft (very high). Thus the injected surfactant solution channels through the fracture.

From the above discussion, we can see that increasing pressure gradient in a chemical flooding may not be effective in fractured shale or tight reservoirs.

11.7 Experimental study of forced imbibition

Tu and Sheng (2019) did some experiments of forced imbibition. The experimental setup was a modified Amott cell, a high-pressure accumulator, and a Quizix pump (Fig. 11.19). A traditional Amott cell is commonly used for the experiments on spontaneous imbibition. However, the Amott cell cannot stand pressure, probably higher than 5 psig. During surfactant injection in a real reservoir, the injection pressure will be higher than the pressure inside matrix. In other words, the imbibition is forced imbibition during a huff or soaking period. To reflect this reality, the Amott cell was modified as shown in Fig. 11.19. The bottom cap with a communication port balances the pressures inside and outside the cell. By submerging the whole Amott cell into the upper portion of the accumulator filled with designated fluid, any target pressures can be simply achieved by injecting water through the Quizix pump into the bottom portion of the accumulator. The balanced pressure in the top space of the accumulator can be recorded from the pressure gauge. The advantage of such apparatus is that the pressurized imbibition occurs inside the cell and any oil coming out the core can be viewed at the cell neck with graduated scales.

A total of eight cycles of pressurized huff (including soaking) and puff tests were performed for each core sample listed in Table 11.11. Each test

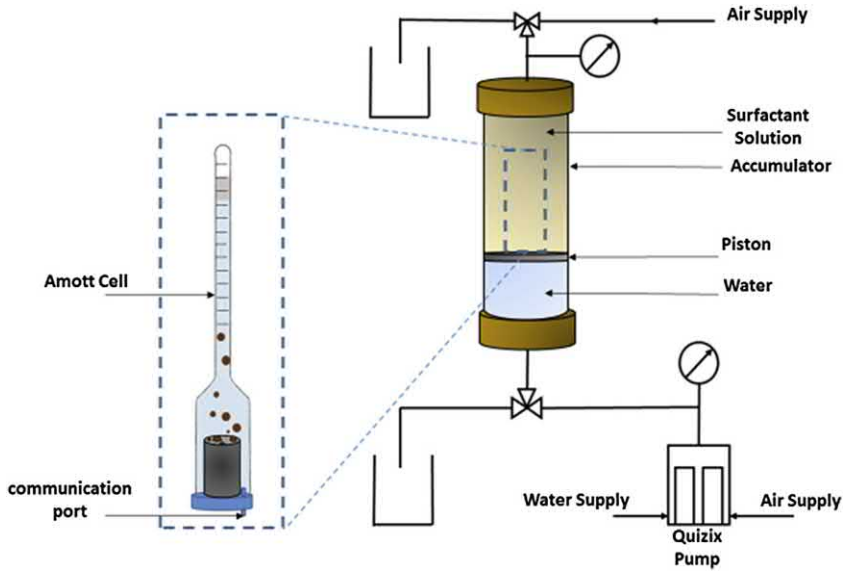

Figure 11.19 Modified high-pressure Amott apparatus.

Table 11.11 Experimental conditions for pressurized soaking and depletion tests.

Core No.	Testing solution	Soaking time, hour	Injection pressure, psi	Depletion time, hour	Production pressure, psi
EF-1	Brine (5% KCl), IFT = 18 mN/m	12	3000	12	14.7
EF-2	High IFT surfactant (3 mN/m)				
EF-3	Intermediate IFT surfactant (0.4 mN/m)				
EF-4	Low IFT surfactant (0.02 mN/m)				

had 12-hour huff (soaking) and 12-hour puff periods. The soaking pressure was controlled to 3000 psi and the cell was depleted to atmospheric pressure. The cores were initially oil-wet (contact angles about 150°) altered by surfactants to 35−40°. Note that during the huff and soaking period, because the pressure could be quickly increased, a huff and soaking period was actually a soaking period.

The oil recovery factors of huff-n-puff for different surfactant solutions and brine are shown in Fig. 11.20. The oil recovery factor was higher when the IFT was higher, the same trend as the spontaneous imbibition. Note that the last two points of high oil recovery factor for the intermediate IFT were caused by fractures created in the core. It implies that the spontaneous imbibition during huff and soaking period is very important. This observation becomes more obvious when the simulation data of pressure and recovery factor are presented in the same plot in which the continuous pressure and oil recovery data are presented. For example, the pressure and oil recovery data for the high-IFT case is presented in Fig. 11.21. Look at a single cycle, the high-pressure step (3000 psig) indicates the huff and soaking period, and the low-pressure step (0 psig) indicates the depletion period. From a close look at the oil recovery data during a single cycle, we can see that the oil coming out of the core during the huff and soaking period is higher than that during the puff (depletion) period. It becomes clear

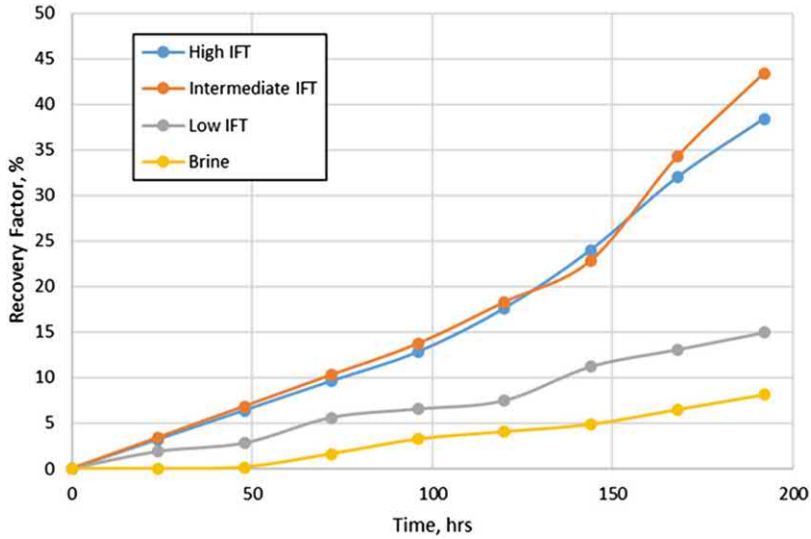

Figure 11.20 Oil recovery factors of huff-n-puff for different solutions with different IFTs and wettability alteration.

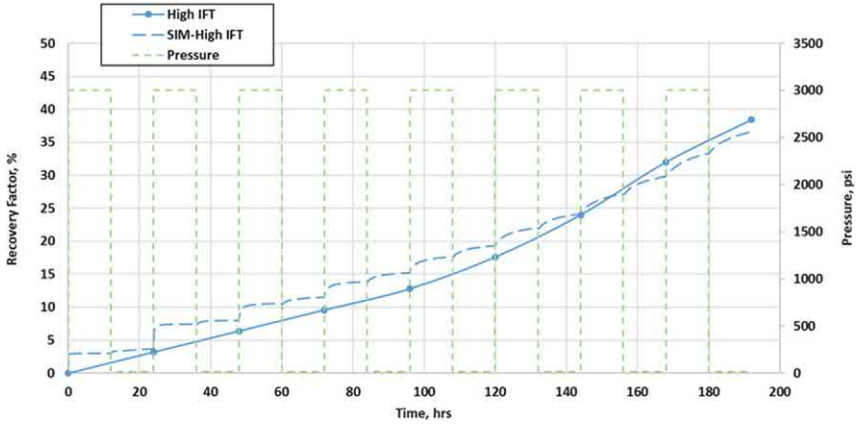

Figure 11.21 Oil recovery factor and pressure during huff-n-puff for the high-IFT solution.

when the oil during the huff and soaking periods is added together compared to the oil added during the puff periods, as shown in Fig. 11.22 (experimental data). In this figure, the huff and soaking time varied, but the depletion (puff) time was the same (12 h), total eight cycles. Interestingly, the oil recovery during the 3 h of huff and soaking was even higher than that during the 12 h of depletion for eight cycles. During the depletion, the pressure was low at practically atmospheric pressure because the pressure was immediately depleted, and the imbibition is actually spontaneous imbibition. These data suggest that the pressurized imbibition is important; in other words, the pressure helps imbibition.

For the above one brine, one low-IFT and one high-IFT surfactant solutions, spontaneous imbibition, forced imbibition, and cyclic injection

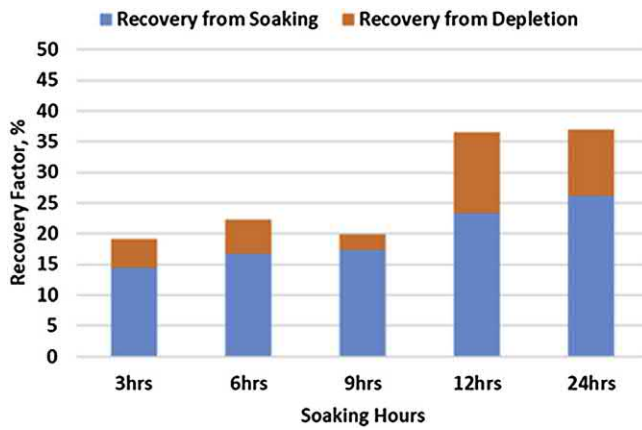

Figure 11.22 Oil recovery factors for different huff and soaking times compared to that during 12 h of depletion (high-IFT cases).

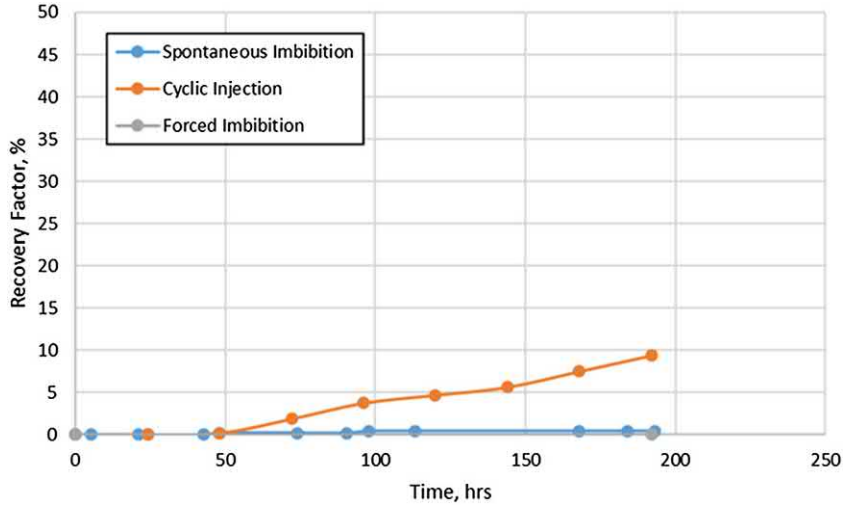

Figure 11.23 Spontaneous imbibition, forced imbibition and cyclic injection for brine.

(huff and soaking and puff injection) were conducted. Fig. 11.23 shows the tests using brine. For the spontaneous and forced imbibition, basically no oil came out of the core because the core was oil-wet. The cyclic injection brought some oil out by depletion. For the low three IFT surfactant solutions, Figs. 11.24 and 11.25 show the oil recovery from forced

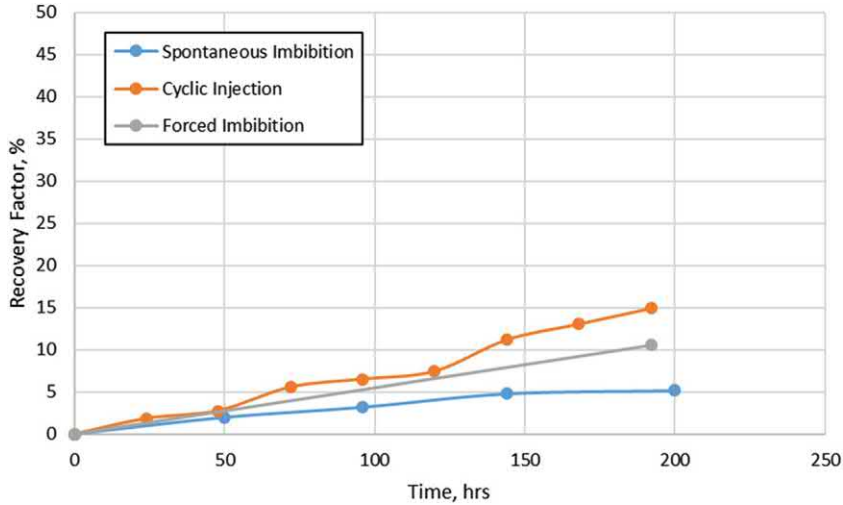

Figure 11.24 Spontaneous imbibition, forced imbibition and cyclic injection for the low-IFT surfactant solution.

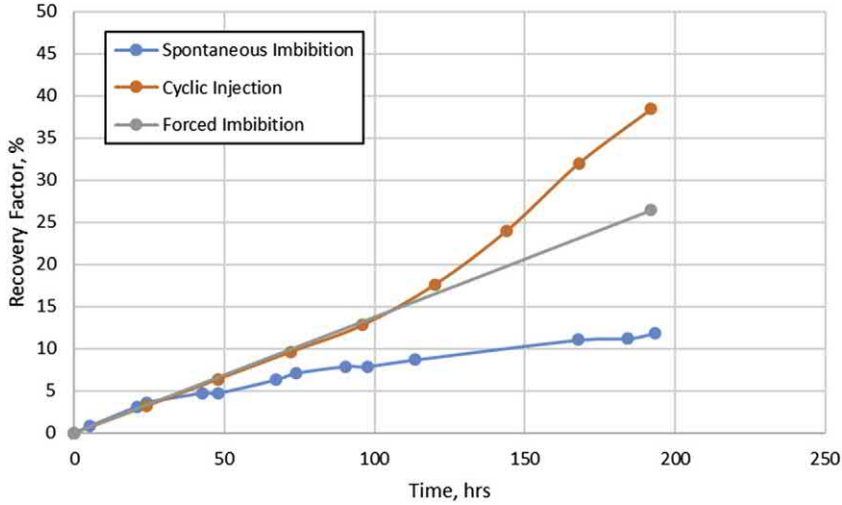

Figure 11.25 Spontaneous imbibition, forced imbibition and cyclic injection for the high-IFT surfactant solution.

imbibition was higher than that from the spontaneous imbibition; the oil recovery from cyclic injection was highest because extra oil was obtained by depleting the core pressure. Those results also show that the forced imbibition had higher oil recovery for the high-IFT solution than that for the low-IFT solution.

11.8 Field tests of surfactant EOR

Surfactants are often added in the fracturing fluid for different reasons, but not necessarily for enhancing oil recovery. There have been few field tests where surfactants were added for the direct EOR purpose.

It is well known that surfactants can change wettability and enhance water imbibition. For conventional oil-wet fractured carbonate reservoirs, many laboratory studies have been conducted using surfactants to stimulate spontaneous imbibition, for example, Chen et al. (2001), Olson et al. (1990), and Hirasaki and Zhang (2004). Some surfactant stimulation tests (injection, soak and flush back) have been tried in the Yates field in Texas (Yang and Wadleigh, 2000), the Mauddud carbonate in Bahrain (Zubari and Sivakumar, 2003), in the Cottonwood Creek field, Wyoming (Xie et al., 2005; Weiss et al., 2006), and in the Baturaja formation in the Semoga field in Indonesia (Rilian et al., 2010). Field results in general showed positive responses to surfactant stimulation (Sheng, 2013a).

The literature on shale oil rocks indicates that they are most likely oil-wet (Phillips et al., 2009; Wang et al., 2011). This oil-wet condition makes it difficult for the aqueous phase to penetrate the matrix and displace the oil out. Surfactants can alter the rock wettability from oil-wet to water-wet or mixed wet (Sheng, 2012). Therefore, most of surfactant-related EOR studies for shale oil reservoirs focus on wettability alternation and water imbibition (e.g., Shuler et al., 2011; Wang et al., 2011; Ferno et al., 2012; Xu and Fu, 2012; Morsy and Sheng, 2014b). Those studies used very thin slices or small cores because the spontaneous imbibition process is very slow (Sheng, 2013b). In practice, if the matrix is too large, the recovery rate by spontaneous imbibition will be uneconomically slow, because the imbibition rate is inversely proportional to a characteristic length, either linearly, or squared (Mattax and Kyte, 1962; Cuiec et al., 1994; Kazemi et al., 1992; Li and Horne, 2006; Ma et al., 1997; Babadagli, 2001). To solve this problem, we need to implement forced imbibition to speed up the imbibition process, like in the fracturing process. Apparently, refracturing shale reservoirs improves recovery (Vincent, 2011). Huff-n-puff surfactant injection may contribute to the process of refracturing and thus enhance oil recovery. Interestingly, huff-n-puff is expected to work better than surfactant flooding in shale reservoirs. However, we did not see a huff-n-puff field case report. Instead, a surfactant flooding in a Bakken formation was studied.

A detailed characterization program consisting of logging, coring, pressure testing, and fluid tracing was carried out to build a reservoir model to evaluate the EOR potential of surfactant flooding in a Middle Bakken formation. The reservoir model is also based on calibrated parameters from history-matching experiments like surfactant adsorption parameters. The permeability in the modeled area is 100 nD to 10 μD. The model consists of a pair of horizontal wells with half-fractures from each well overlapping 60% but not connected. Only half of a fracture from each well is included in the model. The base half-fracture length is 1200 ft, and fracture height is 300 ft. The model predicts that the produced oil in 12.5 years is more than what can be produced from 12.5 years of primary production. A series of economic sensitivity studies shows that the surfactant injection could have not only EOR potential, but also economic potential. However, detailed data in the model were not reported in the paper by Dawson et al. (2015).

CHAPTER TWELVE

Fracturing fluid flow back

Abstract

In this chapter, the flow back and production performance from common shale reservoirs and experimental results are summarized. Mechanisms of low flow back are proposed. The effects of shut-in, initial rock wettability, invasion depth and surfactant additives on flow back are discussed. Finally, some solutions to deal with flow back are summarized.

Keywords: Delay; Flow back; Invasion; Invasion depth; Permeability recovery; Shut in; Surfactant additives; Water blockage.

12.1 Introduction

After hydraulic fracturing, a well can be put in production immediately or after some time. Several terms have been used anonymously to describe the time to defer well production: soak, shut-in, resting, and delay. Strictly speaking, shut-in or resting means a time lapse between two flowing periods, while the delay means the time before the first flowing period. We try to explicitly use the different terms of "shut in" and "delay." The shut-in is sometimes called the first shut-in which is from the end of fracturing stimulation to the start of the first fluid flow back. The shut-in after the first flow back is the second shut-in or subsequent shut-in, which is an intentional or unintentional event in operation.

Generally, fracturing treatments are designed with good fluid stability during the pump time. It is desired to break the fluid as quickly and completely as possible to facilitate rapid cleanup of the well and minimize conductivity damage. It is commonly believed that if the shut-in in the reservoir is too long, fracture conductivity damage may increase. For a multistage fracturing job, it is desirable to flow the treatment fluid back after each stage to recover the fluid, because the shut-in time for the preceding stages will be too long, if the flow back is executed after the fracturing work at the last stage is completed. Then a problem is that offshore and geographically remote well operations often require the use of the drilling rig for completion operations. The time consumed on the completion phase

Enhanced Oil Recovery in Shale and Tight Reservoirs
ISBN: 978-0-12-815905-7
https://doi.org/10.1016/B978-0-12-815905-7.00012-8

of a fractured well can therefore be very expensive. Significant cost savings can be realized after the flow back of fracturing fluid after the last stage is fractured so that the rig is moved quickly. We also need to know whether a long shut-in time is not harmful to the subsequent hydrocarbon production. Therefore, study of shut-in time effect is very important.

There does not appear to be significant impairment of stimulation effectiveness, if delays of up to 2 h occur prior to the start of flow back. There is conclusive evidence that whenever any shut-in occurs during flow back, especially prior to gas breakthrough, damage occurs. Delay in starting flow back is less damaging than shut-ins during flow back. The well should not be shut-in prior to hydrocarbon breakthrough, and even afterward. Delayering breakthrough of hydrocarbon production by maintaining lower flow back rates, not by shutting-in, appears to result in better effective stimulation (Crafton, 1998).

In low-permeability formations, a large amount of proppant is pumped at lower proppant concentrations, requiring an excessive volume of fracturing fluid to transport the proppant. This extends the closure time, allowing proppant to transport away from the wellbore into the fracture after the end of treatment. In such a situation, an early flow back procedure to force proppant bridging at the wellbore in a reverse screen-out mode is essential to restore the proppant pack conductivity near the wellbore (Barree and Mukherjee, 1995). This process can be immensely accelerated by increasing proppant concentration toward the end of the treatment as suggested by Ely et al. (1990), Coulter and Wells (1972), and Cleary et al. (1994). Or small pad volume is used (Cleary et al., 1994).

One of the controversial issues in hydraulic fracturing is the flow back of fracturing fluids. It is intuitive that higher percentage of fracturing fluid flow back should lead to higher hydrocarbon recovery, because the remaining fracturing fluid may block the paths for hydrocarbon to flow to the well during production. However, that has not been always the case. In the case of low-permeability reservoirs, wells with good permeability and flow capacity may often start recovering significant hydrocarbon after very little production of the fracturing fluid (Malone and Ely, 2007).

In this chapter, the flow back and production performance from common shale reservoirs and experimental results are summarized. Mechanisms of low flow back are proposed. The effects of shut-in, initial rock wettability, invasion depth, and surfactant additives on flow back are discussed. Finally, some solutions to deal with flow back are summarized.

12.2 Field observations and experimental results on flow back

The literature information about fracture fluid flow back and production performance related to the flow back are summarized in this section.

12.2.1 Low flow back

The most commonly used fracturing fluid in the shale reservoir stimulation is slick water due to the characteristics of low cost, easily creating complex fracture networks and little reservoir damage (Waltman et al., 2005; Palisch et al., 2010; Cuss et al., 2015). Thousands of barrels of fracturing fluid are injected into the formation during hydraulic fracturing operation. However, field data indicate that only a small fraction of the injected fluid is recovered during the clean-up phase. Most of gas well is less than 50% of the total injection volume (King, 2012; Vengosh et al., 2014; Singh, 2016). Some are even less than 5% (Nicot and Scanlon, 2012). On average, only 6%−10% of the injected water is recovered in the United States across all shale plays (Vandecasteele et al., 2015; Mantell, 2013).

12.2.2 Flow back versus hydrocarbon production

There are no consistent observations or results regarding the effect of flow back on gas or oil production. In some cases, gas production is good when more water flows back. In other cases, gas production is good with a small fraction of water flowing back. Yan et al. (2015) used tight rocks (2−18 μD), and Chakraborty and Karpyn (2015) used shale cores (10−200 nD) to experimentally prove that it was detrimental for water to be further imbibed into shale matrix by capillary redistribution due to the permeability impairment by clay swelling. Ibrahim and Nasr-El-Din (2018) conducted similar experiments in tight sandstones (0.23 mD) and in Marcellus shales (3 nD) showing similar results.

Ghabnari et al. (2013) compared the flow back efficiency with cumulative gas production after 72 h of flow back for the wells drilled in Muskwa, Otter Park, and Evie, as shown in Fig. 12.1. The cumulative water production after 72 h was considered because the majority of fluid flowed back during the first 72 h (Asadi et al., 2008). Overall, there was no clear relationship between the gas production and water flow back. But Ghabnari et al. (2013) grouped the wells into two groups. One group is low water flow back efficiency and high gas production, and the other group is high water flow back efficiency and

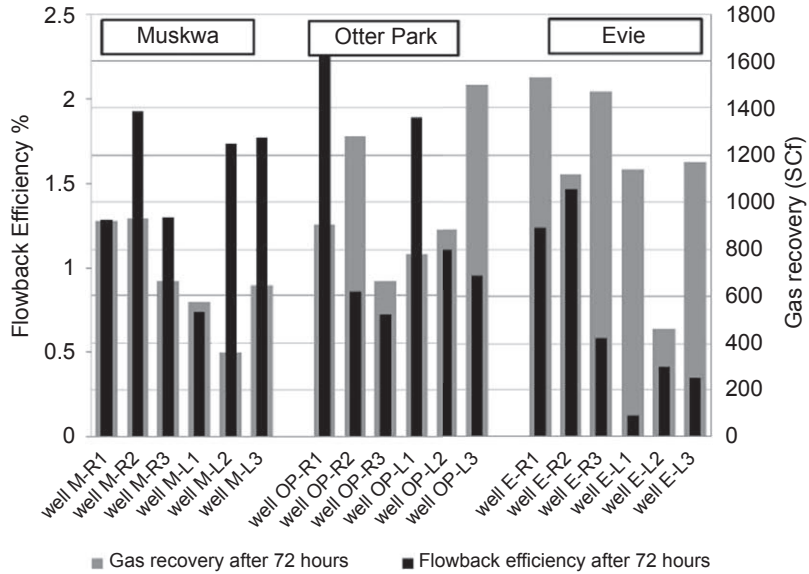

Figure 12.1 Comparison of flow back efficiency with cumulative gas production after 72 h of flow back for three shale gas wells (Ghabnari et al., 2013).

low gas production. They proposed two different fracture systems for the two groups of wells, as shown in Fig. 12.2A for the former group, and Fig. 12.2B for the latter group. In the complex fracture system, at the end of fracturing stimulation, the large primary fractures are filled with proppant and water, but the small but complex secondary fractures are just filled with water. During the shut-in, water imbibes into the complex fracture system, and gas flows

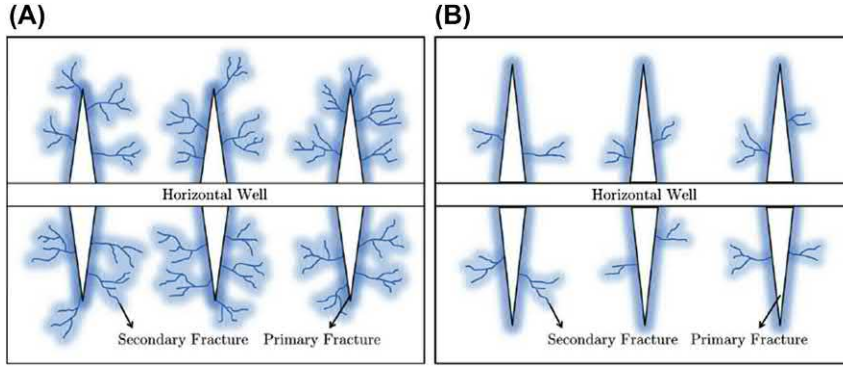

Figure 12.2 Schematic illustration of proposed complex fracture system (A) and simple fracture system (B) (Ghabnari et al., 2013).

into the large fractures by countercurrent flow. During the flow back, the water will be trapped as the small fractures are closed, resulting in low water and high gas production. In the simple fracture system, there are less contact surfaces by water. Thus, less countercurrent flow between water and gas. During the flow back, water can more quickly flow out, the small fractures are closed, resulting in higher water rate, more gas trapped in the matrix and low gas production.

Tangirala and Sheng (2019a) investigated the flow back and oil production in hydraulically fractured water-wet formations using the Lab-on-a-Chip method. A borosilicate glass chip was etched by the process of chemical vapor deposition to form a uniform channel porous medium network (20 × 10 mm footprint). The size of the chip was 45 × 15 mm. The chip was manufactured by Micronit Microtechnologies B.V., Netherlands. The width and height of each channel were 50 and 20 μm, respectively. The porosity of the channel network was 0.6 with two end nodes, End A and End B (Fig. 12.3). A wide pore channel connected to the inlet distributed the injected fluid evenly to the pore network. This portion of the chip represented a fracture.

The chip was housed in a fluidic connect PRO chip holder which was fixed over the mechanical stage of a fluorescence-imaging inverted microscope (Olympus CKX-53). As shown in Fig. 12.4, fluids were pumped by an air compressor whose pressure was controlled by the pressure regulator, a pressure-based flow controller, MFCS-EZ, purchased from Fluigent Inc. The flow rate was measured using the Flow Rate Platform (FRP) also acquired from Fluigent Inc. and having a measurable range of 0—7 μL/min. Before passing through the chip, the fluids were filtered through a 2 μm inline polyether ether ketone (PEEK) filter provided by IDEX corporation.

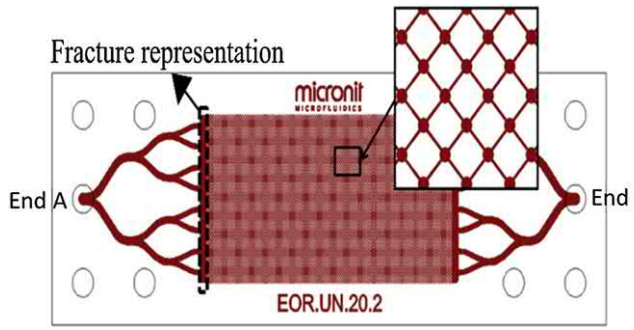

Figure 12.3 A microchip with uniform porous network.

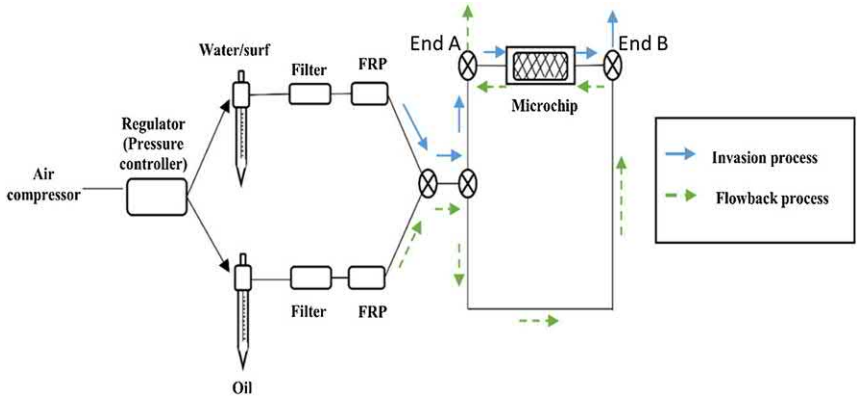

Figure 12.4 Experimental flow chart.

A mineral oil, Soltrol-130, had the viscosity of 2.37 cP. The IFT between the oil and water was 32.92 ± 0.27 mN/m. Two nonionic surfactants, CELB 217-123-8 (Surf-A) and CELB 217-123-2 (Surf-B), supplied by ChemEOR Inc., were diluted to 0.05 and 0.2 wt.%, respectively. The IFTs of Surf-A and Surf-B with oil are 1.64 ± 0.15 mN/m and 3.35 ± 0.34 mN/m, respectively. Those aqueous solutions did not change the initial water-wetness of the network channels. The fluorescein dye purchased from Sigma-Aldrich was soluble only in an aqueous phase and is used to distinguish an aqueous phase from an oil phase. The invasion process and the flow back process are marked by arrows in the figure.

Initially, the microchip representing a porous medium was saturated with oil. During the invasion process (marked by solid arrows), water or a surfactant solution was injected through the valve at End A at a constant pressure of 80 mbar, with the valve at End B open. Both End A and End B had valves with two flow directions. After a designed pore volume (PV) of an aqueous solution was injected, the valves at End A and End B were closed. A saturation image picture was taken. Subsequently, the valve at End A was closed for flow, and the valve at End B for flow was open. Oil was pumped through End B. This process represented a flow back process. After about 10 PVs of oil injection, the flow rate stabilized. During this process, some aqueous solution remained in the network creating some water blocking or formation damage. At the constant pressure difference of 80 mbar, the changes of flow rate might represent the mitigation of formation damage. When the flow rate was stabilized, this flow rate was equal to the oil flow rate through End B. At the end of the process, the values were closed, and an image

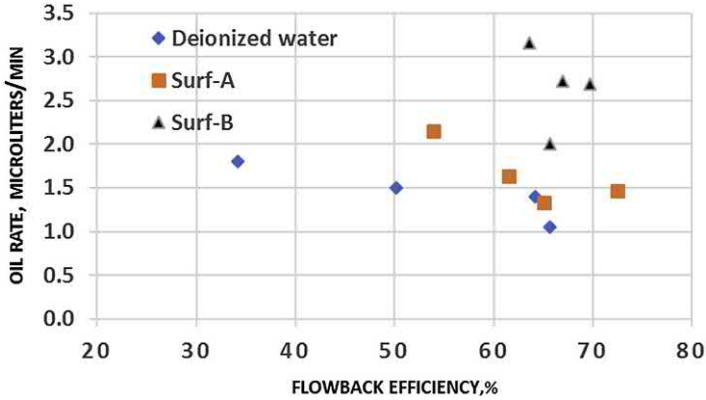

Figure 12.5 Oil rate versus flow back efficiency for different fracturing fluids.

picture was taken. At the end of a cycle of injection and flow back, the chip was flushed by deionized water, followed by isopropanol and air drying was applied to clear the flow passage of any residual fluids. Then this chip was reused for more experiments (different injection volumes or different injected solutions). For experimental details and how to treat image pictures, see Tangirala and Sheng (2019a).

Fig. 12.5 shows the oil rate during flow back when deionized water, aqueous solutions Surf-A and Surf-B were injected and flowed back. The flow back efficiency was calculated by the water saturation at the end of invasion minus the residual water saturation at the end of flow back divided by the water saturation at the end of invasion. The oil flow rate was the stabilized oil flow back rate through End B, and oil was injected through End A at a constant injection pressure. It seems that for the deionized water, the oil rate decreased with the flow back efficiency; for the Surf-A, the three oil rates decreased with the flow back efficiency, but the last oil rate did not continue the trend; Surf-B did not have any trend. In other words, the experimental data did not show that a high flow back led to a high oil production rate. The shortcoming of these experiments is that the constant pressure injection rate was maintained, and the final flow stabilized oil rate was used; in reality, the constant pressure away from fractures may not be maintained and the oil rate is declining.

12.3 Proposed mechanisms of low flow back

Numerous mechanisms could contribute to low-recovery, including extra-trapped water due to changing in natural fracture widths that increase

during injection and decrease during production, and water imbibition into shale matrix by capillary pressure. Generally, formation brine in a shale basin could be high (e.g.,150,000 ppm). And a typical fracturing fluid comprises low-salinity water; in many cases it is in the range of 1000 ppm. The significant salinity contrast can lead to substantial chemical potential differences that can create a large osmotic pressure and drive the filtrate from natural fractures into shale matrix blocks. Current research work shows that the following mechanisms are responsible for the phenomenon of low flow back.

12.3.1 Subirreducible initial water saturation

Some gas reservoirs and many strongly oil-wet reservoirs exhibit abnormally low initial water saturations which is lower than irreducible saturation. This abnormally low initial water saturation is called subirreducible initial water saturation. The corresponding formation is called a dehydrated or desiccated formation. The initial water saturation in some gas reservoirs in Michigan Reef is even close to zero (Katz ad Lundy, 1982). If an oil or gas reservoir was initially 100% saturated with water, then later oil or gas influx could not reduce the water saturation below an irreducible water saturation because water could not move before reaching that low level. In such situations, later fracturing water remains in the formation and cannot flow back if the water saturation is below the irreducible water saturation. Several hypotheses have been proposed to explain the subirreducible water saturation.

12.3.1.1 Vaporization (gas reservoirs)

We know that as the temperature is increased, more water will be vaporized, as shown in Fig. 12.6. If the initial pressure and temperature of a gas reservoir were low, and later they increased due to tectonic and/or geothermal activities, then more water will be vaporized. When gas migrated, the vaporized water would be carried away. Thus the water saturation would be lower than the irreducible water saturation, if the initial water saturation was at the irreducible level.

12.3.1.2 Geological compression and diagenesis

Owing to geological deposition, the increased overburden made the reservoir more compressed, resulting in the initial saturation lower than the originally irreducible water saturation. And reservoir diagenesis processes could contribute to the formation of clays of high surface area and other authigenic

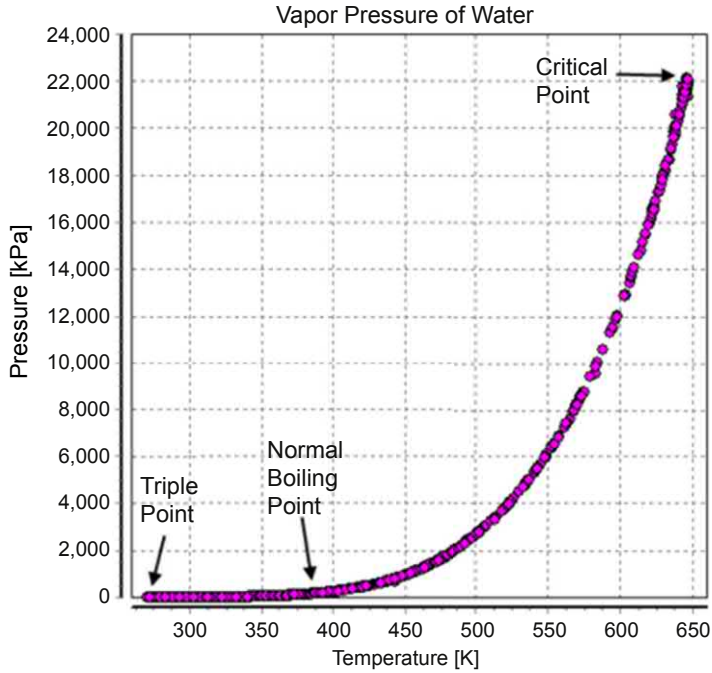

Figure 12.6 Water vapor pressure versus temperature.

materials who could contain water much higher than the originally irreducible water saturation. In these situations, if no additional water flowed into the reservoir, the water saturation in the reservoir would remain at a subirreducible water saturation.

12.3.1.3 Hydration

Many clays and reservoir minerals (e.g., anhydride) may react with water to form hydrated complexes. Such process would remove some water from the pore space.

12.3.2 Capillary imbibition

During drilling, fracturing, and completion, the fluid in the wellbore is lost into the formation, as the wellbore pressure is higher than that in the formation. Generally, the wellbore fluid is aqueous phase, and the formation always has some degree of water-wetness. The aqueous phase will penetrate into the formation away from the wellbore. During the flow back, the pressure drawdown may be lower than the capillary pressure, especially in the cases of shale and tight formations. Then some of the aqueous solutions

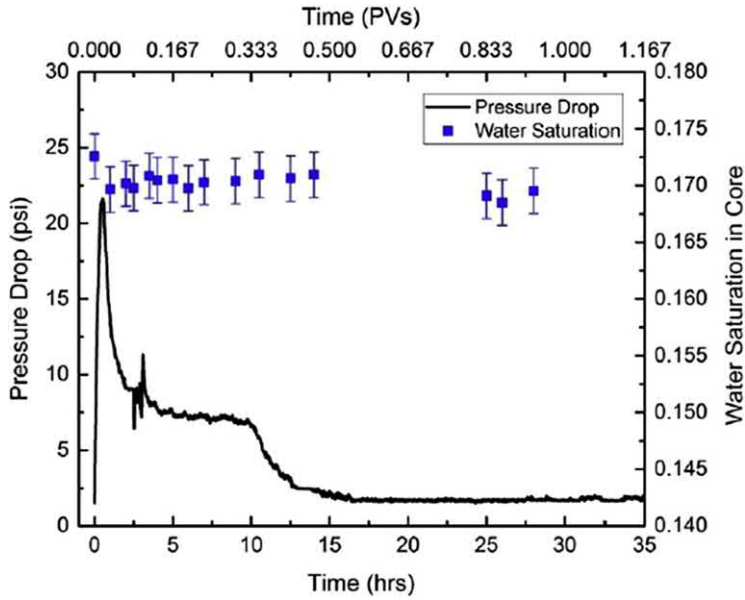

Figure 12.7 Changes of the overall water saturation inside the core (blue [black in print version] discrete data points) and the pressure drop across the core (*black curve*) during flow back (Liang et al., 2017a).

cannot flow back. This capillary imbibition mechanism is supported by many authors (e.g., Settari et al., 2002; Cheng, 2012; Dehghanpour et al., 2012; Pagels et al., 2012; Dehghanpour et al., 2013). In Liang et al.'s (2017a) flow back experiment, pentane was injected from the other end of the core to try to displace injected water out. A typical set of experimental data are shown in Fig. 12.7. When the constant flow rate was low, the overall water saturation did not decrease, but the pressure difference between the two ends of the core decreased, indicating that water imbibed into the core from the inlet side by capillary pressure so that the water blocking was mitigated. In the flow system, deionized water and pentane were used. The late-time plateau of the pressure drop indicated that the further water redistribution by capillary force did not improve the pentane permeability in the matrix. In other words, the formation damage or water block could be permanent if flow rate is low or no remediating chemical is used.

When 20% methanol is added in the fracturing water, the interfacial tension (IFT) between water and pentane decreased from 50 to 23 mN/m. Because of this IFT reduction, the capillary force was lower, resulting in

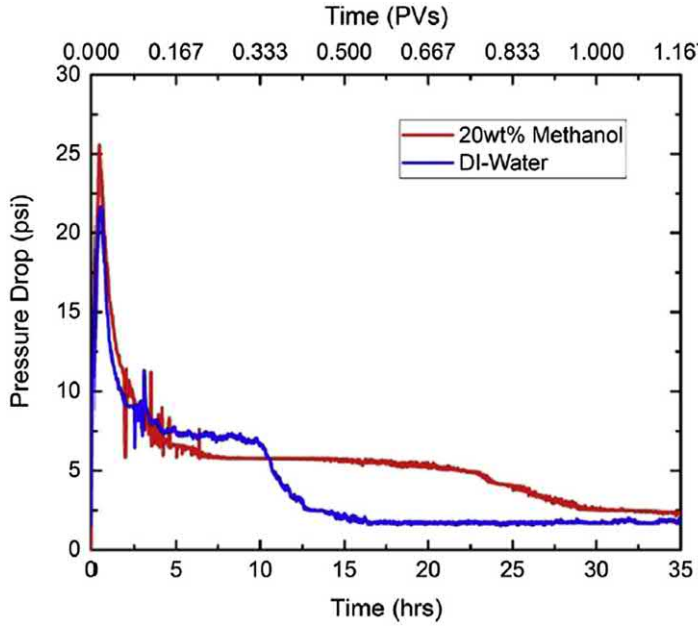

Figure 12.8 Comparison of the pressure drop across the core during flow back between the methanol and water cases (Liang et al., 2017a).

lower imbibition rate deep into the core. In Fig. 12.8 the first plateau of pressure drop for methanol solution lasted almost double that for water only, which was almost the same as the ratio of the two interfacial tensions. Liang et al.'s (2017a) CT data indicated that the duration of the first plateau represented the period of water imbibition from the fracture face deep into the core. Although the imbibition rate was slower, more water flowed back by being displaced out by pentane injection, when methanol was added, as shown in Fig. 12.9. This displacement of water by pentane required more the higher pressure drop as shown in Fig. 12.8.

Bostrom et al. (2014) measured gas permeability on Marcellus and Duvernay cores at reservoir conditions before and after exposure to brines and fracturing fluids. They quantitatively measured the effect of water block formed inside the rock and showed that the effect was time-dependent in most of the samples tested. The core samples tested showed a dramatic decrease in permeability after the exposure to water. Typically, the initial decrease was in the order of 70%. Over the following days, most of the samples showed a subtle and continued rebound in permeability, because the trapped water dissipated. But the degree of rebound varied among the cores tested.

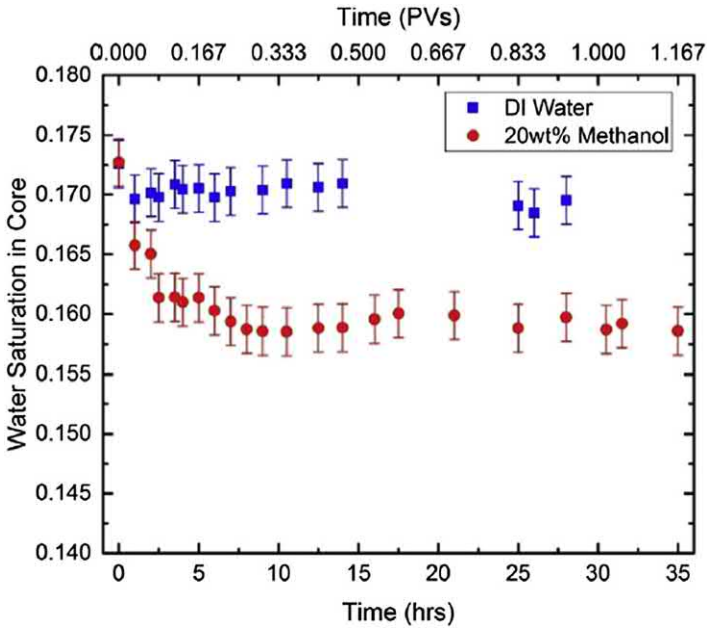

Figure 12.9 Comparison of the overall water saturation during flow back inside the core between the methanol and water cases (Liang et al., 2017a).

12.3.3 Fluid entrapment

During the drawdown, the pore pressure is decreased. Then the net confining stress is increased, resulting in closure of some pores or fractures. Then fluid can be entrapped in the formation (Bertoncello et al., 2014; Ezulike et al., 2016). And incomplete water drainage can occur due to adverse mobility ratio and gravity segregation (Parmar et al., 2013; 2014). In an oil-wet formation, water can be trapped by snap-off (Bertoncello et al., 2014).

12.3.4 Osmosis

In this section, osmosis in shale and its mechanism are introduced, and the implication in shale formation is discussed.

12.3.4.1 Osmosis in shale

Osmosis is the spontaneous movement of solvent molecules (e.g., water) through a semipermeable membrane from a region of lower solute concentration into a region of higher solute concentration. It tends to make the solute concentrations on the two sides equal. A semipermeable membrane is permeable to the solvent, but not the solute. This process can be

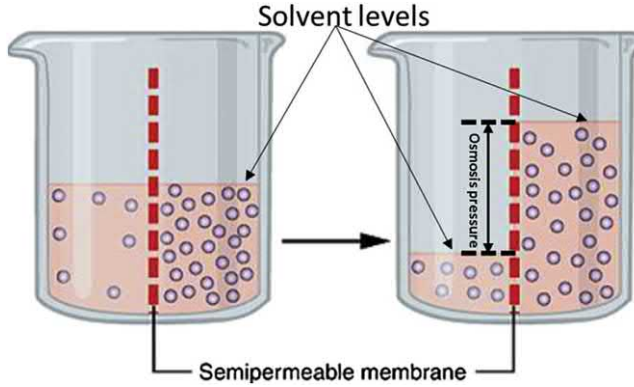

Figure 12.10 Schematic of an osmosis process.

schematically described in Fig. 12.10. In shale formation, clay minerals may serve as a semipermeable membrane. The osmotic pressure (π) can be described by Marine and Fritz (1981):

$$\pi = \frac{RT}{V} \ln\left(\frac{a_I}{a_{II}}\right) \tag{12.1}$$

where a_I and a_{II} are water activities of low-salinity brine I and high-salinity brine II; the water activity for fresh water is 1.0; R is the gas constant equal to 0.082 (liter·atm)/(g-mol·°K); T is the temperature in °K, and V is the molar volume in liter/g-mol.

12.3.4.2 Osmotic mechanism in shale

To understand the osmotic mechanism in shale, we need to introduce the concept of electric double layer. The schematic of electric double layer (EDL) is shown in Fig. 12.11. The length of EDL can typically vary between few nanometers (Johnston and Tombacz, 2002) to tens of nanometers (Tchistiakov, 2000). For dilute solutions, it has been shown (van Olphen, 1963) that the length of EDL can be about 100 nm with monovalent cations and 50 nm with divalent cations. Therefore, it is likely that the thickness of EDL will exceed the pore sizes in shales.

For a shale surface which is negatively charged, the electric potential at the surface is negative. Its absolute value increases as the distance is away from the solid surface. When the distance is at the liquid solution or beyond the diffusion layer, the potential is zero. Within the diffusion layer, the net charge is negative. Therefore, the diffusion layer will impose an electrical repulsion on anions but an attraction on cations. Thus charged particles

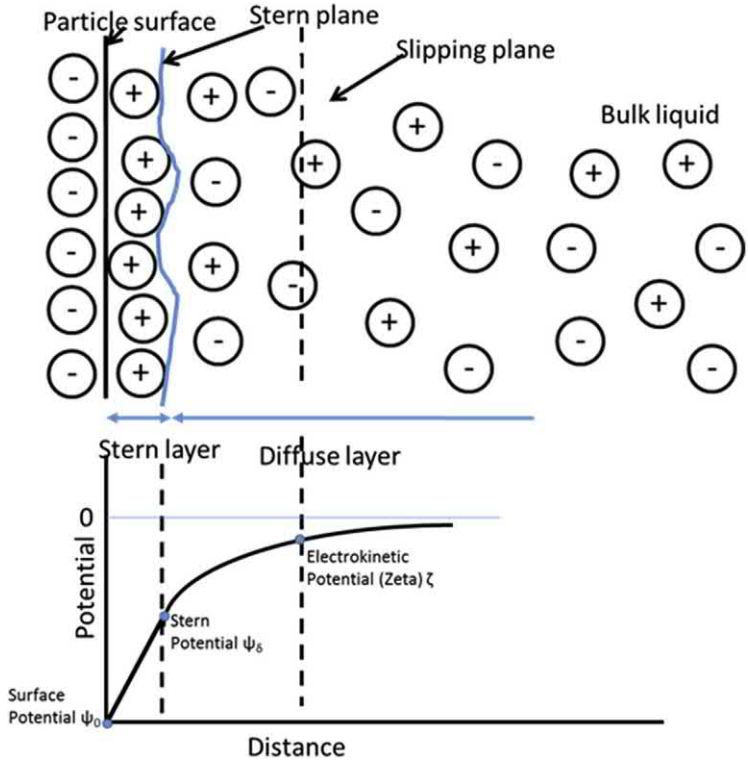

Figure 12.11 Schematic of electric double layer.

cannot pass through the diffusion layer, in the case of shale with such pores that the gap between the solid surfaces is bigger than the electric double layer. Then the electric double layers will overlap each other. As a result, charged particles cannot pass through the pores; but neutrally charged water molecules can flow through the pore center.

The conditions under which osmotic pressures can be observed are rare. A large difference in solute concentration or the existence of clay-rich strata may not be sufficient to generate an osmotic pressure. There must be a very low-permeability barrier between two strata which have very different solute concentrations. Such barrier must be effective in large scale. If there are transmissive fractures between the two strata or units, osmotic pressure may not build up because the fractures behave like short-circuits for solvent (water). Also, for a geologic stratum or unit to have osmotic pressure build up, it must be hydraulically isolated, so that there is no leakage. In a real shale formation, the pore sizes have a wide range. Thus the shale cannot serve as an ideal semipermeable layer. Some solutes in the solvent can pass through,

but the rest cannot. We use the membrane efficiency to describe the effectiveness which is defined as the actual pressure increase across the membrane divided by the theoretical osmotic pressure. The literature information shows that the membrane efficiency is low (less than 5% according to Neuzil and Provost's (2009) review of public experimental data). When Fakcharoenphol et al.'s (2014) history matched experimental data using the TOUGHREACT simulator, they used 5% membrane efficiency. It is possible that theoretical pressures could exceed 30 MPa at a porosity of 0.1 and 10 MPa at a porosity of 0.2 (Neuzil and Provost, 2009). However, the average osmotic pressure measured in laboratory and in situ is 0.128 MPa at the porosity of 0.206 from the published data summarized by Neuzil and Provost (2009). The possible reasons to cause the discrepancy between the theoretical estimation and actual osmotic pressure could be one or more of the following.

(1) Due to the wide range of pore sizes, formation acts as a nonideal semipermeable membrane which only restricts passage of some of the solutes in the solvent (Fakcharoenphol et al. 2014). Ghanbari and Dehghanpour (2015) observed that significant permeability parallel to the laminations acts as a preferential pathway for the imbibing water than the semipermeable clay layers, therefore, reducing the favorable conditions for the development of osmotic pressure.

(2) Some of assumptions in the osmotic theory may not hold in reality (Neuzil and Provost, 2009).

(3) The conditions for the osmosis to occur are difficult to meet (Neuzil and Provost, 2009).

(4) Formations that are effective membranes in tests are ineffective at large scale (Neuzil and Provost, 2009).

However, anomalously high pressures were observed in shales of Triassic Dunbarton Basin, Eastern United States (Marine, 1974; Marine and Fritz, 1981), and in an argillite in the eastern Paris Basin, France (Gueutin et al., 2007). There could be many reasons, such as tectonic deformation, compaction, diagenesis and heating, to cause anomalously high pressure behavior. It seems difficult to explain those anomalously high pressures except by the concept of osmotic pressure.

12.3.4.3 Implications of osmotic phenomenon

The osmotic pressure will drive lower-salinity water like fracturing fluid into higher-salinity shale, displacing oil and gas out of shale formation. Fakcharoenphol et al. (2014) simulated the osmotic effect between a fracture and a

10 ft matrix block being 1 μD and oil-wet. The osmotic pressure reached 40 psi after 30 years imbibition. Oil started to flow from the matrix to the fracture at 20 years. The oil recovery from the matrix reached 35% after 40 years. 5% membrane efficiency was used. Note that the maximum osmotic pressure from their model is more than two times the average pressure (0.128 MPa or 18.9 psi) from Neuzil and Provost's (2009) review mentioned earlier. Such osmotic pressure should be much lower than the capillary pressure. To make oil be able to flow out of matrix, they used almost zero capillary pressure for the oil-wet matrix which is presented in Fig. 12.12. It seems that the significance of the effect of osmotic pressure on oil recovery in a shale or tight formation is questionable. However, in a separate paper (Fakcharoenphol et al., 2016), their simulation shows that the osmotic effect was more significant than the capillary effect on increasing gas rate and decreasing water production.

Some shale formations are oil-wet owing to Ca^{2+}/Na^{+} bridging of oil molecules to the negatively charged clay surface. When low-salinity water invades the high-salinity zone, Ca^{2+}/Na^{+} will detach from the rock surface. As a result, the surface may become more water-wet, resulting in the increase in oil relative permeability and decrease in residual oil saturation (Kurtoglu, 2013). More possible mechanisms for low-salinity waterflooding are summarized in Sheng (2014).

Because of osmosis, some water will be held in the high-salinity zone of a shale or tight formation. That could be one of the reasons to explain less flow

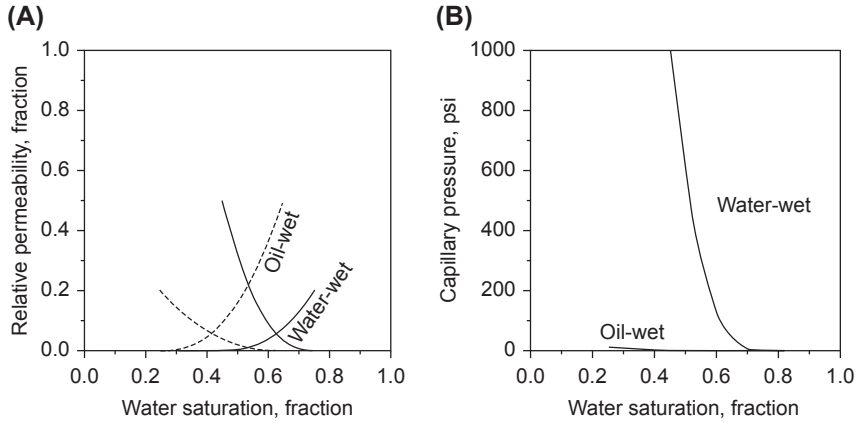

Figure 12.12 (A) Relative permeability, (B) capillary pressure used in Fakcharoenphol et al.'s (2014) model.

back for fracturing fluid. However, as the above discussion about Fakcharoenphol et al.'s (2014) work implies, the osmotic mechanism would be possible only if the shale matrix has higher affinity for aqueous fluid over hydrocarbon, because for an oil-wet shale matrix, they had to use a capillary pressure close to zero which is not the reality. In other words, the shale needs to be water-wet or mixed-wet.

12.3.5 Evaporation

When a gas phase flows through a porous medium that is partially occupied by a volatile liquid phase, evaporation occurs, even if the gas is saturated, due to its volume expansion. This process is referred to as flow-through drying. Such process is important in a wide variety of natural and industrial applications, such as natural gas production, convective drying of paper, catalysts, and membranes. The papers in the petroleum literature mainly discuss the water vaporization near the gas wells.

Another type of drying that is related to flow-through drying is referred to as pass-over drying. In this type of drying, the rate of mass transfer is controlled by the diffusion of volatile species within the pore space. The pressure drop is negligible and the gas flow rate is constant. However, in flow-through drying, the gas flows through a porous medium owing to a pressure drop. Its mass-transfer is controlled by the convection of gas (Mahadevan, 2005).

It is understandable that when gas is unsaturated, water will be vaporized until the water solubility in the gas at the system pressure, temperature and salinity is reached. Fig. 12.13 shows the water solubility in the nonaqueous phase of a methane/NaCl brine system at 121°C as a function of pressure and brine salinity. The symbols represent measured data and the solid lines represent that calculated by the PR EOS (Peng and Robinson, 1976). From this figure, we can see that the mole fraction of water in the hydrocarbon phase is increased, as the pressure is decreased. Then during hydrocarbon gas production, when the reservoir pressure is decreased, more water will be vaporized into the hydrocarbon phase. Therefore, the water blocking near the wellbore will be mitigated as gas is produced. Here we use the PR EOS data to explain water evaporation phenomenon, as the gas is expanded (the pressure is decreased). We can combine the Raoult's law with Dalton's law to explain this phenomenon.

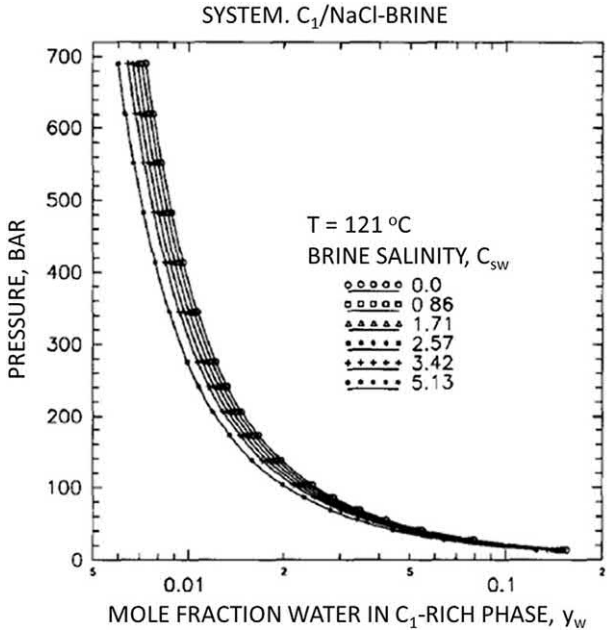

Figure 12.13 Water solubility in the nonaqueous phase of a methane/NaCl brine system at 121°C (Søreide and Whitson, 1992).

Raoult's law states that the partial vapor pressure p_w of the water component w is

$$p_w = x_w p_w^* \tag{12.2}$$

p_w^* is the vapor pressure of the pure water component, x_w is the mole fraction of water component in the water solution.

Dalton's law states that the partial water vapor pressure in the gas phase is

$$p_w = y_w p_g \tag{12.3}$$

Here p_g is the gas phase pressure of the gas mixture of water vapor and hydrocarbon gas, and y_w is the mole fracture of water in the gas mixture. By combining the two laws, we have

$$p_w = x_w p_w^* = y_w p_g \tag{12.4}$$

When the gas phase pressure p_g is reduced, the mole fraction of x_w in the aqueous solution does not change much and p_w^* is fixed for water at a specific temperature. Thus the product of y_w and p_g are almost unchanged. Then

when p_g is reduced, γ_w must be increased. So water must be vaporized as the gas phase pressure is decreased.

However, when more water is vaporized, the salt concentration in the aqueous phase will be increased. As a result, x_w will be decreased. Then the water vaporization will be reduced (Morin and Montel, 1995). Whether more water is vaporized depends on the competitive effect of pressure reduction and the effect of salinity increase. In real gas flow or petroleum problems, the effect of pressure reduction should be more important. When salt precipitation starts to occur, the salinity becomes a constant. Water is vaporized until no water exists, as the pressure declines.

In fracturing shale reservoirs, it has been observed that less water is produced than the pumped fracturing fluid in some cases. Water vaporization is partly attributed to the phenomenon. However, Fig. 12.13 shows that the mole fractions of water vapor in the gas phase changes near 0.01 with a large pressure interval. In other words, even though the pressure changes significantly, the mole fraction in the gas phase remains very small. Then the water vaporization due to pressure drawdown should not be significant, if the gas is saturated with water initially.

Mahadevan and Sharma (2005) conducted corefloods to compare the liquid volumes removed by displacement and evaporation. Fig. 12.14 shows

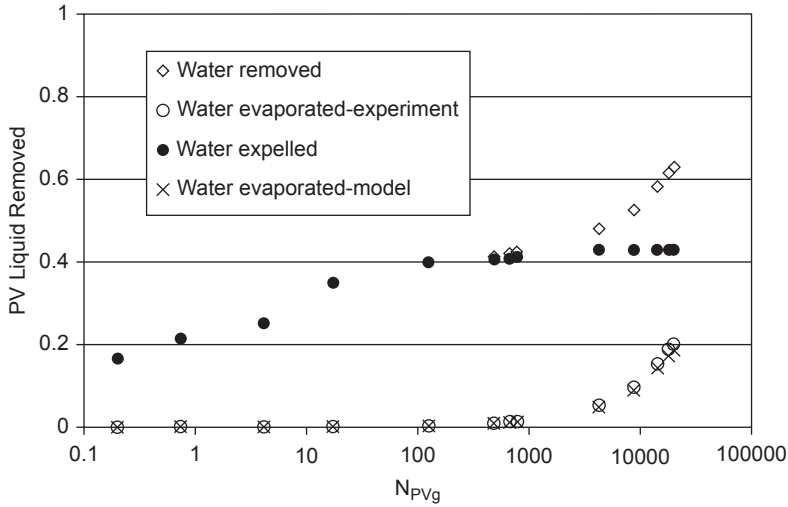

Figure 12.14 Liquid (brine) removed from Texas Cream limestone core by displacement and evaporation ($p_{mean} = 3.0$ atm., $k = 7.2$ mD, and the core length 15.3 cm) (Mahadevan and Sharma, 2005).

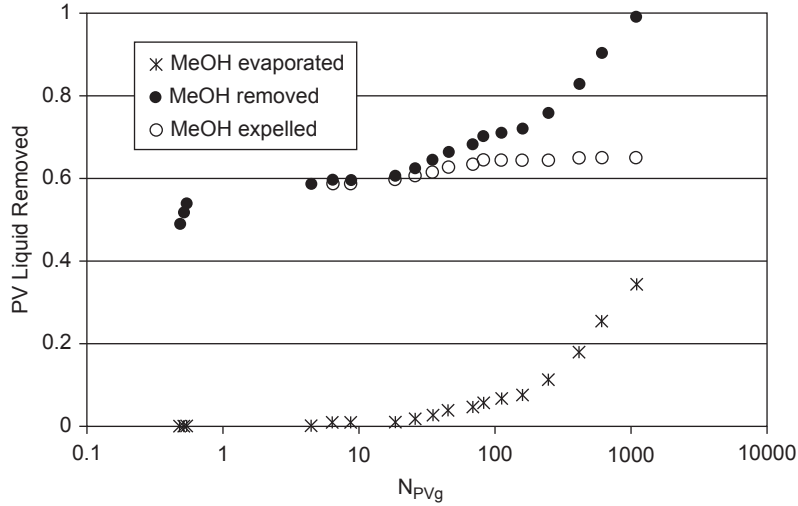

Figure 12.15 Liquid (methanol) removed from Berea sandstone core by displacement and evaporation ($p_{mean} = 1.1$ atm., $k = 327$ mD, and the core length 7.6 cm) (Mahadevan and Sharma, 2005).

the liquid (brine) removed from a Texas Cream limestone core by displacement and evaporation. Evaporation started to remove brine when the flood gas volume reached 1000 pore volumes (N_{PVg}). Fig. 12.15 shows the methanol removed from a Berea sandstone core by displacement and evaporation. Evaporation started to remove brine when the flood gas volume reached 60 N_{PVg}. In this case, the rock permeability was high, and the volatile methanol was used. These conditions are favorable to evaporation (Mahadevan and Sharma, 2005). It can be predicted that in shale and tight reservoirs, it will take much longer time for the evaporation to start to show up.

12.3.6 Permeability jail

Many field cases show that the connate water saturation is immobile at very high saturations in low permeability reservoirs; within a large range of middle saturation, neither gas nor water could flow (Shanley et al., 2004). They term this range of saturation "permeability jail". Ojha et al. (2017) estimated relative permeabilities for shale cores using nitrogen adsorption-desorption data. Their data show that water cannot move for water saturation higher than 50%. Based on these facts, we may hypothesize that during the fracturing operation, high pressure and saturation of fracturing fluid force the fracturing fluid (water) to move deep into a formation, with help of water

imbibition. During the flow back, both the pressure and the saturation are reduced, especially the saturation can be easily decreased to lower than the immobile saturation, thus water cannot flow back when the saturation reaches this level.

12.4 Effect of shut-in time on flow back

From the preceding discussions, the flow back is closely related to the shut-in. There are opposite opinions about the effect of shut-in on flow back. One is that the fracture filtrate (water) near the fracture-matrix interface will dissipate into the deep formation, so that the water blockage is mitigated. The other one is that the fracture filtrate that dissipates into the deep formation will block the gas flow out, and immediate flow back will mitigate the water blockage. Field observations and research results are mixed.

Cheng (2012) presented the performance of a Marcellus shale gas well, as shown in Fig. 12.16. The well was a horizontal well completed with a multi-stage fracturing treatment. After the treatment, it had a short time for flow back, followed by a shut-in of almost a half year. When the well was re-opened, the gas rate was significantly increased, while the water rate was much lower than that before the shut in. Although her simulation work showed the similar trends in gas rate and water rate, the cumulative gas production was almost the same, and the cumulative water production was significantly lower from her simulation from an extended shut-in of 3 or 6 months, compared with the case without an extended shut in. However, the discounted gas production will be lower in the case of extended shut-in, if the accelerated production is considered.

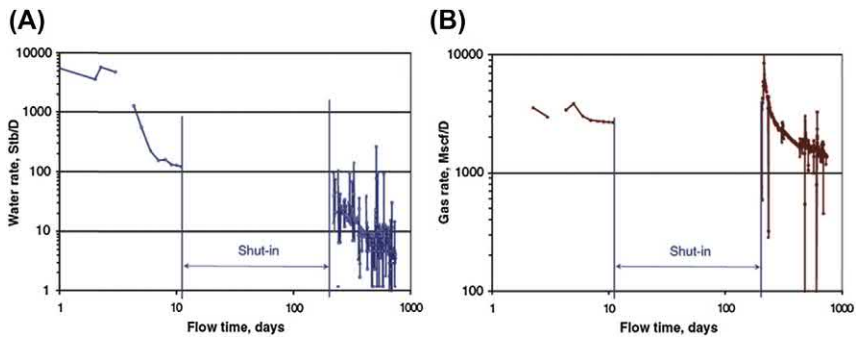

Figure 12.16 Field production data from a well in Marcellus shale, (A) water production and (B) gas production (Cheng, 2012).

Yaich et al. (2015) evaluated the impact of soaking on well performance in the Marcellus shale gas. Their results showed that soaking was possibly beneficial in three out of the four areas investigated. The 30-day average gas rates could be several times those at the end of flow back. The improvement was better with longer soaking time. But most of the improvement in well performance happened during the first 100 days of soaking. The rates were normalized by pressure drawdown. Reduced water production was observed in soaking wells. However, the time loss due to soaking was not included in the evaluation.

Fakcharoenphol et al. (2016) simulated the effect of shut-in time on flow back. The gas rates and cumulative gas production at different shut-in times are shown in Fig. 12.17. They used triple-porosity models to simulate flow in fractures, organic pores, and inorganic pores. The simulator used was TOUGH-REACT (Xu et al., 2012). A shut-in period allows the shale matrix adjacent to the fractures to imbibe the filtrate. Thus the water saturation inside the fractures is reduced. The initial gas rate is increased with a longer shut-in period. However, this effect does not last long. The rates at different shut-in times merge to almost the same curve after about 1 month (Fig. 12.17A); and the cumulative gas production curves almost overlap each other (Fig. 12.17B), indicating that shut-in times do not affect cumulative production. Because water has imbibed deep into the formation, it will be more difficult for water flow out of formation and thus the water production (rate and cumulative) is reduced with longer shut-in times, as shown in Fig. 12.18. It can be expected that the imbibed water may have a long-term impairment on gas production, because the water may block gas flow paths deep inside the formation, and may cause shale swelling. Here, the loss of production time is not included in the comparison. If it is included, the effect of shut-in time on gas production will be worse. But delayed water production may keep the energy inside the reservoir.

Fakcharoenphol et al. (2016) also did a sensitivity study of the effects of other parameters like osmosis and wettability. All their results show the effects are in the early flow back period of less than 100 days. This implies that those effects may not play significant roles in improving gas production.

Bertoncello et al. (2014) simulated the BHPs when the well is shut in 1, 7, and 14 days before the first flow back (or called the first shut-in immediately after well stimulation) at the same gas rate, as shown in Fig. 12.19. It shows that to produce in the well at the gas rate of about 8000 Mscf/d, the BHP required for 1-day shut-in is about 5000 psig, while the required BHP is 2300 psig for 14-day shut-in. These data indicate that earlier flow back

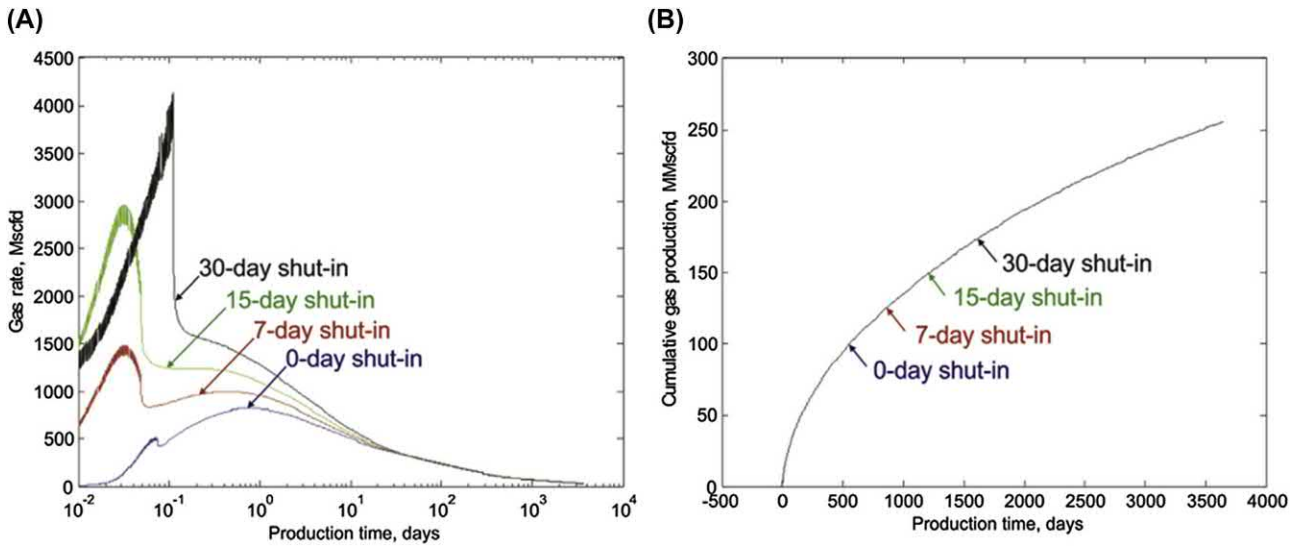

Figure 12.17 Gas production rate (A) and cumulative gas production (B) at the shut-in times of 0 day, 7, 15, and 30 days (Fakcharoenphol et al., 2016).

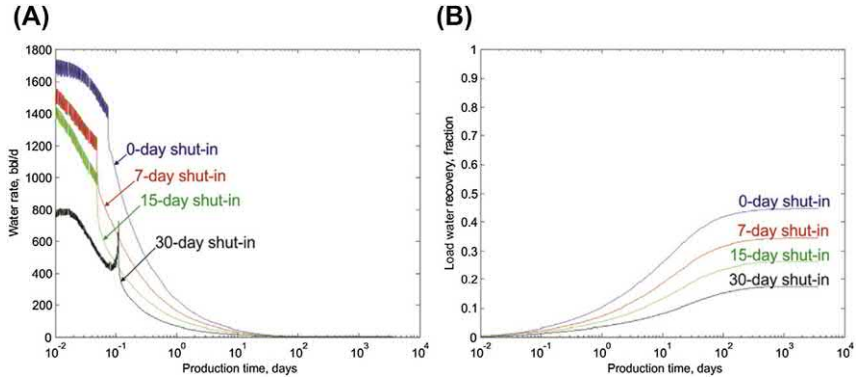

Figure 12.18 Water production rate (A) and cumulative water production (B) at the shut-in times of 0 day, 7, 15, and 30 days (Fakcharoenphol et al., 2016).

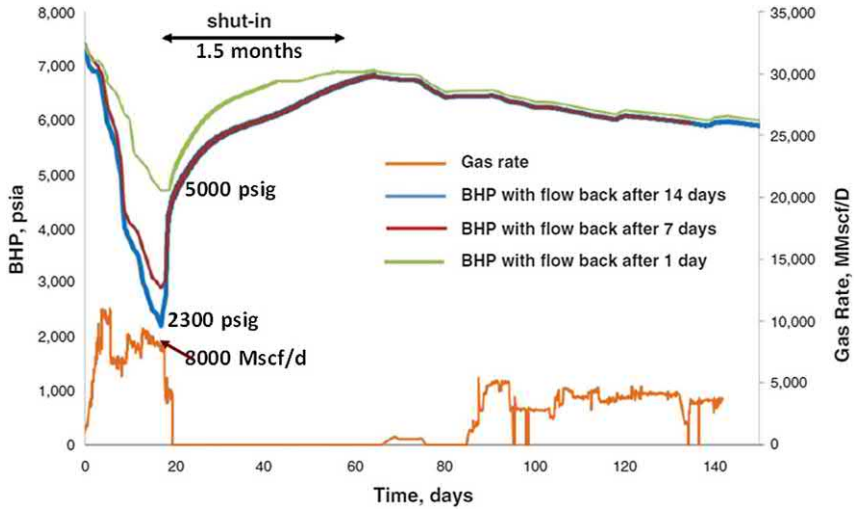

Figure 12.19 Simulated BHP for 1, 7, and 14 days of shut-in before flow back to produce the same gas rates. *Modified from Bertoncello, A., Wallace, J., Blyton, C., Honarpour, M.M., Kabir, S., 2014. Imbibition and water blockage in unconventional reservoirs: well-Management Implications during flowback and Early production. Paper Presented at the SPE/EAGE European Unconventional Resources Conference and Exhibition Held on 25 February. doi:10.2118/167698-PA.*

(shorter shut in before flow back) maintains the reservoir energy so that a higher BHP (lower pressure drawdown) can produce a required gas rate.

Fig. 12.20 shows the BHPs with and without the second shut-in of 1.5 months, when the well produces the same gas rate history shown in

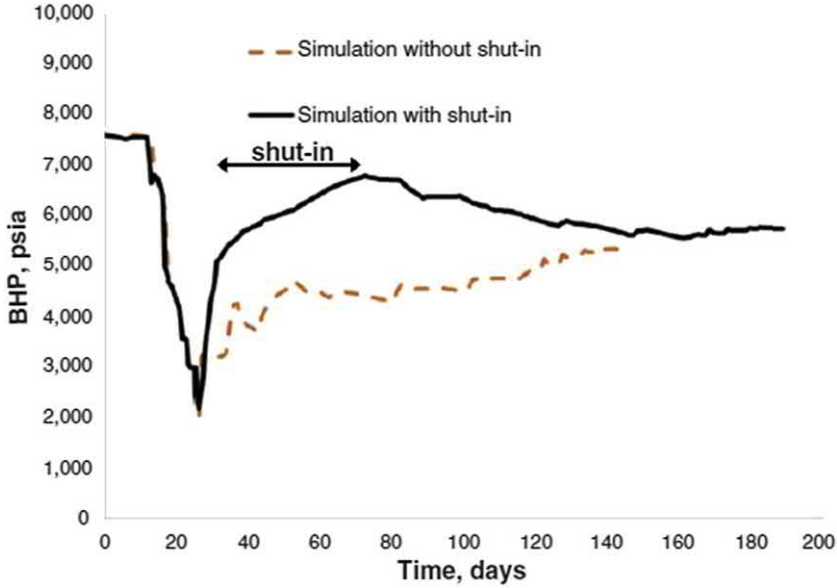

Figure 12.20 Simulated BHPs with and without the second 1.5 months of shut-in when the well produces the same gas rate history shown in the previous figure (Bertoncello et al., 2014).

the previous figure after the initial flow back of 20 days. It shows that the BHP required is higher with the shut-in than that without shut-in. In other words, it is easier to produce the gas rate history with the shut in, indicating the water blockage near the fracture-matrix interface is mitigated and the gas permeability is higher with the shut-in, as shown in Fig. 12.21 which shows the water saturation and k_{rg} at a block near the fracture for the two cases. However, the water saturations in the blocks away from the fracture may be higher with shut-in, resulting in lower gas permeability. They did not show the effect of shut-in on the long-time performance. A different conclusion may be drawn if the long-time gas recovery is analyzed, especially the production loss due to shut-in time is considered.

Bertoncello et al. (2014) further did simulation analysis of shut-in time effect. The initial flow back is 4 days, followed by 1 day or 300 days of shut-in. Produced gas volumes of 90 days are compared. The produced volume for 300 days of shut-in is 20% higher than that for 1 day of shut-in. Their opinion is that an early cleanup period immediately after stimulation before an extended shut-in helps gas production.

However, if 10% discount is used and average constant production rates are assumed, the calculated net present value of the gas produced for the case

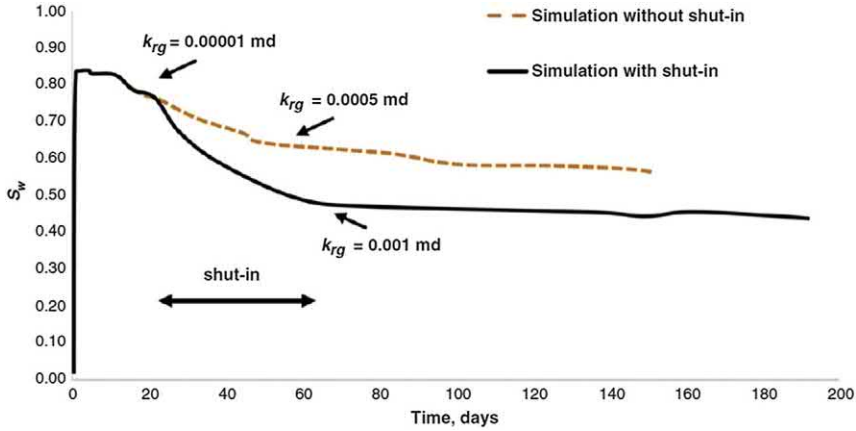

Figure 12.21 Water saturation changes with time at the block closest to the fracture and the effective gas permeability (Bertoncello et al., 2014).

without shut-in is 42% higher than the case with shut-in! This result is based on the assumption that the well produces at constant production rates, and the cumulative produced gas is linearly allocated in the duration of production. If the flow rates are not assumed constant, for example, an exponential decline is assumed; the difference will be higher than 42%, because more gas will be produced in the early time without shut-in.

Liang et al. (2017b) did flow back experiments after different shut-in times. For all the experiments, the flow rate was 0.1 cc/min and the average initial water saturation was 0.2. The core permeability was 8.5 mD. The measured pressure drops are shown in Fig. 12.22. Higher pressure drop represents lower permeability. This figure shows that with a longer shut-in time, the pressure drop was lower in the early time, indicating that the shut-in time dissipated the water blockage and restored to higher permeability. However, when these data are presented in the actual elapse times (including shut-in times) in Fig. 12.23, it can be seen the pressure drop was higher with a longer shut-in time at the same elapse time! This figure clearly demonstrates that the shut-in time wasted the operation (production) time. Both of these figures show that the pressure drops were similar during late-time.

Wijaya and Sheng (2019b) investigated the shut-in effect in removing water blockage in shale-oil reservoirs with stress-dependent permeability considered in their simulation modeling of a sector of half wing fractures and a few natural fractures. The model was validated by matching field production data from a well in the Middle Bakken shale reservoir (Kurtoglu and

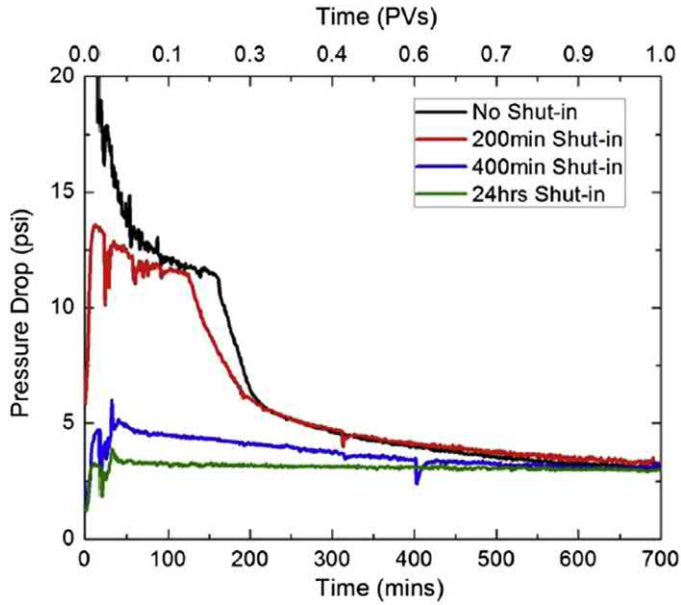

Figure 12.22 Pressure drop across the core during flow back (Liang et al., 2017b).

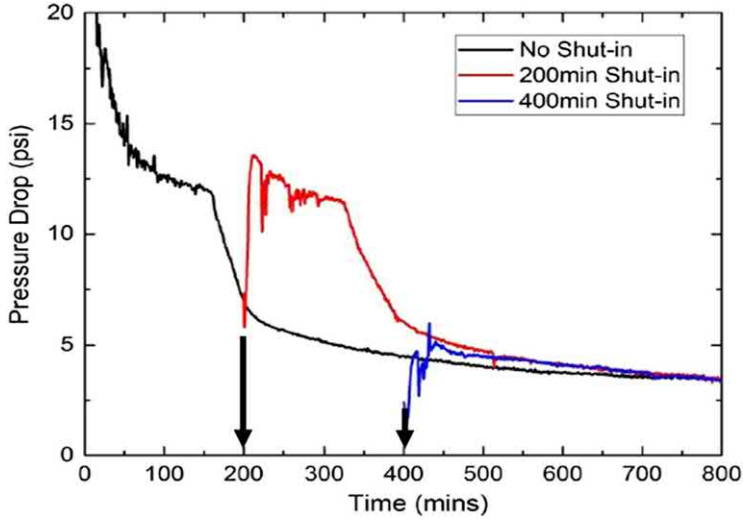

Figure 12.23 Pressure drop across the core during shut-in and flow back. *(Modified from Liang et al., 2017b).*

Table 12.1 Parameter input for matrix, NF, and HF for history match.

Reservoir depth, ft	8000	NF half-length, ft	16
Reservoir thickness, ft	50	HF conductivity, mD-ft	250
Matrix porosity	0.056	HF porosity	0.6
Matrix permeability, nD	300	HF half-length, ft	215
NF conductivity, mD-ft	6.5	Initial reservoir pressure, psi	7800
NF porosity	0.8	Matrix S_{wi}	0.4

Kazemi, 2012). Table 12.1 lists the parameters used in the base model. An exponential stress-dependent-permeability (SDP) model (Raghavan and Chin, 2002) is used:

$$k = k_0 e^{-\beta(\sigma_{eff} - \sigma_{effo})} \tag{12.5}$$

where k is the permeability (mD), k_0 is the permeability at the initial condition (mD), σ_{eff} is the effective stress (psi), σ_{effo} is the effective stress at the initial condition (psi), and β is the stress sensitivity index. Fig. 12.24 shows how the permeabilities of the matrix, natural fractures (NF), and hydraulic fracture (HF) change with the pore pressure during the injection and the production stages. The natural fracture spacing is 2 ft.

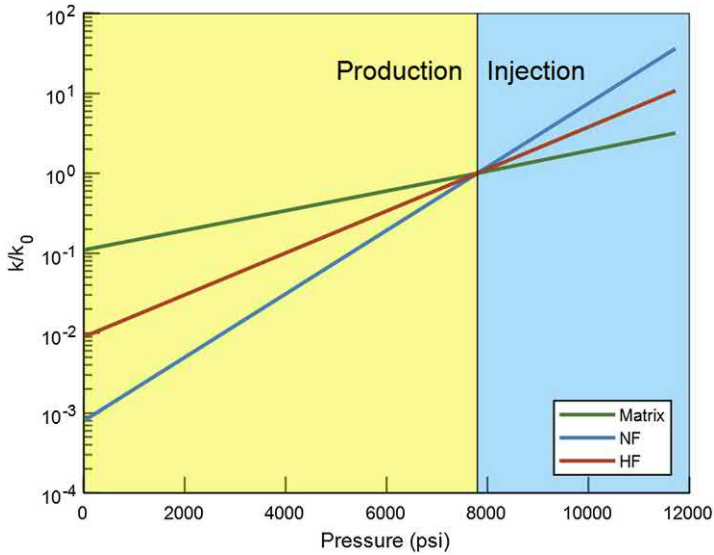

Figure 12.24 Changes of the permeabilities of the matrix, NF, and (HF) with the pore pressure during the injection and production stages.

The bottom hole injection pressure is 12,000 psi to simulate the water-fracturing. After a typical volume of fracturing fluid is injected, flow back is carried after some shut-in times. During the flow back and production, a constant bottom hole pressure of 2000 psi is set.

To investigate the effect of shut-in on oil production, four shut-in times of 0 (immediate flow back), 30, 60, and 300 days are chosen. Fig. 12.25 shows that a longer shut-in results in a higher initial oil rate, which is consistent with most of field observations, and it also justifies the models used. However, it also shows that shut-in does not affect the ultimate oil volume produced. Fig. 12.26 shows the effect of SDP on the cumulative oil production. It shows that when the permeabilities of matrix, NF, and HF are not changed by the pore pressure, the total oil production is higher by 28%.

One believes water will dissipate away from the fracture-matrix interface so that water blockage is mitigated. Fig. 12.27 shows the water saturations S_w at the two locations (2 and 8 inches away from HF) in the two cases of immediate flow back (s0) and 300 days of shut-in (s300). First look at the water saturations (two dotted lines) in the case of 300 days of shut-in. At the location 2 inches away from the HF, S_w keeps increasing until 50 days because

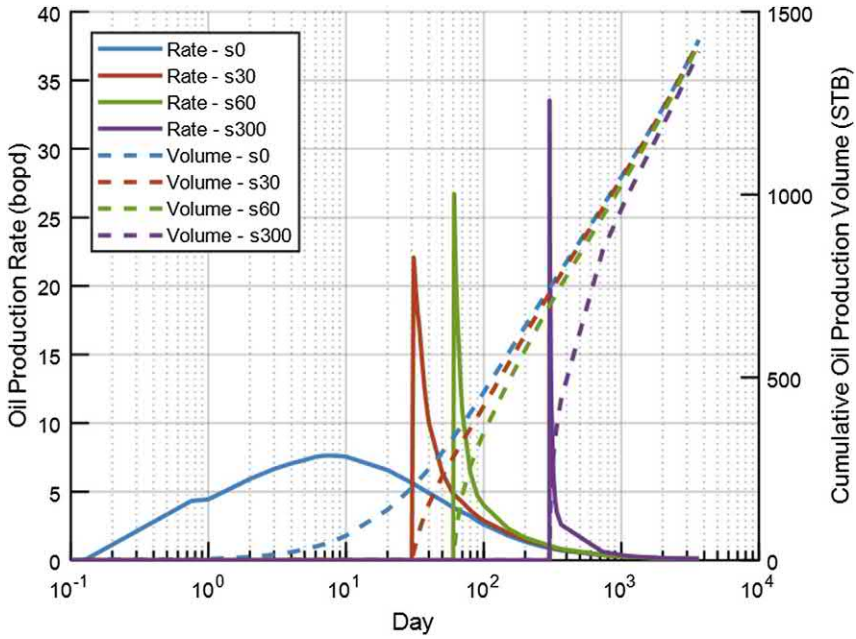

Figure 12.25 Effect of shut-in on oil production rate and cumulative oil production volume.

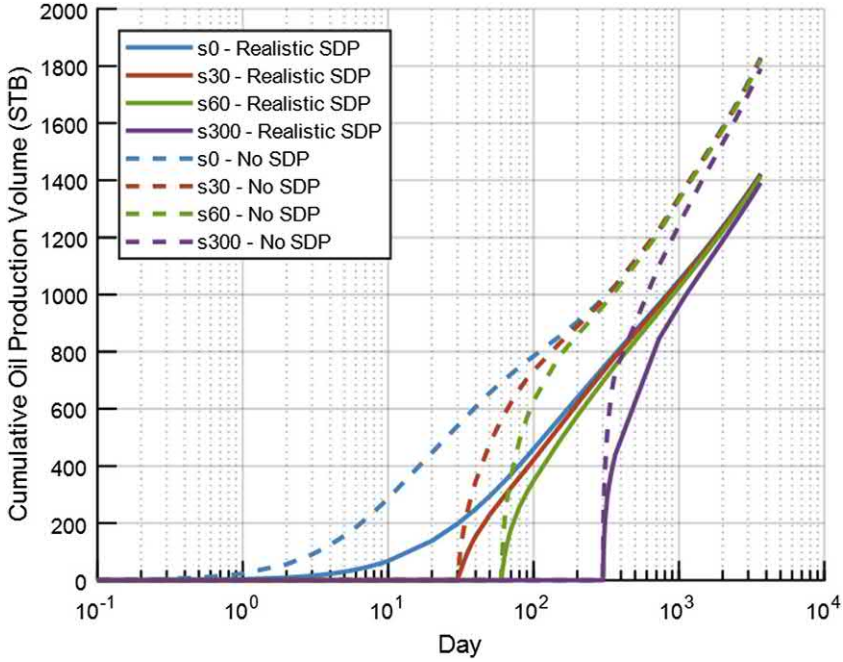

Figure 12.26 Effect of SDP on cumulative oil production.

water in the HF moves to this location. Then S_w decreases until 300 days because of dissipation deep into the matrix. When the flow back starts at 300 days, S_w increases again because the water dissipated earlier flows back! At the location of 8 inches away from the HF, S_w (red dotted line) slightly decreases (<0.02) in the first 10 days because of dissipation, then it increases again until about 150 days because the water closer to the HF dissipates to this location. From 150 to 300 days, S_w decreases because of dissipation deep into the matrix. At 300 days, S_w suddenly decreases for a very short moment because of flow back; then it increases again because the water deep in the matrix flows back. Contradictory to one's belief, the water saturations near the HF-matrix interface in the 300 days of shut-in actually increase during some of 300 days.

Now look at the water saturations in the case of immediate flow back (s0) (two solid curves). S_w (solid blue) at 2 inches away from the HF keeps increasing because the water leaked earlier flows back. Interestingly, the S_w at this location in the s0 case (solid blue) is lower than that (dotted blue) in the s300 case from 0 to 110 days. The S_w (solid red) at 8 inches away from the HF decreases in the first 10 days and then increases again. However, the

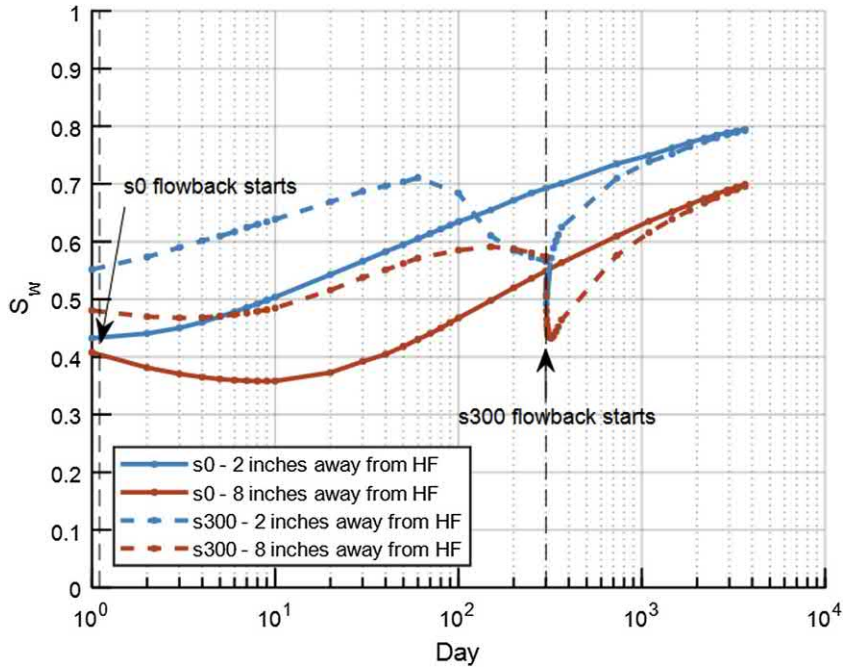

Figure 12.27 Water saturations at the two locations (2 and 8 inches away from HF) in the two cases of immediate flow back (s0) and 300 days of shut in (s300).

S_w (solid red) at this location in the s0 case is lower than that (*dotted red*) in the s300 case from 0 to 300 days!

Furthermore, the water saturation at both locations for the shut-in case (s300 *dashed blue and red lines*) instantaneously before flow back at day 300 is approximately 0.575, which is much higher than that (approximately 0.425) for the immediate flow back case (*solid lines*) at day 1.

The above description demonstrates that the water dissipation is a very slow and inefficient process. Rather, immediate flow back is a quick process to flow water out, mitigating water blockage near the HF-matrix interface, as shown in Fig. 12.28. It shows that the shorter the shut-in, the flow back is more.

We have seen so far that shut-in reduces water flow back; then the water handling cost can be reduced. The shut-in does not significantly affect the cumulative oil production in a long time (data not presented here), but later oil production will devalue the oil production. The question is whether the cost reduction by less water flow back can compensate the value reduction of later oil production.

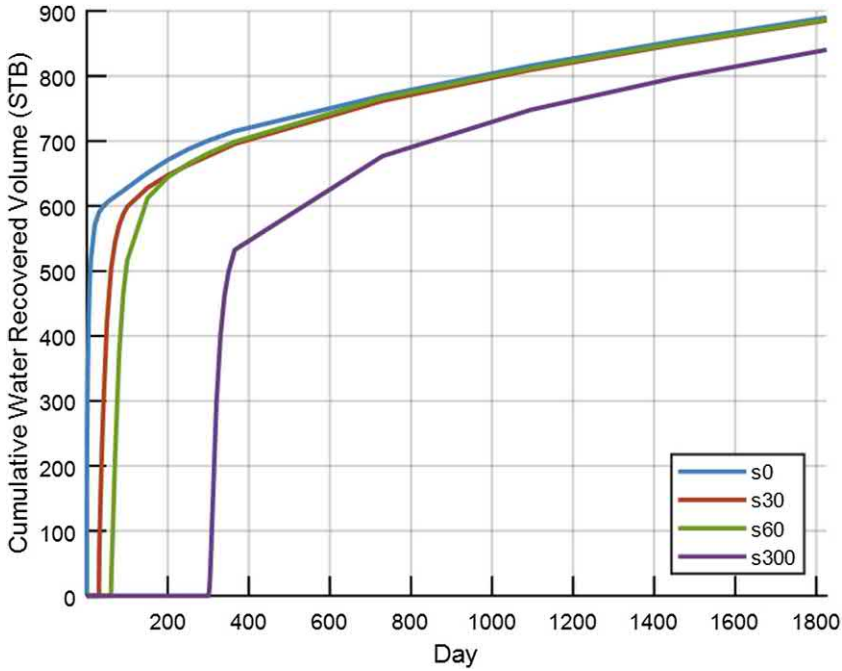

Figure 12.28 Effect of shut-in on the flow back of injected fluid (leaked-off fluid).

The above base model data are used to evaluate the 10-year NPV which is calculated by

$$\mathrm{NPV} = \sum_{i=1}^{10} \frac{V_{o,i}\,\mathrm{OilPrice} - V_{w,i}\mathrm{WaterHandlingCost}}{(1+\mathrm{DiscountRate})^{i}} \tag{12.6}$$

where NPV is the net present value in dollars ($), $V_{o,i}$ is the annual oil production volume in ith year (STB), and $V_{w,i}$ is the annual water recovered volume in ith year (STB). Dollars 70/STB is taken as the oil price; the discount rate is 10%, and the water handling cost is $7/STB water according to Yaich et al. (2015). The other costs are assumed not affected by shut-in time. Fig. 12.29 shows the 10-year NPVs at different shut-in times. The NPV of each scenario is normalized by the NPV of the s0 case (immediate flow back). It shows that the NPV is the highest (normalized NPV = 1) for the immediate flow back. As the shut-in time is longer, the NPV is lower.

Fig. 12.30 presents the effects of matrix permeability and injection value on NPV. The range of injection volumes in barrels is 92,870 (min),106,950 (average), and 122,950 (max).When the permeability is reduced to 20 nD,

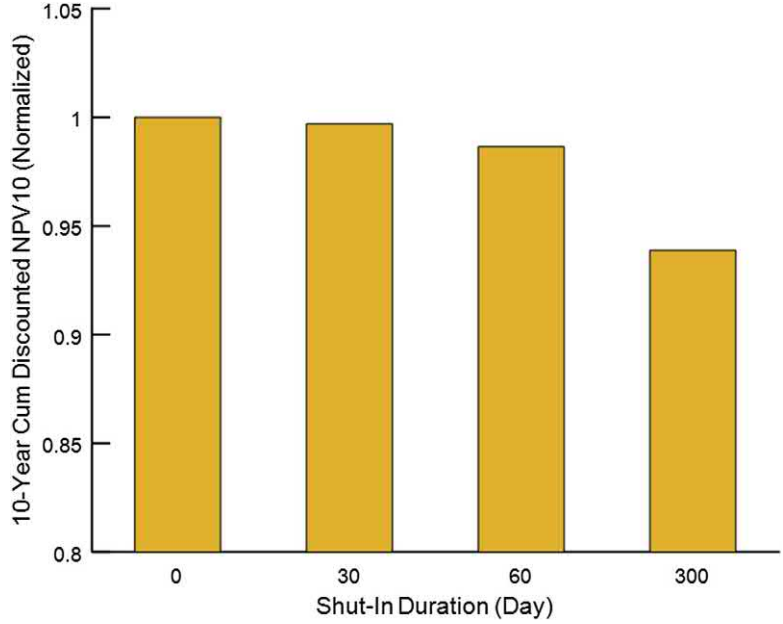

Figure 12.29 Effect of shut-in on the 10-year discounted NPV (10% Discount Rate) for the base case model.

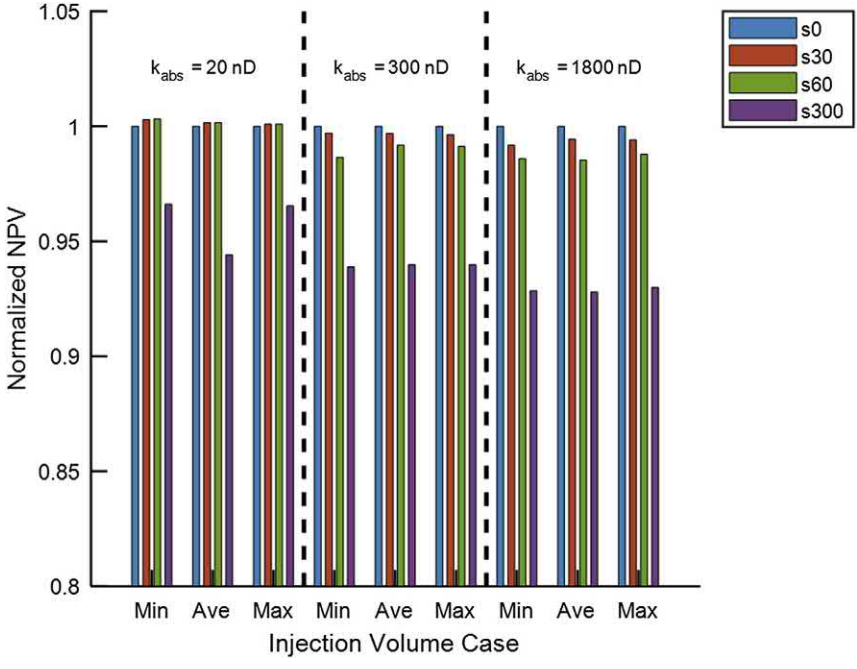

Figure 12.30 Effect of injection volume and matrix absolute permeability on the NPV at different shut-in times.

the NPV increases in the 30-day and 60-day shut-in times over that in the 0-day shut-in are negligible. When the permeability is 300 nD (base model) and 1800 nD, the NPV for the immediate flow back is the highest.

Wijaya and Sheng (2019b) also checked the performance (NPV) of immediate flow back at different oil prices and different water handling costs. Figs. 12.31 and 12.32 show that with the ranges of different prices and costs, the immediate flow back ranks the best.

Earlier, Wijaya and Sheng (2019a) studied the effect of desiccation on shut-in benefits in removing water blockage. Desiccation refers to a state in which the rock's initial water saturation is below the irreducible water saturation, often called subirreducible water. They built simulation models to match Liang et al.'s (2017c) experiments in which a core was initially saturated with oil, then water flooded presenting an invasion process; after some time, the flooding direction was reversed with oil (n-pentane) flooding at a constant flow rate to reach steady state flow; during the oil flooding, regained oil relative permeability k_{ro} was calculated using Darcy's equation assuming a single-phase flow although it was a multiphase flow. Fig. 12.33 shows the effects of desiccation and shut-in before flow back.

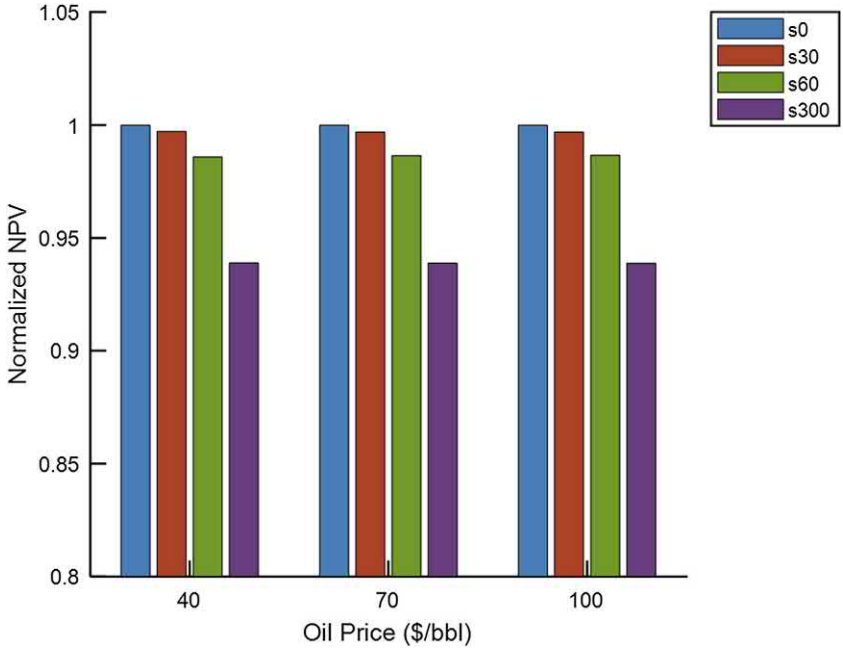

Figure 12.31 Effect of oil price on the NPVs for different shut-in times.

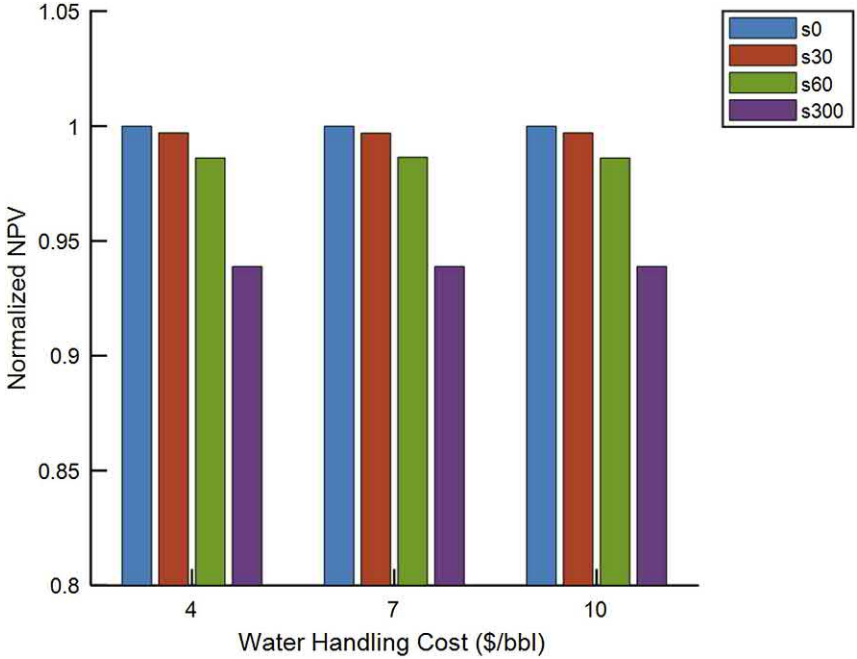

Figure 12.32 Effect of water handling cost on the NPVs for different shut-in times.

The early-time plateau represents the removal of trapped water and oil, while the late-time plateau represents the single-phase oil flow. Several observations may be made. (1) The final regained k_{ro}'s in the desiccated cases are higher than those in the nondesiccated cases, because less mobile water is available in the former cases. (2) The final k_{ro}'s reach the same value at late time because of complete removal of mobile water for the desiccated cases; but for the nondesiccated cases, k_{ro}s cannot reach the same value in realistic time of flow back. (3) for both desiccated cases and nondesiccated cases, the shut-in time decreases the regained k_{ro}.

More generally, the processes of shut-in and flow back are divided into the shut-in immediately after hydraulic fracturing or before the first flow back (pre-flow-back shut-in), flow back, post-flow-back shut-in, and extended flow back (production). Wijaya and Sheng (2019c) studied these pre- and post-flow-back shut-ins. In the literature and earlier in this chapter, the shut-in before the flow back is discussed. Here the shut-in past-flow-back is discussed. The duration of the initial flowback is 10 h in a nondesiccated model. Fig. 12.34 shows that the shut-in time is longer, the regained k_{ro} becomes lower, indicating the shut-in is not beneficial.

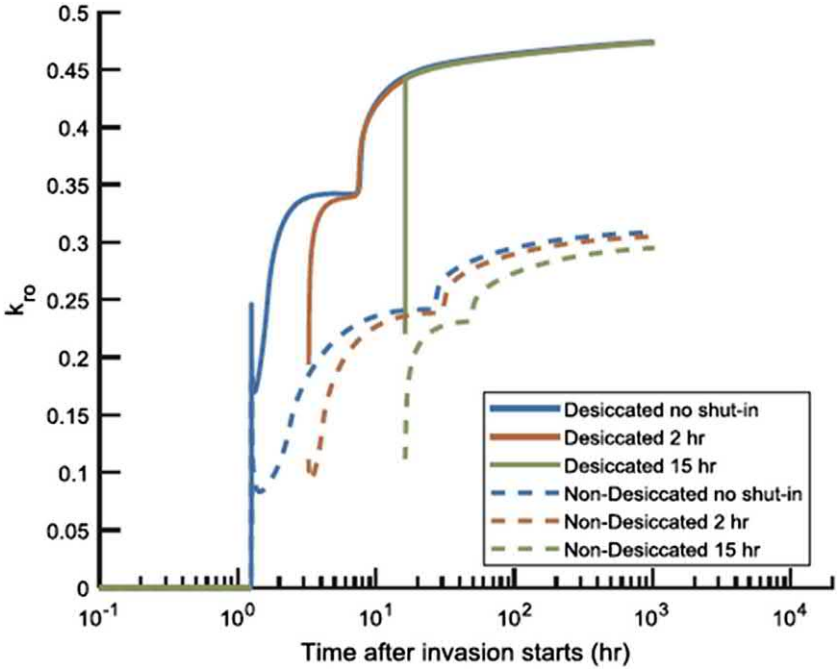

Figure 12.33 Effects of shut-in before flow back and desiccation on regained k_{ro}.

Wijaya and Sheng (2019c) also compared the shut-in performance of the pre-flow-back with that of post-flow-back in a nondesiccated model as shown in Fig. 12.35. It shows that the regained k_{ro} for the shut-in post-flow-back is higher than that pre-flow-back; the k_{ro} without any shut-in is the highest.

In tight gas formations, shutting in wells to allow closure can be very detrimental to ultimate production due to proppant setting in non-cross-linked fluids. Additionally, the supercharge from the treatment is lost. The supercharge is the buildup of leaked fluid near the fracture or wellbore so that the pressure is built up. The stored energy in the compressed minerals, liquids, and gases helps to recover substantial volumes of fluids, even in underpressured reservoirs, if the flow back follows immediately after the treatment. In medium- and high-permeability formations where cross-linked fluids are routinely used and proppant concentrations within the fracture are considerably higher, wells should be shut-in for enough time to allow the fracturing fluid break, then flow back (Malone and Ely, 2007).

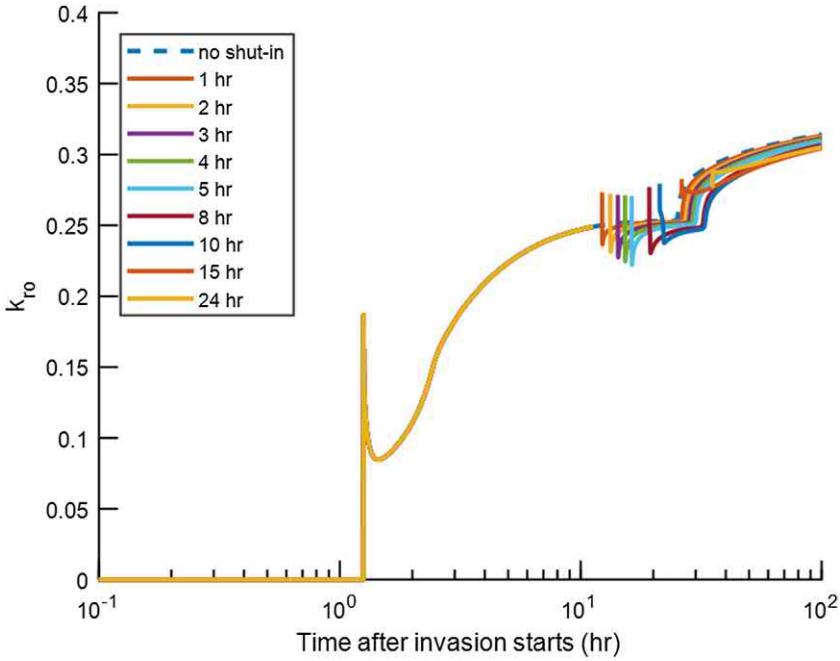

Figure 12.34 Effect of the shut-in post-flow-back on k_{ro} in a nondesiccated model.

12.5 Shut-in time effect on fracture conductivity

To evaluate the shut-in or delay effect, Crafton and Noe (2013) used the well performance metric of connectivity between the reservoir and the wellbore, as measured by "apparent fracture length." In their opinion, the apparent fracture length is not indicative of any measurable entity in the reservoir or adjacent to the wellbore; it is a surrogate to describe the degree of connectivity between the reservoir and the wellbore, nothing more.

Crafton and Noe (2013) reviewed 270 wells' performance in the Marcellus shale. The effect of delay or the first shut-in immediately starting at the end of stimulation is presented in Fig. 12.36. In the figure, the apparent fracture length is normalized by being divided by the millions of pounds of proppant used; ITM is the abbreviation of Interfacial Tension Modifier; the data are from the clean-up wells (thus the length is the *best* apparent fracture length); the log of the normalized length versus the log of delay (soak)

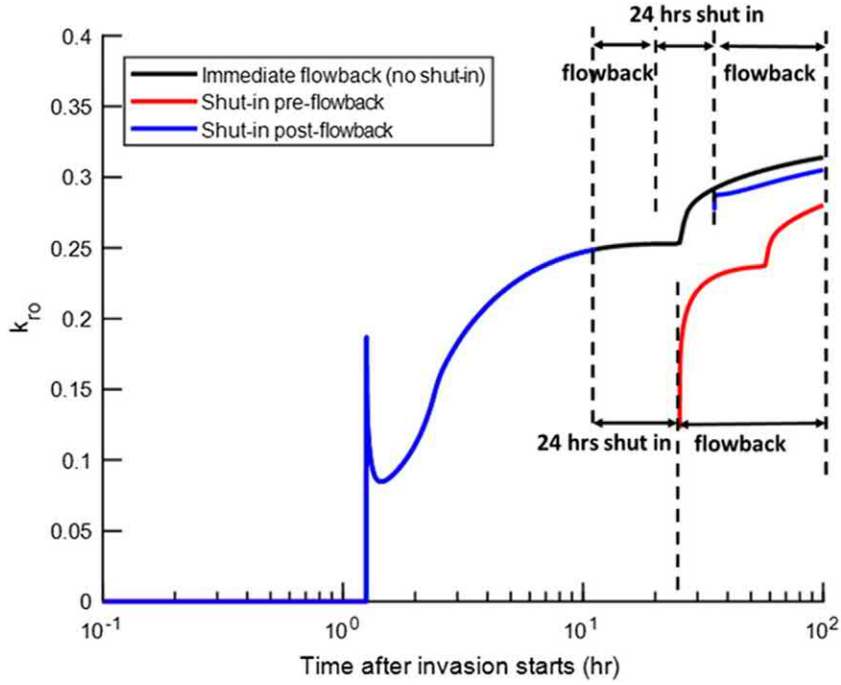

Figure 12.35 Comparison of the shut-in performance of the pre-flow-back with that of the post-flow-back in a nondesiccated model.

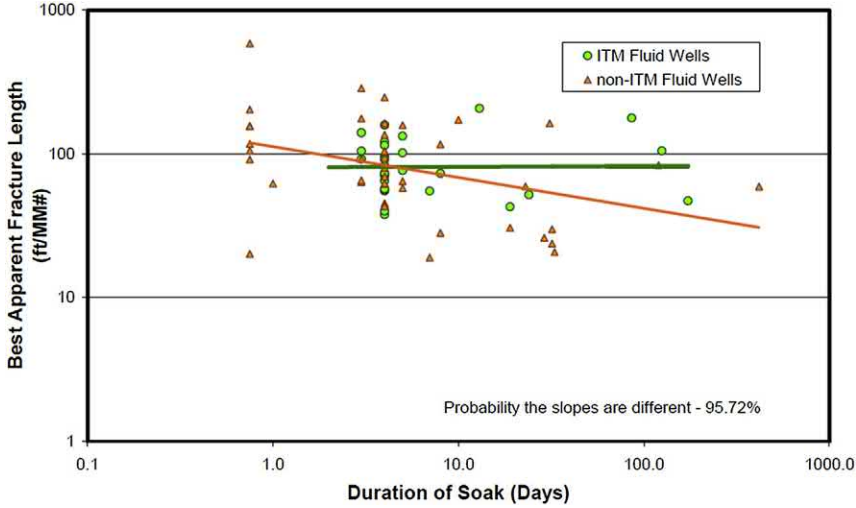

Figure 12.36 Normalized apparent fracture length versus delay or soak time (first shut in) (Crafton and Noe, 2013).

time in days. The figure shows that the apparent length for ITM fluid wells did not change with the delay time, while the apparent length for non-ITM fluid wells decreased as the delay time was longer. Their conclusion or interpretation was that the damage from the delay was quick (damaged observed for short delay times), persistent, and significant. At least, the short delay was not beneficial.

Fig. 12.37 shows the average changes of effective fracture length during a sequence of four shut-ins. The ITM fluid wells and non-ITM fluid wells are separately grouped. The effective fracture lengths at the zero shut-in are the lengths without delay or shut-in. The fracture lengths for the non-ITM fluid wells were shorter than those for the ITM fluid wells. Regardless of ITM and non-ITM fluid wells, the fracture lengths became shorter with more shut-ins being performed. This is a clear and statistical indication that shut-in was not beneficial.

Crafton (1998, 2008) also observed that the delay in starting flow back (the first shut-in) is less damaging than the shut-ins (the second or subsequent shut-ins) during flow back; a high rate of wellhead pressure change (e.g., higher than 250 psi per day) during the first production period are obviously detrimental; there is a minimum flow rate below which the

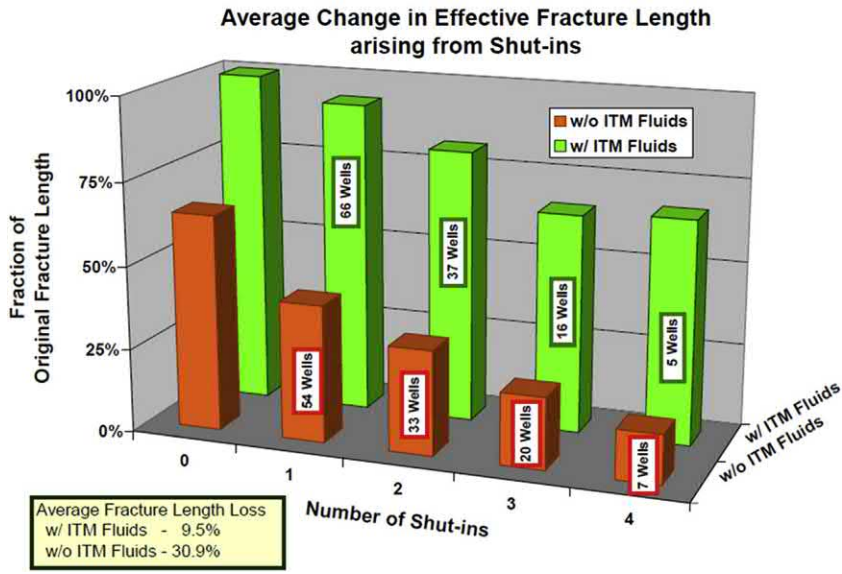

Figure 12.37 Average changes of effective fracture length during a sequence of four shut-ins (Crafton and Noe, 2013).

cleanup is ineffective and formation damage occurs; and there is a critical rate above which severe and permanent damage occurs to the effective fracture length and conductivity.

During the fracture operation, the region near the fracture is compressed and high energy is stored. This energy can help fluid flow back or cleanup. However, this energy will quickly disperse after shutdown. Therefore, it is general to make use of the energy by flowing back as soon as possible after the fracture treatment (Martin and Rylance, 2007). In tight formations, there is a significant elapse time to fracture closure and there is potential for proppant convection away from the pay zone and wellbore; consideration should be given to immediate flow back or forced closure (preclosure) (Ely et al., 1990), or reverse gravel packing (Ely, 1996). However, it is generally accepted that forced closure will lead to reduced fracture width, and therefore reduced conductivity, immediately at the wellbore, and consequently this approach has a limited range of application and should be considered carefully. After the fracture closure is confirmed, the flow back process (postclosure flow back) is begun as soon as the treatment has been shut down. After the fracturing fluids have been produced back toward the wellbore, it is very important to keep the fluids moving and not to halt the process until the well is fully cleaned up. Each time a well is shut-in during fracture fluid recovery, it can become increasingly difficult to reinitiate fluid recovery. This is particularly true if gas is also being recovered with the fracturing fluid, as the multiphase flow effects will tend to decrease the effective permeabilities of both phases. Also, additives in fracturing fluids to prevent formation damage such as demulsifiers, clay stabilizers, and low-tension additives have a limited life, generally in hours not in days or weeks. The longer the fracturing fluids are left in the formation, the less effective these additives will be and the greater the potential for permanent formation or fracture damage (Martin and Rylance, 2007). Hawkins (1988) found that both final permeability and permeability recovery decreased dramatically with increasing shut-in time in his experiments, because of gelling agent becoming more concentrated which reduces permeability.

The flow back process should also be designed to minimize proppant flow back. One method is to control the drawdown or flow rate. A sudden change should be avoided. The choke sizes should be staged slowly up or down as required (Martin and Rylance, 2007).

Bilden et al. (1995) measured fracture conductivity in laboratory and evaluated well skins from well pressure transient analysis. The results did

not find that 7 days of shut-in was detrimental to fracture conductivity and the negative skin values were not indicative of increased polymer damage.

12.6 Effect of initial wettability on flow back

During the flow back, the water saturation changes in a water-wet core (represented by *square points*) and in an oil-wet core (by *circle points*) are shown in Fig. 12.38A. Clearly, the water saturation in the oil-wet core decreased much faster than in the water-wet core. As shown in Fig. 12.38B, the pressure drop in the water-wet core (*black color*) was higher than that (*red*) in the oil-wet core initially, with the same flow-back rate. After the water block near the fracture face was removed in the water-wet core, the pressure drop was lower than that in the oil-wet cores (either with surfactant or without surfactant). These results suggest that *to favor water flow back*, a surfactant should not be added in the fracturing fluid to change oil-wetness to water-wetness. In other words, initial oil-wetness favors the flow back of aqueous fracturing fluid. Note that the water saturation and pressure drop in the oil-wet core with invaded surfactant solution were slightly lower than those in the oil-wet core with invaded water. In the experiment, an anionic surfactant with the IFT of 0.03 mN/m was used, and the water-wetness of the core (Indiana limestone core) was aged with 1.5 wt.% cyclohexanepentanoic acid in n-pentane to have been changed to oil-wetness. These experiments showed that the added surfactant did not significantly improve the flow back performance in the oil-wet core.

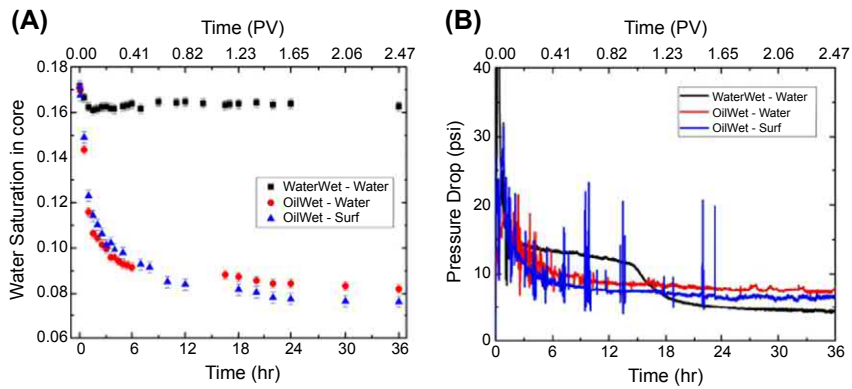

Figure 12.38 Comparison of changes of the total water saturation within the core (A) or the pressure drop across the core (B) during flow back under various conditions (Liang et al., 2017d).

Although the flow back from the above oil-wet case was much more than that from the water-wet case, the regained permeability could be either more or less in the different stages of flow back. Fig. 12.39 shows that the regained permeability to pentane in the initially water-wet core was lower than that in the initially oil-wet core, but higher at late time. This is because in the water-wet core, water imbibed deep into the core by capillary pressure and the flow back of the imbibed water took some time; initially the regained permeability was low; after more water was removed near the fracture face, the permeability was significantly regained, resulting in higher permeability than that in the oil-wet core, because generally the oil permeability in an oil-wet core is depressed. For the case of oil-wet core with a surfactant solution, the regained permeability followed the trend in the oil-wet core without surfactant, but higher. From oil production point of view, it seems that water-wetness is preferred from this example.

Tangirala and Sheng (2019b) compared the surfactant roles in the soaking process and the invasion and flow back processes. The cores were *initially oil-wet* and saturated with a crude oil. Amott type of experiments were conducted to study the soaking process. Three tight cores (crab orchard labeled T1, T2 and T3) of ~11% porosity and three conventional cores (labeled

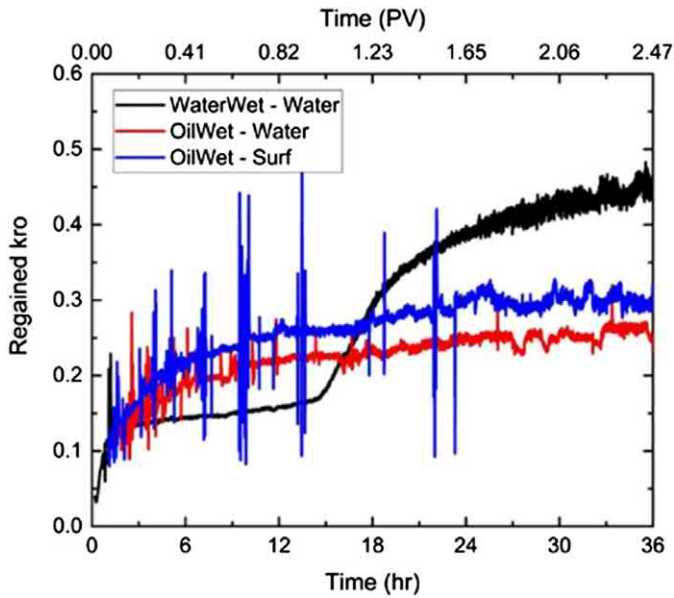

Figure 12.39 Comparison of changes of regained permeability to pentane under various conditions (Liang et al., 2017d).

C1, C2 and C3) of ~18% porosity were used in experiments. Their main mineral component was quartz. Three fluids were used: deionized water, nonionic surfactant, and anionic surfactant. The IFT values and contact angles of these fluids are shown in Table 12.2.

Fig. 12.40 shows the oil recovery by spontaneous imbibition during the soaking process in (a) tight cores and (b) conventional cores. From both types of the cores, the surfactant solution which had the moderate IFT and the function to change oil-wetness to water-wetness had the highest oil recovery, and water had the lowest; the nonionic surfactant even changed the cores more oil-wet but the IFT was reduced, and the oil recovery stood in the middle. Those results are inline with earlier published results.

To study the invasion and flow back processes, the experimental apparatus shown in Fig. 12.41 was used. First, the core was flooded from the end A to the end B using the oil at a constant pressure drop until a steady state oil rate (q_{o1}) was reached. The oil permeability was calculated using Darcy's equation. Then an invasion was performed by injecting about 0.25 pore volumes (PV) of a fluid from the end B of the core at a very small pressure drop (ΔP) to prevent any viscous fingering. Finally, in the flow back phase, the fluids were produced from the end B, and oil was injected from the end A at the same constant pressure (ΔP) to represent the hydrocarbon flow from the deep reservoir to the fractured well. The effluent was collected in a flask and was continuously weighed on a scale. The flow rate during flow back could be calculated from the increment of cumulative fluid production within a unit time. After at least 36 h (1−4 PV) of production from a tight core, or about 10 PV of production from a conventional core, a steady state flow back rate (q_{fb}) was reached. When the flow was steady state, the oil rate (q_{o2}) from the end A should equal the fluid rate at the end B; before that, they are not equal. For a simple comparison, the ratio $R = q_{o2}/q_{o1}$ was used to evaluate the changes of permeability. The flow back efficiency was defined by the flow back volume divided by the invaded volume.

Fig. 12.42 shows the permeability recovery ratios (R) and flow back efficiencies for tight cores, when water, nonionic surfactant solution, and anionic surfactant solution were injected and flowed back. It is against one's intuition that surfactant solutions may help recovery permeability and increase flow efficiency. The figure shows that both permeability recovery ratio and the flow back efficiency for water were higher than those of nonionic and anionic surfactant solutions; the anionic surfactant solution

Table 12.2 IFT and contact angles of the solutions used.

Aqueous fluid	Concentration	IFT with oil mN/m	Rock used	Contact angle, degrees	Primary function of fluid	Designated name for the fluid
DI water	-	25 (±) 1.2	Conventional	120.78 (±) 17.79	Base case	C1
Nonionic surfactant	0.2 wt.%	0.58 (±) 0.06	Berea sandstone	145.62 (±) 6.12	IFT reduction	C2
Anionic surfactant	0.2 wt.%	0.68 (±) 0.04		41.76 (±) 10.45	IFT reduction and wettability alteration	C3
DI water	–	25 (±) 1.2	Tight sandstone—Crab Orchard	112.81 (±) 11.14	Base case	T1
Nonionic surfactant	0.2 wt.%	0.58 (±) 0.06		144.23 (±) 10.48	IFT reduction	T2
Anionic surfactant	0.2 wt.%	0.68 (±) 0.04		44.05 (±) 6.68	IFT reduction and wettability alteration	T3

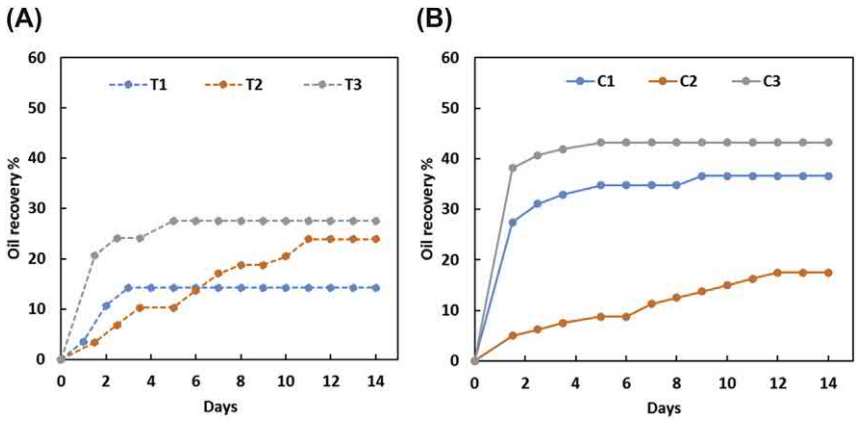

Figure 12.40 Oil recovery by spontaneous imbibition during the soaking process in (A) tight cores and (B) conventional cores.

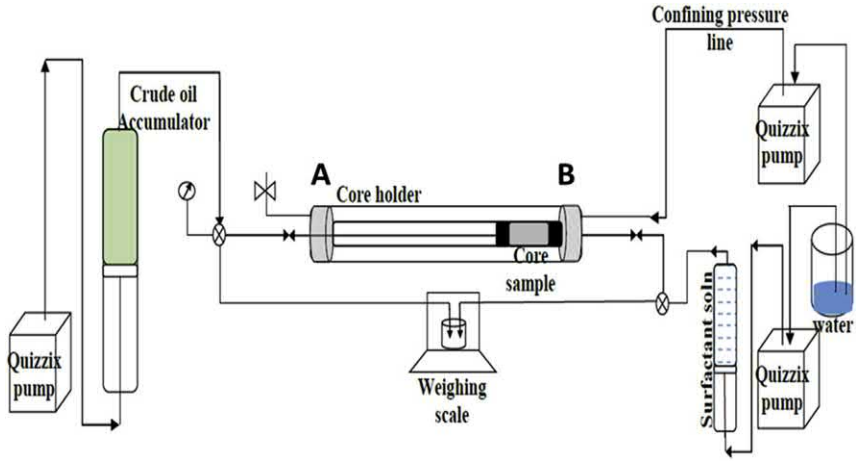

Figure 12.41 Experimental apparatus for invasion and flow back.

which had a low IFT and a water-wetting angle had the lowest permeability ratio and flow back efficiency. In those experiments, the capillary numbers were in the order of magnitudes of 10^{-7}—10^{-6} (Tangirala and Sheng, 2019b). Such low capillary numbers may not make the capillary desaturation mechanism work (Sheng, 2011). Thus, the mechanism that might play in those experiments was wettability. Since the cores were initially *oil-wet*, the invaded zone closer to the end B was oil-wet in the water case. Then the oil from the end A could imbibe into the invaded zone of the core close to the end of B. The capillary pressure was the driving force which helped

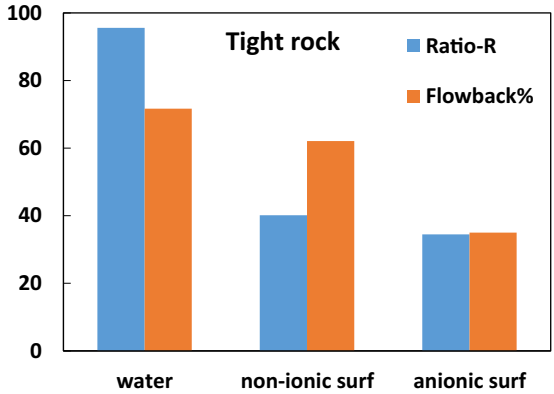

Figure 12.42 Permeability recovery ratios and flow back efficiencies for tight oil-wet cores (*k* in the 10th md) of different fluids.

the fluids flow out (back) through the end B. In addition, the water close to the end B would not stick to the core as the core was oil-wet. As a result, both the permeability ratio and flow back efficiency in the water case were the highest.

In the anionic surfactant case, the invaded zone close to the end B was changed to water-wet, at least partially water-wet. The oil from the end A would have resistance to imbibe into this zone. And the water would preferentially stay inside the core owing to the capillary end effect. The resulting permeability ratio and flow back efficiency would be lowest.

In the nonionic surfactant case, although the *invaded zone remained oil-wet*, the IFT was reduced so that the capillary drive force was lower than that in the water case. Thus, the permeability ratio and flow back efficiency were lower than those in the water case.

Fig. 12.43 shows the permeability recovery ratios (R) and flow back efficiencies for the conventional cores. The performance was similar to that in the tight cores, except that the differences among the cases of different solutions were lower. In the conventional cores, the low IFT and high flow velocity made the capillary numbers in the order of magnitudes of 10^{-5}—10^{-3} (Tangirala and Sheng, 2019b) which made the capillary desaturation work. Thus, the performance in the nonionic and anionic surfactant solution cases was improved, and their differences with those in the water cases became smaller.

However, field data suggest that the IFT reduction decreases the drawdown required to initiate and sustain the flowback; the load recovery from over 200 wells in Cotton Valley, Greater Green River, Piceance, San Juan,

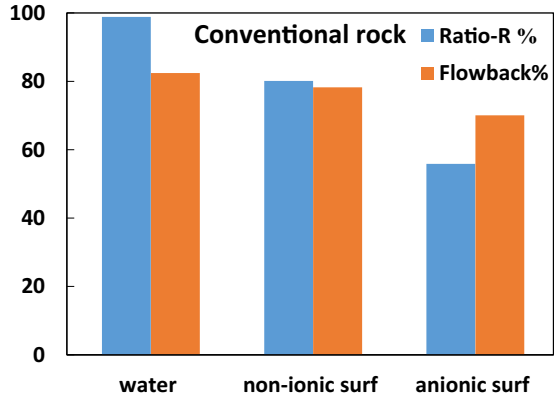

Figure 12.43 Permeability recovery ratios and flow back efficiencies for conventional oil-wet cores (*k* in the range of a few md and tens of md) of different fluids.

Uinta, and Vicksburg Basin treated with surfactants was 50%—100% higher than the load recovery with fracturing water alone (Paktinat et al., 2005; Crafton et al., 2009). Since the flow back can be more easily sustained, surfactants thus demonstrate a much higher load recovery, hence minimum blockage in the reservoir (Crafton et al., 2009; Penny and Pursley, 2007; Butler et al., 2009; Zelenev and Ellena, 2009). Some field operators in the Appalachian, Barnett, and Fayetteville Basin observed an increase in the initial gas production rate from wells treated with microemulsion-forming surfactants (Penny and Pursley, 2007). In those field cases, initial wettability is unknown.

12.7 Effect of invasion depth on flow back efficiency and late time oil rate

Tangirala and Sheng (2019a) studied the effect of invasion depth on flow back efficiency. The invasion depth was represented by the water (aqueous phase) saturation (%) at the end of invasion. The flow back efficiency was defined as the water saturation reduction divided by the water saturation at the end of invasion. The experimental details have been presented earlier in this chapter. They found that as the invasion depth was deeper, the flow back efficiency became higher, especially for the water case, as shown in Figs. 12.44 and 12.45. In the *water-wet* chip, the capillary pressure resisted the water from flowing out. As the invasion was deeper, the positive capillary pressure gradient was lower, and the resistance became weaker. Thus, the flow back efficiency was improved. When the surfactants

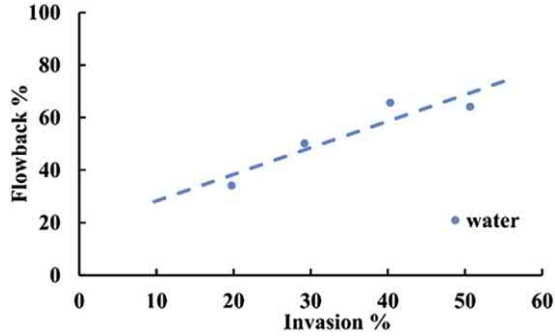

Figure 12.44 Flow back efficiency versus invasion depth in a water-wet chip for deionized water.

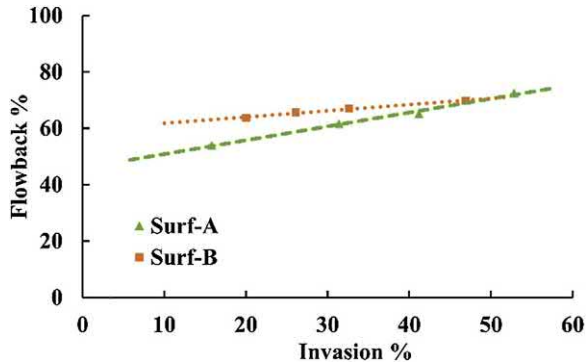

Figure 12.45 Flow back efficiency versus invasion depth in a water-wet chip for two surfactant solutions.

were added, the capillary pressure became lower, and the effect of the capillary pressure gradient became less sensitive to the invasion depth. Note that the surfactants cannot change the chip wettability.

However, the stabilized oil rate during the late-time flow back decreased with the invasion depth, both for water and surfactant solution cases, as shown in Figs. 12.46 and 12.47. Therefore, we wish to have a shallow invasion depth to have higher oil rate. Note this deep invasion was caused by the fluid leak off, not caused by the imbibition during shut-in.

However, when the chip is *oil-wet*, the flow back efficiency decreased with invasion depth, as shown in Fig. 12.48 (Tangirala and Sheng, 2018). During the flow back, the capillary pressure was a driving force. As the invasion depth was increased, the driving pressure gradient was decreased, and the flow back efficiency was decreased. Consequently, the stabilized oil rates

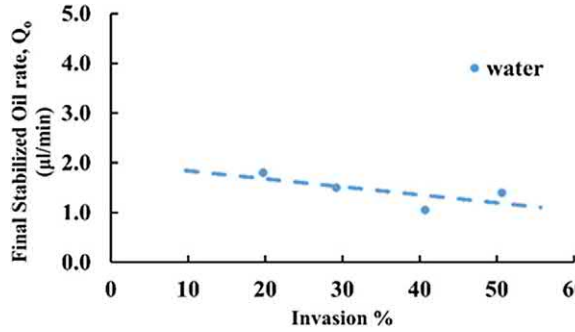

Figure 12.46 Stabilized oil rate versus invasion depth in a water-wet chip for deionized water.

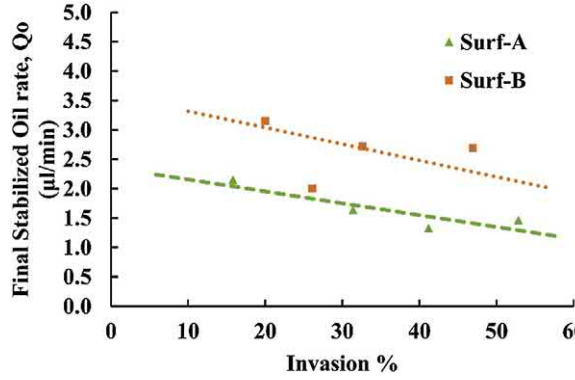

Figure 12.47 Stabilized oil rate versus invasion depth in a water-wet chip for two surfactant solutions.

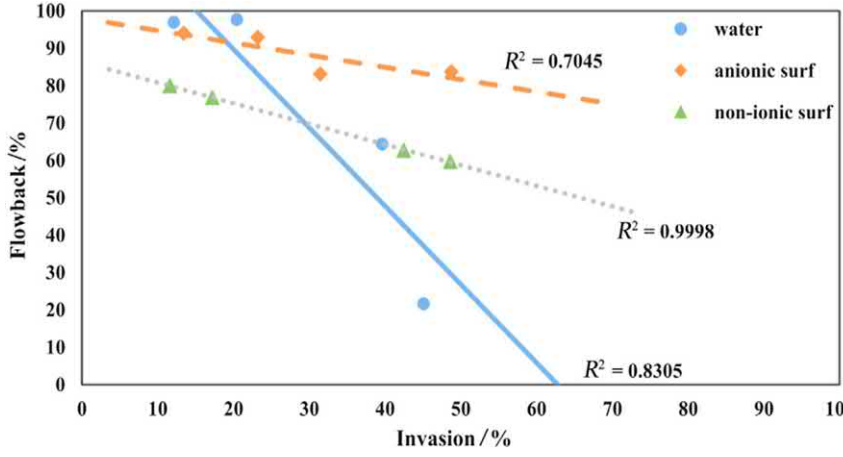

Figure 12.48 Flow back efficiency versus invasion depth in an oil-wet chip.

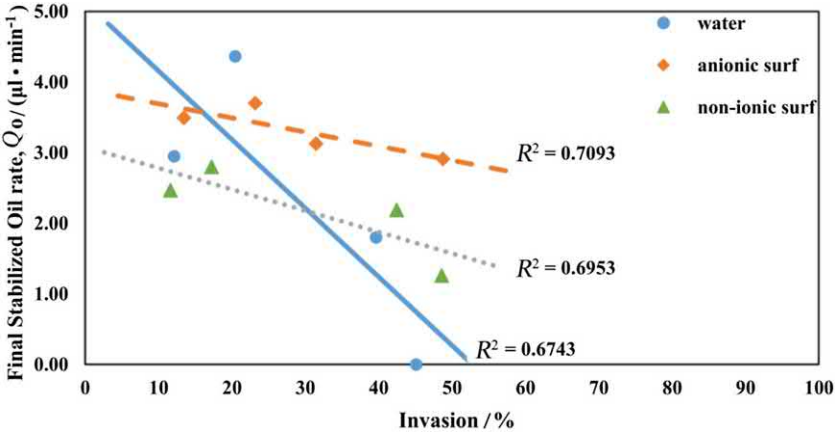

Figure 12.49 Stabilized oil rate versus invasion depth in an oil-wet chip.

decreased with invasion as shown in Fig. 12.49. Those preceding figures show that when the invasion depth was shallower, the flow back efficiency and stabilized oil rate for the water were higher than those for surfactants. This is because the surfactant reduced the capillary pressure gradient; but as the invasion depth became deeper, the surfactant-reduced IFT resulted in higher capillary numbers (in the order of 10^{-4} vs. 10^{-5} for water in the Tangirala and Sheng's (2018) experiments), and the flow efficiency was improved compared with water.

The preceding results and conclusions in oil-wet chips were verified by core flooding results (Tangirala et al., 2019). For the same fixed invasion depth, the remaining (residual) *oil* saturation (S_{w2}) at the end of flow back, the flow back efficiency (*flb*), and the stabilized oil rate (Q_o) were compared for water flooding with and without a surfactant. The following parameters X, Y, and Z were defined:

$$X = \frac{(S_{w2})_{\text{water}} - (S_{w2})_{\text{surf}}}{\left|(S_{w2})_{\text{water}} - (S_{w2})_{\text{surf}}\right|_{\max}} \tag{12.7}$$

$$Y = \frac{(flb)_{\text{surf}} - (flb)_{\text{water}}}{\left|(flb)_{\text{surf}} - (flb)_{\text{water}}\right|_{\max}} \tag{12.8}$$

$$Z = \frac{(Q_o)_{\text{surf}} - (Q_o)_{\text{water}}}{\left|(Q_o)_{\text{surf}} - (Q_o)_{\text{water}}\right|_{\max}} \tag{12.9}$$

In the above equations, the subscripts water and surf represent water and surfactant solution, respectively. The subscript max represents the maximum difference of each variable (S_{w2}, *flb*, and Q_o) at different invasion depth (%). These parameters *X*, *Y*, and *Z* are calculated separately for the experiments in chips and cores. They are shown in Fig. 12.50. The negative values of these parameters mean the fracture fluid with surfactant performed below the water without surfactant. The figure shows that when the invasion was low (<20% for chip flooding, 30% for core flooding), the water performed better than the fracturing fluid with surfactants; in other words, the residual water saturation was higher, the flow back efficiency was lower, and the oil rate was lower for the fracturing fluid with surfactant than those for water only.

From the preceding figures, it seemed that the final stabilized oil rate decreased with the invasion depth, regardless of the initial chip wettability. It could also be derived from those figures that the flow back efficiency was inline with the final stabilized oil rate; that is, the higher the flow back efficiency, the higher the final oil rate was.

For an *oil-wet* chip, it is expected that a higher injection pressure is needed to force water into the chip, or at a pressure, the invasion depth is shallow; and the flow back becomes easier. Therefore, a higher oil rate would be expected, compared with a water-wet chip. Compared with water invasion, a surfactant can reduce the IFT leading to a lower capillary resistance and thus deeper invasion is expected. During the flow back, the capillary pressure is a drive force which is higher for water than for a surfactant solution; the resulting flow back rate or oil rate is higher for water. However, when the invasion became deeper, the flow back efficiency and the stabilized oil rate for water was lower than those for surfactant solutions,

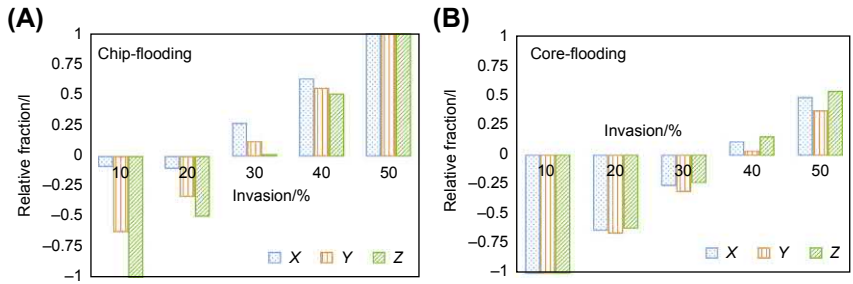

Figure 12.50 Relative performance of fracture fluid with surfactant against the one without surfactant in both (A) Chip flood and (B) Core flood experiments.

because the surfactant solutions reduced IFT and increased capillary number. These expectations are consistent with the experimental results presented in the preceding paragraph. Note that surfactant cannot change the chip wettability from oil-wet to water-wet in this case owing to the chip material. If a surfactant can change the wettability to water-wet, then the capillary pressure becomes a resistance, but the oil relative permeability may be increased during the flow back. The net effect of these two factors determines the oil flow rate for surfactant solution compared with the oil rate for water.

12.8 Effect of surfactants on flow back

In preceding sections, the roles of surfactants are discussed when they are related to shut in, invasion depth, and initial rock wettability. This section is to further discuss the roles in flow back. Surfactants have basically two functions: interfacial tension (IFT) reduction and wettability alteration. Generally, when IFT is reduced, the capillary number is increased, residual saturations are reduced, and relative permeabilities are increased. At oil-wet conditions, oil relative permeability is depressed; similarly, at water-wet conditions, water relative permeability is depressed. From these general observations, surfactant solutions should have high IFT and oil-wetness alteration to mitigate water blockage from favorable p_c point of view; but they should have low IFT and water-wetness alteration to increase k_{ro} and depress k_{rw} from k_r point of view. More detailed ideal functions of surfactants are summarized in Table 12.3. Obviously, the requirements to favor p_c and k_r

Table 12.3 Favorable conditions for invasion, flow back, and oil recovery.

		Less invasion		More flow back		Higher oil recovery	
Favorable	**Initial wettability**	**IFT**	**Wettability**	**IFT**	**Wettability**	**IFT**	**Wettability**
p_c for SI	WW	Low	OW	High	OW	High	OW
k_{rw} for displacement	WW	High	WW	Low	OW		
k_{ro} for displacement	WW					Low	WW
p_c for SI	OW	High	OW	High	OW	High	OW
k_{rw} for displacement	OW	High	WW	Low	OW		
k_{ro} for displacement	OW					Low	WW

are not consistent. This makes the selection of surfactant more complicated. The final selection depends on the net effect of these two functions. In the table, the requirements to favor invasion are also listed which even make the optimization even more difficult. Note that to reduce water imbibition, low IFT is more favorable in an initially water-wet formation.

As mentioned earlier, surfactants added in fracturing fluids seem to remove water blockage more effectively than water, and the regained oil relative permeability k_{ro} is improved as well. Wijaya and Sheng (2019d) conducted mechanistic analysis of the effectiveness of surfactant additive by history matching core flood experiments in *initially water-wet* cores by Liang et al. (2017c). Fig. 12.51 shows the water saturation histories at different distances away from the fracture during the invasion and three periods of flow back in the deionized water (DI) case (A) and the surfactant case (B). Several observations can be made. (1) At the same time, the water front in the DI case is further away from fracture (water invades deep in the matrix), as it is clear when the S_w front from the DI is plotted in the surfactant plot (B). Because of the shallow invasion, removal of invaded water in the surfactant case becomes easier. (2) Flow back is more effective in the surfactant case than the DI water case, as the water saturation during flow back is lower (large area of 0.2—0.25 in B compared to a large area of 0.25—0.3 in A). As a result, the regained k_{ro} or oil recovery from the surfactant case is higher.

The next question is how to optimize the surfactant functions? Wijaya and Sheng (2019e) used the above history matched base model (*initially water-wet*) and run a series of simulation cases to see at what conditions a maximum removal of water blockage and a maximum oil recovery or regained oil relative permeability k_{ro} can be achieved. They look at the conditions in three phases: early-, intermediate-, and late-phases. Corresponding to these phases in order, k_{ro} quickly increases, temporarily decreases, and finally increases or stabilizes. The early phase refers to the period in which the IFT reduction effect is still present. The intermediate phase refers to the period in which the IFT reduction effect is diminished as flow back gradually removes the surfactants out of the rock, and water is not fully cleaned up in the fracture. This leads to further water imbibition into the matrix, causing the temporary decrease in k_{ro}. The late phase refers to the period in which water is fully cleaned up in the fracture, so that k_{ro} gradually increases again or stabilizes because of stabilized oil flow. Fig. 12.52 presents the k_{ro} at different IFTs and oil-wetness at the ends of early phase (A), intermediate phase (B), and late phase (C) for a low-permeability model (3.69 mD). An optimum condition for high k_{ro} seems to be low IFT and water-wetness. This condition corresponds to a condition to favor k_{ro} according to Table 12.3. Similarly, Fig. 12.53 presents the k_{ro} at different IFTs and

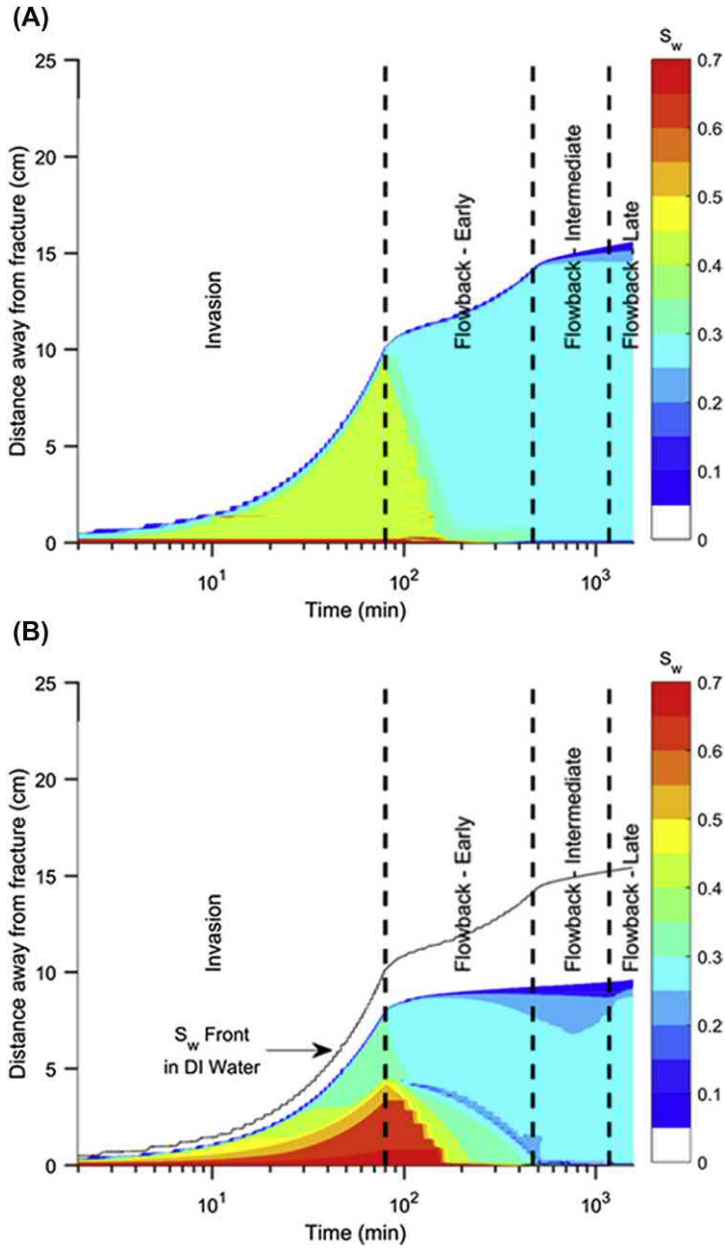

Figure 12.51 Water saturation histories at different distances away from the fracture during invasion and three periods of flowback in the DI water case (A) and the surfactant case (B).

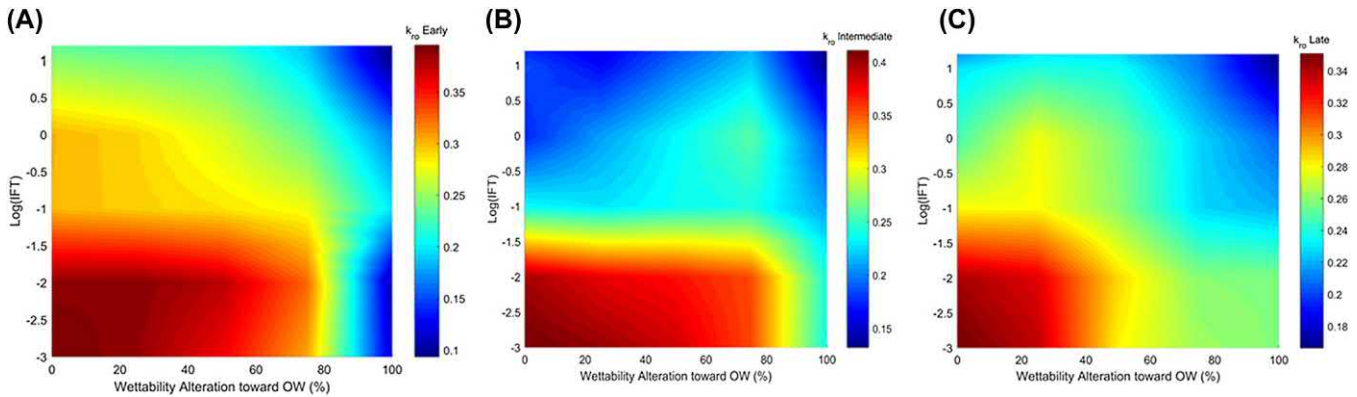

Figure 12.52 k_{ro} at different IFT and oil-wetness at the end of early phase (A), intermediate phase (B), and late phase (C) for a low-permeability model (3.69 mD).

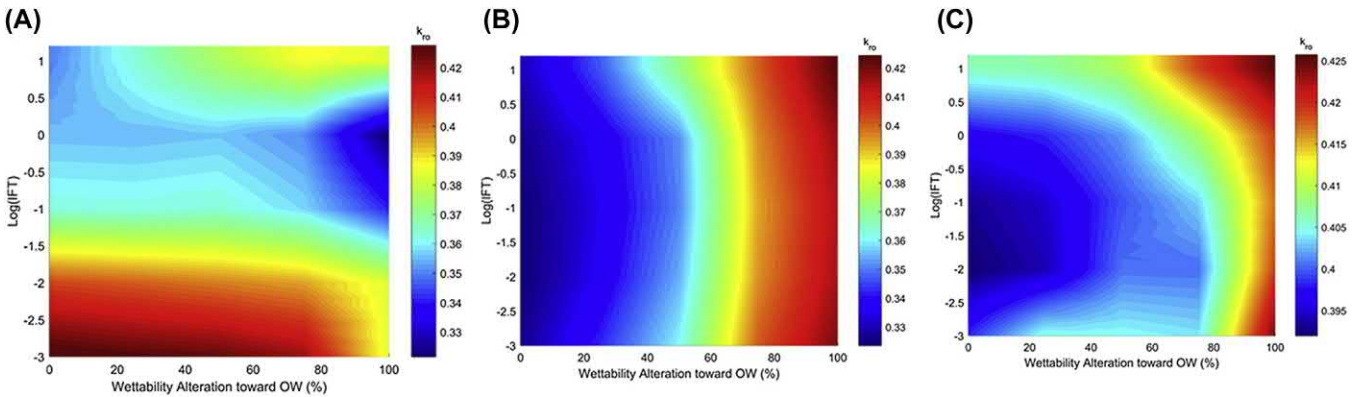

Figure 12.53 k_{ro} at different IFT and oil-wetness at the end of early phase (A), intermediate phase (B), and late phase (C) for a tight model (500 nD).

oil-wetness at the ends of early-phase (A), intermediate-phase (B), and late-phase (C) for a tight model (500 nD). An optimum condition for high k_{ro} appears to be low IFT with a wide range of wettability in the early phase, oil-wetness with a wide range of IFT in the intermediate and late phases. Probably the oil recovery is more related to the late-phase behavior. The oil-wetness is an optimum condition for the tight model. This condition corresponds to a condition to favor negative p_c according to Table 12.3. Apparently, this example indicates that a favorable k_r condition is good for a low-permeability water-wet formation; a favorable p_c condition is good for a tight water-wet formation.

12.9 Solutions to deal with flow back

According to the fundamental flow theory (the concept of relative permeability), higher flow back will enhance oil and gas recovery, because more water blocking is removed. Sometimes, a high oil or gas production rate is observed when the flow back is low. That may be because trapped water near fractures dissipates deep into the formation so that the blocking near fractures is mitigated. In this situation, there may exist a complexity of fracture networks to facilitate quick water dissipation. If a low oil or gas rate is observed even though the flow back is high, the opposite situation may exist where there is not a complexity of fracture networks. In the following sections, several solutions are proposed or practiced to dealing with flow back.

12.9.1 Avoid using trapping fluids

Flow back is to remove phase trapping. Ideally, use of trapping fluids should be avoided. For example, use of water should be avoided in strong water-wet formations. The problem is many shale and tight formations exhibit mixed wettability, either oil or water can spontaneously imbibe into formations. More importantly, which fluid should be used depends on many factors in addition to the trapping issue, like economic and environmental concerns. This solution, in most of cases, is not practical.

12.9.2 Early high drawdown

As the aqueous fluid is more significantly accumulated near fracture faces similar to the capillary pressure end effect in core flood experiments, it causes the blockage to oil and gas flow into the fractures. High pressure drawdown

may help to remove such blockage. However, several factors need to be considered: fine migration, fracture closure, etc. Water blockage is more severe near the fracture face. To effectively remove this blockage, early flow back should be practiced. Here it means that if you plan to perform flow back, early flow back is preferred, because as time elapses, the water may enter deep into the formation and then it will be more difficult to flow back. You may argue that this deep dissipation may mitigate the water blockage. This issue has been discussed earlier.

12.9.3 CO_2 injection

CO_2 dissolves in trapped water and reduces the gas-water interfacial tension. Then the energized water will more easily flow out.

12.9.4 Solvent injection

Injection of a mutual solvent like methanol experienced success in gas reservoirs. Heavier alcohols like isopropanol, butanol (Sharma and Sheng, 2017) are preferred for oil reservoirs.

12.9.5 Use of surfactants

Fig. 12.54 compares the water saturation profiles during flow back. In the experiments, pentane was injected to displace the invaded water from the other end of the core. For the left column, the invaded fluid was water only. For the right column, different types of microemulsions were formed in situ during invasion. First, during water invasion, the saturation in the invaded zone was flat which represented the front saturation, For surfactant solutions, the water saturation near the fracture face (end of core) was high and declined to the front water saturation. Water blocking near the fracture face will be more effective. The water saturations in this figure show that water blocking will be more severe initially when surfactants are added.

In Fig. 12.55, the left column shows the average water saturations in the corresponding cores presented in the earlier figure. Initially, the water saturations with surfactants were higher than those without surfactants. But during the flow back, the water saturations with surfactants quickly declined to levels lower than those without surfactants. Among all three surfactant cases, the type-I microemulsion triggered the most flow back. Note that the type II had a lower viscosity because the pentane oil viscosity was about 0.24 cP that was lower than water viscosity, so that it is easier for the type II solution fingered through the water phase, being less effective

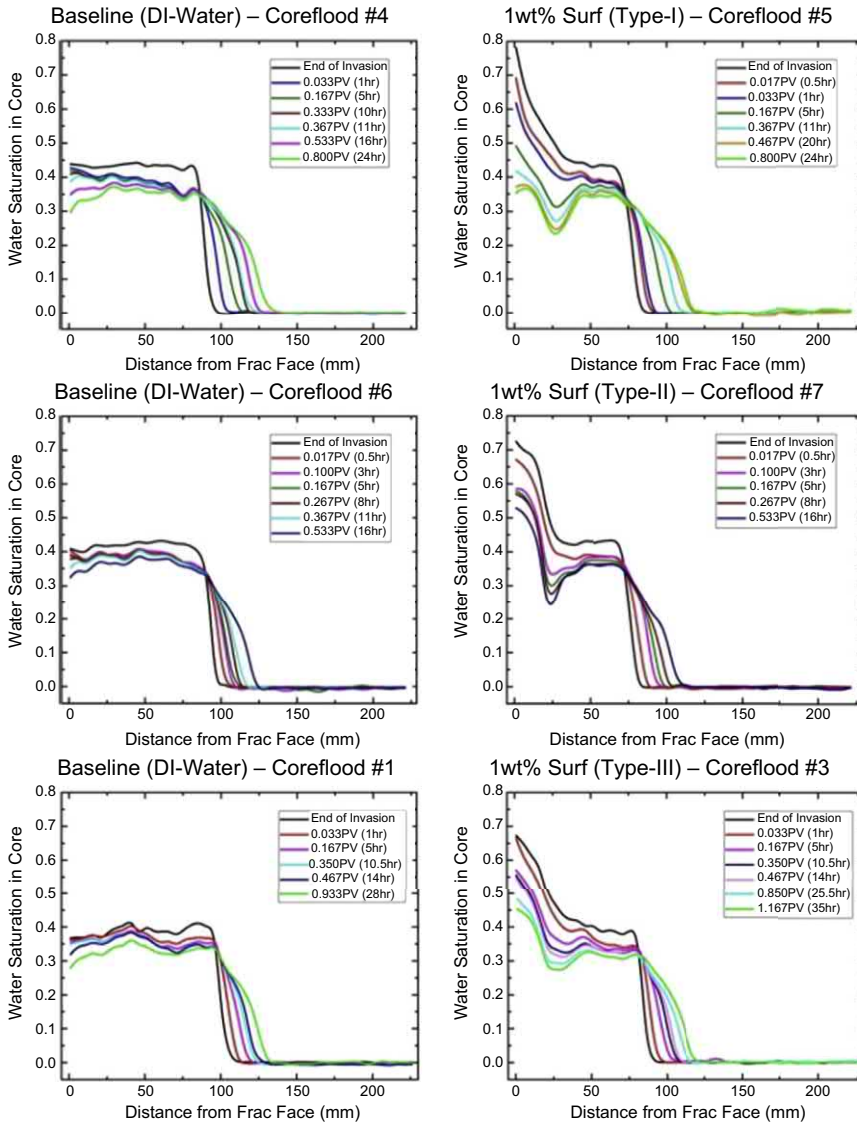

Figure 12.54 Comparison of changes of water saturation profile during flow back and hydrocarbon production among DI water and various surfactant cases (Liang et al., 2017a).

than the type I. Liang et al. (2017a) explained that the low efficiency of the type II was not caused by the fact that water was dispersed in water-in-oil microemulsion; rather it was easier for oil to bypass the type II microemulsion. However, such explanation is not supported by conventional reasoning

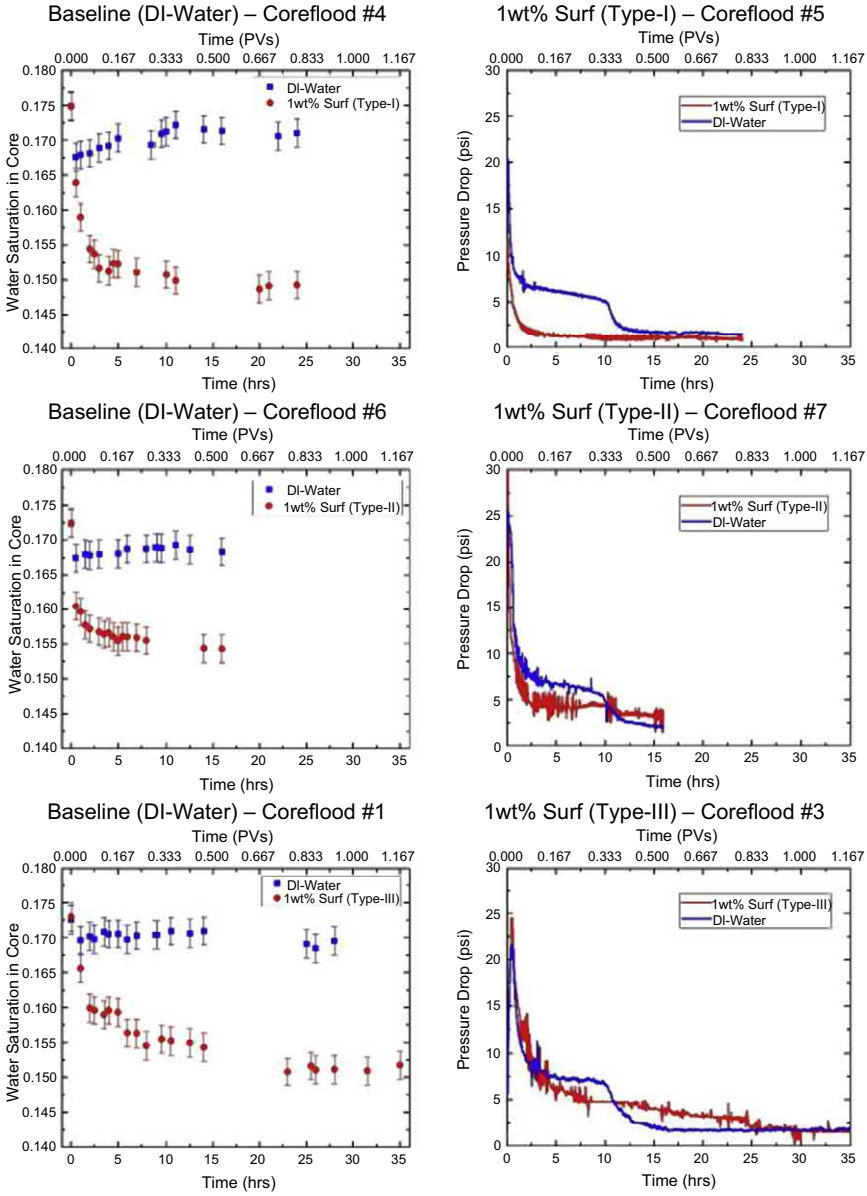

Figure 12.55 Comparison of changes of overall water saturations and the pressure drop across the core during flow back and hydrocarbon production among DI water and various surfactant cases (Liang et al., 2017a).

that a type II microemulsion is oil external and should be able to be well displaced by oil.

The right column of Fig. 12.55 compares the pressure drop for DI-water and three types of microemulsions. For the type I, the pressure drop was lower than that for DI-water, indicating the surfactant solution improved the matrix permeability. For the type II, the pressure drop was lower in the early time, but higher in the late time. For the type III, the pressure drop continued declining but was higher than that for DI-water later for a long time. These data show that the type I was most effective in improving the matrix permeability, followed by the type II, and the worst is the type III.

Overall, laboratory experiments have shown that surfactants regained more hydrocarbon permeability than fracturing water (Ahmadi et al., 2011; Rostami and Nasr-El-Din, 2014; Sayed et al., 2018; Dong et al., 2019).

12.9.6 Injection of dry gas

In principle, dry gas may be injected to vaporize liquid so that liquid phase trapping may be mitigated. Care may be taken if the trapped brine is concentrated with soluble ions. As the brine desiccates, the soluble ions may be precipitated and plug the pores, especially where divalent concentrations are high (Bennion et al., 1999).

This technique is proposed in gas condensate reservoirs in a huff-n-puff process (Meng et al., 2015a,b). This technique also has the mechanism of repressurization. However, it has not been reported in shale and tight reservoirs to remove water blockage, probably due to economic concern and effectiveness.

12.9.7 Formation heating

Formation heating was proposed by Jamaluddin et al. (1995) to remove water-based phase traps and water reactive clay-induced damage in gas reservoirs. Hot gas is injected through the tubing. A zone of 2 m high and 1.5–2 m in the radial depth is treated. Temperatures over 500°C lead to supercritical extraction of trapped water and thermal decomposition and desensitization of reactive clays.

Roychaudhuri et al. (2014) conducted forced imbibition experiments of 60 ppm surfactant solution into shale gas cores. The cores were saturated with gas and confined by 2500 psi. Then the surfactant solution was injected at one end with the other end closed. They found the imbibition rate of the

deionized water or the surfactant solution was not higher, because the capillary pressure might be marginal compared with the injection pressure and the surfactant concentration was too low. But the flow back volume of the surfactant solution was higher than the deionized water because the surfactant changed the rock from strongly water-wet to intermediate-wet.

CHAPTER THIRTEEN

Air injection

Abstract

As air has its vast and free resources, it has its economic benefit. This chapter addresses air injection in shale and tight reservoirs of light oils. In detail, this chapter addresses the following special issues: (1) kinetic parameters; (2) oxidation reactions; (3) spontaneous ignition; (4) thermal effect from low-temperature oxidation (5) oxygen consumption rate in low-temperature oxidation; (6) minimum oil content for combustion; (7) air requirement for combustion; (8) EOR mechanisms and EOR potential in shale and tight reservoirs.

Keywords: Air injection; Air requirement; Combustion; Kinetic parameters; Low-temperature oxidation (LTO); Minimum oil content; Oxidation reactions; Oxygen consumption rate; Spontaneous ignition.

13.1 Introduction

As shale and tight formations have ultralow permeability, gas injection has its advantage in terms of injectivity. Gas injection is a relatively effective method to enhance shale and tight oil and condensate recovery. Natural gas is short of supply as a clean energy in some countries like China. We may try to avoid injecting natural gas to recover oil. CO_2 injection needs building of long pipelines, and thus it is expensive. Air has its vast and free resources. It has its economic benefit. There exists light oil in most of shale and tight oil reservoirs. This chapter addresses air injection in shale and tight reservoirs of light oils.

Initially high-pressure air injection (HPAI) is designed for light oil reservoirs to make use of high-pressure air energy not heat, while in-situ combustion (ISC) is designed for heavy oil. Later air injection in some light oil reservoirs is found to have thermal benefit, for example, in the North and South Dakota portions of the Williston basin. Kumar et al. (2007) stated that more than half of the cumulative oil production was contributed by the thermal effects for the HPAI project in the West Buffalo Red River Unit. As a result, air injection in light oil reservoirs has gained attention.

Enhanced Oil Recovery in Shale and Tight Reservoirs
ISBN: 978-0-12-815905-7
https://doi.org/10.1016/B978-0-12-815905-7.00013-X

This chapter addresses several special issues related to air injection in shale and tight reservoirs:

(1) Kinetic parameters
(2) Oxidation reactions
(3) Spontaneous ignition
(4) Thermal effect from low-temperature oxidation (LTO)
(5) Oxygen consumption rate in low-temperature oxidation
(6) Minimum oil content for combustion
(7) Air requirement for combustion
(8) EOR mechanisms and EOR potential in shale and tight reservoirs

Before addressing these issues, fundamental laboratory measurements about air injection are introduced.

13.2 Laboratory experimental facilities

To facilitate understanding of air injection, equipment and instruments to study air injection are briefly introduced. They are thermogravimetry (TG) and differential scanning calorimetry (DSC), and small batch reactor (SBR), ramped temperature oxidation, combustion tube, and accelerating rate calorimetry (ARC). Turta and Singhal (2001) listed laboratory tests needed for air injection projects.

13.2.1 Thermogravimetry

In a thermogravimetric apparatus, a sample (oil) is put in a crucible which is placed in a sample holder, as shown in Fig.13.1. The holder is heated by a controllable heating program with a continuous gas flow. The gas could be air, pure oxygen, or nitrogen. The gas called purging gas will contact and displace the vapor phase of the sample and the remaining weight of the sample is recorded at different temperatures. The experiment is performed at atmospheric pressure. The experimental data are analyzed in the method described in Section 13.3.1.

13.2.2 Differential scanning calorimetry

In a DSC apparatus, a sample (oil) is put in a container. An example apparatus is shown in Fig.13.2. The sample is heated by a controllable heating program (1−10°C/min) with a continuous gas flow. The gas could be air, pure oxygen, or nitrogen. During the experiment, the heat flow (watt per second) is recorded at different temperatures. The data on positive deviation in heat flow from the crude-oil sample compared with a reference

Figure 13.1 An example of TGA apparatus and its sample crucible.

Figure 13.2 An example of a DSC apparatus.

is collected. Two peaks are seen for crude oils, one for the LTO and the other for high-temperature oxidation (HTO). The experiment is performed at an atmospheric pressure. The experimental data are analyzed in the method described in Section 13.3.2.

13.2.3 Small batch reactor

In a small batch reactor (SBR) experiment (Fig. 13.3), oil and loose sand are mixed and placed in a steel container so that air can contact oil. In the container, there is a free space to fill high-pressure air. During the experiment, excess oil exists, and the oven or system temperature is kept constant.

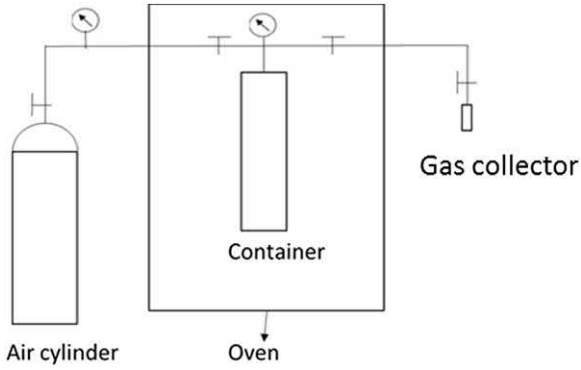

Figure 13.3 Schematic of the SBR experimental apparatus.

In other words, the experiment is under an isothermal condition. As a small volume of gas is collected and the system pressure is high, the pressure drop in the system pressure owing to this small volume withdrawal is considered negligible (Zhang and Sheng, 2016). Owing to oxidation reaction, the oxygen partial pressure is decreased. To analyze the pressure reduction caused by the oxygen consumption, the data are recorded after a steady decline in pressure. And the produced gas is collected, and the gas compositions are analyzed by a GC/MS instrument. The reaction rate is calculated by the moles of oxygen consumed in a unit mass of oil within a time interval. The oxygen partial pressure can be calculated from the air pressure multiplied by oxygen mole fraction. Such experiments are generally conducted at low temperatures, and it is intended to study low-temperature oxidation (LTO). The kinetic parameters like activation energy, preexponential constant (frequency factor), and reaction order in terms of oxygen partial pressure are obtained from such experiment, based on the Arrhenius type of equation. Such experiments assume no significant heat generated in an LTO process.

In such SBR tests, it is assumed that the produced volume is almost same as the oxygen volume consumed so that the overall pressure is maintained. Generally, the amount of carbon oxides produced during LTO reactions is very small or negligible as compared to other LTO products (Adegbesan et al., 1987; Khansari et al., 2014). This observation agrees with the experimental results. Actually, a portion of oxygen is consumed in LTO without producing carbon oxides, resulting in a decrease in the overall pressure (Turta and Singhal, 2001). Ren et al. (1999) found that the pressure reduction could also be due to the gas dissolution in the oil.

In a Greaves et al.'s (2000) LTO experiment (120°C), the oxygen, CO_2, and CO concentrations were 2%, 8%, and 1.2% after 175 h of oxidation, respectively. The experiment indicated that CO_2 and CO were produced in an LTO process. It is believed that 12% CO_2 concentration in the produced gas stream is a good indication of combustion (Montes et al., 2010). A short time of pressure increased in Sarma et al.'s (2002) isothermal aging ARC tests.

13.2.4 Ramped temperature oxidation (RTO)

A ramped temperature oxidation apparatus consists of two identical tubular reactors mounted in a common heating block where both are simultaneously heated at a fixed rate. One is the active reactor packed with a core saturated with oil and water, while the other one is the reference reactor packed with a clean core only. Inert gas is flowed through the reference reactor, whereas an oxygen-containing gas is flowed through the active reactor. The temperatures in the two reactors are compared to isolate exothermic and endothermic events related to oxidation reactions. Apparent atomic H/C ratio, apparent reacted oxygen/fuel ratio, and percentage of reacted oxygen converted to carbon oxides from the active reactor are reported (Moore et al., 1999).

Like TG or DSC tests, when the heating rate is higher than that caused by oxidation reactions, an RTO test may not represent the oxidation reactions that will occur in a reservoir (thermal hysteresis). This is because when the heat generation rate in a reservoir is low, the subsequent higher temperature oxidation may not be able to initiate because of the loss of generated heat into overburden and underburden rocks.

13.2.5 Combustion tube test

The fundamental part of a combustion tube apparatus is the combustion tube which is insulated and heated by a series of heaters. This is to reduce the radial heat loss. However, the heaters should be adjusted so that they do not drive the combustion. This is achieved by maintaining the temperature in the middle of the test tube slightly higher than the wall temperature. The tube is ignited at one end by using heaters. A combustion tube test (CT) is designed to have artificial ignition; LTO is minimized; reaction kinetics are not obtained from a combustion tube. The following data may be obtained from a combustion tube test (Prasad and Slater, 1986):

- Atomic H/C ratio of the burned fuel
- Oxygen-fuel ratio

- Oxygen-sand ratio
- Apparent fuel consumption
- Compositions of produced fluids
- Peak combustion temperature

13.2.6 Accelerating rate calorimeter (ARC)

Accelerating rate calorimeter (ARC) introduced in petroleum literature in 1991 (Yannimaras and Tiffin, 1995) is the only instrument to determine kinetics parameters at high pressure. The basic principle of an ARC is to maintain a sample of oil and rock in an adiabatic condition, during an exothermic reaction period; the adiabatic condition is achieved by maintaining the temperature of the sample container same as that of the system outside the container. The ARC is first heated to a desired temperature and held for some time for thermal equilibrium. Check whether the heating rate is less than a preset rate (e.g., 0.02 °C/min). If it is, the ARC will proceed to the preselected temperature step (5°C, e.g.,), following a heat-wait-search (HWS) sequence, until a self-heat rate is greater than the preset rate. By this time, the ARC is maintained at adiabatic conditions until the experiment is completed, as shown in Fig. 13.4 (Townsend and Tou, 1980). The experimental data are presented as the log of exothermic heat rate versus temperature. Kinetic parameters like activation energy, preexponential factor, and order of reaction can be derived from ARC

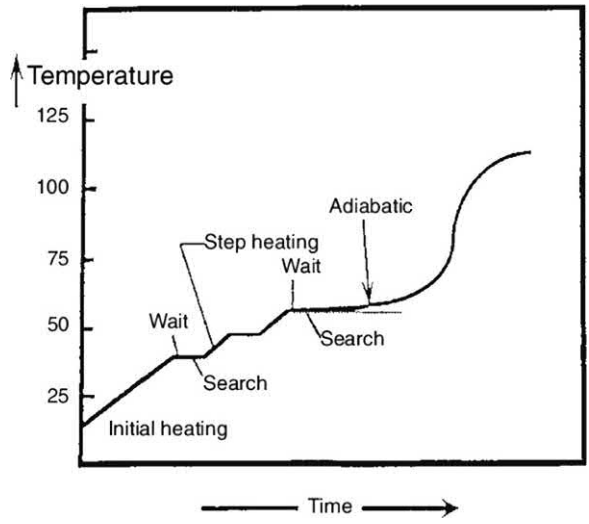

Figure 13.4 Heat-wait-search process of an accelerating rate calorimeter (modified from Townsend and Tou, 1980).

experimental data, along with the starting temperature and the content of exotherms. To reach adiabatic conditions, an oil sample is usually put in a "close" ARC system. But a "flowing" type of ARC testing system is also possible with the oil sample under a high air purge and at a quasiadiabatic operation (Yannimaras and Tiffin, 1995). ARC is similar to DSC or TG except that reactions can be performed at a high pressure in ARC.

13.3 Kinetic parameters

Oxidation reaction rates are described commonly using the Arrhenius type of equation which includes several kinetic parameters: activation energy, frequency factor and reaction order. These kinetic parameters are obtained through thermogravimetry (TG) and Differential scanning calorimetry (DSC), accelerating rate calorimeter (ARC), and small batch reactor (SBR). Example methods to obtain kinetic parameters using TG and DSC are presented next.

13.3.1 Thermogravimetric analysis (TGA)

Oxidation is a thermal decomposition process which needs kinetic parameters to describe it. One of the classic methods is based on the Arrhenius method to estimate the kinetic parameters from thermogravimetric tests or thermogravimetric analysis (TGA) (Coats and Redfern, 1964). The time-derivative thermogravimetric (DTG) data are readily available in TG equipment and sometimes used together with TG data. A TG test is used to measure the mass loss of a substance as the temperature is increased. It is described by the following equation:

$$\frac{dm_t}{dt} = kf(m, C_o, \ldots) \tag{13.1}$$

where $f(m,C_o, \ldots)$ is a function of the mass m_t remaining at time t, oxidation concentration, etc., k is the temperature-dependent rate constant, (m/t), which is described by the Arrhenius equation:

$$k = Ae^{-\left(\frac{E}{RT}\right)} \tag{13.2}$$

where A is the preexponential or frequency factor, $[t^{-1}]$, (s^{-1}). E is the activation energy of the decomposition reaction, $[L^2/t^2]$, (kJ/mol). R is the universal gas constant, $[L^2/Tt^2]$, (kJ/mol K). T is the absolute temperature, $[T]$, (K).

The function $f(m,C_o, \ldots)$ describes how the reaction (mass loss here) depends on the available mass, oxygen concentration, etc. If the reaction is not dependent on any of those parameters, the function is essentially one. The reaction is zero-order. If the reaction depends on one of those parameters, e.g., C_o^n, the function becomes a function of C_o^n which means the nth order of reaction of C_o. Make sure the units are consistent.

For the purpose of simplifying the explanation, it is assumed the reaction order is zero. By combining Eqs. (13.1) and (13.2):

$$\frac{dm_t}{dt} = Ae^{-\left(\frac{E}{RT}\right)} \tag{13.3}$$

For nonisothermal TG tests with a linear heating rate $\beta = \frac{dT}{dt}$, Eq. (13.3) can be written as

$$\frac{dm_t}{dT} = \frac{A}{\beta}e^{-\left(\frac{E}{RT}\right)} \tag{13.4}$$

Taking the logarithm of both sides of Eq. (13.4), it becomes

$$\ln\left(\frac{dm_t}{dT}\right) = \ln\left(\frac{A}{\beta}\right) - \frac{E}{RT} \tag{13.5}$$

When $y = \ln\left(\frac{dm_t}{dT}\right)$ is plotted versus $x = \frac{1}{T}$ for the experimental data, a straight line is obtained that will have a slope of E/R and the intercept of $\ln(A/\beta)$. The value of activation energy E and frequency factor A can be obtained from the slope and the intercept of the linear fit line, respectively. During a TG test, mass loss versus temperature is measured.

Note that as the temperature is increased, oil may be distilled, and the mass will be lost under air or oxygen purge. In other words, the mass loss is not totally by oxidation. Therefore, it is suggested the TG test under nitrogen purge should be carried out as a base line. Fig. 13.5 is an example of TG tests under air and nitrogen purge (Huang et al., 2016a). First, note that the two curves under air and nitrogen purge were not two straight lines in the whole temperature range as Eq. (13.5) suggests, indicating the reactions were not zero order. The figure shows that the two oil mass curves overlapped before 192°C, indicating a distillation-dominant process. After 192°C, oil weight sharply decreased. At around 348°C, weight remaining for the oil sample under air purging was around 9% and 15% for nitrogen purging. The difference of weight remaining at a particular temperature was owing to oxidation reactions at low temperature stages. Some of the

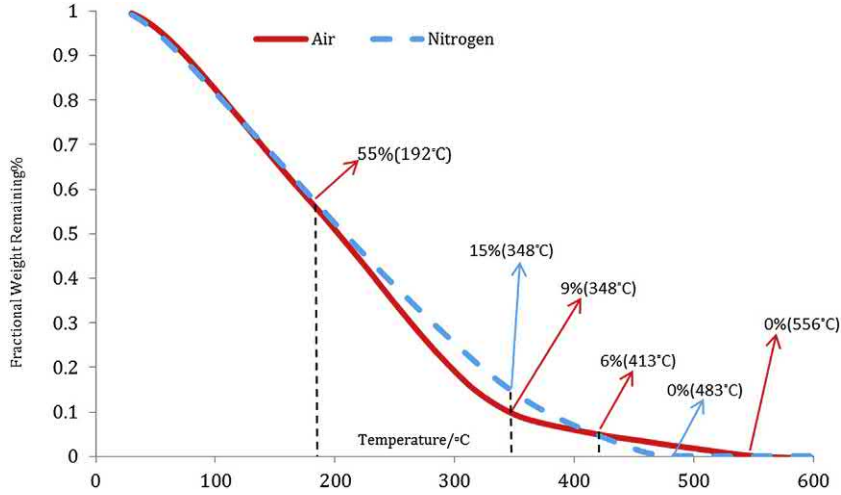

Figure 13.5 Thermograms (TG curves) of comparative tests for nitrogen and air with oil (heating rate = 10°C/min).

light components of crude oil were oxidized, causing a higher mass loss rate (Fassihi et al., 1982). It was observed that between 348 and 413°C, the total mass loss rate under air purge was slower than that under nitrogen purging; and the oil was completed lost at 483°C under nitrogen purge and at 556°C under air purging, respectively. Under nitrogen purging, the process was a distillation and cracking process (nonoxidation). Under air purging, light components of oil reacted with oxygen during a low temperature oxidation stage and generated cokelike fuel during the fuel deposition stage. During this stage, the oil mass loss rate was decreased. Finally in the high temperature range, the oil was fully burned out.

13.3.2 Differential scanning calorimetry (DSC)

Oxidation reaction with oil may generate heat. Differential scanning calorimetry (DSC) is a technique to use the exothermicity and oxidation behavior of crude oil to derive kinetic parameters. Following Eq. (13.1), the released heat (enthalpy) H_t is substituted for m_t, and the function f is defined by H which stands for the enthalpy yet to be released and is equal to $H_o - H_t$. H_o is the total released heat and is known at the end of the DSC test. Then Eq. (13.1) becomes

$$\frac{dH_t}{dt} = Aexp\left(-\frac{E}{RT}\right)H \tag{13.6}$$

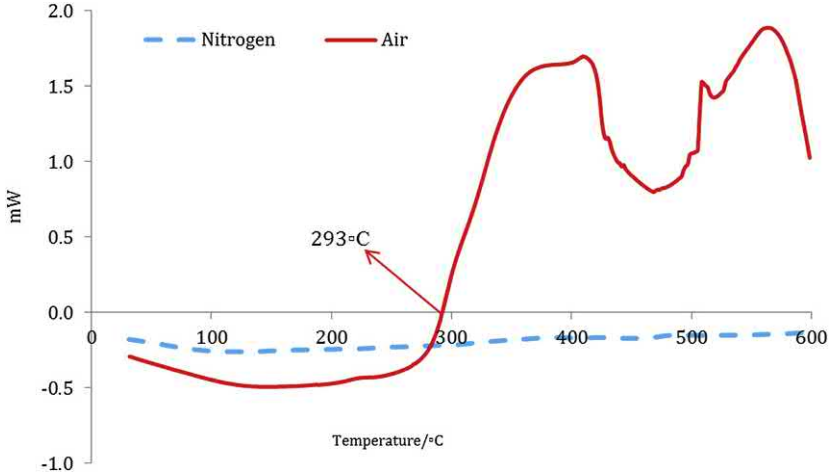

Figure 13.6 Thermograms (DSC curves) of comparative tests for nitrogen and air with oil (heating rate = 10°C/min).

Taking the natural logarithmic form, the above equation becomes

$$\ln\left(\frac{\frac{dH_t}{dt}}{H}\right) = \ln A - \frac{E}{RT} \tag{13.7}$$

The value of the activation energy can be estimated from the slope after plotting $\ln\left(\frac{\frac{dH_t}{dt}}{H}\right)$ versus $1/T$, and the Arrhenius constant is the intercept of the linear fit line (Huang et al., 2016b). Fig. 13.6 (Huang et al., 2016a) shows the DSC curves for the same oil sample used to generate the TG curves in Fig. 13.5. It shows that the heat released from nitrogen is negative, indicating an endothermic distillation process. Before 293°C, an endothermic distillation process also occurred under oxygen purging. The first peak represented the low-temperature oxidation (LTO), and the second peak represented the high-temperature oxidation (HTO) (Bae, 1977). The range between the LTO and HTO represented the fuel deposition process.

13.3.3 Practical values of kinetic parameters

When the analytical method using the Arrhenius type of equation is used to estimate kinetic parameters, only approximately "overall average" values can be obtained, as there are several temperature ranges with each range having

its own kinetic values (refer to Fig. 13.12 later). When the simulation approach is used, initial values are needed. Then what initial values should be used? More practically, a real field project cannot wait for experimental data for the project evaluation; or experiments may never be performed for practical reasons. In these situations, knowledge of practical values, or typical values, of kinetic parameters is very helpful.

Huang and Sheng (2017a) did survey on the values of published kinetic parameters for 22 crude oils with the API gravity from 11 to 44.3. Fig. 13.7 shows the distribution of activation energy data of these crude oils. The mean values for LTO and HTO at the 50% cumulative probability are 33 kJ/mol and 107 kJ/mol, respectively. No relation between the API gravity and the activation energy was found from the surveyed data, which implies that the API gravity of the crude oil cannot be used as an all-descriptive measure of the thermal behavior of crude oil (Bae, 1977).

The values of frequency factor in LTO and HTO from surveyed 11 crude oils are ($0.1—10^5$ s^{-1}) and ($10^4—10^9$ s^{-1}), respectively. The wide ranges may be caused by the fact that the frequency factor is obtained from the intercept of a straight line on the logarithmic axis which is very sensitive to the straight line selected. The API gravity of the crude oil does not have a relation with the frequency factor.

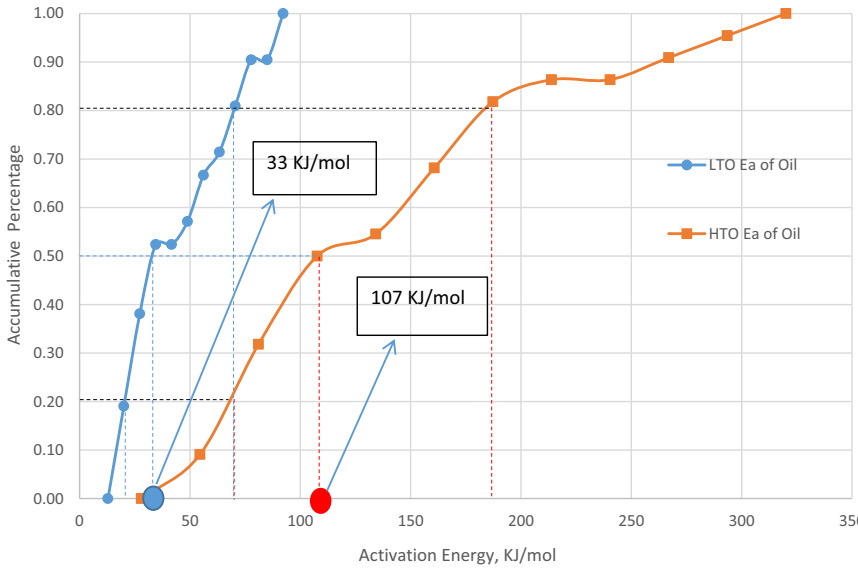

Figure 13.7 Activation energy data of 22 crude oil samples in LTO and HTO.

13.3.4 Exothermic and endothermic behavior

To define reaction schemes, exothermic and endothermic behavior needs to be understood; their data can be obtained experimentally by differential thermal analyzer (DTA), DSC, and accelerating rate calorimetry (ARC). Several temperature regimes can be identified from thermal experiments: low-temperature oxidation (LTO), fuel deposition (FD), and high-temperature oxidation (HTO). It is observed that the API gravity of the oil does not directly correlate with the temperature regions. Huang and Sheng (2017a) found average reaction temperature regions for LTO and HTO to be 149–364°C for the LTO and 415–542°C for the HTO from 19 crude oils' oxidation temperature regimes, as shown in Fig. 13.8 (Huang and Sheng, 2017a). The peak temperatures in LTO and HTO for 13 oils are presented in Fig. 13.9 which shows that the average peak temperatures are 320°C in LTO and 469°C in HTO, respectively. The first peak in LTO was considered caused by liquid hydrocarbon combustion and the second peak in HTO was considered caused by coke combustion (Kök et al., 1997). Coke is defined as the fraction insoluble in toluene. Generally, the second exothermic peak has a much stronger heat generation than the first peak. A lower exothermic peak indicates easier ignition. Thus, exothermic peaks can be used as a method to screen the feasibility of air injection. The data in these two figures were measured from almost the same sources of crude oils.

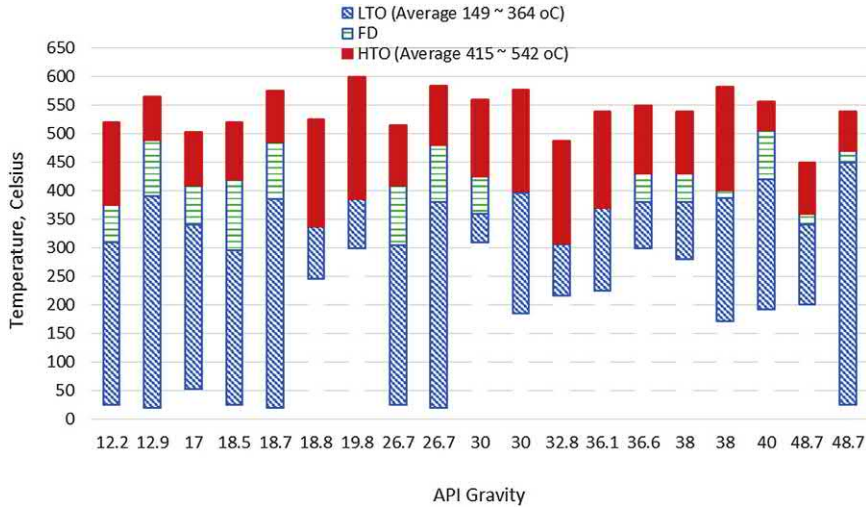

Figure 13.8 LTO, FD, and HTO temperature regions for 19 crude oils.

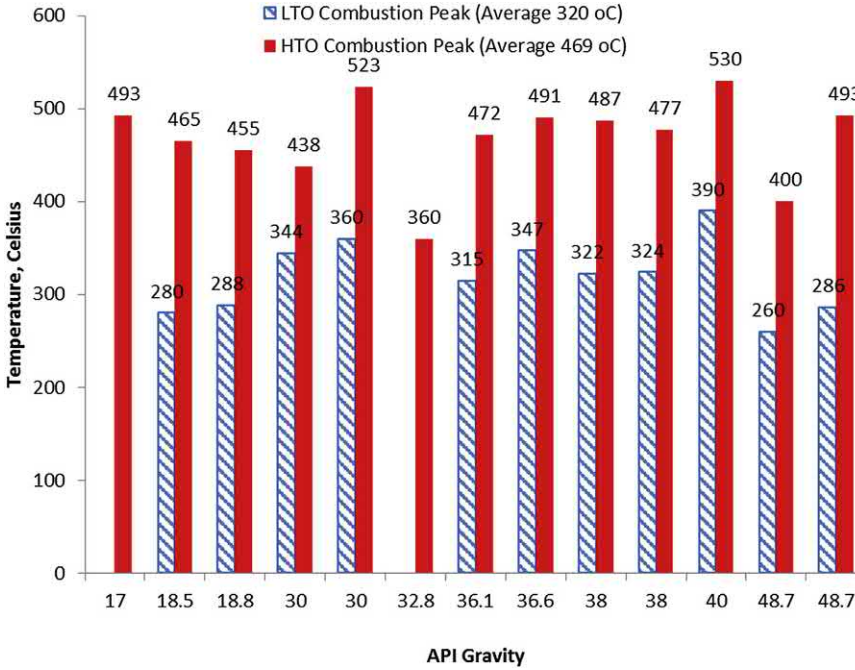

Figure 13.9 LTO and HTO exothermic temperature peaks for 13 crude oils.

The heat release from reactions may be obtained from DSC tests. As a quality check of measured heat data, the heat (enthalpies per unit mass of fuel) from each reaction must be lower than the published value which is for complete combustion. Table 13.1 lists the heating values of combustion reactions (1 and 2) and oxidation reactions (3–7) in kcal/mol O_2 or BTU/ft^3 air at 1 atmospheric and 25°C, with H_2O produced in liquid state. The values in this table show that the order of magnitude of the heat released by the consumption of 1 mol of oxygen in the same type of reaction is independent of the nature of the hydrocarbon molecule. The heat released for the same type of reaction has almost the same value when it is presented in kcal/mol O_2 consumed or in BTU/standard cubic feet of air. From the data in this table, it may be summarized that the heat released is approximately 105 kcal/mol O_2 from complete combustion or partial oxidation to carboxylic acid, 85–95 kcal/mol O_2 for carbonyl compound formation, 70–90 kcal//mol O_2 for hydroxyl compound formation, and 25–35 kcal/mol O_2 for peroxidation.

Table 13.1 Heating values of combustion and oxidation (Burger and Sahuquet, 1972).

#	Type of reaction	CH_4	C_2H_6	C_3H_8	n-C_4H_{10}	n-C_7H_{16}	C_6H_{12}	C_6H_6	$C_6H_5CH_3$
1	$-CH_2- \quad CO_2$	106.40	106.52	106.12	105.84	105.45	104.98	105.21	104.84
2	$-CH_2- \quad CO$	96.77	95.01	93.63	92.76	91.54	89.83	85.17	85.48
3	$-CH_3 \quad -C(=O)-OH$	91.4	101.85	101.5	102.6	109.0	—	—	106.4
4	$-CH_3 \quad -C(=O)-H$	78.7	87.8	92.6	90.55	88	—	—	92.4
5	$-CH_2 \quad -C(=O)-$	—	—	95.3	97.5	99	95.8	—	—
6	$-C(-H)- \quad -C(-OH)-$	60.3	71.6	72.7	76.0	87	92.4	99	82
7	$-C(-H)- \quad -C(-OOH)-$		37.8		27.1	25.4	28.0		

Table 13.2 Gross and net heating (calorific) values of simple fuels (North America Mfg. Co. 1986).

Fuel	Gross (kJ/g)	Net (kJ/g)
Acetylene	50.014	48.309
Butane	49.593	49.771
Carbon	32.78	32.78
Carbon monoxide	10.11	10.11
Ethane	51.923	47.492
Hydrogen	142.11	120.08
Hydrogen sulfide	16.51	15.21
Methane	55.533	49.997
Octane	48.371	44.871
Propane	50.402	46.373
Sulfur	9.257	9.257

Table 13.2 lists the heating values of some simple fuels. When a perfect mixture of fuel and air, originally at 60°F (15.6°C) is ignited and then cooled to 60°F (15.6°C), the total heat release is called the gross heating value of the fuel. The gross heating value minus the heat released by the condensation of the water vapor in the combustion products is called net heating value.

Burger and Sahuquet (1972) defined a general combustion reaction (combined reactions 1 and 2 in Table 13.1):

$$CH_x + \left(\frac{2+\beta}{2(1+\beta)} + \frac{x}{4}\right)O_2 \rightarrow \frac{1}{1+\beta}CO_2 + \frac{\beta}{1+\beta}CO + \frac{x}{2}H_2O \qquad (13.8)$$

In the above reaction, x is the atomic H/C ratio of the fuel and β is CO/CO_2 ratio in the exhaust gases. They also derived the gross calorific value of a unit mass of burned fuel (H_2O being condensed):

$$Q = \frac{265{,}700 + 19{,}850\beta}{(1+\beta)(12+x)} + \frac{31{,}175x - 171{,}700}{12+x}\text{cal/g} \qquad (13.9)$$

or

$$Q' = \frac{478{,}260 + 356{,}130\beta}{(1+\beta)(12+x)} + \frac{56{,}115x - 309{,}060}{12+x}\text{BTU/lb} \qquad (13.10)$$

The heat of reaction in terms of the oxidizer is:

$$Q^* = \frac{265.7 + 197.85\beta}{\left(1 + \frac{\beta}{2} + \frac{x}{4}(1+\beta)\right)} + \frac{31.175x - 171.7}{\frac{2+\beta}{2(1+\beta)} + \frac{x}{4}}\text{kcal/mol } O_2 \text{ or BTU/ft}^3\text{air} \qquad (13.11)$$

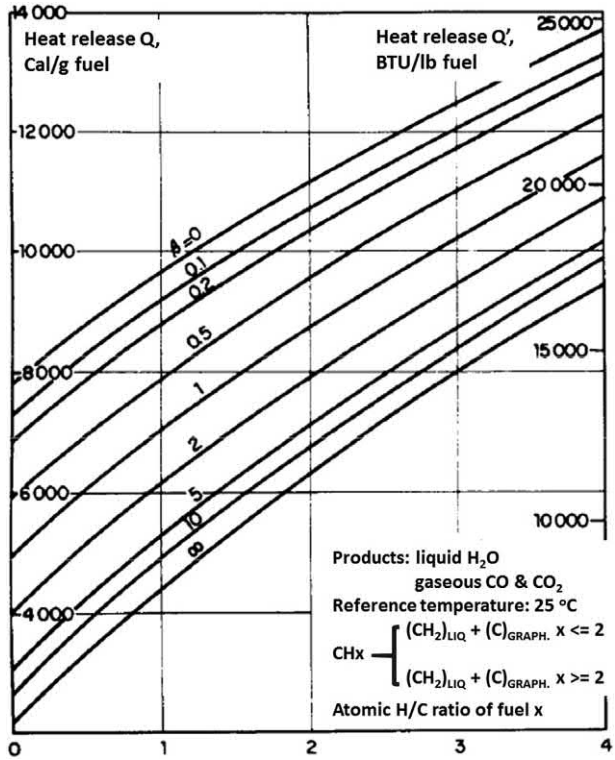

Figure 13.10 Heat of combustion (cal/g and BTU/lb CH_x) as a function of the H/C ratio x of the fuel (in the horizontal axis) and the CO/CO_2 ratio in the produced gases (Burger and Sahuquet, 1972).

The results from Eqs. (13.9) and (13.10) are presented in Fig. 13.10 and the results from Eq. (13.11) in Fig. 13.11. The gross heaving values calculated from Eq. (13.10) for carbon and some hydrocarbons are presented in Table 13.3, together with the experimental data from Perry et al. (1963).

The kinetic parameters can also be measured using ARC and SBR. ARC is used to detect the self-heat rate of the crude oil, and it can maintain nearly perfect adiabatic conditions through the test. During the test, once the self-heat rate is detected, the time, temperature, and pressure data are recorded. Then the thermal data and kinetic data can be derived. The advantage of the ARC is that it can be applied at a very high-pressure condition (till 6000 psi). An SBR has two sample holders, one is the reactor and the other is served as the reference cell. The reactor is subjected to a heating schedule while air is flown through. The heating is continued at the desired rate until the termination is reached and then held at that temperature during the test. During the test, the temperature profiles of both reactor and reference cell

are measured. By comparing these two profiles, the temperature intervals of the exothermic and the endothermic process can be identified. Relevant kinetic data can also be estimated through analyzing SBR data.

13.3.5 A simulation approach to estimate kinetic parameters and heating values

Based on the Arrhenius equation, TG and DSC experimental data should present a straight line with the slope proportional to the activation energy and the intercept representing the frequency factor. However, actual experimental data show straight lines in several temperature ranges, as shown in Fig. 13.12 for one oil sample, because different reactions occur in different temperature ranges. In practice, a straight line for the whole tested temperature range is generated. Obviously, it is an approximation and it is assumed a single reaction occurs. Sakthikumar et al. (1995) observed that the activation energy determined from ARC for LTO could not be used to forecast core flood kinetics. To improve this method, a simulation approach was proposed (Guitirrez et al., 2012) and extensively used by Huang and Sheng (2017a,b,c). In a simulation model, it is possible to define several different reactions in same temperature range, and/or define one reaction covering a large temperature range depending on the values of kinetic parameters (activation energy, frequency factor, and reaction enthalpy), as these kinetic parameters control the reaction rates in different temperature ranges. Such simulation model describes the reactions that actually happen in a reservoir. The description of the reactions is achieved by using several sets of the keywords of STOREAC to input stoichiometric coefficients of reacting components, STOPROD to input stoichiometric coefficients of produced components, EACT (activation energy), FREQFAC (frequency factor), and RENTH (Reaction enthalpy) in CMG's (2016) STARS, with one set being for one reaction scheme. The activation energy gives the dependence of reaction rate on grid block temperature. For chemical reactions (e.g., combustion), it is positive, that is, the reaction rate increases with increasing temperature; the reaction rate is independent of temperature when EACT is zero. To avoid too low or too high reaction rates, two keywords "RTEMLOWR" and "RTEMUPR" in CMG STARS are used to set the two temperature limits. If the reaction temperature is lower (higher) than the RTEMLOWR (RTEMUPR), the reaction rate is set to the one calculated at the temperature RTEMLOWR (RTEMUPR).

Sometimes a modeled reaction has different rate responses at different temperatures, in which case a plot of natural logarithmic of reaction rate

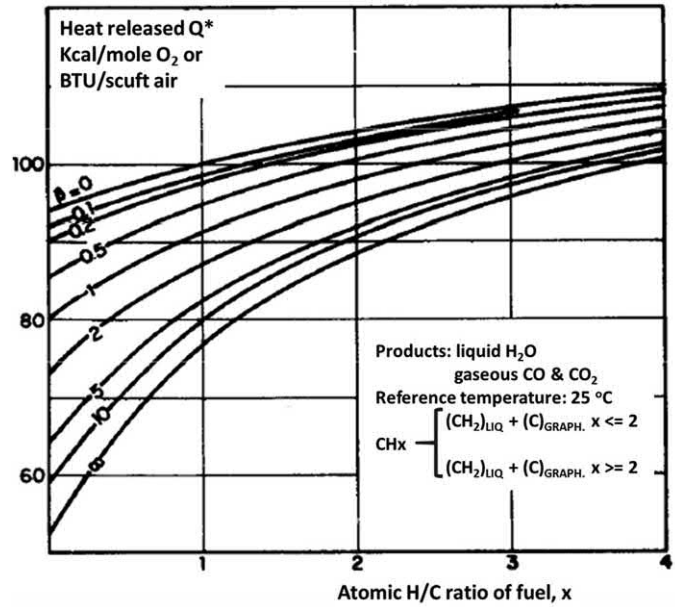

Figure 13.11 Heat of combustion (kcal/mol O_2 or BTU/standard ft^3 air) as a function of the H/C ratio x of the fuel and the CO/CO_2 ratio in the produced gases (Burger and Sahuquet, 1972).

versus $1/T$ will not be a straight line. However, sometimes this plot can be approximated adequately by a series of joined straight lines, each with its own temperature range and slope. This can be modeled with a table of E versus T, where each temperature range uses the same model form as *EACT. The keyword is EXCT_TAB in the form:

EACT_TAB reference temperature number

$T_1\ E_1$

$T_2\ E_2$

…

$T_N\ E_N$

$\{T\ E\}$ is a table of T versus activation energy E, E_i applies to T_i to T_{i+1}, $i = 1$ to $N-1$. The maximum N in STARS is 20. The temperature entries must increase down the table by at least 0.01 degrees. In the following example, the activation energy is 15,000 for the temperature from 150 to 200, 25,000 from 200 to 300, and 4000 from 600 to 700. The activation energy is 15,000 when the temperate is lower than 150, and it is 20,000 when the temperature is higher than 700. In this entry table, the reference temperature number is 3 (third row).

Table 13.3 Heat released by Reaction 8 for some typical fuels (25°C, 1 ATM, H_2O liquid).

Fuel	H/C	CO/CO_2	Perry et al. (1963)	Burger and Sahuquet, 1972
C graphite, solid	0	0	14,090	14,100
		∞	3,960	3,920
$C_6H_5-C_{12}H_{25}$ dodecybenzene, liquid	1.667	0	19,380	19,220
		∞	10,300	10,300
$C_{10}H_{18}$ *cis*-decaline, liquid	1.8	0	19,540	19,580
		∞	10,730	10,730
$C_{20}H_{40}$ leicosene, liquid	2	0	20,180	20,100
		∞	11,500	11,380
C_6H_{12} cyclohexane, liquid	2	0	20,030	20,100
		∞	11,360	11,380
$C_{20}H_{42}$ neicosane, liquid	2.1	0	20,260	20,350
		∞	11,660	11,690
C_4H_{10} butane, liquid/gas	2.5	0	21,110	21,340
		∞	12,750	12,920
C_3H_8 propane, liquid/gas	2.667	0	21,490	21,740
		∞	13,220	13,410
C_2H_6 ethane, gas	3	0	22,300	22,500
		∞	14,220	14,360

```
*EACT_TAB 3
150   15000
200   25000
300   53500 **Reference activation energy
600   40000
700   20000
```

However, a reaction rate is defined by the activation energy and frequency factor according to the Arrhenius equation. Using EACT_TAB is not adequate to describe the variable reaction rates in different temperature ranges. Ideally, the EACT_TAB should add another column with frequency factor values.

To reduce the nonuniqueness of model description, the pseudo-components are defined using nitrogen purging experimental data which are not affected by oxidation reactions. Other fluid properties, for example,

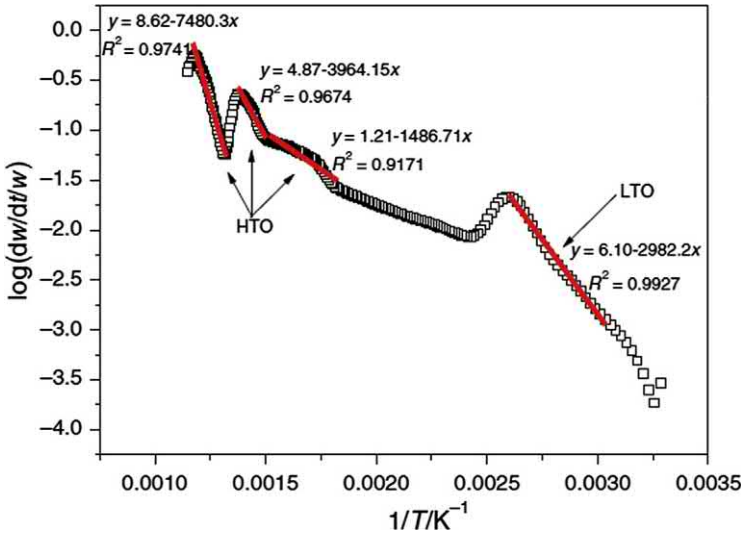

Figure 13.12 DTG curve for an oil sample (Ni et al., 2014).

equilibrium *K*-values, are tuned with some known data using a fluid property model, for example, CMG's WinProp.

The reaction schemes are proposed first based on the understanding of most relevant reaction mechanisms. TG and DSC experimental data are matched by the model prediction by adjusting the kinetic parameters through the above-mentioned keywords. Thus, the kinetic parameters for each reaction scheme are obtained. Note that in a practical simulation model, several reactions are defined, and for each reaction, several kinetic parameters are needed to define the reaction. Therefore, there are many parameters to be used in a simulation model to match kinetic experiments. It can be understood that the parameters obtained from the simulation approach are not unique. The following section presents an example of the simulation approach.

13.3.6 An example to build a kinetic simulation model

In this example, a step-by-step approach is presented to build a kinetic simulation model, based on the work by Huang and Sheng (2017b, 2017c).

Step 1 model grids

To build a simulation model representing TG and DSC experiments, we can use one-dimensional model (e.g., in the *X* direction) with the first block representing the inlet point, and the last block representing the exit point in an experiment. An injection well is in the first block, and a production well in the last block. Between the injection well block and the production

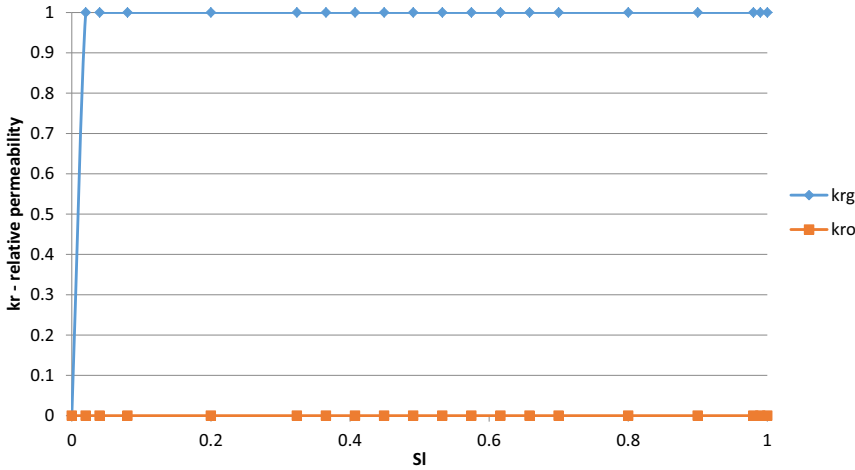

Figure 13.13 Oil and gas relative permeability curves used in the model.

well block, a minimum one block is needed, but several blocks should be used. In this example, only one block is used. In the TG and DSC experiments, liquid oil does not flow, and only gas or vapors are produced. To simulate this fact, liquid oil relative permeability is set zero and the gas relative permeability is set 1 as shown in Fig. 13.13.

Step 2 define pseudocomponents

A crude oil has many components. To reduce the computation burden, several pseudocomponents are defined by lumping together some components into one pseudocomponent. The pseudocomponents are defined based on crude oil fractions, possible oxidation reactions, etc. In this example, seven pseudocomponents are defined, and their properties are presented in Table 13.4.

To confirm the defined pseudocomponents, the simulation model must be able to match the TG experiment under nitrogen purging. In the experiment, no oxidation reaction occurs, and the oil loses weight by thermal distillation. Fig. 13.14 shows the simulation model with seven pseudocomponents matches the TG experiment.

Step 3 define parameters for oxidation reactions

To define reactions, TG and DSC experiments are reviewed. First, the TG experiments under nitrogen purging and air purging at a heating rate of 10°C/min are compared in Fig. 13.15. It shows that before 215°C, the nitrogen purging TG curve overlaps with the air purging TG curve,

Table 13.4 Properties of the pseudocomponents.

Pseudocomponents	P_{crit}	T_{crit}	MW	T_b
	kpa	°C	kg/gmol	°C
C6-9	2735.77	324.85	0.121	277.9913
C10-13	2191.64	390.75	0.161	407.93
C14-16	1925.15	426.85	0.173	463.0484
C17-19	1656.67	476.05	0.237	571.73
C20-22	1455	509.75	0.275	641.93
C23-25	1090.27	584.55	0.372	802.13
C25+	734.636	680.55	0.531	1018.13

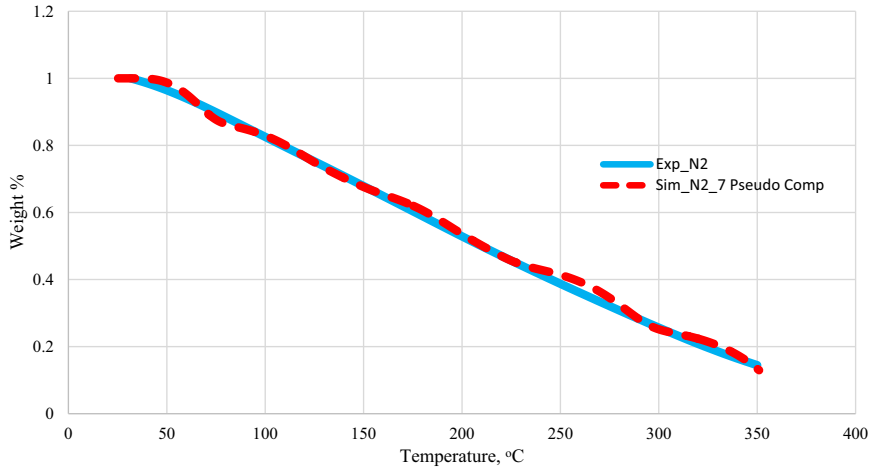

Figure 13.14 Simulation model matches the TG experiment under nitrogen purging.

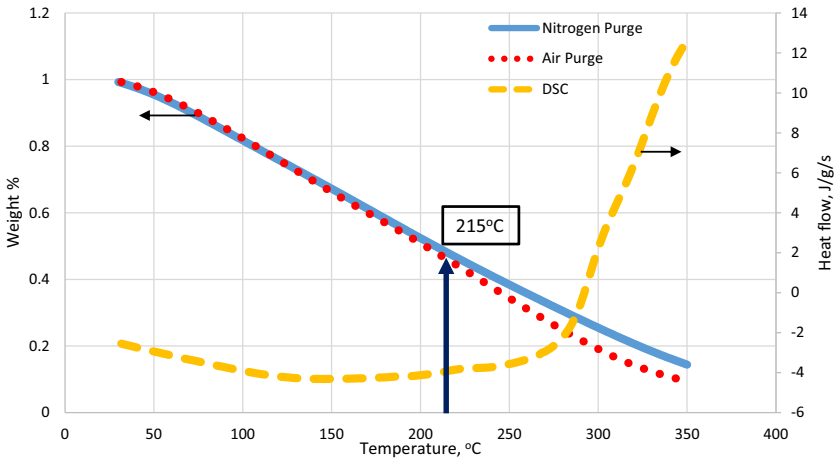

Figure 13.15 Nitrogen purging TG experiment, air purging TG experiment, and air purging DSC experiment (heating rate = 10°C/min).

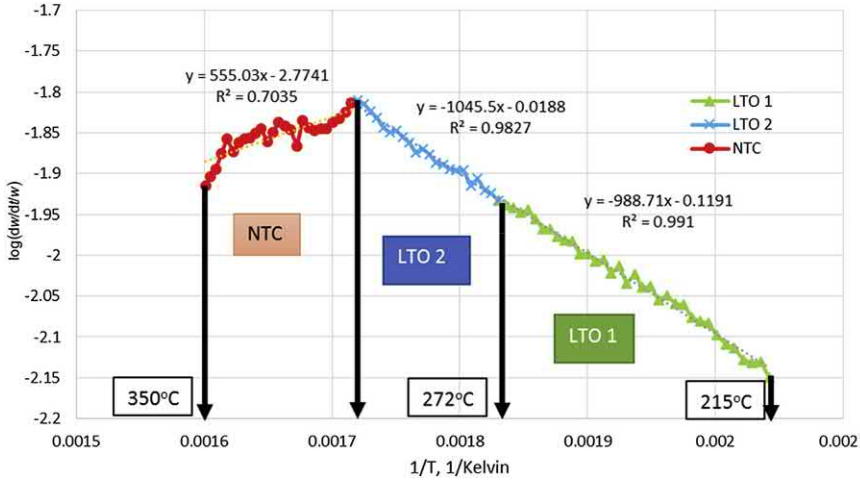

Figure 13.16 Arrhenius method to analyze TG test of the crude oil.

indicating that the distillation process dominates the mass loss of crude oil. Fig. 13.16 also shows the air purging DSC curve of the crude oil. It can be seen that the crude oil behaves endothermically due to the distillation process before 215°C. After 215°C, the heat flow starts to increase with the increase in temperature, indicating LTO reactions. The TG data from 215 to 350°C are analyzed by the Arrhenius method as described in Huang et al. (2016a) and shown in Fig. 13.16. It shows that the LTO can be divided into three reactions: LTO 1 (215–272°C), LTO 2 (272–308 C), and NTC phase (308–350°C). NTC is abbreviation of negative temperature coefficient, or negative temperature gradient (Moore et al., 1999). The NTC region is associated with the generation of the oxidation inhibitors. It occurs between the LTO reaction and the HTO reaction (Fassihi et al., 1984). To achieve the spontaneous ignition, the reaction regime is shifted from the LTO to the NTC and eventually reaches the HTO which is known as the combustion reaction. Because of the existence of the NTC region, the heat generation rate is decreased and became insufficient to compete with the heat dissipation rate to the environment. Therefore, the ignition fails to be achieved eventually. In other words, the NTC effect can also be expressed as the lack of exothermic reactivity of the crude oil samples. If the exothermic reactivity of the crude oil is sufficient to overcome the NTC effect and be able to raise the temperature to the HTO region, the ignition can still be achieved.

Table 13.5 TGA kinetic data of the oxidation reactions.

Reaction	Temperature range for the data used, °C	Slope	Intercept	Activation energy, kJ/gmol	Frequency factor, s^{-1}
LTO1	215–272°C	−989	−0.119	18.93	7.60E-01
LTO2	272–308°C	−1046	−0.019	20.02	9.57E-01
NTC	308–350°C	555	−2.774	−10.63	1.77E + 04

Note that a negative activation energy value is obtained from the experimental data in this temperature. Khansari et al. (2014) also obtained negative activation energy values. The negative activation energies are not physically realistic but suggest that there are competitive reactions occurring within the system. There are intermediate compounds produced during the earlier temperature ranges which are reactive, but they are consumed within the later ranges (Khansari et al., 2014). Also note that the temperature ranges are for the data used to define the reaction kinetic parameters, not the actual reaction temperature ranges. An actual reaction may cover different temperature ranges, depending on the available compositions, values of kinetic parameters, and actual temperature history.

With the three reactions defined, the Arrhenius method is used to analyze TG data. The corresponding activation energy values estimated from the slope and the frequency factor values from the intercept are presented in Table 13.5.

Fig. 13.17 shows the DSC data under air purging and nitrogen purging at the heating rate of 10°C/min. It shows the whole process of nitrogen purging is an endothermic process. For the air purging, it is endothermic before about 290°C. Then the earlier defined LTO 1 is in the endothermic stage. But an LTO process should be exothermic. Where does the heat go? Huang and Sheng (2017c) proposed two explanations. One is that during this marked LTO, the dominant mechanism is distillation. The heat from LTO is used to satisfy the need for distillation. The other one is that there are a number of incomplete oxidation gaseous products during this period which are purged out from the sample holder before being totally oxidized as reported by Fan et al. (2015). Zhao et al. (2012) also reported that light oil components and carbon monoxide are detected by GC at the outlet of the experimental setup. If the first explanation is valid, a better method is needed to analyze the data. If the second explanation is valid, the DSC experimental design needs to be improved. One way to improve such experiment is to use

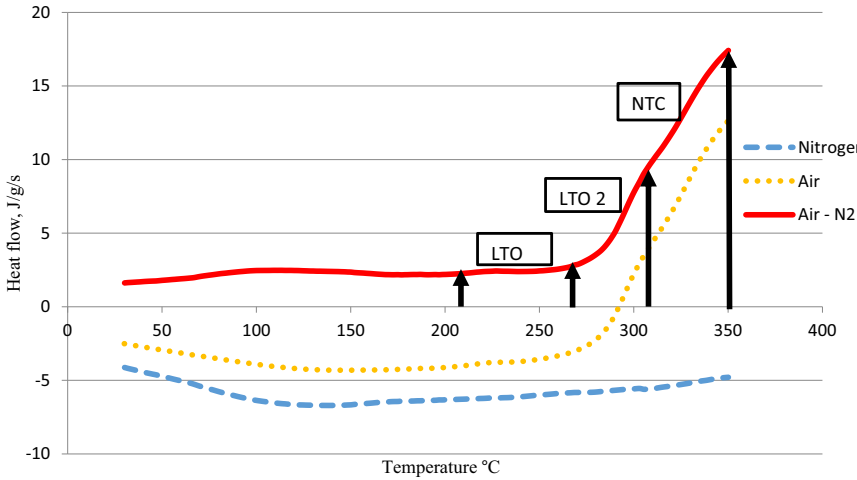

Figure 13.17 Air/nitrogen purging DSC data and subtracted heat flow of oxidation reactions (heating rate = 10°C/min).

pure oxygen instead of air to reduce the emission of oxidized gas and vapor. Another way is to use a large container to hold oxidized products.

Based on the above two explanations or assumptions, the actual enthalpy from LTO is obtained from subtracting the negative enthalpy for the nitrogen purging from the enthalpy for the air purging. The resultant enthalpy is represented by the solid (*red*) curve in Fig. 13.17. Based on the earlier defined three LTO reactions, the enthalpies for LTO 1, LTO 2, and NTC were estimated to be 844.1, 1209.2, and 3327.0 J/g, respectively. These enthalpy values are obtained by integrating the heat flow over the time taken for the corresponding temperature intervals (the heating rate is 10°C/min).

Step 4 define reaction scheme

Note that the previous step describes how the values of the parameters to describe oxidation reactions are obtained. This step discusses how to define reaction schemes briefly.

Since the experiments are conducted below 350°C, the reactions are most likely low oxidation reactions. To define a detailed LTO reaction scheme, we first investigate which pseudocomponents are dominant in LTO reactions. Fig. 13.18 shows the cumulative gas production under nitrogen purging from the simulation model. It is seen that pseudocomponents C6−9, C10−13, C14−16, and C17−19 are almost displaced

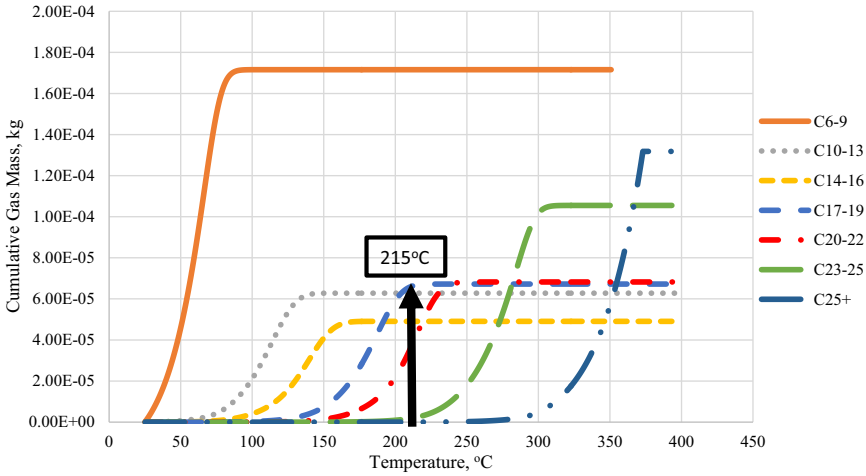

Figure 13.18 Cumulative production of each pseudocomponent by nitrogen purging from simulation model.

by the purging gas in the distillation stage (before 215°C). Practically, only C20−22, C23−25, and C25+ pseudocomponents are involved in LTO.

Generally, an LTO reaction is an oxygen-addition reaction, leading to a heavy component. The lighter components C20−22 form the heavier component C25+ and this reaction is assigned to LTO 1; the medium components C23−25 also form the heavier components C25+ and the reaction is assigned to LTO 2; the heavier component C25+ generates coke and lighter hydroperoxides 1, 2, 3, and the reaction is assigned to the NTC period. To simplify the model, these three hydroperoxides are treated as the lighter pseudocomponents C10−13, C14−16, and C17−19, respectively, and they take the physical properties of their counterparts.

Combining the results from the preceding steps, the final kinetic reaction models can be summarized in Table 13.6. Note that the values of frequency factor are changed, comparing this table with Table 13.5. This is because, to validate the kinetic model using the air purging TG/DSC experiments, it is found that the values of frequency factor need to be adjusted. One justification for this adjustment is that Barzin et al. (2013) found that the experimentally obtained value of frequency factor is not exact in their ramped temperature tests. The final model well matches the air purging TG test as shown in Fig. 13.19. That completes the presentation of an example to build a kinetic model to simulate an air injection experiment.

Table 13.6 Calibrated reaction scheme of air injection process.

Reactions	Activation energy, kJ/gmol	Frequency factor, s^{-1}	Enthalpy, J/g	Reaction schemes
LTO1	18.93	2.40E-03	8.44E + 02	C20-22 + O_2 = C25+
LTO2	20.02	2.80E-03	1.21E + 03	C23-25 + O_2 = C25+
NTC	−10.63	3.40E-04	3.33E + 03	C25+ + O_2 = HP1 + HP2 + HP3 + CO_2 + H_2O + Coke

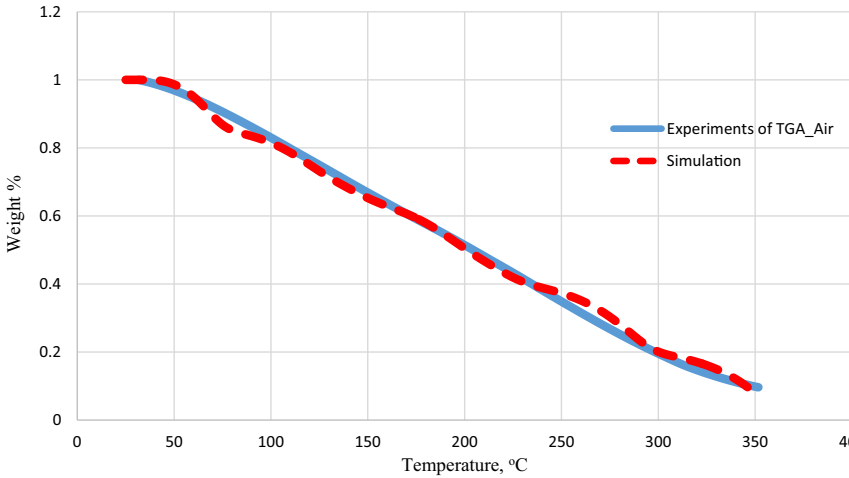

Figure 13.19 Simulation model of seven pseudocomponents matches the air purging TG test.

13.4 Oxidation reactions

In this section, the terminologies and principles to define reaction schemes are summarized, followed by the discussion of factors that affect oxidation reaction.

13.4.1 Terminologies and principles to define reaction scheme

Oxidation reactions between a crude oil and oxygen (air) are very complex. They may be divided into LTO and HTO. Some authors add an intermediate temperature oxidation (e.g., Prasad and Slater, 1986) or medium temperature oxidation (e.g., Turta and Singhal, 2001). LTO yields water and partially oxygenated hydrocarbons such as carboxylic acids, aldehydes,

ketones, alcohols, and hydroperoxides (Burger and Sahuquet, 1972), with negligible amount of carbon oxides (Khansari et al., 2014). In the intermediate temperature oxidation, because the temperature is increased by LTO, distillation coupled with thermal cracking produces hydrogen gas and light hydrocarbon gases. These gases react with oxygen, leaving heavy oil residue on the solid matrix as fuel (Prasad and Slater, 1986). Combustion occurs in HTO, with CO_2 being generated in a complete combustion and CO being generated in an incomplete combustion. HTO operates above 250−300°C (Burger and Sahuquet, 1972) or 400−800°C (Khansari et al., 2014).

There are several other terms to describe oxidation reactions: pyrolysis, fuel deposition (FD), thermal cracking (TC), and bond scission. Pyrolysis refers to the modification of crude oil by thermal effects in the absence of oxygen. Coke and gases are formed through pyrolysis of LTO components. This region operates throughout the entire range of temperature but is mostly found in the temperature range from about 350 to 450°C; it may occur ahead of the LTO zone where the temperature is elevated, but oxygen has been consumed (Khansari et al., 2014). Moore et al. (1992) reported that coke formation occurred rapidly over the temperature range 200−300°C, and coke yield was very dependent on the time that the oil remained with this temperature region. At low temperatures, the pyrolysis is called visbreaking or aquthermolysis in the presence of water; At high temperatures, it is called thermal cracking; in the heavy oil, it is believed that fuel is deposited in liquid and/or solid phase (coke) through pyrolysis, thus it is called fuel deposition (FD) (Barzin et al., 2010). The fuel that actually burns in forward in-situ combustion is not the crude oil in the reservoir. Rather the fuel is primarily the carbon-rich residue resulting from thermal cracking and distillation of the residual crude near the combustion front. Naturally occurring coal, if present in the rock, also can contribute to the fuel available for combustion (Prats, 1982). Aquathermolysis (hydrous pyrolysis) produces additional carbon dioxide and hydrogen sulfide (Khansari et al., 2014). In a bond scission reaction, oxygen breaks up the hydrocarbon molecules to principally produce carbon dioxide and water (combustion type, dominant in light oil 150−300°C but not in heavy oil below 450°C (Moore et al., 2002) (350−700°C (Sarma et al., 2002))). Bond scission reactions are associated with a cokelike fuel; but these reactions could be homogeneous gas phase reactions or liquid phase reactions (Barzin et al., 2010).

In a negative temperature coefficient (NTC) region, the reaction rate decreases with increasing temperature. NTC is due to decomposition of

alkylperoxy radical. It generally occurs in gas-phase reactions above 400−500°C. If it occurs in a liquid phase, the temperature will be higher (Freitag, 2016). If a numerical simulation model of in-situ combustion is valid over a broad range of operating conditions, it must incorporate a reaction scheme capable of predicting the negative temperature gradient region (decreasing oxygen uptake rates with increasing temperature) (Moore et al., 1992).

Freitag (2016) found that the above defined reactions are not adequate to describe the oxidation processes. Based on the chemistry of oil components and reaction characteristics, he found that at least eight groups of fundamental reactions are needed to define the oxidation rates of crude oils and their pyrolysis products for in-situ combustion and high-pressure-air-injection (APAI): two for hydroperoxide formation, one "branching" by hydroperoxides, two governing NTC region, one for oxidation inhibition, one rate-controlling reaction at very high temperature, and one for the combustion of coke that is produced by pyrolysis.

Burger and Sahuquet (1972) defined the reactions in LTO and HTO, and they provided the heat of reactions for HTO (complete and incomplete combustion) based on the general reaction 8. Belgrave et al. (1993) assumed asphaltene and coke were products of LTO; asphaltene, coke, and gas were products of thermal cracking; and CO_2 and water were the products of HTO. Khansari et al. (2014) defined heavy oil LTO reactions in four temperature subranges based on the reaction products.

Many different forms of reactions appear in the literature based on products of reactions (See Table 13.7). However, the reactivity of a given oil is reservoir specific, and no screening guides have yet been published which predict the oxidation characteristics of a specific reservoir. For a light oil, reactivity is pressure-dependent, but not for a heavy oil (Moore et al., 2002). The fundamental approach to define oxidation reactions is to define less pseudocomponents, with kinetic parameters and heat released within subranges of temperature measured from experiments like TG and DSC. These variable parameters can be handled in a simulation model, and the experiments are matched using the simulation approach.

13.4.2 Factors that affect oxidation reactions

It is easy to understand that the activity of crude oil dominates the oxidation reactions and thus kinetic parameters. Many factors could affect the reactions which are not fully understood. This section simply summarizes some of the observations.

Table 13.7 Summary of reaction schemes with kinetic data (Zhang and Sheng, 2017).

Oil	Authors		Reactions	Frequency factor	Activation energy	Enthalpy	Oil density
					Btu/lbmole	Btu/lbmole	API
Bitumen	Belgrave et al. 1993	LTO	Maltenes + O_2 → Asphaltenes Asphaltenes + O_2 → Coke				
		Cracking	Maltenes → Aspaltenes Asphaltenes → Coke Asphaltenes → Gas				
Heavy oil	Lin et al. 1984	Cracking	Heavy oil → 1.06 light oil + 61 coke	4.00E + 06	3.49E + 04	4.00E + 04	13
		Combustion	Light oil + 19.35 O_2 → 14.5 CO_x + 13 H_2O	1.00E + 06	4.30E + 04	4.06E + 06	
			Heavy oil + 87 O_2 → 71 CO_x + 63.4 H_2O	1.00E + 06	4.30E + 04	1.86E + 07	
			Coke + 1.03 O_2 → 1.0 CO_x + 0.25 H_2O	1.00E + 06	3.26E + 04	2.35E + 05	
	Druganova et al. 2010	Cracking	Heavy oil → Light oil + Coke				
		Combustion	Light oil + O_2 → Water + inert gas + energy Heavy + O_2 → Water + inert gas + energy Coke + O_2 → Water + inert gas + energy				
	Mercado Sierra and Trevisan 2014	Cracking	HO → 1.81 LO + 19.35 Coke	6.95E + 03	1.10E + 05	0.00E + 00	
		Combustion	HO + 47.01 O_2 → 16.64 H_2O + 38.69 CO_2	5.03E + 08	2.58E + 05	1.57E + 07	
			LO + 12.97 O_2 → 4.59 H_2O + 10.68 CO_2	5.03E + 08	2.58E + 05	6.77E + 07	
			Coke + 1.12 O_2 → 0.43 H2O + 0.93 CO_2	6.95E + 00	1.09E + 05	1.22E + 06	
		Cracking	C21−C30 → C5−C20 + coke	1.39E + 15	4.87E + 05	0.00E + 00	

	Rodriguez et al. 2012	LTO	C5−C20 + O_2 → C21−C30	2.24E + 05	1.88E + 04	1.58E + 06	
			C21−C30 + O_2 → Coke	4.86E + 01	1.68E + 05	6.05E + 06	
		Combustion	Coke + O_2 → CO_2 + H_2O	5.41E + 05	7.91E + 04	1.31E + 06	
Medium oil	Lin et al. 1984	Cracking	Heavy oil → 3.65 light oil + 10 coke	3.32E + 20	1.44E + 05	4.00E + 04	26.5
		Combustion	Light oil + 13 O_2 → 10 CO_x + 9.6 H_2O	7.25E + 11	7.68E + 04	2.97E + 06	
			Heavy oil + 59 O_2 → 48 CO_x + 43.5 H_2O	7.25E + 10	7.68E + 04	1.28E + 07	
			Coke + 1.15 O_2 → 1.0 CO_x + 0.5 H_2O	1.00E + 06	3.26E + 04	2.25E + 05	
	Kumar 1987	Cracking	HO → LO + Coke	1.73E + 12	7.29E + 04		26
			LO → Coke	2.10E + 09	6.45E + 04		
		Combustion	HO + O_2 → CO_x + H_20	3.02E + 10	5.95E + 04		
			LO + O_2 → CO_x + H_20	3.02E + 10	5.95E + 04		
			Coke + O_2 → CO_x + H_20	4.17E + 04	2.52E + 04		
Light oil	Tingas 2000	Cracking	C21 + → CH_4 + Coke	2.10E + 05	2.50E + 04	0.00E + 00	40.2
			C10−C20 → CH_4 + Coke	2.00E + 05	2.70E + 04	0.00E + 00	
		Combustion	C21 + O_2 → H_2O + CO + Energy	3.02E + 10	1.35E + 04	1.03E + 04	
			C11−C20 + O_2 → H_2O + CO + Energy	3.02E + 10	1.55E + 04	4.92E + 03	
			C6−C9 + O_2 → H_2O + CO + Energy	3.02E + 10	1.55E + 04	2.42E + 03	
			C2−C5 + O_2 → H_2O + CO + Energy	3.02E + 10	1.50E + 04	1.46E + 03	
			Coke + O_2 → H_2O + CO_2 + Energy	3.00E + 05	5.50E + 03	4.61E + 02	
			CH4 + O_2 → H_2O + CO_2 + Energy	3.02E + 10	5.95E + 04	5.03E + 02	

(*Continued*)

Table 13.7 Summary of reaction schemes with kinetic data (Zhang and Sheng, 2017).—cont'd

Oil	Authors		Reactions	Frequency factor	Activation energy	Enthalpy	Oil density
					Btu/lbmole	Btu/lbmole	API
			$CO + O_2 \rightarrow CO_2 + Energy$	1.50E + 05	3.25E + 03	2.84E + 05	
	Fassihi et al. 2000	Cracking	$C12-C17 \rightarrow Coke + C7-C11$	3.35E + 10	7.74E + 04		32.7
			$C18 + \rightarrow Coke + C7-C11$	3.35E + 10	7.74E + 04		
		Combustion	$C7-C11 + O_2 \rightarrow CO_2 + H_2O$	4.00E + 10	4.86E + 04		
			$C12-C17 + O_2 \rightarrow CO_2 + H_2O$	4.00E + 10	4.86E + 04		
			$C18 + + O_2 \rightarrow CO_2 + H_2O$	4.00E + 10	4.86E + 04		
			$Coke + O_2 \rightarrow CO_2 + H_2O$	1.00E + 08	1.50E + 04		
	de Zwart et al. 2008	Heavy oil cracking	$C27 \rightarrow Coke + C7-C15$				36
		Combustion	$C7-C15 + O_2 \rightarrow H_2O + CO_x + heat$				
			$C16-C26 + O_2 \rightarrow H_2O + CO_x + heat$				
			$Coke + O_2 \rightarrow H_2O + CO_x + heat$				
	van Batenburg et al. 2010	Heavy oil cracking	$C26 \rightarrow C7-C15 + Coke$				
		Combustion	$C16-C25 + O_2 \rightarrow H_2O + CO_x + heat$				
			$C26p + O_2 \rightarrow H_2O + CO_x + heat$				
			$Coke + O_2 \rightarrow H_2O + CO_x + heat$				
	Barzin 2013	LTO	$MO + O_2 \rightarrow Asp$	7.60E + 04	1.77E + 05	2.00E + 05	39.7
		Cracking	$Asp \rightarrow LO + HO + Coke$	1.00E + 05	2.33E + 05	0.00E + 00	
		Combustion	$LO + O_2 \rightarrow CO_2 + H_2O$	4.40E + 06	5.35E + 04	9.30E + 06	
			$MO + O_2 \rightarrow CO_2 + H_2O$	1.70E + 08	8.37E + 04	1.67E + 07	
			$HO + O_2 \rightarrow CO_2 + H_2O$	7.00E + 02	1.00E + 05	2.79E + 07	
			$Coke + O_2 \rightarrow CO_2 + H_2O$	1.30E + 06	1.77E + 05	2.00E + 05	

13.4.2.1 Pressure effect

It has been observed that as the system pressure is increased, the reaction rate is increased, more heat is released, and the reactions move to lower temperatures (Bae, 1977; Yoshiki and Phillips, 1985; Nickle et al., 1987; Li et al., 2006). It is believed that higher pressure extends to the flammable limits of distilled hydrocarbon vapor (Li et al., 2006). Fan et al. (2015) even reported that the total amount of heat resulted from LTO reactions of oil had a linear relationship with oxygen partial pressure, as shown in Fig. 13.20. This is not a surprised result, as the higher pressure leads to higher oxygen concentration, and the reaction is a function of oxygen concentration. For this reason, ideally, we should conduct pressurized differential scanning calorimeter (PDSC) tests, instead of DSC tests, to obtain kinetic parameters. PDSC tests need to be performed using accelerating rate calorimeter (ARC). However, such pressure effect can be considered by using a reaction model which is nonzero order in terms of oxygen concentration or oxygen partial

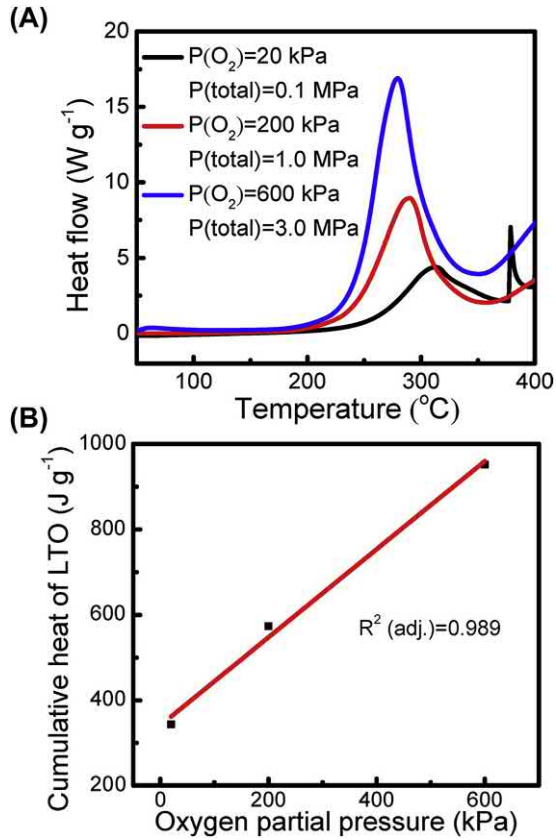

Figure 13.20 Total amount of heat generated in heavy oil LTO versus oxygen partial pressure (Fan et al., 2015).

pressure, and DSC tests should serve the purpose. In addition, the linear relationship shown in Fig. 13.20 may not be extended to very high partial pressures, probably up to several hundred of kPa for liquid oil, even much lower for gas phase (Freitag and Verkoczy, 2005). If extended to a very high partial pressure, the heat released will be unrealistically high.

Bae (1977) and Li et al. (2006) observed that the pressure effect is more enhanced in LTO. However, Yoshiki and Phillips (1985) and Kök and Gundogar (2010) observed that increased pressure did not affect the activation energy in LTO but in HTO (Kök and Gundogar, 2010). Burger and Sahuquet (1972) found that the reaction order of oxygen partial pressure for forward combustion should be less than one by comparing experimental data with simulation data.

13.4.2.2 Catalytic effect of additives

It has been observed that clay minerals can have catalytic effect by reducing activation energy for both LTO and HTO (Vossoughi et al., 1983; Kök, 2006; 2012; Sarma and Das, 2009; Huang et al., 2016a), while Jia et al. (2012a) observed slightly increased activation energy in LTO. The clays include kaolinite, smectite, illite, chlorite, and shale cuttings which have clays, with smectite having the strongest catalytic effect (Jia et al., 2012b). Pu et al. (2015) observed that adding metallic $CuCl_2$ reduced activation energy in LTO and HTO. Burger and Sahuquet (1972) claimed that metallic derivatives of copper, iron, nickel, vanadium, etc. reduced activation energy and formed more coke. Huang and Sheng (2017a) surveyed 25 cases on the effect of additives and found that the activation energy values were 26 and 73 kJ/mol for LTO and HTO, respectively, as shown in Fig. 13.21. Compared with those (33and 107 kJ/mol for LTO and HTO, respectively) in Fig. 13.7, they are lower, but the activation energy for LTO is not significantly lower. More fuel is available in the presence of clay for oxidation reactions. This may be caused by adsorption of hydrocarbons on the clay surface and, hence, low distillation and pyrolysis in porous media (Fassihi et al., 1984).

13.4.2.3 Gas phase versus oil phase

The gas phase has significant amount of vaporized light hydrocarbons with two to six carbon atoms which are aliphatic, and it has much less antioxidants (oxidation inhibitors); the oxygen diffusion into a gas phase is much faster than into a liquid phase; therefore, the vaporized hydrocarbons will oxidize much more quickly (Freitag, 2016).

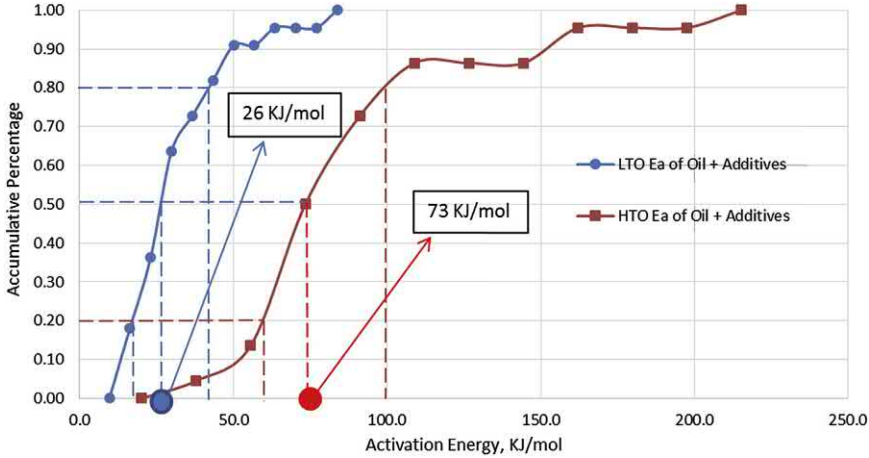

Figure 13.21 Activation energy of 25 crude oil samples with additives.

13.4.2.4 Light oil versus heavy oil

A heavy oil has more heavy components. A light oil has larger amount of light aliphatic hydrocarbons which vaporize into injected air. Thus, a light oil has less oxidation inhibitors like aromatics; and oxidation can more rapidly proceed in the gas phase for a light oil. As a result, a lower temperature peek for a light oil usually occurs earlier than a heavy oil. Because a light oil does not have significant coke to form by pyrolysis, the temperature cannot reach high in a light oil reservoir. Thus, generally LTO occurs in light oil reservoirs.

A heavy oil has more heavy components that are aromatic in nature. Aromatic-based oxidation inhibitors become ineffective near or above 180°C. Thus, as LTO increases the reservoir temperature above 220°C, the aromatic, resin, and asphaltene fractions in a heavy oil enter a new kinetically controlled regime (Freitag and Verkoczy, 2005). Above this temperature, the peroxides that form from aromatic compounds (ROOR) begin to participate in branching and cease to inhibit oxidation. As the temperature is further increased, more coke is formed by pyrolysis. More fuel leads to high combustion temperature (HTO) (Freitag, 2016).

13.5 Spontaneous ignition

Spontaneous ignition (autoignition) occurs when the temperature is raised to a fire point by self-heating (due to exothermic internal reactions). At the fire point, the vapor produced by a given fuel continue to burn for at

least 5 seconds after ignition by an open flame. The flash point is lower than the fire point. At the flash point, the vapor burns briefly, but may not sustain.

During LTO, heat may be released. And oxidation reaction rates increase almost exponentially with temperature, whereas the heat loss rate increases linearly; it is feasible for the LTO reaction to achieve the spontaneous ignition (Gray, 2016).

If spontaneous ignition can occur in reservoirs, the following advantages may be realized:

1. The air injection project will be much more economic.
2. The sweep efficiency of air injection will be more uniform because spontaneous ignition leads to combustion, consuming oxygen, reducing air (oxygen) fingering.

Ignition is fundamentally important for air injection, as many failures in field projects were caused by the failure of ignition (Turta, 2013). Understanding of spontaneous ignition and the resulting thermal effect will aid in designing and optimizing air injection projects so that the advantages of spontaneous ignition and the thermal effects are fully taken of. Therefore, it is important to study spontaneous ignition.

In this section, the field and laboratory observations are reviewed, and simulation results are discussed in terms of the feasibility of spontaneous ignition. Spontaneous ignition is a result of heat accumulation. In other words, it takes some time for spontaneous ignition to occur. Therefore, to discuss the feasibility of spontaneous ignition, ignition delay is discussed.

13.5.1 Field observations

Evidences of in-situ combustion from cores and production performance were observed in the air injection project in the light oil reservoirs in the North and South Dakota portions of the Williston Basin. These fields had permeability less than 20 mD, porosity 11%–19%, and oil viscosity less than 2 cP. The CO_2 content in some of production wells exceeded 12%; a thin-section photomicrograph showed a high content of halite indicating a high temperature experienced by the rock; the core showed a very low oil saturation (4%) and some parts were absent of hydrocarbons (black spots) (Gutierrez et al., 2008). More than half of the cumulative oil production could be attributed to thermal effects in the Red River zone in West Buffalo (Kumar et al., 2007). Production data showed flat gas-oil ratio (GOR) compared with exponential increase in GOR for the wells without thermal effect (Gutierrez et al., 2009). As earlier as in 1956, spontaneous ignition was

observed in the South Belridge field, California; the entire injection wellbore temperature exceeded 538°C after 3 months of air injection (Gates and Ramey, 1958). The oil viscosity was 2700 cP in the reservoir. In the pilot test in the Holt Sand Unit, the reservoir temperature was increased from 200to 230°C (Fassihi et al., 2016). In 25 of the surveyed air injection projects, 5 projects had the evidence of spontaneous ignition (Chu, 1982).

However, Niu et al. (2011) proposed that the possibility of spontaneous ignition was low; the thermal effect was minimum in light oil reservoirs, and the air injection was considered immiscible flue gas injection. Greaves et al. (1999) also believed that LTO, rather than in-situ combustion, prevailed in air injection in light oil reservoirs; the important task was to study whether the oxygen consumption rate was high enough so that the safety requirement could be ensured.

13.5.2 Laboratory observations

From their combustion tube tests, Montes et al. (2010) observed that the GOR was maintained flat, indicating that the combustion front could mitigate gas viscous fingering, and the sweep efficiency was improved. Barzin et al. (2010) conducted a series of ramped temperature oxidation tests for light hydrocarbon oil and observed that when the temperature reached about 180°C, the system suddenly increased about 60°C, indicating that spontaneous ignition occurred through light oil oxidation.

However, Christopher (1995), and Yannimaras and Tiffin (1995) conducted ARC tests using dozens of light oils and found that only 20% of the oil samples had continuous exothermic behavior, and the rest of the oil samples did not show the potential of spontaneous ignition.

Abu-Khamsin et al. (2001) conducted 22 air injection flooding tests using packed-bed reactors. They found that the maximum temperature increase was about 10°C, indicating spontaneous ignition could not occur. They interpreted that the LTO-generated heat was lower than the heat loss. Jia et al. (2012a) conducted air flooding tests using their developed apparatus and real cores to detect heat effect. Their system temperature was maintained at a constant, and the reactor was wrapped using insulating tapes to reduced heat loss. The core temperature was only increased from 80 to 89°C within 22.2 days of experiments. They also attributed such low temperature increase to heat loss through metal thermocouples.

Clara et al. (2000) measured the temperature variation when air flowed through their Handil cores under adiabatic conditions. Although the

temperature was able to increase from 134 to 400°C spontaneously, it could not increase from 92 to 134°C through oxidation; artificial heating was needed, indicating spontaneous ignition could not occur through LTO when the initial core temperature was 92°C or lower.

Huang et al. (2016a, 2016b), and Huang and Sheng (2017c) studied the exothermic behavior of Wolfcamp shale oil using DSC. They found that the oil exhibited exothermic behavior only after the temperature was heated above 300°C. But this high temperature may be caused by the thermal hysteresis owing to the high heating rate (5−15°C/min) in the experiments.

The above reviews (both field and laboratory) indicate that there is no conclusion whether spontaneous ignition can occur in real oil reservoirs. Whether spontaneous ignition can occur or not depends on the balance between heat generation and heat release. If the heat generation is faster than the heat release, a local temperature can reach an ignition point, and spontaneous ignition may occur. In a reservoir, it is believed that heat release is pressed (adiabatic condition), spontaneous ignition may happen. Turta and Singhal (2001) mentioned that spontaneous ignition could occur in reservoirs as low as 30°C. However, spontaneous ignition does not occur in ventilated asphalt (of high activity component) roads, because heat cannot be accumulated (A. K. Singhal, personal communication in 2015). A real reservoir is not adiabatic, but heat load imposed by many of laboratory setups is much higher than what a reaction zone would experience in the field. Just looking at the heat capacity of the apparatus, and the small reaction volume for many of the setups, it is essentially impossible to duplicate the heat loss environment of an oxidation zone operating in the field. That is why it is difficult to duplicate ignition temperatures in the laboratory (Gordon Moore, personal communication on Oct. 20, 2015). Therefore, compared with laboratory conditions, a reservoir condition is relatively "adiabatic" (Malcolm Greaves, personal communication on Oct. 27, 2015); and it is difficult to achieve ignition in the laboratory.

13.5.3 Simulation studies

To study spontaneous ignition experimentally in laboratory, there are two limitations. (1) Spontaneous ignition is induced by thermal energy accumulation from the LTO reactions; but LTO reactions are slow. Thus, it may take an unrealistically long time to reach a high temperature for ignition. (2) A good adiabatic condition may not be able to satisfy. These limitations may be overcome by a simulation approach. In principle, a simulation model

Table 13.8 Reservoir and thermal parameters used in the lab scale simulation model.

Parameter	Value
Reference depth (cm)	0
Porosity (dimensionless)	0.41
Horizontal permeability (mD)	12,700
kv/kh (dimensionless)	1
Oil saturation (dimensionless)	0.882
Reference pressure (kPa)	4100
Original reservoir temperature (°C)	100
Rock volumetric heat capacity (J/(cm^3·°C))	2.35
Rock thermal conductivity (J/(cm·min·°C))	1
Water thermal conductivity (J/(cm·min·°C))	0.36
Oil thermal conductivity (J/(cm·min·°C))	0.077
Gas thermal conductivity (J/(cm·min·°C))	0.083
Temperature of injected gas (°C)	100

can history-match TG/DSC experiments with limited experimental time and heat loss. Using this history-matched model, slow reactions and adiabatic conditions can be simulated, and the feasibility of spontaneous ignition may be studied. A laboratory-scale model may be upscaled to a field model so that spontaneous ignition in field can be studied.

Huang and Sheng (2018) built a 1D laboratory-scale base model of grids of 36 × 1 × 1. The total grid block size was set at 5.08, 9.94, and 9.94 cm in the x, y, z directions, respectively. Air is injected at block (36 1 1) and the production end is at block (1 1 1). The main reservoir properties and thermal properties were taken from Belgrave et al. (1993), presented in Table 13.8. The kinetic parameters and the reaction scheme which contains three reactions with 11 components are from Huang and Sheng (2017c), as presented in Table 13.6. In the base laboratory-scale model, the over/underburden volumetric heat capacity of 2.350 J/(cm^3·°C) and thermal conductivity of formation adjacent to the reservoir of 1.038 J/(cm·min·°C) are used.

Fig. 13.22 shows the temperature profiles at grids (6 1 1), (18 1 1), and (35 1 1) in the base case model and the adiabatic case (Huang and Sheng, 2018). The temperature increase from the original reservoir temperature of 100°C is around 10°C in the base case and around 25°C in the adiabatic case due to LTO reactions. Such temperature increases are close to those reported by Jia et al. (2012a) and Abu-Khamsin et al. (2001). Such low temperature may not lead to spontaneous ignition. Note that in the adiabatic case, the temperatures near the production end (blocks (18 1 1) and (6 1 1)) maintain at the peak temperatures because of no heat loss, while the

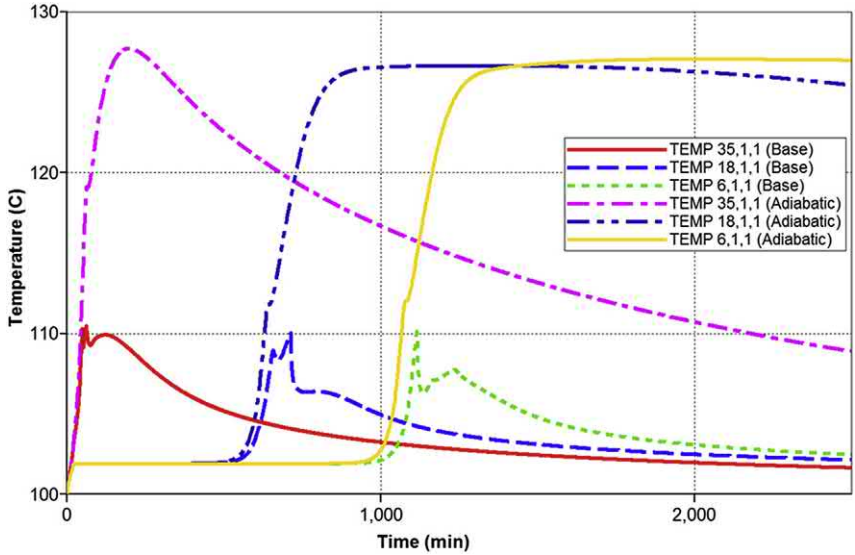

Figure 13.22 Temperature profiles for the base case and the adiabatic case.

temperature at the injection end (block (35 1 1)) decreases because sweeping air takes heat away.

Huang and Sheng (2018) used the base model having heat loss considered to have done sensitivity analyses. The cumulative oils produced from air injection and nitrogen injection are compared and found they are similar, indicating that thermal effect is not significant; increasing the frequency factor or reducing the activation energy can only increase the peak temperature near the injector by 5−8°C; injection of pure oxygen leads a peak temperature near the injector to 38°C increase; doubling the enthalpy due to higher injection pressure increases the peak temperature near the injector by less than 20°C. All these results indicate that a very high temperature cannot be achieved, and thus spontaneous ignition cannot occur, if the heat loss exists. Such sensitivity analyses should have been extended to the adiabatic case to see whether spontaneous ignition is possible under the adiabatic condition.

Huang and Sheng (2018) also used a field model to investigate the spontaneous ignition and thermal effect. The field model is a modified version of Tingas's (2000) model. The thermal properties are same as those presented in Table 13.8. The field model shows that the temperature increase in the middle layer is about 20°C, higher than 10°C in the above base laboratory model and lower than 20°C in the adiabatic laboratory model. The result

does show that heat loss is reduced in the reservoir. However, with such low temperature increase, spontaneous ignition cannot occur in the reservoir.

Huang and Sheng (2018) also used the field model to have done sensitivity analyses, similarly to what is done for the base laboratory model. They found that the cumulative oils produced from air injection and nitrogen injection are similar; the peak temperature near the injector is less than 150°C (the original reservoir temperature 99°C) by increasing the frequency factor, reducing the activation energy causes, injection of pure oxygen, or increasing the enthalpy. All these results indicate that spontaneous ignition cannot occur in the reservoir under low-temperature oxidation reactions.

13.5.4 Delay time of spontaneous ignition

Spontaneous ignition occurs as the heat from oxidation reactions is accumulated so that the temperature is increased to reach an ignition temperature. An analytical solution for the ignition delay time in days was proposed by Tadema and Wiejdema (1970) and then modified by Hou et al. (2011):

$$t_{SI} = \frac{\left[(1-\phi)\rho_r C_r + \phi S_{org}\rho_o C_o + \phi S_{wc}\rho_w C_w + \phi(1-S_{org}-S_{wc})\rho_g C_g\right]E}{R\phi S_{org} Q_{O_2} A p_{O_2}^n} \left\{\left[\left(\frac{RT}{E}\right)^2 + 2\left(\frac{RT}{E}\right)^3\right] exp\left(\frac{E}{RT}\right)\right\}\Bigg|_{T_{SI}}^{T_r} \tag{13.12}$$

In the above equation, ϕ is the effective porosity; ρ_r, ρ_w, ρ_o are the average densities of reservoir rock, water, and oil, respectively, kg/m^3; T_r is the reservoir initial temperature, K; T_{SI} is the spontaneous ignition temperature, K; C_r, C_o, C_w, C_g are the heat capacities of reservoir rock, oil, water, and gas, respectively, kJ/(kg·°C); S_{org} and S_{wc} are the residual oil saturation under gas drive and connate water saturation, respectively; E is the activation energy of the oxidation reaction, J/mol; p_{O_2} is the partial pressure of oxygen, kPa; A is the frequency factor, day^{-1}·kPa^{-n}; R is the universal gas constant which equals to 8.3147 J/(mol·K); n is the reaction order; and Q_{O_2} is the enthalpy of the corresponding reaction, kJ/m^3. Using the above analytical equation, examples of calculated time delay in ignition are shown in Fig. 13.23.

The above equation is derived based on the balance between the heat generated by a low-temperature oxygen-addition reaction $Q_{O_2} \cdot p_{O_2} \cdot A \cdot exp(-E/RT) \cdot dt$ and the heat required $C_f \cdot \rho_f \cdot dT$ to increase the reservoir

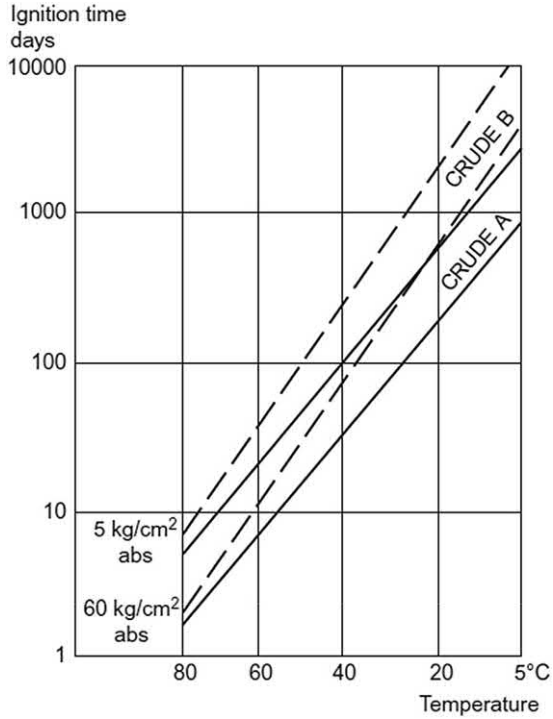

Figure 13.23 Calculated time delay in ignition as a function of temperature at various air injection pressure (Dietz, 1970).

system temperature from T_r to T_{SI}, with the subscript f here representing the formation system.

Spontaneous ignition may be expected when the reservoir temperature is higher than 60–70°C (Turta, 2013). If the delay of spontaneous ignition is practically too long, artificial ignition needs to be considered. Artificial ignition includes electrical heating, injection of steam, injection of chemicals like linseed oil (Turta, 2013) and benzene (Gjini et al., 1999). Linseed oil can start ignition at 33°C. But our tests in laboratory did not experience a very low ignition temperature when linseed oil was used somehow. It might have caused a significant heat loss in the tests. S. Ren (October 5, 2017, personal communication) also found the ignition temperature was still high (250–300°C) when linseed oil was used.

It can be understood that there is also a delay in artificial ignition. It may not be too important to know exactly ignition delay for spontaneous ignition. But it is important for artificial ignition because extension of ignition expenditure is expensive.

13.5.5 Prediction of spontaneous ignition using the Frank-Kamenestskii method

The heat balance equation is

$$\lambda \nabla^2 T + QA(c_o)e^{-\frac{E}{RT}} = 0 \tag{13.13}$$

In the above equation, the first term describes the heat loss to the surrounding in the unit of enthalpy per unit volume of the system (J/m^3), where λ is the thermal conductivity of the system ($W/(m \cdot K)$); and T is the system temperature, K. The second term describes the heat generation, enthalpy per unit volume (J/m^3), where Q is the heat of reaction per unit mass of the fuel, J/mole; $A(c_o)$ represents the chemical reaction rate mole/($m^3 \cdot s$) (the unit of QA(co) should be $J/(m^3 \cdot s)$); E is the activation energy of the reaction, J/mole; R is the universal gas constant, 8.314 J/(mole·K). The product of $Q \cdot A(c_o) \cdot exp(-E/RT)$ is the reaction rate per unit volume, similar to that described by the Arrhenius equation. The above equation describes the heat balance that the heat loss is equal to the heat generated from a reaction.

To convert the above equation into a dimensionless form, the dimensionless parameter δ is defined as

$$\delta = \frac{QEA(co)L^2 e^{\left(-\frac{E}{RT_a}\right)}}{\lambda R T_a^2} \tag{13.14}$$

where L is the characteristic length of the system, with one-half of the smallest dimension of the body being commonly used, m; T_a is the ambient temperature. At some value of δ, spontaneous ignition occurs. This value is called the critical value δ_c. Table 13.9 lists some δ_c corresponding to some geometries.

At a critical condition, the above equation can be written as

$$\ln\left(\frac{\delta_c T_{a,c}^2}{L^2}\right) = \ln\left[\frac{QEA(c_o)}{\lambda R}\right] - \frac{E}{RT_{a,c}} \tag{13.15}$$

Based on the above equation, a plot of $\ln\left(\frac{\delta_c T_{a,c}^2}{L^2}\right)$ versus $\frac{1}{T_{a,c}}$ (critical ambient temperature) will be a straight line with slope of $-E/R$ and intercept $\ln\left[\frac{QEA(c_o)}{\lambda R}\right]$.

Table 13.9 δ_c values for some geometries (Gray, 2016).

Geometry	Dimensions	δ_c
Infinite plane slab	Width 2L	0.878
Rectangular box	Sides 2L, 2r, 2m; L < r, m	$0.873\ (1 + L^{2/12} + L^2/m^2)$
Cube	Side 2L	2.52
Infinite cylinder	Radius L	2.00
Equicylinder	Height 2L, radius L	2.76
Sphere	Radius L	3.32
Infinite square rod	Side 2L	1.70

This method can be used to obtain activation energy when the critical temperature and critical size are measured from the experimental work. On the other hand, this method can also be used as a scaling law to predict the critical ambient temperature for large-scale bodies from small laboratory samples, where L is considered as the argument in the above equation. Or the equation can be used to estimate the critical size L for a certain geometry δ_c at a fixed critical ambient temperature $T_{a,c}$. When doing so, parameters such as reaction rate, activation energy, and heat of the reaction need to be provided. They can be provided by TGA and DSC experiments. Specifically, the TGA is used to obtain kinetic parameters for crude oil oxidation reactions based on the Arrhenius method, and the DSC is used for estimating the heat of reaction. The feasibility of this method is investigated below.

Consider an oil reservoir of the geometry of an infinite slab. The critical dimensionless parameter, δ_c, is 0.878 according to Table 13.9. According to Huang and Sheng (2017a), typical kinetic data for the activation energy E vary from 20 to 70 kJ/mol (median 33 kJ/mol), and the typical values for the frequency factor A from 0.1 s^{-1} to 10^5 s^{-1} (median 50,000 s^{-1}) for LTO. According to Zhang and Sheng (2017), the enthalpy values Q for LTO are from 20 to 3635 kJ/mol. Earlier in Table 13.6, the enthalpy values are 844 and 1210 J/g. If the molecular weight is 200 g/mole, the enthalpy values are 168.8 and 242 kJ/mol, respectively. An average of 200 kJ/mol may be taken. The value of formation thermal conductivity λ used in Green and Willhite (1998) is about 2.6 J/(s·m·K). The oil density of 850 kg/m^3 is taken. The reservoir temperature T_a is assumed to be 80°C. These average values or the base case values are listed in Table 13.10. Using these values, the calculated critical reservoir thickness to lead to spontaneous ignition is 0.00,073 m. This indicates that spontaneous ignition is ready to achieve in the reservoir.

Table 13.10 Average (base) parameters used in the Frank-Kamenestskii method.

δ_c	A	ρ	MW	λ	Q	E	Ta
Dimensionless	1/s	kg/m^3	g/mole	W/(m·K)	J/mole	J/mole	°C
0.878	50,000	850	200	2.6	200,000	33,000	80

In Abu-Khamsin et al.'s (2001) experiments, the maximum temperature increase was about 10°C, indicating spontaneous ignition could not occur. The Frank-Kamenestskii's method is used to check whether spontaneous ignition could occur. In their experiments, radial packed reactor was used. So δ_c is 2 according to Table 13.9. Other required data were not reported in their paper. Using the base values of other parameters above, the critical length L is estimated to be 0.001 m, indicating spontaneous ignition could occur. This mismatch between the theory and the experiment could be caused by incorrect parameter values used. They reported that the failure of spontaneous ignition could be caused by excessive heat loss by sweeping gas or running out of LTO fuel. To simulate an excess heat loss, the thermal conductivity λ is increased by 10,000 times, then the estimated critical length is 0.1 m which is several times the diameter of the sand pack. This analysis shows that the failure was not caused only by heat loss.

Similarly, Jia et al.'s (2012a) experiments are also analyzed using the Frank-Kamenestskii method. In their experiments, a cylinder-shaped core was used. δ_c was 2. The activation energy of 26 kJ/mol was reported by Jia et al. (2012a). For the rest of the other parameter values, the base values above are used. When the thermal conductivity λ is increased by 1000 times, the critical length is 0.1 m. The above two examples and the base case all show that it should be easy to achieve spontaneous ignition. However, the reality did not show that. It seems that the Frank-Kamenestkii method may not predict the reality. Now we conduct a sensitivity study of each parameter in the Frank-Kamenestskii method.

The kinetic parameters E and A, thermal conductivity λ, and the enthalpy Q are studied about their sensitivity on the critical characteristic length L_c at which spontaneous ignition occurs. The reservoir is assumed to be an infinite slab (δ_c is 0.878) and its temperature is 80°C. The results are presented in Table 13.11. The minimum and maximum values of E of 20,000 and 70,000 J/mole, respectively, are tested. Even when the maximum E is used, L_c is 0.28 m, indicating that spontaneous ignition can readily occur. For the rest of three parameters, their base values are increased or decreased by 10 times. The results show that L_c hardly changes and it is

Table 13.11 Critical lengths at different values of each parameter.

E	A	λ	Q	L_c
J/mole	1/s	W/(m·K)	J/mole	m
33,000	50,000	2.6	200,000	0.0007
20,000				0.0001
70,000				0.28
	5,000.0			0.002
	500,000			0.0002
		0.26		0.0002
		26		0.0023
			20,000	0.0002
			2,000,000	0.0002

close to 0.0002 m. Interestingly, it is believed in the literature that because heat loss is so significant spontaneous ignition is difficult to occur in laboratory conditions. However, when λ is increased from 0.26 to 26 W/(m·K) by 100 times, L_c is only increased 10 times; and more importantly, L_c is 0.0023 m (very small), indicating that spontaneous ignition can occur at such high thermal conductivity (heat loss)! This is not in line with what has been believed. The exothermic thermal energy used in the Frank-Kamenestskii method is from a DSC test and it is calculated within a temperature range for an LTO reaction. The method assumes that the thermal energy can accumulate and raise the in-situ temperature to complete the whole reaction. In other words, there is a difference among the thermal energy derived from DSC and that used in the Frank-Kamenestskii method. In addition, the Frank-Kamenestskii method assumes that the oxygen and reactants are sufficient for the exothermic reaction to take place. Whether the Frank-Kamenestskii method can be used to predict the occurrence of spontaneous ignition is a question.

13.5.6 Thermal effect in low-temperature oxidation

When spontaneous ignition cannot occur, or combustion cannot be maintained, what can occur in reservoirs is low-temperature oxidation (LTO) during air injection. In addition to thermal effect caused by heat release from LTO reactions, LTO is an oxygen addition reaction. Products are water and partially oxygenated hydrocarbons such as carboxylic acids, aldehydes, ketones, alcohols, and hydroperoxides (Burger and Sahuquet, 1972), so that the oil viscosity is increased. How can LTO improve oil recovery? To answer this question, Huang et al. (2018) conducted a series of isothermal core flooding tests at different temperatures. Details are presented next.

13.5.7 Experimental

A Berea sandstone core of 5.308 cm length and 3.874 cm diameter was used. The porosity was 19.01% and the nitrogen permeability was about 200 mD. This core plug was repeatedly used for tests at different temperatures and for gas and nitrogen. After each test, the core was cleaned by a Soxhlet extractor for the next test. Wolfcamp crude oil was used. The density of this crude oil is 0.83 g/cc (38.98 API) and the viscosity of this crude oil is 3.66 cP at 25°C and at atmospheric pressure.

The core was saturated by oil and air or nitrogen was injected at 840 psi at the inlet and the back pressure at the outlet was 800 psi. For both nitrogen and air injection tests, isothermal tests were conducted under 80, 100, and 120°C, respectively.

13.5.8 Results and discussion

Fig. 13.24 shows the recovery factors of isothermal air injection tests under 80, 100, and 120°C, respectively (Huang et al., 2018). Their ultimate recovery factors after 8 pore volume injection were 63.4%, 70%, and 74%, respectively. The incremental oil recovery factor from 80 to 100°C was 6.6% for 20°C increase in temperature, while the incremental oil recovery factor from 100 to 120°C was 4%. If the thermal effect is important, it is expected that the recovery increase from 80 to 100°C would be lower than that from 100 to 120°C, because the heat loss is smaller when the temperature is increased and the thermal effect due to LTO would be

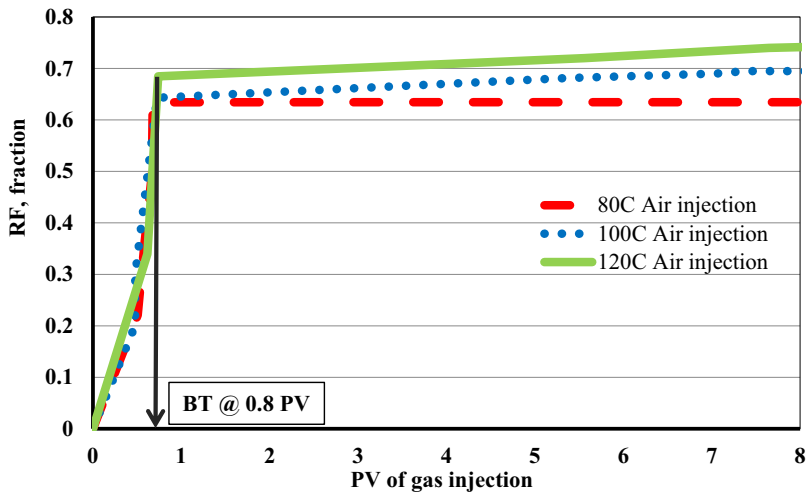

Figure 13.24 Recovery performance of isothermal air injection tests at 80, 100, and 120°C, respectively.

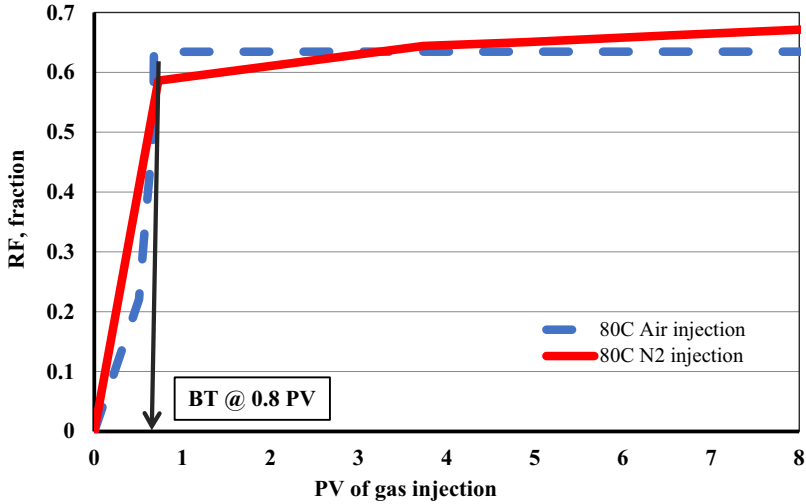

Figure 13.25 Recovery performance of isothermal air injection test and nitrogen injection test at 80°C.

more significant. The experimental data did not show this expectation. The increase in recovery factor as the temperature is increased is due to the decrease in oil viscosity as the temperature is increased. The oil viscosity was decreased from 2.7 to 1.1 cP as the temperature was increased from 80 to 120°C.

Fig. 13.25 compares the oil recovery from nitrogen injection and air injection at 80°C. It is seen that the recovery from nitrogen injection was higher than that from air injection. Such result was also observed when live oil was used. In other words, the difference in oil recovery between nitrogen injection and air injection was not caused by the difference of gas dissolution of different gases. The difference is probably caused by the fact that part of the oxygen was consumed. The consumption of oxygen resulted in less air that actually flooded oil.

During gas injection (either nitrogen or air), gas pushes the oil ahead of it to the producer. Some oil remains behind the displacement front. After some PV (e.g., 8 PV) of nitrogen is injected first so that no more oil is produced, air injection is injected. Then oxidation reactions may occur between the air and the oil remaining from nitrogen injection. If the oxidation can significantly improve oil recovery, incremental oil over nitrogen injection will be recovered. Fig. 13.26 shows such experimental results at 80, 100 and 120°C. At any temperature, when air is injected after 8 PV of nitrogen, no more oil was recovered. Therefore, the LTO thermal effect was not observed under the laboratory conditions where heat loss deemed more

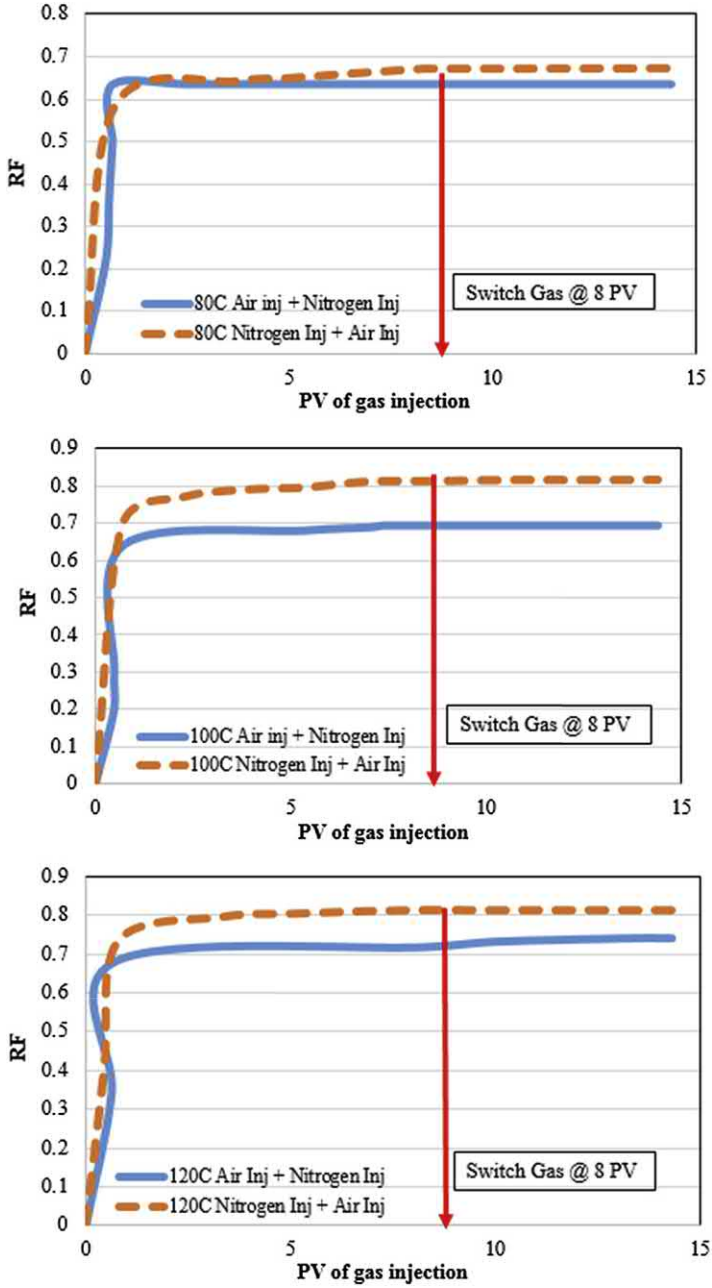

Figure 13.26 Alternate gas injection tests.

significant than in a reservoir. Similarly, after 8 PV of air injection, nitrogen was injected. Fig. 13.26 shows that no more oil was recovered from additional nitrogen injection (Huang et al., 2018), which is expected. At 120°C, it seems that a little more oil was recovered. This more oil was probably experimental error.

13.5.9 Numerical analysis

The LTO effect in the above experiments was further analyzed by numerical simulation. A simulation model was built using the thermal simulator CMG-STARS. The kinetic data and kinetic model for the Wolfcamp oil in the LTO stage were obtained and developed in Huang et al. (2016a) and Huang and Sheng (2017c). 1D Cartesian grids of 5 × 1 × 1 were used to represent the core plug. The main reservoir properties of the model are listed in Table 13.12. The inlet and outlet were located at blocks (5 1 1) and (1 1 1), respectively. The gas-liquid *K*-values in the phase behavior model were obtained through the CMG-WinProp PVT module. This model successfully matched the air injection test at 80°C.

The insignificant thermal effect in the experiments was suspected to be caused by heat loss. To verify this hypothesis, the performance of two laboratory scale models is compared. One model is the history-matched model with heat loss parameters presented in Table 13.12. The other one is at the adiabatic condition under which no conductive heat loss is considered between over/underburden strata. The simulation results are shown in Fig. 13.27 (Huang et al., 2018). It shows the reservoir average temperatures for the models with and without heat loss almost overlap each other; both

Table 13.12 Main parameters used in the laboratory-scale simulation model.

Porosity (dimensionless)	**0.19**
Horizontal permeability (mD)	200
kv/kh (dimensionless)	1
Oil saturation (dimensionless)	0.998
Reference pressure (kPa)	5800
Original reservoir temperature (°C)	80
Rock volumetric heat capacity (J/(cm^3·°C))	2.35
Rock thermal conductivity (J/(cm·min·°C))	1
Water thermal conductivity (J/(cm·min·°C))	0.36
Oil thermal conductivity (J/(cm·min·°C))	0.077
Gas thermal conductivity (J/(cm·min·°C))	0.083
Temperature of injected gas (°C)	80

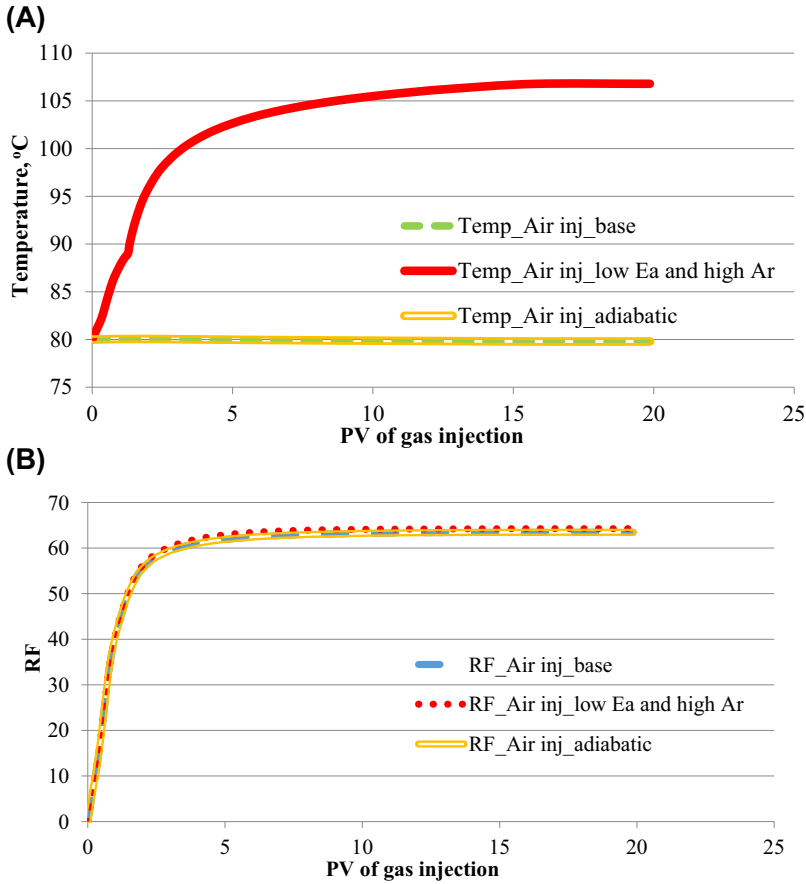

Figure 13.27 Effect of kinetic data and adiabatic condition on (A) reservoir average temperature and (B) oil recovery factor.

models do not show the temperature increase (almost invisible); but lower activation energy (20 kJ/mol) and a higher frequency factor (10^5 s^{-1}) resulted in 25°C increase. During the isothermal experiments discussed in the preceding section, it was observed that there was a 1–2°C difference in the measured temperatures or no difference with and without adiabatic materials used. These simulation results and experimental observations seem to indicate that the absence of thermal effect was not caused by the heat loss in laboratory conditions, but rather attributed to the lack of crude oil exothermic activity (e.g., high activation energy and low frequency factor).

13.6 Oxygen consumption rate in low-temperature oxidation

The preceding section shows that during LTO the oil recovery factor is very close to that from nitrogen injection. It means the combustion cannot occur or maintained, so that thermal effect from LTO is not significant. Then practically, air injection is similar to flue gas injection in terms of oil recovery. However, for air injection, a significant amount of air remaining at the production well will pose a safety issue. Therefore, oxygen consumption rate in LTO is discussed in this section.

The oxygen consumption during LTO was studied by SBR (small batch reactor), oxidation tube, and slim tube tests (Ren et al., 1999; Clara et al., 2000; Niu et al., 2011; Zhang and Sheng, 2016). The oxygen reaction rate can be calculated based on the mass balance. Ren et al. (1999) performed the SBR experiments using North Sea oil and found that less than 3% of oxygen was measured after the SBR test under 120°C with 120 h of reaction time. The reaction rate ranges from 8.92E-6 gmol O_2/(hr·cm^3 sand) to 9.1E-6 gmol O_2/(hr·cm^3 sand). Chen et al. (2013) used the Changqing oil in China in the SBR test and reported that the oxygen concentration decreased from 21% to 1% under 140°C for 108 h of reaction; and a test at 170°C only took 6 h to reduce the oxygen concentration from 21% to 0.2%. However, we did SBR tests, the oxygen concentration was 17.85%, 13.75%, and 5.51% at 100, 120, and 140°C, and by 138, 129, and 134 h, respectively. Ren et al. (1999) performed the oxidation tube tests to study the oxygen consumption by LTO, and they reported that the produced oxygen concentration was less than 2% under the 120°C oxidation tube experiments. Niu et al. (2011) conducted the slim tube experiments with the Zhongyuan oil in China, and they reported that when the temperature was higher than 100°C, the produced oxygen concentration was less than 2%. We also did core flooding tests and observed that the oxygen concentrations were 17%–19% at 100 and 120°C after 3 h of flooding. To prevent the potential fire and explosion hazards in a production well, the oxygen concentration should be lower than 10% (Kuchta. 1985; Ji et al., 2008; Liao et al., 2018). Based on the experience, the oxygen concentration can be as high as 5% in the production well (Hou et al., 2010).

13.7 Minimum oil content for combustion

If spontaneous ignition can occur or artificial ignition is executed, in situ combustion will occur. To maintain this combustion, minimum oil content W_{omin} is required. According to the energy balance over a unit volume near the combustion front (Kharrat and Vossoughi, 1985):

$$W_{omin} = S_o \phi \rho_o = \frac{\rho_{bC_b} \Delta T_f}{\Delta H} \tag{13.16}$$

where

$$\rho_b C_b = (1 - \phi)\rho_s C_s + \phi \rho_g C_g$$

ΔT_f is the front temperature minus room temperature from a combustion tube test, ΔH is the heat value of crude from a DSC test, ϕ is the porosity, ρ is the density, C is the specific heat, S is the saturation, and the subscripts b, o, g, and s are bulk, oil, gas, and solid, respectively. $\rho_b C_b$ may be obtained from Perry et al. (1963). Kharrat and Vossoughi (1985) calculated W_{omin} for three reservoir cases, 0.0465, 0.0511, and 0.604 g/cm^3, the average being 0.0527 g/cm^3. For a shale reservoir, if we assume other parameters are the same as those examples, and if the oil density is 0.85 g/cm3, and the porosity is 0.08, then S_o must be higher than 0.77 to meet this minimum oil requirement. This example calculation indicates that it is difficult to meet the oil requirement in shale reservoirs. As a result, combustion cannot be maintained, even if it is initiated. However, Fassihi and Kovscek (2017) reported a lower range for fuel concentration (0.016–0.04 g/cm^3).

It was found from experiments using heavy oils and field observations that fuel consumed in an in-situ combustion process usually falls within 200–300 barrels per acre-ft of formation burned (Nelson and McNeil, 1961). This number is translated to 2.6%–3.9% porosity, if the oil is completely burned. This number is also converted to 1.6–2.4 lb/ft^3 which is in the high side of the data presented by Showalter (1963). Probably 5%–10% the oil in place is burned in an in-situ combustion project (Hughes and Sarma, 2006).

13.8 Air requirement in combustion

A combustion front can advance only when both air and fuel are available. Air requirement is closely related to available fuel. And a minimum

air requirement is related to minimum fuel required to maintain the combustion. Barzin et al. (2010) reported that the air requirement for typically high gravity oil is 173 m^3 (STC)/m^3; Martin et al. (1958) reported 135 m^3 (STC)/m^3. But several times of these numbers were reported in field projects.

13.9 EOR mechanisms and EOR potential in shale and tight reservoirs

Fassihi and Kovscek (2017) listed these mechanisms of air injection in light oil reservoirs:

(1) stripping and vaporizing light oil components by generated CO_2;
(2) sweeping oil by combustion gases and possible miscibility effects;
(3) oil banking and improved sweep;
(4) pressurization and voidage replacement;
(5) reducing oil viscosity due to increased temperature.

These mechanisms are all related to combustion. However, whether combustion, especially by spontaneous ignition, in light oil reservoirs can occur or sustain is still a question. In high-temperature combustion, pressure is maintained. But in LTO, pressure is reduced as oxygen consumed is greater than carbon dioxide release (Turta and Singhal, 2001). In Zhang and Sheng's (2016) small batch reactor experiments, both the oxygen partial pressure and the total pressure decreased with time (see Fig. 13.28). Therefore, the pressurization (the above mechanism 4) from air injection during LTO is not more effective from nitrogen or flue gas injection.

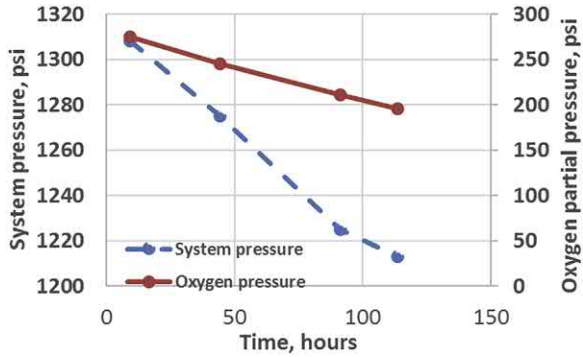

Figure 13.28 Total system pressure and oxygen pressure in an isothermal (124°C) SBR experiment.

Generally, in an LTO process, the temperature increase may not be high, and the viscosity reduction will not be high. And LTO-generated oxygenated compounds such as carboxylic acids, aldehydes, ketones, alcohols, and hydroperoxides (Burger and Sahuquet, 1972) will increase oil viscosity. Thus, the above mechanism 5 may not be feasible. Other mechanisms (the above mechanisms 1−3) from air injection may not outperform a nonoxidation gas process like nitrogen or flue gas injection. Such opinions are supported by Huang et al. (2018) experiments to study the thermal effect in LTO process (see the above Section 13.6 for details).

To have significant benefits from air injection over nonoxidation gas injection, combustion must be able to occur. In a shale and tight formation, even when a combustion process is initiated, sustaining the combustion process requires the availability of minimum fuel and the injectivity of air requirement. To ease the low-permeability problem with shale and tight reservoirs, huff-n-puff air injection was evaluated (Jia and Sheng, 2018). The simulation results show that about 10% oil can be recovered within 20 years. However, it is assumed that combustion can occur in the model.

Jia and Sheng (2017) discussed the favorable and unfavorable conditions of air injection in shale reservoirs. Although shale and tight reservoirs have the disadvantage of low injectivity, and the low-porosity matrix may result in the difficulty to increase oxidation temperature and in the increase of heat loss, the fine-grade matrix provides a high surface area that can promote crude oil oxidation in porous media. A high specific surface area can make the exothermal temperature range shift to a lower temperature range (Drici and Vossoughi, 1985). A rich content of clays in shale rocks have a catalytic effect on crude oil oxidation. Jia et al. (2012b) found that smectite was ranked first, illite was ranked second, and chlorite and kaolinite were ranked third in their catalytic ability for crude oil oxidation.

Oils in shale and tight reservoirs are more likely light oils. Freitag (2016) stated that the aromatics act as the main sources for the oxidation inhibitors during the LTO reaction process. Hence, the difference on exothermic behavior for heavy oil and light oil can be explained based on their different compositions. As the heavy oil contains more aromatic components and the light oil contains more aliphatic contents, therefore, the light oil tends to present more intense exothermic activity in the LTO region than the heavy oil.

The EOR potential of air injection in shale and tight reservoirs cannot be defined, until EOR mechanisms are well understood and quantified.

CHAPTER FOURTEEN

Other enhanced oil recovery methods

Abstract

This chapter briefly presents other enhanced oil recovery (EOR) efforts. The efforts include using sequential method of huff-n-puff gas injection and spontaneous imbibition, chemical blends, air foam drive, branched fractures, zipper fracture, refracturing, diversion technology in fracturing, energized fluids, thermal recovery, and microbial EOR.

Keywords: Air foam; Microbial EOR; Branched fractures; Chemical blend; Diversion technology; Energized fluids; Refracturing; Thermal recovery; Zipper fracture.

14.1 Introduction

In addition to the enhanced oil recovery (EOR) methods described in the preceding chapters, additional efforts were made to enhance oil recovery from shale and tight reservoirs. This chapter briefly presents those efforts. The efforts include using sequential method of huff-n-puff gas injection and spontaneous imbibition, chemical blends, air foam drive, branched fractures, zipper fracture, refracturing, diversion technology in fracturing, energized fluids, thermal recovery, and microbial EOR.

14.2 Sequential method of huff-n-puff CO_2 injection and surfactant-assisted spontaneous imbibition

As we have seen in earlier chapters, huff-n-puff gas injection can improve oil recovery, but the oil production rate will decline with injection cycle; at later cycles, the process may lose economic advantages. During this late time, water may be injected to activate spontaneous imbibition with surfactants added in the water which is called surfactant-assisted spontaneous imbibition (SASI). Zhang et al. (2018) first conducted huff-n-puff CO_2 injection followed by SASI using sidewall cores. Fig. 14.1 shows the recovery factors (RF) from huff-n-puff CO_2 injection and surfactant-assisted

Enhanced Oil Recovery in Shale and Tight Reservoirs
ISBN: 978-0-12-815905-7
https://doi.org/10.1016/B978-0-12-815905-7.00014-1

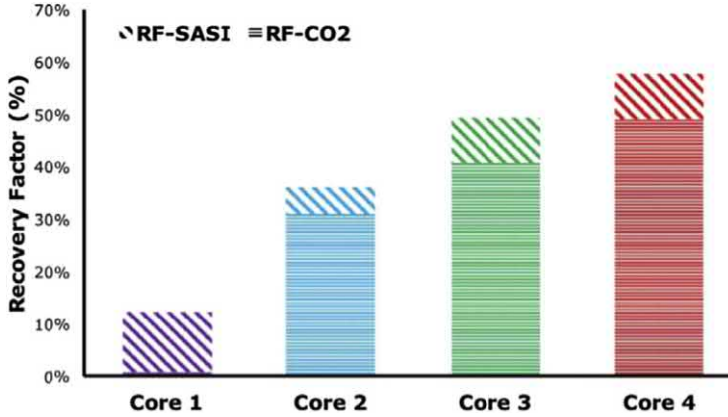

Figure 14.1 Recovery factors from huff-n-puff CO_2 injection and surfactant-assisted spontaneous imbibition (SASI) (Zhang et al., 2018).

spontaneous imbibition (SASI) from four cores. Depending on the injection pressure and number of cycles, the four different cores had different RFs with Core 1 not having a huff-n-puff part. The figure indicates that the RFs from huff-n-puff could reach 50% (Core 4); although different amount of oil was recovered from different huff-n-puff experiments on four cores, the RFs from SASI were almost same from the four cores (top parts), close to 10%. Therefore, a good practice may be that huff-n-puff gas injection is performed first; after not much oil can be recovered any more, switch to the imbibition process.

14.3 Chemical blends

Mohanty et al. (2017) designed and evaluated a chemical blend to enhance oil recovery. The blend consisted of an anionic surfactant (0.1−1 wt.%), an organic solvent (1−10 wt.%), and an oxidizing agent (a weak acid, 0.1−1 wt.%). About 0.1 wt.% clay stabilizer and 0.1 wt.% scale inhibitor were also added. The surfactant lowered the interfacial tension (IFT) and increased water-wetness. The organic solvent solubilized oil and heavy organic components such as asphaltenes, and it cleaned the flow path. The oxidizing agent oxidized some of the kerogen, and a byproduct of oxidation acted as a weak acid which dissolved a part of calcite. Those chemicals were not reported in their paper.

Eagle Ford shale samples rich in calcite (>50 wt.%) were used in laboratory tests. The agent reacted with calcite in the shale. The calcite dissolution by the pure oxidizing agent was higher than the blend solution, even though

the amount of oxidizing agent was the same in the two solutions. Probably, the adsorption of anionic surfactant in the blend solution retarded the calcite dissolution. The dissolution resulted in permeability increase from 54 to 78 μD on the average from three tests. The permeability increase was owing to the microfractures generated or widened on the big fracture surface. The dissolution did not weaken the rock hardness, while HCl decreased the hardness from 200 to 70 MPa, as HCl dissolved more calcite than the blend. The softening of rock might cause mud generation and proppant embedment. However, the dissolution decreased the fracture conductivity by 30%–60%, because the continued flow of the blend solution made the proppant packing tighter. Fortunately, fracture conductivity is generally not the limiting resistance to production; the resistance in the matrix dominates the flow. The solution having the oxidizing agent alone could not produce oil. With just the oxidizing agent in brine, there was some calcite dissolution, but no oil was released by aging a shale core (spontaneous imbibition). In a combination of the organic solvent and the oxidizing agent, the oxidizing agent reacted with the shale and dissolved some calcite. But no oil was produced from the shale.

The organic solvent solubilized oil and oil residues like asphaltene. The spontaneous imbibition type of experiments showed that for a solution of organic solvent alone, only organic solvent floated at the top of the solution, but no oil was produced from the shale. There was no interaction between the organic solvent and the shale.

When the anionic surfactant and oxidizing agent were mixed, there was some wettability alteration, but the calcite dissolution became smaller than the case with oxidizing agent alone, because the surfactant covered some of the calcite.

When the anionic surfactant and organic solvent were mixed, the wettability was altered, but no oil was released in spontaneous imbibition.

When these three components were mixed, the wettability was altered, oil was released, and the calcite was dissolved.

Field trials were performed in several Eagle Ford wells in South Texas. Individual chemicals in 2% NaCl brine were used as a preload to mitigate frac hit. The preload volume of 3000 – 20,000 bbls were pumped at a rate of 2–5 bbls/min, followed by an average shut-in time of 2–5 weeks. A dozen of treated wells showed strong well performance. The incremental cumulative oil and water production were 20,000 bbls and 12,000 bbls, respectively, with 60% of injected water returned in a period of 8 months after 5 weeks of soak. Note that the laboratory tests showed that the shut-in time of 2 days was enough.

Miller et al. (2018) did a similar study of chemical blends in clay-quartz rich (75 wt.%) shale cores. The chemical blends consisted of 0.1−1.0 wt.% anionic surfactant (Calfax), 0.1−1.0 wt.% oxidizing agent (persulfate salt), and 1.0−10.0 wt.% D-Limonene. Chemical blends with sulfate ions delayed the weak acid-carbonate reaction, which permits the acid to reach deep matrix. The blends also increased the shale surface roughness, and the fracture conductivity was reduced minimally.

The performance of the chemical blends summarized above, together with the results of the combinations of surfactants reported by Zeng et al. (2018), show that surfactant blends had better performance, especially in terms of oil recovery, than a single surfactant by synergy.

14.4 Air foam drive

If there are fractures connecting an injector and a producer, injected gas will break through quickly for gas flooding. Some operators reported that even for a huff-n-puff gas injection, gas broke through neighboring wells. In other words, even in shale or tight reservoirs, sometimes we need to deal with a sweep efficiency issue. In conventional reservoirs, one method to deal with the issue is to use foam. Not much work has been reported in the literature on this issue for shale and tight reservoirs. One paper that is close to the subject is the one presented by Singh and Mohanty (2015). In that paper, they reported using foam with wettability alteration capabilities for a carbonate core (vuggy, oil-wet, Silurian dolomite). The core permeability was 792 mD and the porosity was 17.7%, though. The surfactants used were alkyl propoxy sulfate (APS) that had low interfacial tension (IFT), wettability alteration and weak foaming, and alpha-olefin sulfonate (AOS) that had good foaming capacity but no wettability alteration; two zwitterionic foam boosters, lauryl betaine, and cocoamidopropyl betaine, were also added. After secondary water floods, surfactant solutions were coinjected with methane gas at a fixed foam quality. Spontaneous imbibition experiments and contact angle measurements showed that AOS could act as a wettability-altering surfactant in the presence of sodium carbonate, but not alone. A blend of zwitterionic surfactant and AOS was not observed to play a role in stabilizing foam in a water-wet carbonate core. Oil displacement experiments showed that coinjection of wettability-altering surfactant and gas could recover significant amount of oil (33% OOIP) over water flooding. With AOS as the foaming agent, only a weak foam was propagated in a carbonate core, regardless of the

core wettability. A blend of wettability-altering surfactant (AOS and zwitterionic surfactant) not only altered the wettability from oil-wet to water-wet, but also significantly increased the foam resistance factor in the presence of oil.

An air foam test was started to improve injection profile before water injection in An 83 zone in the Chang 7 formation in April 2013. In the 350 m × 150 m well pattern (An 231−45 well pattern), 7824 m^3 of air was injected to generate 3631 m^3 foam. The well production capacity was increased from 0.55 to 0.88 tons/day on the average, a significant increase compared with the capacity of 0.39 tons/day for the neighboring wells. Water injection began in December 2013. The water cut in the corresponding production wells started to increase. This test showed that air foam mitigated water breakthrough (Wang et al., 2015).

14.5 Branched fractures

Branched fractures are generated by adding fiber in the fracturing fluid whose viscosity is reduced gradually. After the main fracture is generated, added fibers (0.1−0.3 wt.%) form a temporary bridge blockage with sand within the fracture. The pressure is increased, and then the fracturing fluid diverts to understimulated intervals along the lateral to form branched fractures (Potapenko et al., 2009). After the fractures are generated, the fluid viscosity is gradually reduced. Thus, the fracture conductivity is achieved (Wang et al., 2013). Branched fractures can be more easily generated when the difference between the maximum and minimum horizontal stresses is small.

Fan and Liu (2016) reported a field case to generate branched fractures by a large-scale fracturing operation in the Hailaer field, Inner Mongolia, China. For such a fracturing operation, 1631 m^3 of fracturing fluid and 161 m^3 sand per well on average were injected. About 7.8 m^3/d of sand was injected per well. For this field, the average porosity was 15.3%, and the permeability was 0.34 mD under an overburden confining condition. After fracturing, the average oil rate was increased by 5.7 tons/day from 0.7 tons/day. After 500 days of fracturing, the average incremental oil per well was 2244 tons. Totally six wells were tested.

Li (2012) reported the oil production performance (oil rate) using different fracturing methods. The oil rates showed that the multistage fracturing method and using polyhydric alcohol fracturing fluid worked better.

14.6 Zipper fracture

Instead of drilling and hydraulically fracturing one well at a time, multiple wells are drilled from a pad site; after one stage in one well is fractured, during the time to prepare for fracture the next stage at this well, wireline and perforation operations take place and a stage is fractured in another well. The fractures have a zipperlike configuration, as shown in Fig. 14.2 in which other configurations are presented. This figure shows two well fracture patterns. A similar pattern can be practiced in four wells and multiple wells. For the conventional fracturing configuration, well 1 and well 2 are independently fractured with each stage fractured sequentially from the toe to the heel. For the zipper fracturing configuration, after one stage from well 1 is fractured, another stage from well 2 is fractured to the early stage, and the sequence is repeated. The objective is to generate the fracture complexity near the tips of fractures. For the Texas two-step configuration, the sequence of fracturing stages for a single well is altered. After the first stage near the toe is fractured, the second stage toward the heel is fractured; next the third fracture is initiated between the two previously fractured. The middle fracture has a reduced half-length because it is generated in the stress alteration region by the previous fractures. In the modified zipper fracturing configuration, the staggered fracture pattern allows the individual stimulated reservoir volume (SRV) extents for each lateral overlap, generating both

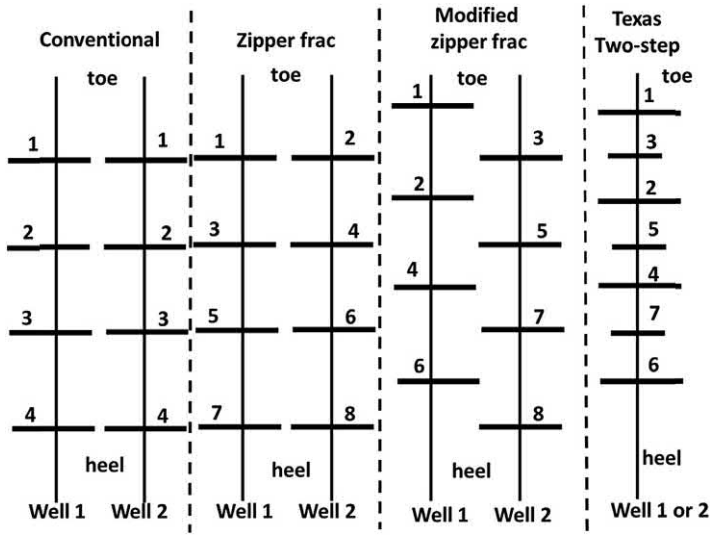

Figure 14.2 Various fracturing figurations (numbers indicate sequence).

near- and far-field complexity with the reservoir. Each fracture stage for the second well propagates into the stress alteration region by the two previously propagated fractures from the first well, combining concepts of the zipper and Texas two-step patterns (Soliman et al., 2010; Curnow and Tutuncu, 2016).

When completing horizontal wells one at a time, after a single stage is fractured, it takes 2–3 h for the wireline operation to set plugs and perforate the next stage. By completing multiple wells, this waiting time can be used. In addition to cut operation time off, zipper and modified zipper fracturing patterns can increase fracture complexity, and therefore, improve oil recovery.

For the multiwell frac patterns to work there are three primary factors (Jacobs, 2014):

(1) Existence of conductive natural fractures,
(2) Impact the stress shadow may have on hydraulic fracturing between two wells,
(3) Ability to change the pressure within the natural fractures between two wells.

14.7 Refracturing

Statistically, refracturing jobs show more field success than field failures. Vincent (2010, 2011) used specific field cases to illustrate refracturing mechanisms. These mechanisms include enlarged fracture geometry, increased fracture height in vertical wells, greater lateral coverage in horizontal wells or initiation of more transverse fractures, restored or increased fracture conductivity, reorientation of existing fractures, etc.

14.8 Diversion technology in fracturing

In displacement processes in conventional reservoirs, diversion technology is used to improve the sweep efficiency of displacing fluids. Similarly, diversion technology in fracturing is to increase the fracturing fluid to enter more or all zones so that more fractures are generated, or sometimes more fracture complexity is obtained. This can be achieved mechanically or chemically. Mechanical diversion uses mechanical parts like different packers, retrievable bridge plugs, sliding sleeves and ball sealers. Chemical diversion uses viscous fluids or soluble particulate diverters. The main purpose of these diversion methods is to divert the fluid from high-permeability zones to lower-permeability zones or temporarily block the

high-permeability zones. The blockage must be able to be removed after the treatment so that oil and gas can flow back or be produced back from all of the zones. In hydraulic fracturing, a fracturing fluid is diverted to less dominant perforations, clusters, or fractures. To remove the blockage, the particulates in the diverting agents must be degraded biologically, chemically, thermally, or when they contact oil.

14.9 Energized fluids

Because gas is a compressible fluid, the compressed gas will release energy (slow down pressure depletion) when the system pressure is decreased. Thus, a fluid with one or more compressible gas components dispersed is called energized fluid. The compressible gases are typically CO_2, N_2 or a combination of gases. However, energized fluids have their drawbacks such as low stability at high temperature, high friction during pumping, and corrosion in the case of CO_2.

Cryogenic liquid N_2 (-320 to $-322°F$) is used in hydraulic fracturing. It is found that liquid N_2 can reduce breakdown pressure and increase fracture complexity (Gomaa et al., 2014). CO_2 can be pumped with conventional equipment in liquid form. As it is heated in a reservoir, it vaporizes to a gas state. The gaseous CO_2 can assist in flow back. Liquid CO_2 has high density which helps in gaining hydrostatic pressure and in carrying proppants. Other benefits include lower interfacial tension and clay inhibition. Water saturated with CO_2 forms carbonic acid which may have some benefits. In many cases, energized fluids in different types of foams are used (Karadkar et al., 2018).

14.10 Thermal recovery

To develop oil shale, in-situ heating to about 650°F may convert kerogen to oil and gas. Although kerogen content in a shale oil rock is much lower (<10%) than a typical oil shale, a shale oil formation may be heated so that the kerogen is converted to oil and gas; probably the formation permeability is increased owing to kerogen decomposition. Egboga et al. (2017) used a compositional thermal simulator to check the feasibility of downhole in-situ heating. They proposed high frequency electromagnetic (microwave) heating at the downhole wellbore to avoid significant heat loss. The microwave energy is introduced into a reservoir from a radiating element located in the horizontal section of a wellbore, heating the reservoir through adsorption of electromagnetic energy by connate water

Table 14.1 Main fluid and rock properties used in the model.

Matrix permeability (mD)	0.0015
Matrix porosity	0.08
Reservoir thickness (ft)	10
Shale thermal conductivity (Btu/ft·day°F)	30
Initial pressure (psi)	6840
Initial temperature (°F)	248
Initial kerogen concentration (weight%)	10
Oil viscosity (cp)	0.31
Hydraulic fracture half-length (ft)	200
Hydraulic fracture spacing (ft)	200
Well spacing (ft)	150
Natural fracture spacing (ft)	28

in the reservoir. The same well is used for production and heating; during the heating, the well is not produced. In their simulation model, the properties of a Bakken oil are used. Table 14.1 lists the main fluid and rock properties used in the simulation model.

The reservoir is initially depleted (the first primary depletion in Fig. 14.3) at 2000 psi bottom hole pressure, followed by heating at 700°F at the heating well, and then followed by the second depletion. Fig. 14.3 shows the average reservoir (model) pressure. It shows that heating increases the reservoir pressure from 3300 psi at the end of first depletion to 7000 psi after 1000 days of heating, indicating thermal pressurization is an important

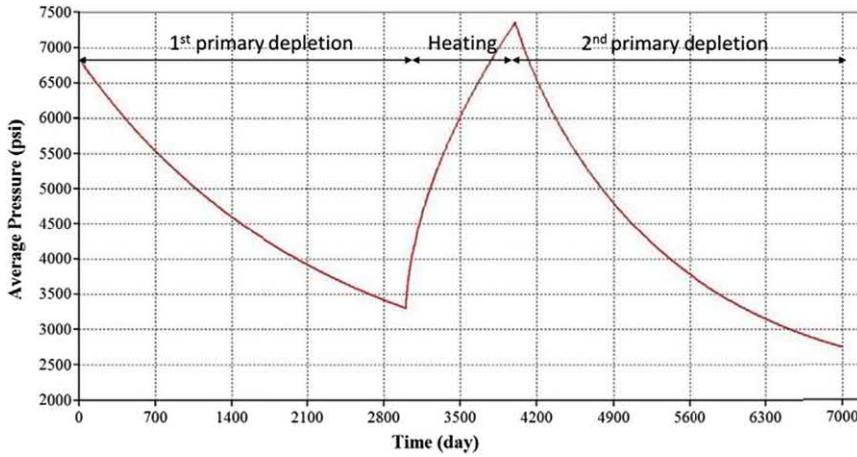

Figure 14.3 Average reservoir pressure during depletion and heating (Egboga et al., 2017).

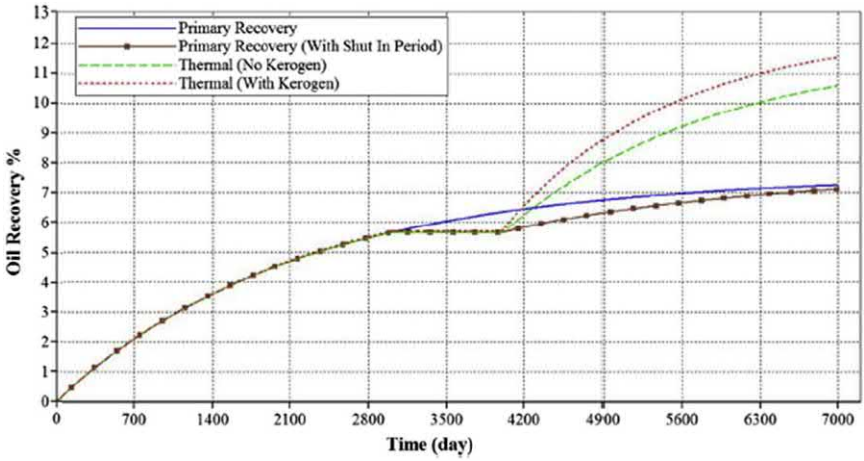

Figure 14.4 Oil recovery from primary depletion and thermal stimulation with and without kerogen (Egboga et al., 2017).

mechanism. At the end of heating, the temperature near the well increases, but the viscosity due to this temperature increase is decreased from 0.3 to 0.23, indicating viscosity reduction is not an important mechanism.

Heating will accelerate kerogen decomposition into oil and gas, and the decomposition will provide more pore space, resulting in an increase in porosity and permeability. It is found that the porosity of the studied model increases from 8% to 10%, and the permeability is increased from 0.0015 to 0.002 mD. From the absolute value increase in permeability, it seems that the effect of stimulation by heating is not very significant. Note their model does not include the mechanism of thermally driven fracturing. The question is "Can such heating increase a local pressure higher than a fracturing pressure?"

Fig. 14.4 shows the oil recovery for 7000 days for different recovery schemes. It shows that the oil recovery from thermal stimulation when the rock has 10% kerogen is 1% higher than that from the thermal stimulation without kerogen, indicating that kerogen decomposition due to heating is not a dominant mechanism. It is because the thermal heating and the resultant kerogen decomposition are concentrated locally near the heater. This observation is consistent with the permeability data.

The simulation model shows the oil recovery is increased from 7.2% for primary depletion to 11.5% for the depletion with 1000 days of heating. A cost analysis shows that the energy cost is $26 to produce an additional barrel of oil, which does not include the capital cost and implementation cost.

14.11 Microbial EOR

Microbial EOR is to inject microbial reaction products in the reservoir or inject microbes and nutrients in the reservoir so that microbial products are generated (Sheng, 2013b). These products could be acids, gases, solvents, biosurfactants, and biopolymers. Their EOR mechanisms are similar to those for gas injection and chemical injection. Microbial EOR is generally applied to formations of low temperature ($<98\ ^{\circ}C$) and high permeability (>50 mD) (Sheng, 2013c). However, one application in a low-permeability reservoir is reported (Liu et al., 2010), as briefed below.

In the MEOR pilot test zone, Wangyao, in Ansai Field, China, the porosity was 14%, the permeability was 5.22 mD, and the reservoir temperature was 45°C. The water cut reached 66.1%, and the average well oil rate was 1.48 tons/d before the test. One injector, Wang 15−5, was chosen with 7 producers around it. Total 1150 m^3 of solution was injected. The solution consisted of two slugs, the first slug being microbes and nutrients, and the second slug being microbial reaction products. The injection was operated from June 28 to August 21, 2009. The response time was 40 days. The injection might be effective within 300 days. By the end of 2009, the cumulative oil increased was 297.65 tons, and the estimated ultimate incremental oil was 550 tons.

Nomenclature

a	empirical constant for Langmuir-type isotherm
A	preexponential or frequency factor, t^{-1}, s^{-1} in Eq. 13.2, or $L^n t^{2n+1}/m^n$, $d^{-1} \cdot kPa^{-n}$ in Eq. 13.12, or area, L^2
$A(c_o)$	chemical reaction rate per unit volume, m/L^3t, $mol/(m^3 \cdot s)$
A_f	fracture surface area, L^2
A_o	rock area covered by oil, L^2
A_w	rock area covered by water, L^2
b	empirical constant for Langmuir-type isotherm
c	a constant, the ratio of the gravity force to the capillary force in Eq. 10.13 dimensionless, or a ratio of two parameters
C	heat capacity, L^2/t^2T, $kJ/(kg \cdot °C)$, or $J/(kg \cdot K)$, or a conversion constant in Eq. 9.45
C_A	precipitated asphaltene concentration in the liquid phase, m/L^3, meq/mL
C_H	empirical constant in Huh's equation
C_{pc}	capillary parameter, m/L^2t^2, $psi(Darcy)^{1/2}$
C_{surf}	surfactant concentration, L^3/L^3, vol.%
$\widehat{C}_{surf}$	adsorbed surfactant concentration, L^3/L^3, vol.%
c_t	total compressibility, Lt^2/m, psi^{-1}
CT	CT number measured in a substance
CT_a	CT number for air
CT_{ar}	CT number for a dry rock saturated with air
CT_g	CT number for gas
CT_{gor}	CT number for a system of gas, oil, and rock
CT_{gr}	CT number for a dry rock saturated with gas
CT_o	CT number for oil
CT_{or}	CT number for a dry rock saturated with oil
CT_r	CT number for a rock
D	pore diameter or penetration depth (Chapter 2), L, ft, or diffusion coefficient, L^2/t, cm^2/s (Chapter 10)
D_{pt}	average pore throat diameter, L
D_{ptc}	critical pore throat diameter, L
E_A	fractional pore volume occupied by asphaltene deposition, L^3, m^3
E	activation energy of the decomposition or oxidation reaction, L^2/t^2, kJ/mol, J/mol
E_{pc}	exponent of a capillary pressure function, dimensionless
F_c	capillary force, mL/t^2
F_v	viscous force, mL/t^2
g	gravitational constant, Lt^{-2}, m/s^2
G	magnetic gradient
h	height, L
H	enthalpy yet to be released, equals to $(H_o - H_t)$, mL^2/t^2, J
H_o	total released heat, mL^2/t^2, J

$\mathbf{H_t}$	release heat (enthalpy) at any time, mL^2/t^2, J
$\mathbf{I_w}$	wetting index, fraction
$\mathbf{k}$	permeability, L^2, mD
$\mathbf{K}$	K value, dimensionless
$\mathbf{k_0}$	permeability at the initial stress σ_0, L^2, mD,
$\mathbf{k_e^*}$	effective permeability of two phases at S_{wf}, mD
$\mathbf{k_r}$	relative permeability, dimensionless, fraction
$\mathbf{l}$	imbibition distance, L, m
$\mathbf{L}$	length, L, ft
$\mathbf{L_a}$	characteristic length, ft
$\mathbf{L_c}$	critical and characteristic length, ft
$\mathbf{M}$	molecular weight, m, g
$\mathbf{M_e}$	effective mobility, L^3t/m
$\mathbf{m_t}$	mass, m, kg
$\mathbf{n}$	reaction order or exponent in a k_r equation, dimensionless
$\mathbf{N_B}$	bond number, dimensionless
$\mathbf{N_C}$	capillary number, dimensionless
$\mathbf{(N_C)_C}$	critical capillary number, dimensionless
$\mathbf{(N_C)_{max}}$	maximum capillary number, dimensionless
$\mathbf{N_{pe}}$	Péclet number, dimensionless
$\mathbf{N_T}$	trapping number, dimensionless
$\mathbf{p}$	pressure, m/Lt^2, kPa, atm., psi
$\mathbf{p_{avg}}$	matrix average pressure, m/Lt^2, kPa
$\mathbf{p_c}$	capillary pressure, m/Lt^2, psi
$\mathbf{P_D}$	dimensionless pressure
$\mathbf{P_e^*}$	capillary pressure at Swf, m/Lt^2, psi
$\mathbf{p_{huff}}$	dimensionless pressure during the huff time
$\mathbf{p_{max}}$	maximum matrix average pressure in one cycle, psi
$\mathbf{p_{O_2}}$	partial pressure of oxygen, m/Lt^2, kPa
$\mathbf{p_{puff}}$	dimensionless pressure during the puff time
$\mathbf{p_w^*}$	vapor pressure of the pure water component, m/Lt^2
$\mathbf{Q}$	gross calorific value per unit mass of burned fuel, L^2/t^2, cal/g in Eq. 13.9, or heat of reaction per unit mass of fuel, L^2/t^2, J/mole in Eq. 13.13
$\mathbf{Q'}$	gross calorific value of per unit mass of burned fuel, L^2/t^2, BTU/lb in Eq. 13.10
$\mathbf{Q^*}$	heat of reaction in terms of the oxidizer, m/Lt^2, kcal/mol O_2 or BTU/ft^3 air in Eq. 13.11
$\mathbf{Q_{O_2}}$	enthalpy of the oxidation reaction, L^2/t^2, kJ/mol
$\mathbf{r}$	capillary or pore radius, L, m
$\mathbf{R}$	recovery factor by spontaneous water imbibition, or gas the constant (8.3147 J/(°K•mol)) or 0.082 (liter•atm)/(°K•mol))
$\mathbf{R^*}$	normalized oil recovery, dimensionless
$\mathbf{RF}$	oil recovery factor, fraction or %
$\mathbf{r_w}$	water drop radius, L
$\mathbf{S}$	saturation, L^3/L^3, fraction
$\mathbf{S_1}$	area representing the integral of average matrix pressure over the huff time (t_{huff}) in a cycle, m/Lt, psi·hour

$\mathbf{S_2}$	area defined by the maximum average matrix pressure during the huff time, p_{max}, times t_{huff}, m/Lt, psi·hour
$\mathbf{S_3}$	area representing the integral of the average matrix pressure over the puff time (t_{puff}) in a cycle, m/Lt, psi·hour
$\mathbf{S_4}$	area defined by the maximum average matrix pressure, p_{max}, times t_{puff}, m/Lt, psi·hour
$\overline{\mathbf{S}}$	normalized saturation, fraction
$\mathbf{S_{huff}}$	area defined by the maximum average matrix pressure during the huff time, m/Lt, psi·hour
$\mathbf{S_{org}}$	residual oil saturation under gas drive, L^3/L^3, fraction or %
$\mathbf{S_{puff}}$	area defined by the maximum average matrix pressure during the puff time, m/Lt, psi·hour
$\mathbf{S_{w2}}$	remaining (residual) *oil* saturation (S_{w2}) at the end of core flood, L^3/L^3, fraction or %
$\mathbf{S_{wc}}$	connate water saturation, L^3/L^3, fraction or %
$\mathbf{S_{wf}}$	water saturation behind imbibition front, L^3/L^3, fraction or %
$\mathbf{S_{wi}}$	initial water saturation, L^3/L^3, fraction or %
$\mathbf{t}$	time, t, s, hours or days
$\mathbf{T}$	temperature, T, °F, °C
$\mathbf{T_2}$	transverse relaxation time in porous medium, t, ms
$\mathbf{T_{2,bulk}}$	transverse relaxation time in bulk liquid t, ms
$\mathbf{T_a}$	ambient temperature, T, °K
$\mathbf{T_{a,c}}$	critical ambient temperature, T, °K
$\mathbf{t_D}$	dimensionless time
$\mathbf{T_E}$	echo spacing of measurement sequence, t, ms
$\mathbf{t_g}$	ratio of viscous force to gravity force
$\mathbf{t_{huff}}$	huff time, t, days
$\mathbf{T_p}$	parameter in a capillary desaturation curve equation for phase p
$\mathbf{t_{puff}}$	puff time, t, days
$\mathbf{T_r}$	reservoir initial temperature, T, °K
$\mathbf{T_{SI}}$	spontaneous ignition temperature, T, °K
$\mathbf{T_j}$	trapping number parameter for phase j, dimensionless
$\mathbf{u_L}$	superficial Darcy velocity, L/t, m/s, ft/d
$\mathbf{U}$	Darcy velocity, L/t, m/s
v or V	volume, L^3, m^3, cm^3
$\mathbf{v_L}$	interstitial velocity, L/t, m/s, ft/d
$\mathbf{v_{Lc}}$	critical interstitial velocity, L/t, m/s, ft/d
$\mathbf{V_o}$	oil volume, L^3, or oil spontaneous imbibition volume, L^3
$\mathbf{V_{o2}}$	normalized oil volume imbibed into the dry plug 2, L^3
$\mathbf{V_{om}}$	volume of oil in the microemulsion, L^3, cm^3
$\mathbf{V_{or}}$	rock bulk volume whose pores are fully saturated by oil, L^3, m^3, cm^3
$\mathbf{V_{osi}}$	oil spontaneous imbibition volume, L^3
$\mathbf{V_p}$	pore volume, L^3, m^3, cm^3
$\mathbf{V_r}$	rock grain volume, L^3, m^3, cm^3
$\mathbf{V_{sm}}$	volume of surfactant in the microemulsion, L^3, cm^3
$\mathbf{V_w}$	water spontaneous imbibition volume, L^3

V_{w1}	normalized water volume imbibed into the dry plug 1, L^3
V_{wsi}	water spontaneous imbibition volume, L^3
W	work, mL^2/t^2
W_{dry}	weight of a dry core, m, g
W_{end}	weight of the core plug at the end of each flood, m, g
W_{exp}	weight of a core after removing the core from the vessel, m, g
W_i	weight of a core with water and oil at the end of cycle i, m, g
WI_o	wettability index of oil
WI_w	wettability index of water
W_{omin}	minimum oil content to maintain in situ combustion defined in Eq. 13.16, m/L^3, kg/m^3
W_{r+w+o}	weight of a core saturated with water and oil initially, m, g
W_{sat}	weight of an oil saturated core, m, g
x	atomic H/C ratio of the fuel, or mole fraction, m/m
χ_o^W	mole fraction of oil in the aqueous phase, m/m, fraction
χ_o^O	mole fraction of oil in the oleic phase, m/m, fraction
χ_w^O	mole fraction of water in the oleic phase, m/m, fraction
χ_w^W	mole fraction of water in the aqueous phase, m/m, fraction
χ_s^O	mole fraction of surfactant in the oleic phase, m/m, fraction
χ_s^W	mole fraction of surfactant in the aqueous phase, m/m, fraction
x_{sw}	surfactant mole fraction in the aqueous surfactant solution, m/m, fraction
y	gas mole fraction in oil, m/m, fraction (Chapter 2)
y_w	mole fraction of water in the gas mixture, fraction

Greek symbols

α	surface deposition rate coefficient, 1/t, 1/day
β	CO/CO_2 ratio in the exhaust gases (Chapter 13), or entrainment rate coefficient, 1/L, 1/ft (Chapter 3), or stress sensitivity index or permeability-stress exponent (Chapters 2 and 12)
γ	plugging deposition rate coefficient, 1/L, 1/ft (Chapter 3), or interpolation parameter for k_r and p_c at different wettabilities (Chapter 9)
γ_g	gyromagnetic ration
γ_i	rate coefficient for instantaneous plugging deposition, 1/L, 1/ft
δ	dimensionless parameter defined in Eq. 13.14
δ_c	dimensionless parameter for the critical condition defined in Eq. 13.15
$\delta_{o,SI}$	fraction of oil volume by spontaneous imbibition in the total oil imbibition volume in Eq. 9.61
$\delta_{w,SI}$	fraction of water volume by spontaneous imbibition in the total water imbibition volume in Eq. 9.60
Δ	operator that refers to a discrete change
ΔH	heat value of crude from a DSC test, mL^2/t^2, J
ΔT_f	front temperature minus a room temperature from a combustion tube test, T, °K
θ	contact angle, degree
θ_{osi}	oil wetting angle during spontaneous imbibition
θ_{wsi}	water wetting angle during spontaneous imbibition
λ	thermal conductivity of the system, mL/t^3T, $W/(m \cdot K)$

μ	viscosity, m/Lt, mPa·s, or attenuation coefficient (Chapter 2)
μ_e	effective viscosity of two phases (but considered as one phase), $mL^{-1}t^{-1}$, mPa·s
μ_{gr}	attenuation coefficient for a core fully saturated with gas
μ_{or}	attenuation coefficient for a core fully saturated with oil
ρ	density, m/L^3, kg/m^3
ρ_{or}	density for a rock bulk fully saturated by oil, m/L^3, kg/m^3
σ	interfacial tension, mt^2, mN/m, or deposition constant for the snowball effect, dimensionless (Chapter 3)
π	constant ratio of the circumference to its diameter of a circle, or osmotic pressure (Chapter 12), m/Lt^2, atm.
ϕ	porosity, dimensionless, fraction or %
Φ	potential, m/Lt^2
Γ_s	adsorbed surfactant concentration, L^3/L^3, vol.%
ω	mixing parameter, fraction
ω_{kr}	interpolation scaling factor for k_r, dimensionless
ω_{pc}	interpolation scaling factor for p_c, dimensionless

Superscripts

e	indicates an end point in a k_r equation
high	at a high capillary or trapping number
L	lower bound
low	at a low capillary or trapping number
mw	mixed wet
U	upper bound
WA	wettability alteration only
ww	water–wet
ow	oil–wet

Subscript

0	initial
a	air
as	air–solid (interface)
b	bulk
b1,b2	dummy phase b1, b2
c	critical
D	dimensionless
f	formation
F	fracture
FI	forced imbibition
fm	fracture to matrix
g	gas
huff	during the huff time
i	initial
j	dummy phase j
j′	conjugate phase of phase j
nw	nonwetting

o	oil or original (initial)
oa	oil–air (interface)
or	residual oil
ow	water–oil (interface)
os	oil–solid (interface)
osa	oil–solid–air system
puff	during the puff time
P	phase
r	rock or residual
R	residual or rock
s	solid
SI	spontaneous imbibition
w, W	water
wa	water–air (interface)
wf	water displacement front
wo	water–oil (interface)
wr	residual water
ws	water–solid (interface)
wsa	water–solid–air system

References

Abousleiman, Y.N., Hoang, S.K., Tran, M.H., 2010. Mechanical characterization of small shale samples subjected to fluid exposure using the inclined direct shear testing device. International Journal of Rock Mechanics and Mining Sciences 47 (3), 355–367.

Abu-Khamsin, S.A., Iddris, A., Aggour, M.A., 2001. The spontaneous ignition potential of a super-light crude oil. Fuel 80 (10), 1415–1420.

Adegbesan, K.O., Donnelly, J.K., Moore, R.G., Bennion, D.W., 1987. Low temperature oxidation kinetic parameters for in situ combustion numerical simulation. Society of Petroleum Engineers Journal 2 (4), 573–582.

Aderibigbe, A.A., Lane, R.H., 2013. Rock/Fluid chemistry impacts on shale fracture behavior. In: Paper SPE 164102 Presented at the SPE International Symposium on Oilfield Chemistry, the Woodlands, Texas, USA, 8-10 April, 2013.

Adibhatla, B., Mohanty, K.K., February 2008. Oil recovery from fractured carbonates by surfactant-aided gravity drainage: laboratory experiments and mechanistic simulations. SPE Reservoir Evaluation and Engineering 119–130.

Adibhatla, B., Sun, X., Mohanty, K.K., 2005. Numerical studies of oil production from initially oil-wet fracture blocks by surfactant brine imbibitions. In: Paper SPE 97687 Presented at the SPE International Improved Oil Recovery Conference in Asia Pacific Held in Kuala Lumpur, Malaysia, 5–6 December.

Advanced Resources International, Inc, 2013. EIA/ARI world shale gas and shale oil resource assessment. In: Report Prepared for U.S. Energy Information Administration/ U.S. Department of Energy, June. Arlington, VA, USA.

Aguilera, R., May 2014. Flow units: from conventional to tight gas to shale gas to tight oil to shale oil reservoirs. SPE Reservoir Evaluation and Engineering 190–208.

Ahmadi, M., Sharma, M.M., Pope, G.A., Torres, D., McCulley, C.A., Linnemeyer, H., 2011. Chemical treatment to mitigate condensate and water blocking in gas wells in carbonate reservoirs. SPE Production and Operations 26 (1), 67–74.

Akbarabadi, M., Saraji, S., Piri, M., Georgi, D., Delshad, D., 2017. Nano-scale experimental investigation of in-situ wettability and spontaneous imbibition in ultra-tight reservoir rocks. Advances in Water Resources 107, 160–179.

Akin, S., Kovscek, A.R., 2003. Computed Tomography in Petroleum Engineering Research, vol. 215. Geological Society, London, Special Publications, pp. 23–28.

Akita, E., Moghanloo, R.G., Davudov, D., Tinni, A., 2018. A systematic approach for upscaling of the EOR results from lab-scale to well-scale in liquid-rich shale plays. In: Paper SPE 190188 Presented at the SPE Improved Oil Recovery Conference Held in Tulsa, Oklahoma, USA, 14–18 April.

Akrad, O.M., Miskimins, J.L., Prasad, M., 2011. The effects of fracturing fluids on shale rock mechanical properties and proppant embedment. In: Paper SPE 146658 Presented at the SPE Annual Technical Conference and Exhibition, Denver, Colorado, USA, 30 October-2 November.

Al-Anazi, H.A., 2003. Experimental Measurements of Condensate Blocking and Treatments in Low and High Permeability Cores. PhD dissertation. University of Texas at Austin, Austin, Texas, USA.

Al-Anazi, H.A., Walker, J.G., Pope, G.A., Sharma, M.M., Hackney, D.F., 2005. A successful methanol treatment in a gas/condensate reservoir: field application. SPE Production and Facilities 20 (1), 60–69.

Al-Bazali, T., 2013. A novel experimental technique to monitor the time-dependent water and ions uptake when shale interacts with aqueous solutions. Rock Mechanics and Rock Engineering 46, 1145–1156.

Al-Bazali, T., Zhang, J.G., Chenevert, M.E., Sharma, M.E., 2007. Factors controlling the compressive strength and acoustic properties of shales when interacting with water-based fluids. International Journal of Rock Mechanics and Mining Sciences 45 (5), 729–738, 2008.

Al-Yami, A.M., Gomez, F.A., AlHamed, K.I., Al-Buali, M.H., 2013. A successful field application of a new chemical treatment in a fluid blocked well in Saudi Arabia. In: Paper SPE 168086 Presented at the SPE Saudi Arabia Section Technical Symposium and Exhibition Held in Al-Khobar, Saudi Arabia, 19–22 May.

Alhammadi, A.M., AlRatrout, A., Singh, K., Bijeljic, B., Blunt, M.J., 2017. In situ characterization of mixed-wettability in a reservoir rock at subsurface conditions. Scientific Reports 7, 10753–10761.

Alharthy, N., Teklu, T., Kazemi, H., Graves, R., Hawthorne, S., Braunberger, J., Kurtoglu, B., 2015. Enhanced oil recovery in liquid-rich shale reservoirs: laboratory to field. In: Paper SPE 175034 Presented at the SPE Annual Technical Conference and Exhibition Held in Houston, Texas, USA, 28–30 September.

Altawati, F.S., 2016. An Experimental Study of the Effect of Water Saturation on Cyclic N_2 and CO_2 Injection in Shale Oil Reservoirs. Master's thesis. Texas Tech University, Lubbock, Texas, USA.

Alvarez, J.O., Neog, A., Jais, A., Schechter, D.S., 2014. Impact of surfactants for wettability alteration in stimulation fluids and the potential for surfactant EOR in unconventional liquid reservoirs. In: Paper SPE 169001 Presented at the SPE Unconventional Resources Conference – USA, The Woodlands, Texas, USA, 1–3 April.

Alvarez, J.O., Schechter, D.S., 2017. Wettability alteration and spontaneous imbibition in unconventional liquid reservoirs by surfactant additives. SPE Reservoir Evaluation and Engineering 20 (01), 107–117.

Alvarez, J.O., Saputra, I.W.R., Schechter, D.S., December 2018. The impact of surfactant imbibition and adsorption for improving oil recovery in the Wolfcamp and Eagle Ford reservoirs. SPE Journal 2103–2117.

Amott, E., 1959. Observations relating to the wettability of porous rock. Transactions of the American Institute of Mining, Metallurgical and Petroleum Engineers, Incorporated (AIME) 216, 156–162.

Anderson, W.G., 1986. Wettability literature survey part 2: wettability measurement. Journal of Petroleum Technology 38 (11), 1246–1262.

Anderson, W.G., 1987. Wettability literature survey-part 5: the effects of wettability on relative permeability. Journal of Petroleum Technology 39 (11), 1453–1468.

Andrew, M., Bijeljic, B., Blunt, M.J., 2014. Pore-scale contact angle measurements at reservoir conditions using X-ray microtomography. Advances in Water Resources 68, 24–31.

Appel, M., 2004. Nuclear magnetic resonance and formation porosity. Petrophysics 45 (03), 296–307.

Artun, E., Ertekin, T., Watson, R., Miller, B., 2011. Performance evaluation of cyclic pressure pulsing in a depleted, naturally fractured reservoir with stripperwell production. Petroleum Science and Technology 29, 953–965.

Asadi, M., Woodroof, R.A., Himes, R.E., May 2008. Comparative study of flowback analysis using polymer concentrations and fracturing-fluid tracer methods: a field study. SPE Production and Operations 147–157.

Ashoori, S., Balavi, A., 2014. An investigation of asphaltene precipitation during natural production and the CO_2 injection process. Petroleum Science and Technology 32 (11), 1283–1290.

Atkin, R., Craig, V.S.J., Wanless, E.J., Biggs, S., 2003. Mechanism of cationic surfactant adsorption at the solid–aqueous interface. Advances in Colloid and Interface Science 103, 219–304.

Atkinson, B.K., 1979. A fracture mechanics study of subscritical tensile cracking of quartz in wet environments. Pure and Applied Geophysics 117, 1011–1024.

Atkinson, B.K., 1982. Subcritical crack propagation in rocks: theory, experimental results and applications. Journal of Structural Geology 4 (1), 41–56.

Atkinson, B.K., Meredith, P.G., 1981. Stress corrosion cracking of quartz: a note on the influence of chemical environment. Tectonophysics 77, T1–T11.

Austad, T., Milter, J., 1997. Spontaneous imbibition of water into low permeable chalk at different wettabilities using surfactants. In: Paper SPE 37236 Presented at the International Symposium on Oilfield Chemistry Held in Houston, Texas, USA, 18-19 February.

Austad, T., Standnes, D.C., 2003. Spontaneous imbibition of water into oil-wet carbonates. Journal of Petroleum Science and Engineering 39, 363–376.

Austad, T., Matre, B., Milter, J., Sævareid, A., Øyno, L., 1998. Chemical flooding of oil reservoirs 8. Spontaneous oil expulsion from oil- and water-wet low permeable chalk material by imbibition of aqueous surfactant solutions. Colloids and Surfaces A: Physicochemical and Engineering Aspects 137 (1–3), 117–129.

Austin, U.T., 2009. A Three-Dimensional Chemical Flood Simulator (UTCHEM, Version 9.95). University of Texas at Austin, Austin, Texas.

Babadagli, T., December 2001. Scaling of concurrent and countercurrent capillary imbibition for surfactant and polymer injection in naturally fractured reservoirs. SPE Journal 465–478.

Bae, J.H., 1977. Characterization of crude oil for fireflooding using thermal analysis methods. SPE Journal 17 (03), 211–218.

Baker, R., Dieva, R., Jobling, R., Lok, C., 2016. The myths of waterfloods, EOR floods and how to optimize real injection schemes. In: Paper SPE 179536 Presented at the SPE Improved Oil Recovery Symposium Held in Tulsa, Oklahoma, USA, 11-13 April.

Bang, V., 2007. Development of a Successful Chemical Treatment for Gas Wells with Condensate or Water Blocking Damage. PhD dissertation. University of Texas at Austin, Austin, Texas, USA.

Bang, V.S.S., Yuan, C., Pope, G.A., Sharma, M.M., Baran, J.R., Skildum, J., Linnemeyer, H.C., 2008. Improving productivity of hydraulically fractured gas condensate wells by chemical treatment. In: Paper OTC 19599 Presented at the Offshore Technology Conference Held in Houston, Texas, USA, 5–8 May.

Bang, V.S.S., Pope, G.A., Sharma, M.M., Baran, J.R., 2009. Development of a successful chemical treatment for gas wells with liquid blocking. In: Paper SPE 124977 Presented at the Annual Technical Conference and Exhibition Held in New Orleans, Louisiana, UAS, 4–7 October.

Bang, V.S.S., Pope, G., Sharma, M.M., Baran, J., Ahmadi, M., 2010. A new solution to restore productivity of gas wells with condensate and water blocks. SPE Reservoir Evaluation and Engineering 13 (2), 323–331.

Barree, R.D., Mukherjee, H., 1995. Engineering criteria for fracture flowback procedures. In: Paper SPE 29600 Presented at the Low Permeability Reservoirs Symposium Held in Denver Calorado, USA, 19-22 March. https://doi.org/10.2118/29600-MS.

Barzin, Y., 2013. An Experimental and Numerical Study of the Oxidation/combustion Reaction Kinetics in High Pressure Air Injection Process. PhD dissertation. University of Galgary, Galgary, Alberta, Canada.

Barzin, Y., Moore, R.G., Mehta, S.A., Ursenbach, M.G., Tabasinejad, F., 2010. Impact of distillation on the combustion kinetics of high pressure air injection (HPAI). In: Paper SPE 129691 Presented at the SPE Improved Oil Recovery Symposium Held in Tulsa, Oklahoma, USA, 24–28 April. https://doi.org/10.2118/129691-MS.

Barzin, Y., Moore, R.G., Mehta, S.A., Ursenbach, M.G., Tabasinejad, F., 2013. A comprehensive kinetics model for light oil oxidation/combustion reactions under high pressure air injection process (HPAI). In: Paper SPE 166483 Presented at the SPE Annual Technical Conference and Exhibition Held in New Orleans, Louisiana, USA, 30 September-2 October.

Behbahani, H.S., Blunt, M.J., 2005. Analysis of imbibition in mixed-wet rocks using pore-scale modeling. SPE Journal 10 (4), 466–474.

Behbahani, T.J., Ghotbi, C., Taghikhani, V., Shahrabadi, A., 2012. Investigation on asphaltene deposition mechanisms during CO_2 flooding processes in porous media: a novel experimental study and a modified model based on multilayer theory for asphaltene adsorption. Energy and Fuels 26 (8), 5080–5091.

Behbahani, T.J., Ghotbi, C., Taghikhani, V., Shahrabadi, A., 2013. A modified scaling equation based on properties of bottom hole live oil for asphaltene precipitation estimation under pressure depletion and gas injection conditions. Fluid Phase Equilibria 358, 212–219.

Behbahani, T.J., Ghotbi, C., Taghikhani, V., Shahrabadi, A., 2015. Experimental study and Mathematical modeling of asphaltene deposition mechanism in core sample. Journal of Oil and Gas Science and Technology 70 (6), 909–1132.

Behnsen, J., Faulkner, D.R., 2011. Water and argon permeability of phyllosilicate powders under medium to high pressure. Journal of Geophysical Research 116, B12203.

Belgrave, J.D.M., Moore, R.G., Ursenbach, M.G., Bennion, D.W., 1993. A comprehensive approach to in-situ combustion modeling. SPE Advanced Technology Series 1 (1), 98–107.

Bennion, D.B., Thomas, F.B., Bietz, R.F., Bennion, D.W., 1999. Remediation of water and hydrocarbon phase trapping problems in low permeability gas reservoirs. Petroleum Society of Canada 38 (08). https://doi.org/10.2118/99-08-01.

Bertoncello, A., Wallace, J., Blyton, C., Honarpour, M.M., Kabir, S., 2014. Imbibition and water blockage in unconventional reservoirs: well-management implications during flowback and early production. In: Paper Presented at the SPE/EAGE European Unconventional Resources Conference and Exhibition Held on 25 February. https://doi.org/10.2118/167698-PA.

Bi, Z., Liao, W., Qi, L., 2004. Wettability alteration by CTAB adsorption at surfaces of SiO_2 film or silica gel powder and mimic oil recovery. Applied Surface Science 221 (1–4), 25–31.

Bilden, D.M., Fletcher, P.A., Montgomery, C.T., Guillory, R.J., Allen, T.P., 1995. The effect of long-term shut-in periods on fracture conductivity. In: Paper SPE 30493 Presented at the SPE Annual Technical Conference and Exhibition Held in Dallas, Texas, USA, 22–25 October. https://doi.org/10.2118/30493-MS.

Bol, G.M., Wong, S.-W., Davidson, C.J., Woodland, D.C., 1994. Borehole stability in shales. SPE Drilling and Completion 9 (2), 87–94.

Bolouri, H., Schaffie, M., Kharrat, R., Ghazanfari, M., Ghoodjani, E., 2013. An experimental and modeling study of asphaltene deposition due to CO_2 miscible injection. Petroleum Science and Technology 31 (2), 129–141.

Boneau, D.F., Clampitt, R.L., 1977. A surfactant system for the oil-wet sandstone of the north burbank unit. Journal of Petroleum Technology 29, 501–506.

Bostrom, N., Chertov, M., Pagels, M., Willberg, D., Chertova, A., Davis, M., Zagorski, W., 2014. The time-dependent permeability damage caused by fracture fluid. In: Paper SPE 168140 Presented at the SPE International Symposium and Exhibition on Formation Damage Control Held in Lafayette, Louisiana, USA, 26-28 February. https://doi.org/10.2118/168140-MS.

Bourbiaux, B.J., Kalaydjian, F.J., 1990. Experimental study of cocurrent and countercurrent flows in natural porous media. SPERE 5 (3), 361–368.

Brooks, R.H., Corey, A.T., 1966. Properties of porous media affecting fluid flow. Journal of the Irrigation and Drainage Division 6, 61–88.

Brown, R.J.S., Fatt, I., 1956. Measurements of fractional wettability of oil field' rocks by the nuclear magnetic relaxation method. In: Paper SPE 743 Presented at Fall Meeting of the Petroleum Branch on AIME Held in Los Angeles, California, USA, 14-17 October. https://doi.org/10.2118/743-G.

Buckley, S.E., Leverett, M.C., 1942. Mechanisms of fluid displacement in sands. Transactions of the American Institute of Mining, Metallurgical and Petroleum Engineers, Incorporated (AIME) 146, 107–116.

Burger, J.G., Sahuquet, B.C., 1972. Chemical aspects of in-situ combustion–heat of combustion and kinetics. SPE Journal 12 (05), 410–422. https://doi.org/10.2118/3599-PA.

Butler, M., Trueblood, J.B., Pope, G.A., Sharma, M.M., Baran Jr., J.R., Johnson, D., 2009. A field demonstration of a new chemical stimulation treatment for fluid-blocked gas wells. In: Paper SPE 125077 Presented at the SPE Annual Technical Conference and Exhibition. New Orleans, Louisiana, USA, 4–7 October.

Cai, J.C., Yu, B.M., 2011. A discussion of the effect of tortuosity on the capillary imbibition in porous media. Transport in Porous Media 89 (2), 251–263.

Cai, J., Yu, B., 2012. Advances in studies of spontaneous imbibition in porous media. Advances in Mechanics 42 (6), 735–754.

Carminati, S., Del Gaudio, L., Zausa, F., Brignoli, M., 1999. How do anions in water-based Muds affect shale stability?. In: Paper SPE 50712 Presented at the SPE International Symposium on Oilfield Chemistry, 16–19 February, Houston, Texas.

Cazabat, A.M., Langevin, D., Pouchelon, A., 1980. Light-scattering study of water-oil microemulsions. Journal of Colloid and Interface Science 73 (1), 1–12.

Chakraborty, N., Karpyn, Z.T., 2015. Gas permeability evolution with soaking time in ultra- tight shales. In: Paper SPE 178740 Presented at the SPE Annual Technical Conference and Exhibition, Houston, Texas, USA, 28–30 September.

Chen, P., Mohanty, K., 2013. Surfactant-mediated spontaneous imbibition in carbonate rocks at harsh reservoir conditions. SPE Journal 18 (1), 124–133. https://doi.org/10.2118/153960-PA.

Chen, P., Mohanty, K.K., 2014. Wettability alteration in high temperature carbonate reservoirs. In: Paper SPE 169125 Presented at the SPE Improved Oil Recovery Symposium, Tulsa, Oklahoma, USA, 12–16 April. https://doi.org/10.2118/169125-MS.

Chen, P., Mohanty, K.K., 2015. Surfactant-Enhanced oil recovery from fractured oil-wet carbonates: effects of low IFT and wettability alteration. In: Paper SPE 173797 Presented at the SPE International Symposium on Oilfield Chemistry Held in Woodland, Texas, USA, 13–15 April. https://doi.org/10.2118/173797-MS.

Chen, Z., Narayan, S.P., Yang, Z., Rahman, S.S., 2000. An experimental investigation of hydraulic behaviours of fractures and joints in granitic rock. International Journal of Rock Mechanics and Mining Sciences 37, 1061–1071.

Chen, H.L., Lucas, L.R., Nogaret, L.A.D., Yang, H.D., Kenyon, D.E., 2001. Laboratory monitoring of surfactant imbibition with computerized tomography. SPE Reservoir Evaluation and Engineering 2, 16–25.

Chen, C., Balhoff, B., Mohanty, K.K., 2013a. Effect of reservoir Heterogeneity on improved shale oil recovery by CO_2 huff-n-puff. In: Paper SPE 164553 Presented at the SPE Unconventional Resources Conference Held in Woodlands, Texas, USA, 10–12 April.

Chen, Z., Wang, L., Duan, Q., et al., 2013b. High-pressure air injection for improved oil recovery: low-temperature oxidation models and thermal effect. Energy and Fuels 27 (2), 780–786. https://pubs.acs.org/doi/abs/10.1021/ef301877a.

Chen, Q., You, L., Kang, Y., Dou, L., Sheng, J.J., 2018. Gypsum-crystallization-induced fracturing during Shale–Fluid reactions and application for shale stimulation. Energy & Fuels 32, 10367–10381.

Chen, C., Balhoff, B., Mohanty, K.K., August 2014. Effect of reservoir heterogeneity on primary recovery and CO_2 huff 'n' puff recovery in shale-oil reservoirs. SPE Reservoir Evaluation and Engineering 404–413.

Chen, Q., Kang, Y., You, Y., Yang, P., Zhang, X., Cheng, Q., 2017. Change in composition and pore structure of Longmaxi black shale during oxidative dissolution. International Journal of Coal Geology 172, 95–111.

Chenevert, M.E., 1969. Adsorptive pore pressures of Argillaceous rocks. In: Paper Presented at the 11th U.S. Symposium on Rock Mechanics (USRMS), June 16–19, Berkeley, CA.

Chenevert, M.E., September 1970. Shale alteration by water adsorption. Journal of Petroleum Technology 1141–1148. https://doi.org/10.2118/2401-PA.

Cheng, Y., 2012. Impact of water dynamics in fractures on the performance of hydraulically fractured wells in gas-shale reservoirs. Journal of Canadian Petroleum Technology 51 (2), 143–151. https://doi.org/10.2118/127863-PA.

Cheng, J.Y., Wan, Z.J., Zhang, Y.D., 2015. Experimental study on anisotropic strength and deformation behavior of a coal measure shale under room dried and water saturated conditions. Shock and Vibration 1–13.

Chou, S.I., Shah, D.O., 1980. The droplet size in oil-external microemulsions using the membrane diffusion technique. Journal of Colloid and Interface Science 78 (1), 249–252.

Christopher, C.A., 1995. Air injection for light and medium gravity reservoirs. In: Paper Presented at the DTI Share Meeting (1) Held in London, 20 July.

Chu, C., 1982. State-of-the-Art review of fireflood field projects. Journal of Petroleum Technology 34 (01), 19–36. https://doi.org/10.2118/9772-PA.

Clara, C., Durandeau, M., Quenault, G., Nguyen, T.-H., 2000. Laboratory studies for light-oil air injection projects: potential application in handil field. SPE Reservoir Evaluation and Engineering 3 (3), 239–248. https://doi.org/10.2118/64272-PA.

Clark, A., 2009. Determination of recovery factor in the Bakken formation, Mountrail County, ND. In: Paper SPE 133719 Presented at the SPE Annual Technical Conference and Exhibition Held in New Orleans, Louisiana, USA, 4–7 October.

Cleary, M.P., Doyle, R.S., Teng, E.Y., Cipolla, C.L., Meehan, D.N., Massaras, L.V., Wright, T.B., 1994. Major new developments in hydraulic fracturing, with documented reductions in job costs and increases in normalized production. In: Paper SPE 28565 Presented at the SPE Annual Technical Conference and Exhibition Held in New Orleans, Louisiana, USA, 25–28 September. https://doi.org/10.2118/28565-MS.

Coats, A.W., Redfern, J.P., 1964. Kinetic parameters from thermogravimetric data. Nature 201, 68–69.

CMG (Computer Modeling Group), 2014. GEM User Guide. Compositional & Unconventional reservoir simulator, Calgary, Alberta, Canada.

CMG (Computer Modelling Group), 2016. STARS User Guide: Advanced Processes & Thermal Reservoir Simulator (Calgary, Alberta, Canada).

Coulter, G.R., Wells, R.D., 1972. The advantages of high proppant concentration in fracture stimulation. Journal of Petroleum Technology 24 (06), 643–650. https://doi.org/10.2118/3298-PA.

Crafton, J.W., 1998. Well evaluation using early time post-stimulation flowback data. In: Paper SPE 49223 Presented at the SPE Annual Technical Conference and Exhibition Held in New Orleans, Louisiana, USA, 27–10 September. https://doi.org/10.2118/49223-MS.

Crafton, J.W., 2008. Modeling flowback behavior or flowback equals "slowback". In: Paper SPE 119894 Presented at the SPE Shale Gas Production Conference Held in Fort Worth, Texas, USA, 14-16 November https://doi.org/10.2118/119894-MS.

Crafton, J.W., Noe, S., 2013. Impact of delays and shut-ins on well productivity. In: Paper SPE 165705 Presented at the SPE Eastern Regional Meeting Held in Pittsburgh, Pennsylvania, USA, 20–22 August. https://doi.org/10.2118/165705-MS.

Crafton, J.W., Penny, G.S., Borowski, D.M., 2009. Micro-emulsion effectiveness for twenty four wells, Eastern Green River, Wyoming. In: Paper SPE 123280 Presented at the Rocky Mountain Petroleum Technology Conference. Denver, Colorado, USA, 14–16 April.

Cude, H.E., Hulett, G.A., 1920. Some properties of charcoals. Journal of the American Chemical Society 42 (3), 391–401.

Cuiec, L.E., Bourbiaux, B., Kalaydjian, F., 1994. Oil recovery by imbibition in low-permeability chalk. SPE Formation Evaluation 9 (3), 200–208.

Curnow, J.S., Tutuncu, A.N., 2016. A coupled geomechanics and fluid flow modeling study for hydraulic fracture design and production optimization in an eagle ford shale oil reservoir. In: Paper SPE 179165 Presented at the SPE Hydraulic Fracturing Technology Conference in The Woodlands, Texas, USA, 9–11 February.

Cuss, R., Wiseall, A., Hennissen, J., Waters, C., Kemp, S., 2015. Hydraulic Fracturing: A Review of Theory and Field Experience. British Geological Survey, Keyworth, Nottingham, NG12 5GG, UK.

Dandekar, A.Y., 2013. Petroleum Reservoir Rock and Fluid Properties, Second Version. CRC Press/Taylor & Francis Group, Boca Raton, Florida, USA.

Dawson, M., Nguyen, D., Champion, N., Li, H., 2015. Designing an optimized surfactant flood in the Bakken. In: Paper SPE 175937 Presented at the SPE/CSUR Unconventional Resources Conference Held in Calgary, Alberta, Canada, 20-22 October.

de Zwart, A.H., van Batenburg, D.W., Blom, C.P.A., Tsolakidis, A., Glandt, C.A., Boerrigter, P., 2008. The modeling challenge of high pressure air injection. In: Paper SPE 113917 Presented at the SPE Symposium on Improved Oil Recovery Held in Tulsa, Oklahoma, USA, 20-23 April. https://doi.org/10.2118/113917-MS.

Dehghanpour, H., Zubair, H.A., Chhabra, A., Ullah, A., 2012. Liquid intake of organic shales. Energy and Fuels 26 (2012), 5750–5758.

Dehghanpour, H., Lan, Q., Saeed, Y., Fei, H., Qi, Z., 2013. Spontaneous imbibition of brine and oil in gas shales: effect of water adsorption and resulting microfractures. Energy and Fuels 27, 3039–3049.

Delshad, M., Najafabadi, N.F., Sepehrnoori, K., 2008. Scale up methodology for wettability modification in fractured carbonates. In: Paper SPE 118915 Presented in the SPE Reservoir Simulation Symposium Held in Woodlands, Texas, USA, 2–4 February.

Dietz, D.N., 1970. Wet underground combustion, state of the art. Journal of Petroleum Technology 22 (5), 605–617.

Donaldson, E.C., Thomas, R.D., Lorenz, P.B., 1969. Wettability determination and its effect on recovery efficiency. SPE Journal 9 (01), 13–20.

Dong, B., Meng, M., Qiu, Z., Lu, Z., Zhang, Y., Zhong, H., 2019. Formation damage prevention using microemulsion in tight sandstone gas reservoir. Journal of Petroleum Science and Engineering 173, 101–111.

Dong, C., Hoffman, B.T., 2013. Modeling gas injection into shale oil reservoirs in the Sanish field, North Dakota. In: Paper SPE 168827 Presented at the Unconventional Resources Technology Conference Held in Denver, Colorado, USA, 12–14 August.

Drici, O., Vossoughi, S., 1985. Study of the surface area effect on crude oil combustion by thermal analysis techniques. Journal of Petroleum Technology 37 (04), 731–735.

Druganova, E.V., Surguchev, L.M., Ibatulin, R.R., 2010. Air injection at Mordovo-Karmalskoye field: simulation and IOR evaluation. In: Paper SPE136020 Presented at the SPE Russion Oil and Gas Conference and Exhibition Held in Moscow Russia, 26–28 October.

Duan, Q.B., Yang, X.S., 2014. Experimental studies on gas and water permeability of fault rocks from the rupture of the 2008 Wenchuan earthquake, China. Science China Earth Sciences 57 (11), 2825–2834.

Dunning, J.D., Lewis, W.L., Dunn, D.E., 1980. Chemomechanical weakening in the presence of surfactants. Journal of Geophysical Research 85, 5344–5354.

Dutta, R., Lee, C.-H., Odumabo, S., Ye, P., Walker, S.C., Karpyn, Z.T., Ayala, H.,L.F., 2014. Experimental investigation of fracturing-fluid migration caused by spontaneous imbibition in fractured low-permeability sands. SPE Reservoir Evaluation and Engineering 17 (1), 74–81.

Egboga, N.U., Mohanty, K.K., Balhoff, M.T., 2017. A feasibility study of thermal stimulation in unconventional shale reservoirs. Journal of Petroleum Science and Engineering 154, 576–588.

EIA, 2018a. Oil and Natural Gas Resources and Technology, Issue in Focus from the Annual Energy Outlook 2018, March, Independent Statistics & Analysis. U.S. Department of Energy, Washington, USA.

EIA, 2018b. Annual Energy Outlook 2018 with Projections to 2050, February. U.S. Department of Energy, Washington, USA.

EIA (Energy Information Administration), 2016. Initial Production Rates in Tight Oil Formations Continue to Rise, 11 February 2016. https://www.eia.gov/todayinenergy/detail.cfm?id=24932.

Ely, J.W., 1996. Experience proves forced fracture closure works. World Oil 217 (1), 37–41.

Ely, J.W., Arnold, W.T., Holditch, S.A., 1990. New techniques and quality control find success in enhancing productivity and minimizing proppant flowback. In: Paper SPE 20708 Presented at the SPE Annual Technical Conference and Exihibition Held in New Orleans, Louisiana, USA, 23–26 September. https://doi.org/10.2118/20708-MS.

Engelder, T., Cathles, L.M., Bryndzia, L.T., 2014. The fate of residual treatment water in gas shale. Journal of Unconventional Oil and Gas Resources 7, 33–48.

Ershaghi, I., Hashemi, R., Caothien, S.C., Abdassah, D., 1986. Injectivity losses under particle cake buildup and particle invasion. In: Paper SPE 15073 Presented at the SPE California Regional Meeting Held in Oakland, California, USA, 2–4 April. https://doi.org/10.2118/15073-MS.

Ewy, R.T., Stankovic, R.J., June 2010. Shale Swelling, Osmosis, and Acoustic Changes Measured under Simulated Downhole Conditions. SPE Drilling & Completion, pp. 177–186. https://doi.org/10.2118/78160-PA.

Ezulike, O., Dehghanpour, H., Virues, C., Hawkes, R.V., Jones, R.S., 2016. Flowback fracture closure: a key factor for estimating effective pore volume. SPE Reservoir Evaluation and Engineering 19 (04), 567–582. https://doi.org/10.2118/175143-PA.

Fai-Yengo, V., Rahnema, H., Alfi, M., 2014. Impact of light component stripping during CO_2 injection in Bakken formation. In: Paper SPE 1922932 Presented at the SPE/AAPG/SEG Unconventional Resources Technology Conference, 25–27August, Denver, Colorado, USA.

Fakcharoenphol, P., Charoenwongsa, S., Kazemi, H., Wu, Y.-S., October 2013. The effect of water-induced stress to enhance hydrocarbon recovery in shale reservoirs. SPE Journal 897–909. https://doi.org/10.2118/158053-PA.

Fakcharoenphol, P., Kurtoglu, B., Kazemi, H., Charoenwongsa, S., Wu, Y.-S., 2014. The effect of osmotic pressure on improve oil recovery from fractured shale formations. In: Paper SPE 168998 Presented at the SPE Unconventional Resources Conference Held in Woodland, Texas, USA, 1–3 April. https://doi.org/10.2118/168998-MS.

Fakcharoenphol, P., Torcuk, M., Kazemi, H., Wu, Y.S., 2016. Effect of shut-in time on gas flow rate in hydraulic fractured shale reservoirs. Journal of Natural Gas Science and Engineering 32 (May), 109–121. https://doi.org/10.1016/j.jngse.2016.03.068.

Fan, W.G., Liu, Q.H., 2016. Development test of tight oil in Hailaer oilfield. Sino-Global Energy 21, 54–57.

Fan, C., Zan, C., Zhang, Q., Shi, L., Hao, Q., Jiang, H., Wei, F., 2015. Air injection for enhanced oil recovery: in situ monitoring the low-temperature oxidation of oil through thermogravimetry/differential scanning calorimetry and pressure differential scanning calorimetry. Industrial and Engineering Chemistry Research 54 (26), 6634–6640.

Fassihi, M.R., Kovscek, A.R., 2017. Low-Energy Processes for Unconventional Oil Recovery. Society of Petroleum Engineers, Richardson, Texas, USA.

Fassihi, M.R., Ramey Jr., H.J., Brigham, W.E., 1982. Laboratory Combustion Tube Studies, Final Report (No. DOE/ET/12056-22). Department of Energy, Washington, DC (USA).

Fassihi, M.R., Brigham, W.E., Ramey, H.J., August 1984. Reaction kinetics of in-situ combustion: Part 2 – Modeling. SPE Journal 408–416.

Fassihi, M.R., Yannimaras, D.V., Newbold, F., Belgrave, J., 2000. Laboratory and simulation characterization of light oil air injection. In Situ 24 (4), 219–249.

Fassihi, M.R., Moore, R.G., Mehta, S.A., Ursenbach, M.G., August 2016. Safety considerations for high-pressure air injection into light-oil reservoirs and performance of the Holt sand unit project. SPE Production and Operations 197–206.

Faulkner, D., Rutter, E., 2000. Comparisons of water and argon permeability on natural clay-bearing fault gouge under high pressure at 20°C. Journal of Geophysical Research 105, 16415–16426.

Feng, L., Xu, L., 2015. Implications of shale oil compositions on surfactant efficacy for wettability alteration. In: Paper 172974 Presented at the SPE Middle East Unconventional Resources Conference and Exhibition, Muscat, Oman, 26–28 January.

Ferno, M.A., Haugen, A., Graue, A., 2012. Surfactant prefloods for integrated EOR in fractured, oil-wet carbonate reservoirs. In: Paper SPE 159213 Presented at the SPE Annual Technical Conference and Exhibition Held in San Antonio, Texas, USA, 8–10 October.

Fischer, H., Morrow, N.R., 2006. Scaling of oil recovery by spontaneous imbibition for wide variation in aqueous phase viscosity with glycerol as the viscosifying agent. Journal of Petroleum Science and Engineering 52 (1–4), 35–53.

Fischer, H., Wo, S., Morrow, N.R., 2006. Modeling the effect of viscosity ratio on spontaneous imbibition. SPE Reservoir Evaluation and Engineering 577–589.

Fontaine, J., Johnson, N., Schoen, D., 2008. Design, execution, and evaluation of a "typical" Marcellus shale slickwater stimulation: a case history. In: Paper SPE 117772 Presented at the SPE Eastern Regional/AAPG Eastern Section Joint Meeting, Pittsburgh, Pennsylvania, USA, October 11–15, 2008. https://doi.org/10.2118/117772-MS.

Fragoso, A., Selvan, K., Aguilera, R., 2018a. Breaking a paradigm: can oil recovery from shales be larger than oil recovery from conventional reservoirs? the answer is yes!. In: Paper SPE 189784 Presented at the SPE Canada Unconventional Resources Conference Held in Calgary, Alberta, Canada, 13–14 March. https://doi.org/10.2118/189784-MS.

Fragoso, A., Selvan, K., Aguilera, R., 2018b. An investigation on the feasibility of combined refracturing of horizontal wells and huff and puff gas injection for improving oil recovery from shale petroleum reservoirs. In: Paper SPE 190284 Presented at the SPE Improved Oil Recovery Conference Held in Tulsa, Oklahoma, USA, 14–18 April. https://doi.org/10.2118/190284-MS.

Freitag, N.P., 2016. Chemical-Reaction mechanisms that govern oxidation rates during in-situ combustion and high-pressure air injection. SPE Reservoir Evaluation and Engineering 19 (04), 645–654. https://doi.org/10.2118/170162-PA.

Freitag, N.P., Verkoczy, B., 2005. Low-Temperature oxidation of oils in terms of SARA fractions: why simple reaction models don't work. Journal of Canadian Petroleum Technology 44 (03), 54–61. https://doi.org/10.2118/05-03-05.

Fu, Y.-F., Wong, Y.-L., Poon, C.-S., et al., 2004. Experimental study of micro/macro crack development and stress-strain relations of cement-based composite materials at elevated temperature. Cement and Concrete Research 34 (5), 789–797.

Gala, D., Sharma, M., 2018. Compositional and geomechanical effects in huff-n-puff gas injection IOR in tight oil reservoirs. In: Paper SPE 191488 Presented at the SPE Annual Technical Conference and Exhibition Held in Dallas, Texas, USA IN 24–26 September. https://doi.org/10.2118/191488-MS.

Gamadi, T.D., Sheng, J.J., Soliman, M.Y., 2013. An experimental study of cyclic gas injection to improve shale oil recovery. In: Paper SPE 166334 Presented at the SPE Annual Technical Conference and Exhibition Held in New Orleans, Louisiana, USA, 30 September–2 October.

Gamadi, T., Elldakli, F., Sheng, J.J., 2014a. Compositional simulation evaluation of EOR potential in shale oil recovery by cyclic natural gas injection. In: Paper SPE 1922690 (URTeC 1922690) Presented at the Unconventional Resources Technology Conference Held in Denver, Colorado, USA, 25–27 August 2014.

Gamadi, T.D., Sheng, J.J., Soliman, M.Y., Menouar, H., Watson, M.C., Emadibaladehi, H., 2014b. An experimental study of cyclic CO_2 injection to improve shale oil recovery. In: Paper SPE 169142 Presented at the SPE Improved Oil Recovery Symposium Held in Tulsa, Oklahoma, USA, 12–16 April.

Ganjdanesh, R., Rezaveisi, M., Pope, G.A., Sepehrnoori, K., 2015. Treatment of condensate and water blocks in hydraulic fractured shale gas-condensate reservoirs. In: Paper SPE 17545 Presented at the SPE Annual Technical Conference and Exhibition Held in Houston, Texas, USA, 28–30 September.

Garrels, R.M., Thompson, M.E., 1960. Oxidation of pyrite by iron sulfate solutions. American Journal of Science 258, 57–67.

Gates, C.F., Ramey, H.J., 1958. Field results of south Belridge thermal recovery experiment. Petroleum Transaction, AIME 203, 236–244.

Ghaderi, S.M., Clarkson, C.R., Kaviani, D., 2012. Evaluation of recovery performance of miscible displacement and WAG processes in tight oil formations. In: Paper SPE 152084 Presented at the SPE/EAGE European Unconventional Resources Conference and Exhibition, Vienna, Austria, 20–22 March.

Ghanbari, E., Dehghanpour, H., 2015. Impact of rock fabric on water imbibition and salt diffusion in gas shales. International Journal of Coal Geology 138 (January), 55–67. https://doi.org/10.1016/j.coal.2014.11.003.

Ghanbari, E., Abbasi, M.A., Dehghanpour, H., Bearinger, D., 2013. Flowback volumetric and chemical analysis for evaluating load recovery and its impact on early-time production. In: Paper SPE 167165 Presented at the SPE Unconventional Resources Conference–Canada Held in Calgary, Alberta, Canada, 5–7 November. https://doi.org/10.2118/167165-MS.

Ghassemi, A., 2012. A review of some rock mechanics issues in geothermal reservoir development. Geotechnical and Geological Engineering 30 (3), 647–664.

Gjini, D., Buzi, X., Mastmann, M., Tare, S., 1999. Experience with cyclic in situ combustion in Albania. In: Paper CIM 99-51 Presented at the 1999 CSPG and Petroleum Society Joint Convention, Digging Deeper, Finding a Better Bottom Line Held in Calgary, Alberta, Canada, June 14–18.

Gomaa, A.M., Qu, Q., Nelson, S., Maharidge, R., 2014. New insights into shale fracturing treatment design. In: Paper SPE 167754 Presented at the SPE/EAGE European Unconventional Resources Conference and Exhibition, Vienna, Austria, 25–27 February.

Gray, B.F., 2016. Spontaneous combustion and self-heating. In: Hurley, M. (Ed.), SFPE Handbook of Fire Protection Engineering. Society of Fire Protection Engineers, New York, USA, pp. 604–632.

Greaves, M., Ren, S.R., Xia, T.X., 1999. New air injection technology for IOR operations in light and heavy oil reservoirs. In: Paper SPE 57295 Presented at the SPE Asia Pacific Improved Oil Recovery Conference Held in Kuala Lumpur, Malaysia, 25–26 October.

Greaves, M., Ren, S.R., Rathbone, R.R., Fishlock, T., Ireland, R., 2000. Improved residual light oil recovery by air injection (LTO process). Journal of Canadian Petroleum Technology 39 (01), 57–61. https://doi.org/10.2118/00-01-05.

Green, D.W., Willhite, G.P., 1998. Enhanced Oil Recovery. Society of Petroleum Engineers, Richardson, Texas, USA.

Grieser, W.V., Wheaton, W.E., Magness, W.D., Blauch, M.E., Loghry, R., 2007. Surface reactive fluid's effect on shale. In: Paper SPE 106815 Presented at the SPE Production and Operations Symposium, Oklahoma City, Oklahoma, USA, 31 March–3 April. https://doi.org/10.2118/106815-MS.

Groisman, A., Kaplan, E., 1994. An experimental study of cracking induced by desiccation. Europhysics Letters 25 (6), 415–420.

Ground Water Protection Council, Consulting, A., 2009. Modern Shale Gas Development in the United States: A Primer. U.S. Department of Energy (DOE) report.

Gueutin, P., Altmann, S., Goncçlvès, J., Cosenza, P., Violette, S., 2007. Osmotic interpretation of overpressures from monovalent based triple layer model, in the callovo-oxfordian at the Bure site. Physics and Chemistry of the Earth 32 (1–7), 434–440.

Guo, W.F., Fang, Y.J., Yang, Y.X., Zhang, Y.J., Ma, H.L., 2004. Cyclic water injection in low-permeability reservoirs. Tuha Oil and Gas 9 (3), 262–265.

Guo, Q., Ji, L., Rajabov, V., Friedheim, J.E., Portella, C., Wu, R., 2012. Shale gas drilling experience and lessons learned from Eagle Ford. In: Paper SPE 155542 Presented at the Americas Unconventional Resources Conference, Pittsburgh, Pennsylvania, USA, 5–7 June. https://doi.org/10.2118/155542-MS.

Gupta, A., Civan, F., 1994. An improved model for laboratory measurement of matrix to fracture transfer function parameters in immiscible displacement. In: Paper SPE 28929 Presented at the SPE Annual Technical Conference and Exhibition, New Orleans, Louisiana, USA, 25–28, September. https://doi.org/10.2118/28929-MS.

Gutierrez, D., Taylor, A.R., Kumar, V., Ursenbach, M.G., Moore, R.G., Mehta, S.A., 2008. Recovery factors in high-pressure air injection projects revisited. SPE Reservoir Evaluation and Engineering 11 (06), 1097–1106. https://doi.org/10.2118/108429-PA.

Gutierrez, D., Miller, R.J., Taylor, A.R., Thies, P., Kumar, V., 2009. Buffalo field high-pressure air injection projects 1977 to 2007: technical performance and operational challenges. SPE Reservoir Evaluation and Engineering 12 (04), 542–550.

Habibi, A., Dehghanpour, H., Binazadeh, M., Bryan, D., Uswak, G., 2016. Advances in understanding wettability of tight oil formations: a montney case study. SPE Reservoir Evaluation and Engineering 19 (04), 583–603. https://doi.org/10.2118/175157-PA.

Hamadou, R., Khodja, M., Kartout, M., Jada, A., 2008. Permeability reduction by asphaltenes and resins deposition in porous media. Fuel 87, 2178–2185.

Handy, L.L., 1960. Determination of effective capillary pressures for porous media from imbibition data. Transactions of the American Institute of Mining, Metallurgical and Petroleum Engineers, Incorporated (AIME) 219, 75–80.

Hawkins, G.W., 1988. Laboratory study of proppant-pack permeability reduction caused by fracturing fluids concentrated during closure. In: Paper SPE 18261 Presented at the SPE Annual Technical Conference and Exhibition Held in Houston, Texas, USA, 2–5 October. https://doi.org/10.2118/18261-MS.

Hawthorne, S., 1990. Analytical-scale supercritical fluid extraction. Analytical Chemistry 62 (11), 633–642.

Hawthorne, S.B., Gorecki, C.D., Sorensen, J.A., Steadman, E.N., Harju, J.A., Melzer, S., 2013. Hydrocarbon mobilization mechanisms from upper, middle, and lower Bakken reservoir rocks exposed to CO. In: Paper SPE 167200 Presented at the SPE Unconventional Resources Conference Held in Calgary, Alberta, Canada, 5–7 November. https://doi.org/10.2118/167200-MS.

Heidug, W.K., Wong, S.W., 1996. Hydration swelling of water-absorbing rocks: a constitutive model. International Journal for Numerical and Analytical Methods in Geomechanics 20 (6), 403–430.

Hemphill, T., Abousleiman, Y., Tran, M., Hoang, S., Nguyen, V., 2008. Direct strength measurements of shale interaction with drilling fluids. In: Paper SPE 117851 Presented at the Abu Dhabi International Petroleum Exhibition and Conference, 3–6 November 2008, Abu Dhabi, UAE.

Hensen, E.J.M., Smit, B., 2002. Why clays smell. Journal of Physical Chemistry B 106 (49), 12664–12667.

Hernandez, I., Farouq Ali, S.M., Bentsen, R.G., 1999. First steps for developing an improved recovery method for a gas condensate reservoir. In: Paper PETSOC 95-09 Presented at the Annual Technical Meeting of Petroleum Society of Canada Held in Calgary, Alberta, Canada, 14–18 June.

Hirasaki, G., Zhang, D.L., June 2004. Surface chemistry of oil recovery from fractured, oil-wet, carbonate formations. SPE Journal 151–162.

Hoffman, B.T., 2018. Huff-N-Puff gas injection pilot projects in the Eagle Ford. In: Paper SPE 189816 Presented at the SPE Canada Unconventional Resources Conference Held in Calgary, Alberta, Canada, 13-–14 March. https://doi.org/10.2118/189816-MS.

Hoffman, B.T., Evans, J.G., 2016. Improved oil recovery IOR pilot projects in the Bakken formation. In: Paper SPE 180270 Presented at the SPE Low Perm Symposium Held in Denver, Colorado, USA, 5–6 May.

Hou, S., Ren, S., Wang, W., et al., 2010. Feasibility study of air injection for IOR in low permeability oil reservoirs of Xinjiang Oilfield China. In: Paper SPE 131087 Presented at in International Oil and Gas Conference and Exhibition Held in Beijing, China, 8–10 June. https://doi.org/10.2118/131087-MS.

Hou, S., Liu, Y., Zhang, J., Ren, S., 2011. A predictive model of spontaneous ignition delay of light-oil air-injection. Petroleum Geology and Recovery Efficiency 18 (3), 61–63.

Hu, Q.H., Ewing, P.R., Dultz, S., 2012. Low pore connectivity in natural rock. Journal of Contaminant Hydrology 133, 76–83.

Hu, Y., Devegowda, D., Striolo, A., Ho, T.A., Phan, A., Civan, F., Sigal, R., 2013. A pore scale study describing the dynamics of slickwater distribution in shale gas formations following hydraulic fracturing. In: Paper SPE 164552 Presented at the SPE Unconventional Resources Conference, Woodlands, Texas, USA, 10–12 April.

Huang, S., Sheng, J.J., 2017a. Discussion of thermal experiments' capability to screen the feasibility of air injection. Fuel 195, 151–164.

Huang, S., Sheng, J.J., 2017b. A practical method to obtain kinetic data from TGA (thermogravimetric analysis) experiments to build an air injection model for enhanced oil recovery. Fuel 206, 199–209.

Huang, S., Sheng, J.J., 2017c. An innovative method to build a comprehensive kinetic model for air injection using TGA/DSC experiments. Fuel 210, 98–106.
Huang, S., Sheng, J.J., 2018. Feasibility of spontaneous ignition during air injection in light oil reservoirs. Fuel 226, 698–708.
Huang, D.Z., Xiang, D., 2004. Mechanisms of huff-n-puff water injection to displace oil. Petroleum Geology and Recovery Efficiency 11 (5), 39–41, 43.
Huang, S., Jia, H., Sheng, J.J., 2016a. Research on oxidation kinetics of tight oil of Wolfcamp field. Petroleum Science and Technology 34 (10), 903–910.
Huang, S., Jia, H., Sheng, J.J., 2016b. Exothermicity and oxidation behavior of tight oil with cuttings from the Wolfcamp shale reservoir. Petroleum Science and Technology 34 (21), 1735–1741.
Huang, S., Zhang, Y., Sheng, J.J., 2018. Experimental investigation of enhanced oil recovery mechanisms of air injection under a low-temperature oxidation process: thermal effect and residual oil recovery efficiency. Energy and Fuels 32 (6), 6774–6781.
Hughes, B., Sarma, H.K., 2006. Burning reserves for greater recovery? Air injection potential in Australian light oil reservoirs. In: Paper SPE 101099 Presented at the SPE Asia Pacific Oil & Gas Conference and Exhibition Held in Adelaide, Australis, 11–13 September. https://doi.org/10.2118/101099-MS.
Huh, C., 1979. Interfacial tension and solubilizing ability of a microemulsion phase that coexists with oil and brine. Journal of Colloid and Interface Science 71, 408–428.
Ibrahim, A.F., Nasr-El-Din, H., 2018. Experimental investigation for the effect of the soaking process on the regain permeability after hydraulic fracturing in tight sandstone and shale formations. In: Paper SPE 193123 Presented at the SPE Abu Dhabi International Petroleum Exhibition & Conference, Abu Dhabi, UAE, 12–15 November.
Idowu, N., Long, H., Øren, P., Carnerup, A.M., Fogden, A., Bondino, I., Sundal, L., 2015. Wettability analysis using micro-CT, FESEM and QEMSCAN, and its applications to digital rock physics. In: Paper Presented at the International Symposium of the Society of Core Analysts Held in St. John's Newfoundland and Labrador, Canada 16–21 August.
Jacobs, S., October 2014. The shale evolution: zipper fracture takes hold. Journal of Petroleum Technology 60–67.
Jadhunandan, P.P., Morrow, N.R., 1995. Effect of wettability on waterflooding recovery for crude oil/brine/rock systems. SPE Reservoir Evaluation and Engineering 10, 40–46.
Jamaluddin, A.K.M., Vandamme, M., Mann, B.K., 1995. Formation Heat treatment (FHT): a state-of-the-art technology for near-wellbore formation damage treatment. In: Paper PETSOC-95-67 Presented at the Annual Technical Meeting Held in Calgary, Alberta, Canada, 7–9 June. https://doi.org/10.2118/95-67.
Jansen, T., Zhu, D., Hill, A.D., 2015. Effect of Rock mechanical properties on fracture conductivity for shale formations. In: Paper SPE 173347 Presented at the SPE Hydraulic Fracturing Technology Conference Held in Woodlands, Texas, USA, 3–5 February.
Javaheri, A., Dehghanpour, H., Wood, J., 2017. Imbibition oil recovery from tight rocks with dual-wettability pore-network a Montney case study. In: Paper SPE 185076 Presented at the SPE Unconventional Resources Conference Held in Calgary, Alberta, Canada, 15–16 February. https://doi.org/10.2118/185076-MS.
Jennings Jr., H.Y., 1957. Surface properties of natural and synthetic porous media. Production Monthly 21 (5), 20–24.
Jerauld, G.R., Rathmell, J.J., 1997. Wettability and relative permeability of Prudhoe Bay: a case study in mixed-wet reservoirs. SPERE 12 (1), 58–65. https://doi.org/10.2118/28576-PA.

Ji, L.J., Geehan, T., 2013. Shale failure around hydraulic fractures in water fracturing of gas shale. In: SPE Paper 167155 Presented at the SPE Unconventional Resources Conference, 5–7 November, Calgary, Alberta, Canada.

Ji, Y.J., Ren, S.R., Zhao, Z.Z., et al., 2008. Study of explosion-proof experiment on oil field air injection process. China Safety Science Journal 2, 014. http://en.cnki.com.cn/Article_en/CJFDTOTAL-ZAQK200802014.htm.

Jia, H., Sheng, J.J., 2017. Discussion of the feasibility of air injection for enhanced oil recovery in shale oil reservoirs. Petroleum 3, 249–257.

Jia, H., Sheng, J.J., 2018. Simulation study of huff-n-puff air injection for enhanced oil recovery in shale oil reservoirs. Petroleum 4, 7–14.

Jia, H., Zhao, J.Z., Pu, W.F., Li, Y.M., Yuan, Z.T., Yuan, C.D., 2012a. Laboratory investigation on the feasibility of light-oil autoignition for application of the high-pressure air injection (HPAI) process. Energy and Fuels 26 (9), 5638–5645.

Jia, H., Zhao, J.Z., Pu, W.F., Liao, R., Wang, L.L., 2012b. The influence of clay minerals types on the oxidation thermokinetics of crude oil. Energy Sources, Part A: Recovery, Utilization, and Environmental Effects 34 (10), 877–886.

Jia, C.Z., Zou, C.N., Li, J.Z., Li, D.H., Zheng, M., 2012c. Assessment criteria, main types, basic features and resource prospects of the tight oil in China. Acta Petrolei Sinica 33 (3), 343–350.

Jia, C.Z., Zheng, M., Zhang, Y., 2014. Four important theoretical issues of unconventional petroleum geology. Acta Petrolei Sinica 35 (1), 1–10.

Jiang, H.-F., Lei, Y.Z., Xiong, X., Yan, L.P., Pi, W.F., Li, X.J., Yu, C.H., 2008. A CO_2 immiscible displacement experimental study aiming at fuyang extra-low permeability layer at the daqing changheng peripheral. Geoscience 22 (4), 659–663.

Johnson Jr., C.E., January 1976. Status of caustic and emulsion methods. Journal of Petroleum Technology 85–92.

Johnston, C.T., Tombacz, E., 2002. Surface chemistry of soil minerals. In: Dixon, J.B., Schulze, D.G. (Eds.), Soil Mineralogy with Environmental Applications. Soil Science Society of America, Madison, Wisconsin, USA, pp. 37–67.

Joslin, K., Ghedan, S.G., Abraham, A.M., Pathak, V., 2017. EOR in tight reservoirs, technical and economical feasibility. In: Paper SPE 185037 Presented at the SPE Unconventional Resources Conference Held in Calgary, Alberta, Canada, 15–16 February.

Karadkar, P., Bataweel, M., Bulekbay, A., Alshaikh, A.A., 2018. Energized fluids for upstream production enhancement: a review. In: Paper SPE 192255 Presented at the SPE Kingdom of Saudi Arabia of Annual Technical Symposium and Exhibition, Dammam, Saudi Arabia, 23–26 April.

Karandish, G.R., Rahimpour, M.R., Sharifzadeh, S., Dadklah, A.A., 2015. Wettability alteration in gas-condensate carbonate reservoir using anionic fluorinated treatment. Chemical Engineering Research and Design 93, 554–564.

Karfakis, M.G., Akram, M., 1993. Effects of chemical solutions on rock fracturing. International Journal of Rock Mechanics and Mining Sciences and Geomechanics Abstracts 30 (7), 1253–1259.

Karpov, V.B., Parshin, N.V., Sleptsov, D.I., Moiseenko, A.A., Ryazanov, A.A., Golovatskiy, Y.A., Petrashov, O.V., Zhirov, A.V., Kurelenkova, Y.V., Ishimov, I.A., Im, P.T., 2016. Tight oil field development optimization based on experience of Canadian analogs. In: Paper SPE 182572 Presented at the SPE Annual Caspian Technical Conference & Exhibition, Astana, Kazakhstan, 1–3 November.

Kathel, P., Mohanty, K.K., 2013. EOR in tight oil reservoirs through wettability alteration. In: Paper SPE 166281 Presented at the SPE Annual Technical Conference and Exhibition Held in New Orleans, Louisiana, 30 September-2 October.

Katz, D.L., Lundy, C.L., 1982. Absence of connate water in Michigan reef gas reservoirs – an analysis. AAPG Buletin 66 (1), 91–98.
Kazemi, H., Gilman, J.R., Elsharkawy, A.M., May 1992. Analytical and numerical solution of oil recovery from fractured reservoirs with empirical transfer functions. SPERE 219–227.
Kelemen, P., Savage, H., Koczynski, T.A., 2017. Methods and Systems for Causing Reaction Driven Cracking in Subsurface Rock Formations. Patent No.: US 9,657,559 B2, 23 May.
Kennedy, H.T., Bruja, E.O., Boykin, R.S., 1955. An investigation of the effects of wettability on the recovery of oil by waterflooding. Journal of Physical Chemistry 59 (Sept.), 867–869.
Khansari, Z., Kapadia, P., Mahinpey, N., Gates, I.D., 2014. A new reaction model for low temperature oxidation of heavy oil: experiments and numerical modeling. Energy 64, 419–428.
Kharrat, R., Vossoughi, S., 1985. Feasibility study of the in-situ combustion process using TGA/DSC techniques. Journal of Petroleum Technology (August), 1441–1445.
Kim, T.-S., Konno, T., Dauskardt, R.H., 2009. Surfactant-controlled damage evolution during chemical mechanical planarization of nanoporous films. Acta Materialia 57, 4687–4696.
King, G.E., 2012. Hydraulic fracturing 101: what every representative, environmentalist, regulator, reporter, investor, university researcher, neighbor and engineer should know about estimating frac risk and improving frac performance in unconventional gas and oil wells. In: Paper SPE 152596 Presented at the SPE Hydraulic Fracturing Technology Conference Held in the Woodlands, Texas, USA, 6–8 February.
Kök, M.V., 2006. Effect of clay on crude oil combustion by thermal analysis techniques. Journal of Thermal Analysis and Calorimetry 84 (2), 361–366.
Kök, M.V., 2012. Clay concentration and heating rate effect on crude oil combustion by thermogravimetry. Fuel Processing Technology 96, 134–139.
Kök, M.V., Gundogar, A.S., 2010. Effect of different clay concentrations on crude oil combustion kinetics by thermogravimetry. Journal of Thermal Analysis and Calorimetry 99 (3), 779–783.
Kök, M.V., Hughes, R., Price, D., 1997a. Combustion characteristics of crude oil-limestone mixtures. Journal of Thermal Analysis 49 (2), 609–615.
Kök, M.V., Sztatisz, J., Pokol, G., 1997b. High-pressure DSC applications on crude oil combustion. Energy and Fuels 11 (6), 1137–1142.
Kong, B., Wang, S., Chen, S., 2016. Simulation and optimization of CO2 huff-and-puff processes in tight oil reservoirs. In: Paper SPE 179688 Presented at the SPE Improved Oil Recovery Conference, Tulsa, Oklahoma, USA, 11–13 April.
Koo, J., Kleinstreuer, C., 2003. Liquid flow in microchannels: experimental observations and computational analyses of microfluidics effects. Journal of Micromechanics and Microengineering 13 (5), 568–579.
Krall, A.H., Sengers, J.V., Kestin, J., 1992. Viscosity of liquid toluene at temperatures from 25 to 150. degree. C and at pressures up to 30 MPa. Journal of Chemical and Engineering Data 37 (3), 349–355.
Ksiezniak, K., Rogala, A., Hupka, J., 2015. Wettability of shale rock as an indicator of fracturing fluid composition. Physicochemical Problems of Mineral Processing 51, 315–323.
Kuchta, J.M., 1985. Investigation of Fire and Explosion Accidents in the Chemical, Mining, and Fuel-Related Industries-A Manual. Bulletin. Bureau of Mines, Washington, DC (USA).

Kumar, M., 1987. Simulation of laboratory in-situ combustion data and effect of process variations. In: Paper SPE 16027 Presented at the SPE Symposium on Reservoir Simulation Held in San Antonio, Texas, USA, 1–4 February. https://doi.org/10.2118/16027-MS.

Kumar, V., Pope, G.A., Sharma, M.M., 2006. Improving the gas and condensate relative permeability using chemical treatments. In: Paper SPE 100529 Presented at the SPE Gas Technology Symposium Held in Calgary, Alberta, Canada, 15–17 May.

Kumar, V.K., Gutierrez, D., Moore, R.G., Mehta, S.A., 2007. Case history and appraisal of the West Buffalo Red River Unit high-pressure air injection project. In: Paper SPE 107715 Presented at the Hydrocarbon Economics and Evaluation Symposium Held in Dallas, Texas, UAS, 1–3 April.

Kumar, K., Dao, E.K., Mohanty, K.K., 2008. Atomic force microscopy study of wettability alteration by surfactants. SPE Journal 13, 137–145.

Kurtoglu, B., 2013. Integrated Reservoir Characterization and Modeling in Support of Enhanced Oil Recovery for Bakken. PhD dissertation. Colorado School of Mines, Golden, Colorado, USA.

Kurtoglu, B., Kazemi, H., 2012. Evaluation of Bakken performance using coreflooding, well testing, and reservoir simulation. In: Paper SPE 155655 Presented at the SPE Annual Technical Conference and Exhibition, San Antonio, Texas, USA, 8–10 October. https://doi.org/10.2118/155655-MS.

Kurtoglu, B., Sorensen, J.A., Braunberger, J., Smith, S., Kazemi, H., 2013. Geologic characterization of a Bakken reservoir for potential CO_2 EOR. In: Paper SPE 168915 Presented at the Unconventional Resources Technology Conference Held in Denver, Colorado, USA, 12–14 August.

Kuuskraa, V.A., 2013. EIA/ARI World Shale Gas and Shale Oil Resource Assessment. EIA Report.

Lan, Q., Dehghanpour, H., Wood, J., Sanei, H., 2015a. Wettability of the Montney tight gas formation. SPE Reservoir Evaluation and Engineering 18 (03), 417–431.

Lan, Q., Xu, M., Binazadeh, M., Dehghanpour, H., Wood, J.M., 2015b. A comparative investigation of shale wettability: the significance of pore connectivity. Journal of Natural Gas Science and Engineering 27 (2015), 1174–1188.

Lei, Q., Latham, J.P., Xiang, J., Tsang, C.F., 2017. Role of natural fractures in damage evolution around tunnel excavation in fractured rocks. Engineering Geology 231, 100–113.

Leverett, M.C., 1941. Capillary behavior in porous solids. Transactions of the American Institute of Mining, Metallurgical and Petroleum Engineers, Incorporated (AIME) 142, 152–169.

Li, Y.-Y., 2011. Application of asynchronous water injection to the Dong-Sheng-Bao reservoir. Petroleum Geology and Engineering 25 (supplemental version), 16–17.

Li, L.L., 2012. Methods to increase well oil production in tight Chang 7 reservoir in Hujianshang field. Petroleum Geology and Engineering 26 (5), 56–58.

Li, X.H., 2015. Huff-n-puff water injection in tight Duha Field. Special Oil and Gas Reservoirs 22 (4), 144–146.

Li, K., Firoozabadi, A., 2000. Experimental study of wettability alteration to preferential gas-wetting in porous media and its effects. SPE Reservoir Evaluation and Engineering 3 (2), 139–149.

Li, K., Horne, R.N., 2006. Generalized scaling approach for spontaneous imbibition: an analytical model. SPE Reservoir Evaluation and Engineering 9 (3), 251–258.

Li, L., Sheng, J.J., 2017a. Numerical analysis of cyclic CH injection in liquid-rich shale reservoirs based on the experiments using different-diameter shale cores and crude oil. Journal of Natural Gas Science and Engineering 39, 1–14.

Li, L., Sheng, J.J., 2017b. Upscale methodology for gas huff-n-puff process in shale oil reservoirs. Journal of Petroleum Science and Engineering 153, 36–46.
Li, J., Yang, C., Xu, C., Ren, G., Tu, X., 2001. Huff-n-puff water injection in energy-deficient wells in the south yellow region. Oil and Gas Geology 22 (3), 221–224, 229.
Li, J., Mehta, S.A., Moore, R.G., Zalewski, E., Ursenbach, M.G., Van Fraassen, K., 2006. Investigation of the oxidation behaviour of pure hydrocarbon components and crude oils utilizing PDSC thermal technique. Journal of Canadian Petroleum Technology 45 (01), 48–53.
Li, K., Liu, Y., Zheng, H., Huang, G., Li, G., 2011. Enhanced gas-condensate production by wettability alteration to gas wetness. Journal of Petroleum Science and Engineering 78, 505–509.
Li, Z.X., Li, J., Qu, X.F., Li, X.W., Lei, Q.H., Fan, J.M., 2015a. Field test to produce tight oil in Chang 7 field, Ordos Basin. Natural Gas Geoscience 26 (10), 1932–1940.
Li, Z.X., Qu, X.F., Liu, W.T., Lei, Q.H., Sun, H.L., He, Y.A., 2015b. Development modes in Chang 7 tight oil reservoir, triassic yangchang formation in Ordos basin, NW China. Petroleum Exploration and Development 42 (2), 217–221.
Li, L., Sheng, J.J., Sheng, J., 2016. Optimization of huff-n-puff gas injection to enhance oil recovery in shale reservoirs. In: Paper SPE 180219 Presented at the SPE Low Perm Symposium Held in Denver, Colorado, USA, 5–6 May.
Li, L., Sheng, J.J., Xu, J., 2017a. Gas selection for huff-n-puff EOR in shale oil reservoirs based upon experimental and numerical study. In: Paper SPE 185066 Presented at the SPE Unconventional Resources Conference Held in Calgary, Alberta, Canada, 15–16 February.
Li, L., Zhang, Y., Sheng, J.J., 2017b. Effect of the injection pressure on enhancing oil recovery in shale cores during the CO_2 huff-n-puff process when it is above and below the minimum miscibility pressure. Energy and Fuels 31, 3856–3867.
Li, L., Sheng, J.J., Su, Y., Zhan, S., 2018. Further Investigation of Effects of Injection Pressure and Imbibition Water on CO_2 Huff-n-Puff Performance in Liquid-Rich Shale Reservoirs. Energy Fuels 32, 5798–6789.
Liang, J., Xiong, X., Liu, X., 2015. Experimental study on crack propagation in shale formations considering hydration and wettability. Journal of Natural Gas Science and Engineering 23, 492–499.
Liang, L., Luo, D., Liu, X., Xiong, J., 2016. Experimental study on the wettability and adsorption characteristics of Longmaxi Formation shale in the Sichuan Basin, China. Journal of Natural Gas Science and Engineering 33, 1107–1118.
Liang, T., Achour, S.H., Longoria, R.A., DiCarlo, D.A., Nguyen, Q., 2017a. Flow physics of how surfactants can reduce water blocking caused by hydraulic fracturing in low permeability reservoirs. Journal of Petroleum Science and Engineering 157, 631–642.
Liang, T., Longoria, R.A., Lu, J., Nguyen, Q.P., DiCarlo, D.A., 2017b. Enhancing hydrocarbon permeability after hydraulic fracturing: laboratory evaluations of shut-ins and surfactant additives. SPE Journal 22 (4), 1011–1023. https://doi.org/10.2118/175101-PA.
Liang, T., Luo, X., Nguyen, Q., DiCarlo, D.A., 2017c. Computed-tomography measurements of water block in low-permeability rocks: scaling and remedying production impairment. SPE Journal 23 (03), 762–771.
Liang, T., Zhou, F., Lu, J., DiCarlo, D.A., Nguyen, Q., 2017d. Evaluation of wettability alteration and IFT reduction on mitigating water blocking for low-permeability oil-wet rocks after hydraulic fracturing. Fuel 209, 650–660.
Liao, G.Z., Yang, H.J., Jiang, Y.W., et al., 2018. Applicable scope of oxygen-reduced air flooding and the limit of oxygen content. Petroleum Exploration and Development 45 (1), 111–117. https://www.sciencedirect.com/science/article/pii/S1876380418300107.

Li, L., Sheng, J.J., 2016. Experimental study of core size effect on CH4 huff-n-puff enhanced oil recovery in liquid-rich shale reservoirs. Journal of Natural Gas Science and Engineering 34, 1392–1402.
Lin, C.Y., Chen, W.H., Lee, S.T., Culham, W.E., 1984. Numerical simulation of combustion tube experiments and the associated kinetics of in-situ combustion process. SPE Journal 24 (06), 657–666.
Lin, Y.Y., Wang, P.P., Li, Q.D., Han, B.M., Li, H.L., Wu, Y.P., He, W.S., 2016. Performance analysis of different modes of huff-n-puff water injection in horizontal wells in An-83 Chang-7 tight oil reservoir. Petrochemical Industry Application 35 (6), 94–97.
Lindman, B., Kamenka, N., Kathopoulis, T.-M., Brun, B., Nilsson, P.-G., 1980. Translational diffusion and solution structure of microemulsions. Journal of Physical Chemistry 84, 2485–2490.
Liu, J., Sheng, J.J., 2019. Experimental investigation of surfactant enhanced spontaneous imbibition in Chinese shale oil reservoirs using NMR tests. Journal of Industrial and Engineering Chemistry 72, 414–422.
Liu, J., Sheng, J.J., Huang, W., 2019. Experimental investigation on microscopic mechanisms of surfactant-enhanced spontaneous imbibition in shale cores. Energy Fuels 33, 7188–7199.
Liu, H., Wang, M.C., Zhou, X., Zhang, Y.P., 2005. EOS simulation for CO_2 huff-n-puff process. In: Paper CIM 2005-120 Presented at the Petroleum Society's 6th Canadian International Petroleum Conference Held in Calgary, Alberta, Canada, June 7–9.
Liu, J.Y., Shen, K., Huang, Z.W., Huai, H.N., Chen, F.L., 2010. A MEOR pilot test in an ansai low-permeability reservoir. Xinjiang Petroleum Geology 31 (6), 634–636.
Liu, J., Sheng, J.J., Wang, X., Ge, H., Yao, E., 2019. Experimental study of wettability alteration and spontaneous imbibition in Chinese shale oil reservoirs using anionic and nonionic surfactants. Journal of Petroleum Science and Engineering 175, 624–633.
Loomis, A.G., Crowell, D.C., 1962. Relative Permeability Studies: Gas-Oil and Water-Oil Systems (No. BM-BULL-599). Bureau of Mines. San Francisco Petroleum Research Lab, San Francisco, Calif. (USA).
Looyestijn, W.J., Hofman, J., 2006. Wettability-index determination by nuclear magnetic resonance. SPE Reservoir Evaluation and Engineering 9 (02), 146–153. https://doi.org/10.2118/93624-PA.
Lu, C.-F., 1988. A new technique for the evaluation of shale stability in the presence of polymeric drilling fluid. SPEPE 3 (3), 366–374.
Ma, S., Morrow, N.R., Zhang, X., 1997. Generalized scaling of spontaneous imbibition data for strongly water-wet systems. Journal of Petroleum Science and Engineering 18 (3–4), 165–178.
MacPhail, W.F.P., Shaw, J.C., 2014. Well injection and production method and system. Patent Cooperation Treaty (PCT). WO2014124533A1, August 21.
Mahadevan, J., 2005. Flow through Drying of Porous Media. PhD dissertation. The University of Texas at Austin, Austin, Texas, USA.
Mahadevan, J., Sharma, M.M., 2005. Factors affecting clean-up of water-blocks: a laboratory investigation. SPE Journal 10 (3), 238–246.
Makhanov, K., 2013. An Experimental Study of Spontaneous Imbibition in Horn River Shales. Master's thesis, University of Alberta, Edmonton, Alberta, Canada.
Makhanov, K., Habibi, A., Dehghanpour, H., Kuru, E., 2014. Liquid uptake of gas shales: a workflow to estimate water loss during shut-in periods after fracturing operations. Journal of Unconventional Oil and Gas Resources 7, 22–32. https://doi.org/10.1016/j.juogr.2014.04.001.
Malone, M., Ely, J.W., 2007. Execution of hydraulic fracturing treatments. In: Economides, M.J., Martin, T. (Eds.), Chapter 9 in Modern Fracturing, Enhancing Natural Gas Production. ET Publishing, Houston, Texas, USA.

Mandal, A., 2015. Chemical flood enhanced oil recovery: a review. International Journal of Oil, Gas and Coal Technology 9 (3), 241–264.
Mantell, M., 2013. Recycling and Reuse of Produced Water to Reduce Freshwater Use in Hydraulic Fracturing Operations. In: Paper Presented in the EPA Hydraulic Fracturing Study Water Acquisition Workshop Held in Arlington, VA, June 4.
Marine, I.W., 1974. Geohydrology of buried triassic basin at Savannah river plant, South Carolina. AAPG Bulletin 58 (9), 1825–1837.
Marine, I.W., Fritz, S.J., 1981. Osmotic model to explain anomalous hydraulic heads. Water Resources Research 17 (1), 73–82. https://doi.org/10.1029/WR017i001p00073.
Marmur, A., 1988. Penetration of a small drop into a capillary. Journal of Colloid and Interface Science 122 (1), 209–219. https://doi.org/10.1016/0021-9797(88)90304-9.
Maroudas, A., 1966. Particles deposition in granular filter media-2. Filtration and Separation 3 (2), 115–121.
Martin III., R.J., 1972. Time-dependent crack growth in quartz and its application to the creep of rocks. Journal of Geophysical Research 77, 1405–1419.
Martin, T., Rylance, M., 2007. Technologies for mature assets. In: Economides, M.J., Martin, T. (Eds.), Chapter 13 in Modern Fracturing, Enhancing Natural Gas Production. ET Publishing, Houston, Texas, USA.
Martin, W.L., Alexander, J.D., Dew, J.N., 1958. Process variables of in situ combustion. Petroleum Transactions, AIME 213, 28–35.
Mattax, C.C., Kyte, J.R., 1962. Imbibition oil recovery from fractured, water-drive reservoir. SPE Journal 2 (2), 177–184.
McCain Jr., W.D., 1989. The Properties of Petroleum Fluids. PennWell Publishing Company, Tulsa, Oklahoma. ISBN: 0-87814-335-1.
McCurdy, R., 2011. EPA Hydraulic Fracturing Workshop 1. In: High Rate Hydraulic Fracturing Additives in NonMarcellus Unconventional Shales, February 24–25, 2011.
McGuire, P.L., Okuno, R., Gould, T.L., Lake, L.W., 2016. Ethane-Based EOR: an innovative and profitable EOR opportunity for a low price environment. In: Paper SPE 179565 Presented at the Improved Oil Recovery Conference Held in Tulsa, Oklahoma, USA, April 11–13.
McKibben, M.A., Barnes, H.L., 1986. Oxidation of pyrite in low temperature acidic solutions: rate laws and surface textures. Geochimica et Cosmochimica Acta 50 (7), 1509–1520.
McWhorter, D.B., Sunada, D.K., 1990. Exact integral solutions for two-phase flow. Water Resources Research 26 (3), 399–413.
Mehtar, M., Brangetto, M., Abou Soliman, A., Mielke, S., Young, S., 2010. Effective implementation of high performance water based fluid provides superior shale stability offshore Abu Dhabi. In: Paper SPE 138564 Presented at the Abu Dhabi International Petroleum Exhibition and Conference, 1-4 November, Abu Dhabi, UAE.
Meng, X., Sheng, J.J., 2016a. Optimization of huff-n-puff gas injection in a shale gas condensate reservoir. Journal of Unconventional Oil and Gas Resources 16, 34–44.
Meng, X., Sheng, J.J., 2016b. Experimental and numerical study of huff-n-puff gas injection to revaporize liquid dropout in shale gas condensate reservoirs. Journal of Natural Gas Science and Engineering 35, 444–454.
Meng, M., Ge, H., Ji, W., Shen, Y., Su, S., 2015. Monitor the process of shale spontaneous imbibition in co-current and counter-current displacing gas by using low field nuclear magnetic resonance method. Journal of Natural Gas Science and Engineering 27, 336–345. https://doi.org/10.1016/j.jngse.2015.08.069.
Meng, X., Sheng, J.J., Yu, Y., 2015a. Evaluation of enhanced condensate recovery potential in shale plays by huff-n-puff gas injection. In: Paper SPE 177283 Presented at the SPE Eastern Regional Meeting Held in Morgantown, West Virginia, USA, 13–15 October.

Meng, X., Yu, Y., Sheng, J.J., Watson, W., Mody, F., 2015b. An experimental study on huff-n-puff gas injection to enhance condensate recovery in shale gas reservoirs. In: Paper URTeC 2153322 Presented at the Unconventional Resources Technology Conference Held in San Antonio, Texas, USA, 20–22 July.

Meng, X., Sheng, J.J., Yu, Y., May 2017. Experimental and numerical study on enhanced condensate recovery by huff-n-puff gas injection in shale gas condensate reservoirs. SPE Reservoir Evaluation and Engineering 471–477.

Mercado Sierra, D.P., Trevisan, O.V., 2014. Numerical simulation of a dry combustion tube test for a Brazilian heavy oil. In: Paper SPE 169335 Presented at the SPE Latin American and Caribbean Petroleum Engineering Conference Held in Maracaibo, Venezuela, May 21–23.

Miller, C., Tong, S., Mohanty, K.K., 2018. A Chemical Blend for Stimulating Production in Oil-Shale Formations. In: Paper URTeC 2900955 Presented at the Unconventional Resources Technology Conference Held in Houston, Texas, USA, 23–25 July. https://doi.org/10.15530/URTEC-2018-2900955.

Mirchi, V., Saraji, S., Goual, L., Piri, M., 2014. Dynamic interfacial tensions and contact angles of surfactant-in-brine/oil/shale systems: implications to enhanced oil recovery in shale oil reservoirs. In: Paper SPE 169171 Presented at the SPE Improved Oil Recovery Symposium Held in Tulsa, Oklahoma, USA, 12–16 April. https://doi.org/10.2118/169171-MS.

Mirzae, M., DiCarlo, D., 2013. Imbibition of anionic surfactant solution into oil-wet capillary tubes. Transport in Porous Media 99, 37–54.

Moghadam, A.A., Chalaturnyk, R., 2015. Laboratory investigation of shale permeability. In: Paper SPE 175919 Presented at the SPE/CSUR Unconventional Resources Conference, Calgary, Alberta, Canada, 20–22 October. https://doi.org/10.2118/175919-MS.

Mohammed-Singh, L.J., Singhal, A.K., Sim, S.S.K., 2006. Screening criteria for carbon dioxide huff 'n' puff operations. In: Paper SPE 100044 Presented at the SPE/DOE Symposium on Improved Recovery Held in Tulsa, Oklahoma, 22–26 April.

Mohanty, K.K., Tong, S., Miller, C., Honapour, M.M., Turek, E., Peck, D., 2017. Improved hydrocarbon recovery using mixtures of energizing chemicals in unconventional reservoirs. In: Paper SPE 187240 Presented at the SPE Annual Technical Conference and Exhibition Held in San Antonio, Texas, USA, 9–11 October.

Monger, T.G., Coma, J.M., 1988. A laboratory and field evaluation of the CO_2 process for light oil recovery. SPE Reservoir Evaluation and Engineering 3 (4), 1168–1176.

Montes, A.R., Gutierrez, D., Moore, R.G., Mehta, S.A., Ursenbach, M.G., 2010. Is high-pressure air injection (HPAI) simply a flue-gas flood? Journal of Canadian Petroleum Technology 49 (02), 56–63. https://doi.org/10.2118/133206-PA.

Moore, T.F., Slobod, R.L., 1956. The effect of viscosity and capillarity on the displacement of oil and water. Producers Monthly 20 (August), 20.

Moore, R.G., Belgrave, J.D.M., Mehta, R., Ursenbach, M., Laureshen, C.J., Xi, K., 1992. Some Insights into the Low-Temperature and High-Temperature In-Situ Combustion Kinetics. In: Paper SPE 24174 Presented at the SPE/DOE Enhanced Oil Recovery Symposium Held in Tulsa, Oklahoma, USA, 22–24 April. https://doi.org/10.2118/24174-MS.

Moore, R.G., Ursenbach, M.G., Laureshen, C.J., Belgrave, J.D.M., Mehta, S.A., 1999. Ramped temperature oxidation analysis of Athabasca oil sands bitumen. Journal of Canadian Petroleum Technology 38 (13), 1–10. https://doi.org/10.2118/99-13-40.

Moore, R.G., Mehta, S.A., Ursenbach, M.G., 2002. A guide to high pressure air injection (HPAI) based oil recovery. In: Paper SPE 75207 Presented at the SPE/DOE Improved Oil Recovery Symposium Held in Tulsa, Oklahoma, USA, 13–17 April. https://doi.org/10.2118/75207-MS.

Moore, J.E., Crandall, D., Lopano, C.L., Verba, C.A., 2017. Carbon Dioxide Induced Swelling of Unconventional Shale Rock and Effects on Permeability. NETL-TRS-9-2017, NETL Technical Report Series. U.S. Department of Energy, National Energy Technology Laboratory, Morgantown, West Virginia, USA.

Moradian, Z., Seiphoori, A., Evans, B., 2017. The role of bedding planes on fracture behavior and acoustic emission response of shale under unconfined compression. In: Paper Presented at the 51st US Rock Mechanics/Geomechanics Symposium, San Francisco, California, USA, 25–28 June.

Morin, E., Montel, F., 1995. Accurate predictions for the production of vaporized water. In: Paper SPE 30719 Presented at the SPE Annual Technical Conference and Exhibition Held in Dallas Texas, USA, 22–25 October. https://doi.org/10.2118/30719-MS.

Morrow, N.R., McCaffery, F.G., 1978. Displacement studies in uniformly wetting porous media. In: Paddy, G.F. (Ed.), Wetting, Spreading and Adhesion. Academic Press, New York, pp. 289–319.

Morrow, N.R., Songkran, B., 1981. Effect of viscous and buoyancy forces on nonwetting phase trapping in porous media. In: Shah, D.O. (Ed.), Surface Phenomena in Enhanced Oil Recovery. Plenum Press, pp. 387–411.

Morsy, S., Sheng, J.J., 2014a. Effect of water salinity on shale reservoir productivity. Advances in Petroleum Exploration and Development 8 (1), 9–14.

Morsy, S., Sheng, J.J., 2014b. Imbibition characteristics of the Barnett shale formation. In: Paper SPE 168984 Presented at the SPE Unconventional Resources Conference Held in Woodlands, Texas, USA, 1–3 April.

Morsy, S., Gomaa, A., Sheng, J.J., Soliman, M.Y., 2013a. Potential of improved water-flooding in acid-hydraulically-fractured shale formations. In: Paper SPE 166403 Presented at the SPE Annual Technical Conference and Exhibition Held in New Orleans, Louisiana, USA, September 30–October 2.

Morsy, S., Sheng, J.J., Soliman, M.Y., 2013b. Improving hydraulic fracturing of shale formations by acidizing. In: Paper SPE 165688 Presented at the SPE Eastern Regional Meeting Held in Pittsburgh, Pennsylvania, USA, August 20–22.

Morsy, S., Sheng, J.J., Ezewu, R.O., 2013c. Potential of waterflooding in shale formations. In: Paper SPE 167510 Presented at the Nigeria Annual International Conference and Exhibition Held in Lagos, Nigeria, August 5–7.

Morsy, S., Gomaa, A., Sheng, J.J., 2014a. Imbibition characteristics of Marcellus shale formation. In: Paper SPE 169034 Presented at the SPE Improved Oil Recovery Symposium Held in Tulsa, Oklahoma, USA, 12–16 April.

Morsy, S., Gomaa, A., Sheng, J.J., 2014b. Improvement of Eagle Ford shale formations water imbibition by mineral dissolution and wettability alteration. In: Paper SPE 168985 Presented at the SPE Unconventional Resources Conference Held in Woodlands, Texas, USA, 1–3 April.

Morsy, S., Hetherington, C.J., Sheng, J.J., 2015. Effect of low-concentration HCl on the mineralogy, physical, and mechanical properties, and recovery factors of some shale. Journal of Unconventional Oil and Gas Resources 9, 94–102.

Morsy, S., Gomaa, A., Sheng, J.J., 2016. Effects of salinity and alkaline concentration on the spontaneous imbibition behavior and rock properties of some shale rocks. International Journal of Petroleum Engineering 2 (3), 209–224.

Muhammad, M., McFadden, J., Creek, J., 2003. Asphaltene precipitation from reservoir fluids: asphaltene solubility and particle size vs. pressure. In: Paper SPE 80263 Presented at the International Symposium on Oilfield Chemistry Held in Houston, Texas, USA, 5–7 February.

Najafabadi, N.F., Delshad, M., Sepehrnoori, K., Nguyen, Q.P., Zhang, J., 2008. Chemical flooding of fractured carbonates using wettability modifiers. In: Paper SPE 113369 Presented at the SPE Symposium on Improved Oil Recovery Held in Tulsa, Oklahoma, USA, 20–23 April.

Nelson, T.W., McNeil, J.S., 1961. How to engineer an in situ combustion project. Oil and Gas Journal 69 (23), 58–65.

Neuzil, C.E., Provost, A.M., 2009. Recent experimental data may point to a greater role for osmotic pressures in the subsurface. Water Resources Research 45, W03410. https://doi.org/10.1029/2007WR006450.

Nghiem, L.X., Hassam, M.S., Nutakki, R., George, A.E.D., 1993. Efficient modelling of asphaltene precipitation. In: Paper SPE 26643 Presented at the SPE Annual Technical Conference and Exhibition Held in Houston, Texas, USA, 3–6 October. https://doi.org/10.2118/26642-MS.

Nguyen, D., Wang, D., Oladapo, A., Zhang, J., Sickorez, J., Butler, R., Mueller, B., April 12, 2014. Evaluation of surfactants for oil recovery potential in shale reservoirs. In: Paper SPE 169085 Presented at the SPE Improved Oil Recovery Symposium, Tulsa, Oklahoma, USA, 12–16 April.

Ni, J., Jia, H., Pu, W., Jiang, H., Yang, J., Ren, Q., 2014. Thermal kinetics study of light oil oxidation using TG/DTG techniques. Journal of Thermal Analysis and Calorimetry 117, 1349–1355. https://doi.org/10.1007/s10973-014-3854-8.

Nickle, S.K., Meyers, K.O., Nash, L.J., 1987. Shortcomings in the use of TGA/DSC techniques to evaluate in-situ combustion. In: Paper SPE 16867 Presented at the SPE Annual Technical Conference and Exhibition Held in Dallas, Texas, USA, 27–30 September.

Nicot, J., Scanlon, B., 2012. Water use for Shale-gas production in Texas, U.S. Environmental Science and Technology 46 (6), 3580–3586.

Niu, B., Ren, S., Liu, Y., Wang, D., Tang, L., Chen, B., 2011. Low-temperature oxidation of oil components in an air injection process for improved oil recovery. Energy and Fuels 25 (10), 4299–4304.

North America Mfg Co, 1986. North American Combustion Handbook, third ed., vol. 1 Cleveland, OH 44105, USA.

North Dakota Council, 2012. Available from: http://www.ndoil.org/?id=78&advancedmode=1&category=Bakken+Basics.

NPC (National Petroleum Council), 2011. Unconventional Oil, Prepared by the Unconventional Oil Subgroup of the Resource & Supply Task Group.

Odusina, E.O., Sondergeld, C.H., Rai, C.S., 2011. NMR study of shale wettability. In: Paper SPE 147371 Presented at the Canadian Unconventional Resources Conference Held in Calgary, Alberta, Cnada, 15-17 November. https://doi.org/10.2118/147371-MS.

Ojha, S.P., Misra, S., Tinni, A., Sondergeld, C., Rai, C., 2017. Relative permeability estimates for Wolfcamp and Eagle Ford shale samples from oil, gas and condensate windows using adsorption -desorption measurements. Fuel 208, 52–64.

Olson, D.K., Hicks, M.D., Hurd, B.G., Sinnokrot, A.A., Sweigart, C.N., 1990. Design of a novel flooding system for an oil-wet central texas carbonate reservoir. In: Paper SPE 20224 Presented at the SPE/DOE Enhanced Oil Recovery Symposium Held in Tulsa, Oklahoma, USA, 22–25 April.

Onaisi, A., Audibert, A., Bieber, M.T., Bailey, L., Denis, J., Hammond, P.S., 1993. X-ray tomography vizualization and mechanical modelling of swelling shale around the wellbore. Journal of Petroleum Science and Engineering 9, 313–329.

Orangi, A., Nagarajan, N.R., Honarpour, M.M., Rosenzweig, J., 2011. Unconventional shale oil and gas-condensate reservoir production, impact of rock, fluid, and hydraulic

fractures. In: Paper 140536 Presented at SPE Hydraulic Fracturing Technology Conference Held in Woodlands, Texas, USA, 24–26 January 2011.
Orozco, D., Fragoso, A., Selvan, K., Aguilera, R., 2018. Eagle ford huff-and-puff gas injection pilot: comparison of reservoir simulation, material balance and real performance of the pilot well. In: Paper SPE 191575 Presented at the SPE Annual Technical and Exhibition Held in Dallas, Texas, USA, 24–26 September. https://doi.org/10.2118/191575-MS.
Otsu, N., 1979. A threshold selection methods from gray-level histograms. IEEE Transactions on Systems, Man, and Cybernetics 9, 62–66. https://doi.org/10.1109/TSMC.1979.4310076.
Pagels, M., Hinkel, J.J., Willberg, D.M., 2012. Measuring capillary pressure tells more than pretty pictures. In: Paper SPE 151729 Presented at the SPE International Symposium and Exhibition on Formation Damage Control Held in Lafayette, Louisiana, USA, 15–17 February. https://doi.org/10.2118/151729-MS.
Paktinat, J., Pinkhouse, J.A., Stoner, W.P., Williams, C., Carder, G.A., Penny, G.S., 2005. Case histories: post-frac fluid recovery improvements of Appalachian Basin gas reservoirs. In: Paper SPE 97365 Presented at the SPE Eastern Regional Meeting, Morgantown, West Virginia, USA, 14–16 September.
Palisch, T.T., Vincent, M., Handren, P.J., 2010. Slickwater fracturing: food for thought. SPE Production and Operations 25 (03), 327–344. https://doi.org/10.2118/115766-PA.
Paria, S., Khilar, K.C., 2004. A review on experimental studies of surfactant adsorption at the hydrophilic solid–water interface. Advances in Colloid and Interface Science 110, 75–95. https://doi.org/10.1016/j.cis.2004.03.001.
Park, J.H., Shin, H.J., Kim, M.H., 2016. Application of montmorillonite in bentonite as a pharmaceutical excipient in drug delivery systems. Journal of Pharmaceutical Investigation 46 (4), 363–375.
Parmar, J.S., Dehghanpour, H., Kuru, E., 2013. Drainage against gravity: factors impacting the load recovery in fractures. In: Paper SPE 164530 Presented at the SPE Unconventional Resources Conference Held in Woodlands, Texas, USA, 10–12 April. https://doi.org/10.2118/164530-MS.
Parmar, J., Dehghanpour, H., Kuru, E., 2014. Displacement of water by gas in propped fractures: combined effects of gravity, surface tension, and wettability. Journal of Unconventional Oil and Gas Resources 5, 10–21.
Parra, J.E., Pope, G.A., Mejia, M., Balhoff, M.T., 2016. New approach for using surfactants to enhance oil recovery from naturally fractured oil-wet carbonate reservoirs. In: Paper SPE 181713 Presented at the SPE Annual Technical Conference and Exhibition Held in Dubai, UAE, 26–28 September.
Pedlow, J., Sharma, M., 2014. Changes in shale fracture conductivity due to interactions with water-based fluids. In: Paper SPE 168586 Presented at the SPE Hydraulic Fracturing Technology Conference Held in Woodlands, Texas, USA, 4–6 February.
Peng, D.-Y., Robinson, D.B., 1976. A new two-constant equation of state. Industrial and Engineering Chemistry Fundamentals 15 (1), 59–64. https://doi.org/10.1021/i160057a011.
Peng, S., Xiao, X., 2017. Investigation of multiphase fluid imbibition in shale through synchrotron-based dynamic micro-CT imaging. Journal of Geophysical Research Solid Earth 122, 4475–4491. https://doi.org/10.1002/2017JB014253.
Penny, G.S., Pursley, J.T., 2007. Field studies of drilling and completion fluids to minimize damage and enhance gas production in unconventional reservoirs. In: Paper SPE 107844 Presented at the European Formation Damage Conference, Scheveningen, the Netherland, 30 May-1 June.
Perry, R.H., Chilton, C.H., Kirkpatrick, S.D., 1963. Chemical Engineers Handbook. McGraw-Hill Book Co., New York.

Petijohn, F.J., 1957. Sedimentary Rocks, second ed. Harper & Row Publishers, New York.
Phillips, Z.D., Halverson, R.J., Strauss, S.R., Layman II, J.M., Green, T.W., 2009. A case study in the Bakken formation: changes to hydraulic fracture stimulation treatments result in improved oil production and reduced treatment costs. In: Paper SPE 108045 Presented at the Rocky Mountain Oil & Gas Technology Symposium Held in Denver, Colorado, USA, 16–18 April.
Potapenko, D.I., Tinkham, S.K., Lecerf, B., Fredd, C.N., Samuelson, M.L., Gillard, M.R., Le Calvez, J.H., Daniels, J.L., 2009. Barnett shale refracture stimulations using a novel diversion technique. In: Paper SPE 119636 Presented at the SPE Hydraulic Fracturing Technology Conference Held in Woodlands, Texas, USA, 19–21 January.
Prasad, R.S., Slater, J.A., 1986. High-Pressure combustion tube tests. In: Paper SPE 14919 Presented at the SPE Enhanced Oil Recovery Symposium Held in Tulsa, Oklahoma, USA, 20–23 April. https://doi.org/10.2118/14919-MS.
Prats, M., 1982. Thermal Recovery. SPE Monograph, vol. 7. American Institute of Mining, Mettallurgical, and Petroleum Engineers, Inc., Dallas, Texas, USA.
Pu, W.F., Liu, P.G., Li, Y.B., Jin, F.Y., Liu, Z.Z., 2015. Thermal characteristics and combustion kinetics analysis of heavy crude oil catalyzed by metallic additives. Industrial and Engineering Chemistry Research 54 (46), 11525–11533.
Qi, C.W., 2015. Hydraulically fractured zone is actually "dead oil zone" in tight reservoir. Inner Mongolian Petrochemical 17, 146–147.
Raghavan, R., Chin, L.Y., 2002. Productivity changes in reservoirs with stress-dependent permeability. In: Paper SPE 77535 Presented at the SPE Annual Technical Conference and Exhibition, San Antonio, Texas, USA, 29 September-2 October. https://doi.org/10.2118/77535-MS.
Rahman, M.K., Hossain, M.M., Rahman, S.S., 2002. A shear-dilation-based model for evaluation of hydraulically stimulated naturally fractured reservoirs. International Journal for Numerical and Analytical Methods in Geomechanics 26 (5), 469–497.
Rai, R.R., 2003. Parametric Study of Relative Permeability Effects on Gas-Condensate Core Floods and Wells. Masters' thesis, University of Texas at Austin, Austin, Texas, USA.
Rai, S.K., Bera, A., Mandal, A., 2015. Modeling of surfactant and surfactant–polymer flooding for enhanced oil recovery using STARS (CMG) software. Journal of Petroleum Exploration and Production Technology 5 (1), 1–11.
Rapoport, L.A., 1955. Scaling laws for use in design and operation of water-oil flow models. Transactions of the American Institute of Mining, Metallurgical and Petroleum Engineers, Incorporated (AIME) 204, 143–150.
Ren, S.R., Greaves, M., Rathbone, R.R., 1999. Oxidation kinetics of North sea light crude oils at reservoir temperature. Trans IChemE 77, 385–394. Part A.
Rilian, N.A., Sumestry, M., Wahyuningsih, 2010. Surfactant stimulation to increase reserves in carbonate reservoir "a case study in Semoga field". In: Paper SPE 130060 Presented at the SPE EUROPEC/EAGE Annual Conference and Exhibition Held in Barcelona, Spain, 14–17 June.
Rodriguez, E., Comes, J., Trujillo, M., Belgrave, J.D.M., 2012. A framework for consolidating air injection experimental data. In: Paper SPE 152048 Presented at the SPE Latin American and Caribbean Petroleum Engineering Conference Held in Mexico City, Mexico, April 16–18.
Roshan, H., Ehsani, S., Marjo, C.E., Andersen, M.S., Acworth, R.I., 2015. Mechanisms of water adsorption into partially saturated fractured shales: an experimental study. Fuel 159, 628–637.
Roshan, H., Al-Yaseri, A.Z., Sarmadivaleh, M., Iglauer, S., 2016. On wettability of shale rocks. Journal of Colloid and Interface Science 475 (August), 104–111. https://doi.org/10.1016/j.jcis.2016.04.041.

Ross, J.K., Bustin, R.M., 2009. The importance of shale composition and pore structure upon gas storage potential of shale gas reservoirs. Marine and Petroleum Geology 26, 916–927.

Rostami, A., Nasr-El-Din, H.A., 2014. Microemulsion vs. surfactant assisted gas recovery in low permeability formations with water blockage. In: Paper SPE 169582 Presented at the SPE Western North American and Rocky Mountain Joint Meeting, Denver, Colorado, USA, 16–18 April.

Roychaudhuri, B., Xu, J., Tsotsis, T.T., Jessen, K., 2014. Forced and spontaneous imbibition experiments for quantifying surfactant efficiency in tight shales. In: Paper SPE 169500 Presented at the SPE Western North American and Rocky Mountain Joint Meeting Held in Denver, Colorado, USA, 17–18 April.

Sagdeev, D., Fomina, M., Mukhamedzyanov, G.K., Abdulagatov, I., 2013. Experimental study of the density and viscosity of n-heptane at temperatures from 298 K to 470 K and pressure upto 245 MPa. International Journal of Thermophysics 34 (1), 1–33.

Sakthikumar, S., Madaoui, K., Chastang, J., 1995. An investigation of the feasibility of air injection into a waterflood light oil reservoir. In: Paper SPE 29806 Presented at the SPE Middle East Oil Show Held in Bahrain, 11–14 March.

Salathiel, R.A., 1973. Oil recovery by surface film drainage in mixed-wettability rocks. Journal of Petroleum Technology 25, 1216–1224. https://doi.org/10.2118/4104-PA.

Salehi, M., Johnson, S.J., Liang, J.-T., 2008. Mechanistic study of wettability alteration using surfactants with applications in naturally fractured reservoirs. Langmuir 24, 14099–14107. https://doi.org/10.1021/la802464u.

Samanta, A., Bera, A., Ojha, K., Mandal, A., 2012. Comparative studies on enhanced oil recovery by alkali–surfactant and polymer flooding. Journal of Petroleum Exploration and Production Technology 2 (2), 67–74.

Sanchez-Rivera, D., Mohanty, K., Balhoff, M., 2015. Reservoir simulation and optimization of huff-and-puff operations in the Bakken shale. Fuel 147, 82–94.

Santos, H., da Fontoura, S.A.B., 1997. Concepts and misconceptions of mud selection criteria: how to minimize borehole stability problems?. In: Paper SPE 38644 Presented at the Annual Technical Conference and Exhibition, San Antonia, 5–8 October https://doi.org/10.2118/38644-MS.

Santos, H., da Fontoura, S.A.B., Gupta, A., Roegiers, J.-C., 1997a. Laboratory tests for wellbore stability in deepwater, Brazil. In: Paper SPE 38977 presented at the fifth Latin American and Caribbean Petroleum Engineering Conference and Exhibition, Rio de Janeiro, Brazil, 30 August–3 September. https://doi.org/10.2118/38977-MS.

Santos, H., Rego, L.F.B., da Fontoura, S.A.B., 1997b. Integrated study of shale stability in deepwater, Brazil. In: Paper SPE 38961 presented at the Latin American and Caribbean Petroleum Engineering Conference, 30 August-3 September, Rio de Janeiro, Brazil.

Sarma, H.K., Das, S.C., 2009. Air injection potential in Kenmore oilfield in Eromanga Basin, Australia: a screening study through thermogravimetric and calorimetric analyses. In: Paper SPE 120595 Presented at the SPE Middle East Oil and Gas Show and Conference Held in Manama, Bahrain, 15–18 March.

Sarma, H.K., Yazawa, N., Moore, R.G., Metha, S.A., Okazawa, N.E., Ferguson, H., Ursenbach, M.G., 2002. Screening of three light-oil reservoirs for application of air injection process by accelerating rate calorimetric and TG/PDSC tests. Journal of Canadian Petroleum Technology 41 (03), 50–61. https://doi.org/10.2118/02-03-04.

Sayed, M.A., Al-Muntasheri, G.A., 2014. Liquid bank removal in production wells drilled in gas-condensate reservoirs: a critical review. In: Paper SPE 168153 Presented at the SPE International Symposium and Exhibition on Formation Damage Control Held in Lafayette, Louisiana, USA, 26–28 February.

Sayed, M., Liang, F., Ow, H., 2018. Novel surface modified nanoparticles for mitigation of condensate and water blockage in gas reservoirs. In: Paper SPE 189959 Presented at the SPE International Conference and Exhibition on Formation Damage Control, Lafayette, Louisiana, USA, 7–9 February.

Schechter, D.S., Denqen, Z., Orr, F.M., 1991. Capillary imbibition and gravity segregation in low IFT systems. In: Paper SPE 22594 Presented at the SPE Annual Technical Conference and Exhibition Held in Dallas, Texas, USA, 6–9 October.

Schechter, D.S., Zhou, D., Orr Jr., F.M., 1994. Low IFT drainage and imbibition. Journal of Petroleum Science and Engineering 11, 283–300.

Schepers, K.C., Nuttall, B.C., Oudinot, A.Y., Gonzalez, R.J., 2009. Reservoir modeling and simulation of the devonian gas shale of eastern Kentucky for enhanced gas recovery and CO2 storage. In: Paper SPE 126620 Presented at the Annual 2009 SPE International Conference on Capture, Storage, and Utilization, Sango, California, USA, 10–11 November.

Schmid, K.S., Geiger, S., 2013. Universal scaling of spontaneous imbibition for arbitrary petrophysical properties: water-wet and mixed-wet states and Handy's conjecture. Journal of Petroleum Science and Engineering 101, 44–61.

Schmidt, M., Sekar, B.K., 2014. Innovative Unconventional2 EOR-A light EOR an unconventional tertiary recovery approach to an unconventional Bakken reservoir in southeast Saskatchewan. In: Paper WPC-21-1921 Presented at the 21st World Petroleum Congress Held in Moscow, Russia, 15–19 June.

Schmitt, L., Forsans, T., Santarelli, F.J., 1994. Shale testing and capillary phenomena. International Journal of Rock Mechanics and Mining Science and Geomechanics Abstracts 31 (5), 411–427.

Scholz, C.H., 1972. Static fatigue of quartz. Journal of Geophysical Research 77, 2104–2114.

Schwartz, M.W., Mukherjee, A.K., 1974. The migration of point defects in crack tip stress fields. Materials Science and Engineering 13, 175–179.

Seethepalli, A., Adibhatla, B., Mohanty, K.K., 2004. Physicochemical interactions during surfactant flooding of fractured carbonate reservoirs. SPE Journal 9 (4), 411–418.

Settari, A., Sullivan, R.B., Bachman, R.C., 2002. The modeling of the effect of water blockage and geomechanics in waterfracs. In: Paper SPE 77600 Presented at the SPE Annual Technical Conference and Exhibition Held in San Antonia, Texas, USA, 29 September –2 October.

Shanley, K.W., Cluff, R.M., Robinson, J.W., 2004. Factors controlling prolific gas production from low-permeability sandstone reservoirs: implications for resource assessment, prospect development, and risk analysis. AAPG Bulletin 88 (8), 1083–1121.

Sharma, M.M., Manchanda, R., 2015. The role of induced un-propped (IU) fractures in unconventional oil and gas wells. In: Paper SPE 174946 Presented at the SPE Annual Technical Conference and Exhibition, Houston, Texas, USA, 28–30 September.

Sharma, M.M., Manchanda, R., Gilmore, E.D., 2013. Systems and methods for injection and production from a single wellbore. In: Patent Cooperation Treaty (PCT) WO2013159007A1, October 24.

Sharma, G., Mohanty, K., August 2013. Wettability alteration in high-temperature and high-salinity carbonate reservoirs. SPE Journal 646–655. https://doi.org/10.2118/147306-PA.

Sharma, S., Sheng, J.J., 2017. A comparative study of huff-n-puff gas and solvent injection in a shale gas condensate core. Journal of Natural Gas Science and Engineering 38, 549–565.

Sharma, S., Sheng, J.J., 2018. Comparison of huff-n-puff gas injection and solvent injection in large-scale shale gas condensate reservoirs. Journal of Natural Gas Science and Engineering 52, 434–453.

Sharma, M.M., Wunderlich, R.W., 1987. The alteration of rock properties due to interactions with drilling-fluid components. Journal of Petroleum Science and Engineering 1 (2), 127–143.

Sharma, S., Sheng, J.J., Shen, Z., 2018. A comparative experimental study of huff-n-puff gas injection and surfactant treatment in shale gas-condensate cores. Energy and Fuels 32, 9121–9131.

Sharp, K.V., Adrian, R.J., Santiago, J.G., Molho, J.I., 2001. Liquid Flow in Microchannels, Chapter 10, the MEMS Handbook (Gad El-Hak, M.). CRC Press.

Shayegi, S., Jin, Z., Schenewerk, P., Wolcott, J., 1996. Improved cyclic stimulation using gas mixtures. In: Paper SPE 36687 Presented at the SPE Annual Technical Conference and Exhibition Held in Denver, Colarado, USA, 6–9 October. https://doi.org/10.2118/36687-MS.

Shen, Z., Sheng, J.J., 2016. Experimental study of asphaltene Aggregation during CO_2 and CH_4 injection in shale oil reservoirs. In: Paper SPE 179675 Presented at the SPE Improved Oil Recovery Conference Held in Tulsa, Oklahoma, USA, 11–13 April.

Shen, Z., Sheng, J.J., 2017a. Experimental study of permeability reduction and pore size distribution change due to asphaltene deposition during CO_2 huff and puff injection in Eagle Ford shale. Asia-Pacific Journal of Chemical Engineering 12 (3), 381–390.

Shen, Z., Sheng, J.J., 2017b. Investigation of asphaltene deposition mechanisms during CO_2 huff-n-puff injection in Eagle Ford shale. Petroleum Science and Technology 35 (20), 1960–1966.

Shen, Z., Sheng, J.J., 2018. Experimental and numerical study of permeability reduction caused by asphaltene precipitation and deposition during CO_2 huff and puff injection in Eagle Ford shale. Fuel 211, 432–445.

Shen, Z., Sheng, J.J., 2019. Optimization strategy to reduce asphaltene deposition associated damage during CO_2 huff-n-puff injection in shale. Arabian Journal for Science and Engineering published online. https://doi.org/10.1007/s13369-018-03701-w.

Shen, Y., Ge, H., Li, C., Yang, X., Ren, K., Yang, Z., Su, S., 2016. Water imbibition of shale and its potential influence on shale gas recovery – a comparative study of marine and continental shale formations. Journal of Natural Gas Science and Engineering 35, 1121–1128.

Shen, Y., Ge, H., Meng, M., Jiang, Z., Yang, X., 2017. Effect of water imbibition on shale permeability and its influence on gas production. Energy and Fuels 31, 4973–4980.

Sheng, J.J., 2011. Modern Chemical Enhanced Oil Recovery: Theory and Practice. Elsevier, Burlington, MA 01803, USA.

Sheng, J.J., 2012. In: Sheng, J.J. (Ed.), Surfactant Enhanced Oil Recovery in Carbonate Reservoirs, Book Chapter in Enhanced Oil Recovery Field Cases. Elsevier.

Sheng, J.J., 2013a. Review of surfactant enhanced oil recovery in carbonate reservoirs. Advances in Petroleum Exploration and Development 6 (1), 1–10.

Sheng, J.J., 2013b. Comparison of the effects of wettability alteration and IFT reduction on oil recovery in carbonate reservoirs. Asia-Pacific Journal of Chemical Engineering 8 (1), 154–161.

Sheng, J.J., 2013c. In: Sheng, J.J. (Ed.), Introduction to MEOR and Field Applications in China, Chapter 19 in EOR Field Case Studies. Elsevier, pp. 543–560.

Sheng, J.J., 2013d. In: Sheng, J.J. (Ed.), Foams and Their Applications in Enhancing Oil Recovery, Chapter 11 in EOR Field Case Studies. Elsevier, pp. 251–280.

Sheng, J.J., 2014. Critical review of low-salinity waterflooding. Journal of Petroleum Science and Engineering 120, 216–224.

Sheng, J.J., 2015a. Preferred calculation formula and buoyancy effect on capillary number. Asia-Pacific Journal of Chemical Engineering 10 (3), 400–410. https://doi.org/10.1002/apj.1883.

Sheng, J.J., 2015b. Increase liquid oil production by huff-n-puff of produced gas in shale gas condensate reservoirs. Journal of Unconventional Oil and Gas Resources 11, 19–26.
Sheng, J.J., 2015c. Status of alkaline flooding technology. Journal of Petroleum Engineering and Technology 5 (1), 44–50.
Sheng, J.J., 2015d. Enhanced oil recovery in shale reservoirs by gas injection, invited review. Journal of Natural Gas Science and Engineering 22, 252–259.
Sheng, J.J., 2017a. Critical review of field EOR projects in shale and tight reservoirs. Journal of Petroleum Science and Engineering 159, 654–665.
Sheng, J.J., 2017b. Optimization of huff-n-puff gas injection in shale oil reservoirs. Petroleum 3, 431–437.
Sheng, J.J., 2017c. What type of surfactants should be used to enhance spontaneous imbibition in shale and tight reservoirs? Journal of Petroleum Science and Engineering 159, 635–643.
Sheng, J.J., Chen, K., 2014. Evaluation of the EOR potential of gas and water injection in shale oil reservoirs. Journal of Unconventional Oil and Gas Resources 5, 1–9.
Sheng, J.J., Maini, B.B., Hayes, R.E., Tortike, W.S., 1997. Experimental study of foamy oil stability. Journal of Canadian Petroleum Technology 36 (4), 31–37.
Sheng, J.J., Maini, B.B., Hayes, R.E., Tortike, W.S., 1998. A non-equilibrium model to calculate foamy oil properties. Journal of Canadian Petroleum Technology 38 (4), 38–45.
Sheng, J.J., Mody, F., Griffith, P.J., Barnes, W.N., 2016. Potential to increase condensate oil production by huff-n-puff gas injection in a shale condensate reservoir. Journal of Natural Gas Science and Engineering 28, 46–51. https://doi.org/10.1016/j.jngse.2015.11.031.
Shi, C., Horne, R.N., 2008. Improved recovery in gas-condensate reservoirs considering compositional variations. In: Paper SPE 115786 Presented at the SPE Annual Technical Conference and Exhibition Held in Denver, Colorado, USA, 21–24 September. https://doi.org/10.2118/115786-MS.
Shoaib, S., Hoffman, B.T., 2009. CO2 flooding the Elm Coulee field. In: Paper SPE 123176 Presented at the SPE Rocky Mountain Petroleum Technology Conference Held in Denver, Colorado, UAS, 14–16 April.
Showalter, W.E., March 1963. Combustion-drive tests. SPE Journal 53–58.
Shuler, P.J., Tang, H., Lu, Z., Tang, Y., 2011. Chemical process for improved oil recovery from Bakken shale. In: Paper SPE 147531 Presented at the Canadian Unconventional Resources Conference Held in Calgary, Alberta, Canada, 15–17 November.
Siddiqui, M.A.Q., Ali, S., Fei, H., Roshan, H., 2018. Current understanding of shale wettability: a review on contact angle measurements. Earth-Science Reviews 181, 1–11.
Siebold, A., Walliser, A., Nardin, M., Oppliger, M., Schultz, J., 1997. Capillary rise for thermodynamic characterization of solid particle surface. Journal of Colloid and Interface Science 186 (1), 60–70.
Sigmund, P.M., 1976. Prediction of molecular diffusion at reservoir conditions. Part II—estimating the effects of molecular diffusion and convective mixing in multicomponent systems. Journal of Canadian Petroleum Technology 15 (3), 53–62.
Singer, P.C., Stumm, W., 1970. Acidic mine drainage: the rate-determining step. Science 167 (3921), 1121–1123.
Singh, H., 2016. A critical review of water uptake by shales. Journal of Natural Gas Science and Engineering 34, 751–766.
Singh, R., Mohanty, K.K., 2015. Foams with wettability-altering capabilities for oil-wet carbonates: a synergistic approach. In: Paper SPE 175027 Presented at the SPE Annual Technical Conference and Exhibition, Houston, Texas, USA, 28–30 September.

Siratovich, P.A., Sass, I., Homuth, S., et al., 2011. Thermal stimulation of geothermal reservoirs and laboratory investigation of thermally-induced fractures. In: Prod., Geothermal Resources Council Annual Meeting 2011, San Diego, California, vol. 35, pp. 1529–1535.

Soliman, M.Y., East, L.E., Augustine, J.R., 2010. Fracturing design aimed at enhancing fracture complexity. In: Paper SPE 130043 Presented at the SPE EUROPEC/EAGE Annual Conference and Exhibition in Barcelona, Spain, 14–17 June.

Song, C., Yang, D., 2013. Performance evaluation of CO_2 huff-n-puff processes in tight oil formations. In: Presented SPE 167217 at the SPE Unconventional Resources Conference Canada, Calgary, Alberta, Canada, 5–7 November. https://doi.org/10.2118/167217-MS.

Song, Y., Zhuo, L., Lin, J., Feng, H., 2015. The concept and the accumulation characteristics of unconventional hydrocarbon resources. Petroleum Science 12, 563–572.

Søreide, I., Whitson, C.H., 1992. Peng-Robinson predictions for hydrocarbons, CO_2, N_2, and H_2S with pure water and NaCI brine. Fluid Phase Equilibria 77, 217–240.

Sorensen, J.A., Hawthorne, S.B., Jin, L., Bosshart, N.W., Torres, J.A., Azzolina, N.A., Kurz, B.A., Smith, S.A., Jacobson, L.L., Doll, T.E., Gorecki, C.D., Harju, J.A., Steadman, E.N., 2017. Subtask 2.20 – Bakken CO2 Torage and Enhanced Recovery Program – Phase II, Final Report to National Energy Technology Laboratory. Department of Energy, USA, April 2018.

Sorensen, J.A., Pekot, L.J., Torres, J.A., Jin, L., Hawthorne, S.B., Smith, S.A., Jacobson, L.L., Doll, T.E., 2018. Field test of CO2 injection in a vertical middle bakken well to evaluate the potential for enhanced oil recovery and CO2 storage. In: Paper URTeC 2902813 Presented at the Unconventional Resources Technology Conference in Houston, Texas, USA, 23–25 July. https://doi.org/10.15530/URTEC-2018-2902813.

Sorensen, J.A., Hamling, J.A., 2016. Historical Bakken Test Data Provide Critical Insights on EOR in Tight Oil Plays. Available from: http://www.aogr.com/magazine/cover-story/historical-bakken-test-data-provide-critical-insights-on-eor-in-tight-oil-p.

Speight, J.G., 2017. Deep Shale Oil and Gas. Elsevier, Cambridge, Massachusetts, USA.

Standnes, D.C., Austad, T., 2000. Wettability alteration in chalk 2. Mechanism for wettability alteration from oil-wet to water-wet using surfactants. Journal of Petroleum Science and Engineering 28, 123–143.

Standnes, D.C., Nogaret, L.A.D., Chen, H., Austad, T., 2002. An evaluation of spontaneous imbibition of water into oil-wet carbonate reservoir cores using a nonionic and a cationic surfactant. Energy and Fuels 16 (6), 1557–1564.

Steiger, R.P., August 1982. Fundamentals and use of potassium/polymer drilling fluids to minimize drilling and completion problems associated with hydratable clays. Journal of Petroleum Technology 1661–1670. https://doi.org/10.2118/10100-PA.

Sun, Y., Bai, B., Wei, M., 2015. Microfracture and surfactant impact on linear cocurrent brine imbibition in gas-saturated shale. Energy and Fuels 29, 1438–1446.

Swain, M.V., Williams, J.S., Lawn, B.R., Beek, J.J.H., 1973. A comparative study of the fracture of various silica modifications using the Hertzian test. Journal of Materials Science 8, 1153–1164.

Tabatabal, A., Gonzalez, M.V., Harwell, J.H., Scamehorn, J.F., May 1993. Reducing surfactant adsorption in carbonate reservoirs. SPERE 117–122.

Tadema, H.J., Wiejdema, J., 1970. Spontaneous ignition of oil sands. Oil and Gas Journal 68 (50), 77–80.

Tagavifar, M., Balhoff, M., Mohanty, K., Pope, G.A., January 2019. Dynamics of low-interfacial-tension imbibition in oil-wet carbonates. SPE Journal 1–16. https://doi.org/10.2118/194194-PA.

Takahashi, S., Kovscek, A.R., 2009. Spontaneous counter current imbibition and forced displacement characteristics of low permeability, siliceous rocks. In: Paper SPE 121354 Presented at the Western Regional Meeting, San Jose, California, USA, 24–26 March. https://doi.org/10.2118/121354-MS.

Taleghani, A.D., Ahmadi, M., Wang, W., Olson, J.E., 2014. Thermal reactivation of microfractures and its potential impact on hydraulic-fracture efficiency. SPE Journal 19 (05), 761–770.

Talens, F.I., Paton, P., Gaya, S., 1998. Micellar flocculation of anionic surfactants. Langmuir 14, 5046–5050.

Tang, G.Q., Firoozabadi, A., 2002. Relative permeability modification in gas/liquid systems through wettability alteration to intermediate gas wetting. SPE Reservoir Evaluation and Engineering 5 (6), 427–436.

Tang, A.-Y., Li, W., 2010. Application of huff-n-puff water injection in Niuquanhu reservoir. Yuha Oil and Gas 15 (3), 274–275.

Tangirala, S., Sheng, J.J., 2018. Effects of invasion of water with and without surfactant on the oil production and flowback through an oil wet matrix – a microfluidic chip based study. Open Journal of Yangtze Gas and Oil 3, 278–292.

Tangirala, S., Sheng, J.J., 2019a. Investigation of Oil Production and Flowback in Hydraulically-Fractured Water-Wet Formations Using the Lab-On-A-Chip Method (accepted for publication in Fuel).

Tangirala, S., Sheng, J.J., 2019b. Roles of Surfactants in Invasion, Soaking and Flow Back in Oil-Wet Cores (submitted for journal publication).

Tangirala, S., Sheng, J.J., Tu, J., 2019. Chip flood (vs) core flood – assessment of flowback and oil productivity in oil-wet hydraulic fractured rocks. Open Journal of Yangtze Gas and Oil 4, 59–78.

Tchistiakov, A.A., 2000. Colloid chemistry of in-situ clay-induced formation damage. Society of Petroleum Engineers. In: Paper SPE 58747 Presented at the SPE International Symposium on Formation Damage Control Held in Lafayette, Louisiana, USA, 23–24 February. https://doi.org/10.2118/58747-MS.

Teklu, T.W., Alameri, W., Kazemi, H., Graves, R.M., 2015. Contact angle measurements on conventional and unconventional reservoir cores. In: Paper SPE 178568 Presented at the Unconventional Resources Technology Conference Held in San Antonia, Texas, USA, 20–22 July. https://doi.org/10.15530/URTEC-2015-2153996.

Thomas, G.A., Monger-McClure, T.G., May 1991. Feasibility of cyclic CO_2 injection for light-oil recovery. SPE Reservoir Evaluation and Engineering 179–184.

Thomas, F.B., Zhou, X., Bennion, D.B., Bennion, D.W., 1995. Towards optimizing gas condensate reservoirs. In: Paper PETSOC 95-09 Presented at the Annual Technical Meeting of Petroleum Society of Canada Held in Calgary, Alberta, Canada, June 7–9.

Thomas, A., Kumar, A., Rodrigues, K., Sinclair, R.I., Lackie, C., Galipeault, A., Blair, M., 2014. Understanding water flood response in tight oil formations: a case study of the lower Shaunavon. In: Paper SPE 171671 Presented at the SPE/CSUR Unconventional Resources Conference Held in Calgary, Alberta, Canada, 30 September–2 October.

Tiab, D., Donaldson, E.C., 2004. Petrophysics – Theory and Practice of Measuring Reservoir Rock and Fluid Transport Properties, second ed. Elsevier, Burlington, Massachusetts.

Tian, M., Lin, H., Sun, Y.W., Xu, Y.B., Gao, P., 2003. Huff-n-Puff test of oil extraction in a low-permeability and fractured reservoir. Global Geology 22 (3), 279–283.

Tingas, J., 2000. Numerical Simulation of Air Injection Processes in High Pressure Light & Medium Oil Reservoirs. PhD dissertation. University of Bath, Somerset, England.

Todd, M.R., Longstaff, W.J., 1972. The development, testing, and application of a numerical simulator for predicting miscible flood performance. Journal of Petroleum Technology 24 (7), 874–882.

Tovar, F.D., Eide, O., Graue, A., Schechter, D.S., 2014. Experimental investigation of enhanced recovery in unconventional liquid reservoirs using CO_2: a look ahead to the future of unconventional EOR. In: Paper SPE 169022 Presented at the SPE Unconventional Resources Conference Held in Woodlands, Texas, USA, 1–3 April.

Townsend, D.I., Tou, J.C., 1980. Thermal hazard evaluation by an accelerating rate calorimeter. Thermochimica Acta 3791, 1–30.

Tu, J., Sheng, J.J., 2019. Experimental and numerical study of shale oil EOR by surfactant additives in fracturing fluid. In: Paper URTeC 295 Presented at the Unconventional Resources Technology Conference Held in Denver, Colorado, USA, 22–24 July.

Turta, A.T., 2013. In: Sheng, J.J. (Ed.), Situ Combustion, Chapter 18 in EOR Field Case Studies. Elsevier, pp. 447–541.

Turta, A.T., Singhal, A.K., 2001. Reservoir engineering aspects of light-oil recovery by air injection. SPE Reservoir Evaluation and Engineering 4 (04), 336–344. https://doi.org/10.2118/72503-PA.

van Batenburg, D.W., de Zwart, A.H., Doush, M., 2010. Water alternating high pressure air injection. In: Paper SPE 129882 Presented at the SPE Improved Oil Recovery Symposium Held in Tulsa, Oklahoma, USA, April 24–28.

van Olphen, H., 1963. An Introduction to Clay Colloid Chemistry: For Clay Technologists, Geologists, and Soil Scientists. Interscience Publishers.

van Olphen, H., 1977. Clay Colloid Chemistry, second ed. John Wiley & Sons Inc., New York City.

Van Oss, C.J., Giese, R.F., Li, Z., Murphy, K., Norris, J., Chaudhury, M.K., et al., 1992. Determination of contact angles and pore sizes of porous media by column and thin layer wicking. Journal of Adhesion Science and Technology 6 (1992), 413–428.

Vandecasteele, I., Marí Rivero, I., Sala, S., Baranzelli, C., Barranco, R., Batelaan, O., Lavalle, C., 2015. Impact of shale gas development on water resources: a case study in northern Poland. Environmental Management 55 (6), 1285–1299.

Vengosh, A., Jackson, R., Warner, N., Darrah, T., Kondash, A., 2014. A critical review of the risks to water resources from unconventional shale gas development and hydraulic fracturing in the United States. Environmental Science and Technology 48 (15), 8334–8348.

Vijapurapu, C.S., Rao, D.N., 2004. Compositional effects of fluids on spreading, adhesion and wettability in porous media. Colloids and Surfaces A: Physicochemical and Engineering Aspects 241 (1–3), 335–342.

Vincent, M.C., 2010. Refracs - why do they work, and why do they fail in 100 published field studies?. In: Paper SPE 134330 Presented at the SPE Annual Technical Conference and Exhibition, Florence, Italy, 19–22 September.

Vincent, M.C., 2011. Restimulation of unconventional reservoirs: when are refracs beneficial? Journal of Canadian Petroleum Technology 50 (5), 36–52.

von Engelhardt, W., Lubben, H., 1957. Study of the influence of interfacial stress and contact angle on the displacement of oil by water in porous material, 11-test results. Erdol und Kohle 10 (12), 826–830.

Vossoughi, S., Willhite, G., El Shoubary, Y., Bartlett, G., 1983. Study of the clay effect on crude oil combustion by thermogravimetry and differential scanning calorimetry. Journal of Thermal Analysis 27 (1), 17–36.

Waltman, C., Warpinski, N., Heinze, J., 2005. Comparison of single and dual array microseismic mapping techniques in the Barnett Shale. SEG Technical Program Expanded Abstracts 1 (24), 1261.

Wan, T., Sheng, J.J., 2015a. Compositional modelling of the diffusion effect on EOR process in fractured shale-oil reservoirs by gas flooding. Journal of Canadian Petroleum Technology 54 (2), 107–115.

Wan, T., Sheng, J.J., 2015b. Evaluation of the EOR potential in hydraulically fractured shale oil reservoirs by cyclic gas injection. Petroleum Science and Technology 33, 812–818.

Wan, T., Sheng, J.J., Soliman, M.Y., 2013a. Evaluation of the EOR potential in shale oil reservoirs by cyclic gas injection. In: Paper SPWLA-D-12-00119 Presented at the SPWLA 54th Annual Logging Symposium Held in New Orleans, Louisiana, 22–26 June.

Wan, T., Sheng, J.J., Soliman, M.Y., 2013b. Evaluation of the EOR potential in fractured shale oil reservoirs by cyclic gas injection. In: Paper SPE 168880 or URTeC 1611383 Presented at the Unconventional Resources Technology Conference Held in Denver, Colorado, USA, 12–14 August.

Wan, T., Meng, X., Sheng, J.J., Watson, M., 2014a. Compositional modeling of EOR process in stimulated shale oil reservoirs by cyclic gas injection. In: Paper SPE 169069 Presented at the SPE Improved Oil Recovery Symposium Held in Tulsa, Oklahoma, USA, 12–16 April.

Wan, T., Yu, Y., Sheng, J.J., 2014b. Comparative study of enhanced oil recovery efficiency by CO_2 injection and CO_2 huff-n-puff in stimulated shale oil reservoirs. In: Paper 358937 Presented at the AIChE Annual Meeting Held in, Atlanta, Georgia, USA, 16-21 November.

Wan, T., Yu, Y., Sheng, J.J., 2015. Experimental and numerical study of the EOR potential in liquid-rich shales by cyclic gas injection. Journal of Unconventional Oil and Gas Resources 12, 56–67.

Wang, Y.Y., 2015. CO_2 flooding test in Fayang reservoir in Daqing Yushulin oilfield. Petroleum Geology and Oilfield Development in Daqing 34 (1), 136–139.

Wang, J., Rahman, S.S., 2015. An investigation of fluid leak-off due to osmotic and capillary effects and its impact on micro-fracture generation during hydraulic fracturing stimulation of gas shale. In: Paper SPE 137924 Presented at the EUROPEC, Madrid, Spain, 1–4 June.

Wang, X.K., Sheng, J.J., 2017a. Discussion of liquid threshold pressure gradient. Petroleum 3, 232–236.

Wang, X.-K., Sheng, J.J., 2017b. Effect of low-velocity non-darcy flow on well production performance in shale and tight oil reservoirs. Fuel 190, 41–46.

Wang, S., Civan, F., Strycker, A.R., 1999. Simulation of paraffin and asphaltene deposition in porous media. In: Paper SPE 50746 Presented at the SPE International Symposium on Oilfield Chemistry Held in Houston, Texas, USA, 16–19 February.

Wang, X., Luo, P., Er, V., Huang, S.S.S., 2010. Assessment of CO_2 flooding potential for Bakken formation, Saskatchewan. In: Paper SPE 137728 Presented at the SPE Canadian Unconventional Resources and International Petroleum Conference Held in Calgary, Alberta, Canada, 19–21 October.

Wang, D., Butler, R., Liu, H., Ahmed, S., 2011. Flow-Rate behavior and imbibition in shale. SPE Reservoir Evaluation and Engineering 14 (4), 485–492.

Wang, X.J., Shang, L.T., Zhang, M.H., Yang, W.Y., 2013. Field test of degradable fiber fracturing fluid. Petroleum Geology and Oilfield Development in Daqing 32 (2), 141–144.

Wang, P.P., Li, Q.D., Yang, B., Chai, H.Q., Li, L.L., Hu, G., Luo, D., Bo, G.P., 2015a. On the formation energy supplement in an 83 Zone in Chang 7 tight formation. Petrochemical Industry Application 34 (3), 58–62.

Wang, G., Zhao, Z., Li, K., Li, A., He, B., 2015b. Spontaneous imbibition laws and the optimal formulation of fracturing fluid during hydraulic fracturing in Ordos Basin. Procedia Engineering 126, 549–553.

Washburn, E.W., 1921. Dynamics of capillary flow. Physical Review 17 (3), 273–283.

Wei, F.R., 2016. Discussion of high-volume water injection and soaking effect in an ultra-low permeability tight formation. Exploration and Development 3, 155–157, 180.
Weinheimer, R.M., Evans, D.F., Cussler, E.L., 1981. Diffusion in surfactant solutions. Journal of Colloid and Interface Science 80 (2), 357–368.
Weiss, W.W., Xie, X., Weiss, J., Subramanium, V., Taylor, A., Edens, F., 2006. Artificial intelligence used to evaluate 23 single-well surfactant-Soak treatments. SPE Reservoir Evaluation and Engineering 6, 209–216.
Weng, X., Sesetty, V., Kresse, O., 2015. Investigation of shear-induced permeability in unconven tional reservoirs. In: Paper ARMA-2015-121 Presented at the 49th US Rock Mechanics/Geomechanics Symposium Held in San Francisco, CA, USA, 28 June-1 July.
Wiederhorn, S.M., 1978. Mechanisms of subcritical crack growth in glass. In: Bradt, R.C., Hasselman, D.P.H., Lange, F.F. (Eds.), Fracture Mechanics of Ceramics, vol. 4. Plenum Press, New York, pp. 549–580.
Wijaya, N., Sheng, J.J., 2019a. Effect of desiccation on shut-in benefits in removing water blockage in tight water-wet cores. Fuel 244, 314–323.
Wijaya, N., Sheng, J.J., 2019b. Shut-in effect in removing water blockage in shale-oil reservoirs with stress-dependent permeability considered. SPE Reservoir Evaluation and Engineering, 1–12.
Wijaya, N., Sheng, J.J., 2019c. Comparative study of well soaking timing (pre vs. Post flowback) for water block removal from matrix-fracture interface. Petroleum, in press.
Wijaya, N., Sheng, J.J., 2019d. Mitigating near-fracture blockage and enhancing oil recovery in tight reservoirs by adding surfactants in hydraulic fracturing fluid. Revision submitted to Journal of Petroleum Science and Engineering.
Wijaya, N., Sheng, J.J., 2019e. Maximizing long-term oil recovery in tight reservoirs by adding surfactants in hydraulic fracturing fluid: optimum interfacial tension and wettability criteria. Submitted to Colloids and Surfaces A: Physicochemical and Engineering Aspects.
Wong, R.C.K., 1998. Swelling and softening behaviour of La Biche shale. Canadian Geotechnical Journal 35, 206–221.
Wood, T., Milne, B., 2011. Waterflood Potential Could Unlock Billions of Barrels: Crescent Point Energy. http://www.investorvillage.com/uploads/44821/files/CPGdundee.pdf.
Xie, X., Weiss, W.W., Tong, Z., Morrow, N.R., 2005. Improved oil recovery from carbonate reservoirs by chemical stimulation. SPE Journal 10 (3), 276–285.
Xie, W., Shi, L.H., Lv, Y.H., Zeng, J., Wang, J.C., Zhang, L., 2016. Cyclic waterflooding scheme for heterogeneous reservoirs of ultra-low permeability. Unconventional Oil and Gas 3 (1), 47–52.
Xu, M., Dehghanpour, H., 2014. Advances in understanding wettability of gas shales. Energy and Fuels 28 (7), 4362–4375. https://doi.org/10.1021/ef500428y.
Xu, L., Fu, Q., 2012. Ensuring better well stimulation in unconventional oil and gas formations by optimizing surfactant additives. In: Paper SPE 154242 Presented at the SPE Western Regional Meeting Held in Bakersfield, California, USA, 21–23 March.
Xu, T., Spycher, N., Sonnenthal, E., Zhang, G., Zheng, L., Pruess, K., 2012. TOUGHREACT User's Guide: A Simulator Program for Non-isothermal Multiphase Reactive Transport in Variably Saturated Geological Media. Version 2.0.
Xue, H., Zhou, S., Jiang, Y., Zhang, F., Dong, Z., Guo, W., 2018. Effects of hydration on the microstructure and physical properties of shale. Petroleum Exploration and Development 45 (6), 1146–1153.

Yaich, E., Williams, S., Bowser, A., Goddard, P., Diaz de Souza, O.C., Foster, R.A., 2015. A case study: the impact of soaking on well performance in the Marcellus. In: Paper Presented at the Unconventional Resources Technology Conference Held in San Antonio, Texas, USA, 20–22 July. https://doi.org/10.15530/URTEC-2015-2154766.

Yan, Q., Lemanski, C., Karpyn, Z.T., Ayala, L.F., 2015. Experimental investigation of shale gas production impairment due to fracturing fluid migration during shut-in time. Journal of Natural Gas Science and Engineering 24, 99–105.

Yang, H.D., Wadleigh, E.E., 2000. Dilute surfactant IOR – design improvement for massive, fractured carbonate applications. In: Paper SPE 59009 Presented at the SPE International Petroleum Conference and Exhibition Held in Villahermosa, Mexico, 1–3 February 2000.

Yang, Y.D., Yang, Z.Z., Gan, Z.W., Jiang, H., Yi, Z.K., 2006. Application of huff-n-puff water injection in a single well in Tuha Field. Natural Gas Exploration and Development 29 (2), 32–35.

Yang, H., Li, S.X., Liu, X.Y., 2013. Characteristics and resource prospects of tight oil, shale oil in Ordos Basin. Acta Petrolei Sinica 34 (1), 1–11.

Yang, W., Feng, Y., Yang, Y., Fu, X., Feng, Y., 2015a. Conditions of shale oil accumulation and distribution of favorable areas in China. Xinjiang Petroleum Geology 36 (3), 253–257.

Yang, L., Ge, H., Shen, Y., Zhang, J., Yan, W., Wu, S., Tang, X., 2015b. Imbibition inducing tensile fractures and its influence on in-situ stress analyses: a case study of shale gas drilling. Journal of Natural Gas Science and Engineering 26, 927–939.

Yang, D., Song, C., Zhang, J., Zhang, G., Ji, Y., Gao, J., 2015c. Performance evaluation of injectivity for water-alternating-CO_2 processes in tight oil formations. Fuel 139, 292–300.

Yang, L., Ge, H., Shi, X., Cheng, Y., Zhang, K., Chen, H., Shen, Y., Zhang, J., Qu, X., 2016. The effect of microstructure and rock mineralogy on water imbibition characteristics in tight reservoirs. Journal of Natural Gas Science and Engineering 34, 1461–1471.

Yannimaras, D.V., Tiffin, D.L., 1995. Screening of oils for in-situ combustion at reservoir conditions via accelerating rate calorimetry. SPE Reservoir Engineering 10 (01), 36–39.

Yassin, M.R., Begum, M., Dehghanpour, H., 2017. Organic shale wettability and its relationship to other petrophysical properties: a Duvernay case study. International Journal of Coal Geology 169, 74–91.

Yoshiki, K.S., Phillips, C.R., 1985. Kinetics of the thermo-oxidative and thermal cracking reactions of Athabasca bitumen. Fuel 64 (11), 1591–1598.

Yu, Y., Sheng, J.J., 2015. An experimental investigation of the effect of pressure depletion rate on oil recovery from shale cores by cyclic N_2 injection. In: Paper URTeC 2144010 (SPE 178494) Presented at the Unconventional Resources Technology Conference Held in San Antonio, Texas, USA, 20–22 July.

Yu, Y., Sheng, J.J., 2016a. Experimental evaluation of shale oil recovery from Eagle Ford core samples by nitrogen gas flooding. In: Paper SPE 179547 Presented at the SPE Improved Oil Recovery Conference Held in Tulsa, Oklahoma, USA, 11–13 April.

Yu, Y., Sheng, J.J., 2016b. Experimental investigation of light oil recovery from fractured shale reservoirs by cyclic water injection. In: Paper SPE 180378 Presented at the SPE Western Regional Meeting Held in Anchorage, Alaska, USA, 23–26 May.

Yu, Y., Sheng, J.J., 2017. A comparative experimental study of IOR potential in fractured shale reservoirs by cyclic water and nitrogen gas injection. Journal of Petroleum Science and Engineering 149, 844–850.

Yu, W., Al-Shalabi, E.W., Sepehrnoori, K., 2014a. A sensitivity study of potential CO_2 injection for enhanced gas recovery in Barnett shale reservoirs. In: Paper SPE 169012

Presented in SPE Unconventional Resources Conference Held in Woodlands, Texas, USA, 1–3 April.

Yu, W., Lashgari, H., Sepehrnoori, K., 2014b. Simulation study of CO_2 huff-n-puff process in Bakken tight oil reservoirs. In: Paper SPE 169575 Presented at the SPE Western North American and Rocky Mountain Joint Meeting Held in Denver, Colorado, USA, 17–18 April. https://doi.org/10.2118/169575-MS.

Yu, Y., Sheng, J.J., Barnes, W., Mody, F., 2015. Evaluation of cyclic gas injection EOR performance on shale core samples using X-ray CT scanner. In: Paper 407411 Presented at the 2015 AIChE Annual Meeting Held in Salt Lake City, Utah, USA, 8–13 November.

Yu, Y., Li, L., Sheng, J.J., 2016a. Further discuss the roles of soaking time and pressure depletion rate in gas huff-n-puff process in fractured liquid-rich shale reservoirs. In: Paper SPE 181471 Presented at the SPE Annual Technical Conference and Exhibition Held in Dubai, UAE, 26–28 September 2016.

Yu, Y., Meng, X., Sheng, J.J., 2016b. Experimental and numerical evaluation of the potential of improving oil recovery from shale plugs by nitrogen gas flooding. Journal of Unconventional Oil and Gas Resources 15, 56–65.

Yu, Y., Li, L., Sheng, J.J., 2017. A comparative experimental study of gas injection in shale plugs by flooding and huff-N-puff processes. Journal of Natural Gas Science and Engineering 38, 195–202.

Yuan, B., Wang, Y., Zeng, S., 2018. Effect of slick water on permeability of shale gas reservoirs. Journal of Energy Resources Technology 140, 1–7, 112901.

Zelenev, A.S., Ellena, L., 2009. Microemulsion technology for improved fluid recovery and enhanced core permeability to gas. In: Paper SPE 122109 Presented at the 8th European Formation Damage Conference, Scheveningen, The Netherlands, 27–29 May.

Zeng, T.,S., Miller, C., Mohanty, K., 2018. Application of surfactants in shale chemical EOR at high temperatures. In: Paper SPE 190318 Presented at the SPE Improved Oil Recovery Symposium Held in Tulsa, Oklahoma, USA, 14–18 April. https://doi.org/10.2118/190318-MS.

Zhang, F., Adel, I.A., Park, K.H., Saputra, I.W.R., Schechter, D.S., 2018. Enhanced oil recovery in unconventional liquid reservoir using a combination of CO_2 huff-n-puff and surfactant-assisted spontaneous imbibition. In: Paper SPE 191502 Presented at the SPE Annual Technical Conference and Exhibition, Dallas, Texas, USA, 24–26 September.

Zhang, J., Liu, H., 1991. Determination of viscosity under pressure for organic substances and its correlation with density under high pressure. Journal of Chemical Industry and Engineering 3, 269–277.

Zhang, Y., Sheng, J.J., 2016. Oxidation kinetics study of the wolfcamp light oil. Petroleum Science and Technology 34 (13), 1180–1186. https://doi.org/10.1080/10916466.2016.1190753.

Zhang, S., Sheng, J.J., 2017a. Effect of water imbibition on hydration induced fracture and permeability of shale cores. Journal of Natural Gas Science and Engineering 45, 726–737.

Zhang, S., Sheng, J.J., 2017b. Study of the propagation of hydration-induced fractures in Mancos shale using computerized tomography. International Journal of Rock Mechanics and Mining Sciences 95 (2017), 1–7.

Zhang, S., Sheng, J.J., 2017c. Effects of salinity and confining pressure on hydration-induced fracture propagation and permeability of Mancos shale. Rock Mechanics and Rock Engineering 50 (11), 2955–2972.

Zhang, Y., Sheng, J.J., 2017d. The mechanism of the oxidation of light oil. Petroleum Science and Technology 35 (12), 1224–1233.

Zhang, S., Sheng, J.J., 2018. Effect of water imbibition on fracture generation in Mancos shale under isotropic and anisotropic stress conditions. Journal of Geotechnical and Geoenvironmental Engineering 144 (2), 1–10, 04017113.
Zhang, S., Sheng, J.J., Qiu, Z.S., 2016. Water adsorption on kaolinite and illite after polyamine adsorption. Journal of Petroleum Science and Engineering 142, 13–20.
Zhang, S., Sheng, J.J., Shen, Z., 2017. Effect of hydration on fractures and permeabilities in Mancos, Eagleford, Barnette and Marcellus shale cores under compressive stress conditions. Journal of Petroleum Science and Engineering 156, 917–926.
Zhang, F., Saputra, I.W.R., Adel, I.A., Schechter, D.S., 2018. Scaling for wettability alteration induced by the addition of surfactants in completion fluids: surfactant selection for optimum performance. In: Paper URTeC 2889308 Presented at the Unconventional Resources Technology Conference Held in Houston, Texas, USA, 23–25 July. https://doi.org/10.15530/URTEC-2018-2889308.
Zhang, F., Saputra, I.W.R., Parsegov, S.G., Adel, I.A., Schechter, D.S., 2019. Experimental and numerical studies of EOR for the wolfcamp formation by surfactant enriched completion fluids and multi-cycle surfactant injection. In: Paper SPE 194325 Presented at Te SPE Hydraulic Fracturing Technology Conference and Exhibition Held in the Woodlands, Texas, USA, 5–7 February. https://doi.org/10.2118/194325-MS.
Zhao, J.Z., Jia, H., Pu, W.F., Wang, L.L., Peng, H., 2012. Sensitivity studies on the oxidation behavior of crude oil in porous media. Energy and Fuels 26 (11), 6815–6823.
Zhao, H., Ning, Z., Zhao, T., Che, F., Zhang, R., Hou, T., 2015. Applicability comparison of nuclear magnetic resonance and mercury injection capillary pressure in characterisation pore structure of tight oil reservoirs. In: Paper SPE 177026 Presented at the Asia Pacific Unconventional Resources Conference and Exhibition, Brisbane, Australia, 2015. https://doi.org/10.2118/177026-MS.
Zhao, W., Hu, S., Hou, L., 2018. Connotation and strategic role of in-situ conversion processing of shale oil underground in the onshore China. Petroleum Exploration and Development 45 (4), 537–545.
Zheng, T.Y., Pang, X.R., Zhang, K., Zhou, L.M., 2017. Determination of the lower properties of an effective reservoir for the tight west slope of Mahu Sag. Science Technology and Engineering 17 (24), 196–203.
Zhou, Q.F., Yang, G.F., 2012. Definitions and applications of tight oil and shale oil terms. Oil and Gas Geology 33 (4), 541–544, 570.
Zhou, X., Morrow, N.R., Ma, S., 2000. Interrelationship of wettability, initial water saturation, aging time, and oil recovery by spontaneous imbibition and waterflooding. SPE Journal 5 (02), 199–207.
Zhou, Z., Abass, H., Li, X., Teklu, T., 2016. Experimental investigation of the effect of imbibition on shale permeability during hydraulic fracturing. Journal of Natural Gas Science and Engineering 29, 413–430.
Zhu, P., Balhoff, M.T., Mohanty, K.K., 2015. Simulation of fracture-to-fracture gas injection in an oil-rich shale. In: Paper SPE 175131 Presented at the SPE Annual Technical Conference and Exhibition Held in Houston, Texas, USA, 28–30 September.
Zoback, M.D., Kohli, A., Das, I., Mcclure, M.W., 2012. The importance of slow slip on faults during hydraulic fracturing stimulation of shale gas reservoirs. In: Paper SPE 155476 Presented at the SPE Americas Unconventional Resources Conference Held in Pittsburgh, Pennsylvania, USA 5–7 June.
Zolfaghari, A., Dehghanpour, H., Noel, M., Bearinger, D., 2016. Laboratory and field analysis of flowback water from gas shales. Journal of Unconventional Oil and Gas Resources 14, 113–127. https://doi.org/10.1016/j.juogr.2016.03.004.
Zou, C.N., Zhu, R.K., Wu, S.T., Yang, Z., Tao, S.Z., Yuan, X.J., He, L.H., Yang, H., Xu, C.C., Li, D.H., Bai, B., Wang, F., 2012. Types of accumulation, characteristics,

mechanisms and prospects of conventional and unconventional oil and gas formations, a case study of tight oil and gas formations in China. Acta Petrolei Sinica 33 (2), 173–187.
Zou, C.N., Tao, S.Z., Bai, B., Yang, Z., Zhu, R.K., Hou, L.H., Yuan, X.J., Zhang, G.S., Wu, S.T., Pang, Z.L., Wang, L., 2015. Differences and relations between unconventional and conventional oil and gas. China Petroleum Exploration 20 (1), 1–16.
Zubari, H.K., Sivakumar, V.C.B., 2003. Single well tests to determine the efficiency of alkaline-surfactant injection in a highly oil-wet limestone reservoir. In: Paper SPE 81464 Presented at the Middle East Oil Show Held in Bahrain, 9–12 June.

Index

Note: 'Page numbers followed by "*f*" indicate figures and "*t*" indicate tables'.

A

Accelerating rate calorimetry (ARC), 402, 406–407, 412, 416–417, 433–434
Acid preflush, 198
Activation energy (EACT), 417
Adibhatla et al. (2005) model, 221–223
AEO-9. *See* Alcohol ethoxylate (AEO-9)
AES. *See* Alcohol ether sulfate (AES)
Air foam drive, 460–461
Air injection
  air requirement in combustion, 453–454
  EOR mechanisms and EOR potential in shale and tight reservoirs, 454–455
  kinetic parameters, 407–426
  laboratory experimental facilities, 402–407
    ARC, 406–407
    combustion tube test, 405–406
    DSC, 402–403
    RTO, 405
    SBR, 403–405
    TG, 402
  minimum oil content for combustion, 453
  oxidation reactions, 427–435
  spontaneous ignition, 435–451
Air requirement in combustion, 453–454
Alcohol ether sulfate (AES), 243–245, 303–304
Alcohol ethoxylate (AEO-9), 243–245, 303–304
Alcohol olefin sulfonate (AOS), 303–304
Alkali sodium metaborate ($NaBO_2 \cdot 4H_2O$), 304–307
Alkaline precipitation, 304–307
Alkyl propoxy sulfate (APS), 460–461
Alpha olefin sulfonate (AOS), 243–245, 460–461
Ammonium persulfate ($(NH_4)_2S_2O_8$), 209–211
Amott method, 253–254
Amott–Harvey method. *See* Amott method
Anionic fluorosurfactant mixture, 102–103
Anionic surfactants, 303–304
  bilayer mechanism by, 236–237, 237f
  micellar solubilization of organic component by, 237
AOS. *See* Alcohol olefin sulfonate (AOS); Alpha olefin sulfonate (AOS)
APS. *See* Alkyl propoxy sulfate (APS)
Aquthermolysis, 428
Aragonite. *See* Calcite ($CaCO_3$)
ARC. *See* Accelerating rate calorimetry (ARC)
Argon permeability, 187
Aromatics, 455
Arrhenius equation, 407, 410–411, 417, 424
Artificial ignition, 442
Asphaltene precipitation and deposition, 61, 63f
  effect of asphaltene deposition on huff-n-puff optimization, 75–80
  binary interaction coefficients, 72t
  comparison of permeability before and after huff and puff injection, 68f
  comparison of predicted oil recovery with experimental data, 75f
  deposition mechanisms, 69–71
  experiments of permeability reduction and, 61–69
  fractions, 64f
  numerical analysis, 71–75
  particle sizes, 62f
  pore throat size distribution for shale cores, 65f
  tuned parameters of asphaltene deposition model, 74t
Atomic force microscope, 256–257

Attapulgite, 194
Autoignition. *See* Spontaneous ignition
Autolab-1000 servo-hydraulic operated system, 187

B

Back-pressure regulator (BPR), 37–38
Barnett shales, 202–203, 202f, 205
Barrels of oil equivalent (BOE), 94
Base shale model, 300, 310–315
  capillary pressure curves, 311f
  grid parameters of simulation model, 311t
  model parameters of relative permeabilities and capillary pressure, 312t
  parameters for capillary desaturation curves, 315t
  relative permeability curves for matrix, 313f
Bedding effect, 186
Behaviors of surfactants, 303–307
BHFP. *See* Bottomhole flowing pressure (BHFP)
BHP, 362–363
Bilayer mechanism by anionic surfactants, 236–237, 237f
Binary interaction coefficients for Bakken oil, 119–120, 120t
Block oil saturations, 89–90, 89f
BOE. *See* Barrels of oil equivalent (BOE)
Bond number, 298, 300
Bond scission reaction, 428
Borosilicate glass chip, 343
Bottomhole flowing pressure (BHFP), 122
BPR. *See* Back-pressure regulator (BPR)
Branched fractures, 461
Brazilian tests, 212
Brooks-Corey model, 223
BTC 8358 (quaternary amine surfactant), 242–243

C

CAC. *See* Cationics (CAC)
Calcite ($CaCO_3$), 205–206, 209–210
Capillary desaturation curve (CDC), 214, 224, 312
  for water, oil, and microemulsion phases, 215f
Capillary force, 302–303
Capillary imbibition, 309, 347–349
Capillary number (N_c), 226, 295
Capillary pressure, 231, 254–255, 293, 302–303, 314–315, 389–390
  change, 321
  effect on forced imbibition, 322–326, 325t
Capillary rise method, 254–255
Carbon dioxide (CO_2), 205–206
  EOR, 200–201
    in fractured shale and tight reservoirs, 48f
    huff-n-puff in Bakken formation, Elm Coulee field, 55
    huff-n-puff in Burning Tree-State No. 36–2H well, 55–57
    huff-n-puff tests, experimental setup, 39f
  injection, 36, 396
    in Song-Fang-Dun Field, Daqing, 147–148
    in Yu-Shu-Lin Field, Daqing, 148
  MMP for Wolfcamp oil, 38
  potential in Bakken formation, 143
  sequestration, 144–145
Carbonate cores, 68–69, 246
Carbonated water, 200–201
  effects in fluid-rock interactions, 197–201
    oil recovery of forced displacement, 201f
    oil recovery of spontaneous countercurrent imbibitions, 200f
    tensile fractures in organic-rich shale, 198f
    woodford shale frac, 199t–200t
Carboxylates, 242–243
Catalytic effect of additives, 434
Cationic surfactants, 238
Cationics (CAC), 233–234
CDC. *See* Capillary desaturation curve (CDC)
Changed phase behavior, 114–115
Channeling, 320
Chemical blends, 458–460
Chlorite, 194

Clay, 2, 194
  stabilizers, 197
  swelling, 191
Claystone, 2
CMG PVT simulator, 77–78
CMG-STARS model, 224–226
CMM. *See* Computer Modeling Group (CMM)
CO_2 mole fraction in oil (CO_{2oil}), 40–41, 41f, 53
Cocurrent flow, 301–303
Coke, 412
Combined Amott-USBM method, 253–254
Combustion
  air requirement in, 453–454
  minimum oil content for, 453
Combustion tube test (CT), 405–406
Compositional thermal simulator, 464
Computer Modeling Group (CMM), 138
Condensate recovery
  at every cycle, 84–85, 86f
  during gas flooding experiment, 86, 87f
Condensate saturation at every cycle, 84–85, 86f
Confining stress effect, 179–186, 184f
  anisotropic core holder and related CT parts, 184f
  CT images after oil and water imbibition tests, 185f
  CT images of Mancos shale core under various icps, 181f
  cutaway view of Hoek triaxial cell, 182f
  Swelling strain of Mancos, 183f
  test conditions and masses after imbibitions, 185t
Contact angle, 222–223, 253–255
Cooling effect of injected water, 204–205
Core flooding system, 69, 69f
Core saturation with oil, 9–11
Core size effect, 18–20
Core-scale modeling of gas and solvent performance, 91–98
Corey-type of equation, 311–312
Corrected recovery factor (RF_c), 101, 102f
Counter-current flow, 301–303
Crack propagation, 195
Critical capillary number ($(N_C)_c$), 214–215
Cryogenic liquid (N_2), 464
Crystallization of solid minerals, 205–206
CT. *See* Combustion tube test (CT)
CT scanner, 9–10, 14–15
  number, oil saturation, and cumulative oil recovery, 15f
  number comparison between dry and oil saturated core, 12f
  number cumulative distribution, 15f
  slice images of oil saturated core plug, 11f
Cycle time effect, 107, 107t

D

Dalton's law, 356
Darcy's equation, 372–373, 381
Deionized water (DI water), 188–190, 391
Delay, 339
  time of spontaneous ignition, 441–442
Deposition mechanisms for asphaltene precipitation and deposition, 69–71
Desiccation, 372–373
DI water. *See* Deionized water (DI water)
Differential scanning calorimetry (DSC), 402–403, 407, 409–410, 412, 444
Differential thermal analyzer (DTA), 412
Diffusion effect, 41–43, 42f
  in spontaneous imbibition, 296–297
Dimensionless capillary number (N_C), 214
Dimensionless parameter, 443
Dimensionless time, 283–284
Dimeric surfactants, 212
Discrete particle model, 197
Displacement equipment, 14–15, 16f
Dissolved lime (CaO), 205–206
Divalent scavengers, 242–243
Diversion technology in fracturing, 463–464
Dodecyl trimethylammonium bromide (DTAB), 212
Dolomite ($CaMg(CO_3)_2$), 209–210
Dry gas injection, 399
DSC. *See* Differential scanning calorimetry (DSC)

DTA. *See* Differential thermal analyzer (DTA)
DTAB. *See* Dodecyl trimethylammonium bromide (DTAB)
DTG. *See* Time-derivative thermogravimetric (DTG)
Dual permeability model, 118–119

E

Eagle Ford, 175–176
  core, 307
  outcrop cores, 133–134
  project in La Salle County, TX, 57–58
EDL. *See* Electric double layer (EDL)
Effective mobility for cocurrent flow, 284
Electric double layer (EDL), 351
End-point relative permeabilities and exponents, 223
Endothermic behavior, 412–417
Energized fluids, 464
Enhanced oil recovery (EOR), 1, 457
  air foam drive, 460–461
  branched fractures, 461
  chemical blends, 458–460
  diversion technology in fracturing, 463–464
  energized fluids, 464
  experimental setup, 16f
  mechanisms and EOR potential in shale and tight reservoirs, 454–455
  methods, 309
  performance with number of cycles, 29–31
  refracturing, 463
  sequential method of huff-n-puff CO_2 injection and SASI, 457–458
  thermal recovery, 464–467
  zipper fracture, 462–463
EO. *See* Ethoxylate (EO)
EOR. *See* Enhanced oil recovery (EOR)
Ethane, 36
Ethomeen, 245–246
  Ethomeen T/25, 245–246
Ethoxy sulfates, 242–243
Ethoxylate (EO), 245–246
Ethoxylate sulfates, 242–243
Ethoxylated aliphatic amine, 245–246
Exothermic behavior, 412–417
Exponential SDP model, 364–366
ExxonMobil, 4–5

F

Favor water flow back, 379
FD. *See* Fuel deposition (FD)
Feasibility of gas flooding, 149
Field applications of gas flooding, 145–149
Field model, 440–441
Field performance, 151
Field tests of surfactant EOR, 336–337
Flooding, 5, 5f, 7, 83–84
  general experimental setup for, 83f
Flow back, 341–345
  efficiency, invasion depth effect on, 385–390, 386f
  initial wettability effect on, 379–385
  procedure, 340
  process, 378
Flow Rate Platform (FRP), 343
Flow-through drying process, 355
Fluid entrapment, 350
Fluid production, 7
Fluid-rock interactions, 173
  bedding effect, 186
  confining stress effect, 179–186
  cooling effect of injected water, 204–205
  evidences of existing natural fractures reopening, 173–179
  existing natural fracture effect, 186
  high-pH water effect, 202–203
  low-pH and carbonated water effect, 197–201
  microfractures generation evidences, 173–179
  permeability changes from water-rock interactions, 187–191
  reaction-induced fractures, 205–211
  rock mechanical properties, effect on, 191–193
  surfactant effects, 212
  views and hypotheses, 194–197
    fracture creation during desiccation, 194f
    internal shear stress and promoted fracture creation, 196f

Fluorinated surfactant, 102–103
Fluorocarbon surfactants, 219, 253
Forced imbibition, 309. *See also* Spontaneous imbibition
  base shale model, 310–315
  effect of capillary pressure, 322–326, 325t
  experimental study, 331–336
    experimental conditions for pressurized soaking and depletion tests, 332t
    modified high-pressure Amott apparatus, 331f
    spontaneous imbibition, forced imbibition and cyclic injection, 335f–336f
  field tests of surfactant EOR, 336–337
  effect of pressure gradient, 326–330
  relative permeability change *vs.* capillary pressure change, 321
  shale rock *vs.* sand rock, 315–321
Formation damage, 61, 64–65, 71
Formation heating, 399–400
Fractional wettability, 253
Fracture conductivity, shut-in time effect on, 375–379
Fracture permeability, 328–329
  of fractured Bakken shale, 201
Fracture-to-fracture gas-flooding scheme, 136–137
Fractured reservoirs, 320
Fracturing
  diversion technology in, 463–464
  fluid, 341
  treatments, 339–340
Fracturing fluid flow back, 340
  field observations and experimental results on flow back, 341–345
    flow back *vs.* hydrocarbon production, 341–345
    low flow back, 341
  invasion depth effect on flow back efficiency and late time oil rate, 385–390
  low flow back mechanisms, 345–359
  shut-in time effect
    on flow back, 359–374
    on fracture conductivity, 375–379
  solutions to deal with flow back, 395–400
    avoid using trapping fluids, 395
    CO_2 injection, 396
    early high drawdown, 395–396
    formation heating, 399–400
    injection of dry gas, 399
    solvent injection, 396
    use of surfactants, 396–399
  surfactants effect on flow back, 390–395
Frank-Kamenestskii method, spontaneous ignition prediction using, 443–446
Frequency factor (FREQFAC), 417
FRP. *See* Flow Rate Platform (FRP)
Fuel deposition (FD), 412, 428
Fundamental flow theory, 395

G

Gas condensate reservoir, 81–82
  core-scale modeling of gas and solvent performance, 91–98
  distribution, 82f
  experimental setup, 83–84
  factors affecting huff-n-puff gas injection performance, 105–109
  field case of methanol injection, 101–102
  huff-n-puff gas injection, 84–85
  huff-n-puff *vs.* gas flooding, 86–91
  mechanisms of huff-n-puff injection, 110–115
  optimization of huff-n-puff injection, 109–110
  phase diagram, 82f
  reservoir-scale modeling of gas and solvent performance, 98–101
  surfactant treatment, 102–105
Gas flooding, 86–91, 133. *See also* Waterflooding
  in Bakken formation in North Dakota, 147
  CO_2 injection
    in Song-Fang-Dun Field, Daqing, 147–148
    in Yu-Shu-Lin Field, Daqing, 148
  experimental setup for, 134f
  feasibility, 149

Gas flooding (*Continued*)
field applications, 145–149
gas saturation profiles, 136f
huff-n-puff gas injection *vs.*, 137–145
oil recovery factors at different flooding pressures, 135f
performance, 148–149, 149t
comparison of huff-n-puff, 87f
research results, 133–137
section, 154
in Viewfield Bakken field, Saskatchewan, 145–147
Gas injection, 7, 162–165, 401, 448–450
testing, 161
Gas penetration depth, 51–54
Gas relative permeabilities, 119–120, 121f
Gas reservoirs. *See* Vaporization
Gas-oil ratio (GOR), 436–437
GEM simulator, 72
GOR. *See* Gas-oil ratio (GOR)
Gravity effects in spontaneous imbibition, 297–300
Guerbet alkoxy sulfate, 242–243
Gypsum, 210

H

Half-fractures, 137–138
Handy method, 282–283
Heat balance equation, 443
Heat-wait-search sequence (HWS sequence), 406–407
Heavier alcohols, 396
Heavy oil, 435
High-pH water effects in fluid-rock interactions, 202–203
High-pressure air injection (HPAI), 401, 429
High-temperature oxidation (HTO), 402–403, 410, 412. *See also* Low-temperature oxidation (LTO)
History matched base model, 391–395
History-matched model, 438–439
Hoek triaxial cell, 182
Horizontal injectors, 155–156
Horizontal well drilling and fracturing, 4–5
HPAI. *See* High-pressure air injection (HPAI)
HTO. *See* High-temperature oxidation (HTO)
Huff-n-puff, 7, 61, 83–84, 86–91, 151
effect of asphaltene deposition on optimization, 75–80
CO_2 injection
in Parshall field, 57
performance, 108–109, 109t
diffusion effect, 41–43
effect
of core size, 18–20
of injected gas composition, 31–36
of pressure and pressure depletion rate, 20–25
of soaking time, 25–29, 25f–26f
EOR performance with number of cycles, 29–31
experimental methods, 9–18
core saturation with oil, 9–11
experimental setup, 83f
experimental verification of effectiveness, 17–18
factors affecting huff-n-puff gas injection performance, 105–109
effect of cycle time, 107, 107t
effect of huff pressure, 105–106, 106t
effect of puff pressure, 106–107, 106t
effect of soak time, 107–108, 108t
field projects, 54–60, 56t
gas huff-n-puff performance, 60
gas injection, 84–85
gas flooding *vs.*, 137–145
gas penetration depth, 51–54
initial simulation studies of injection, 8
injection
mechanisms, 110–115
optimization, 109–110, 109t
mechanisms, 46–51
minimum miscible pressure, 37–41
mode, 5, 5f
nitrogen injection performance, 17f
oil recovery histories for different soaking times, 28f
sequential method of CO_2 injection, 457–458

stress-dependent permeability effect, 45–46
system pressure profile, 27f
water injection, 166–167, 169–171
water saturation effect, 43–45
Huff-n-puff gas injection optimization, 117–118
base simulation model, 118–121, 119f
effect of huff-n-puff times, 123t
matrix and fracture properties, 119t
near-wellbore block pressures, 124f–125f, 127f
number of cycles, 130
optimum huff time and puff time, 122–129
optimum soaking time, 129–130, 129t
principles, 121–122
start time of huff-n-puff, 130–132
Huff-n-puff injection optimization, 109–110, 109t
Huff-soak-puff process, 7
HWS sequence. *See* Heat-wait-search sequence (HWS sequence)
Hydration, 347
of clays, 194
softening of shale, 196
swelling, 191, 196
Hydraulic fracturing, 186, 463–464
operation, 198
Hydrocarbon production, flow back *vs.*, 341–345
Hydrogen peroxide (H_2O_2), 206, 208
Hydrous pyrolysis. *See* Aquthermolysis

I

IAE. *See* Isomeric alcohol ethoxylates (IAE)
IFT. *See* Interfacial tension (IFT)
Illite, 194
IMEX (black oil simulator), 138
In-situ combustion (ISC), 401
Incremental oil recovery, 231
Initial water content effects on spontaneous imbibition, 301
Initial wettability effect
on flow back, 379–385
in spontaneous imbibition, 290–293
Initially water-wet, 391–395
Injected gas composition effect, 31–36, 34f–35f
Injected water, cooling effect of, 204–205
Injection
modes, 5–6
pressure, 136–137
rate, 326–330
Interfacial tension (IFT), 114, 279, 293, 348–349, 460–461
effect in spontaneous imbibition, 293–296
simulation analysis, 295–296
theoretical and experimental analysis, 293–295
reduction, 213–214, 390–395
capabilities, 247t–248t
mechanisms, 214–217
wettability alteration *vs.*, 226–236
effects, 227–236, 241–242
mathematical treatments, 220–226
relative importance, 230–231
Interfacial Tension Modifier (ITM), 375–377
Internal olefin sulfonate (IOS), 242–243
International Union of Pure and Applied Chemistry (IUPAC), 281–282, 304
Interpolation parameter, 226
Invaded zone remained oil-wet, 384
Invasion, 344–345
depth effect on flow back efficiency and late time oil rate, 385–390
Ion-pair mechanism, 237–239, 239f
IOS. *See* Internal olefin sulfonate (IOS)
IPA. *See* Isopropyl alcohol (IPA)
ISC. *See* In-situ combustion (ISC)
Isomeric alcohol ethoxylates (IAE), 243–245, 303–304
Isopropanol. *See* Isopropyl alcohol (IPA)
Isopropyl alcohol (IPA), 36, 97
ITM. *See* Interfacial Tension Modifier (ITM)
IUPAC. *See* International Union of Pure and Applied Chemistry (IUPAC)

K

K-value for component, 225

Kaolinite, 194
Kerogen, 4
Kinetic parameters for oxidation reaction rates, 407–426
  DSC, 409–410
  example to build kinetic simulation model, 420–426
    defining parameters for oxidation reactions, 421–425
    defining pseudocomponents, 421, 422t
    defining reaction scheme, 425–426
    model grids, 420–421
  exothermic and endothermic behavior, 412–417
  practical values of, 410–411
  simulation approach to estimating heating values and, 417–420
  TGA, 407–409
Klinkenberg effect, 187
Known 1/3–1/7 rule-of-thumb, 61–62

L

Lab-on-a-Chip method, 343
Laboratory-scale model, 438–439
Langmuir-type isotherm, 224–225
Late time oil rate, invasion depth effect on, 385–390
Leverett-J function, 314–315
Li and Horne method, 284–285
Light oil, 435
Liquid blockage, 83
Liquid condensate, 81–82, 82f
Liquid recovery factor, 43, 45f, 104, 159–160
Local porosity after asphaltene deposition, 72–73
Longitudinal relaxations, 257
Low flow back, 341, 345–359
  capillary imbibition, 347–349
  evaporation, 355–358
  fluid entrapment, 350
  osmosis, 350–355
  permeability jail, 358–359
  subirreducible initial water saturation, 346–347
Low-pH effects in fluid-rock interactions, 197–201
  oil recovery
    of forced displacement, 201f
    of spontaneous countercurrent imbibitions, 200f
  pump schedule in Woodford shale frac. job, 199t–200t
  tensile fractures in organic-rich shale, 198f
Low-temperature oxidation (LTO), 403–404, 410, 412, 424–425
  oxygen consumption rate in, 452
  thermal effect in, 446

M

Mancos, 175–176
Marcellus, 175–176
Mattax and Kyte method, 283–284
Maximum capillary number ($(N_C)_{max}$), 214–215
Maximum injection pressure, 127
mD. *See* MilliDarcy (mD)
Meridian Oil, 154
Methane huff-n-puff injection, 104
Methane-n-butane mixture
  liquid dropout curve, 85f
  phase diagram of, 84, 85f
Methanol, 36
  injection field case, 101–102
Micellar solubilization of organic component by anionic surfactants, 237
Microbial EOR, 467
Microchip, 344–345
Microemulsion, 225–226
Microfractures, 209–210
  generation, 173–179
Micropore, 2
Microtomography, 256–257
Microwave energy, 464–465
Middle Bakken data, 118
Middle Woodford shale, 193
MilliDarcy (mD), 2
Minimum miscible pressure (MMP), 37–41, 38f–39f
Minimum oil content for combustion, 453
Minimum production pressure, 127
Miscibility
  of gas and oil, 37–38

model, 138
MMP. *See* Minimum miscible pressure (MMP)
Mohr circle, 204–205
Monolayer adsorption by nonionic surfactants, 240–241, 241f
Montmorillonite, 194
Mudstone, 2

N

n-heptane reverse flooding test, 69, 70f
N_2 huff-n-puff tests, 11–13, 12f
Nano-CT, 257
NanoDarcies (nD), 2
NaPA. *See* Sodium polyacrymide (NaPA)
Natural fractures (NF), 364–366
  effects on fluid-rock interactions, 186
  reopening, 173–179
    Barnett Shale with clear fractures parallel, 175f
    Mancos, Barnett, Marcellus, and Eagle Ford samples, 175f
    mancos rock samples, 174f
    Oil RF, 175f
    shale permeability changes with immersion time, 177f
    water imbibition times, 178f
Natural gas, 401
Natural gas liquid (NGL), 147
nD. *See* NanoDarcies (nD)
Negative temperature coefficient (NTC), 428–429
Net present value (NPV), 149, 370
NF. *See* Natural fractures (NF)
NGL. *See* Natural gas liquid (NGL)
Nitrogen
  flooding, 139, 149
  purging, 424–425
NMR method. *See* Nuclear magnetic resonance method (NMR method)
Nonionic fluorinated polymeric surfactants, 242–243
Nonionic fluorinated surfactant, 103
Nonionic surfactants, 245–246
  monolayer adsorption by, 240–241
Nonswelling minerals, 188
Nonwetting phase velocity, 285
NPV. *See* Net present value (NPV)
NTC. *See* Negative temperature coefficient (NTC)
Nuclear magnetic resonance method (NMR method), 257–261, 290
Numerical analysis for asphaltene precipitation and deposition, 71–75
Numerical simulation approach, 309

O

Oil recovery, 1, 133–134
  mechanisms of wettability alteration, 217–219
Oil recovery factor (Oil RF), 13, 18, 158, 164–165, 175f, 288, 291t, 316–317, 333–334. *See also* Recovery factor (RF)
  with and without including asphaltene deposition, 77f
  for cores, 19f
  at different huff pressures with asphaltene deposition, 79f
  at different puff pressures with asphaltene deposition, 80f
  at different soaking pressures and cycles, 39f
  dimensionless time *vs.*, 22f
  and matrix average pressure *vs.* operation time, 21f
  reductions by asphaltene deposition, 78f–79f
Oil relative permeabilities, 119–120, 120f–121f
Oil RF. *See* Oil recovery factor (Oil RF)
Oil saturation, 138–139, 138f, 318–319
Oil shale, 2, 4–5
Oil-wet(ness), 391–395
  chip, 386–390
  surfaces, 257
  system, 289
One-dimension (1D)
  laboratory-scale base model, 439
  simulation model, 110–112
Organic-rich shale reservoir, 197

Osmotic/osmosis, 350–355
  implications of osmotic phenomenon, 353–355
  osmotic mechanism in shale, 351–353
  phenomenon implications, 353–355
  pressure, 350–351
  in shale, 350–351
Oxidation, 407
Oxidation reactions, 427–435
  factors affecting oxidation reactions, 429–435
    catalytic effect of additives, 434
    gas phase *vs.* oil phase, 434
    light oil *vs.* heavy oil, 435
    pressure effect, 433–434
  rates, 407
  reaction schemes with kinetic data, 430t–432t
  terminologies and principles to defining reaction scheme, 427–429
Oxidative reagents, 206
Oxidizer, 415
Oxygen consumption rate in LTO, 452

P

Pass-over drying process, 355
PDSC tests. *See* Pressurized differential scanning calorimeter tests (PDSC tests)
Péclet number (N_{pe}), 41–42
PEEK. *See* Polyether ether ketone (PEEK)
Penetration depth, 53
Peng-Robinson EOS parameter, 119–120, 120t
Permeability changes
  due to water imbibition, 191f
  from water-rock interactions, 187–191
    axial displacement measurements, 190f
    swelling of sample with DI water injection, 189f
    upstream pressure measurements *vs.* time, 188f
Permeability jail, 358–359
Permeability recovery ratios, 381–384, 384f
Plugging deposition rate coefficient, 72–73
Plugging mechanism, 68–69
Poly-oxyethylene alcohol (POA), 233–234
Polyether ether ketone (PEEK), 343
Pore size distributions (PSD), 65
  for EF#1 core before and after huff and puff CO_2 injection, 66f
  for EF#2 core before and after huff and puff CO_2 injection, 67f
  for EF#5 core before and after huff and puff CO_2 injection, 67f
  of tested core samples before and after CO_2 huff and puff injection, 66f
Pore sizes, 3
Pore throat, 61, 64–65
Pore volumes (PV), 37–38, 344–345
Pore-space imaging methods, 256–257
Porosity, 10
Pressure
  depletion rate, 20–25
    comparison of experimental and simulation data, 24f
    effect of, 23f
    on oxidation reactions, 433–434
  gradient effect in alkali injection, 326–330, 326t
  maps, 138–139, 138f
Pressurized differential scanning calorimeter tests (PDSC tests), 433–434
Primary forced imbibition, 254
Propoxy sulfates, 242–243
PSD. *See* Pore size distributions (PSD)
Pseudocomponents, 421, 422t
Puff pressure, 78
  effect, 106–107, 106t
Purging gas, 402
PV. *See* Pore volumes (PV)
Pyrite (FeS_2), 209–211
Pyrolysis, 428

Q

Quantitative NMR wettability index, 259
Quizix pump, 156–158

R

Ramped temperature oxidation (RTO), 405
Raoult's law, 356
Reaction enthalpy (RENTH), 417
Reaction-induced fractures, 205–211
Recovery factor (RF), 14, 28, 94, 99–101, 136, 140–141, 285–288, 457–458. *See also* Oil recovery factor (Oil RF)
  of nitrogen flooding and huff-n-puff injection, 141f
Recovery ratios (*R*), 381–384
Reference time, 298
Refracturing, 463
  shale reservoirs, 337
Relative permeability
  change, 321
  for water phase, 216–217
Replacement reaction process, 210
Reservoir
  diagenesis processes, 346–347
  fluid composition, 119–120
  model, 88, 337
  pressure maps, 138–139, 139f
  reservoir-scale modeling of gas and solvent performance, 98–101
Residual saturations, 224
Retorting, 4–5
Revaporization by gas, 110–113
RF. *See* Recovery factor (RF)
Rock mechanical properties, fracturing fluids effect on, 191–193
  fracture conductivity reduction, 193f
  stress and CT images, 192f
  water imbibitions, 191f
  Young's moduli, 192f
RTO. *See* Ramped temperature oxidation (RTO)

S

S/V. *See* Surface-to-volume ratio (*S/V*)
Sand rock, 315–321
SASI. *See* Surfactant-assisted spontaneous imbibition (SASI)
Sasol's Alf-38 and Alf-69, 237
SBR. *See* Small batch reactor (SBR)
"Scab-liner" technique, 145–146
Scaling theories, 289
SDBS. *See* Sodium dodecyl benzenesulfonate (SDBS)
SDP. *See* Stress-dependent-permeability (SDP)
Secondary forced drainage, 254
Sequential method of huff-n-puff CO_2 injection, 457–458
Shale, 196–198
  EOR mechanisms and EOR potential in, 454–455
  formation, 3, 3t–4t
  gas permeability, 187
  oil, 2, 4–5
  osmosis in, 350–351
  osmotic mechanism in, 351–353
  rock, 315–321
Shale and tight
  formations wettability, 277–278
  reservoirs, 2–6
    production technologies, 6
  resources, 6
Shut-in time
  effect on 10-year discounted NPV, 371f
  effect on flow back, 359–374
    comparison of shut-in performance of pre-flow-back, 376f
    gas production rate, 361f
    pressure drop across core during flow back, 365f
    pressure drop across core during shut-in and flow back, 365f
    simulated BHP, 362f
    water production rate, 362f
    water saturation changes with time, 364f
    water saturations, 369f
  effect on fracture conductivity, 375–379
  effect on oil production rate and cumulative oil production volume, 367f
  initial wettability effect on flow back, 379–385
Shut-in, 339–340
  time effect on flow back, 359–374
Siltstone, 2

Simple interpolation technique, 221, 224
Simulation
  analysis, 295–296
  approach to estimating kinetic parameters and heating values, 417–420
  model, 438–439, 450, 466
  studies, 438–441
Sliding crack, 196–197
Small batch reactor (SBR), 402–405, 404f, 407
Smectite clays, 195–196
Soak time effect, 107–108, 108t
Soaking process, 15–17, 381
Soaking time, 5, 129–130, 129t, 140–141
  effect, 25–29, 25f–26f
Sodium dodecyl benzenesulfonate (SDBS), 212
Sodium hypochlorite (NaOCl), 206
Sodium peroxydisulfate ($Na_2S_2O_8$), 206
Sodium polyacrymide (NaPA), 242–243
Soltrol-130, 344
Solvents, 83, 91–92, 97, 101, 114
  injection, 396
  soaking process, 18
Spontaneous ignition, 435–451
  delay time of, 441–442
  experimental, 447
  field observations, 436–437
  laboratory observations, 437–438
  numerical analysis, 450–451
  oxygen consumption rate in LTO, 452
  prediction using Frank-Kamenestskii method, 443–446
  simulation studies, 438–441
  thermal effect in LTO, 446
Spontaneous imbibition, 279, 309. *See also* Forced imbibition
  behaviors of surfactants, 303–307
  countercurrent flow *vs.* cocurrent flow, 301–303
  diffusion effect, 296–297
  experiments, 227
  gravity effect, 297–300
  IFT effect, 293–296
  initial water content effect, 301
  effect of initial wettability and wettability alteration, 290–293
  method, 255–256
  effect of permeability and porosity, 285–290
    experimental observation, 289–290
    simulation results, 285–287
    theoretical considerations, 287–289
  theoretical equations, 279–285
    Handy method, 282–283
    Li and Horne method, 284–285
    Mattax and Kyte method, 283–284
    Washburn's equation, 280–282
  viscosity ratio effect, 301
5-spot pattern model, 204–205
Stimulated reservoir volume (SRV), 4–5, 118, 462–463
Stoichiometric coefficients of produced components (STOPROD), 417
Stoichiometric coefficients of reacting components (STOREAC), 417
Stress corrosion, 195
Stress-dependent-permeability (SDP), 364–366
  effect, 45–46
Stripping process of oil film, 241–242, 242f
Subirreducible initial water saturation, 346–347
  geological compression and diagenesis, 346–347
  hydration, 347
  vaporization, 346
Subirreducible water, 372–373
Sulfonates, 242–243
Sulfuric acid (H_2SO_4), 209–210
Surface deposition, 72–73
Surface-to-volume ratio (S/V), 290
Surfactant EOR
  field tests of, 336–337
  mechanisms relating to shale and tight formations, 236–242
    bilayer mechanism by anionic surfactants, 236–237
    effect of IFT reduction on wettability alteration, 241–242
    ion-pair mechanism, 237–239

micellar solubilization of organic component by anionic surfactants, 237
monolayer adsorption by nonionic surfactants, 240–241, 241f
surfactant adsorption mechanism, 239–240
Surfactant(s), 289, 295
additives, 340, 391
adsorption
isotherm, 224–225
mechanism, 239–240
behavior, 303–307
effect on flow back, 390–395
favorable conditions for invasion, flow back, and oil recovery, 390t
IFT and oil-wetness at end of early phase, 393f–394f
water saturation histories at different distances, 392f
effects in fluid-rock interactions, 212
injection, 166–167, 213–214
property data, 235–236, 235t
selection for wettability alteration, 242–253
treatment, 102–105
uses in flow back, 396–399
Surfactant-assisted spontaneous imbibition (SASI), 457–458
Swelling
effect, 47
by solvent, 114
Synergy ofwettability alteration and IFT reduction, 234–235, 235f

T

TAN. *See* Total acid number (TAN)
TBN. *See* Total base number (TBN)
TC. *See* Thermal cracking (TC)
Tetramethyl ammonium chloride ($Me_4N^+Cl^-$), 197
TG. *See* Thermogravimetry (TG)
TGA. *See* Thermogravimetric analysis (TGA)
Thermal cracking (TC), 428
Thermal effect in low-temperature oxidation, 446
Thermal pressurization, 464–465
Thermal recovery, 464–467
microbial EOR, 467
Thermal stimulation, 204
Thermogravimetric analysis (TGA), 407–409, 444
Thermogravimetry (TG), 402, 407
Thin layer wicking method, 254–255
3D simulation model, 227
Tight formation, 2–3, 3t–4t
Tight oil, 3
Tight reservoirs, EOR mechanisms and EOR potential in, 454–455
Time-derivative thermogravimetric (DTG), 407
TOC. *See* Total organic carbon (TOC)
Toluene reverse flooding test, 69, 71f
Total acid number (TAN), 246
Total base number (TBN), 246
Total hydrocarbons, 94, 97f
recovery factors
in different huff-n-puff time, 94f
in different injected pore volume, 95f
vs. injected BOE volume, 100f
in terms of costs, 96f
*vs.*time, 99f
Total organic carbon (TOC), 2, 277
TOUGHREACT simulator, 352–353
Traditional Amott cell, 331
Transverse relaxations, 257
Trapping fluids avoiding flow back, 395
Trapping number, 221–222
Two-phase Darcy equation, 279–280
Type I microemulsion phase, 225–226
Type II microemulsion phase, 226

U

U.S. Bureau of Mines method (USBM method), 253–254
Ultralow permeability formation, 2
Ultralow-permeability rocks, 176
Upscaling theories, 279
UTCHEM model, 220–221, 311–312

V

Vaporization, 346
Velocity equation, 280

Visbreaking, 428
Viscosity ratio effects on spontaneous imbibition, 301
Volume fracturing, 4–5
Volume solubilization ratio, 226

W

WAG. *See* Water-alternating-gas (WAG)
Washburn's equation, 280–282
Water
  adsorption by clay minerals, 195
  blockage, 359, 362–364, 367–368, 395–396
  imbibition, 279
  leak-off model, 195–196
  relative permeabilities, 119–120, 120f
  saturation effect, 43–45
  vaporization, 357
Water huff-n-puff injection, 156–162
  in Bakken formation in North Dakota, 160
  different huff and soaking times, 159f
  different injection pressures, 160f
  huff-n-puff CO_2 injection in Parshall Field, 161
  oil recovery from water and gas injection over primary depletion, 162t
  in Parshall Field, 160–161
  performance, 161, 161t
  water huff-n-puff tests, 157f
Water injection, 151, 162–165, 173, 309
  asynchronous, 169
  in China, 167–171
  gas injection, *vs.*, 162–165
  huff-n-puff water and surfactant injection, 166–167
  performance of Chinese projects, 168t
  pulsed, 167–169
  WAG, 166
  water huff-n-puff and nitrogen huff-n-puff, 165f
  water huff-n-puff injection, 156–161
  waterflooding, 151–156
    vs. huff-n-puff water injection, 162
Water-alternating-gas (WAG), 166
Water-cooling effect, 205
Water-oil
  capillary pressure, 217, 220–221
  IFT, 225
  system, 288–289
Water-rock interactions, 173–174, 187–191
  axial displacement measurements, 190f
  deionized water injection, 189f
  permeability changes from, 187–191
  time during fracture permeability test, 188f
  upstream pressure measurements, 188f
Water-wet chip, 385–386
Waterflooding, 151–156, 162, 163f
  Bakken and lower Shaunavon, Saskatchewan, 153–154
  Bakken area in North Dakota, 155f
  in Bakken formation
    in Montana, 154–155
    in North Dakota, 154
  in Bakken viewfield in Saskatchewan, 155–156
  in Pembina Cardium in Alberta, 156
  performance, 156, 157t
  in Vinogradova field in Russia, 156
  water imbibition in matrix and fractured matrix, 153f
Well bottom-hole pressure, 121, 121f
Wettability
  determination of, 253–276
  indices, 255–256, 258
  methods to determining, 262–276
  of shale and tight formations, 277–278
Wettability alteration, 213–214, 309, 311–312, 314–316, 322, 328, 390–391
  of anionic surfactant in carbonate rock, 240f
  capabilities, 247t–248t
  of cationic surfactant in siliceous rock, 240f
  effect in spontaneous imbibition, 290–293
  effect of IFT reduction, 241–242
  IFT reduction *vs.*, 226–236
    effect of, 227–230
    relative importance, 230–231
  mathematical treatments and IFT effect, 220–226

mechanisms on oil recovery, 217–219
capillary pressure curves for different wettabilities, 218f
steady-state oil/water relative permeabilities, 218f
ultimate oil recovery as function of wettability index, 219f
from oil-wet to water-wet by ion-pairs, 238f
surfactant selection for, 242–253
Wettability index of oil (WI_o), 255
Wettability index of water (WI_w), 255
Wetting angle conversion, 276–277
Wetting phase viscosity, 301
Winprop simulator, 72, 77–78
Wolfcamp oil, 65
Wolfcamp siliceous cores, 246–252
Woodford frac job, 198–200
pump schedule in, 199t–200t

Z

Zero-soaking time, 28–29
Zeta potential measurements (ζ-potential measurements), 261–262
Zipper fracture, 462–463

Enhanced Oil Recovery in Shale and Tight Reservoirs

James J. Sheng

Today's unconventional reservoirs are more complex, and engineers are still learning fundamentals on how to adjust current known enhanced oil recovery (EOR) methods and mechanisms to solve and optimize more reservoirs which have immense potential to meet future oil and gas demand. ***Enhanced Oil Recovery in Shale and Tight Reservoirs*** delivers a current state-of-the-art resource in this unknown area for engineers trying to manage unconventional hydrocarbon resources. Going beyond the traditional EOR methods, this product answers key challenges on the proper methods, technology, and options available that can be applied in the production process, followed by the most current field applications. The first of its kind to be offered in one source, ***Enhanced Oil Recovery in Shale and Tight Reservoirs*** provides engineers and researchers with a systematic list of EOR methods and addresses the issues related to EOR in shale and tight reservoirs, including gas huff-n-puff injection, gas and water flooding, air injection, asphaltene deposition, water–rock interactions, surfactant EOR mechanisms, spontaneous and forced imbibition, fracturing fluid flow back, and other EOR methods. It gives engineers and researchers the knowledge needed to tackle the most complex oil and gas assets.

Key Features

- Understand methods and mechanisms for EOR technology specifically for shale and tight oil reservoirs
- Obtain deep analyses through author's research on available EOR methods as well as recent practical case studies
- Learn about practical design solutions for EOR methods and related operation solutions like fracturing fluid flow back and selection of surfactants

About the Author

James J. Sheng is a distinguished SPE member, currently a professor in petroleum engineering at Texas Tech University and an honorary professor at China University of Petroleum specializing in oil recovery research. He worked in the oil industry for 20+ years before entering academia. He has authored two books, both with Elsevier, and over 200 papers, and he earned five patents to date. He earned a PhD and MSc from the University of Alberta, and a BSc from China University of Petroleum, all in petroleum engineering. James received the SPE Regional Technical Awards (Southwestern US region) (2013 and 2015), TTU Whitacre Engineering Excellent Research Award (2015), Most Influential Faculty Member (2015, 2017), the Fulbright Specialist Grant (2013), the Outstanding Technical Editor Award (2005) and the Outstanding Associate Editor Award for SPEREE (2008), and the Best Paper Award in JCPT (1997). He was an associate editor (2005–2009) for SPEREE and Journal of Petroleum Science and Engineering (2008–2011). He is also a member of the SPE "A Peer Apart" group.

Related titles

- *Modern Chemical Enhanced Oil Recovery: Theory and Practice* by Sheng, Oct-2010, ISBN: 978-0-08-096163-7
- *Enhanced Oil Recovery Field Case Studies* by Sheng, May-2013, ISBN: 978-0-12-386546-5
- *Shale Oil and Gas Handbook: Theory, Technologies and Challenges* by Zendehboudi & Bahadori, Nov-2016, ISBN: 978-0-12-802113-2

ELSEVIER

Gulf Professional Publishing
An imprint of Elsevier
elsevier.com/books-and-journals

ISBN 978-0-12-815905-7